LIÈGE université
Sciences Appliquées

Hydro-Mechanical Modelling of Gas Transport Processes in Clay Host Rocks in the Context of a Nuclear Waste Repository

Thesis submitted in partial fulfilment of the requirements for the degree of *Philosophiæ Doctor* (Ph.D) in Applied Sciences

Presented by

Gilles CORMAN

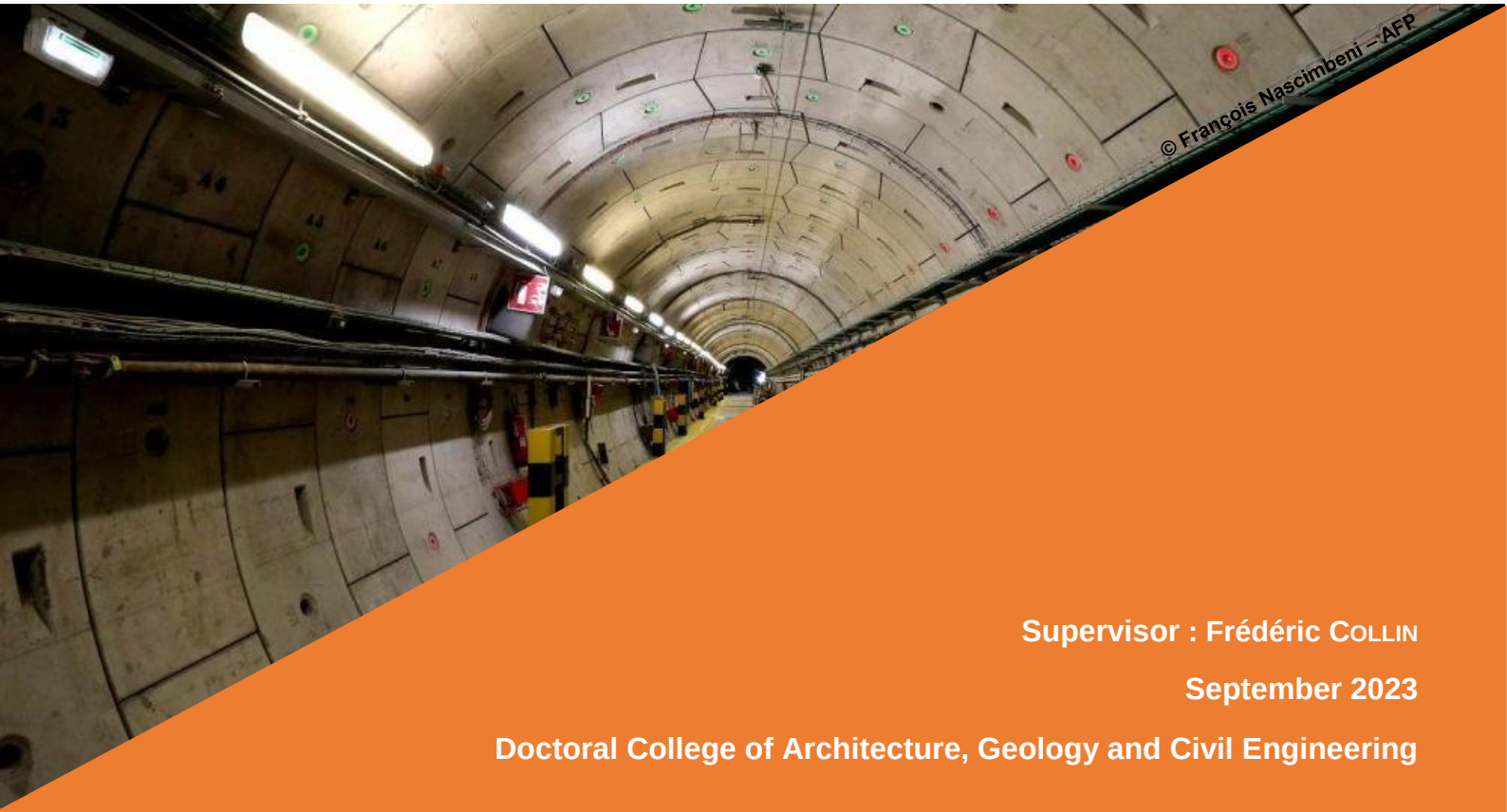

Supervisor : Frédéric COLLIN

September 2023

Doctoral College of Architecture, Geology and Civil Engineering

University of Liège
Faculty of Applied Sciences
Urban & Environmental Engineering

Hydro-Mechanical Modelling of Gas Transport Processes in Clay Host Rocks in the Context of a Nuclear Waste Repository

Thesis submitted in partial fulfilment of the requirements
for the degree of *Philosophiæ Doctor* (Ph.D) in Applied Sciences

Presented by

Gilles CORMAN

October 2023

Generated on October 19, 2023

This research was funded by the
EURAD project:

The European Joint Programme on Radioactive Waste Management which has received funding from the European Union's Horizon 2020 research and innovation programme under grant agreement No 847593.

Jury:

Prof. Frédéric COLLIN	(Supervisor)	University of Liège (Belgium)
Prof. Anne-Catherine DIEUDONNÉ		Delft University of Technology (The Netherlands)
Prof. Cedric GOMMES		University of Liège (Belgium)
Dr. Séverine LEVASSEUR		ONDRAF/NIRAS (Belgium)
Dr. Jean TALANDIER		ANDRA (France)
Prof. Jean-Michel PEREIRA		Ecole des Ponts - ParisTech (France)
Prof. Pierre BÉSUELLE		University of Grenoble (France)

À mes parents et grands-parents,
Merci de m'avoir inspiré depuis mes tous premiers pas.

Remerciements

Octobre 2017, gare de Liège-Guillemins. Pour son premier jour de travail, un jeune ingénieur fraichement diplômé s'apprête à embarquer à destination des Alpes françaises, en vue d'assister à un congrès sur la géomécanique. Le coup de sifflet du contrôleur résonne alors comme le début d'une formidable aventure scientifique et humaine.

Six ans plus tard presque jour pour jour, au moment de mettre un point final à l'écriture de la thèse que vous vous apprêtez à lire, je me remémore, non sans émotion, les différentes étapes de ce périple. En fin de compte, il m'apparait que le chemin parcouru importe tout autant que les résultats obtenus. Cet aboutissement est le fruit d'un travail personnel jalonné de rencontres et interactions humaines l'ayant façonné en retour. Je voudrais profiter de ces quelques lignes pour adresser mes plus sincères remerciements à toutes les personnes qui ont fait de cette expérience l'une des plus belles pages de ma vie.

Tout d'abord, ce travail n'aurait pu aboutir sans Frédéric. Il parait qu'un promoteur se situe quelque part entre un patron, un mentor et un collègue de bureau. J'ai eu la chance que le mien soit un savant mélange des trois. Ses judicieux conseils, ses critiques constructives, ses questions déroutantes jamais moins pertinentes m'ont permis de garder le cap tout au long du projet ; son énergie communicative, sa disponibilité sans faille ainsi que sa grande générosité furent les ingrédients d'une expérience doctorale sereine et épanouie. *Je sais tout ce que cette thèse te doit, tout ce que je te dois. Merci infiniment !*

A travers la thématique l'enfouissement des déchets radioactifs en couches géologiques, j'ai eu l'opportunité d'explorer un sujet stimulant, mêlant enjeux sociétaux et défis techniques. I am particularly grateful to the WorkPackage GAS of the EURAD project, not only for its financial support but also for the enthralling interactions that prevailed among all members throughout the process. A ce titre, j'aimerais créditer tout spécialement Séverine Levasseur de l'ONDRAF ainsi que Jean Talendier, Rémi de la Vaissière et Minh-Ngoc Vu de L'ANDRA, pour avoir partagé avec moi leur expertise pointue sur le sujet lors de nos fructueuses collaborations. *To all of you, thank you so much !*

Tout au long du parcours scientifique, j'ai pu compter sur le support ponctuel mais essentiel de chercheurs chevronnés. Parmi ceux-ci, je ne peux oublier Benjamin Cerfontaine dont la supervision attentive et dévouée de mon mémoire de fin d'études, a su stimuler ma volonté de poursuivre dans le monde de la recherche. Merci également à Anne-Catherine, Cédric, Tristan et Robert d'avoir contribué à nourrir ma réflexion lors de nos réunions du comité de thèse. J'ai une pensée tout particulière pour Robert Charlier, dont j'ai pu apprécier les grandes qualités humaines et professionnelles à de maintes reprises ces dernières années. François Bertrand est aussi de ceux qui ont donné une autre dimension à ce travail. Collègue admirable autant qu'attachant, il a su me mettre dans les meilleures dispositions possibles pour aborder les aspects multi-échelles. Enfin, j'ai à cœur de remercier l'ensemble des membres de mon jury, qui ont accepté de consacrer une partie de leur temps à la lecture et à l'évaluation de ce manuscrit. *Merci à vous d'avoir apporté votre pierre à l'édifice !*

Le doctorat, c'est bien plus qu'un chercheur solitaire, isolé derrière son écran, dans un bureau au fond d'un couloir de l'université ; c'est surtout et avant tout un travail d'équipe. Et quelle équipe ! Cette thèse est le reflet de l'environnement de recherche exceptionnel dans lequel j'ai eu le privilège d'évoluer au quotidien ces six dernières années. Que ce soit par un éclat de rire partagé, un encouragement délivré,

ou un conseil avisé, autour d'une bière, d'un génépi, ou d'une tarte au riz, lors d'une conférence, d'une mise au vert à Aussois ou d'un resto-bowling, chacun de mes collègues passés ou présents a marqué cette expérience de son empreinte. Qu'ils en soient chaleureusement remerciés : Simon, Julien, Albert, Liliana, Kien, Giulio, Sanae, François, Hangbiao, Arthur, Benjamin D., Adriana, Abhishek, Hesam, Bertrand, Sophie, Aoxi, Cyrille, Max. Mentions spéciales à Sanae, d'abord : *Ton accueil amical au -1/537 ainsi que tes conseils bienveillants au cours des deux premières années m'ont mis sur de bons rails pour aborder la suite sereinement,* `Choukran!` Arthur, ensuite : *L'atmosphère de franche camaraderie au bureau a su me remobiliser en fin de parcours, ta prise en main des TPs (et pas que) dans ma (longue) dernière ligne droite fut bénéfique, mille mercis ! Bon courage pour la fin de ta thèse. Je sais déjà qu'elle sera à l'image de la personne que tu es : de qualité.*

Comment ne pas aborder ensuite le vélotaf, pratique qui a assurément changé ma vie. A ce sujet, des chiffres valent mieux que des mots : 272 trajets domicile-travail, 13600 kilomètres parcourus, et environ 1.5 tonne de CO_2 évitée. Merci à tous les vélotafeurs du plateau - Adri, Renaud, Oli, Loris - pour leur joyeuse compagnie. *Et à très vite pour un Ritz !*

Je me dois aussi de mettre en lumière les travailleuses de l'ombre, qui par leurs aptitudes respectives m'ont été d'un précieux support : le personnel administratif du département, et en particulier Stéphanie pour sa disponibilité et son inoxydable bonne humeur ; les agents de nettoyage, et en particulier Christine pour sa gentillesse ; Alexandra Elbakyan dont le site Sci-Hub m'a ouvert l'accès à tous les articles dont j'avais besoin. Ce manuscrit a de surcroit gagné en qualité grâce à la relecture de Floriane, qui a su débusquer les faux dans la langue de Sheakspeare. *A vous toutes, un grand merci !*

Enfin, je ne saurais conclure ces quelques lignes sans penser à celles et ceux dont la présence au quotidien m'est devenue si familière que j'en oublie bien trop souvent de les remercier pour ce qu'ils et elles sont/font.

A mes amis de toujours, de secondaires, de Blegny, et du basket, *merci pour votre amitié indéfectible, ainsi que tous ces fabuleux moments partagés, et tous ceux à venir.*

Antoine, Virginie, *qui aurait pu imaginer qu'autour d'une table d'un café gantois allaient se nouer des liens si forts ? Merci pour cette amitié durable, devenue depuis familiale.*

Elise, *merci d'être une sœur (presque) parfaite, sur qui je peux toujours compter en cas de besoin.*

Adrien, *ta présence à mes côtés depuis le berceau est un cadeau inestimable, qui a illuminé chacune des étapes de ma vie jusqu'ici. Rien n'aurait été pareil sans toi !*

Papy, *ta simplicité, ta générosité et ta résilience sont une source d'inspiration depuis mes premiers pas. La personne que je suis devenue te doit énormément, merci !*

Papa, Maman, *les mots me manquent face à la reconnaissance que je souhaite vous exprimer. A cet instant précis, je mesure toute la chance que j'ai de vous avoir à mes côtés. Merci pour cet amour inconditionnel que vous me (nous) portez depuis toujours et pour toujours.*

Last but not least, Fanny, *tu es de loin ma plus belle découverte ! Mon petit rayon de soleil qui a ce pouvoir de rendre les mauvais jours moins moroses, et les belles journées infiniment plus éclatantes. Merci d'être là. Merci d'être toi, tout simplement.*

Gilles Corman
Septembre 2023

Abstract

To date, the concept of a deep geological disposal is recognised as one of the most viable options for safely and durably storing high and intermediate level radioactive waste away from the biosphere. This mode of repository relies on a multi-barrier confinement system, which comprises a series of engineered and natural layers, aimed at delaying the radionuclide migration on a timescale consistent with the radioactive decay period. Due to their excellent insulation properties, clay materials are being considered in numerous repository designs not just as parts of the artificial barriers but also as a potential host formation, such as the Boom Clay in Belgium and the Callovo-Oxfordian claystone in France. Among the various multi-physics processes that could affect the long-term safety function of the geological barrier, the release of gases induced by the corrosion of the metal components within the system is a crucial issue. Given the impermeable nature of the host rock, an undesirable accumulation of gas in the system could trigger a succession of gas transport processes as a function of the gradual pressure build-up, jeopardising the long-term safety function of the repository.

In this context, the present work is dedicated to the modelling of the complex coupled hydro-mechanical processes governing gas flows in low-permeable clay materials, using the finite element code `LAGAMINE`. The aim is to gain a more comprehensive understanding of which transport regime prevails under which conditions in various zones of the geological barrier.

- The first model is developed to reproduce the gas transport processes in the excavation damaged zone, which are assumed to be controlled by the hydraulic properties modifications caused by fracturing. This requires to simultaneously capture the multi-physics interactions related to gas transfers and the development of fractures. Particular attention is paid to the specific hydro-mechanical couplings between the transfer properties and the damage. The model is applied to simulate field-scale gas injection experiments in the Boom Clay on the one hand, and a large-scale storage gallery set up in the Callovo-Oxfordian claystone on the other hand.
- The second model is developed to reproduce the gas transport processes in the undisturbed rock layers, which are assumed to be controlled by the rock structure at a micro-level. This requires to define a representative element volume that provides a detailed representation of the material microstructure with an explicit description of each constituent on their respective length scales. A comprehensive hydro-mechanical constitutive model can then be formulated at the micro-scale, which can be integrated into a multi-scale framework. This way, it is possible to capture the microstructure-induced phenomena that affect macroscopic gas flows. The model is applied to simulate lab-scale gas injection tests in the Boom Clay, as well as up-scaled configurations.

Through the development of these innovative numerical models, the aim of the research is to enhance the conceptualisation of the gas transport mechanisms in clay materials, to gain insight into the observed transport modes and their primary controls, and to provide a modest contribution to the mechanistic understanding of the hydro-mechanical phenomena associated with gas-induced failure.

Résumé

A l'heure actuelle, l'enfouissement en couches géologiques profondes apparait comme l'une des solutions les plus pérennes pour assurer le confinement à long terme des déchets radioactifs de moyenne et haute activités, à distance de la biosphère. Ce mode de stockage repose sur le concept de confinement multi-barrières, qui offre une série de couches de protection artificielles et naturelles visant à ralentir la migration des radionucléides sur des échelles de temps proches de la période de décroissance radioactive. En raison de leurs excellentes propriétés d'isolement, les matériaux argileux sont envisagés aussi bien pour les composants des barrières artificielles, qu'en tant que formation hôte pour le stockage, comme c'est le cas pour l'argile de Boom en Belgique et pour l'argile du Callovo-Oxfordien en France. Parmi les processus multi-physiques susceptibles d'affecter le bon fonctionnement de la barrière géologique, la production de gaz induite par la corrosion des parties métalliques du système constitue un enjeu de premier plan. Compte tenu de la nature peu perméable de la roche hôte, l'accumulation de gaz dans le système est susceptible d'entrainer l'activation progressive de différents modes de transport suivant la montée en pression.

Dans ce contexte, le travail présenté dans cette thèse est consacré à la modélisation des processus hydromécaniques couplés régissant les écoulements gazeux dans les matériaux argileux peu perméables, à l'aide du code aux éléments finis `LAGAMINE`. L'objectif poursuivi est de comprendre sous quelles conditions ont lieu les différents régimes de transport de gaz, dans différentes zones du stockage.

- Le premier modèle développé vise à reproduire les processus de transport de gaz dans la zone endommagée par l'excavation, qui sont supposés être contrôlés par la modification des propriétés hydrauliques induites par la fracturation. Il nécessite de capturer à la fois les interactions multi-physiques liées aux transferts de gaz, ainsi que l'initiation des fractures. Une attention particulière est portée aux couplages hydromécaniques liant les propriétés de transfert à l'endommagement. Le modèle est finalement mis en application pour reproduire des expériences d'injection de gaz à grande échelle dans l'argile de Boom, et le stockage à plus grande échelle dans une alvéole creusée dans l'argilite du Callovo-Oxfordien.
- Le deuxième modèle développé vise à reproduire les processus de transport de gaz dans les couches de roche saine, supposés être contrôlés par la structure rocheuse au niveau microscopique. Il convient de définir un volume élémentaire représentatif offrant une représentation détaillée de la microstructure du matériau avec une description de chacun des micro-constituants. Un modèle constitutif hydromécanique complet peut ensuite être formulé à cette échelle élémentaire et intégré dans une approche multi-échelle pour reproduire l'impact des phénomènes à petite échelle sur les écoulements gazeux macroscopiques. Le modèle est finalement mis en application pour reproduire des tests d'injection de gaz à l'échelle du laboratoire dans l'argile de Boom et simuler des configurations plus générales à plus grande échelle.

Grâce aux développements numériques proposés, cette recherche vise à améliorer la conceptualisation des mécanismes de transport de gaz dans les matériaux argileux, à mieux comprendre les modes de transport observés et leurs leviers d'activation, et à apporter une modeste contribution à la compréhension mécanistique des phénomènes hydromécaniques liés aux dégradations induites par les transferts de gaz.

Preface

The research outlined in this thesis has been the object of publications in scientific journals (or currently under consideration) and presentations at various conferences and seminars. Below is a detailed list of the main dissemination activities grouped according to the two main parts of the work.

Modelling gas transport in the excavation damaged zone

- **Article**

[Corman et al., 2022] Corman, G., Vu, M.-N., and Collin, F. Numerical investigation of the couplings between strain localisation processes and gas migrations in clay materials. *International Journal of Solids and Structures*. (2022).
doi:10.1016/j.ijsolstr.2022.111974

- **Presentations**

Study of the gas impact on clayrock integrity with a second gradient model. The Biot-Bažant Conference on Engineering Mechanics and Physics of Porous Materials. Evanston (United States). 1-3 June 2021.

A second gradient H²M model to investigate gas migrations in clay materials. 8^{th} International Conference on Clays | Clay Conference. Nancy (France). 13-16 June 2022.

- **Poster**

A second gradient Thermo-Hydro-Mechanical model to investigate gas transfer processes in low-permeable media. 30^{th} ALERT Geomaterials Workshop. Aussois (France). 30 September - 1 October 2019.

Modelling gas transport in sound rocks

- **Article**

(In preparation) Corman, G., Gonzalez-Blanco, L., and Collin, F. Hydro-mechanical modelling of gas transport processes in clay materials using a multi-scale approach. (2024).

- **Presentations**

A multi-scale model to investigate gas migrations in clay materials. 3^{rd} International Workshop on the Finite Element Code `LAGAMINE` | Lagashop. Villard-de-Lans (France). 5-7 July 2022.

A multi-scale model to study gas transport processes in clay materials. 3^{rd} International Symposium on Energy Geotechnics | SEG23. Delft (The Netherlands). 3-5 October 2023.

- **Poster**

A multi-scale model to investigate gas migrations in clay materials. 8^{th} International Conference on Clays | Clay Conference. Nancy (France). 13-16 June 2022.

Contents

"En vérité, le chemin importe peu, la volonté d'arriver suffit à tout."
(In truth, the path does not matter, the will to achieve is enough.)

— Albert Camus (1942)

Part I

Introduction

1. Context of the research

1.1 A story of energy

In modern societies, energy is more essential than ever to support daily life and to drive both social and economic developments. Nowadays, primary energy sources are used to meet human energy needs, such as providing fuel for transportation, heating and cooling residential and industrial buildings or generating power. While for millennia mankind has relied almost entirely on limited amounts of renewable energy, largely biomass, its consumption of primary energy has increased exponentially since the beginning of the industrial revolution by the end of the 18th century, along with the emergence of the thermo-industrial civilisation we know today [Steffen et al., 2015]. As highlighted in Figure I–1a, this period of growth was achieved through the discovery and extensive exploitation of fossil fuels – namely, coal, oil and gas – subsequently supplemented by new sources of renewable energy – namely solar and wind – and nuclear energy.

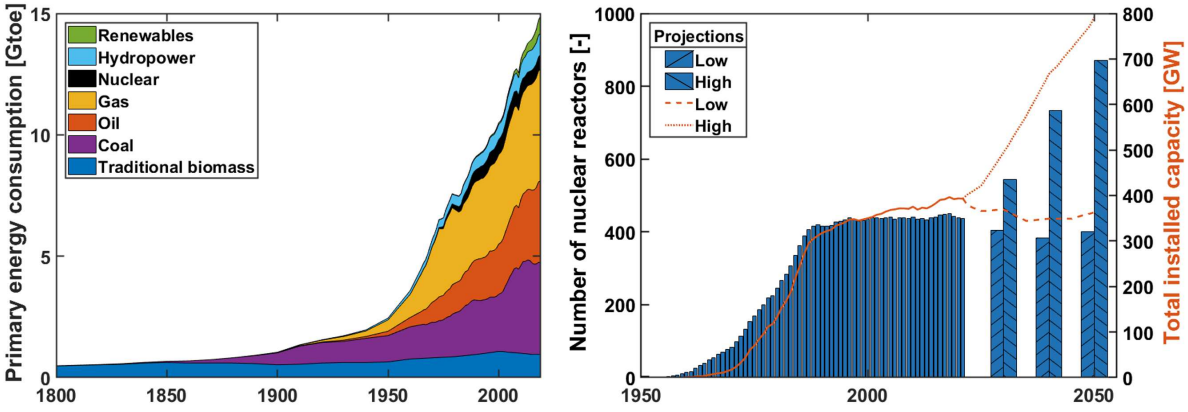

(a) (b)

Figure I–1 – (a) World primary energy consumption by fuel source in Gigatonne of oil equivalent [Gtoe], 1800-2019. *Based on data compiled from BP Statistical Review of World Energy* [BP, 2022] *and* [Smil, 2016]. (b) Historical number of nuclear reactors (bar) and related total installed capacity (line), 1951-2021 with IAEA low and high projections, 2030, 2040, 2050. *Data from* [IAEA, 2021].

Since its introduction in the mid-1950s, nuclear power has become a leading source of energy in many civil applications, including the stable and massive generation of electricity in nuclear power plants [IAEA, 2021]. The nuclear reactors as currently operated use Uranium-235 as fuel and initiate and control a self-sustaining chain reaction, called nuclear fission, to produce energy. In this process, the nucleus of an atom of Uranium bombarded by a neutron splits into several smaller nuclei, and extra neutrons. These neutrons cause in turn fission of surrounding heavy atoms of Uranium, thereby triggering a domino effect. The reaction releases large amounts of energy in the form of heat, which is converted into steam and then into electricity in a turbine [Galindo, 2022].

Following the first successful self-sustaining nuclear reaction performed by Fermi [1] in 1942 [Metzger, 1977], the nuclear power industry experienced an early robust growth during the 1960s, mainly in industrialised countries. Over 15 years, more than 75 nuclear reactors were commissioned in 14 countries around the globe for a nuclear generated capacity of 14.1 GW [Schneider et al., 2021], as reported in Figure I–1b. The oil price shocks further reinforced this trend in the 1970s and early 1980s as nuclear power was promoted as a suitable substitute to fossil fuels [Char and Csik, 1987]. However, since the 1990s, the growth of the nuclear energy sector has stagnated, with several nuclear projects being cancelled. This was largely due to the negative public perception following the major accidents at Three Mile Islands [2] (the US, 1979) and Chernobyl [3] (ex-USSR, 1986), together with the electricity market deregulation, slower growth of electricity demand and economic reforms in Russia and Eastern Europe [Omoto, 2005].

The first quarter of the 21st century is being characterised by a spatial reconfiguration of the world geography of nuclear energy. Developed countries are undergoing a clear slowed-down trend, where the Fukushima Daiichi accident [4] (Japan, 2011) definitely undetermined public confidence in nuclear power [Rogner, 2013]. Germany has adopted an aggressive policy leading to the permanent closure of eight of its reactors, with the remaining nine to be shut down by 2022 [Wiliarty, 2013]. Belgium decided in 2003 to ban the building of new nuclear power plants, and to decommission its entire fleet of seven reactors by 2025. Recent issues related to the security of energy supply in the country have encouraged the Belgian government to extent the lifetime of two reactors beyond 2025 [BelGov, 2003]. With a high nuclear energy share, France plans to gradually scale back nuclear energy, and to rapidly reduce its fraction in the electric mix from 75% to 50% by 2025 [Andrews-Speed, 2022]. With 93 operating reactors and the largest base of installed nuclear capacity, the United States (US) continue to have a prevailing presence in this sector and yet with only one reactor started up in the past 20 years, the US nuclear industry is in decline [Schneider et al., 2021]. Many factors such as low shale gas prices, financing hurdles, difficulties to meet waste management conditions or greater regulatory burdens can explain that the US fleet continues to age, with a mid-2021 average of 40.7 years [Kramer, 2018].

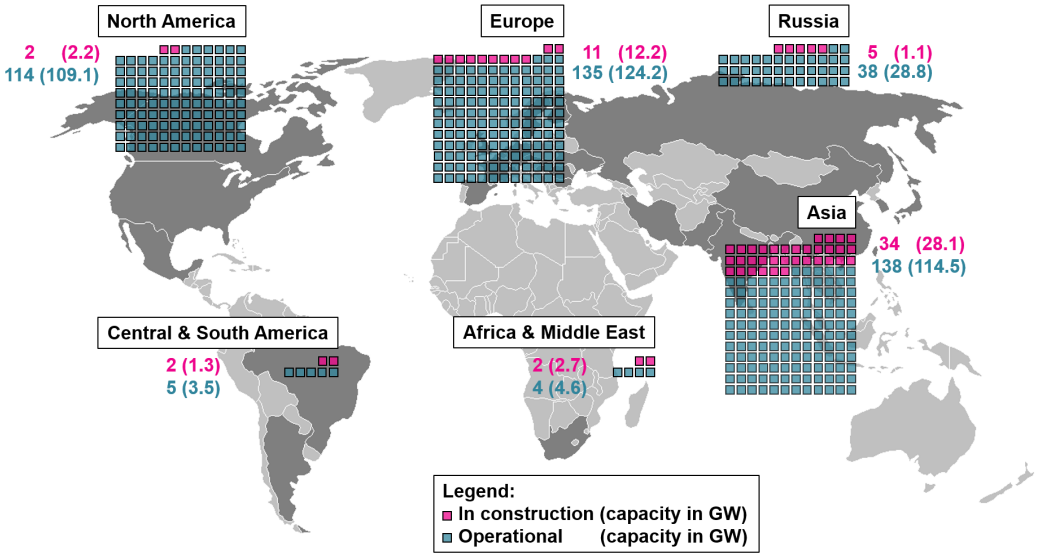

Figure I–2 – Global civil nuclear energy in a nutshell. *Data collected from the International Atomic Energy Agency* [IAEA, 2021]. *Modified from* [Kernenergie, 2022].

1. Chicago Pile-1 was the first experimental reactor designed by Fermi's team at the University of Chicago. The use of nuclear energy for civil purposes dates back to 1954, with the commissioning of the first nuclear reactor in the Soviet Union.
2. Accident of level 5 on the International Nuclear and radiological Event Scale (INES), which groups nuclear events in seven classes based on their severity [IAEA, 2008].
3. First accident of level 7 on the INES rating scale.
4. Second most severe nuclear event of level 7 on the INES rating scale, occurring after the earthquake on March 11, 2011, and subsequent tsunami, that inundated the nuclear power facilities.

Conversely, developing countries and emerging economies with growing energy requirements hold a different view on nuclear power [Rogner, 2013]. The Indian authorities are strongly supporting the development of nuclear power facilities and forecast the percentage of domestic nuclear power generation to reach 25% by 2050, with a view to coping with environmental degradation and reducing energy import dependency [Frankenbach et al., 2021]. Nuclear power has expanded rapidly in China over the last decade following the regime's goal of vigorously promoting this sector. Nowadays, China operates by far the youngest nuclear fleet with 40 units connected to the grid within the past ten years and 16 units under construction [IAEA, 2021], and the industry continues to thrive as domestic nuclear power technology improves and local market demand rises [Hou et al., 2011].

As of today [5], a total of 437 nuclear reactors are operating in 32 countries around the world (including Taiwan [6], Figure I–2), and 56 additional units are reportedly under construction, mainly in Asian countries. The current world fleet has a total nominal electric net capacity of about 393 GW. During the last four decades, nuclear energy consumption has increased by more than 40% worldwide, generating 9.8% of the global electricity and accounted for 4.25% of global primary energy demands in 2021. In the European Union (EU), 103 nuclear power reactors were operating in 13 of the 27 member states in 2021, supplying about one-quarter of the electric demand throughout Europe. More specifically, in Belgium and in France, 7 and 56 nuclear power plants are currently running, bringing the nuclear share of total electricity generation to 52% and 69%, respectively (2021).

The prediction of global energy consumption over the rest of this century remains a complex issue. Based on a compilation of hundreds of recent scenarios [IAEA, 2020a] [7], the future estimates of energy demand by 2050 ranges from 220 to 900 exajoules (EJ), compared with around 418 EJ in 2019 [IEA, 2021] [8]. However, all projections point to an overall increase of 20% to 330% in the current electricity demand by 2050, due to global population growth and increased economic activities, efforts to achieve sustainable development goals [UN, 2015], and above all the necessity of ambitious strategies to mitigate climate change. It is now scientifically recognised that most of human activities in the world emit carbon dioxide (CO_2) by burning fossil fuels, which leads to increasing atmospheric concentrations of greenhouse gases [9] (GHGs), along with a rise in temperature, and ultimately modifies the global and regional climatic attributes [IPCC, 2021]. To prevent the disasters to which both people and nature would be exposed in the event of uncontrolled global warming, the international community has reached an agreement to regulate GHG emissions and to limit the temperature increase to 1.5°C above pre-industrial levels [10] by the end of the century [IPCC, 2022].

To achieve these goals, global energy production and use, just like other sectors need to be fully decarbonised by around 2050, while it currently accounts for around 70% of total emissions in recent years. Within this segment, 22% of global emissions is attributable to electricity generation [IAEA, 2020a] [11], which faces the immense challenge of shifting almost entirely to low-carbon energy sources in the next decades. It must be kept in mind that in these ambitious mitigation scenarios, electrification plays an even more predominant role to support decarbonisation of other energy-based sectors like transport and industry. This trend towards an intense electrification of world's energy requirements brings into focus the key role of power generation in a gradual transition to clean energy. With average emissions of about 12 gCO_2eq/kWh electricity produced over the course of its life-cycle [IPCC, 2014] [12], nuclear energy emerges as a promising alternative for electric production, being the second-largest source of low-carbon

5. Last update of energy data provided by BP until December 31, 2021 [BP, 2022].

6. The political status of Taiwan is contentious.

7. Synthesis of over 400 recent scenarios of energy demand from international, governmental, non-governmental, private sector and academic organisations presented in [IAEA, 2020a].

8. The high scattering is related to the different assumptions and approaches, together with the high level of uncertainty underlying the key driving factors related to the demographic, technological, climatic, economic, and geopolitical aspects.

9. Emissions from energy also comprise methane from fuel extraction and nitrous oxide formed during combustion.

10. 1850-1900 period.

11. synthesis of 7 sources compiling global greenhouse gas emissions by sectors

12. compared for instance to 820 gCO_2eq/kWh for coal, 490 gCO_2eq/kWh for gas, 48 gCO_2eq/kWh for solar, 24 gCO_2eq/kWh for hydropower and around 10 gCO_2eq/kWh for wind.

power generation in use after hydro-power. Although literature reviews [Siqueira et al., 2019, Li et al., 2022] report a certain cleavage about the suitability of nuclear power to contribute to the phase-out of fossil fuels [Schaffer, 2007, Adamantiades and Kessides, 2009, Kampan and Tanielian, 2016, Roth and Jaramillo, 2017] or not [ORG, 2007, Verbruggen, 2008, Dellano-Paz et al., 2015, Prăvălie and Bandoc, 2018], most scenarios addressing the imperative transition of the energy sector expect a substantial increase in global nuclear power capacity [IEA, 2019, IAEA, 2021, IPCC, 2022] as presented in Figure I–1b, combined with renewables, a higher energy efficiency and some unavoidable levels of sufficiency.

As a well-established electricity generation process, nuclear power benefits from several driving factors that make it a suitable option to meet the requirements of a sustainable global future. Climatically, nuclear power is labelled as a low-carbon system that releases little amount of CO_2 emissions in the atmosphere [Mathew, 2022], even after accounting for the whole life cycle from ore mining to spent fuel waste management. With massive investments to boost the installed capacity by 2050, nuclear power could therefore provide some of the highest contribution to CO_2 reductions [Prăvălie and Bandoc, 2018]. Environmentally, nuclear power is also promoted as a technology with fewer emissions of air pollutants such as sulfur and nitrogen oxides than fossil fuel plants, thus avoiding ecosystems degradations and health troubles on local and regional scales [Van Der Zwaan, 2008]. Economically and strategically, nuclear power remains an important component of energy security and socio-economic development in nuclear states. Nuclear facilities are more immune to fuel cost volatility relative to gas-fired stations, and help reduce the dependence on energy imports with all the risks of disrupted power supplies, and vulnerabilities it entails, especially in emerging countries with increasing energy needs [Adamantiades and Kessides, 2009]. Energetically, nuclear power is considered as a reliable and affordable source of energy operating at nearly constant capacity throughout its useful life. This way, it can meet fluctuations in energy demand and provide stability to electrical grids, particularly those with high fractions of intermittent renewable sources such as solar and wind power [Mathew, 2022].

However, even though it has been proven that nuclear energy can benefit human societies in many ways, it remains perhaps one of the most controversial way to generate electricity. The main concern being the non-negligible risk of radioactive contamination with global-scale repercussions in the event of radionuclides leak from nuclear installations. Focussing solely on nuclear energy for commercial purposes [13], the past three decades have seen two major nuclear disasters that still colour public opinion on this form of energy today. Although unlikely, the occurrence of a major accident at any of the currently operated reactor would affect extensive areas, expose dozens of millions of people to radioactive contamination and cause considerable environmental and socio-economic damages regionally and even globally [Lelieveld et al., 2012]. Over the years, it can be argued that safety science has benefited from the accumulated operating experience, resulting in the addition of several built-in physical barriers and provisions deemed necessary, ensuring safer installations [Högberg, 2013]. Even though the risk of accidents tends to diminish, the problematic management of nuclear waste is another critical issue the sector is facing. High-level radioactive waste is the most hazardous, as it persists in the environment for up to one hundred thousand years, which makes safe and permanent storage very challenging [Horvath and Rachlew, 2016].

As of today, burying such waste in deep geological repository is the approach most favoured by the technical experts in the field [IAEA, 2003]. And yet, despite the amounts of waste produced by nuclear energy over more than half a century, such underground facilities have not yet been completed anywhere around the globe. To guarantee the feasibility of such a solution, it is of paramount importance to fully understand the geological barrier response to the loading imposed by the nuclear waste storage throughout the system lifespan. Since the overall barrier performance is a highly complex problem to tackle, involving multiple coupled Thermo-Hydro-Mechanical (THM) perturbations, numerical modelling constitutes an effective technique to perform predictions at the time-scale of the storage [Gens et al., 1998]. In particular, it is now of great interest to improve the understanding of the migration of gas from the ge-

13. Some risks are also associated with the proliferation of nuclear weapons worldwide.

ological disposal facilities into the rock formation, as it may open preferential flow paths and ultimately affect the safety function of the geological barrier in the long term [Rodwell et al., 1999]. This study aims to contribute to research in this perspective. First, few concepts related to nuclear waste management, geological disposal solution and gas-related issues are presented in this introductory part of the thesis to understand the issues addressed in this work.

1.2 Management of nuclear wastes

Energy consumption - whether of fossil, renewable or fissile source - inevitably alters the biosphere through its production process, the required facilities or the wastes it generates. Nuclear energy - like any source of power - produces wastes but in markedly smaller quantities compared with the pollutions released by fossil fuel plants, for instance. Generating 1 GW of electricity for one year with atomic plants releases on average 25-30 tons of spent nuclear fuel and a few hundred cubic meters of other wastes [IAEA, 2009b].

Yet, nuclear waste is not a singular category of pollution since it contains radionuclides *i.e.* large unstable atoms that tend to achieve stability by releasing atomic energy in the form of radioactivity, that is, emissions of $\alpha-$ and $\beta-$particles, $\gamma-$rays and neutrons. Upon exposure, this type of invisible ionising radiation can damage biological life forms. Through the process of radioactive decay illustrated in Figure I–3a, a radionuclide looses its radioactivity in an exponential way over time, and is thence characterised at any time by the activity of its hazardous content and the half-life period of its radioactive isotopes, *i.e.* the time required for one-half of the atoms to become stable. This period ranges from few fractions of seconds to millions of years according to the type of material [GSL, 2020].

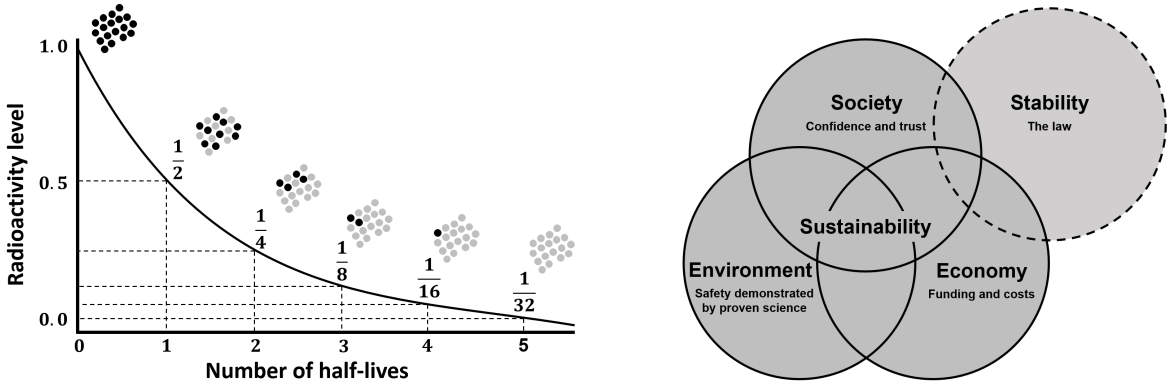

(a) (b)

Figure I–3 – (a) Schematic representation of the radioactive decay concept, *modified after* [GSL, 2020]. (b) Venn diagram of the 4-circles concept for the sustainable development of radioactive waste management strategies, *modified after* [Sanders and Sanders, 2016].

In fact, radioactive waste includes any non-recoverable materials, that are either intrinsically radioactive or that have been contaminated through exposure to radioactive sources. These by-products are generated in all forms of nuclear science and technology processes in the world: from the power industry, to medical, industrial and defence sectors, and research activities [IAEA, 2018b]. Hospitals and pharmaceutical labs use a large range of radionuclides in different medical processes for diagnosis, therapeutic and treatment purposes, producing non-negligible amounts of nuclear waste [WHO, 1999]. Numerous non-nuclear industries deal with radioactive materials as part of their daily operations and generate nuclear wastes in the form of contaminated equipments and liquids or as technologically enhanced naturally occurring radioactive materials (TENORM). These latter refer to radioactive elements which have always been in the earth's crust and have been concentrated and exposed by human activities

like mining, or smelting processes, undertaken by various extractive industries [Doyi et al., 2015]. Also, a certain number of nuclear research institutes and academia around the world resort to multiple types of radioactive sources to conduct R&D experiments, out of which post-irradiation contaminated devices are declared as radioactive wastes [IAEA, 2001]. However, most of the radioactive waste produced around the globe stems from the use of nuclear fission to generate electricity. This production of radwaste occurs at highly variable levels of quantity and activity throughout the nuclear cycle, from the initial refining of uranium ore to the final decommissioning of nuclear power plants [Darda et al., 2021].

The front end of the cycle starts with the extraction of uranium ore in open-pit and underground mines, followed by the refinement of the extracted substances into a so-called yellow cake (mostly U_3O_8), *i.e.* a concentrated uranium oxide that is packaged in drums, further enriched and converted into uranium dioxide (UO_2) pellets in order to be used as fuel in nuclear reactors. This upstream process creates both solid and liquid tailings, that contain long-lived radionuclides [IAEA, 2002]. The back end of the cycle corresponds to the uranium fuel discharged from the reactors after use. The spent fuel as a whole contains emitting fission products that are temporarily stored on-site at the reactor facilities in order to be cooled before going into reprocessing or long-term disposal. The reprocessing of spent fuel consists in separating the recoverable fissile elements from the waste by chemicophysical reactions to produce recycled fuels such as uranium and plutonium-based mixture (MOX), reusable in certain reactors [Supko, 2016]. Fuel recycling avoids misspending resource and reduces the volume and radiotoxicity of waste. Finally, the decommissioning process where nuclear power plants or other nuclear fuel cycle facilities are dismantled to the point that it no longer requires measures for radiation protection is another vector of radioactive waste production [IAEA, 2018a], which encompasses steel and concrete components, soil, or reactor pressure vessel that have been exposed to long-term irradiation [Zohuri, 2020].

Unlike natural background radiation that people interact with on a daily basis without safety concern in most areas around the globe, radioactive waste from the aforementioned human activities poses a severe risk to the biosphere on a timescale much longer than the human lifetime. It is therefore imperative to properly design the nuclear waste management strategies to ensure a secure, efficient and permanent disposal of such material, bearing in mind that the burden of managing radwaste should rest on the shoulders of present-day producers and consumers of nuclear energy, and not on those of future generations [Decamps and Dujacquier, 1997]. A challenging task, that has been pragmatically quoted by the Swedish National Council for Nuclear Waste [KASAM, 1998]:

> *We have a responsibility to search for the optimum solution on the basis of the knowledge that we have today. Since our knowledge of the long-term evolution of the repository is imperfect, our assessment of the consequences of our solution will be uncertain. For this reason, we must choose a solution that is sufficiently open to allow future generations freedom of choice. However, there are inevitably crucial cutoff points in time, in terms of both preserving freedom of choice and taking responsibility for the consequences of our actions.*

To meet such arduous challenges, the evaluation of the ingredients needed for the implementation of long-term strategies is currently based on the popular three-pillar conception of sustainability [Meadows et al., 1972, Giddings et al., 2002]. Specifically applied to the sustainable development of a nuclear waste management program [Sanders and Sanders, 2016], this tripartite description is translated into an economic circle which encompasses the funding aspect to build a storage site, an environmental circle which requires science and technology to demonstrate that waste can be stored with minimal impact on all stakeholders at large, and a societal circle ensuring that all decisions are taken in an ethical manner that reflects the will of the society, with sustainability being at the intersection, as shown in Figure I–3b. However, beside the technical challenges raised by the long-term management of radioactive substances, an additional stabilising structure is required to ensure the sustainability of the actions undertaken. This aspect is often reflected by a fourth circle representing the law, which must guarantee that all actions are performed in accordance with the rule of law applied within the society [Sanders and Sanders, 2016]. As a consequence, most nuclear countries have progressively set up regulatory bodies and enacted laws, providing the legal framework for radioactive waste management policies. National agencies have been

created to coordinate, supervise and centralise all activities related to radwaste management to a degree that varies from country to country [Decamps and Dujacquier, 1997]. ONDRAF/NIRAS in Belgium and ANDRA in France are both examples of institutions responsible for finding, implementing and guaranteeing safe management solutions for all the waste produced in their respective country. Among their missions is the drawing up of a national inventory showing the conditions and location of all radwaste stored on the territory.

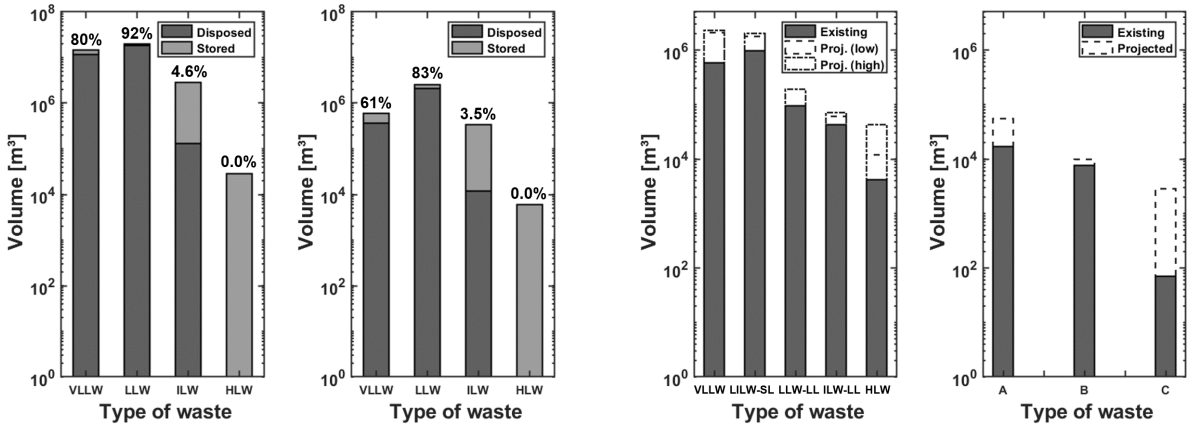

(a) Global scale (b) EU scale (c) France (d) Belgium

Figure I–4 – Reported radioactive waste in storage and in disposal (with percentage), as at the end of 2016 at (a) the global scale and (b) in the EU. *Data from* [IAEA, 2018b, EC, 2019]. Radioactive waste inventory as at the end of 2020 in (c) France and (d) Belgium, with future estimates based on specific scenarios, *from* [ONDRAF, 2018, EC, 2019, ANDRA, 2020, ONDRAF, 2021].

The classification of radioactive waste varies according to the country and the type of waste generated. Six main categories are proposed in the IAEA reference system [IAEA, 2009a], based on the amount of radioactivity contained:

- **Exempt waste (EW)** contains radionuclides at a level close to natural background radiation that can be cleared from regulatory control without provisions for radiation protection.
- **Very short lived waste (VSLW)** contains only very short half-life radionuclides, which can be stored on site facility for a waiting period before being disposed of as conventional waste.
- **Very low level waste (VLLW)** consists of material whose level of radioactivity is considered non-harmful to the biosphere, and does not require a high level of containment and isolation.
- **Low level waste (LLW)** covers a broad range of materials from trace amounts of short-lived radionuclides at higher levels of radioactivity to long-lived radionuclides at relatively low levels of radioactivity, and requires robust isolation and containment for several hundred years.
- **Intermediate level waste (ILW)** consists of materials with relatively long-lived radionuclides which require a greater degree of isolation and containment for periods beyond several hundred years, but no (or only limited) provision for heat dissipation during storage.
- **High level waste (HLW)** contains the most hazardous materials available, with large amounts of long-lived radionuclides, and levels of activity which are high enough to generate significant quantities of heat, thus requiring immediate cooling and shielding for the storage extending over tens of thousands of years.

The profiles shown in Figures I–4a and I–4b represent the estimated total inventory of radioactive waste that is either in storage or disposed of by the end of 2016, at the global and EU scale respectively [IAEA, 2018b, EC, 2019]. The overall worldwide volume of waste generated in the past 60 years of

nuclear activity is about 38 million cubic meters, of which 30 million cubic meters (81%) have already been disposed of, while a further 7.2 million cubic meters (19%) are in storage awaiting final disposal. Zooming in on EU territory, the total volume for the same period amounts to 3.5 million cubic meters, of which a large part (72%) is already disposed of and the rest (28%) is in storage and will have to be managed in the future. With a specific focus on the French and Belgian contexts addressed in this work, the national agencies have established their own radioactive waste categorisation schemes, based on the activity level (risk) and half-life period (duration) of the radionuclides contained in the materials at the time of conditioning, with a conversion to the IAEA standard classification system [IAEA, 2009a] proposed in Table I–1, and the total amount of waste of each class at the end of 2020 given in Figures I–4c and I–4d respectively. Long-term estimates of the volumes of waste to be managed by the end of the activities relating to the decommissioning of all existing nuclear facilities are also presented, assuming that the nuclear phase-out is completed by 2025 in Belgium [ONDRAF, 2021] and that different scenarios of nuclear power renewal or substitution are implemented in France [ANDRA, 2020]. In both cases, a large part of this waste already exists or will inevitably be produced. One specificity related to nuclear waste management is that HLW accounts for a small percentage of the total volume, but represents more than 95% of the total radioactivity of the waste produced, whereas LLW comprises some 90% of the volume but only about 1% of the radioactivity of all radioactive waste [IAEA, 2018b]. Specific repository facilities must thus be envisaged with a growing degree and duration of isolation related to the increasing waste harmfulness [Van Dorp et al., 1989, ICRP, 1985].

Half-life / Activity	Very short-lived	Short-lived	Long-lived
Very low	VLLW (LLW)		
Low	VSLW (-)		LLW-LL (ILW)
Intermediate		LILW-SL (LLW)	ILW-LL (ILW)
High	Not applicable		HLW (HLW)

(a) France

Half-life / Activity	Short	Long
Low	A (LLW)	B (ILW)
Intermediate	A (LLW)	B (ILW)
High	C (HLW)	C (HLW)

(b) Belgium

Table I–1 – Radioactive waste classification in (a) France [ANDRA, 2020] and (b) Belgium [ONDRAF, 2021], and its equivalence with IAEA classification in brackets [IAEA, 2009a].

After treatment operations to reduce waste volume, and conditioning to prepare for transportation [Garamszeghy, 2011, IAEA, 2020b], VLLW and LLW containers are generally stored in near-surface disposal facilities [Han et al., 1997], implemented either in caverns at depths of tens of meters or at ground level in constructed vaults which are backfilled when full and covered with a protective layer of top-soils. With this approach adopted in France for the LILW-SL and VLLW and in Belgium for the A-type waste, the sites are maintained at least for a few decades. As for ILW and HLW, a common repository strategy could be considered because the risk that they present extends over similar timescales, from several tens to hundreds of millennia. In the past, many disposal options have been imagined [McKinley et al., 2007], from long-term above ground storage to disposal in outer space, at sea, in sub-sea bed, in subduction zones, in ice sheets, by deep rock melting, or deep well injection. Most of them were rejected for safety concerns or prohibited by international agreements, until a worldwide scientific consensus dating back to the late 20th century [Witherspoon, 1991, IAEA, 1993, Savage, 1996, NEA, 1999, EC, 2000] recognised the deep geological disposal as the most promising solution for the long-lasting storage of nuclear wastes [Bredehoeft et al., 1978, Chapman and McKinley, 1987]. The topic of the present work focuses on the higher activity wastes that might be destined for geological disposal.

1.3 Deep geological disposal

While for centuries, the commonly accepted practise for disposing of environmentally unfriendly solid material that could not be burned was to bury them hasty at shallow depth [Miller et al., 1994], the concept of geological disposal has been taken to a greater degree of sophistication by the nuclear sector, reflecting the extremely demanding performance requirements to achieve. Within this framework, it specifically refers to the repository of radioactive waste in a geological disposal facility (GDF) located underground in a stable geological formation, without intention to retrieve the waste, although such a possibility is not ruled out [IAEA, 2011b]. In particular, the GDF must be designed with the specific objectives of [IAEA, 2011a]:

(i) Confining the waste;

(ii) Preventing, reducing and delaying the migration of radionuclides at any time;

(iii) Isolating the waste from the accessible biosphere for extended periods of time.

These prescriptions must ensure that any residual radionuclide release reaching the surface remain at concentrations that are below some prescribed limits or insignificant compared with the natural background levels of radioactivity. And at the same time, the system must provide a reasonable assurance that any risk from inadvertent human intrusion would be very small.

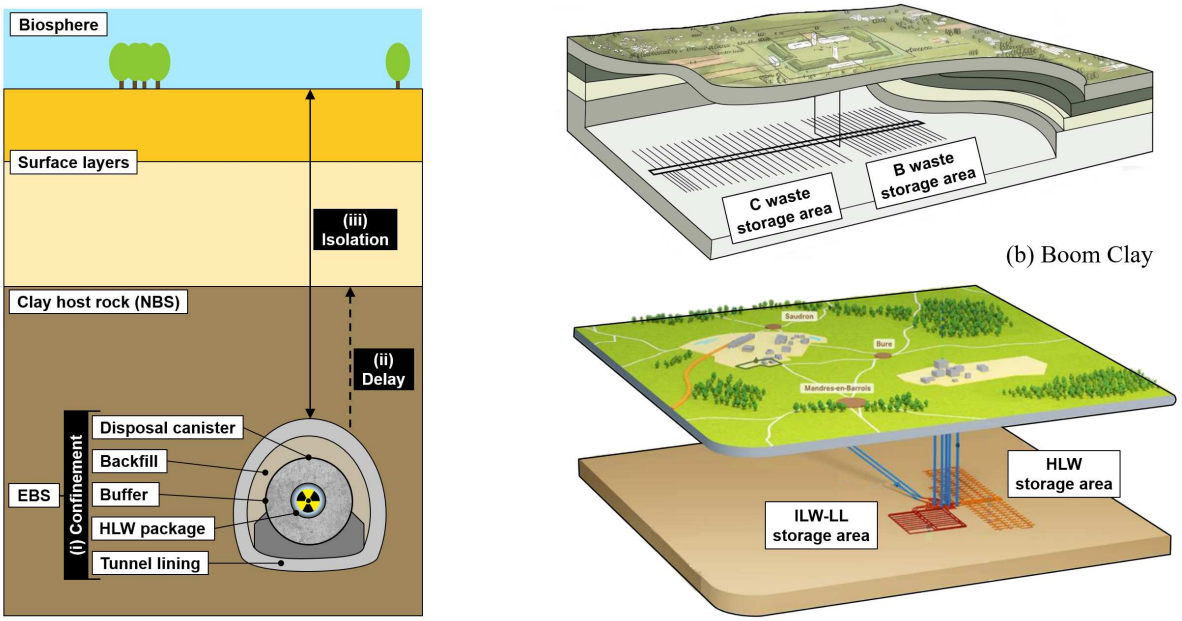

(a)

(b) Boom Clay

(c) COx claystone

Figure I–5 – Conceptual schemes of a deep geological repository, (a) illustrating the concept of multi-barrier system, and according to (b) the Belgian concept in Boom Clay [ONDRAF, 2020] and (c) the French concept in the COx claystone [Andra, 2023].

Of the dozens of countries with significant nuclear power activities to date, only a few of them [14] have approved the geological disposal of all or part of their radioactive waste in facilities constructed at an appropriate depth in stable geological formations in the next decades. Depending on the country, different concepts of disposal in specific geological environments have been considered as shown in Figures I–5b and I–5c [Hicks et al., 2008]. Yet in all cases the conceptual basis of geological disposal has been based upon the passive multi-barrier system, illustrated in Figure I–5a. It typically comprises the natural (geological) barrier system (NBS) and an engineered barrier system (EBS), acting together to isolate the

14. Canada, Finland, France, Sweden, and Switzerland.

waste and contain its associated radionuclides [Ewing et al., 2016, Ojovan and Steinmetz, 2022].

The EBS corresponds to the underground structures and includes the different manufactured components. Typically, the high-level waste is vitrified, forming a first chemically inert barrier, before being put in canisters made of steel or copper, in order to build a second physical barrier. These substances are in turn possibly encapsulated in standard concrete containers before being emplaced and sealed in horizontal storage drifts or in vertical boreholes using backfill materials. This generic EBS design differs according to the repository concept adopted in each country. For instance, in the current version of the French Cigéo project [Labalette et al., 2011], the space between the canisters and the host rock is filled by claystone-based backfill materials, while bentonite-based backfill materials are used in access galleries and shafts. In the supercontainer concept as envisaged in Belgium, the canister is enveloped in a cement-based material, over-packed by a thin carbon steel layer [Van Humbeeck et al., 2008].

The NBS corresponds to the surrounding geological medium in which the entire repository is located. This host rock formation is selected according to key factors including long-term stability, good confining conditions in terms of permeability and geochemical interactions, and high geomechanical properties, in order to provide the most predictable environment possible. Depending on these geological characteristics of the underground varying from one region to another, the preferred host materials fall into the broad categories of crystalline [Bäckblom, 1991], clay-based [Félix et al., 1996, Neerdael and Boyazis, 1997], or salt [Langer, 1999, Behlau and Mingerzahn, 2001] rocks. Among these geological formations, this work focuses more specifically on the Callovo-Oxfordian claystone which is envisaged in France, and the Boom Clay which is currently under investigation in Belgium.

Although the NBS constitutes the main and most reliable component, the overall safety of a GDF is achieved through a sensible balance of its different constituents [Chapman and Hooper, 2012]. The EBS ensures the confinement of the radioactive substances and is usually designed to resist for thousands of years. After this period, such artificial components will inevitably degrade and the NBS will then play its role by delaying and slowing down the radionuclide migration on a time-scale consistent with the radioactive decay period. This series of barriers should provide a safe isolation of the radioactive waste from all living organisms and their environments. Nevertheless, to ensure that the described safety functions are maintained, an in-depth understanding of the processes affecting the long-term behaviour of the barriers is needed.

1.4 Gas-related issues in a context of coupled processes

During the lifetime of a nuclear waste isolation project, various coupled thermal-hydraulic-mechanical-chemical (THMC) processes arise in the geological host formation under the joint influence of thermal gradients, liquid and gas pressure changes, rock mechanical stresses and geochemical reactions [Birkholzer et al., 2019]. It implies that the response of the rock mass cannot be predicted with confidence by considering each process individually or in direct succession, but by considering that each process is potentially affected by the initiation and progress of the other processes [Tsang, 1987]. Such coupled phenomena have received a particular attention in the field of rock mechanics and engineering over the past decades [Kohl et al., 1995, Stephansson et al., 1996, Neaupane et al., 1999, Tsang et al., 2000, Hudson et al., 2001], involving numerical models as a complement to experimental studies. Sustained efforts have been made to model these process interactions occurring in different stages of the lifespan of a GDF, as is the case at the University of Liège with the finite element code `LAGAMINE`.

Initially, the excavation of the storage galleries causes unavoidable stress redistribution that triggers damage and cracks propagation in the close vicinity of the excavated cells, leading to the creation of a so-called excavation damaged zone (EDZ) [Tsang et al., 2005, EC, 2005a], with significant changes in the hydro-mechanical properties [Armand et al., 2014]. Then, the air ventilation required during the op-

eration phase initiates water drainage and desaturation of the host rock which may induce extra cracking [EC, 2005b]. Numerical modelling of such binary HM interactions has been performed for instance by [Pardoen, 2015] and [Salehnia, 2015]. The nuclear waste packages are subsequently placed in their cells and sealed with swelling clay (bentonite) and concrete during the proper post-closure repository phase. In the short term, hydraulic resaturation in the near-field of the storage drift is the dominant process at work, which has been numerically tackled by [Dieudonné, 2016] and [Gramegna, 2021]. In the medium term, the heat release from the high-level radioactive waste will induce thermal effects on the damaged zone, a TM coupled process investigated by [Dizier, 2011], and expose the host rock to desiccation effects and potential cracking under shrinkage, as studied by [Hubert, 2018]. In the long term, other coupled processes can potentially affect migration of radionuclides, such as geo-chemical processes or gas production from the degradation of repository engineering materials, as explored by [Gerard, 2011]. The work presented here aims to address these latter gas-related issues from a numerical perspective.

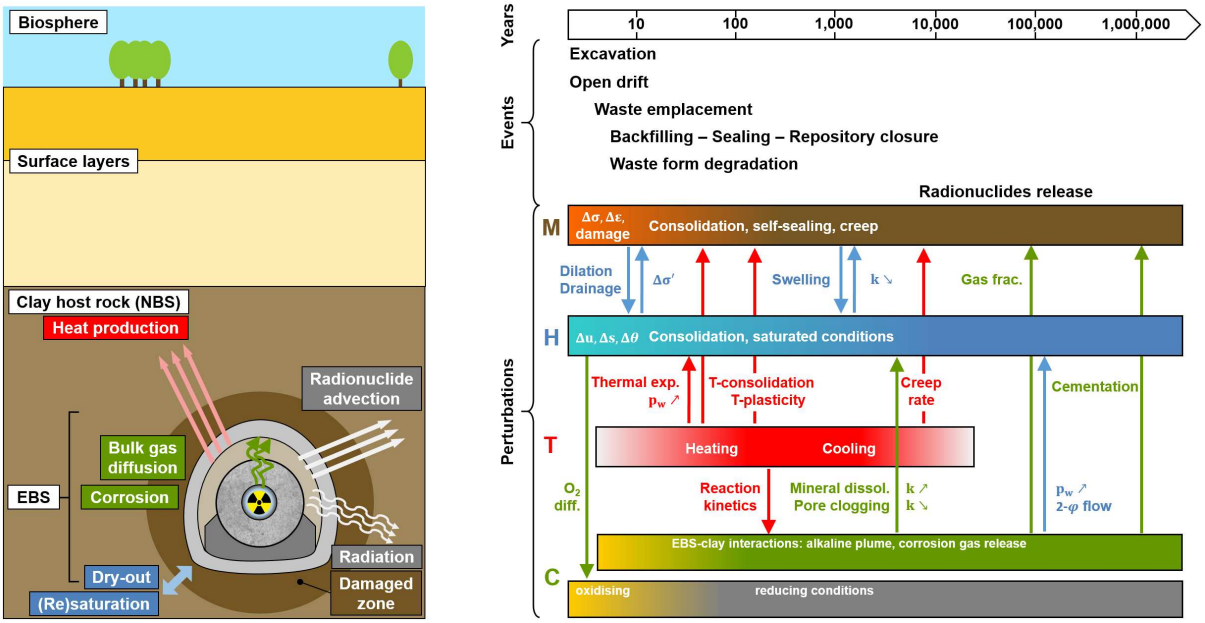

(a) (b)

Figure I–6 – Conceptual scheme of a deep geological repository with (a) the major THMC processes affecting the system and (b) the related coupled effects occurring over its lifetime, *after* [Sillen, 2012].

Gas generation from radioactive waste under final repository conditions is unavoidable and stems from the nature of certain essential components of the storage system. Since the amounts and types of gases have been recognised as potential safety concerns for the long-term integrity of a repository, major efforts have been made to characterise the gas generating modes and their generation potential [Rodwell et al., 1999]. A number of mechanisms have been identified, as potentially contributing to the total gas generation rate and cumulative gas generation to varying degree, depending on the geo-physico-chemical conditions at the specific site, the disposal concept, and the waste characteristics.

The anaerobic corrosion of all the reactive metallic constituents of the waste products, their packages and the components used in the EBS will lead to the formation of Hydrogen in the absence of oxygen and in the presence of water [Rodwell et al., 2003]. In nearly all disposal concepts, this mechanism is expected to have the strongest impact on total gas generation. The decomposition of water and certain organic matter in the packages by all kinds of radiation is another gas generation mechanism termed radiolysis yielding small additional amounts of Hydrogen [Voinis et al., 1997]. Gas generation from microbial degradation is another well-known phenomenon confined to organic material-containing waste of LLW or ILW type, which gives carbon dioxide and methane as the chief products [Francis et al., 1997].

Even though the gas production processes are generally slow, it is important to verify that these will not be detrimental to the good functioning of the disposal system. Indeed, the low permeability of clays, from which the containment function of a repository benefits, also limits the evacuation of the generated gases. Four basic transport mechanisms for gas migration in low-permeable porous media have been identified, including the advection and diffusion of dissolved gas, the visco-capillary two-phase flow, the dilatancy-controlled flow, and the macro-fracture flow [Marschall et al., 2005]. Under these circumstances, the generally accepted assumption [15] in most DGF concepts is that the original transport of dissolved gas in the liquid phase by advection and diffusion will not be sufficiently rapid to prevent the local pore water from becoming saturated with dissolved gas and the appearance of a discrete gas phase. If this gas phase cannot disperse through the engineered barriers and into the host rock as fast as it is generated, gas could continue to accumulate, causing the pressure in the repository to build up. At a certain level of pressure, the accumulated gas could then escape from the repository by creating discrete gas-specific pathways through the EBS and/or the host rock, as illustrated in Figure I–6a. In the event that the over-pressurisation reaches the gas fracturing threshold, the resulting damage might open up pathways through which radioactive contaminants might subsequently leak from the repository. Given that the generation, accumulation and release of gases from a GDF may significantly affect the long-term safety function of the repository [NEA, 2001b], this topic has been the subject of several research activities focussing on both experimental and numerical modelling aspects in a series of international research projects [16] [Volckaert et al., 1995, Ortiz et al., 1997, Haijtink and Rodwell, 1995, Manai, 1997, Rodwell, 2000, Rodwell et al., 2003, Shaw, 2015, Tamayo-Mas and Harrington, 2020]. Building on these previous works, the present contribution aims to advance understanding and modelling of the gas impact on the hydro-mechanical behaviour of clayey rocks as part of the work package (WP) GAS of the EURAD [17] EC project [Garcia et al., 2020].

15. Further developed in Part II.

16. MEGAS (1991-1994), EVEGAS (1994-1996), PROGRESS (1996-1999), GASNET (1998-2002), FORGE (2009-2013), DECOVALEX (2016-2019) to name the most important ones.

17. European Joint Programme on Radioactive Waste Management.

2. Objectives of the study

In the first reference status report on the basic understanding of gas transport processes in the context of an underground radioactive waste repository [Rodwell et al., 1999], it was stated that *there are few problems in geoscience more complex than the quantitative prediction of gas migration fluxes through an argillaceous rock formation*. Taking over from the continued effort deployed for the past 20 years on the subject, the WP GAS of the EURAD EC project aims to improve the mechanistic understanding of gas transport processes in natural and engineered clayey materials, their couplings with the mechanical behaviour and their effects on the properties of these materials, as well as to evaluate their potential impact on clayey barrier integrity and repository performance [Levasseur et al., 2022].

The work presented in this thesis focuses on task 2 of this WP, dedicated to the main transport mechanisms at play in the post-closure phase of a disposal system, and on part of task 3, dealing with the barrier integrity. Among all the objectives of the WP, the work presented in this thesis aims to contribute to:

- Conceptualise the transport mechanisms both at micro- and macro-scale (sub-task 2.2).
- Improve understanding of the observed gas transport modes and their main control (sub-task 2.2).
- Gain a mechanistic understanding of the hydro-mechanical phenomena associated with gas-induced failure, within the EDZ and the host rock (sub-task 3.1).
- Evaluate achievements by the application of the newly developed modelling tools on *in situ* experiments (sub-task 3.3).

More particularly, in the case of saturated plastic clays with low diffusion coefficients and subjected to high gas production rates, there is now a growing body of evidence [Harrington and Horseman, 1999, Harrington et al., 2012b, Cuss et al., 2014b, Gonzalez-Blanco et al., 2016, Harrington et al., 2017a] that, classic concept of porous medium two-phase flow characterised by intrinsic hydraulic properties are unsuitable to numerically capture the complex coupled hydro-mechanical processes governing gas flows in porous media. This thesis is thus motivated by the challenging task of suitably modelling which transport regime prevail under which conditions in different zones of the geological barrier and for different argillaceous materials, with the emphasis on the two primary modes for gas flow as a separate phase, *i.e.* the visco-capillary flow and the formation of discrete gas-filled pathways.

This investigation therefore requires to develop novel and robust numerical models that can realistically simulate the gas transport mechanisms in low permeability media as well as the accompanied HM processes. More specifically, the doctoral research activities undertaken to meet the objectives of the WP listed above can be summarised as follows:

- The **identification** of the conditions, main features and fundamental properties of the clayey materials to be modelled, namely the Boom Clay and the Callovo-Oxfordian claystone, the **characterisation** of the possible gas transport mechanisms and related HM couplings to be considered in the numerical models, and the **inventory** of the numerical tools available for the modelling of gas migrations in low permeable media, in order to highlight the research gaps in these numerical studies. This part of the work is essentially based on an extensive literature review of the current state of the art.

- The **development** of a series of numerical models able to reliably reproduce the key experimentally observed gas transport processes in low permeable clay materials. Two distinct zones of the repository system have been more specifically identified in Figure I–7, dividing the task into two sub-objectives:
  - A **second gradient H^2M model**: In the excavation damaged zone (EDZ), the gas migration is supposed to be governed by the hydraulic properties modification induced by the fracturation following the storage drifts excavation [Tsang et al., 2005, Armand et al., 2014]. A first contribution aims thus at extending the second gradient method [Chambon et al., 1998] to two-phase flow hydro-mechanically coupled conditions in order to simultaneously capture the multi-physics interactions related to gas transfers and the development of fractures.
  - A **multi-scale model**: In the sound clay rock, the gas migration is supposed to be governed by the rock structure at a micro-level [Harrington et al., 2012b, Gonzalez-Blanco et al., 2016]. A second contribution aims thus at building a multi-scale model which captures the micro-scale effects on the macroscopic gas flow, by embedding the description of the microstructure constituents, like the pore network and the separation planes, on a representative element volume (REV).
- The **implementation** of the developed models in the framework of the finite element code `LAGAMINE`, and the **verification** of their efficiency and robustness. For an extensive description of the code, the reader should refer to [Charlier, 1987, Habraken, 1989].
- The **application** of the developed models at different scales, to demonstrate their ability to qualitatively mimic the experimental data at the lab or *in situ* scales, in such a way as to provide a better understanding of the gas transport processes that can be active at the scale of a geological disposal system.

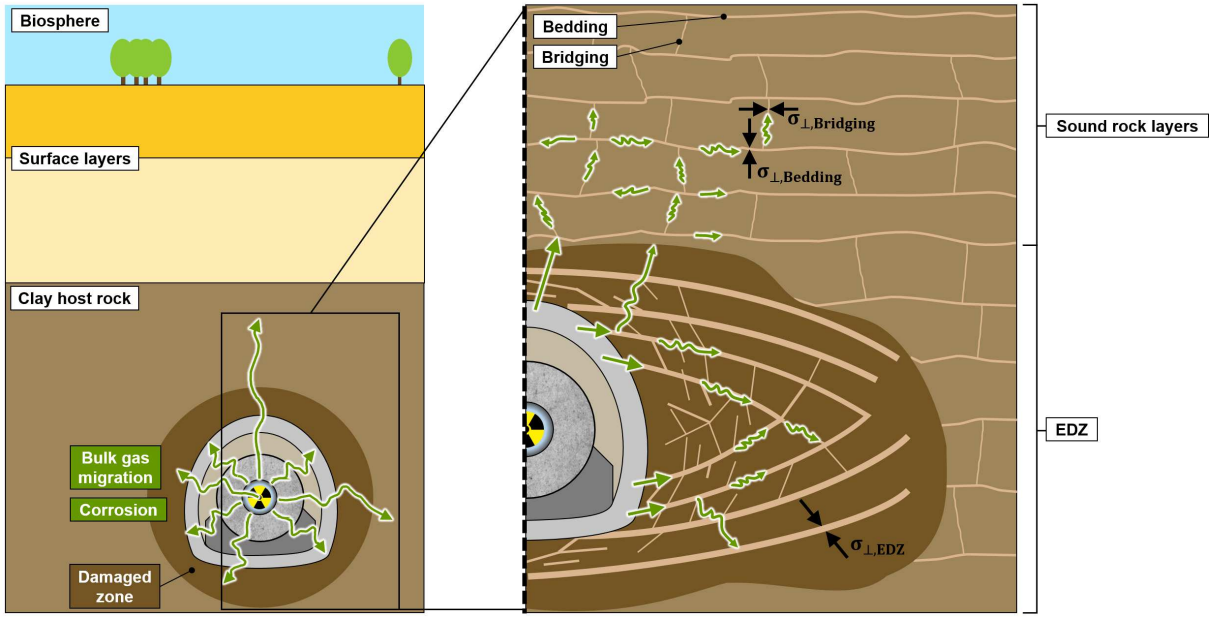

Figure I–7 – Conceptual scheme of a deep geological repository (a) focussing on the gas generation process with (b) the potential expected gas transport modes in the EDZ and the sound rock layers, *inspired from* [Levasseur et al., 2024].

3. Outline of the thesis

The thesis global frame consists of five main parts articulated following the key objectives and briefly introduced hereafter.

Context of the research. This opening part (I) provides a general introduction to the research topic, by presenting the background information about the nuclear power industry, radioactive waste types, and the concept of a deep geological disposal. In addition, a first insight into the gas-related issues in clayey rocks is given and the objectives of the thesis are delineated.

Basics of multiphase flows in clay materials. The second part (II) of the thesis gives a general overview of the state of knowledge with respect to the gas transport processes that may take place in the Boom Clay and the COx claystone. These two investigated materials are first characterised in detail, and the key experimental results on gas transport in these two rocks, as well as the insight acquired on the conceptualisation of the gas flow process through geological disposal systems, are highlighted. A description of the current modelling approaches for simulating gas migrations in saturated clayey materials is also provided to establish the starting point for numerical developments.

Modelling gas transport in the EDZ. The third part (III) is dedicated to the presentation of a second gradient H^2M model to reproduce gas transport processes through the excavation damaged zone. The path from experimental observations of strain localisation in geomaterials, to the practical implications of its numerical implementation, via the theorising of this concept, is first outlined. The key ingredients of the model required to properly reproduce the development of fractures, and simultaneously capture the multi-physics processes inherent to gas migrations are also described. Finally, this numerical tool is used for the modelling of a small-scale gas injection test in Boom Clay and a large-scale storage gallery in the COx claystone.

Modelling gas transport in sound rocks. The fourth part (IV) is dedicated to the elaboration of a detailed micro-scale hydraulic constitutive model for partially saturated clay materials, integrated into a multi-scale scheme employing homogenisation and localisation equations for the transition from one scale to the other. The sequential steps behind the double-scale procedure are first summarised, and then used for the development of the HM multi-scale model. The complex microstructure of the clay material is idealised as an assembly of fractured and tubular constituents in the horizontal and vertical directions, described by their own constitutive laws. This multi-scale HM model is used to reproduce gas injection experiments carried out in Boom Clay, from the laboratory scale to a larger scale, which raises the questions related to the variability of the material properties and the up-scaled impact of the microstructure-induced processes on gas migrations.

Conclusions The closing part (V) of the thesis presents the main conclusions drawn from the different contributions of the research, together with the recommendations for future work.

Part II

Basics of multiphase flows in clay materials

Introduction Part II

Before proceeding to modelling, this part of the thesis aims to better apprehend the complex and specific transport processes inherent to gas release from geological disposal facilities, the materials to be modelled in this specific context, and the modelling tools available. These aspects, briefly contextualised in the introduction part, are now further clarified by way of a literature review.

Among the different materials for deep geological repository, the focus has been put on the behaviour of the Boom Clay and the Callovo-Oxfordian claystone envisaged respectively in Belgium and France. The main properties of these two argillaceous formations used in the modelling parts III and IV are first summarised. This general description covers different aspects, including the geological setting of the materials, the materials structure, the geotechnical properties, with a special focus on the expected favourable attributes such as low permeability and on the implications induced by the creation of an excavation damage zone in the material.

The second chapter of the state of the art intends to draw up a broad picture of the gas transport taking place in the framework of geological disposal, without being exhaustive but based on the currently shared mechanistic understanding of the transfer processes [Levasseur et al., 2021]. So, the main mechanisms that allegedly operate gas migrations through low-permeability clayey materials (Figure II–1) are individually reviewed [Marschall et al., 2005]: *(i)* advection and diffusion of dissolved gas, *(ii)* visco-capillary two-phase flow, *(iii)* dilatancy-controlled gas flow, and *(iv)* gas flow in fractures.

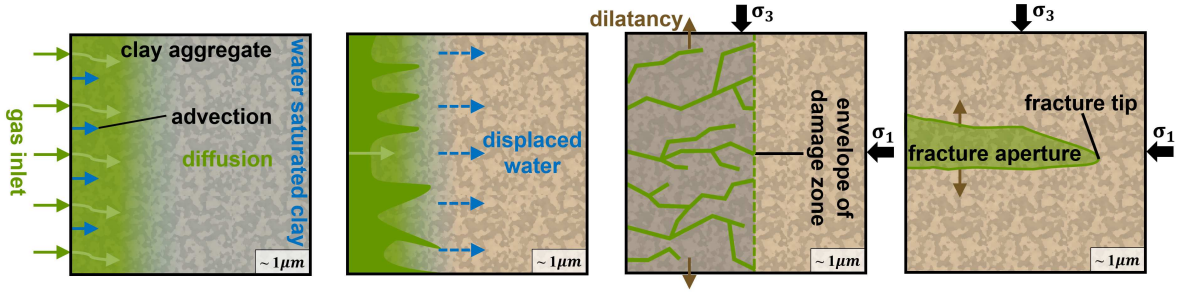

Figure II–1 – Phenomenological description of the basic modes of gas transport in low-permeability rocks. *After* [Marschall et al., 2005].

The final objective of Part II is to describe the fundamental basics for modelling gas transport in clayey materials. Gas flows are represented both from the perspective of the gas and considering the couplings with the mechanical behaviour of the porous media. In particular, classical hydro-mechanical models of a porous medium in partially saturated conditions are detailed and some other improved models able to capture the development of preferential flows are also introduced. The idea is to give a foretaste of the implementation procedure in the used `LAGAMINE` tool, and to provide a quick scan of what exists in terms of gas transport in the modelling sphere, which will serve as a basis for the numerical developments in the following parts.

4. General description of the clay host formations

For many decades now, a broad number of studies have been conducted to apprehend all the specificities of gas migrations in a variety of materials, including clays, generally related to a specific subsurface activity, whether it is conventional and unconventional hydrocarbons industry [Krooss et al., 1992, Clayton and Hay, 1994, Schlömer and Krooss, 1997], reservoir engineering [Gray, 1987, Gilman and Beckie, 2000, Gensterblum et al., 2015] or more recently the carbon dioxide sequestration projects [Christensen and Larsen, 2004, White et al., 2005]. Nevertheless, all these latter have been most often performed on very site-specific and briefly characterised materials which contrasts with the few clay formations studied in detail for the disposal of radioactive waste and on which a large body of experiments have been carried out. As of today, many countries in Europe are deploying great efforts to examine clays as a potential formation for hosting the radioactive waste disposals. France has approved an indurated clay rock known as Callovo-Oxfordian (COx) formation to dispose of its high-level and long-lived intermediate-level nuclear waste, while the technical option currently recommended in Belgium is the deep geological disposal envisaged in a poorly indurated clay, known as Boom Clay.

This chapter aims thus to provide a general overview of these two clay formations that are numerically modelled further in this work. First, an overview of the favourable attributes of clay rocks as host formations for radioactive waste storage is presented. Then the occurrence area of both studied formations is contextualised. The following part of this chapter proposes to describe the fundamental physical and geotechnical properties of the Boom Clay and the COx claystone from a general point of view, ending with an overall summary for the two considered host rock formations.

4.1 Expected favourable attributes

The natural geological barrier provided by the clay host formation and its surroundings is the key component of the multi-barrier system owing to its excellent properties for the confinement of contaminants. Intensive researches have been conducted over the past decades to properly characterise these favourable attributes of clay which encompass [Norris, 2017]:

- **Stability**: the selected host rocks and their associated properties have remained unchanged over millions of years.
- **Lateral continuity**: the geological structures encompassing the selected clay host rocks are characteristed by a large-scale lateral continuity.
- **Vertical homogeneity**: the selected host rocks present very uniform transport properties throughout their entire thickness.
- **Limited water movement**: the selected host rocks have a very low permeability, considerably restraining water movements and the radionuclide transfer via this medium.
- **Diffusive transport**: the chemical species migration through the selected host rocks is essentially diffuse, by means of concentration gradient and not the pore water movement.
- **Retention capacity**: the selected host rocks are defined by a strong capacity to delay the transfer of many radionuclides and chemical contaminants.

- **Buffer effect**: the selected host rocks display a substantial buffer effect with regard to chemical perturbations.
- **Self-sealing capacity**: any fissure created in the selected host rocks could close with time under given conditions.

Looking more fundamentally at the transport of gases through such clays, it emerges that this process is conditioned by the sub-microscopic dimensions of the interparticle spacing [Nelson, 2009], the strong physico-chemical interactions between pore water and substrate [Abdullah et al., 1999], a low permeability [Neuzil, 1994] and a deformable matrix, which results in a hydro-mechanical coupled response of the considered materials [Barnichon and Volckaert, 2003]. At this point, the rest of this chapter intends to demonstrate that many properties of the Boom Clay and the Callovo-Oxfordian claystone are favourable to the choice of these formations as safe host rocks.

4.2 Site investigation

The following subsections summarise the occurrence area and geological origin of the formations for the two host clays and how the specific site can be thoroughly characterised at large scale by underground research laboratories (URL).

4.2.1 Geological setting

The Boom Clay formation is a detrital marine deposit belonging to the Rupelian age in the Tertiary Period on a geological timescale [Dumont, 1849]. This sedimentary formation is composed of rhythmically alternating clay-rich and silt-rich materials with variations in organic matter content which have been deposited in layers in the Campine Basin according to the climate and geological conditions change [Vandenberghe et al., 2014]. The Boom Clay layer is located in the north part of Belgium and covers a surface of about 5000 km^2, according to the geographic distribution visible in Figure II–2a. The formation remains almost horizontal with a gentle dip of 1-2% towards the northeast and its thickness increases from a few decameters at the outcrop to more than 150 meters in the deeper part of the basin [Heremans et al., 1977, Bernier et al., 2007a]. At this location, water bearing sand layers are situated above and below the layer, as presented in Figure II–2b.

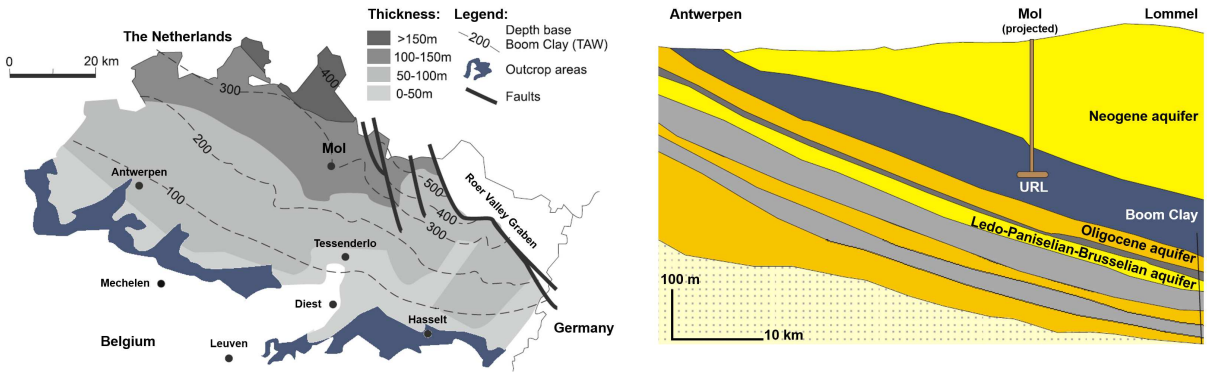

(a) (b)

Figure II–2 – (a) Extension of the Boom Clay formation in the north part of Belgium, *from* [ONDRAF, 2001] *modified after* [Honty et al., 2010]. (b) Geological cross-section through the occurrence area, *modified after* [Wemaere et al., 2008].

The Callovo-Oxfordian claystone, also called argillite, is part of the largest sedimentary basin in France, *i.e.* the Paris basin, known to be stable over the 365 million years of its geological history [Mégnien et al., 1980, Guillocheau et al., 2000]. This geological area is constituted of a succession of

quasi-horizontal sedimentary layers of clay, limestone and marls among which the Callovo-Oxfordian formation deposited 160 million years ago, in an open and calm marine environment. The COx sedimentary series remains almost horizontal with a general dip of about 1° to the West [Linard et al., 2011], and is located between 400 and 600 m depth, as displayed in Figure II–3. The formation is surrounded above and below by the Dogger and the Oxfordian limestones, and is vertically divided into three major geological sub-layers based on clay mineral content [Lerouge et al., 2011, Armand et al., 2016], namely the argillaceous unit, the transition unit and the silty-carbonated unit. The former constitutes the interval of interest for the planned repository.

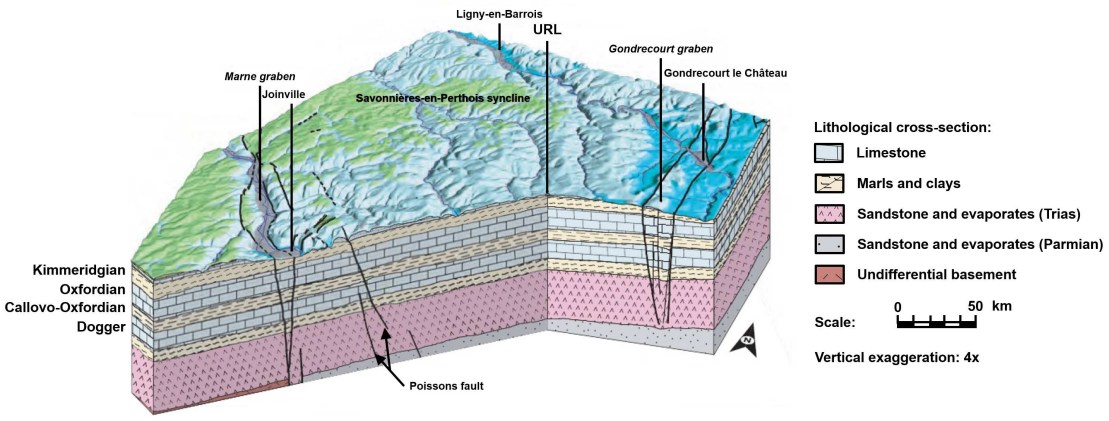

Figure II–3 – Geological map of the Meuse/Haute-Marne area in Eastern France, where the Callovo-Oxfordian claystone is located in a layer at around 500m depth, *modified after* [Andra, 2005].

4.2.2 Underground research laboratory

Given that the comprehension of the geomechanical behaviour of the candidate host rocks is an essential issue to assess the practicability and the long-term safety of a repository, a more direct access to deep geological formations turns out to be necessary. For this reason, a certain number of nuclear power generating countries, such as Belgium and France, have undertaken to build underground research facilities to acquire all the required *in situ* data and carry out research and development projects [Kickmaier and McKinley, 1997, Birkholzer et al., 2012, Delay et al., 2014]. In the context of radioactive waste disposal, an Underground Research Laboratory, usually known by the generic acronym URL, is a facility in which experiments are carried out so as to establish and to demonstrate the feasibility of constructing and operating a radioactive waste disposal facility within a geological formation [NEA, 2001a, NEA, 2001c].

As of today, Belgium operates the oldest URL in clay medium. The first construction phase of the HADES [1] URL dates back to 1980 at a depth of about 223 m in the Mol-Dessel area (Figure II–4a) where the Boom Clay is supposed to be present between 190 m and 290 m beneath the surface [Mertens et al., 2004]. Since then, the HADES laboratory has played a major role in the development of a scientific-technical basis for the disposal in Boom Clay, thanks to a large number of experiments performed under *in situ* repository conditions [Bernier et al., 2007a, Bastiaens and Bernier, 2006]. This type of URL falls in the methodological laboratories category [Blechschmidt and Vomvoris, 2010] since it is located at a site with representative rock, but is not designated to host a repository.

In France, the Meuse/Haute-Marne URL was built at the very end of 20th century and has been in operation since then in the framework of ANDRA's research program. The Laboratory consists of two shafts providing access to a multi-purpose experimental area at 445 m depth level and to a set of technical and experimental drifts at the main level at 490 m depth [Piguet, 2001, Delay et al., 2005], as presented in Figure II–4b. This latter depth corresponds to the median depth of the COx formation

1. High-Activity Disposal Experimental Site.

on the site which extends from approximately 422 m to 552 m. The first objective of the ongoing underground research was to characterise the confining properties of the argillaceous rock through *in situ* hydrogeological tests, chemical measurements and diffusion experiments [Delay et al., 2007]. After establishing the geological conditions, the subsequent studies have to demonstrate how the rock reacts to the construction and operation of the geological disposal [Armand et al., 2015]. Thus, such a site-specific URL serves a research purpose on the one hand, through the monitoring of the construction of the lab itself, and is also expected to have a prototyping and performance confirmation function on the other hand, which means that full-scale mock-ups of an eventual repository tunnel are built for early testing of engineered and natural barrier components [Blechschmidt and Vomvoris, 2010].

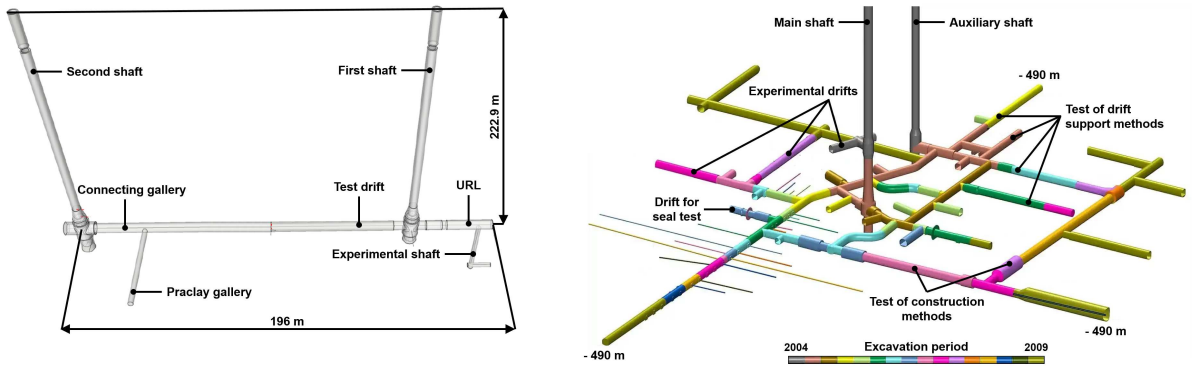

(a) HADES URL (Boom Clay) (b) Meuse/Haute-Marne URL (COx claystone)

Figure II–4 – Schematic representation of the gallery network of (a) the HADES URL in the Boom Clay, *after* [Bernier et al., 2007a, Verstricht, 2013] and (b) the Meuse/Haute-Marne URL in the Callovo-Oxfordian claystone, *after* [Armand et al., 2014, Souley et al., 2022].

4.3 Geotechnical properties and *in situ* conditions

4.3.1 From lithology to mineralogy

The Boom Clay is a silty clay or argillaceous silt whose horizontal layered structure constitutes its most striking characteristic. Within this vertical layering, several marker horizons with distinct properties are detected, as a consequence of variations in grain size or mineralogical content among the bands. These disparities result from sedimentary depositional processes and subsequent limited burial history [Vandenberghe, 1978]. In the horizontal direction, however, the Boom Clay formation presents an extended lateral continuity [Vandenberghe et al., 1997, Honty and De Craen, 2012].

In term of mineralogical composition, the present-day assemblage of the Boom Clay consists mainly of clay minerals dominated by illite, kaolinite and smectite and a complementary non-argillaceous fraction mostly constituted by quartz and feldspar. This composition is very homogeneous in the vertical profile from a qualitative point of view, although the proportions of the various minerals vary from one clay-dominated layer to another silt-dominated one [De Craen, 1998]. The presence of beds containing diagenetic sequences such as carbonates or pyrite as well as fractions of natural organic matter is also detected in smaller quantities in Boom Clay mineralogy [Van Geet et al., 2003, Bruggeman and De Craen, 2012]. Detailed information about the history of Boom Clay and its main mineralogical composition has been compiled by [DeCraen et al., 2004, Volckaert et al., 2005, Li et al., 2007, Wemaere et al., 2008], and further updated by [Zeelmaekers et al., 2015] and [Frederickx, 2019].

The Callovo-Oxfordian claystone forms a predominantly homogeneous clayey layer between 422 m and 552 m in depth directly above the underground laboratory. Only slight variations in the main constituents of the mineral composition into three distinct sedimentary sequences are perceptible, which are the expression of weak cyclic variations of the sea level at the time of the deposition of the layer. It is the

median sequence with the highest clay mineral proportion that is especially studied for the implantation of a possible repository. Laterally, this clayey layer does globally not exhibit any discontinuities likely to modify the favourable properties of the argillite which testifies to the stable tectonic and sedimentary context during the period of deposition [Andra, 2005].

In terms of mineralogical composition, the main phases of COx claystone consist of clay minerals dominated by illite and smectite, a complementary non-argillaceous fraction mostly constituted by silicates and carbonates grains, and a minor part of organic matter. Detailed information about the history of COx claystone and its main mineralogical composition has been compiled in [Andra, 2005].

4.3.2 From granulometry to porosity

The Boom Clay is an uncemented fine-grained compacted clay with a well-developed particle alignment according to the bedding plane. This microscopically well-developed arrangement arises from the geological history of the clay, which has been deposited in a marine environment and submitted to different vertical loads during its history [Mertens et al., 2003]. This preferential alignment of the clay particles has been observed in [Dehandschutter et al., 2004] using scanning electron microscopy (SEM) technique. Moreover, a small-scale characterisation of the pore network, with the determination of the distribution, orientation and shape of pores down to a few nanometres in size has been performed in [Desbois et al., 2010, Hemes et al., 2011] by combining Broad Ion Beam cross-sectioning and high-resolution SEM imaging.

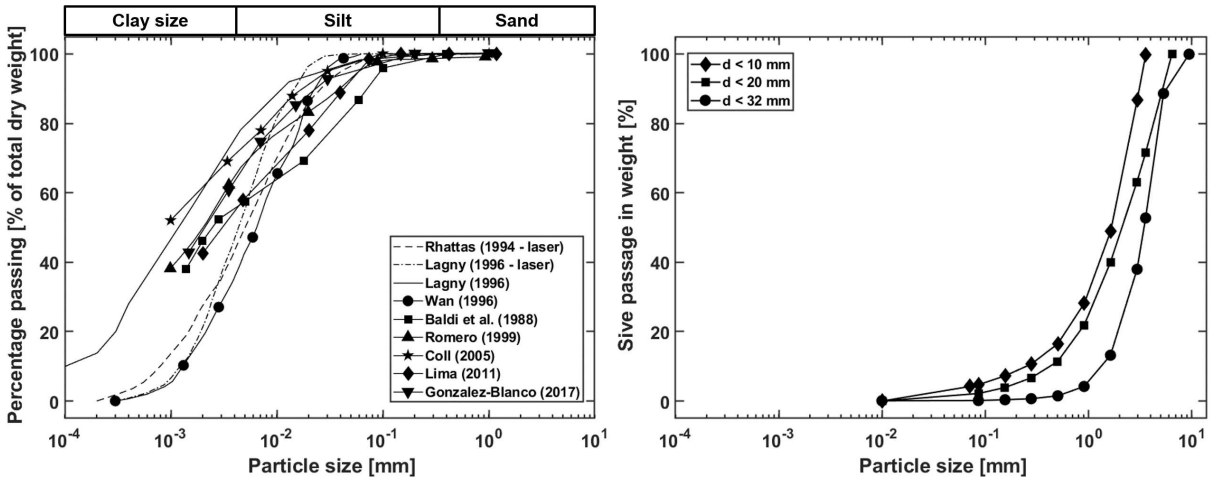

(a) Boom Clay

(b) COx claystone

Figure II–5 – Particle size distribution curves for (a) Boom Clay samples, *compiled by* [Lima, 2011, Gonzalez-Blanco, 2017], and (b) crushed COx claystone samples, *after* [Zhang, 2014].

In Figure II–5a, the compilation of several granulometric curves from different studies and methods [2] provided by [Lima, 2011] and further enriched by [Gonzalez-Blanco, 2017] reveals that the Boom Clay composition includes more than 60% of very fine particles (fine silt and clay-size particles). The analysis of the pore size distribution of Boom Clay measured by [Dehandschutter et al., 2004, Lima, 2011] on freeze-dried (natural) and air-dried samples with Mercury Intrusion Porosimetry (MIP) and presented in Figure II–19a of Section 5.3, shows that the majority of the pores have a radius comprised between 0.001 μm and 0.1 μm with a peak of the unimodal distribution around 0.01 μm. Although clay can be considered as an open structure with high porosity [Dehandschutter et al., 2004], assessing the porosity morphology in fine-grained sediments such as Boom Clay is quite complex due to the small pore sizes

2. Including: [Rhattas, 1994, Lagny, 1996, Wan, 1996, Baldi et al., 1988, Romero, 1999, Coll, 2005, Lima, 2011, Gonzalez-Blanco, 2017].

of this material. The total porosity of Boom Clay derived from the water content and diffusion experiments with tritiated water [Aertsens et al., 2005, Aertsens et al., 2008] ranges from 0.31 to 0.45, with the highest porosities detected in the bands.

The Callovo-Oxfordian claystone is an indurated clay with a preferential orientation of clay particles and aggregates parallel to the bedding plane [Robinet et al., 2012] that is not as pronounced as in the case of other indurated clays such as Opalinus Clay [Wenk et al., 2008], but still leads to a slight anisotropy of most of rock properties. The grain size distribution curves assessed by [Zhang, 2014] on crushed claystone produced by drift excavation at the main level of the URL are depicted in Figure II–5b. Pore network characterisation studies using MIP [Sammartino et al., 2003] demonstate that most of the porosity is located within the clay matrix, and there is a strong correlation between clay content and porosity values at the scale of the Callovo-Oxfordian geological layer [Robinet et al., 2015]. Figure II–19b of section 5.3 presents the reference pore size distribution curve of the COx claystone obtained by using MIP [Andra, 2005] that indicates that the network of pores mainly comprises meso- and micropores with a predominant pore population at approximately 10 nm to 30 nm [Song et al., 2015], and that this network has an extremely low connectivity for pore sizes larger than 40 nm [Robinet et al., 2012, Song et al., 2015, Armand et al., 2016].

According to [Esteban, 2006], the total porosity measurements lie between 13% in the carbonate-rich intervals to 19.5% at levels having the highest clay content, porositites as high as 27.5% are likely to be found in layers containing a significant quantity of pyrite, as mentioned in [Robinet, 2008], while the porosity of samples from the lower layers of the COx argillite deposit are generally around 22% as given in [Mohajerani et al., 2011]. In the end, the average porosity in the middle of the argillaceous unit of interest is assumed to be around 18%.

4.3.3 Density and water content

The density of Boom Clay has been widely characterized in the literature for several decades now. The reported value of the solid density ρ_s, namely the density of the solid grains, varies from 2650 $\frac{kg}{m^3}$ in [Mertens et al., 2003] to 2682 $\frac{kg}{m^3}$ in [Bernier et al., 2007a], by way of 2670 $\frac{kg}{m^3}$ in [Belanteur et al., 1997, Lima, 2011, Gonzalez-Blanco, 2017]. As for the values of the bulk (saturated) density ρ, these fall within the range 1900-2100 $\frac{kg}{m^3}$ following different studies [Heremans et al., 1977, De Bruyn et al., 1988, Mertens et al., 2003, Mertens et al., 2004, Dehandschutter et al., 2004, Bernier et al., 2007a], while the values of the dry density ρ_d that represents the density of soil when it is completely dry, range from 1490 $\frac{kg}{m^3}$ to 1900 $\frac{kg}{m^3}$ according to [De Bruyn et al., 1988, Baldi et al., 1988, Mertens et al., 2003, Dehandschutter et al., 2005, Li et al., 2007, Lima, 2011, Gonzalez-Blanco, 2017] and has been presented as function of depth in Figure II–6a [Gens, 2013], following previous reviews [Hoteit et al., 1999, Gens et al., 2007].

The typical water content of Boom water is thus about 20%, which is consistent with the water content weight range from 19% to 30% reported by [De Bruyn et al., 1988, Mertens et al., 2003, Mertens et al., 2004, DeCraen et al., 2004, Dehandschutter et al., 2004].

As for the density in Callovo-Oxfordian claystone, the value of the density of the solid grains ρ_s and the total bulk density ρ have been clearly established around 2700 $\frac{kg}{m^3}$ and 2420 $\frac{kg}{m^3}$ respectively [Andra, 2005, Conil et al., 2018, Zhang et al., 2019]. Since the COx formation is divided into multiple rheological layers, it is often observed that the dry density ρ_d rises with increasingly higher carbonate content and decreasing clay content. Thence, the values of the dry density range from 2210 $\frac{kg}{m^3}$ to 2330 $\frac{kg}{m^3}$, as reported in [Andra, 2005, Su, 2007, Zhang et al., 2010], and have been presented according to the depth in Figure II–6a [Gens, 2013].

The typical water content of Callovo-Oxfordian claystone falls in the range 5.3% to 8.8 % [Andra, 2005, Su, 2007, Zhang et al., 2010] with a reference value for the layer of interest of around 7.1% [Conil et al., 2018, Zhang et al., 2019]. A comparative visualisation of the water content of different clay rocks

envisaged for hosting a deep geological disposal, as a function of the uniaxial compressive strength is presented in Figure II–6b [Su, 2007].

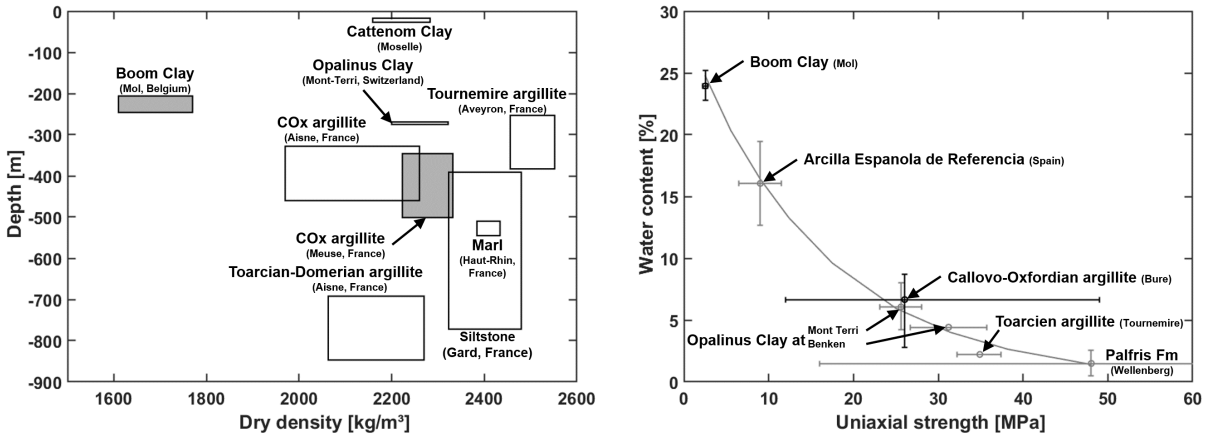

(a) (b)

Figure II–6 – (a) Dry densities of several argillaceous rocks at different depths, *modified after* [Heitz and Hicher, 2002, Gens, 2013]. (b) Cross-plot of water content and uniaxial compressive strength for different argillaceous rocks, *modified after* [Su, 2007].

4.3.4 Hydraulic conductivity

Since clays and other argillaceous lithologies are known to be among the least permeable geomaterials [Neuzil, 2019, Asem and Gardoni, 2022], their hydraulic conductivity, defined as the measure of their ability to transmit fluids, is consequently a crucial parameter for a nuclear waste disposal application.

The Boom Clay is characterised by a very low conductivity of the order of $10^{-12}\ \frac{m}{s}$ for the most argillaceous part of the formation, and exhibits an anisotropy of this parameter, ensuing a limited hydraulic gradient over the formation. A large investigation through various national [ONDRAF, 1989, ONDRAF, 2001, Yu et al., 2011] and international [Beaufays et al., 1994, Volckaert et al., 1995, Bernier et al., 2007b] programs has been running for more than 40 years to assess the value of hydraulic conductivity, with experiments carried out on different scales ranging from continuous lab tests to *in situ* tests in the HADES URL or from boreholes at the surface [ONDRAF, 2012]. In the laboratory, the hydraulic conductivity may be determined by different techniques, including pulse injection tests [Aertsens et al., 2004], constant pressure measurements [Wemaere et al., 2008] or back analyses [Horseman et al., 1987]. The former method has led to the establishment of a vertical hydraulic conductivity of $2.3 \times 10^{-12}\ \frac{m}{s}$, an average value which corresponds to an intrinsic vertical permeability of $2.3 \times 10^{-19}\ m^2$ and has been confirmed since then by [Lima, 2011, Yu et al., 2011]. In addition, the application of a mechanical load can cause change in the size of voids and so in porosity, which can reduce the value of the permeability and must therefore be taken into account under *in situ* conditions. Yet, considering a confining pressure of 2-2.3 MPa similar to the *in situ* stress level as in [Horseman et al., 1987, Ortiz et al., 1997, Coll, 2005, Bésuelle et al., 2014] gives similar values to those observed from non-stress-controlled testing techniques. Figure II–7b shows a compilation of the permeability evolution as a function of the isotropic effective stress from these different studies. The Boom Clay hydraulic conductivity has also been estimated by back analysis from MIP results in [Lima, 2011] following the approach developed in [Romero, 1999], getting the same orders of magnitude as in the other methods. Finally, a review of laboratory and *in situ* hydraulic conductivity measurements for the Boom Clay detailed in [Yu et al., 2011, Yu et al., 2012, Yu et al., 2013] has proposed a geometric means of 1.7×10^{-12} and $4.4 \times 10^{-12}\ \frac{m}{s}$ for the vertical and horizontal hydraulic conductivities respectively with an anisotropy ratio $\frac{k_h}{k_v}$ of about 2.5.

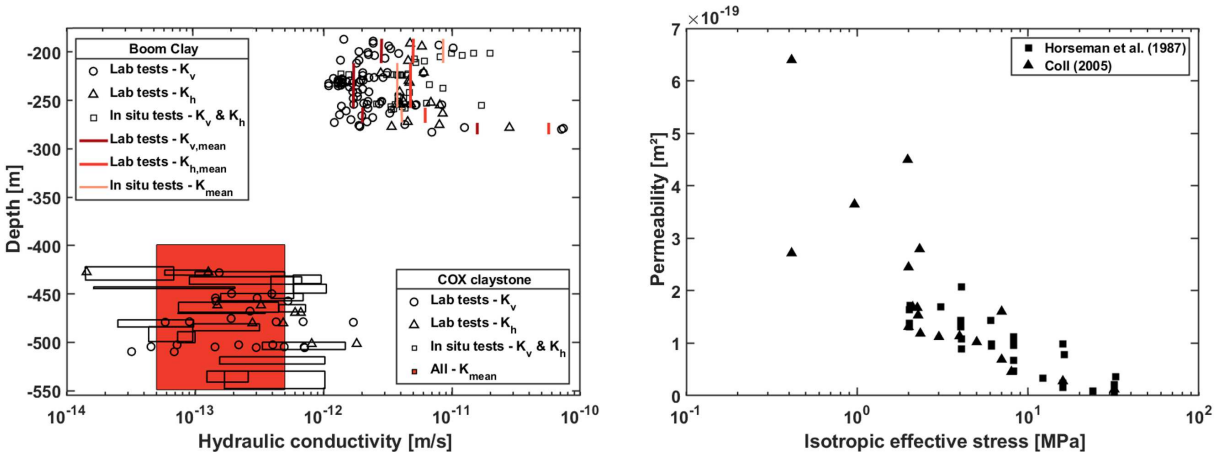

Figure II–7 – (a) Hydraulic conductivity profile of Boom Clay and Callovo-Oxfordian claystone on the site of respective URL, *after* [Yu et al., 2013] *and* [Delay et al., 2006]. (b) Permeability of Boom Clay as a function of isotropic effective stress, *after* [Horseman et al., 1987, Coll, 2005].

The Callovo-Oxfordian claystone belongs to low-permeable argillaceous rocks, with a hydraulic conductivity estimated around $10^{-13}\ \frac{m}{s}$ over the entire thickness of the formation. In order to refine the evaluation of this parameter, a large number of geomechanical and hydraulic measurements have been performed since the early 1990s whether from *in situ* instrumented boreholes [Delay et al., 2006, Distinguin and Lavanchy, 2007], or from the laboratory, either by using the pulse test method in saturated state [Coste et al., 2000, Escoffier, 2002, Heitz and Hicher, 2002, Homand et al., 2004, Koriche, 2004, Escoffier et al., 2005, Laego, 2005] or by exploiting the kinetics of drying tests via a linearised diffusivity coefficient in partially saturated conditions [De Greef et al., 2004, Homand et al., 2004, Hoxha and Auvray, 2005, Pham, 2010, Pham et al., 2007, Boulin, 2008, Boulin et al., 2008a, Semete et al., 2008, Malinsky, 2009]. In the end, the values of permeability commonly accepted range from 5×10^{-20} to $5 \times 10^{-21}\ m^2$, with a relatively low anisotropy (2 to 3 ratio) and a reference value of $4 \times 10^{-21}\ m^2$ corresponding to the median value of the measurements obtained in steady-state tests [Enssle et al., 2011, Armand et al., 2014, Armand et al., 2016].

4.3.5 *In situ* stress state

Characterising the *in situ* stress state at the planned location is of prime importance to understand the hydro-mechanical behaviour of the host rock and its long-term evolution. In particular, it has been widely evidenced that the transport properties of clays are highly sensitive to the effective stress state [Neuzil, 1994, Dewhurst et al., 1999, Katsube, 2000]. Changes in the effective stress can be caused by a variation in the confining pressure, the pore fluid pressure, or the development of anisotropic conditions. This latter can be influenced by the variation in the burial depth, or result from the creation of weakness planes, called bedding planes, owing to metamorphism and diagenetic processes, or is induced by the loading history and deformation following the material deposition [Arthur et al., 1977].

At the level of the HADES URL [3], the total vertical stress σ_v imposed by the weight of the overlying layers, the total horizontal stress σ_h and the undisturbed pore pressure p_w corresponding to a hydrostatic distribution up to the water table are respectively defined as follows [Bernier et al., 2007a]:

$$\sigma_v = 4.5\ MPa, \quad \sigma_h = 3.9\ MPa, \quad p_w = 2.3\ MPa \tag{II–1}$$

Laboratory measurements and *in situ* investigations confirm that the *in situ* stress state in the far field of HADES URL is transverse isotropic, with the major stress component being vertical [Bernier et al.,

3. At a depth of 223 m below the ground surface.

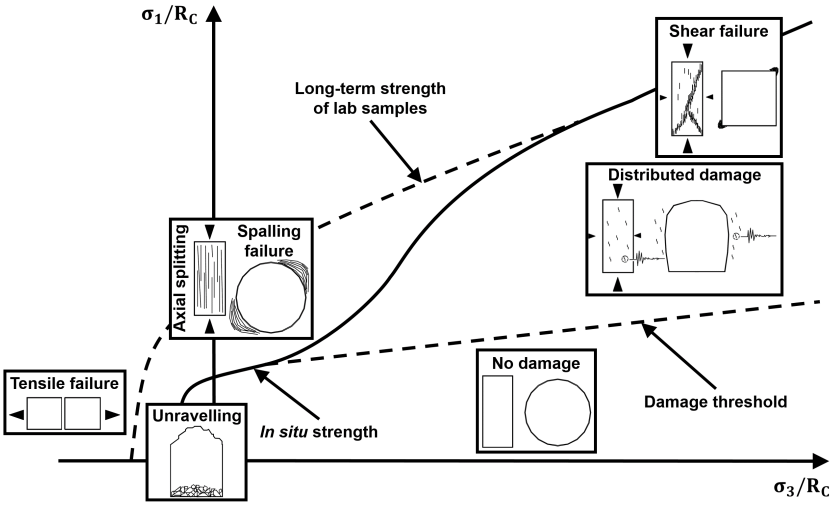

Figure II–8 – Mechanisms of rock mass brittle failure around a tunnel, *modified from* [Diederichs, 2003].

2002]. The value of the coefficient of earth pressure at rest $K_0 = \frac{\sigma'_h}{\sigma'_v}$ ranges from 0.7 to 0.8, hence the total horizontal stress is expected to be the minor principal stress, without indication of stress anisotropy in the horizontal plane [ONDRAF, 2012].

At the level of the Meuse/Haute-Marne URL [4], the stress regime is anisotropic and characterised by a major principal stress in the horizontal direction and a vertical stress more or less equal to the minor principal horizontal stress. Quantitatively, the stress state is defined as follows [Wileveau et al., 2007]:

$$\sigma_v = 12 - 12.7\ MPa, \quad \sigma_h = 12 - 12.4\ MPa, \quad \sigma_H = 14.4 - 16.1\ MPa, \quad p_w = 4.5 - 4.7\ MPa \quad \text{(II–2)}$$

The usual value that is considered for the ratio $\frac{\sigma_H}{\sigma_h}$ is closer to $1.2 - 1.3$, even if it varies with the rheological material properties and the depth [Armand et al., 2013, Armand et al., 2014].

4.3.6 Excavation Damaged Zone

An important aspect that goes along with the construction of a deep geological disposal in argillaceous rocks is the *in situ* stress redistribution that triggers damage propagation in the surrounding medium during the process of underground excavation. This leads to the creation of a so-called Excavation Damaged Zone (EDZ) close to the storage drift wall, dominated by hydro-mechanical properties modifications that are mainly irreversible and which induce important changes in flow and transfer properties [Tsang et al., 2005]. In particular, permeabilities are higher and gas entry pressures are low for damaged clay host rocks in such a way that the gas phase can enter and be transported through such zones much more easily. The EDZ has thus the potential to play an important role in gas transport, which is why it has been extensively investigated in terms of fracture development, transfer properties variations, and accurate numerical reproduction.

In terms of rock fracturing characterisation, tensile, opening, shear and mixed-modes are the different primary behaviours of fractures occurring in geotechnical applications [Whittaker et al., 1992]. Among the distinct brittle failure mechanisms (Figure II–8) prone to occur in the rock mass around underground galleries due to the damage propagation and microcracks coalescence [Diederichs, 2003], macroscale shear failure appears to be predominant in case of high-stress environment, as encountered in the context of deep geological disposal [EC, 2005a, Blümling et al., 2007]. In the vicinity of the Meuse/Haute-Marne URL, many *in situ* observations and measurements of fractures induced by the drilling process

4. At a depth of 490 m below the ground surface.

are performed to characterise the strike, dip and sense of the superficial cracks as well as the overall extent of the damaged zone [Armand et al., 2007]. The fracturing pattern analysis proposed in [Cruchaudet et al., 2010b, Armand et al., 2014] and presented in Figure II–9b reveals that shearing (mode II) is the main failure mechanism for this material, which causes the developement of explicit shear fractures in chevron deeper in the rock, and a zone of mixed fractures with minor spalling and extensional cracks in the zone close to the tunnel. The EDZ in the COx claystone presents an elliptical shape of several meters whose extension is mainly governed by the anisotropy of the stress state and of the material [Armand et al., 2013]. In the vicinity of the HADES URL, *in situ* observations during the construction of the connecting gallery were used to determine the fracture pattern in the surrounding formation [Bastiaens et al., 2003, Mertens et al., 2004]. The fracturing pattern analysis proposed in [Wileveau and Bernier, 2008] and presented in Figure II–9a reveals that two conjugate fracture planes develop in the upper part, dipping towards the excavation direction, and in the lower part, dipping towards the opposite direction, with a radial fracture extent of about one meter. All in all, the observed chevron or herringbone fracture pattern is similar to what is observed in the COx claystone [Wileveau and Bernier, 2008].

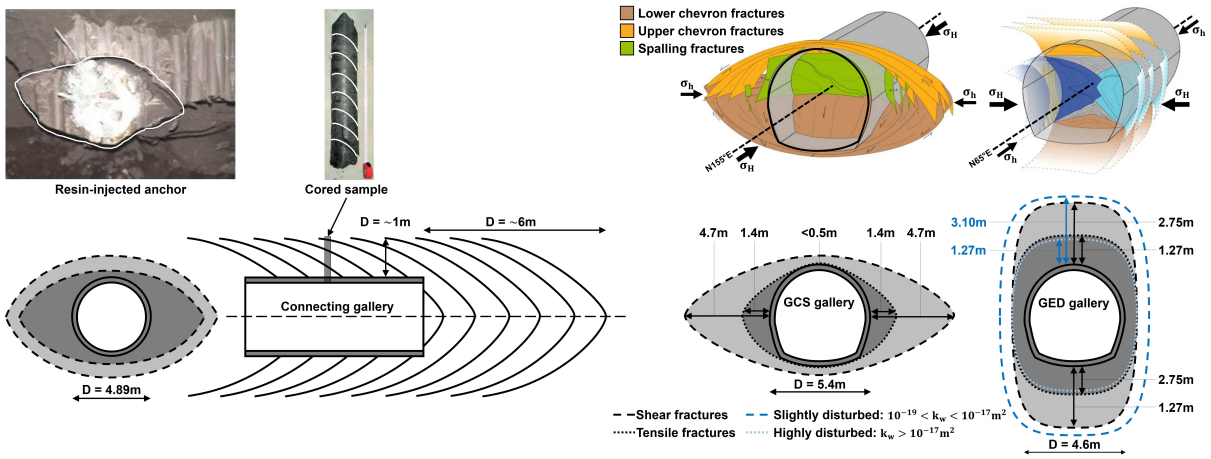

(a) Boom Clay (b) COx claystone

Figure II–9 – Conceptual scheme of induced fractures (a) in Boom Clay around the connecting gallery, with details of the damage on a resin-injected anchor (left) and on a cored sample (right), *from* [Mertens et al., 2004, Van Marcke and Bastiaens, 2010], and (b) in the COx claystone around drifts parallel to the major (left) and minor (right) horizontal principal stresses, *from* [Armand et al., 2014, Pardoen et al., 2016].

In terms of transport properties evolution, it is commonly assumed that the appearance of cracks and fractures concentrated in the EDZ deteriorates the flow properties of the surrounding material, such as permeability and porosity. This makes it easier for the gas to enter this zone of potentially lower strength, which constitutes a major issue since it may provide a preferential route for the transport of gas, bypassing the geologial barrier [Blümling et al., 2007]. As a consequence, the characterisation of the material transport properties and of the transfer kinetics occurring in the EDZ needs to be investigated thanks to experimental measurements conducted in the URLs.

For the COx claystone, severe increases in the hydraulic permeability up to several orders of magnitude have been measured in the fractured zone [Armand et al., 2014], thanks to boreholes drilled around galleries in different directions. Multiple zones of permeability variations can be highlighted in Figure II–10b [Cruchaudet et al., 2010a], which can be related to the location of induced shear fractures or interconnected fractures and thus vary according to the tunnel orientation and the stress state anisotropy.

For the Boom Clay, excavation induces a temporary increase in the hydraulic conductivity which is limited and often less than one order of magnitude as presented in Figure II–10a. This is attributable to the more ductile behaviour of Boom Clay where fractures develop predominantly in shearing without

large opening. Moreover, the affected permeabilities tend to evolve towards those of undisturbed clay as a consequence of the self-sealing capacity of Boom Clay that has been evidenced at different scales [Bastiaens et al., 2007, X. Li et al, 2007, Chen et al., 2012]. Nevertheless, indications that the hydraulic properties of the damaged zone would be completely restored by closing initiated fractures, before the time interval for the release of gas from the system, is yet to be quantified [Bastiaens et al., 2007, Bernier et al., 2007b].

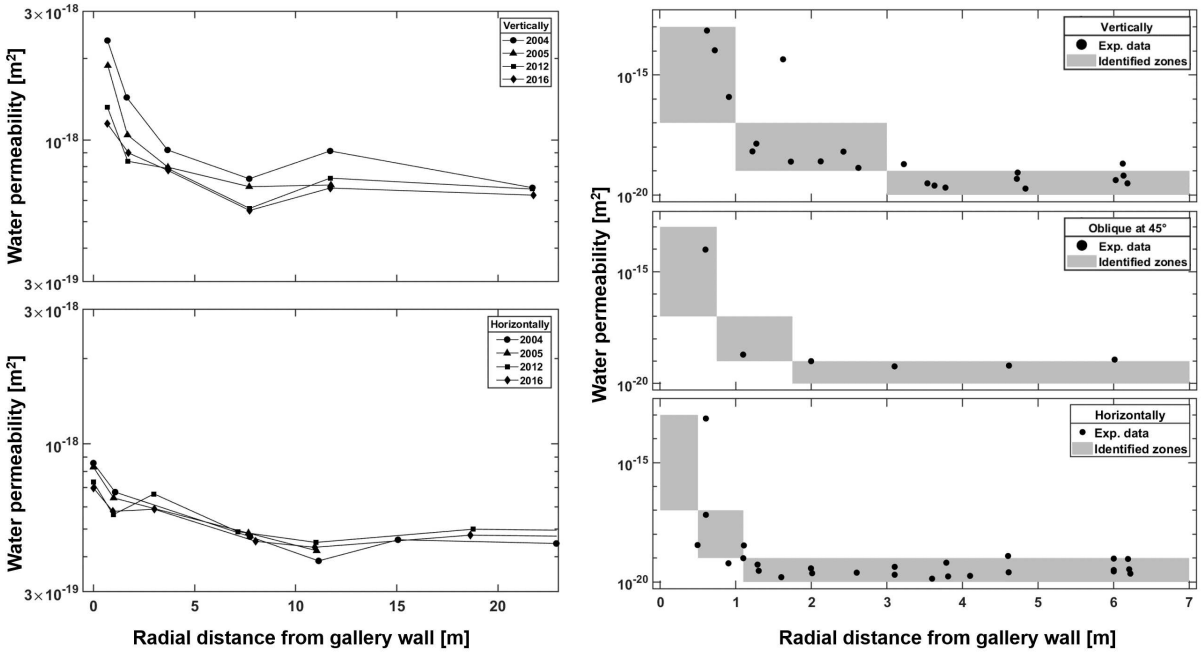

(a) Boom Clay

(b) COx claystone

Figure II–10 – Evolutions of the hydraulic permeability (a) along vertical (top) and horizontal (bottom) piezometers drilled around the connecting gallery in Boom Clay, *from* [Bernier et al., 2007b], and (b) along vertical (top), oblique at 45° (middle) and horizontal (bottom) boreholes drilled around the GED gallery in the COx claystone, *from* [Armand et al., 2014].

In terms of numerical approach, significant efforts have been made to tackle the computational complexity behind the modelling of the EDZ. The numerous approaches elaborated over the past decades focus on the short-term [Lisjak et al., 2015] or long-term [Rutqvist et al., 2009] rock mass response, integrate a damaged-based constitutive law [Pellet et al., 2009, Golshani et al., 2007] or include hydro-mechanical couplings [Plassart et al., 2013, Jia et al., 2008], permeability variations [Levasseur et al., 2013], flow transfers [Charlier et al., 2013], strain localisation [Pardoen and Collin, 2017] or all these aspects at once [Pardoen et al., 2016]. Among the several options convenient to represent rock fractures, a strain localisation approach in shear band mode is adopted in the present work [Pardoen et al., 2015b]. Chapters 7 and 8 are respectively dedicated to the experimental evidence of strain localisation in the geomaterials of interest and to the numerical approaches that are proposed to model such phenomenon.

4.4 Synthesis for the clay host formations

In brief, Table II–1 gives an overview of some typical ranges of values for basic geotechnical characteristics of the Boom Clay and the COx claystone, obtained by lumping together several sources, namely [Mertens et al., 2004, Bastiaens et al., 2006, Bernier et al., 2007a, ONDRAF, 2012, Dizier et al., 2018] and [Andra, 2005, Gens et al., 2007, Wileveau and Bernier, 2008, Malinsky, 2009, Armand et al., 2015]

to name a few.

Many of these properties prove to be favourable to the choice of these formations as host rocks for radioactive waste repository. Yet, it constitutes a necessary but not a sufficient condition, given that clay host formations are characterised by a non-linear stress-strain response under thermo-hydro-mechanical solicitations of which a certain number of the associated hydro-mechanical parameters and properties have been provided in [Villar et al., 2020].

In particular, with regard to gas transport behaviour that is the theme of the present work, the next chapter of this literature review specifically focusses on the characterisation of the main gas transport mechanisms which are expected to take place in a disposal system, and the properties required to adequately describe gas transport in the targeted host rocks.

Table II–1 – Overview of some geotechnical properties of Boom Clay and Callovo-Oxfordian claystone.

Host formations			Boom Clay	Callovo-Oxfordian claystone
Property	Symbol	Unit		
Bulk density	ρ	$[kg/m^3]$	$1900 - 2100$	$2300 - 2400$
Dry density	ρ_d	$[kg/m^3]$	$1490 - 1900$	$2210 - 2330$
Solid density	ρ_s	$[kg/m^3]$	$2650 - 2682$	2700
Porosity	ϕ	$[\%]$	$35 - 40$	18
Water content	w	$[\%]$	$19 - 30$	$5.3 - 8.8$
Poisson's ratio	ν	$[-]$	$0.2 - 0.4$	$0.18 - 0.37$
Young's modulus	E	$[GPa]$	$0.125 - 0.450$	$4 - 5.6$
Parallel	$E_{\parallel}$	$[GPa]$	0.4	5
Perpendicular	$E_{\perp}$	$[GPa]$	0.2	4
Friction angle	φ	$[^\circ]$	$11 - 19.5$	$20 - 25$
Cohesion	c	$[MPa]$	$0.3 - 1.2$	$3 - 7$
Dilatancy angle	ψ	$[^\circ]$	$0 - 10$	$0.0 - 0.5$
Compressive strength	R_c	$[MPa]$	$2.0 - 2.8$	$20 - 30$
Hydraulic conductivities	K_v	$[m/s]$	1.7×10^{-12}	1.0×10^{-13}
	K_h	$[m/s]$	4.4×10^{-12}	3.0×10^{-13}

5. Characterisation of gas transport processes

To evaluate the impact of gas on the integrity of deep geological repositories, adequate understanding of possible gas transport modes through clay barriers is essential. This chapter aims to provide a brief compilation of the scientific knowledge on the main gas transport processes that are expected to occur through clayey materials in the context of a disposal system [Marschall et al., 2005]: *(i)* the diffusive transport of dissolved gas, when gas produced within the system can dissolve in the pore water (Section 5.2), *(ii)* the visco-capillary gas flow, if a free gas phase develops as the gas production rate exceeds the rate at which gas can be dissolved and evacuated by diffusion (Section 5.3) and *(iii)* the formation of discrete gas-filled pathways or (*iv*) the gas-induced failure of clay-based geomaterials in the case of excessive gas pressures build-up (Section 5.4) .

In particular, a special attention is paid to the key results from previous experimental programs on the transport of gas in the Boom Clay and the Callovo-Oxfordian claystone, and insight gained alongside these campaigns for the characterisation of each gas process, which will serve as the basis for the modelling activities.

5.1 Processes relevant to gas transport

There is a number of processes governing the transport of gases from a geological disposal facility through the engineered barrier and the low-permeability clay-rich host formation. Beside the hydraulic and mechanical characteristics of the rock mass, *i.e.* porosity, intrinsic permeability and rock strength, the rate and amount of gases generated and the hydro-mechanical state of the rock, *i.e.* pore water pressure, stress state and water saturation, play also an important role in gas flow mechanisms. According to the widely accepted phenomenological description proposed by [Marschall et al., 2005] and given in Figure II–11, the processes relevant to gas transport can be splitted into four primary components:

- **Gas transport in solution**

The transport of gases in solution (Figure II–11a-i) under fully saturated conditions involves two major gas transport mechanisms, namely diffusion of the dissolved gas species and advection in the liquid phase. The former is characterised by the solubility of gas in pore water (Henry's law) and caused by a concentration gradient in the pore water pressure (Fick's law) [Helmig, 1997], while the latter is driven by a pressure gradient in the pore water (Darcy's law). The relative importance of each process depends on the properties of the host rock and of the dissolved gas. Since the studied argillaceous rocks are characterised by a low hydraulic conductivity, there are very little water flows, so the transport of gas in solution is mainly governed by diffusion as slow background process.

The key parameters affecting the gas transport in solution are the solubility of the gaseous species, the aqueous diffusion coefficient of each gas, the porosity and tortuosity of the porous medium and the hydraulic conductivity of the formation.

- **Visco-capillary two-phase flow**

Two-phase flow conditions (Figure II–11a-ii) take place when gas invades a water-filled porous medium as a separate phase [Bear, 1972]. To enter the pore network, the non-wetting phase (gas) has to displace

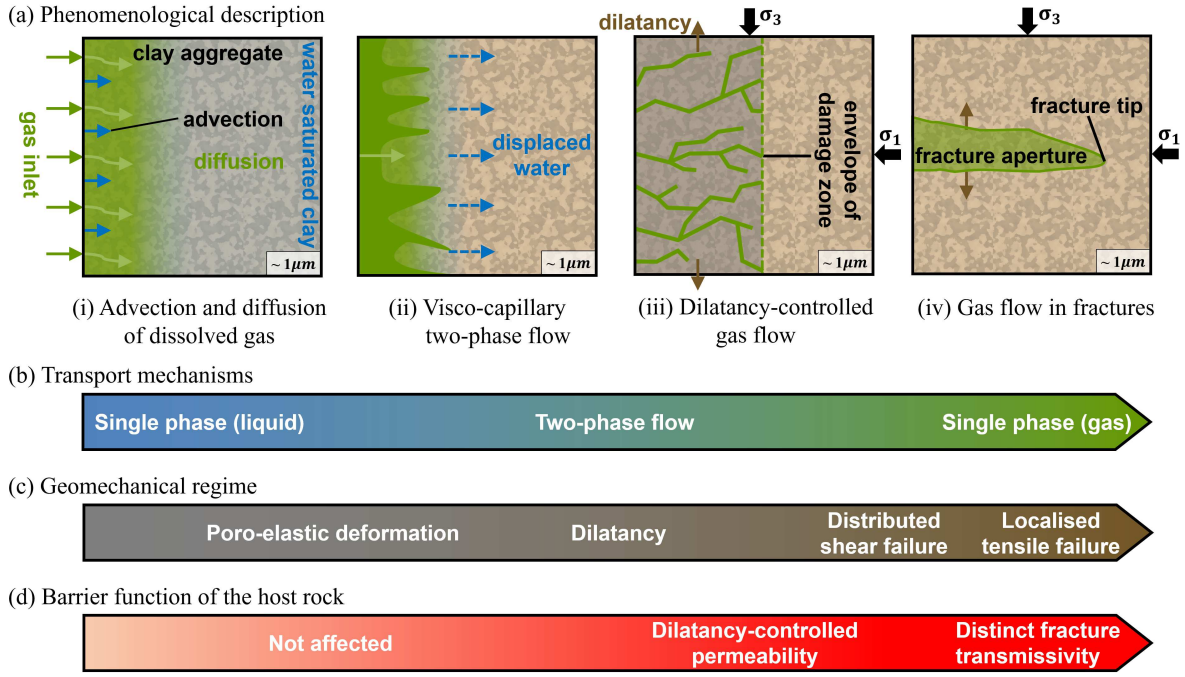

Figure II–11 – Classification and analysis of the processes relevant to gas transport in low-permeable rocks, *after* [Marschall et al., 2005]: (a) phenomenological description, (b) basic transport mechanisms, (c) geomechanical regime and (d) effect of gas transport on the barrier function.

the wetting phase (water), under the complex interactions of gravity, viscous forces and capillary effects (instable invasion), or as an immiscible displacement of the pore water front (stable propagation).

The key parameters affecting the two-phase flow is the gas entry pressure, which is the capillary threshold pressure a gas must exceed for it to be transported into a water-saturated material. Once the gas entry pressure has been exceeded, the gas mobility is controlled mostly by the intrinsic permeability of the formation, the relative permeabilities to water and gas depending on the saturation (relative permeability curves), and the variation of the capillary pressure with saturation (water retention curve).

- **Dilatancy-controlled gas flow**

Gas transport by pathway dilation (Figure II–11a-iii) is a flow mechanism of special importance for low-strength argillaceous rocks [Horseman et al., 1996] in which visco-capillary two-phase flow is difficult. In such materials, there is no transport of gas phase until a significant gas pressure has built up. Such pressures may allow localised consolidation of the clay-rich rocks which cannot withstand long-term gas pressures with a magnitude greater than the minimum principal stress acting on the rock mass. As a result, additional porosity in the form of micro-fractures is created, leading to the development of pathways along which the gas phase can be transported. Yet, the process of gas-driven micro-fracturing may remain intermittent for some materials with closure of the additional pathways in the event that gas transport by pathway dilation is faster than any continued gas generation.

The key parameters affecting the dilatancy-controlled gas flow include the state of deformation of the porous medium, *i.e.* the mechanical properties, and the variation of the transport properties of the solid phase, *i.e.* porosity, permeability, relative permeabilities to water and gas, and capillary pressure, according to this latter.

- **Gas fracturing**

Gas transport by macroscopic fracturing (Figure II–11a-iv) is a flow mechanism occurring in low-strength materials where the combined effect of pore water displacement and formation of small-scale fractures is not sufficient to counterbalance continued gas pressure build-up under high gas generation rates. Then, a macroscopic tensile fracture, *i.e.* gasfrac, develops when the gas pressure is larger than the

sum of the minimum principal stress and the tensile strength of the rock [Valko and Economides, 1997]. Such a fracture can provide a substantial local increase in the bulk permeability of the treated rock, establishing a single-phase flow process. Depending on the self-sealing capacity of the clayey materials, fractures are however expected to close and seal once the gas pressure is released and falls below the shut-in pressure of the fracture.

The key parameters affecting the gas fracturing process include the minimum principal stress and the tensile strength of the material, together with the gas generation rate.

As it can be seen in Figures II–11b and II–11c, the complex hydro-mechanical processes are decomposed into a problem of transport of immiscible fluids and a geomechanical problem respectively, with the effect of gas transport on the hydraulic barrier function of the rock highlighted in Figure II–11d. The basic principles of the processes related to gas transport introduced in this section are now further detailed in the following sections regarding the clayey materials of interest within this work.

5.2 Gas transport in solution

This section deals with gas transport in solution from the perspective of the gas, which means that even if different modes of gas transfer are activated, namely the diffusion of the dissolved gas species within the liquid phase and the advection with the liquid phase, only the former gas-active mechanism will be described in this section, while the latter one will be dealt with in the next section. General principles of this mode of gas transport are first exposed, followed by the main experimental procedures to capture this process, and the key results in the Boom Clay and the COx claystone.

5.2.1 Process overview

When the quantities of gas are small, the gas is completely dissolved in the liquid phase, and this dissolved gas then migrates mainly via diffusion within the liquid phase. The process of dissolution of gas molecules in the pore water of (partially) saturated clayey materials continues until the solubility limit of the gas is reached. It is described by Henry's law [Henry, 1803] which states that the amount of gas that dissolves in a volume of liquid is directly proportional to the partial pressure of dry gas according to:

$$p_g = K_{dg}^{eq}(T) x_{dg} \tag{II–3}$$

where K_{dg}^{eq} is an equilibrium constant depending on the temperature and x_{dg} is the mole fraction of dissolved gas in the liquid.

The underlying process behind diffusion is the movement of gas molecules dissolved in clay pore water from regions of high concentration to regions of low concentration, in absence of bulk transport. It is governed in its simplest form by Fick's law [Fick, 1855] which states that the diffusive flux is proportional to the gradient of mass fraction of species, where the hydrodynamic dispersion coefficient plays the role of the proportionality coefficient. The diffusion of dissolved gas within liquid phase reads:

$$i_{dg} = -D_{dg/w}^{*} \rho_w \frac{\partial}{\partial x}\left(\frac{\rho_{dg}}{\rho_w}\right) \tag{II–4}$$

where $D_{dg/w}^{*}$ is the effective diffusion coefficient for the dissolved gas in liquid water. As real pores in unsaturated porous media are typically of various diameters and twisted, the path for diffusion of the molecules within the pores is tortuous. This coefficient is thus directly related to the porous volume of the material and its structure through a capacity factor and to its water content and can be decomposed as [Philip and de Vries, 1957]:

$$D_{dg/w}^{*} = \phi R_f S_{r_w} \bar{\tau} D_{dg/w} \tag{II–5}$$

where ϕ is the accessible porosity, S_{r_w} is the water degree of saturation, $D_{dg/w}$ is the apparent diffusion coefficient, R_f is the retardation factor, which accounts for retention of the diffusing species by chemo-physical interactions with the solid phase, *e.g.* gas sorption processes, and is generally set to one for the gases of interest [Jacops et al., 2015, Jacops et al., 2016, Jacops et al., 2017b], and $\bar{\tau}$ is the tortuosity of the porous medium, which characterizes the fact that the path followed by the dissolved gas particles between the solid grains is not rectilinear. It corresponds to an obstruction factor lower or equal to one, usually defined as a power function of the ratio between the straight line distance and the effective length covered by the molecule [Jacops et al., 2017a], which attempts to account for the longest distance traversed in the pores, as idealised in Figure II–12.

Finally, it is worth noting that a constrictivity factor can be taken into account to characterise the reduction of the effective diffusion coefficient due to a drag by the pore wall, which is equal to one in the case of large pores and takes importance if the solute diameter has the same order of magnitude as the pore diameter. This phenomenon, known as the Knudsen effect, is all the more important as the gas injection pressure is low, which increases the probability of interactions with the pore wall and not with other molecules [Boulin, 2008].

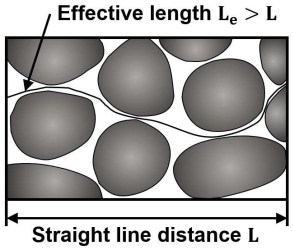

Figure II–12 – Concept of tortuosity in granular porous media.

5.2.2 Experimental procedures

It is possible to experimentally study the kinetics of gas diffusion and to determine a diffusion coefficient of the dissolved gas within the liquid phase, although these tests are particularly slow and the injected quantities of gas are very low. Three types of experiments are envisaged in the literature to assess the gas transport in solution via diffusion:

- **Outgassing from clay samples or boreholes:** Taking advantage of the natural presence of dissolved gas in the clay due to the alpha-decay of naturally-occurring radioactive elements, this first method consists in measuring the time evolution of the gas releases from clay samples [Bigler et al., 2005] or from the formation directly into boreholes [Gómez-Hernández, 2000]. The diffusion coefficient determined by these techniques must be interpreted with care because the outgassing starts directly upon drilling or after the sampling, which reduces the precision of the measurements.
- **Natural tracer profiles:** Based on the gases naturally present in the clay, like He, Ar and CH_4, this method consists in measuring the vertical concentration profile of these natural tracers by outgassing, in combination with assumptions about their environmental boundary conditions and production rate [Bensenouci et al., 2011]. Again, the determination of the diffusion coefficient with this technique suffers from the uncertainty on the initial state of the system, as well as from the difficulty of extrapolating the results acquired for the natural tracers to the gases of interest.
- **In- or through-diffusion experiments:** The third method consists in bringing a clay sample into contact with one or two reservoirs of water depending on whether it is based on the in- or through-diffusion experiment respectively [Rebour et al., 1997]. Initially, the reservoir connected to the inlet of the diffusion cell contains a high concentration of dissolved gas. By measuring the time evolution of the dissolved gas concentration in the low-concentration and/or the high-concentration reservoir, the diffusion parameters can be estimated by fitting the solution of a transport model

based on Fick's law to the experimental data. Provided that the set-up is well designed and that the sample conditions are representative, this technique is supposed to be the most reliable.

5.2.3 Boom Clay

Regarding the transport of solutes in Boom Clay, all the solubility data for key radionuclides were compiled in [Salah and Wang, 2014] using various thermochemical databases available in the literature [Wang et al., 2011]. Then, the first set of gas diffusion parameters for Hydrogen in Boom Clay were obtained from the MEGAS [1] project [Volckaert et al., 1995], where in- and through-diffusion experiments were performed. Given that these tests suffered from several leakage and outgassing disturbances, an uncertainty of up to two orders of magnitude on the diffusion coefficient evaluated in the range of 6.9×10^{-11} to 9.8×10^{-10} $\frac{m^2}{s}$ has been reported. Re-evaluation of the MEGAS experimental protocol by [Aertsens et al., 2009] demonstrated that the applied procedure did indeed not allow a more precise determination of the diffusion coefficient, which led to an estimated apparent value in the range of 5×10^{-12} to 4×10^{-10} $\frac{m^2}{s}$. Thereafter, a new experimental methodology to measure diffusion coefficients of dissolved gases in Boom Clay with high precision and accuracy has been developed based on a double through-diffusion technique presented in Figure II–13a, and detailed in [Jacops et al., 2013]. Further improvement combining different sterilisation techniques to obtain reliable diffusion coefficients for Hydrogen despite leakage and microbial activity have been designed by [Jacops et al., 2015].

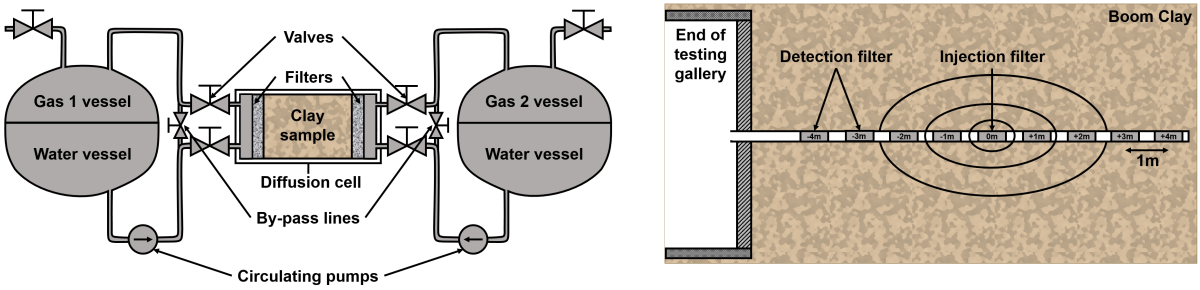

(a) (b)

Figure II–13 – Schematic overview of (a) the double through-diffusion technique set-up, *after* [Jacops et al., 2013], and (b) the CP1 experimental set-up, *after* [Bruggeman et al., 2015].

As for *in situ* characterisation, two large-scale migration experiments have been running for decades in HADES URL [Aertsens et al., 2013, Van Laer, 2018]. Concretely, a known quantity of a non-retarded radioactive tracer has been injected in a piezometer filter located at some distance from the laboratory as depicted in Figure II–13b, and tracer concentrations are monitored at adjacent detection filters, disposed either on the same multi-piezometer or on neighbouring devices. The comparison of these *in situ* concentration measurements with blind predictions of a strictly diffusive model, which uses diffusion coefficients measured in laboratory experiments [Aertsens et al., 2005], shows good correlation. Including a relatively small advective component and the anisotropy of the pore diffusion coefficient in the model further improves the agreement between experimental and modelling results, as reported in [Weetjens et al., 2014].

Diffusion coefficients for a series of gases including He, Ne, H_2, Ar, CH_4, Xe, and C_2H_6 have been measured parallel as well as perpendicular to the bedding planes for several samples of Boom Clay [Jacops et al., 2017b, Jacops et al., 2017a], as reported in Table II–2 (top). This typical layering of clay platelets causes an anisotropy of diffusion in Boom Clay, which is known to be higher in the horizontal direction than in the vertical one [Aertsens et al., 2009], with an average anisotropy factor of 1.5 for

1. Modelling and Experiments on Gas Migration in Repository Host Rocks.

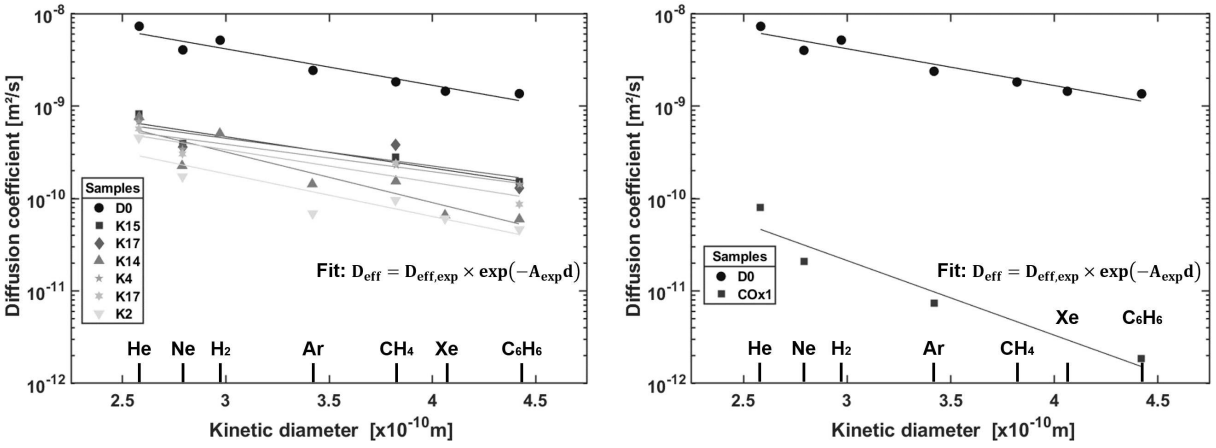

(a) Boom Clay

(b) COx claystone

Figure II–14 – Effective diffusion coefficients for dissolved gases in (a) Boom Clay and (b) COx claystone, *modified after* [Jacops et al., 2017b].

the commonly measured gases. Regarding the correlations between diffusion coefficient of the studied gases, the plot in Figure II–14a of the effective diffusion coefficient D_{eff} of all samples of Boom Clay versus the kinetic diameters d of the gases shows that D_{eff} decreases as a function of d, which means that despite some deviations, a larger molecule exhibits a smaller effective diffusion coefficient. Trend lines for this dependency have been inferred, which helps predicting the diffusion coefficient of a gas based on its molecular size and the experimental results from two other gases as performed by [Jacops et al., 2017b]. Finally, it is worth notifying that with a view to assess the impact of lithological variations in the Boom Clay on its transport properties, a detailed petrographical study was performed on the samples of the Boom Clay, with all the correlation results available in [Jacops et al., 2020a, Jacops et al., 2020b].

5.2.4 COx claystone

When looking in the literature, the first diffusion coefficient for the COx claystone was obtained by [Rebour et al., 1997] by means of a through-diffusion experiment with Helium as pure gas phase. The reported value of $D_{app} = 5 \pm 1 \times 10^{-11} \frac{m^2}{s}$ was later reviewed by [Bigler et al., 2005] concerning the reliability of the measured porosity, the origin of the tested sample or the complications such as anisotropy effects around the data. In this latter study, an outgassing experiment was performed on a spherical sample of COx claystone which resulted to an *in situ* pore diffusion coefficient D_p in the range $0.8 - 7.2 \times 10^{-10} \frac{m^2}{s}$. Yet, these measured values correspond rather to a mixed diffusion coefficient with respect to the bedding plane orientation, showing a large uncertainty of almost one order of magnitude owing to the disturbed nature of the sample. Later on, diffusion coefficients were reported in [Jacops et al., 2016] using the through-diffusion set-up for dissolved gases described for Boom Clay in Figure II–13a and in [Jacops et al., 2013], which has proven to provide consistent results. Finally, notable variations in the transport properties and thus in the diffusion coefficient according to the different lithofacies of the Oxfordian have been related in [Descostes et al., 2008].

Diffusion coefficients for a series of gases including He, Ne, Ar and C_2H_6 have been measured parallel as well as perpendicular to the bedding planes for samples of COX claystone [Jacops and Maes, 2015, Jacops et al., 2016], as compiled in Table II–2 (bottom). The measured anisotropy ratios for He and Ar are respectively 1.23 and 1.74, leading to an average anisotropy ratio of 1.5.As with Boom Clay, diffusion coefficients in Callovo-Oxfordian claystone decrease with increasing size of the diffusing molecule, which can be approximated with an exponential relation as presented in Figure II–14b.

Table II–2 – Overview of the measured effective diffusion coefficients (including the 95% confidence interval of the fit), for the Boom Clay (BC, top) and the Callovo-Oxfordian claystone (COx, bottom) *collected from* [Jacops et al., 2016, Jacops et al., 2017b, Jacops et al., 2017a]. *nm* means not measured, *TAW* refers to Tweede Algemene Waterpassing (Second General Levelling), D_0 values are taken from [Boudreau, 1997], kinetic diameters are taken from [Hirschfelder et al., 1964], D_{eff} of H_2 for the COx claystone are deduced by [Boulin, 2008].

			He	HTO	Ne	H_2	Ar	CH_4	Xe	C_2H_6
Kinetic diameter d $[\times 10^{-10} m]$			2.58	2.75	2.79	2.97	3.42	3.82	4.06	4.42
D_0 $[\times 10^{-9} \frac{m^2}{s}]$			7.28	2.20	4.03	5.11	2.44	1.84	1.47	1.38
Core	Orient.	Depth	D_{eff}							
$[-]$	$[-]$	$[mTAW]$	$[\times 10^{-11} \frac{m^2}{s}]$							
*BC*48a	$\perp$	167.92-168.02	51.0±2.0	17.6±0.9	*nm*	*nm*	*nm*	8.4±0.2	*nm*	*nm*
*BC*48a	$\perp$	168.02–168.12	50.0±0.6	20.6±0.6	*nm*	*nm*	*nm*	11.0±0.1	*nm*	*nm*
*BC*84b	$\perp$	203.29–203.39	46.8±1.7	18.7±0.6	17.5±0.3	*nm*	6.9±0.2	9.7±0.3	6.1±0.2	4.6±0.2
*BC*112a	$\perp$	231.11–231.31	45.0±1.0	16.0±0.5	*nm*	*nm*	*nm*	8.8±0.3	*nm*	*nm*
*BC*127b	$\parallel$	245.89–245.99	74.7±2.0	27.8±0.9	22.9±1.0	51.2±1.1	14.5±0.2	15.5±0.5	6.6±0.9	5.9±0.1
*COx*1	$\perp$	478.52m	8.1±0.2	*nm*	2.1±0.1	6.0	0.7±0.0	*nm*	*nm*	0.2±0.01
*COx*2	$\parallel$	490m	10.0±0.2	*nm*	*nm*	6.0	1.3±0.3	*nm*	*nm*	*nm*

5.3 Gas transport under visco-capillary two-phase flow conditions

This section presents the gas transport by means of visco-capillary two-phase flow, from the perspective of the gas. General principles of this mode of gas migration are first exposed. Then, the water retention model is presented to account for the relation between the capillary pressure and the quantity of fluids in the pores and for the capillary phenomenon governing the flow of two immiscible fluids within porous media. Afterwards, the permeabilities to water and gas are introduced since they constitute other flow parameters controlling the fluids transfers in partially saturated conditions. Finally, the key results in the Boom Clay and the COx claystone are given.

5.3.1 Process overview

In its conventional form, visco-capillary two-phase flow, also known as flow of immiscible fluids in porous media is described as a transport process whereby pore water in the pore volume is displaced by gas under the influence of viscous and capillary forces, as stated for example in [Bear, 1972]. The propagation of an immiscible gas front in an initially fully saturated porous medium is controlled by the complex interactions between the viscous and capillary forces (and gravity), from which three major flow regimes can be identified according to [Lenormand et al., 1988, Méheust et al., 2002]:

- **Stable displacement:** The viscosity of the injected fluid controls the invasion process. Capillary effects and pressure drop in the defending fluid are also negligible. The resulting pattern presents a rather flat front with some irregularities at the scale of a few pores, Figure II–15a.
- **Capillary fingering:** The viscous forces are negligible in both fluids and the capillary forces thus control the invasion process. The resulting pattern presents fingers growing in all directions and forming loops which trap the displaced fluid, Figure II–15b.
- **Viscous fingering:** The viscosity of the displaced fluid controls the invasion process. Capillary effects and pressure drop in the invading fluid are also negligible. The resulting pattern presents fingers with side branches but without loops, growing towards the exit, Figure II–15c.

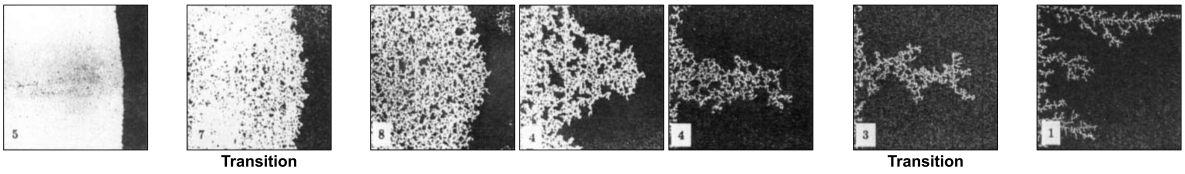

(a) (b) (c)

Figure II–15 – Major flow regimes from a glucose solution or air (white) invading oil (dark), *after* [Lenormand et al., 1988]: (a) stable displacement, (b) capillary fingering, (c) viscous fingering.

Capillary fingering can be assumed as the prevailing regime when a gas front invades the initially saturated matrix of a low-permeability host rock, while viscous fingering is the governing process when gas is released through a re-activated fault or along the EDZ, which creates a distinct precursor flux, *i.e.* an early gas breakthrough.

To enter the porosity, gas has to displace water, overcoming capillary effects. The controlling factor for the two-phase flow is thus the gas entry pressure, also known as the capillary threshold pressure. It represents the difference between the pressure in the non-wetting phase (here the gas) and the pressure in the wetting phase (here the pore water) needed to displace the pore water from the initially fully saturated medium. Once the gas entry pressure has been exceeded, visco-capillary two-phase flow establishes in the porous medium, accounting for the individual phase fluxes. The advection of both liquid and gas phases is described by a version of Darcy's law [Darcy, 1856] generalised to unsaturated cases, which reads:

$$q_{\alpha,i} = -\frac{k_{r_\alpha} k_{ij}^{int}}{\mu_\alpha}\left(\frac{\partial p_\alpha}{\partial x_j} + \rho_\alpha g_j\right) \tag{II–6}$$

where $q_{\alpha,i}$ is the advective flux (Darcy velocity vector) of phase α, k_{r_α} is th relative permeability of phase α, k_{ij}^{int} is the intrinsic permeability tensor, μ_α is the dynamic viscosity of phase α, p_α is the pressure in phase α, and g_j is gravitational acceleration.

The gas mobility is governed mostly by flow parameters such as the permeabilities of the liquid and gas phases and the degree of saturation of the porous medium. The analysis of multiphase fluid flow under partially saturated conditions therefore requires to define:

- **A retention model** linking the capillary pressure to the degree of water saturation;
- **Permeability-saturation relationships** for the evolution of the permeabilities of the liquid and gas phases with the saturation.

5.3.2 Retention model

In the context of a deep geological repository, gas migration in low-permeable media or rock desaturation at the gallery wall are specific issues involving two-phase flows (water and a certain gas) in porous medium under partially saturated conditions. Capillary forces tend to initiate and develop between the grains of the material, and are related to the quantity of water filling the porous space. From then on, it is interesting to study the link between this amount of fluids within the pore volume and the resulting capillary pressure p_c, because it directly conditions multiphase flows.

Notion of capillarity

The contact between two immiscible fluids gives birth to an interface where surface tensions are exerted. These stresses result from the difference in intermolecular forces acting on particles either in the fluid or at the interface, as shown in Figure II–16a. While all the forces acting on a particle within the fluid are balanced, surface tensions σ_{GL} are created for particles at the interface between the liquid and

the gaseous phases to restore equilibrium. Considering more particularly two fluids, L and G in contact with a perfectly plane solid surface S, then the equilibrium between the surface tensions exerted at the interface reads, according to Young-Dupré's formulae [Dupré and Dupré, 1869]:

$$\sigma_{SG} = \sigma_{SL} + \sigma_{GL} cos\theta \tag{II–7}$$

where θ is the contact angle. For $\theta < 90^\circ$ such as W in Figure II–16a, the fluid is said to be a wetting fluid whereas for $\theta > 90^\circ$ such as G in Figure II–16a, the fluid is called a non-wetting fluid.

The applied surface tensions are responsible for the so-called capillary effect, which has been evidenced by the well-known experiment of a tube plunged into a bask of water, showing that the water level rises into the tube until a certain height at equilibrium (Figure II–16b), analytically given by Young-Laplace's Equation:

$$p_c = p_g - p_w = \rho_w g H = \frac{2\sigma_{GL} cos\theta}{r} \tag{II–8}$$

where p_c is the capillary pressure expressed as the difference between the gas pressure p_g and the water pressure p_w, r is the radius of the tube, ρ_w is the water density, g is the gravity and H is the height in the tube. For information only, a gas entry pressure of 8 MPa (respectively 7 MPa) would correspond to a pore radius of the order of 18 nm (respectively 21 nm), considering a surface tension of 0.073 $\frac{N}{m}$ at 20°C and a wetting angle of 0° for the hydrogen – water contact.

This notion of capillarity can be transposed to granular materials and explains the phenomena taking place in an unsaturated porous medium with two fluids [Delage, 1987]. Depending on the capillary pressure and the pore radius, water meniscus forms in the smallest pores of the solid skeleton, at the interfaces between the grains as depicted in Figure II–31. The more the medium desaturates, the smaller the menisci become with a small radius of curvature thus generating a high value of the capillary pressure. However, in fine-grained soils such as argillaceous materials considered in this work, mechanisms other than the capillary effect arise due to the structure of the rock and the subsequent physico-chemical interactions between water molecules and clay minerals that can be encompassed under the term of suction.

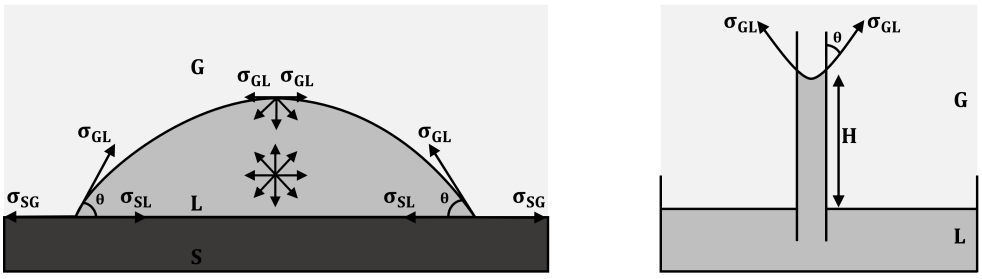

(a) (b)

Figure II–16 – (a) Molecular forces on a particle of water, *modified after* [Collin, 2003]. (b) Physical model of capillary phenomenon.

Concept of suction

The concept of suction often relates to capillary effects and is popular as an alternative to the internal potential, especially in soil mechanics. The water total potential in an unsaturated porous medium can be defined as the amount of work per unit mass of pure water needed to transport and extract the water from the medium and is expressed as the sum of four contributions as [Aitchison, 1965, Collin, 2003]:

$$\psi = \psi_g + \psi_p + \psi_m + \psi_o \tag{II–9}$$

where ψ is the total potential, ψ_g is the gravitational potential, ψ_p is the external pressure potential, and ψ_m and ψ_o are respectively the matrix and osmotic potentials, gathered together as the internal potential.

Yet, in constitutive modelling of soils, only this internal potential is relevant [Gens, 2010] and so the total suction can be expressed as a negative potential made of two contributions as:

$$s_t = s + s_{osm} \tag{II–10}$$

where s is the matrix suction related to the interactions between liquid and solid, and s_{osm} is the osmotic suction which depends on difference in solute concentrations in solutions and corresponds to the osmotic pressure.

In this work, the hydromechanical behaviour of the clayey materials is supposed to be independent of the osmotic effects, so that the total suction corresponds to the matrix suction. This latter is seen here as a quantitative expression of the degree of attachment between liquid and solid (capillary suction), regardless of the attraction mechanisms (adsorption suction) [Baker and Frydman, 2009]. In the end, the total suction can be defined as the gas pressure in excess of the water pressure, and is associated with the capillary phenomena just as explained and defined by Equation (II–8):

$$s = p_g - p_w \tag{II–11}$$

Water retention curve

The retention behaviour of a granular material is usually represented by a so-called retention curve presented in Figure II–17, and defined as the relationship between the amount of water stored in a porous medium, which is quantified by the degree of water saturation S_{r_w}, and the medium suction, which is linked to the capillary pressure. Four main domains characterise a typical shape of a retention curve for geomaterials:

1. **Gas entry limit:** Full saturation of the material is achieved below a suction termed gas-entry pressure s_{GE}, which is the minimal capillary pressure needed to desaturate the material pores. For gas pressures above this threshold, the gas phase starts to displace water from the pore system.
2. **The funicular state:** Higher capillary pressure leads to further desaturation. Liquid phase is continuous while gas phase forms bubbles.
3. **The pendular state:** Desaturation is further continued. Water forms bonds between grains. Generally, the wetting fluid (water) occupies the smallest pores and is in direct contact with the pore walls while the non-wetting fluid (gas) tends to minimise its contact area with the pore walls.
4. **The residual state:** The saturation of the sample takes a residual value $S_{r_{res}}$ which represents a threshold value below which the water can not be extracted from the medium, except in the form of water vapour. Liquid phase is discontinuous while gas phase is continuous.
5. **Resaturation:** A decrease in pressure leads to the resaturation of water, reducing the interconnected pathways of gas until flow stops. Trapped amounts of gas within the pore network lead to a saturation hysteresis between the first drainage and resaturation processes [Kleppe et al., 1997].

Among the large number of analytical expressions available in the literature to represent the retention behaviour of porous media, the constitutive model of van Genuchten's type [van Genuchten, 1980] presented in Figure II–18a is widely used and expressed as:

$$S_{r_w} = S_{r_{res}} + (S_{max} - S_{r_{res}}) \left(1 + \left(\frac{p_c}{P_r} \right)^{\mathcal{N}} \right)^{\frac{1}{\mathcal{N}} - 1} \tag{II–12}$$

where P_r is a parameter identified as the gas entry pressure, S_{max} and $S_{r_{res}}$ are the maximum and residual degrees of water saturation, $\mathcal{N}$ is a model parameter controlling the curve shape, and $p_c = s$ is the capillary pressure or suction.

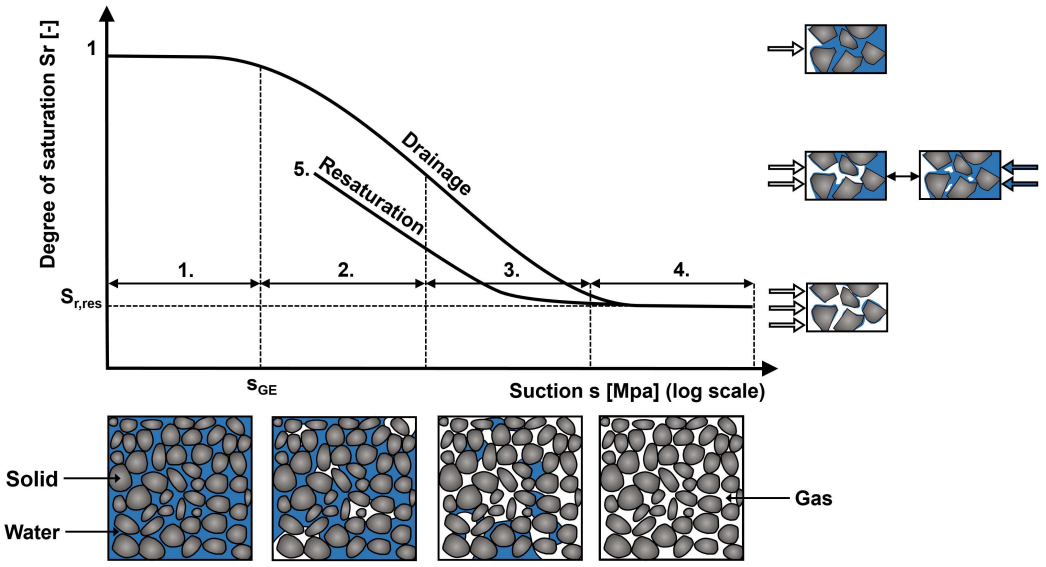

Figure II–17 – Water retention curve and conceptual sketch of the saturation stages (bottom) and the capillary processes during gas invasion. *Modified after* [Nuth and Laloui, 2008] *and* [Busch and Amann-Hildenbrand, 2013].

Another popular capillary pressure model is the Brooks-Corey relationship [Brooks and Corey, 1964] which is based on the following empirical function:

$$S_r^* = \left(\frac{P_r}{p_c}\right)^{\mathcal{K}} \tag{II–13}$$

where $\mathcal{K}$ is a model parameter, and S_r^* is the effective degree of saturation corresponding to the normalised wetting phase saturation:

$$S_r^* = \frac{S_{r_w} - S_{r_{res}}}{S_{max} - S_{r_{res}}} \tag{II–14}$$

A precise characterisation of the retention properties is essential since it contributes to the coupled hydro-mechanical behaviour of the material. Soil deformations affect the degree of saturation whereas variations in the degree of saturation lead to mechanical effects.

5.3.3 Permeabilities evolution

The evolution of permeability, whether to water or to gas, is strongly dependent on the degree of saturation as long as non-reactive porous media are considered. Since gas and water flows are simultaneously encountered in porous media, the widely-used concept of relative permeability k_r is introduced into Darcy's generalised Equation (II–6) to account for the reduction in permeability between fully and partially saturated conditions. The fluid effective permeabilities are consequently generally formulated as:

$$k_{w,ij} = k_{ij}^{int} k_{r_w}(S_{r_w}) \qquad \text{(II–15)} \qquad\qquad k_{g,ij} = k_{ij}^{int} k_{r_g}(S_{r_w}) \qquad \text{(II–16)}$$

where k_{ij}^{int} is the intrinsic permeability tensor for the formation, *i.e.* the water permeability in fully saturated conditions, which depends on the microstructure of clay and varies thus between saturated and unsaturated states [Villar and Lloret, 2001], and k_{r_w} and k_{r_g} are the water and gas relative permeabilities which are functions of the degree of saturation. By contrast to the intrinsic permeability tensor which depends exclusively on the material and not on the considered fluid, the hydraulic conductivity is related

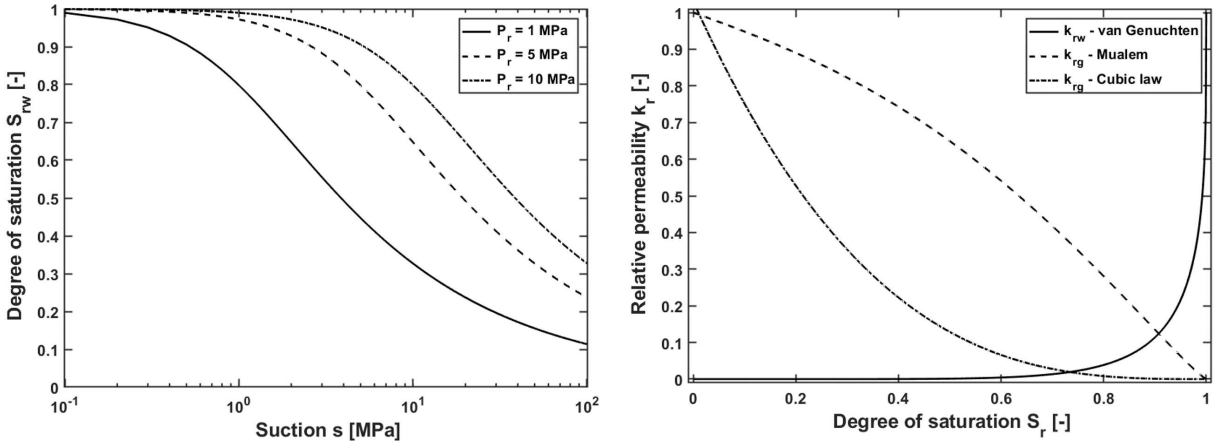

(a) (b)

Figure II–18 – (a) van Genuchten retention curve for $\mathcal{N} = 1.49$ and different value of the P_r parameter of gas entry pressure. (b) Water and gas relative permeability curves for $\mathcal{M} = 0.32886$.

to the fluid characteristics and is defined as:

$$K_{ij}^{sat} = \frac{k_{ij}^{int} \rho_w g_i}{\mu_w} \tag{II–17}$$

For a given saturation degree, the water relative permeability is defined as the ratio between the unsaturated water permeability and the saturated water permeability and is comprised between zero in theoretically completely dry conditions and one in fully saturated conditions. As for the gas relative permeability, it is defined as the ratio between the unsaturated gas permeability and the gas permeability for totally dry conditions. A large number of empirical expressions to assess water and gas relative permeabilities have been proposed in the literature based on the degree of saturation.

Water relative permeability

Based on the interpretation of the retention curve in terms of cylindrical pore size distribution, the following analytical expression has been obtained by [van Genuchten, 1980] and reads:

$$k_{r_w} = \sqrt{S_{r_w}} \left(1 - \left(1 - S_{r_w}^{\frac{1}{\mathcal{M}}} \right)^{\mathcal{M}} \right)^2 \tag{II–18}$$

where S_{r_w} is the water degree of saturation, $\mathcal{M} = 1 - \frac{1}{\mathcal{N}}$ is a model parameter, and $\mathcal{N}$ is the model parameter that is *a priori* used in van Genuchten's retention curve (see Equation (II–82)). This water relative permeability curve presented in Figure II–18b relates the water permeability to the degree of saturation and reproduces the decrease in water permeability during the drying process of a material.

The model developed by [Brooks and Corey, 1964] can also be cited, and reads:

$$k_{r_w} = (S_r^*)^{3+\frac{2}{\mathcal{K}}} \tag{II–19}$$

where S_r^* is the effective degree of saturation defined in Equation (II–14), and $\mathcal{K}$ is the model parameter that is *a priori* used in Brooks-Corey's curve (see Equation (II–13)).

Gas relative permeability

On the other hand, the gas relative permeability curve relates the gas permeability to the degree of saturation and would reproduce an increase under drying of the material. From Van Genuchten's retention curve interpreted in terms of pore size distribution, an analytical formulation has been derived by [Mualem, 1976], and reads:

$$k_{r_g} = \sqrt{S_{r_g}} \left(1 - S_{r_w}^{\frac{1}{\mathcal{M}}}\right)^{2\mathcal{M}} \tag{II–20}$$

where $S_{r_g} = 1 - S_{r_w}$ is the gas degree of saturation, $\mathcal{M} = 1 - \frac{1}{\mathcal{N}}$ is a model parameter, and $\mathcal{N}$ is the model parameter that is *a priori* used in van Genuchten's retention curve (see Equation (II–82)).

On the other hand, a polynomial law, generally cubic [Brooks and Corey, 1964, Mualem, 1978], is also regularly used to describe the gas relative permeability, and reads:

$$k_{r_g} = (1 - S_r^*)^{\mathcal{L}} \tag{II–21}$$

where $\mathcal{L}$ is a model parameter and S_r^* is the normalised wetting phase saturation, defined in Equation (II–14). An example of these two gas relative permeability curves is presented in Figure II–18b which relates the gas permeability to the degree of saturation.

5.3.4 Boom Clay

To characterise the Boom Clay pore network in which the mobility of the liquid/gas phase takes place, Mercury Intrusion Porosimetry (MIP) tests have been performed on freeze-dried (natural) and air-dried samples [Lima et al., 2012], and were complemented by nitrogen adsorption tests [Gonzalez-Blanco, 2017] following the Barrett, Joyner and Halenda (BJH) method using the desorption information.

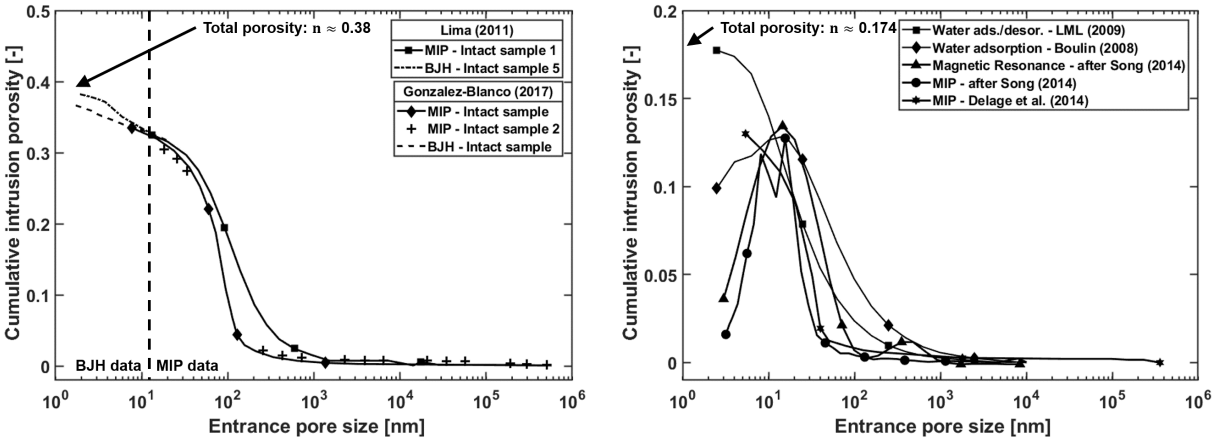

(a) Boom Clay

(b) COx claystone

Figure II–19 – Cumulative intrusion porosity from different methods, for (a) the Boom Clay, *compiled after* [Lima, 2011, Gonzalez-Blanco, 2017] and (b) the COx claystone, *compiled after* [Boulin, 2008, Delage et al., 2014, Song, 2014].

Figure II–19a shows the cumulative intrusion pore volume normalised by solid volume (intrusion void ratio), plotted against the entrance pore size for Boom Clay intact samples, while Figure II–20a represents the Pore Size Density (PSD) function. From the wide range of pore sizes covered by these techniques, one dominant pore family stands out around 70 nm, and a smaller peak is observed around 3 nm.

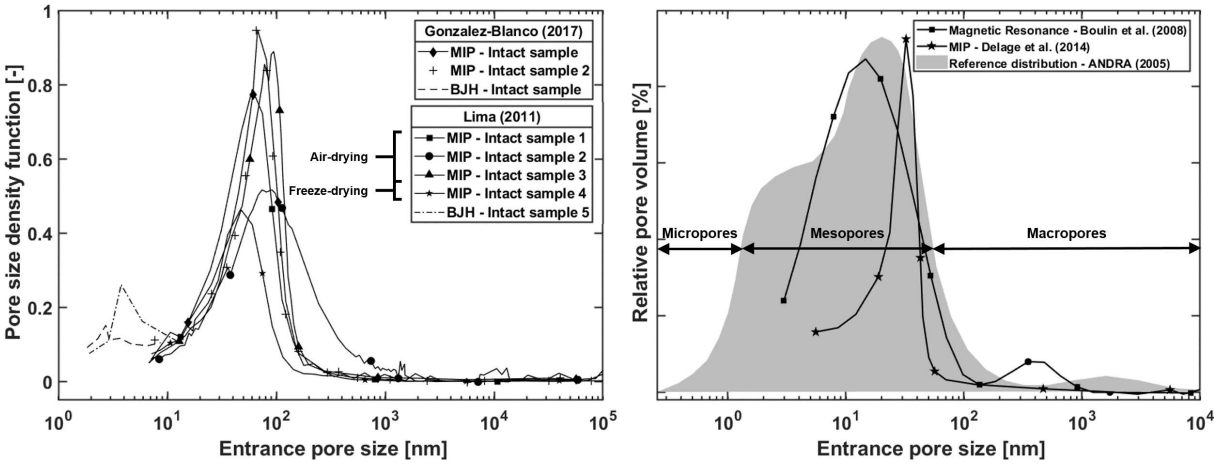

(a) Boom Clay (b) COx claystone

Figure II–20 – Pore size density function for (a) Boom Clay using different techniques, *after* [Lima, 2011, Gonzalez-Blanco, 2017], and (c) the Callovo-Oxfordian claystone, with the conceptual model in background, *after* [Andra, 2005], and experimental data *from* [Boulin, 2008, Delage et al., 2014]

Different complementary techniques for both drying and wetting paths have been used to characterise the water retention properties of Boom Clay, covering a wide range of suction [Le, 2007, Lima, 2011, Gonzalez-Blanco, 2017]. Figure II–21a shows the Boom Clay water retention curve evaluated from a dew-point psychrometer on specimens first dried in steps and then wetted in steps following identical procedure until saturation, together with MIP data and the fitted van Genuchten's Equation (II–12). The gas entry value corresponding to the dominant pore mode detected from MIP data has been estimated to be around 4-5 MPa [Le, 2007, Gonzalez-Blanco, 2017] while a value of 3 MPa was obtained by filter paper by [Salager et al., 2011]. These values can be considered as reasonably similar, considering the differences in test protocols or measurement techniques. As for the material parameter P_r related to the gas entry pressure in van Genuchten's formulation, the proposed values for fitting experimental data oscillate between 10 MPa [Gonzalez-Blanco et al., 2016] and 16.6 MPa [Prime et al., 2016].

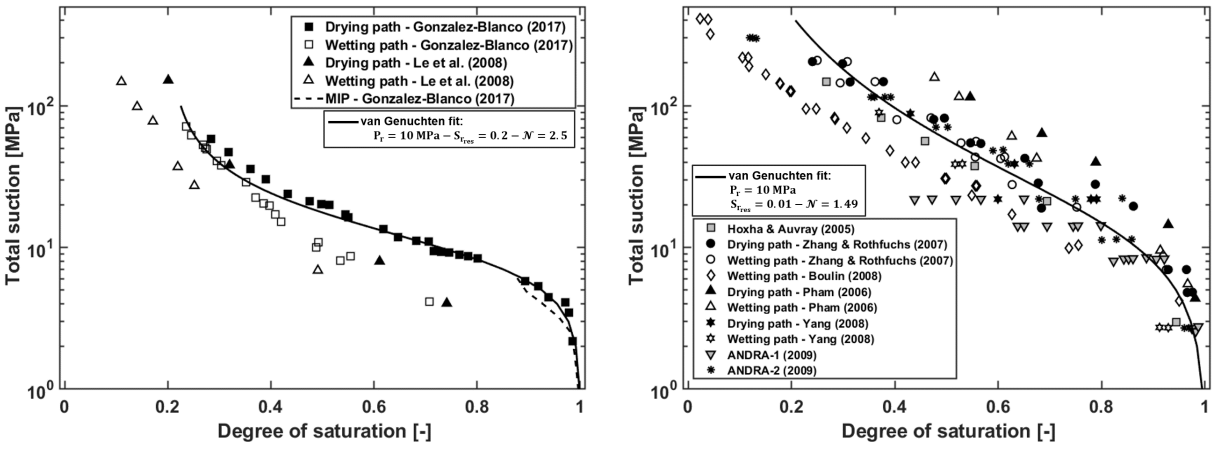

(a) Boom Clay (b) COx claystone

Figure II–21 – Experimental data for water retention curve together with van Genuchten's model fitting for (a) Boom Clay *compiled from* [Gonzalez-Blanco, 2017] and (b) the COx claystone, *compiled from* [Charlier et al., 2013, Armand et al., 2016].

The intrinsic permeability tensor of the matrix k_{matrix} depends on the pore structure and can be related to the porosity ϕ through Kozeny-Carman's law [Carman, 1937], which reads:

$$k_{matrix}(\phi) = k_0 \frac{\phi^3}{(1-\phi)^2} \frac{(1-\phi_0)^2}{\phi_0^3} \tag{II–22}$$

where $k_0 = 4.2 \times 10^{-19}\ m^2$ is the intrinsic permeability for the reference porosity $\phi_0 = 0.363$.
Gas injection and dissipation experiments carried out by [Gonzalez-Blanco, 2017] on samples with bedding planes parallel and perpendicular to flow provided the mean values of intrinsic permeability related to the average void ratio as displayed in Figure II–22a, with fitted Kozeny's model. The results highlight a good agreement between permeability data reported by several authors, with a clear dependence of the water permeability on the porosity. The lower values of water intrinsic permeability compared to gas intrinsic permeability, regardless of the sample orientation suggest that gas flows occur along preferential pathway depending on the volume of this later, while higher water intrinsic permeability values for flows parallel to bedding highlight the important role played by the deformation of the material along the injection stages.

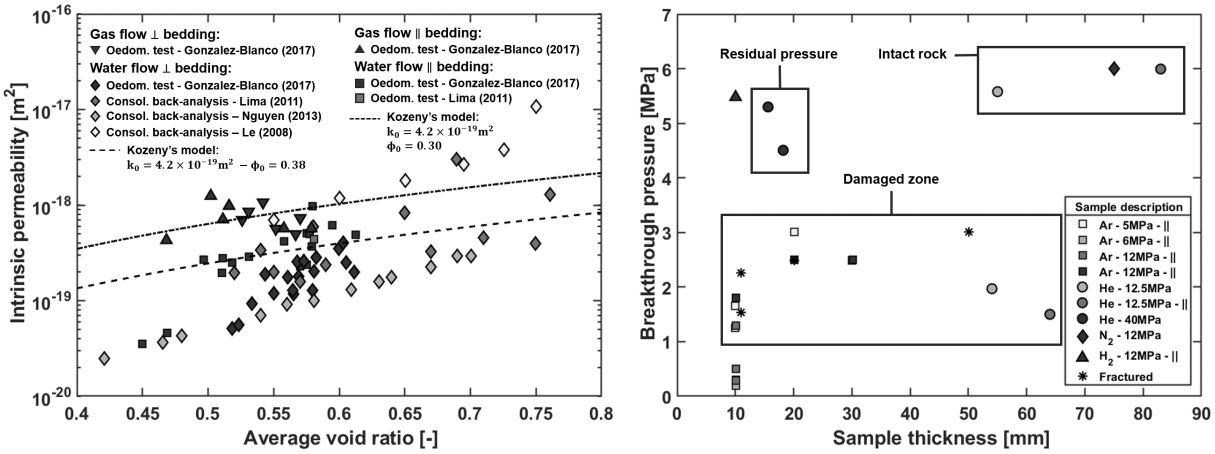

(a) Boom Clay (b) COx claystone

Figure II–22 – Experimental data (a) of intrinsic permeability plotted against the average void ratio after injection of air or water in Boom Clay, *compiled after* [Gonzalez-Blanco, 2017], and (b) of gas breakthrough pressure plotted against sample thickness, *compiled after* [Didier, 2012, M'Jahad, 2012, Cuss et al., 2014a, Song et al., 2016].

According to [Delahaye and Alonso, 2002], the relative permeability of liquid and gaseous phases of Boom Clay can be expressed as a generalised power law similar to Equations (II–19) and (II–21), which can be fitted on experimental data [Volckaert et al., 1995], as presented in Figure II–23a:

$$k_{r_w} = S_r^{*\mathcal{K}} \tag{II–23}$$

$$k_{r_g} = (1 - S_r^*)^{\mathcal{L}} \tag{II–24}$$

$$\text{with } S_r^* = \frac{S_{r_w} - S_{r_{res}}}{S_{max} - S_{r_{res}}}$$

where k_{r_w} and k_{r_g} are the water and gas relative permeability, S_r^* is the effective degree of saturation, and $\mathcal{K}$ and $\mathcal{L}$ are material parameters equal to 1.48 and 2.8 respectively.

5.3.5 COx claystone

A good knowledge of the microstructure is needed to fully understand gas transfer through Callovo-Oxfordian claystone. Porosity is studied with different complementary experimental methods, ranging from logging techniques such as Nuclear Magnetic Resonance (NMR) to assess the *in situ* porosity at

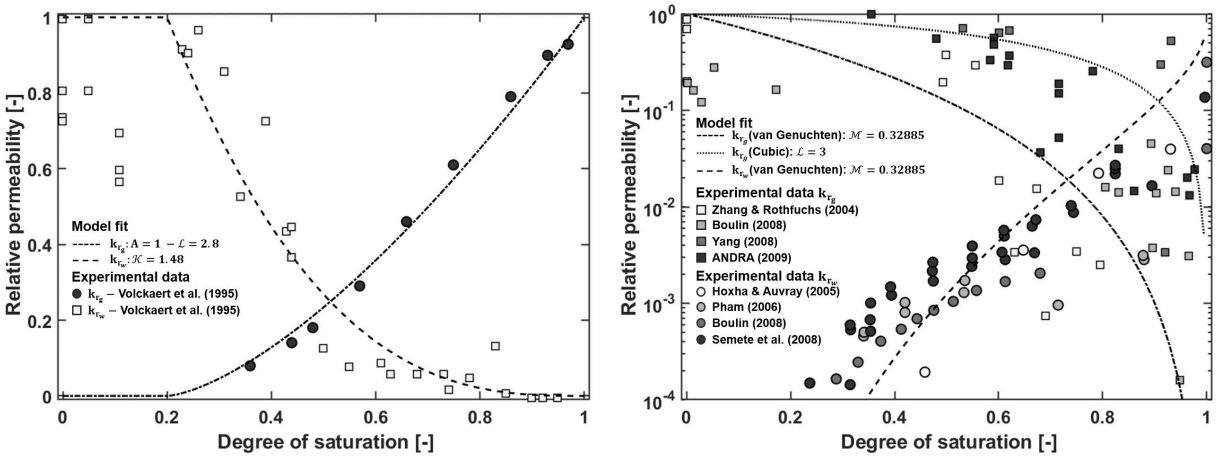

(a) Boom Clay (b) COx claystone

Figure II–23 – Experimental data for relative permeability together with van Genuchten's and cubic models fitting for (a) Boom Clay, *after* [Volckaert et al., 1995, Delahaye and Alonso, 2002] and (b) the Callovo-Oxfordian claystone, *compiled from* [Charlier et al., 2013].

the field scale, to several lab methods such as MIP or μ-CT providing access to the pore network structure, or high resolution techniques available more recently [Song et al., 2015]. Figure II–19b shows the cumulative intrusion pore volume plotted against the entrance pore size for a freeze-dried specimen, while Figure II–20b represents the PSD function, showing a well defined single pore population (with an average diameter of 32 nm) that is typical of the clay matrix [Robinet et al., 2012, Delage et al., 2016].

To characterise the water retention properties of the COx claystone, a whole array of experimental measurements was carried out to define the relationship between suction and water saturation using different techniques [Hoxha and Auvray, 2005, Pham, 2010, Boulin, 2008], as depicted in Figure II–21b. The main method consists of monitoring the mass evolution of a sample submitted to a controlled relative humidity atmosphere, which gives the progress of the wetting/drying process till an equilibrium state is reached. It is worth noting that hysteresis effects can be observed depending on the hydration path followed. As for the analysis of the gas entry pressure measurements, it reveals a first group of values between 0.3 and 3 MPa which are representative of damaged material and other values of the order of or greater than 5 MPa (Figure II–22b) that can be considered as values approaching the gas entry pressure in sound COx claystone. Nevertheless, the knowledge acquired on the pore network connectivity [Robinet, 2008, Song et al., 2015], indicates that these values are probably a minimum for the breakthrough pressure in COx which would be between 6 and 10 MPa. From all these available data, water retention curves are fitted with the van Genuchten's Equation (II–12), considering a calibration parameter $\mathcal{N} = 1.49$ and a gas entry parameter $P_r = 15$ MPa [Charlier et al., 2013, Gerard et al., 2014, Pardoen et al., 2015b].

As mentioned in section 4.3.4, many data are available on the gas and water permeability in the COx claystone, either perpendicular or parallel to the bedding. In Figure II–23b, the selected data and the fitting curves for relative permeability are given, using the widely used van Genuchten's formulation (II–18) for water and either the Mualem's formulation (II–20) [Gerard et al., 2008] or a power law function similar to Equation (II–21) [Charlier et al., 2013, Gerard et al., 2014] for gas, which can be reminded as:

$$k_{r_w} = \sqrt{S_{r_w}}\left(1-\left(1-S_{r_w}^{\frac{1}{\mathcal{M}}}\right)^{\mathcal{M}}\right)^2 \qquad k_{r_g} = \sqrt{S_{r_g}}\left(1-S_{r_w}^{\frac{1}{\mathcal{M}}}\right)^{2\mathcal{M}} \qquad k_{r_g} = (1-S_r^*)^{\mathcal{L}} \quad \text{(II–25)}$$

where k_{r_w} and k_{r_g} are the water and gas relative permeability, S_{r_w} and S_{r_g} are the water and gas degrees of saturation, and $\mathcal{M}$, $\mathcal{L}$ are material parameters equal to 0.32885 and 3 respectively.

When measuring gas permeability, a correction should be applied considering the Klinkenberg effect [Klinkenberg, 1941], which can be seen as a sliding mechanism of the gaseous particles on the pore wall of the material, which has the effect of reducing the permeability of the gaseous phase. This process is all the more important that the size of the pores of the material is small, which is the case for clayey rocks, and the injected gas pressure is low. It has however been observed [Boulin et al., 2008a, Didier, 2012] that the corrections to be added to effective gas permeability as saturation increases remains very small in most cases and integrated into the natural dispersion of the material.

5.4 Gas transport by pathway dilation and macroscopic fracturing

This section investigates the gas transport by means of gas-filled pathway or macroscopic fracturing, from the perspective of the gas. The main principles behind this mode of gas migration are presented, and the prevalent results from experimental investigations at the scale of the laboratory and at larger *in situ* scale for both the Boom Clay and the COx claystone are subsequently exposed.

5.4.1 Process overview

Gas-induced failure of clay-rich barrier materials is controlled by the interplay between water retention behaviour and deformation behaviour. On the one hand, clayey materials exhibit generally a high water retention capacity, inherently associated with a high gas entry pressure value, which originates from their special microstructure, consisting of a fine-grained solid skeleton and a poorly connected pore network, as evidenced in Chapter 4. On the other hand, the mechanical characteristics of clay-rich materials cover a wide property range in terms of strength and stiffness, representing the full spectrum of deformation behaviour in the transition between soft soils and weak rocks [Gens, 2013].

Thence, when an initially water-saturated clay host rock with a high water retention capacity is invaded by a gas phase, the gas generation rate may exceed the capacity for pore water displacement by visco-capillary or the gas entry pressure may exceed the strength of the material, giving rise to local failure. The propagation of the damage front takes place by subcritical crack growth, *i.e.* pathway development, if the gas production rate is balanced steadily by the newly created pore volume at the crack tip, or by supercritical crack growth, *i.e.*gas fracturing, for rapid gas pressure build-up [Valko and Economides, 1997]. From a phenomenological perspective, the former is still controlled by phase interactions between wetting and non-wetting fluids (visco-capillary forces), while the latter can be seen as a single-phase flow process.

In particular, separation planes such as bedding planes or pre-existing fractures in a porous medium represent preferred weaknesses for the process of gas-driven microfracturing. These are characterised by abrupt changes in stiffness and material strength and may exhibit a very small, but well-connected fraction of the total pore volume. When gas invades such a discontinuity of an initially fully water-saturated porous material, further hydro-mechanical interactions, either dilatancy-controlled gas flows (pathway dilation) or gas flows in macroscopic fractures (gas fracturing), may enhance gas transport along discrete features. The conceptual model of gas transport in deformable porous media is essentially an extension thereof, assuming that the porous medium can undergo irreversible deformation. As a consequence, an opening of the pore space is noted and the transport properties of the solid phase *i.e.* rock permeability, relative permeability, capillary pressure relationship, can no longer be viewed as invariants since they depend on the state of deformation of the rock.

In the past two decades, comprehensive knowledge has been collected from the laboratory scale to larger scales to catch the fracturing pressure, which refers to the capillary pressure necessary to obtain a gas breakthrough through the material, and the related transfer properties variation, in response to gas

invasion processes. The most common test characterising this mode of gas transport consists in injecting gas at one side of a sample and detecting the breakthrough of the gas at the opposite side. Depending on the injection conditions, whether at controlled pressure or injection rate, or at constant volume, the gradual development of preferential flow paths can be demonstrated. Beyond the injection kinetics, these lab tests also show the dependence of gas flow to other experimental factors, such as the mechanical loading [Horseman et al., 1999], the sample size [Duveau et al., 2011], the initial nature, saturation [Graham et al., 2002] or damage [Davy et al., 2007] of the sample, or the presence of interfaces between materials [Davy et al., 2009]. Large-scale *in situ* experiments consisting typically in injecting gas in chambers located in boreholes and isolated by packers, have highlighted the creation of preferential paths in the host rocks, that are in agreement with laboratory observations. In addition, such an up-scaling process raises questions about the scale effect of such experiments, that could result in a more extensive heterogeneity of the rock mass and thus in a larger probability of development of preferential pathways at the scale of the repository.

5.4.2 Boom Clay

A significant body of gas experimentation from laboratory scale to field scale was conducted on Boom Clay in the 1990s, particularly within the framework of the MEGAS [Volckaert et al., 1995, Ortiz et al., 1997] and PROGRESS [Rodwell, 2000] EC projects, periodically enriched over the last decades by more recent studies [Harrington et al., 2012b, Gonzalez-Blanco, 2017].

Laboratory investigation

Primary laboratory findings from [Horseman and Harrington, 1994] and [Volckaert et al., 1995] demonstrated that, specifically for Boom Clay, gas breakthrough pressure could be directly related by several empirical relationships to the hydraulic conductivity or the intrinsic permeability, as had earlier been postulated by [Davies, 1991] for salt.

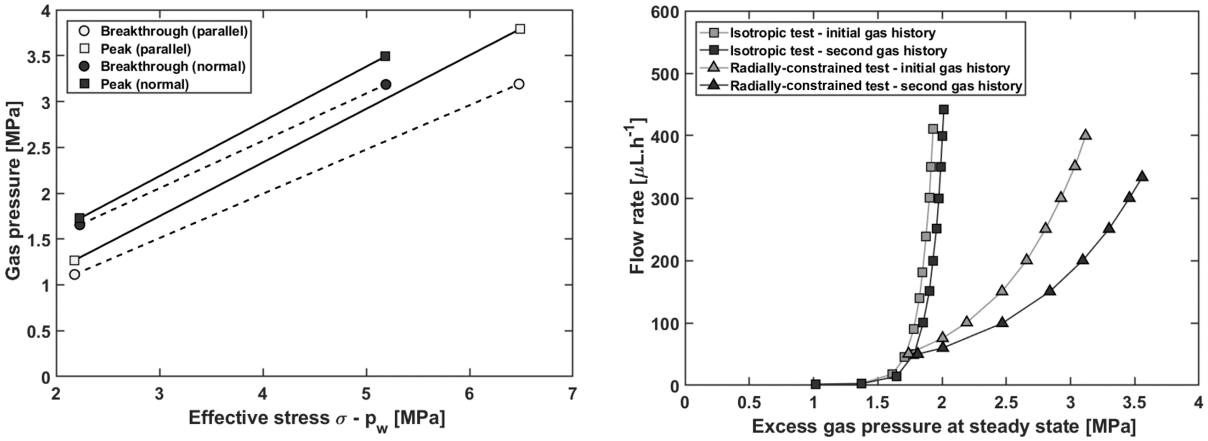

(a) (b)

Figure II–24 – Cross-plot (a) of data showing average breakthrough and peak gas pressures against effective stress for samples normal and parallel to bedding, and (b) of steady state gas flow data for comparable flow rates from both isotropic and radially-constrained tests, *after* [Rodwell, 2000].

Gas injection experiments conducted by the BGS [Harrington and Horseman, 1999] and the SCK•CEN [Ortiz et al., 2002], as part of the PROGRESS EC project [Rodwell, 2000] both indicate that gas pressure has to overcome a threshold before getting an advective mobility for the gas, and that gas flows tend to cease if pressure is allowed to fall below this threshold again. According to the authors, this could demonstrate hydro-mechanical coupling of gas flow and be an indication of possible transfers by pathway development. Gas breakthrough pressures and gas permeabilities were measured for samples under

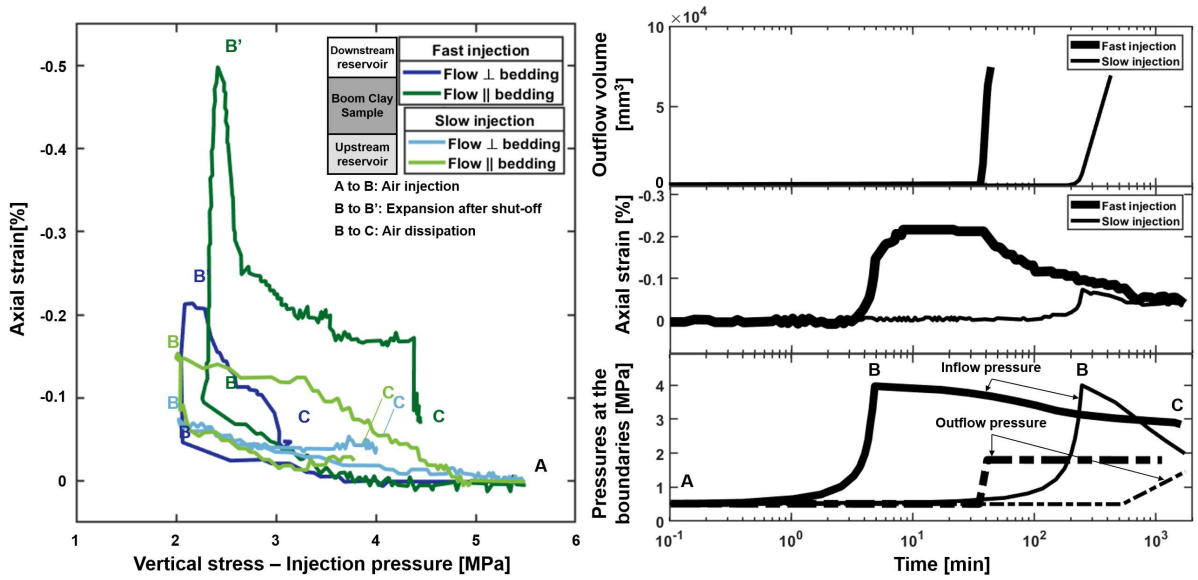

(a) (b)

Figure II–25 – Air injection tests under oedometer conditions [Gonzalez-Blanco et al., 2016, Gonzalez-Blanco, 2017]: (a) evolution of the axial strains with vertical stresses for slow and fast injection rates, and (b) time evolutions of outflow volume (top) axial strain (middle) and pressures at the injection and recovery boundaries (bottom) for the two injection rates.

external boundary conditions and under flow either perpendicular and parallel to the bedding (BGS), or only perpendicular to the bedding (SCK•CEN). Gas breakthrough pressures for a virgin clay are found to vary from 0.48 to 3.57 MPa and from 0.47 to 2.25 MPa respectively, while effective gas permeability measurements range from 6.6×10^{-19} to 0.5×10^{-20} m^2 and from 0.7×10^{-20} to 9.5×10^{-20} m^2 respectively. The cross-plot of the average values for breakthrough and peak pressures against effective stress in Figure II–24a provides approximate trends for estimating breakthrough and peak gas pressures for flow parallel and normal to bedding at repository depth [Wiseall et al., 2015b].

Other observations have also evidenced the effect of boundary conditions imposition with higher gas pressures occurring at lower flow rates for the radially-constrained samples as illustrated in Figure II–24b, which attests to the clear correlation between the nature of the stress field and boundary conditions applied to the sample and the processes governing the migration of gas through Boom Clay. It is worth noting that a series of scoping gas tests have been recently performed on Boom Clay, in the context of Dutch GDF [2], assuming greater repository depths [Harrington et al., 2017b] which has confirmed the influence of effective stress (and consolidation history) upon gas entry properties of the clay.

In order to assess the size and distribution of dilatant pathways during gas flows, nano-particle tracers have been used during gas injection testing of Boom Clay samples that were subsequently splitted and examined [Harrington et al., 2012b]. Observations indicate that the nano-particles have been transported along transient pathways, through the clay matrix and around boundaries of coarser grains, during gas injection. It would appear that these fractures then sealed, trapping any nano-particles that were being transported in the gas stream. The size of the trapped nano-particle aggregates thence point to a minimum aperture of the pathways generated during gas transport.

The impact of gas transport on mechanical integrity of Boom Clay has been investigated by [Gonzalez-Blanco, 2017], by performing slow (2 mL/min) and fast (100 mL/min) air injection tests under oedometer conditions on initially saturated samples with bedding planes oriented parallel and normal to the direc-

2. The OPERA project is the 3^{rd} national program managed by COVRA in the Netherlands during the period 2011 to 2017.

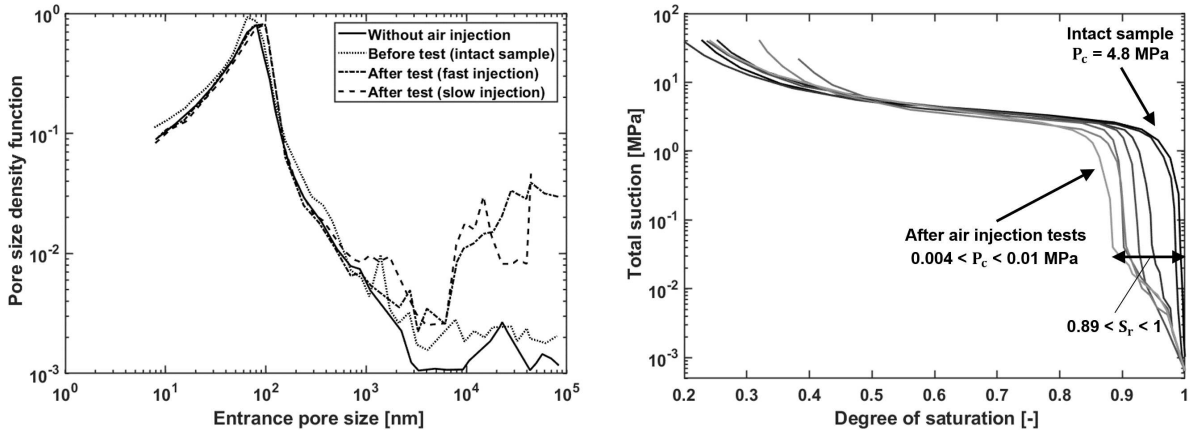

Figure II–26 – Changes in Boom Clay properties between intact samples and after air injection tests [Gonzalez-Blanco et al., 2016]: (a) pore size distribution curves, (b) water retention curves, with the gas entry value determined with the dominant entrance pore size.

tion of water and gas flows. Concretely, the air pressure at the upstream boundary was increased in time (A–B in the figure II–25), followed by shut-off (point B) and dissipation at closed air injection line (B–C). This experiment will be the object of specific application of the multi-scale model developed in Part IV, where it will be properly detailed [Gonzalez-Blanco et al., 2016]. Here, only selected relevant results are presented.

The main finding put in evidence the fundamental role of natural discontinuities in the development of gas flows which tend to take advantage of these existing bedding planes. As depicted in Figure II–25a, samples with bedding planes normal to flows undergo higher expansions on gas equalisation (A-B) and larger compression on the gas dissipation stage (B-C) than samples with bedding planes parallel to the direction of gas flow, which means that gas pathways develop more easily along bedding planes in these oedometric conditions.

Then, taking a look at the results recorded during the air injection and dissipation stages with bedding planes parallel to flow, Figure II–25b shows the time evolution of the air injection pressure at the upstream boundary and the outflow pressure and volume at the downstream boundary, jointly with the average axial strain. The time of breakthrough is clearly visible through a rapid increase of the flow rate through the sample and an increase of the outflow pressure in the downstream reservoir. Note that the increase in injection pressure is accompanied by expansion, *i.e.* negative axial strains in Figure II–25a. These results suggest that some changes in the pore size distribution of the samples could take place during injection. As presented in Figure II–26a, a new family of large pores associated with the expansion undergone by the material, which was not detected on intact samples, is observed. This new class of porosity can be interpreted in terms of permeability and water retention properties of the Boom Clay. The increase in intrinsic permeability of the matrix as a function of void ratio has already been presented in Figure II–22a, while Figure II–26b presents the modification of the water retention curve between intact sample and after air injection tests, and the resulting estimation of the gas entry pressure.

All in all, the results confirm that deformation history should play a role on gas transport properties which are then dependent on the stresses rather than on the material itself.

In situ investigation

Field-scale gas injection testing, referred to as the E4 and E5 *in situ* experiments was conducted in Boom Clay using Helium, as part of the MEGAS EC project [Volckaert et al., 1995, Ortiz et al., 1997]. The former consists of a vertical piezometer with several injection filters installed under the bottom of the first shaft at HADES URL, while the latter is composed of four horizontally installed piezometers along

the first meters of the test drift, the central one being for gas injection and the other three for monitoring. An overview of the set-ups and locations is given in Figure II–27.

A number of key observations were reported from the gas injection through two different filters of the E4 set-up, including a lower gas breakthrough pressure than expected, around 0.6 MPa. It may come from the damage resulting from drilling of the borehole, though it was suggested that convergence over the long-term would minimise this behaviour. At least one preferential pathway was generated along the length of the piezometer which caused the test to be stopped.

As for the E5 set-up, hydraulic testing was first conducted to determine baseline parameters such as total stress, pore pressure and water permeability, which was followed by injection of Helium by increments of 0.1 MPa, until breakthrough occurs. A preferential pathway was detected in a neighbouring filter on the same piezometer, in which gas inflow of a similar magnitude to those encountered in laboratory testing was observed.

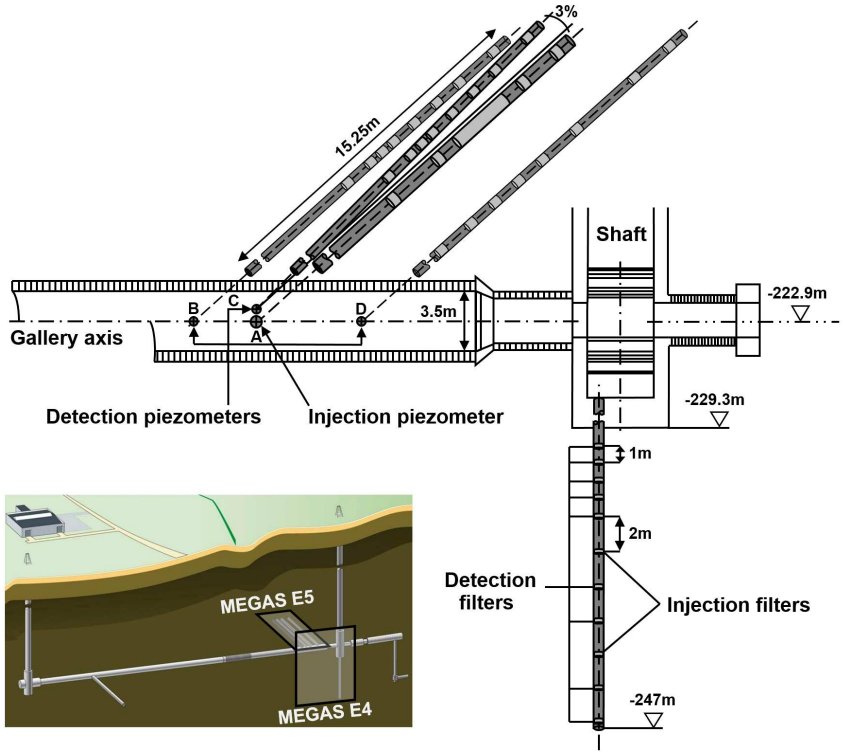

Figure II–27 – Set-up and location of the E4 and E5 gas injection experiments in the HADES URL, *modified after* [Volckaert et al., 1995].

Additional *in situ* testing were conducted to examine the self-sealing properties of the formation [Rodwell, 2000, Ortiz et al., 2002]. Further details about the design and course of the *in situ* tests in Boom Clay will be given in section 10.1.1, as part of the numerical modelling of these experiments.

5.4.3 COx claystone

Many tests have been conducted to explore the consequences of gas breakthrough on the hydro-mechanical behaviour of COx claystone and to detect possible modifications of fabric. In parallel, several *in situ* experiments dedicated to the study of gas injection and gas fracturing in the COx claystone have been carried out in the Meuse/Haute-Marne URL and from the surface. They have been implemented with the particular objective of evaluating the influence of the gas injection rate on the threshold gas fracturing pressure, the consequences on the rock permeability.

Laboratory investigation

First of all, estimated values for dry gas permeability of the order of 10^{-18} m^2 were obtained from gas flow tests on COx samples, using a triaxial cell to provide isotropic confinement at stress conditions below these found *in situ* [Boulin et al., 2008a].

Then, a series of experiments examining the gas transport through samples of COx claystone were performed using either an isotropic loading arrangement [Harrington et al., 2012a, Jacops et al., 2014] or a triaxial permeameter cell [Harrington et al., 2013, Cuss et al., 2014a]. Unexpectedly low values of excess gas entry pressure (2 MPa) was measured in the former case, whereas a more conventional value in excess of 6 MPa was estimated in the latter. It has been suggested that the low entry pressures relate to localised features within the claystone, and that the major gas penetration occurring in the second case was well attributable to pathway dilatancy.

In addition, gas breakthrough was estimated to happen at 10.5 MPa and 6 MPa as a result of triaxial testing of COx samples undertaken in two independent experimental studies [Cuss and Harrington, 2011, Cuss et al., 2014a]. A secondary evidence of gas entry was identified for one of these two experiments. A clear dilation deformation was however detected at the onset of gas flow for both experimental set-ups, interpreted as being the result of the formation of dilatant pathways. The three-stage conceptual model of the onset and establishment of a gas flow network in COx claystone presented in Figure II–28 derives from these observations.

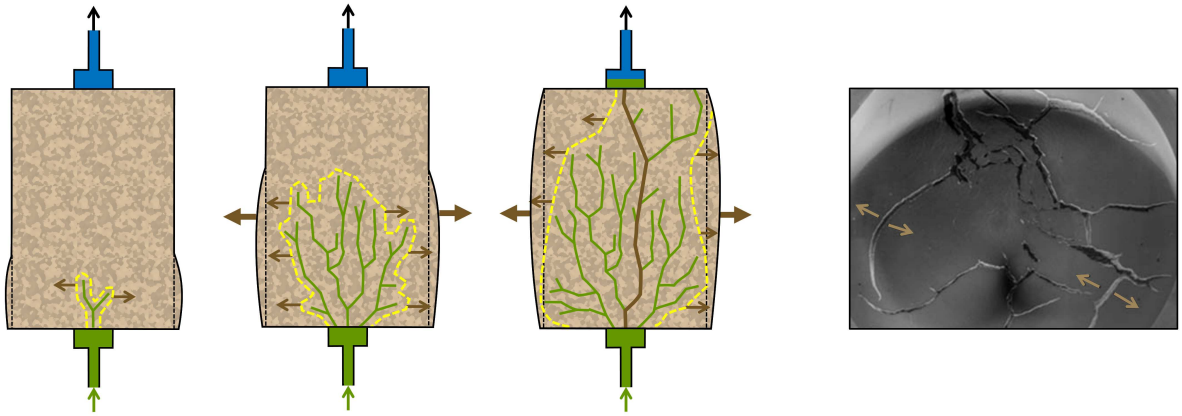

(a) (b)

Figure II–28 – (a) Conceptual model of the onset of gas flow in a COx sample, as idealised by [Cuss et al., 2014a], confronted with (b) the experimental observation of gas-induced fracturing on clay-rich materials, *from* [Wiseall et al., 2015b].

The development of preferential flow paths could be explained by the presence of discontinuities in the material, prior to gas injection. Although closed during the confinement of the sample, such discontinuities can open under the action of gas pressure and give rise to flow channels. The fact that increasing confining pressure results in a decrease in gas permeability parallel to the bedding plane is reported in [Zhang and Rothfuchs, 2004]. This effect was further investigated from gas permeability measurements performed on samples of COx argillite initially fractured by traction during Brazilian tests [Davy et al., 2007]. By comparing reported gas breakthrough pressures from test data compiled from triaxial permeameter and isotropic tests [Harrington et al., 2017a], the observations indicate that sample damage may be one possible explanation for the discrepancy between low and high entry pressures in COx claystone, and that gas entry pressures in excess of 5 MPa may well reflect the properties of intact claystone at *in situ* conditions.

In situ investigation

A first Gas Threshold Pressure Test (GTPT) was conducted in a 5-metre interval of a vertical borehole drilled at the Meuse/Haute-Marne URL to better understand gas transport processes in the low-permeability clay formation under constant gas injection conditions [Senger et al., 2006]. The rapid injection has led to a dynamic stressing of the rock, with a gas fracturing observed at a gas pressure in the chamber of about 11.9 MPa, as shown in Figure II–29a.

The CDZ *in situ* experiment is dedicated to study the evolution of the EDZ hydrogeological properties of the COx claystone under mechanical compression and artificial hydration [de La Vaissière et al., 2015]. The experimental layout consists of six boreholes (CDZ1301 to CDZ1306) equipped with multi-packer systems for hydraulic measurement, and surrounded by additional boreholes providing extensometer and seismic tomography measurements [de La Vaissière et al., 2014b]. Gas conductivity measurements were used to establish the initial value of the permeability and the connectivity of the damaged zone through interference testing. These results have particularly evidenced a well-interconnected fracture zone with high hydraulic conductivity values, that tends to progressively close with the increasing mechanical stress applied on the drift wall.

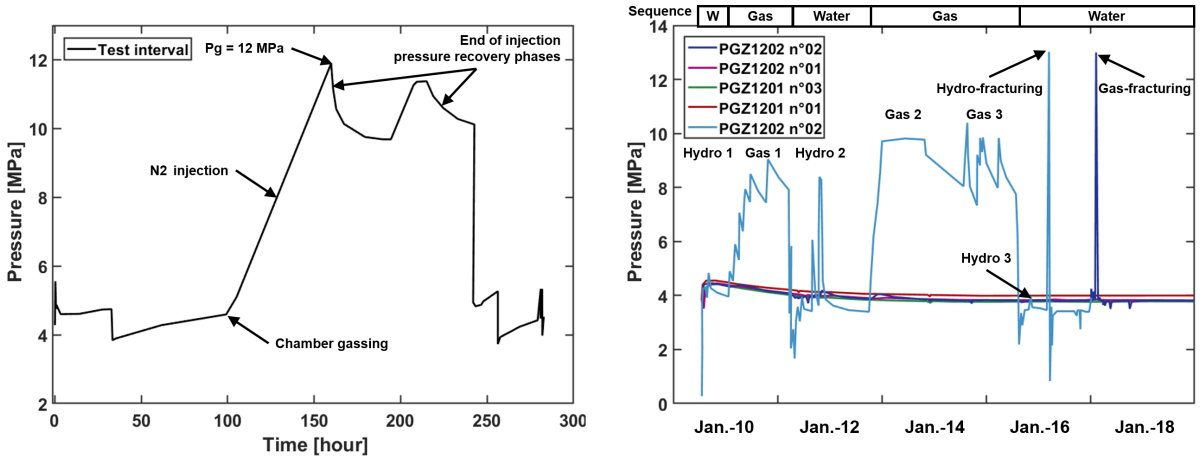

(a) (b)

Figure II–29 – Measurements of the pressure in boreholes during gas injection tests: (a) gas fracturing test performed from the surface (EST363), *modified after* [Senger et al., 2006], (b) sequence of water and gas injection tests performed in the URL (PGZ-1), *modified after* [de La Vaissière et al., 2014b].

The PGZ-1 *in situ* experiment is dedicated to identify the gas percolation mechanisms into the sound COx host rock, for different pressure levels. The experimental layout consists of two multi-packer equipped boreholes (PGZ1201 and PGZ1202) drilled parallel to the direction of the *in situ* maximal stress from the GED drift, and a third borehole (PGZ1031) for axial deformation monitoring, drilled at an inclination of 48° from the GEX drift, as illustrated in Figure II–30. A continuous sequence of alternating water and nitrogen injection tests was conducted in the second interval of borehole PGZ1201. The first two injection tests aimed at characterising the regimes of gas transfer in the saturated claystone while remaining under fracturing pressure, have demonstrated that a gas pressure of the order of 9.1 MPa (GAS1) or 9.8 MPa (GAS2) did not induce the initiation of a fracture [Harrington et al., 2012a, de La Vaissière et al., 2014a]. In a second phase, gas injections at a relatively slow flow rate of 1 mL/min (GAS3) and at high flow rates of about 500 mL/min (GAS-FRAC) were imposed. Gas fracturing was detected at a pressure of 10.45 MPa and 14.1 MPa respectively, that is to say below and above the minimum principal stress ($\sim$ 12.5 MPa). These gas injection tests confirm that the gas-fracture threshold depends not only on the stress fields around the injection zone but also on the kinetics of the fluid injection rate and certainly on the geometry of the damaged zone around the drift. For high gas injection rates, the

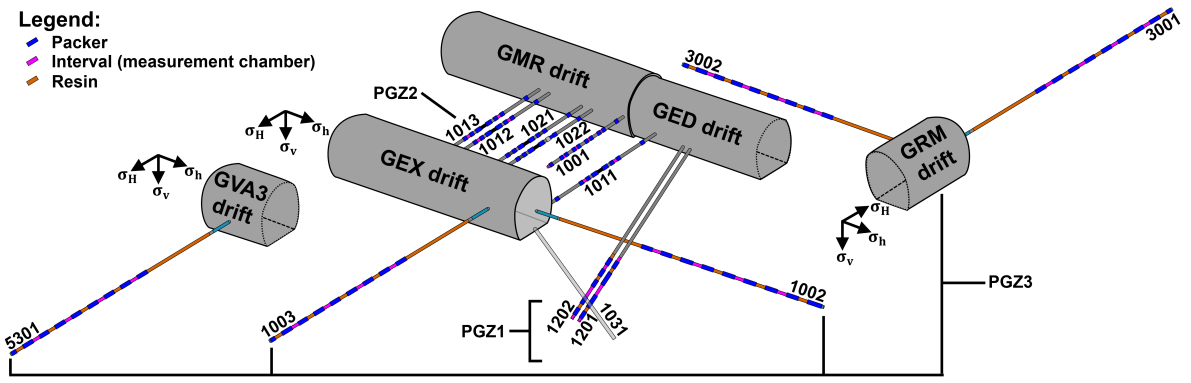

Figure II–30 – Set-up and location of the *in situ* gas injection experiments in the Meuse/Haute-Marne URL, *modified after* [de La Vaissière et al., 2014b, de La Vaissiere and Vinsot, 2019].

gas fracturing pressure is consistent with the natural minor principal stress and the estimated level of the material tensile strength, while for low injection rates, gas starts to penetrate the surrounding media before gas fracturing initiation and in particular the damaged zone which is more accessible to gas due to lower gas entry pressure [de La Vaissière et al., 2019].

The PGZ-2 *in situ* experiment is dedicated to the impact of gas production on the hydro-mechanical behaviour of the plugs designed to close the storage galleries, by studying the competing effects of hydration from the host rock (resaturation) and gas injection (desaturation) [Gatabin et al., 2016]. The experimental layout consists of two parallel boreholes (PGZ1013 and PGZ1011) drilled between the GEX and GMR/GED galleries, and both equipped with a bentonite plug for monitoring hydration and gas injection effect respectively, and a third borehole (PGZ1001) drilled from the GMR gallery parallel to the first two boreholes, to measure the hydraulic head gradient (Figure II–30). A gas breakthrough with a small differential gas pressure between 0.5 to 1.5 MPa is noted, well below the swelling pressure set between 4.5 to 5.5 MPa. The gas injection sequence has revealed that the gas escaped on each side of the core of the plug at the interface or through the borehole damaged zone [de La Vaissière, 2013].

The PGZ-3 *in situ* experiment has been conducted more recently in the continuity of PGZ-1 campaign, with the objective of studying the effect of the stress orientation and of gas injection kinetics on the gas fracturing process [de La Vaissière, 2021]. The experimental layout consists of five identical boreholes equipped with a multi-packer system to monitor water and gas pressure, drilled parallel to the minor (PGZ1002) or major (PGZ1003) horizontal stress from the GEX drift, parallel to the major (PGZ3001) or minor (PGZ3002) horizontal stress from the GRM drift, and parallel to the major horizontal stress from the GVA3 drift (PGZ5301), as reported in Figure II–30. The test protocol includes phases of slow or fast gas injection at constant flow rate (1 mLn/min) through the intervals of the boreholes, until a fracture is created. Then the system undergoes a pressure recovery stage, followed by a new phase of injection with the aim of reopening the fracture to identify its closure pressure and deduce if possible its orientation. This sequence is repeated alternately several times. To date, a water permeability testing campaign has been conducted in the PGZ1002 and PGZ1003 boreholes converging to a hydraulic conductivity value close to $4\times10^{-13}\ \frac{m}{s}$. Three series of fast gas injection tests have also been performed in one interval of PGZ1002 and PGZ1003 boreholes, with a maximum gas pressure achieved between 13.01 to 14.53 MPa.

5.5 Synthesis for the clay host formations

In brief, the present chapter gives a state-of-the-art characterisation of the gas transport processes in low-permeability clay materials based on experimental observations. These latter have especially

evidenced four main mechanisms as a function of the increasing injection pressure, leading to gas breakthrough in the material.

When the amount of gas remains marginal, the gas is dissolved in solution and primarily transported via diffusion within the liquid phase. Comprehensive data sets of diffusion coefficients for the principal dissolved gases have been acquired for Boom Clay and the Cox claystone, as summarised in Table II–2.

Once the injection pressure exceeds the capillary threshold pressure known as the gas entry pressure, the gas is transported via visco-capillary two-phase flows, which are mainly restricted to the sparse network of macropores, because micro- and mesopores are hardly invaded by the gas phase due to their high gas entry pressure. Multiphase flows of water and gas in porous media are governed by the intrinsic permeability of the formation (see previous Chapter 4), the permeability-saturation relationships (relative permeability curves), and the capillary pressure-saturation relationship (water retention curve). Experimental data for these curves have been collected for both the Boom Clay and the Cox claystone, on which different models can be fitted with the respective appropriate parameters given in Table II–3.

Table II–3 – Summary of the fitting parameters for the retention curve and the relative permeability curves of Boom Clay and Callovo-Oxfordian claystone.

Host formations			Boom Clay	Callovo-Oxfordian claystone
Property	Symbol	Unit		
van Genuchten's retention curve − Equation (II–12)				
Max. degree of water saturation	S_{max}	$[-]$	1	1
Residual degree of water saturation	$S_{r_{res}}$	$[-]$	$0.01 - 0.2$	0.01
Gas entry pressure (1^{st} coeff. of S_{r_w})	P_r	$[MPa]$	$10 - 16.6$	15
Model parameter (2^{nd} coeff. of S_{r_w})	$\mathcal{N}$	$[-]$	2.5	1.49
van Genuchten's relative permeability curves − Equations (II–18) and (II–20)				
Model parameter (coeff. of k_{r_w} and k_{r_g})	$\mathcal{M}$	$[-]$	$0.6 - 1$	0.33
Brooks and Corey's water relative permeability curve − Equation (II–19)				
Model parameter (coeff. of k_{r_w})	$\mathcal{K}$	$[-]$	1.48	–
Polynomial gas relative permeability curve − Equation (II–21)				
Model parameter (coeff. of k_{r_g})	$\mathcal{L}$	$[-]$	$2.8 - 3.0$	3.0

Once the injection pressure reaches a certain breakthrough pressure, the gas is transported through the initiation of preferential flow pathways within the rock formation. The laboratory experiments on clay-rich rocks indicate that gas pressures, close to the applied confining pressure are required to invade the fully saturated material. In response to gas invasion, the material first exhibits a continuous volume expansion as long as the gas front propagates through the specimen, followed by contraction when gas breakthrough is reached. In addition to the heterogeneity and bedding fissility of the material, the gas-induced failure is also controlled by the speed of gas pressure build-up and by the applied boundary conditions. A phenomenon of gradual damage evolution is observed at low pressure build-up rates and high confining stresses, which may be attributed to the process of pathway dilatancy, *i.e.* a subcritical crack growth that balances the gas production rate. As for sudden fracture initiation, this phenomenon seems to be triggered by high pressure build-up rates or sudden changes of the confining pressure, which may be attributed to the process of gas fracturing, *i.e.* a supercritical crack growth driven by high uniform gas pressure.

In situ investigation at a larger scale has also been conducted in order to complete this understanding of the transfer mechanisms in clayey rocks and to attest that it is transposable to the scale and to the

mechanical loading conditions characteristic of a disposal site. These experiments highlight the strong hydro-mechanical couplings at work during gas transfer processes, lower breakthrough pressures than in the lab, given the scale effect and the discontinuities created during the boreholes excavation, as well as the important role played by the interfaces between materials as preferential flow paths for gas.

All in all, the analysis of gas transport processes detailed in this chapter clearly highlights how gas migration in clayey rocks relies on various and complex coupled phenomena. It is on the basis of this characterisation that hydro-mechanical numerical models capable of reproducing the behaviour of a clayey rock mass subjected to continuous gas production are implemented. Owing to the importance of the mechanical behaviour of clayey rocks to induce the development of preferential flow pathways, the next chapter of this literature review intends to examine how these hydro-mechanical couplings are taken into account from a numerical point of view.

6. Modelling of gas transport processes

Under repository conditions, the geological barrier system undergoes complex and strongly coupled hydro-mechanical processes. In this context, numerical modelling turns out to be an effective technique, in order to predict the overall barrier performance throughout the system lifespan. Regarding more particularly the gas transfer mechanisms, a number of numerical modelling techniques are currently used for the interpretation of experimental gas test results or the prediction of gas migration in host rock formations. The four main processes experimentally identified in the previous Chapter 5 (Figure II–11) tend to develop gradually in clayey materials with increasing gas pressure, which requires specific and adapted modelling approaches.

For gas pressure lower than a threshold pressure, the transport of gas in porous media is captured by classical hydro-mechanical two-phase flow models that commonly exist in geomechanics [Thomas and He, 1995, Olivella et al., 1996, Collin et al., 2002]. The first objective of the present chapter is thus to present the general framework adopted in this work to model the hydro-mechanical behaviour of multiphase porous media, to which the candidate clay rocks for hosting repositories belong (Section 6.1 to 6.5). First, some general concepts related to the theory of partially saturated porous media are presented. The adopted representation allows continuum mechanics to be applied, and a proper referential has also to be defined. Then, the balance equations governing the porous medium are established. A number of constitutive laws is required to reproduce the behaviour of geomaterials in partially saturated conditions. They include a multiphase flow model, together with a water retention model and a mechanical constitutive model. The necessary restrictions ensuring the thermodynamic equilibrium between the different phases of the porous medium are also expressed. Finally, the theoretical developments leading to the formulation of a coupled finite element, including the linearisation of the field equations and the finite element discretisation are proposed.

Nevertheless, these classical models are not able as such to reproduce all the features of the gas flow processes. Beyond a certain threshold pressure, preferential flow pathways for gas develop in clay rocks, which are strongly dependent on the heterogeneity and microstructure of the material, as well as chosen experimental conditions. Such behaviour can not be captured by conventional two-phase flow models that include constant flow parameters. The second objective of this chapter is thus to review the advanced hydro-mechanical models that are available to improve the modelling response by introducing stronger couplings between the gas flow and the mechanical behaviour of the clayey material (Section 6.6).

Rather than any original contribution, this chapter set the basis for the numerical developments introduced in Parts III and IV.

6.1 General framework

This section constitutes a short summary which highlights fundamental basics of the macroscopic theory implemented in the `LAGAMINE` code that are useful for the present work. The interested reader should refer to [Charlier, 1987, Barnichon, 1998, Collin, 2003] for an extensive description of the code.

6.1.1 Porous medium representation

The structure of geomaterials such as clay rocks is rather complex to describe accurately. It is commonly assumed that such materials approximate a porous medium, composed of several phases: solid, fluid and gas [Coussy and Ulm, 1995, Lewis and Schrefler, 1998]. Therefore, in the theory of the porous media, an elementary volume $d\Omega$ of a granular material (see Figure II–31a) can be defined as the superposition in time and space of different constituents:

- **The solid skeleton**, which constitutes the so-called matrix of the material and corresponds to a continuous juxtaposition of solid grains. The volume of the solid portion is equal to the volume of the grains, denoted $d\Omega_s$, and its specific mass is noted as ρ_s. Since solid grains are usually deemed incompressible, the overall behaviour of the material is due to the rearrangement of the grains and not to their deformations.
- **The void volume**, which characterises the porous space between the grains filled with fluids of specific mass ρ_f in liquid and/or gaseous phases. If the void volume is completely filled by a liquid phase, then the porous medium is defined as saturated whereas if it is filled by a combination of fluids, then it is said to be unsaturated or partially saturated. In this case, the fluid mixture is composed of wetting and non-wetting fluids corresponding to the liquid and the gaseous phases, respectively. The present work specifically deals with this latter case, involving a binary fluid mixture composed of water and specific gas such as Hydrogen.

Since a precise description of this system turns out to be an arduous task, three main modelling approach exist to describe the porous media in a simplified manner. Basically, they propose to substitute the real discontinuous porous medium with an idealised homogeneous superposition of several continua.

- **Macroscopic theories**: In macroscopic theories, based on the consolidation theory introduced by Terzaghi [Terzaghi, 1936] and further extended by Biot [Biot, 1941, Biot, 1956, Biot, 1962] with additional contributions of Coussy [Coussy and Ulm, 1995] and Dormieux [Dormieux et al., 1995], the porous medium and all the related concepts (such as stresses) are examined at the macroscopic scale. In addition, the balance equations are derived for the entire porous medium, without treating the different phases and species separately.
- **Averaging theories**: In averaging theories [Hassanizadeh and Gray, 1979a, Hassanizadeh and Gray, 1979b], the porous medium is studied at two structural levels, namely a micro-scale, corresponding to the pore level and a macro-scale, corresponding to the Representative Element Volume (REV). At the microscopic level, the system is symbolised as the superposition of interpenetrating continua that occupy only a part of the space and separated from the others by interfaces with their own thermodynamic properties. The balance equations and eventually the constitutive relationships are introduced at this scale. Averaging techniques are then applied to get the homogenised field equations over the REV.
- **Theories of mixtures**: In theories of mixture, based on the ideas and methods of modern continuum mechanics [Truesdell and Noll, 1965], the porous medium is studied at the macroscopic scale but the balance equations are expressed for each phase separately. Every point of the idealised system consists of a mixture of phases because all phases are assumed to occupy the same region of space simultaneously, as an overlapping of different continua (see Figure II–31b).

In this part of the work, the homogenisation of the real discontinuous porous medium relies on a theory of mixture at macroscopic scale. This approach is extended to multiphase porous media through the definition of volume fractions [Bowen, 1980, Coussy and Ulm, 1995]. This concept allows continuum mechanics to be applied by creating some homogenised continua of reduced densities.

The volume fraction Ξ_π of the phase π is defined as:

$$\Xi_\pi = \frac{\Omega_\pi}{\Omega} \tag{II–26}$$

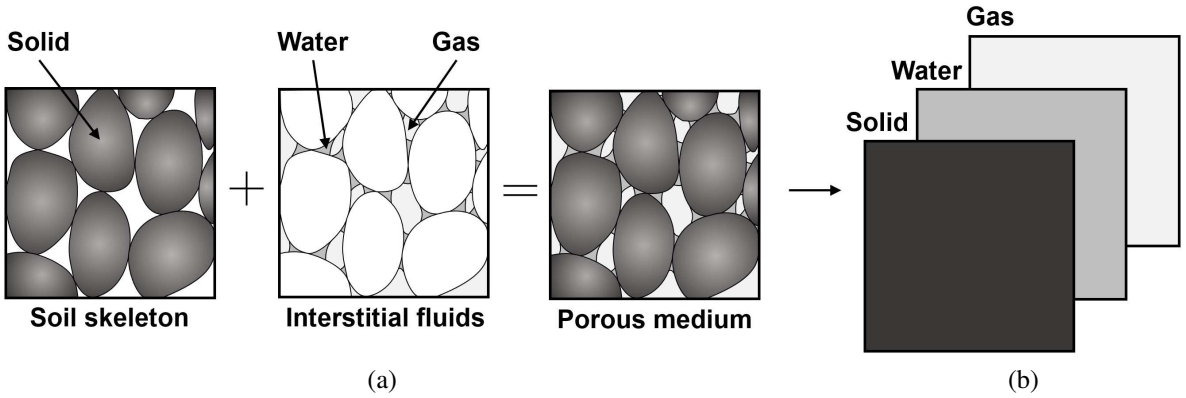

Figure II–31 – Representation of a porous medium: (a) cross-section of a representative element volume, *after* [Barnichon, 1998], and (b) definition of superimposed continua, according to theories of mixtures.

where Ω_π is the volume of the phase π and Ω is the total volume of the control space, which corresponds to the sum of the different volume fractions of all phases and is equal to 1. In particular, this work investigates the gas transfers in clay materials, which are represented as three-phase porous media made of solid, liquid and gaseous phases. Accordingly, the following volume fractions are defined:

$$\Xi_s = 1 - \phi \qquad \Xi_l = S_r \phi \qquad \Xi_g = (1 - S_r)\phi \tag{II–27}$$

where the subscripts s, l and g identify the solid, liquid and gas phases respectively, ϕ is the total porosity defined as the ratio between the total void volume Ω_v and the total volume Ω, such that:

$$\phi = \frac{\Omega_v}{\Omega} = \frac{\Omega_v}{\Omega_s + \Omega_v} = \frac{\Omega_l + \Omega_g}{\Omega_s + \Omega_l + \Omega_v} \qquad \in [0,1] \tag{II–28}$$

and S_r is the water saturation degree, defined as the ratio between the volume of the liquid phase Ω_l and the porous volume Ω_v, such that:

$$S_r = \frac{\Omega_l}{\Omega_v} \qquad \in [0,1] \tag{II–29}$$

6.1.2 Aspects of continuum mechanics

It is possible to use continuum mechanics with the adopted representation of the porous medium. One can hence emphasise the notion of internal stress in solids, from a random cross section inside a given body, as exemplified in Figure II–32a. Let us assume that on this purely conceptual surface element of area ΔA of the body, a force vector whose components are ΔF_i in an orthogonal coordinate system is acting. The limiting value of the ratio of force over area can be derived following the hypothesis of continuity as:

$$t_i = \lim_{\Delta A \to 0} \frac{\Delta F_i}{\Delta A} = \frac{dF_i}{dA} \tag{II–30}$$

where t_i is called the traction vector, or stress vector.

The surface assigned to this stress vector is characterised by an unit-length normal vector n_j which allows to derive the related stress tensor σ_{ij} as:

$$t_i = \sigma_{ij} n_j \tag{II–31}$$

In the following, the force per unit area in the current, deformed configuration refers to as Cauchy stress tensor [Cauchy, 1823] to distinguish it from other stress tensors.

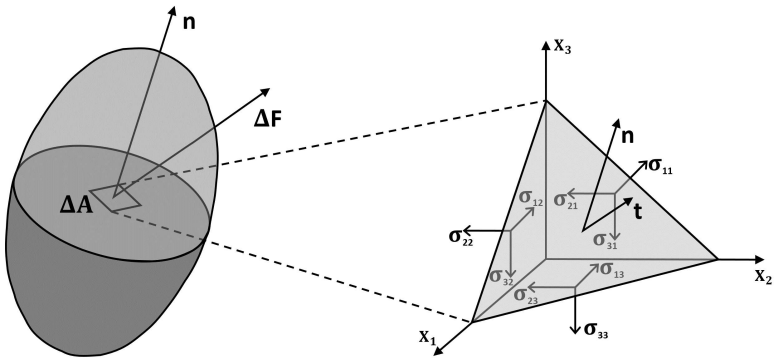

(a) (b)

Figure II–32 – (a) Cross section on a body with an internal force ΔF acting on a surface ΔA with normal vector n. (b) Infinitesimal tetrahedral portion of material externalising the full stress tensor.

In the general three-dimensional context, the Cauchy stress tensor is a symmetrical tensor composed of six independent components, which can be gathered into a 3×3 matrix. Figure II–32b offers a physical representation of the stress tensor components on a tetrahedron constituted of three triangles parallel to the orthogonal coordinate planes and a fourth triangle whose orientation is defined by n_j.

$$\sigma_{ij} = \begin{bmatrix} \sigma_{11} & \sigma_{12} & \sigma_{13} \\ & \sigma_{22} & \sigma_{23} \\ \text{Sym.} & & \sigma_{33} \end{bmatrix} \tag{II–32}$$

It is worth notifying that invariants of the stress tensor are usually employed for a complete representation of the stress state independently of the referential frame. In the field of geomechanics, the stress tensor is conveniently described by a triplet of stress invariants $[I_\sigma, II_{\hat{\sigma}}, III_{\hat{\sigma}}]$, acting as a new polar coordinate system.

The first invariant is the trace of the stress tensor, defined as:

$$I_\sigma = \sigma_{ii} \tag{II–33}$$

The second and third invariants of the stress tensor are computed according to:

$$II_{\hat{\sigma}} = \sqrt{\frac{1}{2}\hat{\sigma}_{ij}\hat{\sigma}_{ij}} \tag{II–34}$$

$$III_{\hat{\sigma}} = \frac{1}{3}\hat{\sigma}_{ij}\hat{\sigma}_{jk}\hat{\sigma}_{kl} \tag{II–35}$$

where the deviatoric stress tensor $\hat{\sigma}$ is defined as:

$$\hat{\sigma}_{ij} = \sigma_{ij} - \frac{I_\sigma}{3}\delta_{ij} \tag{II–36}$$

where δ_{ij} refers to the special Kronecker delta.

Furthermore, the first and the second invariants of the stress tensor can be reformulated into another set of quantities (p,q), *i.e.* the mean stress and the deviatoric stress, that are frequently used to define yield surfaces of geomaterials:

$$p = \frac{I_\sigma}{3} \tag{II–37}$$

$$q = \sqrt{3} II_{\hat{\sigma}} \tag{II–38}$$

Finally, it is worth noting that in this work, the sign convention of geomechanics is adopted, meaning that the compression stress and compaction strains are counted positive.

6.1.3 Referential definition

An appropriate definition of the referential system must be formulated in order to describe the kinematics of the material at work in the investigated coupled phenomena. For small deformation problems which supposes that the initial and final configurations are identical, an infinitesimal description of the deformation remains valid. On the other hand, for large deformation problems which presume a distinction between the deformed and the initial configurations, the non-linearity of kinematics becomes important, revoking the validity of the infinitesimal description. Initially dedicated to the modelling of metal forming [Charlier, 1987], the finite element code LAGAMINE is associated to the latter that requires thence to account for large strains and/or displacements and rigid body motions. In large deformation continuum mechanics the non-linearity of kinematics is generally subdivided into two main categories [Malvern, 1969]:

- **Lagrangian description**: The problem is formulated with regard to the reference configuration but the referential mesh is linked to the material points and evolves with it. In Lagrangian frame, the movement of each individual particle is tracked (Figure II–33a).
- **Eulerian description**: The problem is formulated with regard to the deformed configuration but the referential mesh is considered fixed. In the Eulerian frame, the movement of each individual particle is described in a spatially fixed mesh (Figure II–33b).

Given the multiphasic nature of the porous medium, the kinematic description of each phase, *i.e.* solid and fluids, must be defined considering the coupling effects between them.

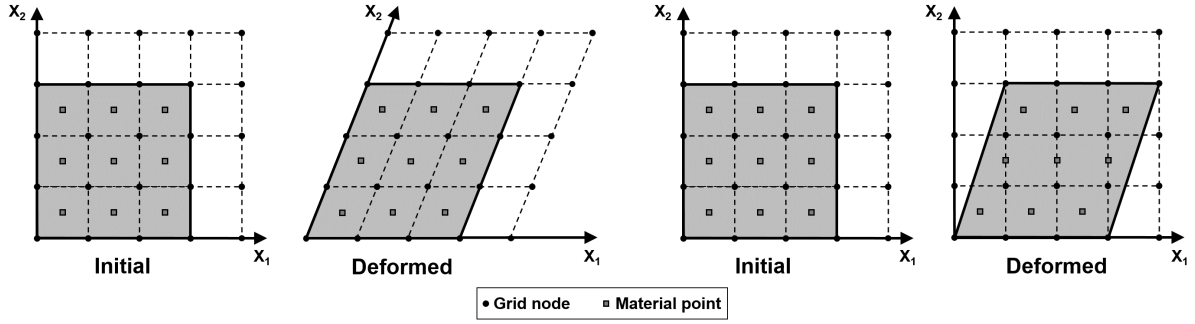

Figure II–33 – Schematic representation of (a) Lagrangian and (b) Eulerian referentials.

Solid phase kinematics

In the present work, the equilibrium of the solid skeleton is expressed by means of an updated Lagrangian formulation, for which the reference configuration evolves at each step. Concretely, it differs from a total Lagrangian formulation because the variables of the problem are defined with regard to an updated configuration (X_1, X_2), and not to the initial referential basis (X_1^0, X_2^0), as illustrated in Figure II–34. In this referential, the transformation from the reference configuration X_i to the current configuration x_i is characterised by a deformation gradient whose components in indicial notations are given by:

$$F_{ij} = \frac{\partial x_i}{\partial X_j} \tag{II–39}$$

The velocity of a material point in the current configuration is given by:

$$v_i = \frac{dx_i}{dt} = \dot{x}_i \tag{II–40}$$

where t denotes time and u_i is the displacement vector.

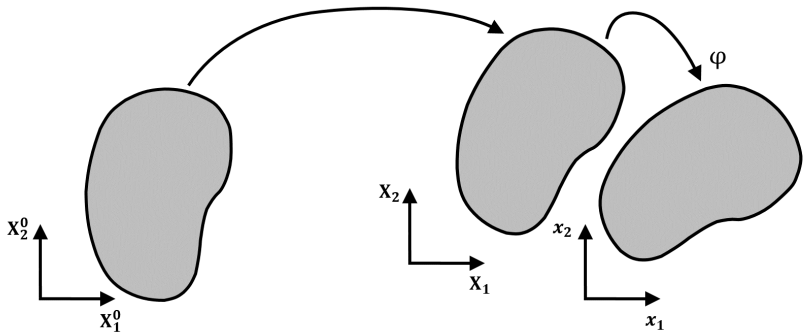

Figure II–34 – Updated Lagrangian formulation with initial configuration in the initial basis (X_1^0, X_2^0), the reference configuration in the updated reference basis (X_1, X_2) and the deformed configuration in the current basis (x_1, x_2). φ is the mapping that associates a material point of the reference configuration with its current position: $x_i = \varphi(X_i)$.

Consequently, the gradient of the velocity in the current configuration is given by:

$$L_{ij} = \frac{dv_i}{dx_j} \tag{II–41}$$

which can be decomposed into its symmetrical and anti-symmetrical parts.

The symmetrical part of this velocity gradient corresponds to the Cauchy strain rate and reads:

$$\dot{\varepsilon}_{ij} = \frac{1}{2}(L_{ij} + L_{ji}) \tag{II–42}$$

and the spin rate tensor is given as the anti-symmetric part of this velocity gradient and reads:

$$\dot{w}_{ij} = \frac{1}{2}(L_{ij} - L_{ji}) \tag{II–43}$$

The Cauchy stress tensor introduced in Equation (II–32) is related to the Cauchy strain rate and is applicable for stress analysis of materials bodies undergoing small deformations. However, switching to large deformation problems with incremental formulation requires an objective stress rate computation so that any rigid-body motion does not induce modification of stress within the material. Among the different available schemes [Ponthot, 2002], the Jaumann objective stress rate $\tilde{\sigma}$ [Jaumann, 1911] is therefore adopted in the following to describe large strains and rotations:

$$\tilde{\sigma}_{ij} = \dot{\sigma}_{ij} - w_{ij}\sigma_{ij} + \sigma_{ij}w_{ij} \tag{II–44}$$

where $\dot{\sigma}_{ij}$ is the Cauchy stress rate.

Fluid phase kinematics

The kinematic approach introduced for the solid part of the continuum porous medium cannot be applied equivalently to the fluid phase. Any elementary volume of the porous network might indeed exchange fluids with the outer environment in the course of the system evolution, thus establishing an open continuum [Coussy, 1991]. Moreover, the fluid behaviour is also coupled to the solid phase since the void volume might evolve, *i.e.* increase or decrease, according to the mechanical behaviour of the solid skeleton. Hence a different kinematic configuration must be adopted for the fluid phase. Generally, the Eulerian approach is used to define a control volume, without identifying individual fluid particles, so that all flow properties such as pressure or velocity are described as fields within the control volume. Nevertheless, in the finite element code `LAGAMINE`, a so-called hybrid description of the fluid flow is implemented in the sense that the movement of the referential is dictated by the deformations of the solid skeleton while the fluid flow follows an Eulerian description inside this solid framework.

6.2 Balance equations

Following the concepts introduced in the previous Subsection 6.1, the material considered in the developed model is treated as an unsaturated porous medium composed of three species, namely an assembly of grains forming the solid matrix and a binary fluid mixture filling the voids between the grains. As illustrated in Figure II–35, these species are supposed to be distributed into three phases, namely solid, liquid and gas. In the present formulation, it is considered that each of the fluid phases corresponds to a combination of two constituents, that is to say the liquid phase includes liquid water and dissolved gas while the gaseous phase is an ideal mixture of dry gas and water vapour. Furthermore, it is also assumed that the mineral species and the solid phase coincide, and that solid and fluid phases are immiscible. Unless otherwise specified in the rest of the manuscript, the subscripts s, l and g concern the solid, liquid and gas phase properties respectively, whereas the subscripts w and v refer to the properties of liquid water and water vapour respectively. As for the properties of the dry and dissolved gas, the subscript is directly related to the type of gas species that is envisaged *i.e.* mainly Hydrogen in this work but extensions to nitrogen, helium or argon are possible.

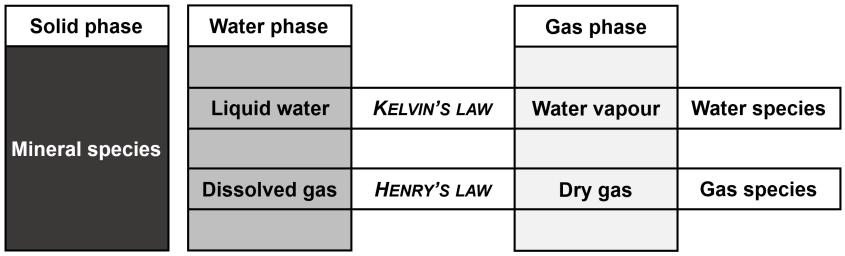

Figure II–35 – Definition of phases, species and equilibrium restrictions of an unsaturated porous medium. *After* [Collin, 2003].

The state of the material is therefore described by its displacement field u_i, liquid pressure field p_w, and gas pressure field p_g. The problem is also restricted to isothermal conditions despite the fact that this assumption may be questionable given the amount of heat released by the packages in the context of applications related to radioactive waste insulation. In the following, the required balance equations for the coupled hydro-mechanical problem under study are presented in usual differential local form using an updated Lagrangian configuration which corresponds to the current porous material configuration (as stated in Subsection 6.1.3). These equations consist of the balance of momentum of the mixture, the solid mass balance equation and the fluids mass balance equations, both for the water and gas species.

6.2.1 Momentum balance equation

The general balance equation of momentum can be established from the equation of motion, *i.e.* Euler's first law [Euler, 1749] extending Newton's second law [Newton, 1687], postulating that the rate of change of linear momentum of a continuum volume is equal to the resultant F_i of all forces acting on the rigid body:

$$F_i = \int_\Omega \rho \frac{\partial v_i}{\partial t} d\Omega \tag{II–45}$$

Considering a deformable porous medium Ω (Figure II–36a) loaded by gravity volume forces ρ_i and contact forces T_i, with g_i the gravity acceleration vector and ρ the specific mass of the mixture, then any chosen control volume Ω^* inside the porous medium is subjected to the same volume forces and to surface forces t_i. At equilibrium, the balance of linear momentum writes:

$$\int_A t_i dA + \int_\Omega \rho g_i d\Omega = \int_\Omega \rho \frac{\partial v_i}{\partial t} d\Omega \tag{II–46}$$

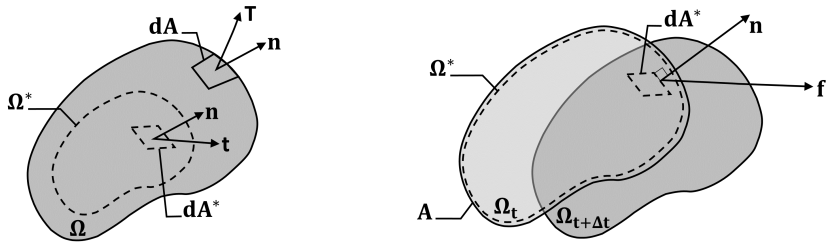

Figure II–36 – Balance on a control volume Ω^* of a deformable porous medium Ω: (a) momentum balance under volume and surface forces, (b) mass balance under flux imposed at the surface at time t and $t+\Delta t$.

Applying Gauss's divergence theorem after introducing Cauchy's Equation (II–31) gives:

$$\int_{\Omega}\left(\frac{\partial \sigma_{ij}}{\partial x_j}+\rho g_i\right)d\Omega=\int_{\Omega}\rho\frac{\partial v_i}{\partial t}d\Omega \tag{II–47}$$

Reformulating this arbitrary balance independently of the chosen control volume for quasi-static loading (the right-hand side member vanishes) gives the general momentum balance equation in differential form:

$$\frac{\partial \sigma_{ij}}{\partial x_j}+\rho g_i=0 \tag{II–48}$$

Developing the mixture homogenised density in this equation gives:

$$\rho_{mix}=\rho_s(1-\phi)+\rho_w S_{r_w}\phi+\rho_g(1-S_{r_w})\phi \tag{II–49}$$

where $\phi=\frac{\Omega_v}{\Omega}$ is the porosity with Ω the current volume of a given mass of skeleton and Ω_v the corresponding porous volume, ρ_s is the solid grain density, ρ_w is the water density, ρ_g is the gas density, and S_{r_w} is the water degree of saturation.

6.2.2 Mass balance equations

The general balance equation for an extensive property $M(t)$ such as the mass of a species can be established quite straightforwardly by introducing the density as the quantity $M(t)$ by unit volume, over a corresponding control volume Ω delimited by a surface A with the unit vector n_i oriented normally to this surface and the inflow/outflow flux f_i injected through this surface (Figure II–36b):

$$M(t)=\int_{\Omega}\rho(x_i,t)d\Omega \tag{II–50}$$

Then, relying on Leibnitz's integral rule, the temporal variation of the mass is given as:

$$\frac{\partial M}{\partial t}=\frac{\partial}{\partial t}\int_{\Omega}\rho d\Omega=\int_{\Omega}\frac{\partial \rho}{\partial t}d\Omega \tag{II–51}$$

At that point, the Reynolds transport theorem [Reynolds et al., 1903] states that the rate of change of a system property defined over a control volume is equal to the sum of the rate of change of the property within the control volume - what is consumed/created by sinks and sources inside this volume - and the difference between property outflow and inflow through the control surface - what is gained/lost through the boundaries of the volume - which gives:

$$\int_{\Omega}\frac{\partial \rho}{\partial t}d\Omega=\int_{A}-(n_i\cdot f_i)dA+\int_{\Omega}Qd\Omega \tag{II–52}$$

Further moving to an integral over a volume according to Gauss's divergence theorem leads to:

$$\int_{\Omega} \left(\frac{\partial \rho}{\partial t} + \frac{\partial f_i}{\partial x_i} - Q \right) d\Omega = 0 \tag{II–53}$$

where the first term is the storage term, Q is the source term and the divergence of the fluxes f_i expresses the variation between the input and the output fluxes over the arbitrary volume.

Finally, reformulating this arbitrary balance independently of the chosen control volume gives the general balance equation in differential form:

$$\frac{\partial \rho}{\partial t} + \frac{\partial f_i}{\partial x_i} - Q = 0 \tag{II–54}$$

The formulation of the mass balance equations follows the compositional approach of [Panday and Corapcioglu, 1989], which balances chemical species rather than phases, thence cancelling out the terms related to phase transfer. The model is elaborated for a single gas species corresponding to the predominant gas release in the case of deep geological repository of high-level nuclear wastes.

Solid mass balance equation

Thanks to a Lagrangian description (see Subsection 6.1.3), the reference system follows the solid phase and the conservation of the solid mass is necessarily met. For a given volume of mixture, the solid mass balance equation in a strong form reads:

$$\dot{M}_s = \frac{\partial}{\partial t} \left(\rho_s (1 - \phi) \Omega \right) = 0 \tag{II–55}$$

where M_s is the solid mass inside the current porous material configuration Ω, and ρ_s is the density of solids, *i.e.* the clay rock matrix density.

Water mass balance equation

Thanks to the expression obtained in Equation (II–54), the balance equations for water in the liquid and gas phases can be formulated by integrating the respective mass of the species within the considered phase, and reads:

$$\dot{M}_w + \frac{\partial f_{w,i}}{\partial x_i} + \dot{E}^{w-v}_{H_2O} = Q^w_l \tag{II–56}$$

$$\dot{M}_v + \frac{\partial f_{v,i}}{\partial x_i} - \dot{E}^{w-v}_{H_2O} = Q^w_g \tag{II–57}$$

where $f_{w,i}$ and $f_{v,i}$ are the mass flows of liquid water and water vapour defined in the two-phase flow model of Section 6.3.1, Q^w_g and Q^w_l are the liquid water and water vapour source/sink terms respectively, $\dot{E}^{w-v}_{H_2O}$ is the mass of liquid water transformed into vapour, and M_w and M_v are the masses of liquid water and water vapour respectively, which are given in rate form to express the change in fluid storage:

$$\dot{M}_w = \frac{\partial}{\partial t} \left(\rho_w \phi S_{r_w} \Omega \right) \tag{II–58}$$

$$\dot{M}_v = \frac{\partial}{\partial t} \left(\rho_v \phi S_{r_g} \Omega \right) \tag{II–59}$$

where ρ_w and ρ_v are the densities of liquid water and water vapour respectively. Variations in porosity directly having an impact on the water storage capacity, these relationships initiate a kind of coupling between mechanical and hydraulic problems.

Given the compositional approach, the different contributions can be combined to express a mass balance equation for the whole water species rather than for each phase. The water mass balance equation thus accounts for the liquid water as well as the water vapour and reads for a unit porous medium ($\Omega = 1$) in a strong form:

$$\underbrace{\frac{\partial f_{w,i}}{\partial x_i} + \frac{\partial}{\partial t} \left(\rho_w \phi S_{r_w} \right)}_{\text{Liquid water}} + \underbrace{\frac{\partial f_{v,i}}{\partial x_i} + \frac{\partial}{\partial t} \left(\rho_v \phi S_{r_g} \right)}_{\text{Water vapour}} - Q_w = 0 \tag{II–60}$$

Gas mass balance equation

Thanks to the expression obtained in Equation (II–54), the balance equations for gas in the liquid and gas phases can be formulated by integrating the respective mass of the species within the considered phase, and reads:

$$\dot{M}_g + \frac{\partial f_{g,i}}{\partial x_i} + \dot{E}_{gas}^{g-dg} = Q_g^g \qquad \text{(II–61)} \qquad \dot{M}_{dg} + \frac{\partial f_{dg,i}}{\partial x_i} - \dot{E}_{gas}^{g-dg} = Q_l^g \qquad \text{(II–62)}$$

where $f_{g,i}$ and $f_{dg,i}$ are the mass flows of dry gas and dissolved gas defined in the two-phase flow model of Section 6.3.1, Q_g^g and Q_l^g are the dry gas and dissolved gas source/sink terms respectively, $\dot{E}_{gas}^{g-dg}$ is the mass of dry gas transformed into dissolved gas into water, and M_g and M_{dg} are the masses of dry gas and dissolved gas respectively, which are given in rate form to express the change in fluid storage:

$$\dot{M}_g = \frac{\partial}{\partial t}\left(\rho_g \phi S_{r_g} \Omega\right) \qquad \text{(II–63)} \qquad \dot{M}_{dg} = \frac{\partial}{\partial t}\left(\rho_{dg} \phi S_{r_w} \Omega\right) \qquad \text{(II–64)}$$

where ρ_g and ρ_{dg} are the densities of dry gas and dissolved gas respectively. Variations in porosity having direct impacts on the gas storage capacity, these relationships initiate another kind of coupling between mechanical and hydraulic problems.

Given the compositional approach, the different contributions can be combined to express a mass balance equation for the whole gas species rather than for each phase. The gas mass balance equation thus accounts for the dry gas as well as the dissolved gas and reads for a unit porous medium ($\Omega = 1$) in a strong form:

$$\underbrace{\frac{\partial f_{g,i}}{\partial x_i} + \frac{\partial}{\partial t}\left(\rho_g \phi S_{r_g}\right)}_{\text{Dry gas}} + \underbrace{\frac{\partial f_{dg,i}}{\partial x_i} + \frac{\partial}{\partial t}\left(\rho_{dg} \phi S_{r_w}\right)}_{\text{Dissolved gas}} - Q_g = 0 \qquad \text{(II–65)}$$

6.3 Constitutive equations

A certain number of dependent variables such as the degree of saturation, fluid flows or densities are involved in the balance equations presented in the previous Section 6.2. All these variables are directly dependent on the main unknowns of the problem (u_i, p_w, p_g). The constitutive equations are the specific relationships that make the link between them, in order to fully describe the behaviour of a multiphasic porous medium. In the context of a multiphasic porous medium, the required constitutive equations include the mechanical models, the multiphase flow model and the retention model.

6.3.1 Two-phase flow model

The fluid mass balance Equations (II–60) and (II–65) involve mass fluxes of water and gas which must be related to the main variables fields of the hydro-mechanical problem. In partially saturated porous media, fluid transport processes occur in the pore spaces between the solid skeleton. However, for the sake of simplicity when simulating flow over large domains, phenomenological continuum approach will be favoured to direct modelling at the porescale level. In this section, the description of the different fluid flows is introduced by means of a two-phase flow transfer model.

Fluid transfer equations

The mass flows in both liquid and gas phases are a combination of advective and non-advective fluxes, that is to say the advection of each phase (phase movement) using the generalised Darcy's law [Darcy, 1856], and the diffusion of the components within each phase (motion of species within phases) by Fick's law [Fick, 1855]. The different mass fluxes of liquid water, water vapour, dry gas and dissolved gas are respectively expressed as:

$$f_{w,i} = \rho_w q_{l,i} \quad \text{(II–66)} \qquad f_{v,i} = \rho_v q_{g,i} + i_{v,i} \quad \text{(II–67)}$$

$$f_{g,i} = \rho_g q_{g,i} + i_{g,i} \quad \text{(II–68)} \qquad f_{dg,i} = \rho_{dg} q_{l,i} + i_{dg,i} \quad \text{(II–69)}$$

where ρ_w, ρ_v, ρ_g and ρ_{dg} are the densities of liquid water, water vapour, dry gas and dissolved gas respectively, $q_{l,i}$ and $q_{g,i}$ are the advective fluxes respectively of the liquid and the gaseous phases, $i_{v,i}$, $i_{g,i}$ and $i_{dg,i}$ are the diffusive fluxes respectively for the water vapour, the dry gas, and the dissolved gas. It is assumed that the amounts of dissolved gas in the liquid phase are small enough to neglect the liquid water diffusion within the liquid phase in Equation (II–66). It is worth noted that these relationships can be particularised to any binary mixture of water and gas species.

Advective fluxes

The advection of both liquid and gas phases is described by the generalisation of Darcy's law [Darcy, 1856] to unsaturated cases. In averaging theories, this specific law has been derived from the equation of the linear momentum balance for the liquid phase, under the assumptions of negligible inertial, viscous and phase change effects [Hassanizadeh and Gray, 1980]. This law thus turns out to be valid for sufficiently slow fluid flows [Lewis and Schrefler, 1998], as it is the case in low-permeable clay materials. Following the Eulerian description, these advective fluxes correspond to the average macroscopic velocity of each phase with respect to the solid phase. The advection of liquid mixture and gaseous phase respectively reads:

$$q_{l,i} = q_{w,i} = -\frac{k_{w,ij}}{\mu_w}\left(\frac{\partial p_w}{\partial x_j} + \rho_w g_j\right) \quad \text{(II–70)} \qquad q_{g,i} = -\frac{k_{g,ij}}{\mu_g}\left(\frac{\partial p_g}{\partial x_j} + \rho_g g_j\right) \quad \text{(II–71)}$$

where $k_{w,ij}$ and $k_{g,ij}$ are the water and gas permeabilities of the partially saturated medium, commonly formulated as $k_{w,ij} = k_{ij}^{int} k_{r_w}(S_{r_w})$ and $k_{g,ij} = k_{ij}^{int} k_{r_g}(S_{r_w})$ respectively, and μ_w and μ_g are the dynamic viscosities of liquid water and an ideal mixture of dry air and water vapour respectively, the latter being dependent on the dynamic viscosity of each component of the mixture as [Pollock, 1986]:

$$\mu_g = \frac{1}{\frac{\rho_g}{\rho_g \mu_g} + \frac{\rho_v}{\rho_g \mu_v}} \quad \text{(II–72)}$$

where μ_g and μ_v are the dry gas and water vapour dynamic viscosities.

Diffusive fluxes

As introduced in Section 5.2, the diffusion of the components within each phase is governed by Fick's law [Fick, 1855], stating that the diffusive flux is proportional to the gradient of mass fraction of species, where the hydrodynamic dispersion coefficient plays the role of the proportionality coefficient. The diffusion of water vapour within gas phase and of dissolved gas with liquid phase respectively reads:

$$i_{v,i} = -D^*_{v/g} \rho_g \frac{\partial}{\partial x_i}\left(\frac{\rho_v}{\rho_g}\right) = -i_{g,i} \quad \text{(II–73)} \qquad i_{dg,i} = -D^*_{dg/w} \rho_w \frac{\partial}{\partial x_i}\left(\frac{\rho_{dg}}{\rho_w}\right) \quad \text{(II–74)}$$

where $D^*_{v/g}$ and $D^*_{dg/w}$ are the effective diffusion coefficients respectively in the gaseous mixture (dry gas - water vapour) and for the dissolved gas in liquid water, which are directly related to the porous volume of the material, its structure and its water content and can be decomposed as [Philip and de Vries, 1957]:

$$D^*_{v/g} = \phi(1 - S_{r_w})\bar{\tau} D_{v/g} \quad \text{(II–75)} \qquad D^*_{dg/w} = \phi S_{r_w} \bar{\tau} D_{dg/w} \quad \text{(II–76)}$$

where ϕ is the porosity, S_{r_w} and $(1-S_{r_w})$ are the liquid and gas degrees of saturation respectively, with the product $\phi(1-S_{r_w})$ stipulating that vapour diffusion takes place through the gas phase of the porous medium for a contribution of the total porosity to the vapour diffusion, and $\bar{\tau}$ is the tortuosity of the porous medium, as defined in Section 5.2 and represented in Figure II–12.

In Equations (II–75) and (II–76), the parameters $D_{dg/w}$ and $D_{v/g}$ are the molecular diffusion coefficients for the the dissolved gas in the water phase and for water vapour in the gas phase respectively. The determination of these phenomenological coefficients is naturally the most critical part of the equations. At standard conditions ($T = 293K$ and $p_w = p_g = 0.1MPa$), the common values of the former coefficient are reported in Table II–5 for air, Hydrogen, Helium and Nitrogen respectively. The latter coefficient $D_{v/g}$ is supposed to vary with the gas pressure and the absolute temperature but independently of the considered porous material and reads respectively for a gas mixture of water vapour and dry air [Philip and de Vries, 1957] or for a gas mixture of water vapour with any other gas species:

$$D_{v/g} = 5.893 \times 10^{-6} \left(\frac{T^{2.3}}{p_g} \right) \qquad \text{and} \qquad D_{v/g} = D_{v/g,0} \left(\frac{p_{g,0}}{p_g} \right) \left(\frac{T}{T_0} \right)^{1.75} \tag{II–77}$$

where $D_{v/g,0}$ is the diffusion coefficient of the gas mixture at $T = 273.15K$ and $p_w = p_g = 0.1MPa$.

Liquid density variation

The fluid phase behaviour is characterised by compressible fluids which implies variation of liquid density. The isotropic compressibility of water is assumed to respect the following relationship [Lewis and Schrefler, 1998], which predicts an increase in water density as a function of water pressure:

$$\frac{\dot{\rho}_w}{\rho_w} = \frac{\dot{p}_w}{\chi_w} \tag{II–78}$$

where χ_w is the water compressibility reported in Table II–4, or $\frac{1}{\chi_w}$ is the liquid water isotropic bulk modulus.

This equation can be linearised to be implemented in a finite element code, thus expressing the liquid water density ρ_w in isothermal conditions as a function of the pore water pressure p_w according to:

$$\rho_w = \rho_{w,0} \left(1 + \frac{p_w - p_{w,0}}{\chi_w} \right) \tag{II–79}$$

where $\rho_{w,0}$ and $p_{w,0}$ are the initial values of water density and pore water pressure.

Gas density variation

The fluid phase behaviour is characterised by compressible fluids which implies variation of gas density. For the gaseous mixture of dry gas and water vapour, the ideal gas law is assumed (Clapeyron's equation [Clapeyron, 1834] and Dalton's law [Dalton, 1802]). The classical state equation of ideal gas applied to the considered gas mixture is used to write the gas densities as:

$$\rho_g = \rho_\alpha + \rho_v \qquad \text{and} \qquad p_g = p_\alpha + p_v \tag{II–80}$$

where p_α and p_v are the partial pressures of the gas species α and water vapour respectively, and ρ_α and ρ_v are the densities of the gas species α and water vapour which respectively reads:

$$\rho_\alpha = \frac{m_\alpha}{RT} p_\alpha \qquad \text{and} \qquad \rho_v = \frac{m_v}{RT} p_v \tag{II–81}$$

where R is the universal gas constant ($= 8.3143\ J/mol \cdot K$), T is the absolute temperature in *Kelvin*, and m_α and m_v are the molar masses of the dry gas species α (Table II–5) and the water vapour.

Table II–4 – Accepted values for the main parameters of liquid water used in numerical modelling.

Parameter	Symbol	Value	Unit
Compressibility	χ_w	5×10^{-10}	$[1/Pa]$
Density	ρ_w	10^3	$[kg/m^3]$
Dynamic viscosity	μ_w	10^{-3}	$[Pa.s]$
Molar mass	m_w	0.018	$[kg/mol]$

Table II–5 – Accepted values for the main parameters of the different gases used in numerical modelling ($T = 20°C$, $p_g = p_w = 0.1MPa$).

Parameter	Symbol	Air	Hydrogen	Nitrogen	Helium	Unit
Dynamic viscosity	μ_g	18.6×10^{-6}	9×10^{-6}	17.9×10^{-6}	20×10^{-6}	$[Pa.s]$
Dissolved gas in water phase	$D_{dg/w}$	5.03×10^{-9}	4.6×10^{-9}	2×10^{-9}	7.28×10^{-9}	$[m^2/s]$
Water vapour in gas phase	$D_{v/g}$	Eq (II–77)	9.5×10^{-5}	2.42×10^{-5}	7.81×10^{-5}	$[m^2/s]$
Density	ρ_g	1.205	0.0838	1.1652	0.1663	$[kg/m^3]$
Henry coefficient	H_g	0.0234	0.0190	0.0149	0.0091	$[-]$
Molar mass	m_g	0.0288	0.002	0.028	0.004	$[kg/mol]$

6.3.2 Retention and relative permeability curves

As described in Section 5.3.2, a retention curve is required to derive the saturation degree from the primary unknowns of the problem, namely the water and gas pressures. The constitutive model of van Genuchten's type [van Genuchten, 1980] already presented in Equation (II–12) is used in the following and expressed as:

$$S_{r_w} = S_{r_{res}} + (S_{max} - S_{r_{res}}) \left(1 + \left(\frac{p_c}{P_r} \right)^{\frac{1}{1-\mathcal{N}}} \right)^{-\mathcal{N}} \tag{II–82}$$

where P_r is a parameter identified as the gas entry pressure, S_{max} and $S_{r_{res}}$ are the maximum and residual degrees of water saturation, $\mathcal{N}$ is a model parameter controlling the curve shape, and $p_c = s$ is the capillary pressure or suction.

A precise characterisation of the retention properties is essential since it contributes to the coupled hydro-mechanical behaviour of the material. Soil deformations affect the degree of saturation whereas variations in the degree of saturation lead to mechanical effects.

On the other hand, it has been demonstrated in Section 5.3.3 that fluid flows are mainly governed by flow parameters such as fluid permeabilitites that are influenced by unsaturated conditions. If both water and gas flows occur concurrently in the porous medium, it is necessary to extent the numerical model to unsaturated conditions and to introduce the concept of relative permeability into Darcy generalised Equations (II–70) and (II–71) as a measure of the reduction in permeability of a given phase that takes place between partially and fully saturated conditions. As introduced in the literature review Part II, two groups of relative permeability models are commonly used to simulate gas flows in clay host rocks, *i.e.* the well-known van Genuchten model [Mualem, 1976, van Genuchten, 1980] on the one hand, and the power law model on the other hand.

The van Genuchten model is a close-form analytical formulation to predict the relative permeability of unsaturated soils, which has been widely applied in the unsaturated rocks [Xu et al., 2013b, Fall et al., 2014, Nguyen and Le, 2015, Senger et al., 2014, Senger et al., 2018, Mahjoub et al., 2018]. The relative permeability for water and gas relates water and gas to the degree of saturation, which respectively reads:

$$k_{r_w} = \sqrt{S_{r_w}} \left(1 - \left(1 - S_{r_w}^{\frac{1}{\mathcal{M}}}\right)^{\mathcal{M}}\right)^2 \qquad \text{(II–83)} \qquad k_{r_g} = \sqrt{S_{r_g}} \left(1 - S_{r_w}^{\frac{1}{\mathcal{M}}}\right)^{2\mathcal{M}} \qquad \text{(II–84)}$$

where S_{r_w} is the water degree of saturation and $S_{r_g} = 1 - S_{r_w}$ is the gas degree of saturation, $\mathcal{M} = 1 - \frac{1}{\mathcal{N}}$ is a model parameter, and $\mathcal{N}$ is the model parameter that is *a priori* used in the van Genuchten retention curve (see Equation (II–82)).

The power law model was developed from the experimental approach [Brooks and Corey, 1964, Mualem, 1978], which has been used in a large panel of numerical applications [Olivella and Alonso, 2008, Arnedo et al., 2013, Charlier et al., 2013, Gerard et al., 2014, Gonzalez-Blanco et al., 2016]. The empirical relation for water and gas is expressed as:

$$k_{r_w} = (S_r^*)^{\mathcal{L}} \qquad \text{(II–85)} \qquad k_{r_g} = (1 - S_r^*)^{\mathcal{L}} \qquad \text{(II–86)}$$

where $\mathcal{L}$ is a model parameter related to the pore size distribution of the rock, and S_r^* is the normalised wetting phase saturation, defined as:

$$S_r^* = \frac{S_{r_w} - S_{r_{w,res}}}{1 - S_{r_{w,res}} - S_{r_{g,res}}} \qquad \text{(II–87)}$$

6.3.3 Mechanical constitutive model

The mechanical behaviour of porous media is not entirely controlled by the total stress, but it is also influenced by the presence of fluids in the pore space. This behaviour is thus described by alternative stress definitions. The mechanical behaviour of the clay host formations is envisaged with a classical (visco-)elasto-plastic model to reproduce the hydro-mechanical couplings that are observed experimentally in clayey rocks. The objective here is therefore not to have recourse to a complex and rock-specific mechanical model, but to present a general law that will be used in the numerical applications of Parts III and IV whether it deals with the Boom Clay or with the COx claystone.

6.3.3.1 Effective stress definition

The hydro-mechanical coupling implied by the effect of fluid pressures on the Cauchy total stress field σ_{ij} was early envisaged by the concept of effective stress [Terzaghi, 1936], which represents the stresses effectively acting between the solid skeleton. For porous materials fully saturated with water, the effective stress field σ'_{ij} is defined as the difference between the confining pressure and the pore pressure. Terzaghi's effective stress definition reads:

$$\sigma'_{ij} = \sigma_{ij} - p_w \delta_{ij} \qquad \text{(II–88)}$$

where σ'_{ij} is the effective stress field, assumed to be positive in compression under soil mechanics convention, p_w is the pore water pressure, δ_{ij} is the Kronecker symbol, *i.e.* the identity tensor.

The material compressibility can be introduced in the effective stress definition of saturated materials by scaling down the effect of the pore water pressure as a function of the relative deformability of the solid structure [Biot, 1941]. Biot's effective stress definition reads:

$$\sigma'_{ij} = \sigma_{ij} - b p_w \delta_{ij} \qquad \text{(II–89)}$$

where b is the Biot's coefficient that represents the compressibility of the solid grains relative to the skeleton compressibility and is defined for isotropic materials as:

$$b = 1 - \frac{K}{K_s} \qquad \text{(II–90)}$$

where K is the drained bulk modulus of the material and K_s is the bulk modulus of the solid grains. For unconsolidated materials with a low bulk modulus of the porous material in comparison to the solid bulk modulus, b is close to 1. On the countrary for consolidated materials, *e.g.* consolidated rocks with a more rigid grain skeleton, the value of b is smaller than 1. Note that the coefficient b has actually the form of a tensor b_{ij} in the general case of anisotropy.

Accounting for partially saturated conditions, an extension of Terzaghi's postulate has been proposed by combining both liquid and gas pressures [Bishop, 1959]. Bishop's effective stress definition reads:

$$\sigma'_{ij} = \sigma_{ij} - p_g \delta_{ij} + \chi(p_g - p_w)\delta_{ij} \tag{II–91}$$

where χ is the effective Bishop's stress parameter which depends on the saturation and the stress state and varies from 0 in dry state to 1 in fully saturated state, recovering Terzaghi's postulate. This parameter is linked to the degree of water saturation by an elementary relationship $\chi = S_{r_w}$ [Schrefler, 1984].

Under this most commonly used assumption, and presuming that compressibility effects and partial saturation can be considered together, the equation of effective stress can be rewritten in a simplified form as:

$$\sigma'_{ij} = \sigma_{ij} - b_{ij}(S_{r_w} p_w \delta_{ij} + (1 - S_{r_w})\, p_g \delta_{ij}) \tag{II–92}$$

where the b_{ij} is the Biot tensor that represents more particularly the compressibility of the solid grain skeleton relative to the skeleton compressibility, expressed in orthotropic axes as [Cheng, 1997]:

$$b_{ij} = \delta_{ij} - \frac{C^e_{ijkl}}{3K_s} \tag{II–93}$$

where K_s is the isotropic bulk modulus of the solid grains, and C^e_{ijkl} is the elastic stiffness tensor of the material. It is worth noting that including the plastic material behaviour in case the medium is not assumed elastic requires an extension to poroplasticity, as proposed by [Coussy and Ulm, 1995]. Yet, these developments are not included in the present work.

6.3.3.2 Solid density variation

The isotropic variation of solid density is linked to the variations of pore water pressure, gas pressure and mean effective stress according to [Detournay and Cheng, 1993]:

$$\frac{\dot{\rho}_s}{\rho_s} = \frac{(b_{ij} - \phi)(S_{r_w}\dot{p}_w + S_{r_g}\dot{p}_g) + \dot{\sigma}'}{(1-\phi)K_s} \tag{II–94}$$

where ρ_s is the solid grain density, ϕ is the porosity and σ' is Bishop's mean effective stress.

6.3.3.3 Behaviour of the clay host formations

An elasto-(visco-)plastic model with cross-anisotropy and horizontal isotropic bedding planes is envisaged for the mechanical behaviour of the host rock formations and described in the following. In the general framework of elasto-visco-plasticity, the region of elastic deformation is limited with a loading surface in the stress state and viscosity is taken into account by splitting the plastic strain as a time-independent instantaneous plastic deformation and a time-dependent creep deformation. This principle makes it possible to break down the total strain rate $\dot{\varepsilon}_{ij}$ into elastic $\dot{\varepsilon}^e_{ij}$, plastic $\dot{\varepsilon}^p_{ij}$ and viscous $\dot{\varepsilon}^{vp}_{ij}$ components:

$$\dot{\varepsilon}_{ij} = \dot{\varepsilon}^e_{ij} + \dot{\varepsilon}^p_{ij} + \dot{\varepsilon}^{vp}_{ij} \tag{II–95}$$

Elastic component

The linear elastic behaviour of the rock is based on the classical Hooke's law linking the stress rate $\dot{\sigma}^e_{ij}$ to the reversible strain rate component $\dot{\varepsilon}^e_{kl}$:

$$\dot{\sigma}^e_{ij} = C^e_{ijkl}\, \dot{\varepsilon}^e_{kl} \iff \dot{\varepsilon}^e_{ij} = D^e_{ijkl}\, \dot{\sigma}^e_{kl} \tag{II–96}$$

where C^e_{ijkl} is the elastic stiffness tensor and D^e_{ijkl} is the elastic compliance tensor corresponding to the inverse of the matrix C^e_{ijkl}.

For an isotropic material, the elastic compliance tensor is expressed as a function of only two parameters which can be the Poisson's ratio ν and the Young modulus E, or the shear modulus G and the bulk modulus K. Switching to a material with anisotropic elasticity increases the total number of required independent parameters. However, anisotropic geomaterials often exhibit limited forms of anisotropy such as orthotropy or cross-anisotropy [Lekhnitskii, 1963]. In such materials with axes of symmetry, the number of parameters is reduced. In orthotropic materials where the anisotropy is induced by three mutually orthogonal symmetry planes, the elastic matrix is defined with 9 parameters:

$$D^e_{ijkl} = \begin{bmatrix} \frac{1}{E_1} & -\frac{\nu_{21}}{E_2} & -\frac{\nu_{31}}{E_3} & 0 & 0 & 0 \\ -\frac{\nu_{12}}{E_1} & \frac{1}{E_2} & -\frac{\nu_{32}}{E_3} & 0 & 0 & 0 \\ -\frac{\nu_{13}}{E_1} & -\frac{\nu_{23}}{E_2} & \frac{1}{E_3} & 0 & 0 & 0 \\ 0 & 0 & 0 & \frac{1}{2G_{12}} & 0 & 0 \\ 0 & 0 & 0 & 0 & \frac{1}{2G_{13}} & 0 \\ 0 & 0 & 0 & 0 & 0 & \frac{1}{2G_{23}} \end{bmatrix} \tag{II–97}$$

where the symmetry of the stiffness matrix imposes that:

$$\frac{\nu_{21}}{E_2} = \frac{\nu_{12}}{E_1}, \quad \frac{\nu_{31}}{E_3} = \frac{\nu_{13}}{E_1}, \quad \frac{\nu_{23}}{E_2} = \frac{\nu_{32}}{E_3} \tag{II–98}$$

In cross-anisotropic materials, such as the Callovo-Oxfordian or the Boom Clay formations, the behaviour remains isotropic in the parallel bedding planes which requires only 5 independent parameters [Amadei, 1983]:

$$\begin{cases} E_1 = E_3 = E_\parallel, \quad E_2 = E_\perp \\ \nu_{13} = \nu_{31} = \nu_{\parallel\parallel}, \quad \nu_{12} = \nu_{32} = \nu_{\parallel\perp}, \quad \nu_{21} = \nu_{23} = \nu_{\perp\parallel} \\ G_{12} = G_{32} = G_{\parallel\perp}, \quad G_{13} = \frac{E_\parallel}{2(1+\nu_{\parallel\parallel})} = G_{\parallel\parallel} \end{cases} \tag{II–99}$$

where the subscripts $\parallel$ and $\perp$ refer respectively to the direction parallel to the isotropic bedding plane (directions 1 and 3 here) and perpendicular to the bedding (direction 2).

Plastic component

The irreversible plastic strain component in Equation (II–95) can be expressed as the derivative of a plastic potential g [Taylor and Quinney, 1931]:

$$\dot{\varepsilon}^p_{ij} = \dot{\lambda}^p \frac{\partial g}{\partial \sigma'_{ij}} \tag{II–100}$$

where $\dot{\lambda}^p$ is called the plastic multiplier.

A yield surface f is usually defined to delimit the boundary between the elastic and the plastic domain. The plastic multiplier is then derived from the consitency condition which rules that the stress state stays on the limit surface during plastic flow:

$$df = \frac{\partial f}{\partial \sigma'_{ij}} \dot{\sigma}'_{ij} + \frac{\partial f}{\partial \kappa} \dot{\kappa} \tag{II–101}$$

where κ is the hardening variable.

The elasto-plastic behaviour of the clay host formations is characterised by an internal friction model with a non-associated plasticity and a Van Eekelen yield surface [Van Eekelen, 1980] (under soil mechanics convention with positive compressive stress) defined as:

$$f \equiv II_{\hat{\sigma}} - m\left(I_{\sigma} + \frac{3c}{\tan\phi}\right) = 0 \tag{II–102}$$

where c is the cohesion, ϕ is the friction angle, m is a parameter of the yield surface, $I_{\sigma'} = \sigma'_{ij}\delta_{ij} = \sigma'_{ii}$ is the first invariant of stresses, $II_{\hat{\sigma}'} = \sqrt{0.5\hat{\sigma}'_{ij}\hat{\sigma}'_{ij}}$ is the second invariant of deviatoric stresses, $\hat{\sigma}'_{ij}$ is the deviatoric part of the effective stress tensor. Plots of the yield surface in the plane of the first and second invariants of stresses and in the plane of deviatoric stresses are presented in Figures II–37a and II–37b respectively.

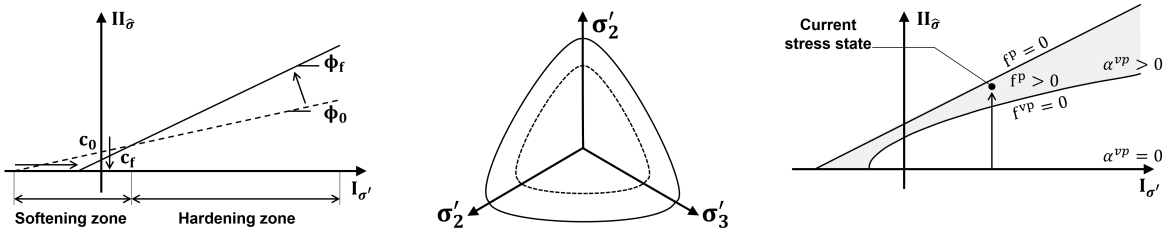

(a) (b) (c)

Figure II–37 – Van Eekelen's yield surface in the (a) stress invariant plane, and the (b) deviatoric plane. (c) Visco-plastic surface in the effective stress invariant plane.

A dependency to the third invariant $III_{\hat{\sigma}'}$ is introduced through the parameter m:

$$m = d_1\left(1 + d_2\ sin(3\beta)\right)^{\eta_c} \tag{II–103}$$

where d_1, d_2 and η_c are material parameters, which have to verify:

$$d_1 > 0, \qquad d_2\eta_c > 0, \qquad -1 < d_2 < 1 \tag{II–104}$$

In addition, the parameter η_c controls the shape of the yield surface in the deviatoric plane (Figure II–37b), and is chosen equal to -0.229 to ensure the convexity of this latter. More details about the parameters d_1 and d_2 are reported in [Pardoen et al., 2015b].

Furthermore, the model allows isotropic hardening or softening of the cohesion and of the friction angles upon loading. In the following, the evolution of these strength parameters between initial and final values is introduced via hyperbolic expressions as a function of the Von Mises equivalent plastic strain ε^p_{eq} [Barnichon, 1998]:

$$c = c_0 + \frac{(c_f - c_0)\langle\hat{\varepsilon}^p_{eq} - dec_c\rangle}{B_c + \langle\hat{\varepsilon}^p_{eq} - dec_c\rangle} \tag{II–105}$$

$$\varphi_c = \varphi_{c,0} + \frac{(\varphi_{c,f} - \varphi_{c,0})\langle\hat{\varepsilon}^p_{eq} - dec_\varphi\rangle}{B_\varphi + \langle\hat{\varepsilon}^p_{eq} - dec_\varphi\rangle} \tag{II–106}$$

$$\varphi_e = \varphi_{e,0} + \frac{(\varphi_{e,f} - \varphi_{e,0})\langle\hat{\varepsilon}^p_{eq} - dec_\varphi\rangle}{B_\varphi + \langle\hat{\varepsilon}^p_{eq} - dec_\varphi\rangle} \tag{II–107}$$

where c_0 and c_f are the initial and final values of cohesion respectively, $\varphi_{c,0}$ and $\varphi_{c,f}$ are the initial and final values of the compression friction angle respectively, $\varphi_{e,0}$ and $\varphi_{e,f}$ are the initial and final values of the extension friction angle, $\hat{\varepsilon}^p_{eq} = \sqrt{\frac{2}{3}\hat{\varepsilon}^p_{ij}\hat{\varepsilon}^p_{ij}}$ is the Von Mises equivalent deviatoric plastic strain with $\hat{\varepsilon}^p_{ij} = \varepsilon^p_{ij} - \frac{\varepsilon^p_{kk}}{3}\delta_{ij}$ the deviatoric part of the plastic strain tensor ε^p_{ij}, coefficients dec_c and dec_φ are the

equivalent deviatoric plastic strain threshold initiating hardening/softening, $\langle\rangle$ are the Macaulay brackets, with $\langle x\rangle = x$ if $x \geq 0$ and $\langle x\rangle = 0$ if $x < 0$, and finally coefficients B_c and B_ϕ are evolution parameters governing the rate of hardening/softening. In particular, these latter represent respectively the values of equivalent plastic strain for which half of the hardening/softening on friction angle and cohesion is achieved, as depicted in Figure II–38.

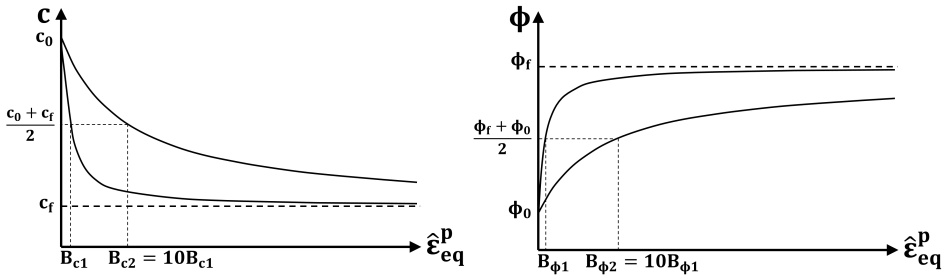

(a) (b)

Figure II–38 – Hardening and softening rules: hyperbolic evolution of (a) friction angle and (b) cohesion with plastic strain.

Viscoplastic component

Viscoplasticity is also taken into account to reproduce the creep deformations characterising the long term behaviour of the clay materials [Shao et al., 2003]. The plastic strain is hence assumed to be composed of a time-independent instantaneous strain ε_{ij}^{p} and of a time-dependent creep strain ε_{ij}^{vp}, which corresponds to a delayed plastic deformation [Perzyna, 1966]. The approach adopted hereafter consists in a single viscoplastic flow mechanism decoupled from elastoplasticity, with the following viscoplastic loading surface f^{vp} (Figure II–37c) controlled by a delayed viscoplastic hardening function α^{vp} [Jia et al., 2008, Zhou et al., 2008]:

$$f^{vp} \equiv \sqrt{3} II_{\tilde{\sigma}} - \alpha^{vp} R_c \sqrt{A\left(C_s + \frac{I'_\sigma}{3R_c}\right)} = 0 \tag{II–108}$$

$$\alpha^{vp} = \alpha_0^{vp} + \left(1 - \alpha_0^{vp}\right) \frac{\varepsilon_{eq}^{vp}}{B^{vp} + \varepsilon_{eq}^{vp}} \tag{II–109}$$

Where R_c is the uniaxial compressive strength, A is an internal friction coefficient, C_s is a constant cohesion coefficient, α_0^{vp} is the initial threshold for the viscoplastic flow, B^{vp} is a hardening parameter, and ε_{eq}^{vp} is the equivalent viscoplastic strain.

Further details about the elasto-plastic model are available in [Pardoen et al., 2015b], while a complete description of the viscoplastic model is available in [Jia et al., 2008, Zhou et al., 2008] and details about its implementation in the gallery excavation can be found in [Pardoen and Collin, 2017].

6.4 Equilibrium restrictions

Equilibrium restrictions arise from thermodynamic equilibrium between the different phases of the species. They constitute equilibrium equations for each chemical species that are necessary to close the mass balance equations, as highlighted in Figure II–35.

6.4.1 Kelvin's law

In porous media, if both gaseous and liquid phases are present in the pore network, then an equilibrium restriction is required to link both phases of the water species, *i.e.* the liquid water and the water

vapour. Assuming that the two phases are thermodynamically equilibrated, then Kelvin's law gives the concentration of water vapour in the gas phase as a function of suction according to:

$$RH = \frac{p_v}{p_{v,0}} = \frac{\rho_v}{\rho_{v,0}} = \exp\left(\frac{-s\, m_v}{RT\rho_w}\right) \tag{II–110}$$

where RH is the relative humidity of the gaseous phase, $p_{v,0}$ and $\rho_{v,0}$ are the pressure and density of saturated water vapour respectively, which remain constant for a given temperature [Garrels and Christ, 1965, Ewen and Thomas, 1989], p_v and ρ_v are the partial pressure and density of water vapour respectively, $s = p_g - p_w$ is the suction defined as the gas pressure in excess of the water pressure (see Section 5.3.2), m_v is the molar mass of water vapour, ρ_w is the density of water, R is the universal gas constant and T is the absolute temperature in *Kelvin*.

6.4.2 Henry's law

In porous media, if both gaseous and liquid phases are present in the pore network, then an equilibrium restriction is required to link both phases of the gas species, *i.e.* the dry gas and the dissolved gas. Assuming that the two phases are thermodynamically equilibrated, then Henry's law [Weast, 1987] states that under partially saturated and isothermal conditions, the amount of dissolved gas is proportional to the partial pressure of dry gas according to:

$$p_g = K_{dg}^{eq}(T) x_{dg} \tag{II–111}$$

where K_{da}^{eq} is an equilibrium constant depending on the temperature and x_{da} is the mole fraction of dissolved air. By assuming the ideal gas law, the equilibrium equation can be rewritten in terms of the dry gas and dissolved gas densities as follows:

$$\rho_{dg} = H_g(T)\rho_g \tag{II–112}$$

where H_g is Henry's coefficient that determines the dissolved gas volume in water [Gawin and Sanavia, 2009]. Its value depends on gas type and temperature, although this latter influence is neglected under isothermal conditions. At standard conditions, this coefficient is equal to $H_g = 0.0234 - 0.0190 - 0.0091$ for air, Hydrogen and Helium respectively.

6.5 Finite element formulation

The classical hydro-mechanical model introduced so far in this chapter is governed by a set of balance equations in a strong form expressing the local equilibrium at the level of an arbitrary control volume. In order to obtain a well-posed problem, initial and boundary conditions are also mandatory besides balance equations (Section 6.5.1). Furthermore, with a view to solving the problem with finite element analysis [Zienkiewicz and Taylor, 2000], the balance equations need to be expressed in a weak form (Section 6.5.2). It also requires to linearise the field equations (Section 6.5.4), and discretise continuous time and space into finite time steps and finite elements (Sections 6.5.3 and 6.5.5). Finally, solving the system of linear equations (Section 6.5.6) gives the global solution of the problem (Section 6.5.7). All these theoretical developments leading to the formulation of a coupled finite element are summarised hereafter.

6.5.1 Initial and boundary conditions

For a proper finite element implementation of the coupled hydro-mechanical problem, initial and boundary conditions are required to complete the balance equations. While these equations characterise the static equilibrium of an elementary volume, boundary conditions ensure the equilibrium at the external surface of the domain and initial conditions are needed for model closure.

The initial conditions describe the entire fields of displacement, water pressures and gas pressures to start from at the beginning of the simulation ($t = t_0$):

$$\mathbf{u} = \mathbf{u_0} \qquad p_w = p_{w,0} \qquad p_g = p_{g,0} \qquad \text{on } \Omega \tag{II–113}$$

The boundary conditions of Dirichelet type correspond to imposed displacements, fluid pressures at the boundary of the system (at all time $t > t_0$):

$$\mathbf{u} = \hat{\mathbf{u}} \text{ on } \delta\Gamma_{\mathbf{u}} \qquad p_w = \hat{p}_w \text{ on } \delta\Gamma_{p_w} \qquad p_g = \hat{p}_g \text{ on } \delta\Gamma_{p_g} \tag{II–114}$$

The boundary conditions of Neumann type correspond to imposed force or fluid flux. For the displacement field, the classical traction force per unit area acting on a part of the external surface reads (see Equation (II–31)):

$$\bar{t}_i = \sigma_{ij} \cdot n_j \tag{II–115}$$

where n_i is the normal vector to the boundary, $\bar{t}_i$ is the imposed traction vector and σ_{ij} is the Cauchy total stress tensor.

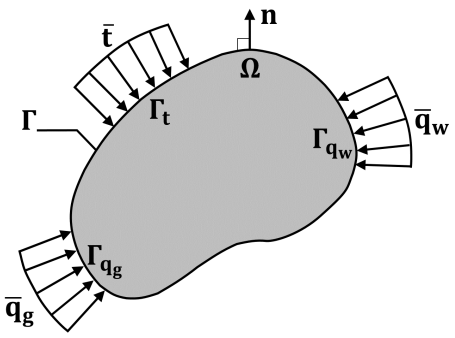

Figure II–39 – Current configuration of the material system with boundary conditions.

Similarly, the boundary conditions for prescribed water and gas fluxes on the boundary, on a part Γ_{q_w} or Γ_{q_g} of Γ are:

$$\bar{q}_w + (f_{w,i} + f_{v,i}) \cdot n_i = 0 \text{ on } \delta\Gamma_{q_w} \qquad \bar{q}_g + (f_{g,i} + f_{dg,i}) \cdot n_i = 0 \text{ on } \delta\Gamma_{q_g} \tag{II–116}$$

where $\bar{q}_w$ and $\bar{q}_g$ are the input water and gas masses (positive for inflow) per unit area imposed on $\bar{\Gamma}_{q_w}$ and $\bar{\Gamma}_{q_g}$ respectively and $f_{w,i}$ and $f_{g,i}$ are internal total fluxes of water and gas species in both liquid and gas phases, as defined in the constitutive equations in Section 6.3. The different boundary conditions of the material system in the current configuration Ω are represented schematically in Figure II–39.

6.5.2 Weak form of the balance equations

The governing Equations (II–48), (II–55), (II–60) and (II–65) presented in Section 6.2 are written in usual differential local form. However, a weak formulation of these equations is required in order to address boundary-value problems over large domains within a finite element framework.

Momentum balance equation

A weak form of the local momentum balance Equation (II–48) is obtained by using the principle of virtual work. It states that for any kinematically admissible virtual field, *i.e.* which respects the solid continuity and boundary conditions, the equality between the internal W_I^* and external W_E^* virtual power (produced by all stresses and forces acting on a mechanical system) ensures the local equilibrium at every point of the domain, and thus the global equilibrium of the solid.

For classical kinematic theory of first gradient, the virtual motion is defined with a kinematically admissible virtual (macro) displacement field u_i^* (and its first derivative F_{ij}^* which refers to Equation (II–39)) on a system with current configuration Ω. In the classical continuum mechanics, the expression of the internal virtual work of a given body reads for any virtual quantities:

$$W_I^* = \int_\Omega \sigma_{ij} \frac{\partial u_i^*}{\partial x_j} d\Omega \tag{II–117}$$

where σ_{ij} is the Cauchy total stress field.

On the other hand, assuming that the boundary Ω is regular, the external virtual work W_{ext}^* reads:

$$W_{ext}^* = \int_\Omega \rho_{mix} g_i u_i^* d\Omega + \int_{\Gamma_\sigma} \bar{t}_i u_i^* d\Gamma \tag{II–118}$$

where ρ_{mix} is the mass density of the mixture defined in Equation (II–49), g_i is the gravity and $\bar{t}_i$ is the classical external traction force per unit area acting on a part Γ_t of the boundary Γ.

The principle of virtual works implies that the internal virtual work is equal to external one, which leads to the following weak form of the momentum balance equation:

$$\underbrace{\int_\Omega \sigma_{ij} \frac{\partial u_i^*}{\partial x_j} d\Omega}_{W_I^*} = \underbrace{\int_\Omega \rho_{mix} g_i u_i^* d\Omega + \int_{\Gamma_\sigma} \bar{t}_i u_i^* d\Gamma}_{W_E^*} \tag{II–119}$$

As this principle holds for any u_i^*, the local equilibrium equations, namely the momentum balance Equation (II–48) and the boundary condition (II–115), are thus deduced inside the domain Ω and for any point on the boundary Γ.

Water mass balance equation

The water mass balance equation is written in a weak form in a similar way as the momentum balance equation. For every kinematically admissible virtual water pressure field p_w^*, it reads:

$$\int_\Omega \left[\dot{M}_w p_w^* + \dot{M}_v p_w^* - f_{w,i} \frac{\partial p_w^*}{\partial x_i} - f_{v,i} \frac{\partial p_w^*}{\partial x_i} \right] d\Omega = \int_\Omega Q_w p_w^* d\Omega - \int_{\Gamma_q} \bar{q}_w p_w^* d\Gamma \tag{II–120}$$

where $\dot{M}_w$ and $\dot{M}_v$ are the mass variations of liquid water and water vapour respectively (see section 6.2.2), $f_{w,i}$ and $f_{v,i}$ are the mass flows of liquid water and water vapour respectively (see Section 6.3.1), Q_w is the sink mass term of water, and Γ_q is the part of the boundary where the input water mass per unit area $\bar{q}_w$ is prescribed.

As Equation (II–120) holds for any p_w^*, the local equilibrium equations, namely the liquid water and water vapour mass balance Equations (II–58) and (II–59) and the hydraulic boundary condition (II–116) can be deduced.

Gas mass balance equation

Similarly, the gas mass balance equation is written in a weak form in the same way as the momentum balance equation. For every kinematically admissible virtual gas pressure field p_g^*, it reads:

$$\int_\Omega \left[\dot{M}_g p_g^* + \dot{M}_{dg} p_g^* - f_{g,i} \frac{\partial p_g^*}{\partial x_i} - f_{dg,i} \frac{\partial p_g^*}{\partial x_i} \right] d\Omega = \int_\Omega Q_g p_g^* d\Omega - \int_{\Gamma_q} \bar{q}_g p_g^* d\Gamma \tag{II–121}$$

where $\dot{M}_g$ and $\dot{M}_{dg}$ are the mass variations of dry gas and dissolved gas respectively (see Section 6.2.2), $f_{g,i}$ and $f_{dg,i}$ are the mass flows of dry gas and dissolved gas respectively (see Section 6.3.1), Q_g is the

sink mass term of gas, and Γ_q is the part of the boundary where the input gas mass per unit area $\bar{q}_g$ is prescribed.

As Equation (II–121) holds for any p_g^*, the local equilibrium equations, namely the dry gas and dissolved gas mass balance Equations (II–63) and (II–64) and the hydraulic boundary condition (II–116) can be deduced.

6.5.3 Time discretisation

The balance Equations (II–119) to (II–121) should be verified at any time t. Yet, the continuous loading process has to be discretised into finite time steps Δt to be able to numerically solve this non-linear problem. The time derivative of the problem unknown fields are defined using a fully implicit difference scheme, expressed for the rate of any quantity a as:

$$\dot{a}_i^{t+\Delta t} = \frac{a_i^{t+\Delta t} - a_i^t}{\Delta t} = \frac{\Delta a_i}{\Delta t} \tag{II–122}$$

6.5.4 Linearisation

The coupled hydromechanical model detailed here hinges on a series of balance Equations (II–119), (II–120) and (II–121) expressed in a weak form in order to be implemented in finite element code. Solving the loading process of a boundary condition problem consists in determining the unknown fields (u_i, p_w, p_g) for which the equilibrium equations are valid. However, given that the governing equations include numerous hydromechanical couplings and advanced constitutive relationships, the whole system is characterised by high non-linearities which make the analytical resolution almost impossible. Since this system of highly non-linear relations is *a priori* not numerically satisfied at any instant t, an iterative procedure of Newton-Raphson type is employed. The aim of this section is to define an auxiliary linear problem deriving from the non-linear system following the approaches of [Borja and Alarcón, 1995, Chambon et al., 2001b], and to find a solution for the unknown fields for which equilibrium is achieved.

To this end, time discretisation into finite time steps Δt (Section 6.5.3) is a prerequisite which leads to two configurations. One configuration Ω^t is assumed to be known and in equilibrium with the boundary conditions at a given time t of the loading, while the other configuration Ω^τ is not at equilibrium at a time ($\tau = t + \Delta t$). The objective of the iterative procedure is to find a new configuration in equilibrium at the end of the time step. Consequently, a first guess of this new configuration close to the solution but for which the equilibrium is not met is proposed and denoted as $\Omega^{\tau 1}$. Both configurations at time t and $\tau 1$ are assumed to be known and non-equilibrium forces, *i.e.* residuals $\Delta_1^{\tau 1}$, $\Delta_2^{\tau 1}$, $\Delta_3^{\tau 1}$ and $\Delta_4^{\tau 1}$ appear in the four governing equations respectively:

$$\int_{\Omega^{\tau 1}} \sigma_{ij}^{\tau 1} \frac{\partial u_i^*}{\partial x_j^{\tau 1}} d\Omega^{\tau 1} - \int_{\Omega^{\tau 1}} \rho_{mix}^{\tau 1} g_i u_i^* d\Omega^{\tau 1} - \int_{\Gamma_\sigma^{\tau 1}} \bar{t}_i^{\tau 1} u_i^* d\Gamma^{\tau 1} = \Delta_1^{\tau 1} \tag{II–123}$$

$$\int_{\Omega^{\tau 1}} \left[\dot{M}_w^{\tau 1} p_w^* + \dot{M}_v^{\tau 1} p_w^* - f_{w,i}^{\tau 1} \frac{\partial p_w^*}{\partial x_i^{\tau 1}} - f_{v,i}^{\tau 1} \frac{\partial p_w^*}{\partial x_i^{\tau 1}} \right] d\Omega^{\tau 1} - \int_{\Omega^{\tau 1}} Q_w^{\tau 1} p_w^* d\Omega^{\tau 1} + \int_{\Gamma^{\tau 1}} \bar{q}_w^{\tau 1} p_w^* d\Gamma^{\tau 1} = \Delta_2^{\tau 1} \tag{II–124}$$

$$\int_{\Omega^{\tau 1}} \left[\dot{M}_g^{\tau 1} p_g^* + \dot{M}_{dg}^{\tau 1} p_g^* - f_{g,i}^{\tau 1} \frac{\partial p_g^*}{\partial x_i^{\tau 1}} - f_{dg,i}^{\tau 1} \frac{\partial p_g^*}{\partial x_i^{\tau 1}} \right] d\Omega^{\tau 1} - \int_{\Omega^{\tau 1}} Q_g^{\tau 1} p_g^* d\Omega^{\tau 1} + \int_{\Gamma^{\tau 1}} \bar{q}_g^{\tau 1} p_g^* d\Gamma^{\tau 1} = \Delta_3^{\tau 1} \tag{II–125}$$

The aim is now to find another configuration denoted $\Omega^{\tau 2}$ close to $\Omega^{\tau 1}$ for which the non-equilibrium forces (residuals) vanish:

$$\int_{\Omega^{\tau 2}} \sigma_{ij}^{\tau 2} \frac{\partial u_i^*}{\partial x_j^{\tau 2}} d\Omega^{\tau 2} - \int_{\Omega^{\tau 2}} \rho_{mix}^{\tau 2} g_i u_i^* d\Omega^{\tau 2} - \int_{\Gamma_\sigma^{\tau 2}} \bar{t}_i^{\tau 2} u_i^* d\Gamma^{\tau 2} = 0 \tag{II–126}$$

$$\int_{\Omega^{\tau 2}} \left[\dot{M}_w^{\tau 2} p_w^* + \dot{M}_v^{\tau 2} p_w^* - f_{w,i}^{\tau 2} \frac{\partial p_w^*}{\partial x_i^{\tau 2}} - f_{v,i}^{\tau 2} \frac{\partial p_w^*}{\partial x_i^{\tau 2}} \right] d\Omega^{\tau 2} - \int_{\Omega^{\tau 2}} Q_w^{\tau 2} p_w^* d\Omega^{\tau 2} + \int_{\Gamma^{\tau 2}} \bar{q}_w^{\tau 2} p_w^* d\Gamma^{\tau 2} = 0 \tag{II–127}$$

$$\int_{\Omega^{\tau 2}} \left[\dot{M}_g^{\tau 2} p_g^* + \dot{M}_{dg}^{\tau 2} p_g^* - f_{g,i}^{\tau 2} \frac{\partial p_g^*}{\partial x_i^{\tau 2}} - f_{dg,i}^{\tau 2} \frac{\partial p_g^*}{\partial x_i^{\tau 2}} \right] d\Omega^{\tau 2} - \int_{\Omega^{\tau 2}} Q_g^{\tau 2} p_g^* d\Omega^{\tau 2} + \int_{\Gamma^{\tau 2}} \bar{q}_g^{\tau 2} p_g^* d\Gamma^{\tau 2} = 0 \tag{II–128}$$

Rewriting the field equations related to $\Omega^{\tau 2}$ in configuration $\Omega^{\tau 1}$ (using the Jacobian transformation), assuming in addition that g_i, $\bar{t}_i$, $\bar{q}_w$, $\bar{q}_g$, Q_w, Q_g are independent of the different unknown fields, and subtracting after all the balance equations for the two configurations yields:

$$\int_{\Omega^{\tau 1}} \frac{\partial u_i^*}{\partial x_l^{\tau 1}} \sigma_{ij}^{\tau 2} \frac{\partial x_l^{\tau 1}}{\partial x_j^{\tau 2}} det(F) - \sigma_{il}^{\tau 1} - u_i^* \left(\rho_{mix}^{\tau 2} det(F) - \rho_{mix}^{\tau 1} \right) g_i d\Omega^{\tau 1} = -\Delta_1^{\tau 1} \tag{II–129}$$

$$\begin{aligned} &\int_{\Omega^{\tau 1}} p_w^* \left(\dot{M}_w^{\tau 2} det(F) + \dot{M}_v^{\tau 2} det(F) - \dot{M}_w^{\tau 1} - \dot{M}_v^{\tau 1} \right) \\ &- \frac{\partial p_w^*}{\partial x_k^{\tau 1}} \left(f_{w,i}^{\tau 2} \frac{\partial x_k^{\tau 1}}{\partial x_j^{\tau 2}} det(F) + f_{v,i}^{\tau 2} \frac{\partial x_k^{\tau 1}}{\partial x_j^{\tau 2}} det(F) - f_{w,k}^{\tau 1} - f_{v,k}^{\tau 1} \right) d\Omega^{\tau 1} = -\Delta_2^{\tau 1} \end{aligned} \tag{II–130}$$

$$\begin{aligned} &\int_{\Omega^{\tau 1}} p_g^* \left(\dot{M}_g^{\tau 2} det(F) + \dot{M}_{dg}^{\tau 2} det(F) - \dot{M}_g^{\tau 1} - \dot{M}_{dg}^{\tau 1} \right) \\ &- \frac{\partial p_g^*}{\partial x_k^{\tau 1}} \left(f_{g,i}^{\tau 2} \frac{\partial x_k^{\tau 1}}{\partial x_j^{\tau 2}} det(F) + f_{dg,i}^{\tau 2} \frac{\partial x_k^{\tau 1}}{\partial x_j^{\tau 2}} det(F) - f_{g,k}^{\tau 1} - f_{dg,k}^{\tau 1} \right) d\Omega^{\tau 1} = -\Delta_3^{\tau 1} \end{aligned} \tag{II–131}$$

where $\frac{\partial x_i^{\tau 2}}{\partial x_j^{\tau 1}}$ is the Jacobian matrix of the transformation between the two configurations, and $det(F) = \left| \frac{\partial x_i^{\tau 2}}{\partial x_j^{\tau 1}} \right|$ is the Jacobian determinant.

By making the two configurations tend towards each other, which leads to the limit $\tau 2 = \tau 1$ the variations of any quantity of the problem can be defined as:

$$da^{\tau 1} = a^{\tau 2} - a^{\tau 1} \tag{II–132}$$

Taking these variations into account and using a Taylor expansion of Equations (II–129) to (II–131) while discarding terms of degree greater than one gives, after some algebra, a linearised system of field equations (more exhaustive analytical developments are available in [Chambon et al., 2001b, Chambon and Moullet, 2004, Collin et al., 2006]). This makes it possible to assess the corrections of the unknown fields to be added to the respective current values to obtain a new configuration closer to a well-balanced configuration.

6.5.5 Space discretisation

The classic finite element method lies on the spatial discretisation of the continuum medium Ω into n_e finite elements of volume Ω_e such that it is approximated by (Figure III–13b):

$$\Omega = \bigcup_{e=1}^{n_e} \Omega_e \tag{II–133}$$

In this part of the work, the coupled finite element developed to model the solid bodies is referred to as the MWAT element in the LAGAMINE code [Collin, 2003]. This 2D isoparametric element is composed of eight nodes with 5 degrees of freedom for the displacement fields u_i, the water pressure field p_w and the gas pressure field p_g (and the temperature T), and four integration points as presented in Figure II–40c.

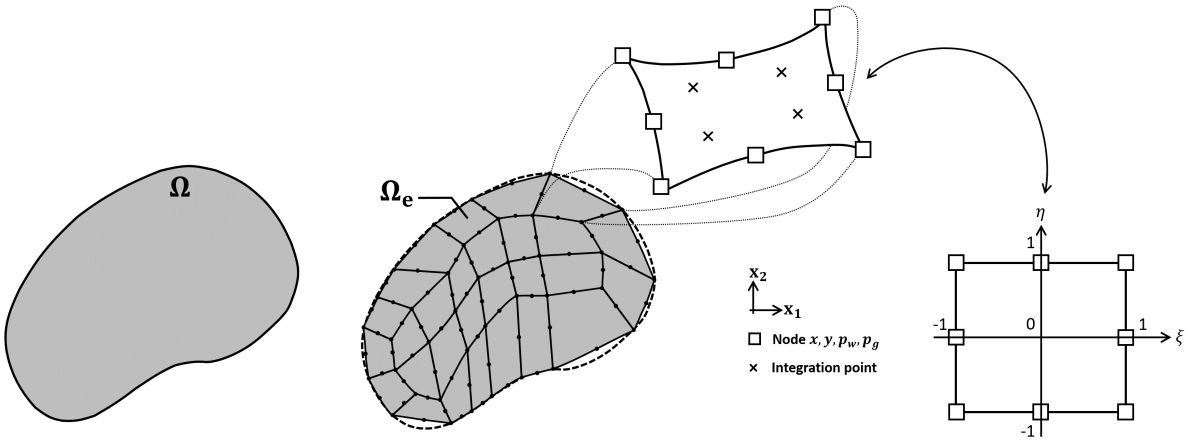

(a) Continuum (b) Discretisation (c) MWAT element

Figure II–40 – Spatial discretisation of the continuum: (a) continuum volume Ω, (b) discrete counterpart composed by n_e finite elements Ω_e, (c) 2D finite element MWAT (top left) and its corresponding parent element (right), *after* [Collin, 2003].

The Jacobian matrix J_{ij} of the transformation from the global (natural) coordinates (x_1, x_2) to the local (parent) coordinates (ξ, η) is defined by:

$$J_{ij} = \begin{bmatrix} \frac{\partial x_1}{\partial \xi} & \frac{\partial x_1}{\partial \eta} \\ \frac{\partial x_2}{\partial \xi} & \frac{\partial x_2}{\partial \eta} \end{bmatrix} \tag{II–134}$$

Let us specify the nodal unknowns coordinates u_{l_k}, each node k having l degrees of freedom, then the coordinates $u_l^e(\xi,\eta)$ and displacements $\Delta u_l^e(\xi,\eta)$ are interpolated over the parent element using the shape functions $\mathcal{F}^k(\xi,\eta)$:

$$u_l^e(\xi,\eta) = \sum_{k=1}^{n_e} \mathcal{F}^k(\xi,\eta) u_{l_k} \qquad \text{and} \qquad \Delta u_l^e(\xi,\eta) = \sum_{k=1}^{n_e} \mathcal{F}^k(\xi,\eta) \Delta u_{l_k} \tag{II–135}$$

where $n_e = 8$ is the number of nodes of the element Ω_e, and $l = 5$ since each node has 5 degrees of freedom: two global coordinates x_1, x_2, the pore water pressure p_w, the gas pressure p_g and the temperature [1].

Using Equation (II–119) to express the mechanical part of the virtual internal power of a single element Ω_e, together with a Gauss integration scheme and the Jacobian matrix of Equation (II–134), one

1. The present work is restricted to isothermal conditions, the energy balance equation required to solve non-isothermal problems can be found in [Collin, 2003].

can express the mechanical internal nodal forces of that element $\left[F_{I,i_k}^{\Omega_e}\right]^T$. Similary deriving hydraulic nodal forces from the expressions of internal virtual work of Equations (II–120) and (II–121), all these nodal forces can be gathered in a generalised equivalent vector $\left[F_{I,l_k}^{\Omega_e}\right]^T$. According to Equation (II–133), the global vector of internal energetically equivalent nodal forces is obtained by assembling the contributions of the n_e individual finite elements composing the continuous body:

$$F_{I,l_k} = \bigcup_{e=1}^{n_e} F_{I,l_k}^{\Omega_e} \tag{II–136}$$

It is worth notifying that the global vector of external energetically equivalent nodal forces is derived in the same way from external virtual power.

6.5.6 From the element computation to the global solution

Formulating the balance Equations (II–129) to (II–131) of the linear auxiliary problem in matrix form helps defining the stiffness (tangent) matrix of an element.

$$\int_{\Omega^t} \left[U_{(x_1,x_2)}^{*,t}\right]^T \left[E^t\right] \left[dU_{(x_1,x_2)}^t\right] d\Omega^t = -\Delta_1^t - \Delta_2^t - \Delta_3^t \tag{II–137}$$

where $[E^t]$ is the stiffness matrix, $\left[dU_{(x_1,x_2)}^t\right]$ is the vector of the unknown increments of nodal variables, $\left[U_{(x_1,x_2)}^{*,t}\right]$ is a vector having the same structure with the corresponding virtual quantities. These two latter are defined as:

$$\left[dU_{(x_1,x_2)}^t\right]_{28\times 1} = \left[\frac{\partial du_1^t}{\partial x_1^t} \frac{\partial du_1^t}{\partial x_2^t} \frac{\partial du_2^t}{\partial x_1^t} \frac{\partial du_2^t}{\partial x_2^t} du_1^t du_2^t \frac{\partial dp_w^t}{\partial x_1^t} \frac{\partial dp_w^t}{\partial x_2^t} dp_w^t \frac{\partial dp_g^t}{\partial x_1^t} \frac{\partial dp_g^t}{\partial x_2^t} dp_g^t\right]^T \tag{II–138}$$

$$\left[U_{(x_1,x_2)}^{*,t}\right]_{1\times 28} = \left[\frac{\partial u_1^*}{\partial x_1^t} \frac{\partial u_1^*}{\partial x_2^t} \frac{\partial u_2^*}{\partial x_1^t} \frac{\partial u_2^*}{\partial x_2^t} u_1^* u_2^* \frac{\partial p_w^*}{\partial x_1^t} \frac{\partial p_w^*}{\partial x_2^t} p_w^* \frac{\partial p_g^*}{\partial x_1^t} \frac{\partial p_g^*}{\partial x_2^t} p_g^*\right] \tag{II–139}$$

The finite element spatial discretisation is introduced in Equation (II–137) using the transformation matrices $[T^t]$ and $[B]$ that connect the current element vector $\left[dU_{(x_1,x_2)}^t\right]$ to the parent element vector $\left[dU_{(\xi,\eta)}^t\right]$ and to the nodal variables $\left[dU_{(Node)}^t\right]$:

$$\left[dU_{(x_1,x_2)}^t\right] = \left[T^t\right] \left[dU_{(\xi,\eta)}^t\right] = \left[T^t\right] \left[B\right] \left[dU_{(Node)}^t\right] \tag{II–140}$$

Integrating Equation (II–137) on each parent element yields:

$$\int_{\Omega^t} \left[U_{(x_1,x_2)}^{*,t}\right]^T \left[E^t\right] \left[dU_{(x_1,x_2)}^t\right] d\Omega^t = \left[U_{(x_1,x_2)}^{*,t}\right]^T \underbrace{\int_{-1}^{1}\int_{-1}^{1} [B]^T \left[T^t\right]^T \left[E^t\right] \left[T^t\right] [B]\, det(J^t) d\xi d\eta}_{[k^t]} \left[dU_{(x_1,x_2)}^t\right] \tag{II–141}$$

where $[k^t]$ is the local element stiffness matrix, $det(J^t)$ is the determinant of the Jacobian matrix of the transformation between the parent (ξ,η) and the current (x_1,x_2) elements, and $[E^t]$ is the stiffness matrix storing the different terms of the linearised balance equations, which reads:

$$\left[E^t\right] = \begin{bmatrix} E_{MM}^t & E_{WM}^t & E_{GM}^t \\ E_{MW}^t & E_{WW}^t & E_{GW}^t \\ E_{MG}^t & E_{WG}^t & E_{GG}^t \end{bmatrix} \tag{II–142}$$

where the matrices $[E_{MM}^{\tau 1}]$, $[E_{WW}^{\tau 1}]$, $[E_{GG}^{\tau 1}]$ are the classical stiffness matrices for mechanical, water flow and gas flow problems, while the off-diagonal matrices contain the multi-physical coupling terms. As an example, the matrix E_{MW} expresses the influence of mechanics (M) on water flows (W).

In Equation (II–137), the residual terms are computed locally for each element from this relationship including the elementary out of balance force vector $[f_{OB}^t]$:

$$-\Delta_1^t - \Delta_2^t - \Delta_3^t = \left[U_{Node}^{*,t}\right]^T \left[f_{OB}^t\right] \tag{II–143}$$

6.5.7 Global solution

The global solution is found once the energetically equivalent internal nodal forces F_I and the external ones F_E are balanced. This might not be the case at the beginning of any arbitrary time step, owing to the loading process and the transient effect. The so-called out-of-balance forces providing a quantification of the imbalance within the system are given by:

$$F_{OB,l_k} = F_{E,l_k} - F_{I,l_k} \tag{II–144}$$

Considering that the out-of-balance forces will most probably not be exactly null, a numerical criterion has to be adopted in order to decide if the equilibrium is reached or not. By expanding the out-of-balance forces in a first order Taylor series around the last known approximation, it comes:

$$F^{t+\Delta t}_{OB,l_k} \approx F^{t}_{OB,l_k} + \frac{\partial F^{t}_{OB,l_k}}{\partial u_{m_n}} \Delta u_{m_n} \tag{II–145}$$

where the derivative term is the variation of the nodal force F^t_{OB,l_k} relative to the degree of freedom l at node k, due to a variation u_{m_n} of the degree of freedom m at node n.

The equilibrium is reached at time $t+\delta t$ in the case the out-of-balance forces are equal to zero:

$$F^{t+\Delta t}_{OB,l_k} = 0 \tag{II–146}$$

Accordingly, the correction of the generalised degrees of freedom is computed at each iteration as:

$$\Delta u_{m_n} = -\left[\frac{\partial F^{t}_{OB,l_k}}{\partial u_{m_n}}\right]^{-1} F^{t}_{OB,l_k} = -\left[K^{t}_{l_k m_n}\right]^{-1} F^{t}_{OB,l_k} \tag{II–147}$$

or passing to finite coordinate increments:

$$\left[\delta U^{t}_{Node}\right] = -\left[K^{t}\right]^{-1}\left[F^{t}_{OB}\right] \tag{II–148}$$

where $\left[\delta U^t_{Node}\right]$ is the global correction vector of the nodal degrees of freedom, $[K^t]$ and $\left[F^t_{OB}\right]$ are the global stiffness matrix and the global out-of-balance force vector, obtained by assembling the elementary stiffness matrices and the elementary out-of-balance force vectors computed from Equations (II–141) and (II–143) respectively. Practically, the components of the former must be re-evaluated at each iteration of the Newton-Raphson strategy as the variation of the equivalent nodal forces due to a variation of the generalised coordinates:

$$K^{t}_{l_k m_n} = \frac{\partial F^{t}_{OB,l_k}}{\partial u_{m_n}} \tag{II–149}$$

Considering the presence of multi-physical coupling terms in the off-diagonal terms, a monolithic (fully coupled) procedure seems more appropriate to solve the stiffness matrix. This computation can be done analytically if an analytical solution of Equation (II–149) is available. Otherwise, another way to compute the stiffness matrix is to approximate Equation (II–149) by a finite difference such as:

$$K^{t}_{l_k m_n} \approx \frac{F^{t}_{OB,l_k}(u_{m_n}+\varepsilon) - F^{t}_{OB,l_k}(u_{m_n})}{\varepsilon} \tag{II–150}$$

where $F^t_{OB,l_k}(u_{m_n}+\varepsilon)$ is the out-of-balance response after perturbing the u_{m_n} coordinates with ε, $F^t_{OB,l_k}(u_{m_n})$ is the out-of-balance response for the unperturbed state, and ε is the perturbation. The size of this numerical perturbation has to be small enough to actually compute a derivative and large enough not to be influenced by the numerical imprecision of the constitutive relation.

Finally, once the stiffness matrix is known, the corrections defined in Equation (II–147) are added to their respective generalised degrees of freedom as follows:

$$u^{t+\Delta t}_{l_k} = u^{t}_{l_k} + \Delta u_{l_k} \tag{II–151}$$

which allows to find an actualised configuration closer to the equilibrium. This latter is verified, leading to a next iteration or to the end of the loading step considering the iterative scheme given in Figure II–41.

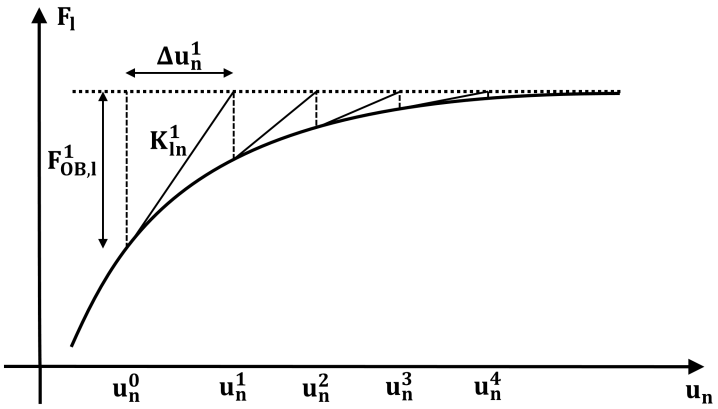

Figure II–41 – Illustration of the Newton-Raphson iterative scheme for solving a non-linear problem.

6.6 Advanced hydro-mechanical models

The conventional HM multiphase models for partially saturated materials like the one presented in detail in Sections 6.1 to 6.5 are essential to reproduce the two-phase water-gas flow mechanism in porous media. In these models, the coupling between the fluid flows and the mechanical behaviour is straightforward, in the sense that the evolution of pore pressure affects the effective stress distribution on the one hand, and the fluid storage is a function of the mechanical deformation on the other hand. Given that these classical models include constant flow parameters such as permeabilities and retention curves, they are however not able as such to reproduce all the features of gas flow processes, such as the impact of a damaged host rock on gas flow, nor the development of gas-filled pathways in the intact host rock. Different numerical methods can therefore be adopted to improve the modelling response, by introducing stronger couplings between the gas flow and the mechanical behaviour of clayey materials.

Among the different existing techniques, the finite element approaches are based on the continuum mechanics hypothesis that averaged properties of the porous medium operate on a representative element volume. Five of these options are presented in the following. On the other hand, discontinuum-based approaches rely on the discrete hypothesis that treats the rock mass as separate matrix blocks or particles, thus enabling to properly simulate strong discontinuities. A brief review of the different types of models related to this second category brings the present section to an end.

6.6.1 Natural heterogeneity based models

This approach relies on the natural and initial heterogeneity of the material for assuming that the pressurised gas is transported preferentially through the areas that are less resistant to both flow and fracturing. The idea is to have recourse to a spatially auto-correlated random field [Phoon and Kulhawy, 1999] that follows a log-normal distribution [Santillán et al., 2017] to construct a heterogeneous distribution of some specific HM properties of the clay material, such as intrinsic permeability, gas entry value, fracture aperture or pore space. A heterogeneous distribution of the permeability in a continuous two-phase flow model was initially proposed by [Delahaye and Alonso, 2002], highlighting the emergence of pathways with higher initial permeability. It was later adapted to a non-uniform distribution of porosity coupled to the permeability according to the Kozeny-Carman law [Olivella and Alonso, 2008], and specifically applied to reproduce some experimental gas transport observations on clay samples

[Gonzalez-Blanco et al., 2016]. This approach was further extended to other HM properties to enhance its ability to simulate the preferential gas flow in clay-rich materials [Guo and Fall, 2019].

6.6.2 Intrinsic permeability based models

The intrinsic permeability directly controls the gas transport processes in the host rocks, which is why this key parameter has stimulated the formulation of a great number of numerical models capable of simulating the development of preferential pathways in an implicit manner.

The gas pressure based model given in Equation (II–152) [Xu et al., 2013b, Xu et al., 2013a] was proposed following the experimental observations that the permeability value experiences an abrupt increase once the applied gas pressure reaches a critical threshold, triggering a gas breakthrough event. However, this phenomenologically based model does not suitably capture the deformation dependent phenomenon that is caused by the confining pressure change, and provides less information about the evolution of the pore size and the pore structure, which are yet fundamental factors affecting the intrinsic permeability.

To address this behaviour, the porosity-based model given in Equation (II–153) [Rutqvist et al., 2002] proposes to use exponential laws to reproduce the permeability evolution due to pore volume change in air injection tests [Senger et al., 2014, Senger et al., 2018], possibly enriched to take into account the fracturing induced pore structure change [Yang and Fall, 2021c].

In a similar way, the damage-based model given in Equation (II–154) [Dagher et al., 2019, Fall et al., 2014] proposes to define the permeability as a function of the pore volume change and a damage variable. This way, both the abrupt increase in permeability due to damage propagation, and the reversible process caused by gas induced porosity change can be captured by the model, while it remains impossible to accurately reflect the characteristics of the microstructure network, such as the size, density and orientation of the fractures.

The strain-based model given in Equation (II–155) [Le and Nguyen, 2014, Nguyen and Le, 2015] shares similar conceptual underpinnings with the damage-based model, in the sense that the effects of permeability variation come from two contributions, *i.e.* the effective plastic strain and the total volumetric deformation. The former is beneficial to achieve the rapid increase of gas outflow rate under tensile failure, while the latter reflects the change in the pore space. Other relations linking the intrinsic permeability to strains have been formulated to reproduce excavation damaged zone developing around tunnels or boreholes. Considering the fractured rock at the macroscale as a continuous medium, the proposed power (cubic) laws summarised under Equation (II–156) relate the permeability tensor either to the porosity [Chavant and Fernandes, 2005] to highlight the volumetric deformation effect, or to the deviatoric [Pardoen et al., 2016] and tensile [Shao et al., 2006] plastic strain, to highlight the strain localisation effect in shear band mode.

$$k_{ij}(p_g) = \begin{cases} k_{ij,0}\,(1 + A_1 p_g) & \text{if } p_g < p_{thr} \\ k_{ij,0}\,(1 + A_1 p_{thr} + A_2(p_g - p_{thr})) & \text{otherwise} \end{cases} \tag{II–152}$$

$$k_{ij}(\phi) = k_{ij,0} \exp\left(A_3 \left(\frac{\phi}{\phi_0} - 1\right)\right) \tag{II–153}$$

$$k_{ij}(\phi, d_{max}) = k_{ij,UD} + k_{ij,D} = k_{ij,0} \exp\left(A_4 \left(\frac{\phi}{\phi_0} - 1\right)\right) + \frac{d}{d_{max}}(k_{max} - k_{UD}) \tag{II–154}$$

$$k_{ij}(\varepsilon) = \begin{cases} k_{ij,0} \left(10^{A_5 \Delta\varepsilon_v} \exp(A_6 \Delta\bar{\varepsilon}_p)\right) & \text{compression} \\ k_{ij,0} \left(10^{A_7 \Delta\varepsilon_v} \exp(A_6 \Delta\bar{\varepsilon}_p)\right) & \text{tension} \end{cases} \tag{II–155}$$

$$k_{ij}(\gamma_{per}) = k_{ij,0} \left(1 + A_8 \langle \gamma_{per} \rangle^3\right) \tag{II–156}$$

where k_{ij} is the intrinsic permeability tensor, p_g and p_{thr} are the gas pressure and threshold pressure, ϕ and ϕ_0 are the porosity and initial porosity, ε_v and $\bar{\varepsilon}_p$ are the volumetric strain and effective plastic

strain, $k_{ij,UD}$ and $k_{ij,D}$ are the undamaged and damaged permeabilities respectively, k_{max} is the maximum permeability corresponding to the maximum damage variable d_{max}, A_i is an empirical parameter in the model, γ_{per} is a deformation parameter for which different expressions can be envisaged, and $\langle\rangle$ are the Macaulay brackets.

6.6.3 Embedded fracture models

Given that microscopic observations in saturated clayey rocks under gas pressure built-up indicate the prevalence of the gas-induced micro-fracturing process, implicitly accounting for these pre-existing micro-fractures in the macroscopic modelling framework is the guideline of the so-called embedded fracture models.

Originally put forward by [Alonso et al., 2006] from previous purely macroscopic and continuous approaches [Snow, 1969, Liu et al., 1999], the embedded fracture model has been widely adopted to simulate gas migration in clay barriers [Chen et al., 2007, Olivella and Alonso, 2008, Gerard et al., 2011, Levasseur et al., 2010, Arnedo et al., 2013, Gerard et al., 2014, Gonzalez-Blanco et al., 2016] because it conveys more information at the macroscopic scale about the fracturing process and the geometric representation of the fracture network. In this approach, the rock is conceptualised at the micro-scale as a series of parallel fracture sets embedded into a porous matrix, as illustrated in Figure II–42. The equivalent permeability of the rock within a representative volume is thence computed as the average of the flow properties of the matrix and the fractures, as:

$$k_{ij} = k_{ij,matrix} + k_{ij,frac} \tag{II–157}$$

where $k_{ij,matrix}$ is the intrinsic permeability of the matrix, described by Kozeny-Carman model introduced in Equation (II–22) [Carman, 1937], while $k_{ij,frac}$ is the intrinsic permeability of the fracture, which is traditionally expressed as a function of the fracture opening, assuming laminar flow in the direction of the discontinuity [Darcy, 1856, Witherspoon et al., 1980]:

$$k_{ij,frac} = \frac{b^2}{12} \tag{II–158}$$

In the case of a fractured medium, the permeability through a set of parallel fractures of equal aperture, oriented parallel to flow direction, is given by [Bear et al., 1993]:

$$k_{ij,frac} = \frac{b^3}{12w} = \frac{(b_0 + w(\varepsilon - \varepsilon_0))^3}{12w} \tag{II–159}$$

where w is the characteristic dimension of a specific rock representing the mean distance between adjacent fractures, and b is the fracture aperture, which consists of an initial aperture b_0 and an aperture change Δb, calculated in dependence of the tensile strain in the direction normal to the fracture, such as:

$$\begin{aligned} b &= b_0 + \Delta b && \text{for} && \Delta b \geq 0 \\ \Delta b &= w\Delta\varepsilon = w(\varepsilon - \varepsilon_0) && \text{for} && \Delta\varepsilon > 0 \end{aligned} \tag{II–160}$$

where ε is the tensile strain within the element at the macroscopic scale, b_0 is the initial opening of the fractures at $\varepsilon = 0$ and ε_0 is the threshold strain associated with fracture initiation.

Several other variants of the embedded fracture model have been proposed up to now, defining the variation of the fracture aperture with respect to the volumetric strain [Dymitrowska et al., 2014] or to the stress normal to the fracture [Rutqvist et al., 2020]. Moreover, extensions of the model incorporating the normal stiffness of embedded fractures into the equivalent stiffness tensor of the rock have been implemented to account for the non-linear effect of the fractures on the mechanical behaviour, and applied to the modelling of coalbed methane recovery [Bertrand et al., 2017], CO_2 sequestration [Martinez

et al., 2013], or the behaviour of bentonite and clay host rock under gas injection tests [Guo and Fall, 2018, Yang et al., 2020]. And lastly, by assuming the rock as a layered structure divided into soft parts undergoing large strains and permeability increase, and hard parts subject to a smaller degree of deformation, the two-part Hooke's model [Liu et al., 2009, Liu et al., 2011] is conceptually close in spirit to the embedded fracture model.

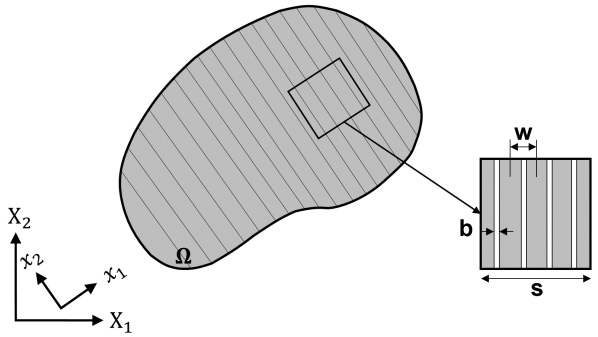

Figure II–42 – Conceptual scheme of the embedded fracture model, *after* [Olivella and Alonso, 2008].

Next to the intrinsic permeability, the gas entry value is another hydraulic property that plays a key role in controlling the gas migration process since it affects the amount of gas entering the saturated porous medium. At intact state, the clayey rock has a high gas entry value due to its extremely small pore size that inhibits the gas migration process. Once gas-induced microfractures initiate under high gas pressure, this value will be significantly decreased, which accelerates the desaturation process. This aspect has been integrated into the embedded fracture model [Olivella and Alonso, 2008] by supposing that the pore radius regarded as equal to the fracture aperture b, increases following the opening of discontinuities, so that decrease in the gas entry pressure is observed. The capillary gas entry pressure, necessary to desaturate a fracture is thus derived by combining the cubic law (II–159) for intrinsic permeability of fractures and the Young-Laplace Equation (II–8):

$$P_r = \frac{2T_s}{b} = \frac{2T_s}{b_0}\frac{b_0}{b} = P_{r,0}\frac{\sqrt[3]{k_{ij,0}}}{\sqrt[3]{k_{ij}}} \tag{II–161}$$

where P_r is the van Genuchten's parameter for the current gas entry pressure, $P_{r,0}$ is the van Genuchten's parameter for the initial value of gas entry pressure, k is the current permeability, k_0 is the initial permeability, and $T_s = 2\sigma_{GL}cos\theta$ is the surface tension acting on the gas-liquid interface.

Some numerical models [Dagher et al., 2019, Damians et al., 2019] propose to express the gas entry value as an exponential function of the void ratio or porosity, although less physically based, while other numerical models [Arson and Pereira, 2012, Pereira and Arson, 2013] intend to study the influence of deformation and damage on the permeability and retention properties thanks to the introduction of micro-scale information into a macroscopic damage model.

6.6.4 Micro-macro based models

Considering that the coupling between micro-mechanical effects and permeability is a fundamental aspect in rocks, the multi-level approach offers an alternative description to the phenomenological laws formulated in the macroscopic HM framework. The guiding principle of this method is to propose a Representative Element Volume (REV) which contains a detailed model of the material microstructure with an explicit description of each constituent on their specific length scale. The physical behaviour of the material at the macro-scale is then derived from suitable averages over the REV, where the computations are performed using different approaches.

For instance, a homogenisation methodology has been elaborated by [Dormieux and Kondo, 2004, Dormieux et al., 2006] in the micro-mechanical framework to estimate the permeability of a media with dense networks of micro-fractures, and was extended in the context of opened micro-cracks by [Barthélémy, 2009]. Such a micro-macro approach (Figure II–43a) of damage-induced permeability evolution has been further applied to the qualitative prediction of the damaged zone in an indurated clay candidate for radioactive waste repository by [Levasseur et al., 2013].

Another class of two-scale damage models (Figure II–43b) has been developed by [Dascalu and Bilbie, 2007, Dascalu, 2009], to obtain macroscopic damage laws from the propagation of micro-fractures in a microstructure that contains an explicit distance between neighbouring micro-cracks. This model has been successively used and extended to represent the brittle failure [Dascalu et al., 2010], the subcritical damage propagation [François and Dascalu, 2010] or the dynamic fracture propagation with branching instabilities [Atiezo and Dascalu, 2017]. Yet, despite the analysis of the coupled thermo-mechanical problem induced by micro-cracking [Dascalu and Gbetchi, 2019], this model is mainly limited to pure mechanical cases.

Conversely, other numerical models are capable of incorporating the HM couplings in the multi-scale framework. For example, in the successive works by [Frey et al., 2013, Marinelli et al., 2016, van den Eijnden et al., 2016, Pardoen et al., 2018], the computational homogenisation has been implemented in the finite element square method (FE^2), where the finite element method is considered for the numerical solutions at both scales, in order to simulate the coupled hydro-mechanical behaviour of a saturated porous medium, and to analyse the cracking-induced localisation phenomena. This HM double-scale model (Figure II–43c) was the starting point of the developments carried out by [Bertrand et al., 2020] to account for partially saturated conditions, and reproduce the coupled phenomena associated with multiphase flows in fractured reservoirs. It is also worth mentioning the multi-scale model developed by [Zhuang et al., 2017] to simulate the hydraulic fracturing phenomenon.

As for the aim of explicitly reproducing the dominant process of gas migration by preferential pathways initiated from the microscopic phenomena, a two-scale time-dependent damage model under single [Yang and Fall, 2021b] and two-phase flow conditions [Yang and Fall, 2021a] has been constructed from the framework introduced by [Dascalu and Bilbie, 2007]. Specifically applied to gas injection experiments, this model makes it possible to simulate the gas induced fracturing process, in which the damage propagation and the dilatant gas pathways are rather well captured.

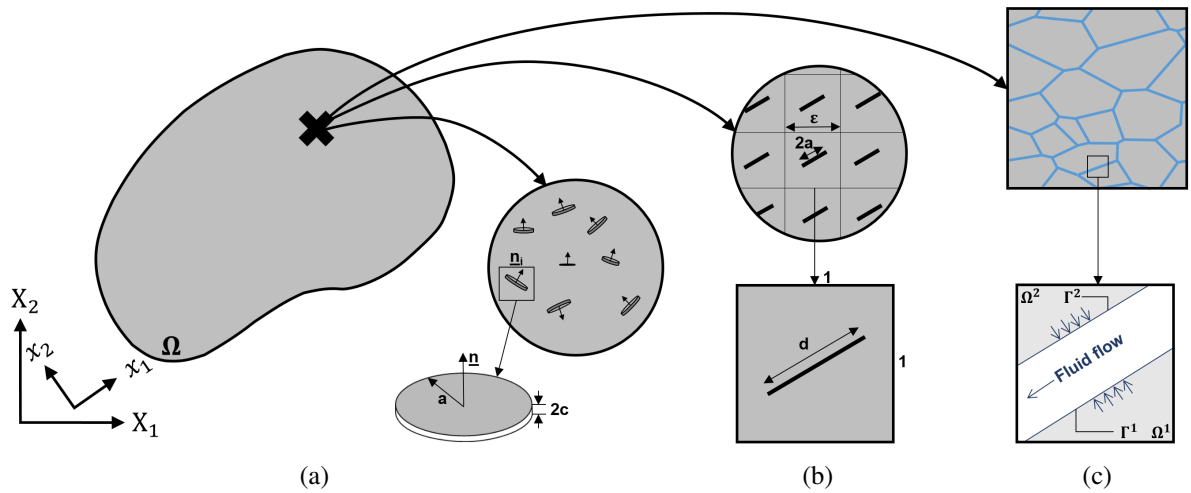

Figure II–43 – Conceptual scheme of micro-macro based models, with microstructure definitions of a micro-cracked material, *after* (a) [Levasseur et al., 2013], (b) [François and Dascalu, 2010], and (c) [van den Eijnden et al., 2016].

6.6.5 Explicit fracture based models

The interest in the use of fracture theories is driven by the need to explicitly simulate the fracturing process behind the formation of preferential gas pathways that accompanies the advective movement of gas through saturated clay rocks.

With the embedded discontinuity models, the modelling of the displacement jump inside the fracture does not require any modification of the mesh, but is directly introduced in the finite element by different techniques [Jirásek, 2000], such as an additional degree of freedom [Dvorkin et al., 1990].

Next to those hybrid models, another common treatment to simulate discrete fractures with the standard continuous FEM that is not able to describe the displacement jump, consists in inserting a zero-thickness interface element between two adjacent bulk elements. Such elements presented in Figure II–44 manage the opening and contact between the two facing walls of the material, and have been developed in saturated [Segura and Carol, 2008a, Segura and Carol, 2008b], and partially saturated [Cerfontaine et al., 2015] conditions, to account for both longitudinal and transversal flows of water and gas, together with fluid storage. An extension of this interface element has been recently implemented as part of a Pneumo-HM model, to simulate existing or induced discontinuities under gas injection in saturated clay samples [Liaudat et al., 2023].

In the context of the FEM with a zero-thickness interface element to predefine the fracture path, the fracture behaviour is generally described by the Cohesive Zone Model (CZM). As the CZM ha been commonly applied to hydraulic fracturing [Carrier and Granet, 2012, Nguyen et al., 2017] or desiccation cracking [Amarasiri and Kodikara, 2013, Vo et al., 2017], it seems to cover the main features of the gas-induced fracturing process in saturated clayey rocks such as the fluid-driven cracking [Faivre et al., 2016], the multiphase flow [Réthoré et al., 2008] or the possible plastic behaviour [Gui et al., 2016], which makes such a method an appropriate candidate for the modelling of gas-induced preferential pathways. Apart from FEM, the CZM is also compatible with other computational methods such as the eXtended Finite Element Method (XFEM) or the Discrete Element Method (DEM). In particular, the XFEM provides an alternative method to handle the arbitrary fracture propagation during gas propagation in porous media independently of the mesh and thus without introducing interface elements [Salimzadeh and Khalili, 2015].

Finally, the Phase-Field Method (PFM) is a suitable approach to explicitly simulate the fracture propagation and branching in FEM without special treatments on the discontinuity parts of the mesh. Initially implemented for hydraulic fracturing of rocks [Lee et al., 2016] and dessication cracking in soils [Heider and Sun, 2020], the PFM has been integrated into a typical two-phase HM model by [Guo and Fall, 2019] to account for the propagation of gas fractures in clay-based materials.

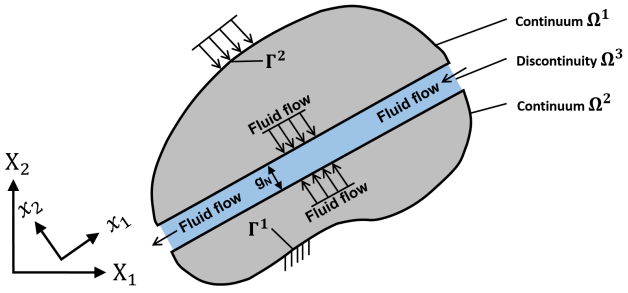

Figure II–44 – Definition of the multiphase flow problem: porous medium, discontinuity and boundaries. *After* [Cerfontaine et al., 2015].

6.6.6 Discontinuum-based methods

The grain-scale mechanistic model developed by [Jain and Juanes, 2009] is able to simulate various modes of gas migration in saturated deformable media, where fracture propagation dominates in fine-

grain sediments, while capillary invasion is favoured in coarse-grain sediments, which is consistent with the experimental findings. Yet, the multiphase flow and fluid interactions are handled in a very basic manner with this model.

For a more realistic representation of the capillary effects, the Lattice Boltzmann Method (LBM) [Liu et al., 2016a] can be coupled with the DEM to investigate the multiphase flow through porous media from a grain scale, as in [Kano et al., 2020, Wang et al., 2020].

Other lattice models propose to define the porous medium as a set of pore bodies or tubes forming the microstructure, where fluids flow within these tubes are controlled by capillary forces. For instance, in the capillary bundle approach first suggested by [Fatt, 1956], the porous medium is expected to be made of a collection of non-intersecting tubes characterised by a tortuosity and a constant radius over the length of the sample. This model has been applied to the field of nuclear waste repository [Rodwell and Nash, 1992, Grindrod et al., 1994], and especially to simulate the development of preferential flow pathways in Boom Clay [Ortiz et al., 1996]. An extension of this approach through a superposition of branching lattices of capillaries with different radii, that represents the porous medium has been further reported. In parallel, a specific technique linking the density functions of capillarities within each lattice to experimental observations on the material microstructure has been elaborated by [Xu et al., 1997] and latter applied on clayey materials by [Boulin et al., 2008b]. By considering a generalised Darcy's law and the Jurin's law to relate the radius the tubes to the gas entry pressure, such a network model allows to reproduce the development of preferential flow pathways together with the complex dynamics of flows during the post-peak phase [Impey et al., 1997].

6.7 Synthesis for the modelling

In brief, the present chapter gives a state-of-the-art description of modelling gas transport processes in low-permeability clay materials, which echoes to the characterisation of gas transport processes proposed in Chapter 5.

As long as the overall gas pressure remains lower than a threshold pressure, a continuous two-phase flow model integrating weak hydro-mechanical couplings is able to reproduce the predominant contributions to gas transport in clay rocks, namely the advection of the gas phase in the unsaturated zones and the diffusion of dissolved gas in the saturated zones. Such a coupled HM model has been meticulously presented in Sections 6.1 to 6.5 as it will constitute the backbone of the different numerical tools elaborated in the rest of the work.

Once gas pressure reaches the threshold pressure, the transport of free gas in the studied low-permeability clayey materials close to saturation takes place through the opening of preferential gas pathways, which translate into sample dilatancy and the (re-)activation of discontinuities in the material that is being tested [Shaw, 2015]. In order to improve the modelling response and to reproduce the development of these specific gas pathways, a number of authors have been trying to incorporate these findings into numerical models, for instance by means of additional hydro-mechanical couplings. A non-exhaustive review of various numerical strategies built to capture such gas-rock interactions has been the object of Section 6.6. Some more extensive state-of-the-art analyses of existing advanced HM models for gas migration in saturated rocks can be found in [Guo and Fall, 2021, Yang and Fall, 2021c, Levasseur et al., 2021]. Yet, the majority of these models still fail being predictive. Thence, this clear need for better mechanistic understanding of the gas flow processes is the starting point of the elaboration and implementation of the different numerical tools presented in the rest of the work.

Conclusion Part II

This thesis aims to model gas transport processes into clay rocks. For this purpose, this state-of-the-art part of the work intends to lay the physical, phenomenological, and numerical foundations for the main core of the thesis which aims to develop original numerical models that can realistically simulate the gas transport mechanisms in low permeability media, and the related hydro-mechanical couplings.

First of all, a general description of the clay host formations that are under study, *i.e.* the Callovo-Oxfordian claystone and the Boom Clay has been proposed. This made it possible to highlight the commonly accepted ranges of values for the geotechnical characteristics of these two rocks. A particular attention has been paid to the properties that govern the gas movements inside the formation such as the pore distribution, the porosity, the conductivity, and how they are affected in the damaged zone.

Then, a characterisation of the main gas transport processes through these low-permeability clay materials has been established based on the current experimental knowledge acquired in clay materials.

Finally, a description of the currently existing strategies to handle the numerical modelling of these predominant gas transport processes in clay-based materials has been proposed.

The task now is to develop advanced hydro-mechanical models that can contribute to a better mechanistic understanding of these gas flow processes. In particular, different zones of the repository, *i.e.* the excavation damaged zone in Part III and the sound rock layer in Part IV, and different scales are investigated in the rest of the thesis.

Part III

Modelling gas transport in the EDZ

Introduction Part III

Experimental observations on geomaterials clearly indicate the activation of localised deformation fields, characterised by the coalescence of cracks, shear bands or rupture lines, which can lead to failure of geotechnical works subjected to strong loading [Desrues, 2005, Bésuelle, 2021]. This phenomenon, known as the strain localisation process, is therefore a crucial issue to address when modelling geotechnical problems. As exemplified in Section 4.3.6, the underground galleries of a deep geological repository are no exception. During the construction phase, the drilling process inevitably generates stress modifications, cracks and eventually fractures in the surrounding medium, that concentrate in the vicinity of the storage cell in a so-called excavation damaged zone [Tsang et al., 2005]. In this zone, significant and irreversible modifications of the hydro-mechanical properties of the host rock are observed [Armand et al., 2014] which may interfere with the gas flows occurring in the long term, and thus alter the safety function of the geological barrier by creating preferential pathways for the migration of radionuclides to the biosphere.

This part of the thesis presents a consistent second gradient H^2M model to reproduce gas transport processes through the excavation damaged zone. One the one hand, this model is based on the second gradient theory as regularisation technique [Collin et al., 2006] to properly reproduce the fractures around the storage drift with strain localisation in shear band mode. On the other hand, the model incorporates the features of a two-phase flow transfer approach [Gerard et al., 2008] to deal with the multi-physics mechanisms inherent to gas migrations. Given that gas flows through the EDZ are supposed to be governed by the hydraulic properties modifications induce by fracturation, specific HM couplings [Pardoen et al., 2014] of the permeability and the retention behaviour with the rock deformation are integrated to capture the impact of fracturing on the kinetics of gas transport. This way, it is for instance possible to reproduce a significant permeability increase within the shear bands as highlighted in Figure III–1.

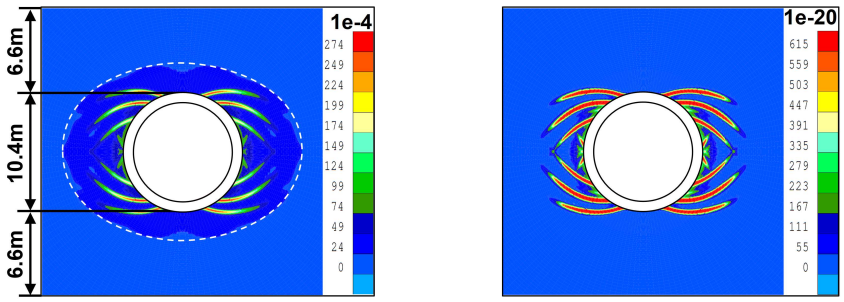

Figure III–1 – Development of shear bands and related modification of the intrinsic permeability in the vertical direction, by the end of the excavation of a storage drift in the COx claystone.

This part is divided into four main sections. The first one presents some highlights of the experimental observations of strain localisation in geomaterials and how this concept has been theorised. The second one details the practical aspects behind the numerical implementation of such a process. The third section focusses on the novelties implemented to the second gradient model, and the last section deals with applications of the model from the field scale with the modelling of *in situ* gas injection tests, to the repository scale via the drilling and operation of a nuclear waste storage drift.

7. Strain localisation in geomaterials

The objective of this chapter is to give a brief overview of some strain localisation aspects, required to subsequently provide a robust numerical reproduction of this failure mechanism in geomaterials. Starting with a general definition, a review of the experimental observations of strain localisation as a mode of material rupture is then conducted before properly formalising the theoretical background for the onset of strain localisation.

7.1 General definition

Converging towards an accurate definition of failure in materials and its related analysis is an essential but intricate question. From a physical perspective, rupture criteria state that some limit stress states cannot be exceeded by the material for any possible loading path. At such a state, any additional load applied to the material induces brutal changes, *e.g.* large deformations, cracks, fragmentation, which roughly corresponds to failure. Failure of geomaterials in the broad sense has been largely investigated in geomechanics, since it directly conditions the design of geotechnical structures subjected to strong solicitations, such as boreholes, tunnel excavation, dams, or shallow foundations. In particular, early works on the stability of retaining walls a few century ago [Coulomb, 1773] already highlighted the concept of rupture surface in the collapse mechanisms. As presented in the next section, experimental works have amply demonstrated the development of localised rupture in soil and rock masses leading up to failure [Desrues, 1984]. This mode of rupture is usually preceded by the emergence of strain localisation, defined as the intense accumulation of large shear strain into narrow thin bands [Vardoulakis et al., 1978]. Basically, the stress redistribution causes damage that triggers microcracks initiation, accumulation and propagation within the material once the damage threshold is reached. This translates into cracks coalescence - or macrocracks - and the onset of interconnected fractures - or rupture lines - followed by a rapid loss of the overall strength of the material and a sudden collapse [Diederichs, 2003].

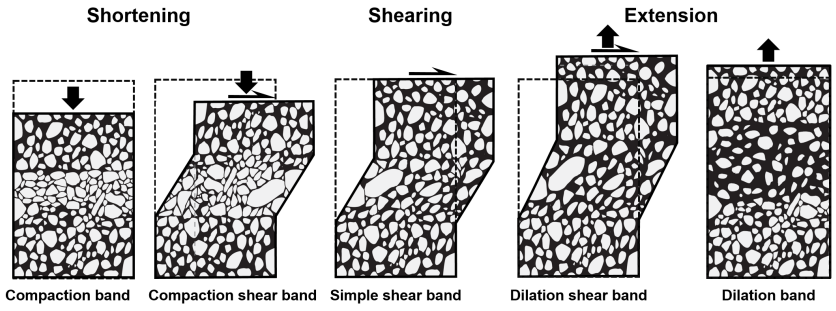

Figure III–2 – Kinematic classification of strain localisation modes. *After* [Fossen et al., 2007].

It is worth noting that under specific conditions, a homogeneous failure mode, coined as diffusive failure that does not display any localisation can also be obtained [Daouadji et al., 2011]. Yet, in most laboratory experiments, observations attest to the onset of strain localisation, which provokes a sudden transition from a homogeneous deformation state to a highly heterogeneous one. Depending on the kinematic that characterises this grains reorganisation, which is mainly related to the material properties and

the loading, different modes of strain localisation can initiate. The deformation bands do not systematically deform in pure shearing, even if shear bands are predominantly described in the literature. For instance, early stages of shear band formation also involve a component of dilation [Bésuelle, 2001] for most geomaterials (inelastic volume increase), poorly consolidated sands can exhibit pure dilation bands [Du Bernard et al., 2002] formed in predominantly opening mode and the contractive behaviour of loose materials can also generate compaction shear bands or pure compaction bands [Issen and Rudnicki, 2000] (inelastic volume increase), which complete the spectrum of localised deformation modes shown in Figure III–2. This strain localisation process is therefore an important issue when considering the material rupture that has been widely investigated both experimentally and theoretically.

7.2 Experimental evidences

Strain localisation in geomaterials being both a rich and complex process with potentially significant effects, it has motivated numerous experimental studies in the field of geomechanics, especially since the 1970s [Bésuelle, 2021]. The acquired understanding about the strain localisation phenomenon has helped to gradually enhance the theoretical knowledge and served as a keystone for the development of mathematical and numerical models. In the following, a brief review of the experimental background of strain localisation, with an emphasis on the multiphysics processes as precursor to localisation is presented, and serves as a basis for highlighting the successive physical mechanisms leading to rupture.

7.2.1 Background

Failures of geomaterials are generally associated with strain localisation in shear band mode [Desrues, 2005]. For more than fifty years now, a large amount of experimental works has attempted to properly characterise localised phenomena in soils and rocks and to describe the occurrence and patterns of shear bands. Strain localisation in soils and granular materials (mainly sand) has received particular attention through studies performed by Vardoulakis and co-workers [Vardoulakis et al., 1978, Vardoulakis and Graf, 1985, Han and Vardoulakis, 1991], Tatsuoka and co-workers [Tatsuoka et al., 1986, Tatsuoka et al., 1990], Finno and co-workers [Finno et al., 1996, Finno et al., 1997], and Desrues and co-workers [Desrues, 1990, Desrues and Viggiani, 2004] to name a few among others. On the contrary, only limited studies have been devoted to investigating the development of strain localisation in fine-grained geomaterials (*e.g.* clayey soils) [Lade and Tsai, 1985, Hicher et al., 1994, Jiang and Shen, 1998, Viggiani et al., 2004] and rocks [Bésuelle et al., 2000, Bésuelle, 2001, Lenoir et al., 2007, Lanata, 2015]. It is respectively due to the size of the clay particles that makes observations inside the shear bands more difficult, and to the high strength and stiffness of quasi-brittle rock specimens which requires to design appropriate testing devices [Bésuelle and Lanatà, 2016].

Since most of these tested materials are characterised by low tensile strength, the vast majority of the researches have focussed on the description of the compression behaviour up to rupture. These small-scale lab tests are usually conducted on axisymmetric triaxial or plane-strain biaxial compression equipments. This latter apparatus has the advantage that the localisation zone is clearly evidenced while it may remain more or less hidden inside the sample in triaxial compression tests. In any case, all these experimental campaigns require specific techniques such as False Relief Stereophotogrammetry (FRS) [Desrues and Viggiani, 2004], Digital Image Correlation (DIC) [Bornert et al., 2008] or X-ray Computed Tomography (X-ray CT) [Vervoot et al., 2004] in order to capture the gradual development of strain localisation processes inside the samples. A short description together with representative results of some methods of visualisation applicable in the field of experimental geomechanics are given in the following.

In pioneering researches, the localisation of strains has initially been described via postmortem or destructive analysis. Specific shear strain localisation features such as band orientation and pattern, or grain scale damage were examined at the end of the loading path with regard to the imposed experimental conditions [Bésuelle, 2021]. Afterwards, laboratory investigation of strain localisation has been

pursued extensively with full-field measurement techniques, which made it possible to migrate to non-destructive imaging and quantification of fields of internal properties over the entirety of an object (an overview of the different available methods is provided in [Viggiani and Hall, 2008] and later updated in [Viggiani and Hall, 2012]). The FRS, initially applied to soil mechanics experiments in the early 1970s by Butterfield *et al.* [Butterfield et al., 1970], is a technique based on the analysis of successive snapshots of a deformable sample taken from a fixed viewpoint, at different times during the loading procedure [Desrues and Viggiani, 2004]. The successive deformation states of the specimen are tracked by recording the local displacement of some points at the surface of the sample, perpendicular to the shooting direction. This provides a full-field measurement of the incremental strain as a fictitious relief within the specimen throughout the test. An illustrative example of such photographs taken by this technique during a biaxial plane strain compression test on dry Hostun sand specimen [1] is presented in Figure III–3(a) [Mokni and Desrues, 1999]. Results show a series of incremental strain maps obtained at different states on the stress-strain response, evidencing the initiation of localisation just before the peak load, between steps 3 and 4. The main downside of the method is that it is limited to two-dimensional cases, tested under plane strain state in order to minimise measurements inaccuracies. On top of that, results obtained with FRS suffer from a low level of spatial resolution which prevents the detection of the start of localisation for small-scale micro-cracks, and paved the path for another range of techniques capable of capturing the developing mechanisms at the grain scale, such as the DIC and the X-ray CT.

And so, the enhancement of the aforementioned technique has been achieved by having recourse to the simplicity of digital image analysis. Originally implemented in the 1980s [Peters and Ranson, 1982], DIC benefits from the computer technology by switching from analogue to digital photographs. The computer software allows to assess the full-field surface displacement in material under deformation by tracking and comparing a set of points at the specimen surface from one reference state to the next one. The displacement field then corresponds to the transformation that matches the reference image to the deformed one [Hall, 2012]. Initially applied to pictures of a 2D plane surface of a specimen [Sutton et al., 1983], DIC has then been extended to 3D volumetric applications [Viggiani et al., 2010]. An illustrative example of such technique during a plane strain compression test on Norwegian quick clay specimen [2] is presented in Figure III–3(b) [Thakur et al., 2018]. Results show a series of slices of the strain field obtained at different states on the stress-strain response, evidencing the transition from an initial homogeneous strain field to a localised regime with a distinct shear band emerging from the upper left edge of the specimen prior to the peak.

Next to the DIC, X-ray CT is another high-resolution technique elaborated at first to the field of medicine [Hounsfield, 1975], which has then been transposed as a valuable tool to help understanding stress- and time-dependent deformations in porous materials [Desrues et al., 1996], among a wide range of other geosciences applications [Ketcham and Carlson, 2001, Cnudde and Boone, 2013]. The use of traditional X-ray imaging in experimental geomechanics dates back to the 1960s, providing valuable qualitative results on localisation patterning in granular materials while suffering from a lack of quantitative data on density changes and restriction to 2D images. X-ray CT is an improved imaging method that has been devised to overcome these limitations. The principle of X-ray CT measurement practically consists of recording X-ray radiographs of a sample at many different angular positions all around the specimen. These multiple projections are assembled together to reconstruct a 3D image of the investigated object applying relevant back-projection algorithms [Baruchel et al., 2000]. This way, it allows quantitative observation of the specimen by giving information on the evolution of the density field and internal features, and providing a 3D volume imaging. Since density transitions correspond to boundaries between materials and phases, these data are valuable to detect shear bands in specimens undergoing mass density changes (dilatancy or compaction). Nevertheless, in general the volumetric strain in a shear band is small compared to the shear strain, and so if the localised deformation is isochoric, *i.e.* closed shearing cracks with no volume change, then it is invisible in X-ray CT snapshots. This is

1. The Hostun sand is a fine angular siliceous sand coming from a natural sand deposit in Hostun, Drôme, France.
2. The clay chosen for this study is defined as quick clay because it liquefies completely upon remolding and was sampled in Tiller, Norway.

why X-ray CT and DIC are often complemented as an effective extension method to track the zones of localised deformation, by quantifying not only the volume strain (mass density change) but the full strain field including shear strain [Viggiani and Hall, 2012]. An illustrative example of such a technique during a triaxial compression test on dry Hostun sand specimen is presented in Figure III–3(c) [Hall et al., 2009]. Results show a series of vertical slices through the X-ray tomography images at different stages in the test (top row), in which the specimen starts to lean to one side with a rotation of the upper platen in the latter part of the test, but without clear evidence of localised deformation. If 3D volumetric DIC is additionally carried out on consecutive pairs of 3D image volume, the incremental displacement and strain fields are provided. This indicates relatively continuous displacement fields together with the clear appearance of a localised band that traverses the sample diagonally. Lastly, it is worth pointing out that with a view to further investigating the microstructure of shear bands, the last decades have seen the emergence of the technique of micro-computed tomography (μ-CT), which enables the precise detection of individual material grains, providing detailed particle position as well as contact maps and calculation of void ratios [Oda et al., 2004].

This abundance of experimental works devoted to the investigation of strain localisation in geomaterials over the last decades has made it possible to gradually gain a refined knowledge of the phenomenon. So far, the interpretation of strain localisation as the initiation of a sudden shear band or the propagation of shear bands from a diffuse strain field related to the stress peak of the specimen's response has prevailed. This concept originates at first from observations of the samples after the tests from which a first series of conclusions were drawn especially for soils and granular materials, listed as follows [Desrues and Chambon, 2002, Desrues, 2005]:

- *Strain localisation in shear band mode can be observed in most, if not all, laboratory tests leading to rupture in geomaterials (at least at sufficiently low temperature and pressure).*
- *Complex localisation patterns may be the result of specific geometrical or loading conditions.*
- *Well marked stress peaks in stress–strain curves can be considered as the signature of an established shear band system over the specimens.*
- *Simple measurements can be made to get an estimation of the orientation of the shear bands.*
- *Strain localisation is observed in both drained and undrained specimens, with a number of specific features in the latter.*

It was also demonstrated that several factors can impact the strain localisation process, including confining pressure, porosity, anisotropy of the granular deposit, or size and shape of both grains and specimens. Geomaterials can also differ widely with respect to their mechanical and physical properties, and cover a wide range of materials, either granular or cohesive, with fine or coarse grains, and ductile or brittle. Thus, while shear band analysis is relevant for the prediction of the onset of strain localisation in granular materials, it is not necessarily the case in rocks and other brittle materials for which the failure mode belongs more to planar rupture surfaces. Furthermore, thanks to more advanced experimental and imaging devices, recent investigations on a broad range of soils and porous rocks throughout the test have provided important data concerning not only shear band features, but also patterns of shear band formation and evolution. The results suggest that the transition from a diffuse regime to a localised one is a progressive process. Localisation starts well before stress peak under the form of numerous parallel and conjugated shear bands. Some of these bands are progressively deactivated leaving only a few bands stay active close to the stress peak which are prone to compaction or dilatancy (volume strain) depending on the material and stress state [Bésuelle, 2021]. The acquired understanding about the onset and development of strain localisation in geomaterials has been mainly established from a purely mechanical point of view or from hydro-mechanical coupled problems. Yet, weakening mechanisms triggering the occurrence of instabilities in geomaterials can be of various origins: mechanical, hydraulic, thermal, chemical, *etc*. So, despite the lack of experimental investigation of the strain localisation process in other multipysics context, there is a wide range of complex multiphysical loading likely to induce instabilities that might be appropriate to briefly explore.

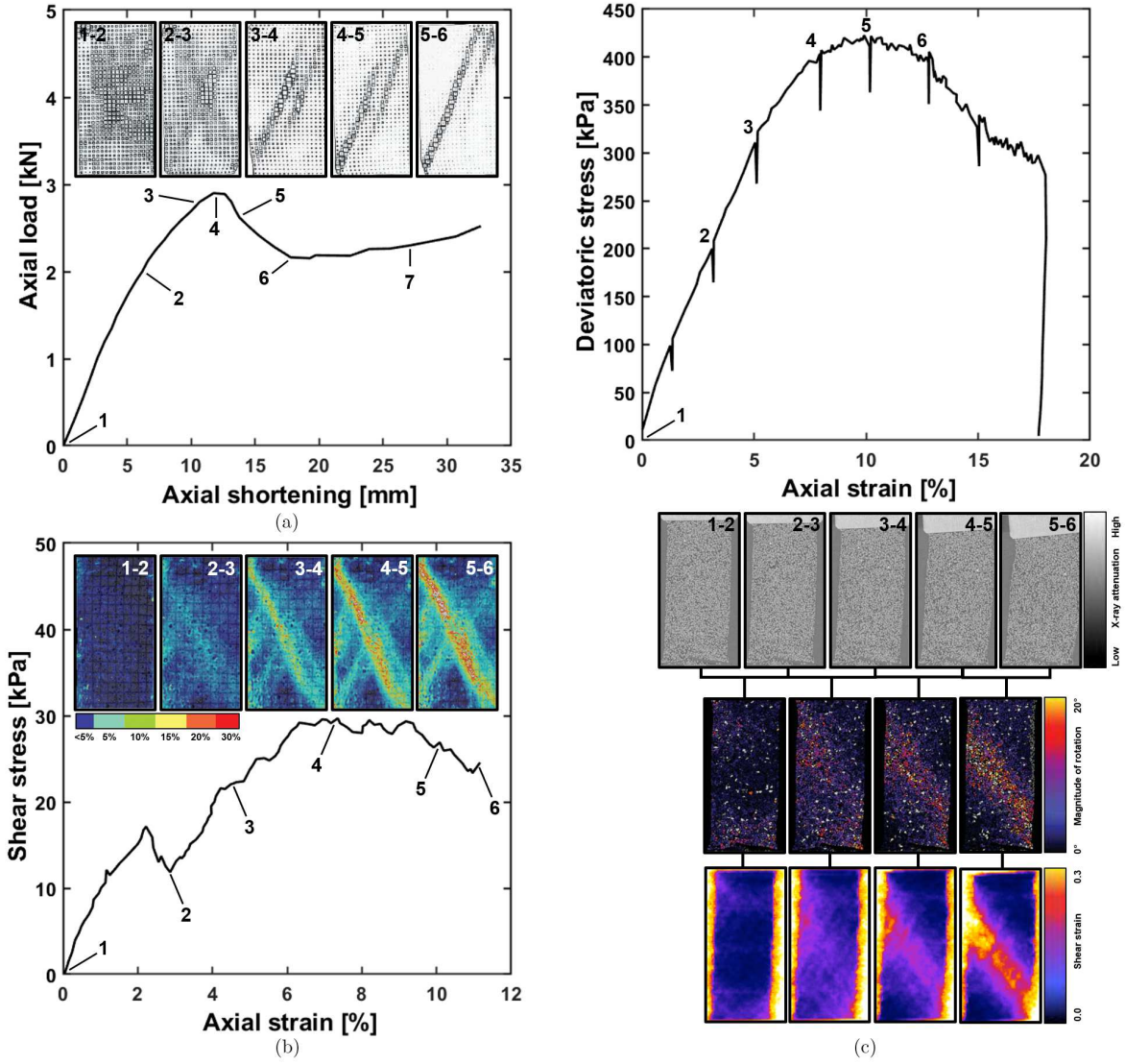

Figure III–3 – Formation of shear strain localisation during compression tests with respect to different steps in the global response curve: (a) results presented for the Hostun sand using a FRS method (*modified after* [Mokni and Desrues, 1999]), (b) total shear strain distribution computed for the Norwegian quick clay using a DIC tool (*modified after* [Thakur et al., 2018]), and (c) vertical slices of the Hostun sand extracted from the X-ray CT technique (top row), completed by discrete DIC-derived incremental grain rotaion (middle row) and DIC-derived incremental maximum shear strain (bottom row, *all modified after* [Hall et al., 2009, Hall et al., 2010]).

7.2.2 Multiphysics processes

The occurrence of strain localisation as a precursor to failure in soils and rocks is now well evidenced. More specifically, this phenomenon is largely favoured by the softening character of the material, although shear banding can occur with positive or negative rate of strain hardening [Rudnicki and Rice, 1975]. This softening behaviour corresponds to a degradation of the material properties which can arise from a trigger of any sort. Apart from the classical weakening mechanism induced by purely mechanical loading, *e.g.* microcracks initiation, grain crushing or grain size reduction [Das et al., 2011], an array of other multiphysical processes can be responsible for enhancing strain localisation in geomaterials [Hueckel, 2021], either hydraulic like pore fluid pressurisation, thermal like shear heating, or chemical like dissolution. These complex phenomena are often interpreted as scenarios of processes that are either simultaneous or sequential, and that are coupled or result from an accumulation of dissipative processes. The study of strain localisation in light of these coupled multiphysic processes is of importance in the context of the present research. On the one hand, the rock formation hosting the deep geological repository is considered as a porous medium, where the pore space is filled with one or several fluids, which means that the rock behaviour does not only depend on the skeleton response to a given loading (solid phase), but also on the interactions taking place between the different phases of the medium. And on the other hand, the long-term behaviour of the structure involve multiple external solicitations that are highly thermo-hydro-mechanically coupled [Tsang et al., 2012]. Some of the main long-term phenomena acting in the context of a deep geological disposal are succinctly described in the following.

The effect of an infiltrated pore fluid (liquid water) that interacts with a rock mass, can have a potential impact on the localisation process [Collin et al., 2009b]. This phenomenon is conditioned by the hydro-mechanical properties of the material and the boundary conditions of the problem. A hardening or softening behaviour of the material can be obtained depending on the volumetric response of the rock, either dilatant or contractant. For hydro-mechanical experiments under globally drained boundary conditions, there is no impact of fluid flows on the localisation process as far as the permeability is high enough with respect to the loading rate to avoid overpressure generation. Experimental findings then correspond to the results under dry and purely mechanical conditions. Conversely, for hydro-mechanical experiments under undrained boundary conditions, overpressures appear in the sample that impact the localisation process. Due to the localised effects, fluid flows can occur through the sample even in an undrained state. For instance, among other experimental campaigns, plane strain undrained tests carried out on sands [Roger et al., 1998, Mokni and Desrues, 1999] have highlighted that while strain localisation develop in loose specimens, it tends to be inhibited by liquid water transfers in dense dilatant specimens. The onset of shear bands is delayed and occurs only until cavitation takes place within the pore fluid, which could be also investigated numerically [Sieffert et al., 2014].

The effect of a fast heating of a saturated geomaterial induces thermal dilation of water, and pore fluid pressurisation, which corresponds to another weakening mechanism that can thus have a potential impact on the localisation process. Especially, the significant differential thermal expansion between soil constituents, namely pore water and clay, draws particular attention in the field of nuclear waste disposal in clay formations [Gens and Olivella, 2001]. The heat resulting from nuclear decay of the waste in the canisters could strongly affect the thermo-mechanical behaviour of the surrounding medium and potentially lead to instability, which has been highlighted experimentally for undrained heating at constant total stress conditions [Hueckel and Pellegrini, 1991], and is even more exacerbated by the relatively high thermal conductivity of the host rock compared to the very low permeability [Hueckel et al., 2011].

The effect of chemical reactions such as dissolution, precipitation or mineral transformation on the solid phase of the medium is another mechanism prone to cause mechanical degradation and material softening triggering possible strain localisation. The experimental evidence of strong chemo-poro-mechanical coupling in soils and rocks [Xie et al., 2011] has been been validated in many works for a wide class of geomaterials [Nova et al., 2003, Hu and Hueckel, 2007, Buscarnera, 2012]. On the one

hand, chemical dissolution leads to an important increase in the porosity as a result of the degradation of the intergranular connections, making the material more ductile and collapsible. On the other hand, compaction of saturated geomaterials progressively engenders a mechanical degradation of the solid skeleton which amplifies the interface area of the reactants and consequently accelerates the rate of dissolution of the solid phase. Chemical softening thus operates as a well-known feedback process [Rimstidt and Barnes, 1980] that gradually damages the overall mechanical properties of the system, whose stability is no more guaranteed. CO_2 injection in a porous carbonate reservoir is another topical example in which the interaction between gas and surrounding rock causes the system to be out of chemical equilibrium. As a consequence, the material softens in due course of carbonate dissolution, providing the required instability conditions for which compaction bands formation is possible [Stefanou and Sulem, 2014].

Lastly, the effect of drying process is highly coupled with the pore fluid flow which can lead to localisation and subsequent cracking in geomaterials. In the field of soil mechanics, drying commonly refers to the loss of water by evaporation linked either to preconsolidation or air invasion mechanisms [Terzaghi, 1936]. The fluids flowing out of the specimen induce a negative liquid pressure (or suction) in the deformable soil that is subjected to shrinkage in response. At that point, the ensuing phenomenon of air entry can give rise to an instability of the fluid/gas interface which constitutes a defect around which a stress concentration arises. This process could result in a tensile failure of the material in the form of drying cracking.

7.2.3 Global response analysis

The fundamental aspects behind the localisation process in geomaterials can be generalised based on the global stress-strain response obtained experimentally. Thanks to the abundant literature covering the well-known uniaxial compression test performed on a wide variety of soils and rocks (*e.g.* granite [Peng and Johnson, 1972], limestone [Olsson, 1974], clay [Hicher et al., 1994] or poorly consolidated sands [Du Bernard et al., 2002]), it is possible to characterise the distribution and organisation of the specific physical mechanisms inducing rupture. The typical response curve for a dominant brittle behaviour material presented in Figure III–4 highlights a number of phases in the fracturing process which can be classified as follows:

- The Zone I corresponds to the primary contraction of the sample under very low stress level which may result in closure of the pre-existing micro-cracks and pores inside the sample. This tightening phase is all the more reduced as a confining pressure is applied beforehand.
- The Zone II is a phase of either linear or non-linear elasticity. Most of the strain in the linear part of the curve are attributable to elastic deformation of the pores and grains, while non-elastic strains are sometimes observed, due to small displacements and relative sliding of the grains [Walsh, 1965]. The related energy dissipation results in a hysteresis effect during load-discharge cycles [Cook and Hodgson, 1965]. The rock stiffness is indeed dependent on the confining pressure and increases with it [Wilhelmi and Somerton, 1967]. At that point, the material is not yet tended to micro-cracks reopening nor creation of new ones.
- The Zone III refers to the threshold of micro-cracking. As a result of the increase in the deviatoric stress increment, one observe the initiation, accumulation and stable propagation of first cracks at simultaneous multiple locations within a large part of the specimen. The proliferation of these micro-cracks is accompanied by a dilatancy tendency and appears to be more stable under confinement.
- The Zone IV covers the pre-peak phase until the resistance peak. This phase first deals with the intensification of micro-cracking. The creation of new cracks is observed which is followed by the propagation and early coalescence of these micro-cracks. Confinement tends to have a stabilising effect on the development of these cracks. The onset of micro-cracking processes depends on local stress concentrations at the grain scale, which are directly influenced by local heterogeneities and imperfections. Then in a second time, the unstable development and connection of cracks

is observed. The strains in the specimen become strongly inhomogeneous at this time and are localised in a thin band. The multiple mechanisms of localised deformation are then in competition as the strain increases, and finally one of them takes over the others at peak stress to complete a full formation of a shear band throughout the specimen, which corresponds to the future macro-fracture.

- The Zone V corresponds to the post-peak (or post-localisation) phase where the macro-fracture can initiate a progressive damage leading up to the general collapse of the sample. Especially in triaxial conditions, the evolution of localisation in shear band mode after the peak is usually well discernible. This process coincides with specimen softening, *i.e.* a drop in the material strength.

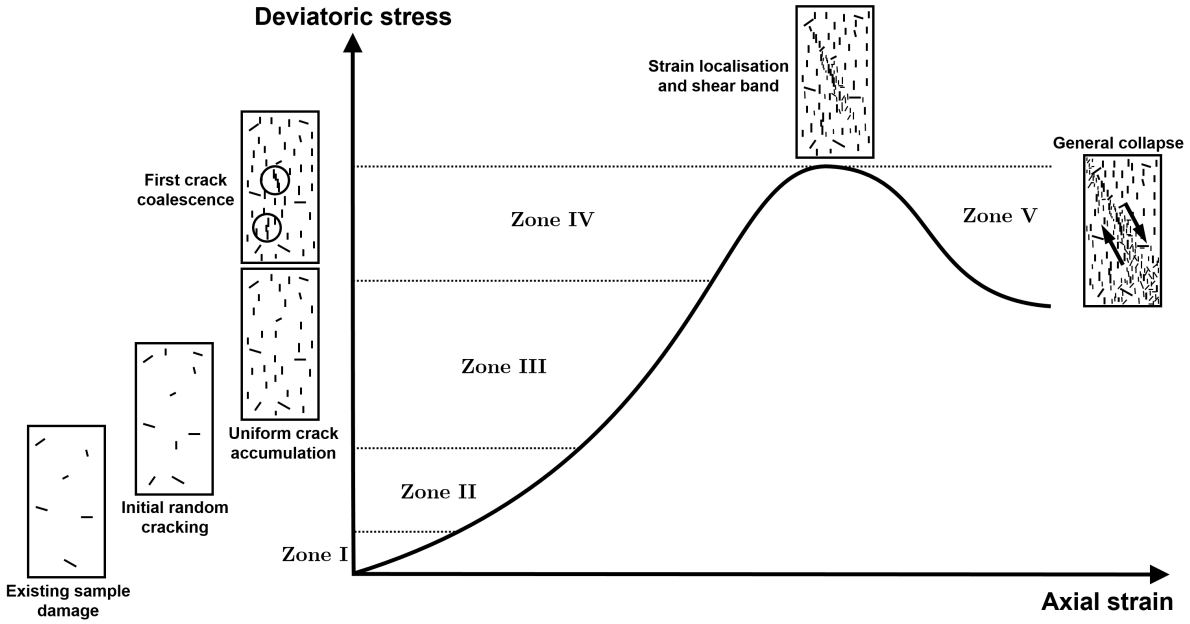

Figure III–4 – Schematic representation of the global stress-strain response of a material under uniaxial compression test, highlighting the main deformation zones occurring during the fracturing process. *Modified after* [Haïed, 1995].

7.3 Theoretical framework

It is easily understood that the analysis of a material response in the failure regime, especially when the strength is suddenly dropping, requires to understand what failure physically means. From an experimental perspective, the large number of work performed on geomaterials and summarised in the previous section 7.2 has highlighted that what appears as a failure plane is in fact a zone of strain localisation in shear band mode. By evidencing the physical processes that control strain localisation, these numerous studies [Vardoulakis, 1980, Sulem et al., 1999, Bésuelle et al., 2000, Desrues and Viggiani, 2004] have served as basis for the formulation and validation of a robust theoretical framework. The latter has thus to account for strain localisation onset, post-peak material behaviour, as well as hydro-mechanical couplings.

7.3.1 Background

From a theoretical perspective, the strain localisation process refers to the stability theory [Lyapunov, 1892], stating that a system is physically stable if a small perturbation of the initial conditions does not increase with time. With reference to this definition, the strain localisation process can be seen as an instability that can be predicted from the pre-failure constitutive behaviour of the material [Sulem, 2010].

In this sense, it is now generally linked to the bifurcation theory, referring to the loss of uniqueness of the solutions of a given boundary problem [Hill, 1958, Rice, 1976, Chambon and Caillerie, 1999]. As conceptually displayed in Figure III–5a, it corresponds to a point in the stress-state domain, for which it exists an alternative solution in addition to the fundamental one for the next loading increment during the evolution of a physical process. At this point, the material is thence subjected to spontaneous change of deformation mode (instability) following the branch of alternative solution. Among the various modes proposed in the literature to characterise the bifurcation phenomenon such as necking [Hill and Hutchinson, 1975], diffuse loss of homogeneity [Vardoulakis, 1979, Vardoulakis, 1981], surface wave [Triantafyllidis, 1980], or shear banding [Rice, 1976], the emphasis is on the strain localisation in shear band mode in this work, because it is the failure mechanism that is mainly evidenced in geomaterials [Finno et al., 1996, Vardoulakis et al., 1978, Desrues and Viggiani, 2004, Desrues, 2005]. The bifurcation phenomenon is illustrated in Figure III–5b for a material under compression or shear [Thakur, 2007]. During the first compression part, the load-displacement curve of the global response of the material firstly exhibits a linear behaviour. Under this elastic regime, the solution is unique corresponding to a uniform distribution of strain. Then under elastoplastic softening regime at the peak stress, there is a loss of uniqueness of the post-peak solution as a consequence of the strain softening in the material behaviour. In fact, once the strength decreases beyond the peak strength, the material response can either continue along the elastic unloading curve or follow the plastic loading curve, thus undergoing a plastic strain increase and instigating an infinity of localised solutions with non-uniform strain distribution. For the compression experiment of Figure III–5b, the loss of uniqueness may result in the development of shear bands among the potential types of localised solutions. Such a discontinuity is characterised by an elastic unloading outside the shear band, while the material remains under plastic loading inside the shear band with a concentration of plastic strain.

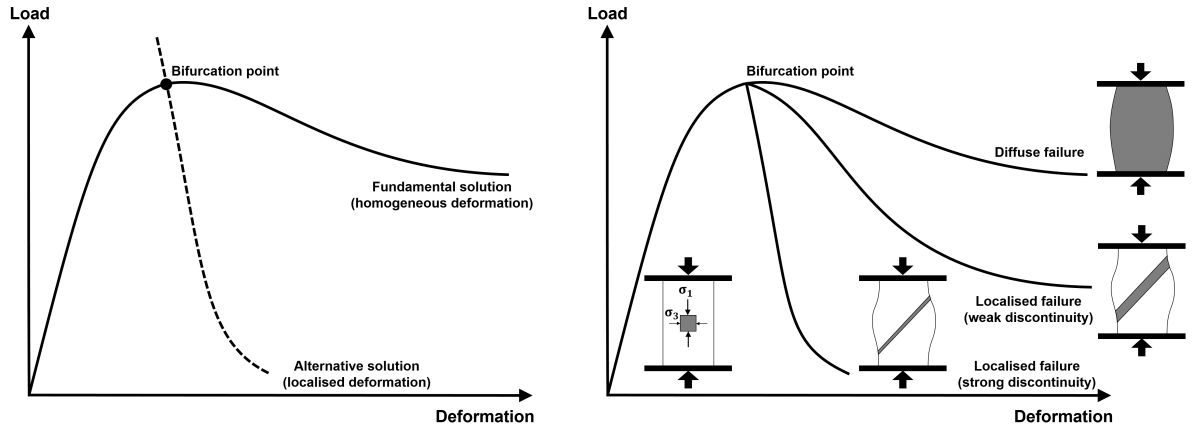

Figure III–5 – (a) Conceptual scheme of a bifurcation problem with fundamental and alternative solutions and (b) example of a post-peak behaviour for a specimen under uniaxial compression. *Modified after* [Thakur, 2007].

The necessary criterion for the emergence of localisation is determined by seeking the possible critical conditions for which a bifurcation point could exist and an alternative solution, corresponding to a localised deformation into a planar band is possible [Rice, 1976, Vardoulakis, 1996a, Vardoulakis, 1996b]. A certain number of studies have been dealing with the development of appropriate constitutive relationships which can predict satisfactory the initiation of failure in the form of the incipient of a shear band. It has been especially particularised for soils [Rudnicki and Rice, 1975, Vardoulakis et al., 1978] and soft rocks [Bésuelle, 1999, Sulem et al., 1999, Vardoulakis, 1984], considering non-associative laws [Bigoni and Hueckel, 1991a, Bigoni and Hueckel, 1991b] and hypoplastic laws [Cham-

bon, 2000, Desrues, 1989, Kolymbas, 1981, Tamagnini et al., 2000]. In the following is summarised the criterion for strain localisation proposed by Rice and co-workers [Rudnicki and Rice, 1975, Rice, 1976], which is based on the theoretical studies of material stability for elastic materials [Hadamard, 1903] and later extended to inelastic materials [Thomas, 1961, Hill, 1962, Mandel, 1966].

7.3.2 Strain localisation criterion

The shear band, is regarded as a very thin layer bounded by two parallel material discontinuity surfaces B_1 and B_2 (shear band boundaries), separated by a distance $2b$ (shear band thickness), with an incremental displacement gradient [Hill, 1962]. The theoretical scheme of a shear band is presented in Figure III–6 where the superscripts ^{0} and ^{1} denote quantities outside and inside the shear band respectively. The so-called Rice bifurcation criterion is defined to analyse the stress state and investigate the eventuality of bifurcation occurrence in the stress and strain paths, for incrementally linear behaviour. At the strain localisation appearance, the stress and strain fields are assumed to be continuous on a solid body, and the discontinuity appears on the interfaces between the shear band and the outer material, for the stress field rate $\dot{\sigma}_{ij}$ and for the corresponding velocity gradient field L_{ij}. Concretely, this criterion is based on a static condition, a kinematic condition and on the constitutive equation.

The static condition expresses the surface equilibrium of the shear band interfaces with the outer material and the discontinuity of the stress field rate. In rate form, it reads:

$$n_i \left(\dot{\sigma}^1_{ij} - \dot{\sigma}^0_{ij}\right) = 0 \tag{III–1}$$

where $\dot{\sigma}_{ij}$ is the Cauchy stress rate, and n_i is the normal unit vector to the shear band.

The kinematic condition expresses the discontinuity of the velocity gradient field L_{ij} across the shear band interfaces in its normal direction as a dilatant strain jump and a shear strain jump, but without any longitudinal strain jump:

$$L^0_{ij} = L^1_{ij} + \varsigma_i n_j \tag{III–2}$$

which is equivalent to:

$$\varsigma_i n_j = \frac{\partial\left(\dot{u}^1_i - \dot{u}^0_i\right)}{\partial x_j} \tag{III–3}$$

where $\dot{u}_i$ is the velocity field, and ς_i is an additional velocity gradient field of the shear band that specifies the band mode and is defined as:

$$\varsigma_i = \frac{\partial\left(\dot{u}^1_i - \dot{u}^0_i\right)}{\partial \xi} \tag{III–4}$$

where ξ is the shear band normal coordinate axis.

The constitutive law expresses the relationship between the stress and strain fields increments. Materials usually exhibit elasto-plasticity with an incrementally non-linear relationship. However, the strain localisation criterion was initially established for classical materials under associated plasticity and incrementally linear behaviour. Thence, following the rather strong assumption of linearity, the constitutive law reads in the general form:

$$\dot{\sigma}_{ij} = C_{ijkl} L_{kl} \tag{III–5}$$

where C_{ijkl} is the elastoplastic constitutive tangent tensor for small strains and rotations.

If continuous constitutive tensors are supposed across the shear band, that is to say $C^0_{ijkl} = C^1_{ijkl} = C_{ijkl}$, then a continuous bifurcation is the first possibility of bifurcation appearance. Yet it is much more common for a bifurcation phenomenon to be discontinuous [Rice and Rudnicki, 1980]. It implies plastic loading inside the shear band and elastic unloading in the outer material, for which different constitutive tensors are assumed, *i.e.* $C^0_{ijkl} = C^e_{ijkl}$ and $C^1_{ijkl} = C_{ijkl}$ respectively. Hence, considering a discontinuous

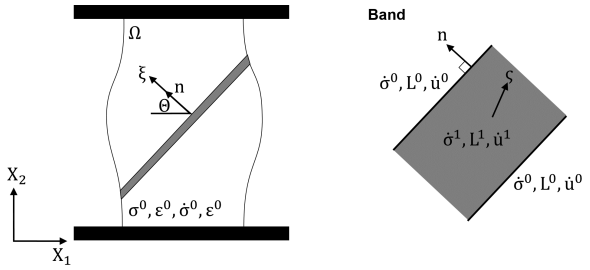

Figure III–6 – Theoretical scheme of a shear band.

bifurcation and using the static condition (III–1), the kinematic condition (III–2) and the constitutive equation (III–5) gives a third order equation system where the unknown is the vector ς_i:

$$n_i \left(C^1_{ijkl} \left(L^0_{kl} + \varsigma_k n_l \right) - C^0_{ijkl} L^0_{kl} \right) = 0 \tag{III–6}$$

The trivial solution $\varsigma_i = 0$ is always possible but means that no shear band can occur for the unique solution $L^1_{ij} = L^0_{ij}$. Other non-trivial solutions can be found for $\varsigma_i \neq 0$ although the difference between the constitutive tensors inside and outside the shear band makes the bifurcation analysis more intricate. Assuming that continuous bifurcation always precedes discontinuous bifurcation [Rice and Rudnicki, 1980, Simo et al., 1993], the bifurcation condition (III–6) can be particularised as follows:

$$\left(n_i C_{ijkl} n_l \right) \varsigma_k = 0 \tag{III–7}$$

The non-trivial solutions $\varsigma_i \neq 0$ in this case are met if and only if the determinant of the acoustic tensor is less or equal to zero, *i.e.* $det\left(n_i C_{ijkl} n_l \right) \leq 0$. Provided that C_{ijkl} is the elastoplastic constitutive tensor, it has been demonstrated that this criterion holds in the case of a classical single-mechanism elastoplastic model [Chambon, 1986].

It is worth noted that the strain localisation criterion can be extended to two-dimensional plane state problems, for which a double orientation of the shear is obtained, indicating that shear band can initiate in two conjugated bifurcation directions. The criterion can also be generalised to large strain problems [Wang, 1993] given that the elastoplastic constitutive tangent tensor is written for large strains and rotations, to no-classical (non-associated) elastoplasticity [Raniecki and Bruhns, 1981], or to materials exhibiting hardening of the plastic properties in addition to softening [Rudnicki and Rice, 1975]. Finally, it should be pointed out that all these developments are valid for pure mechanical analysis. In a multiphysics context, it has been shown that evenif the much more complex localisation patterns can be obtained in coupled hydro-mechanical problems [Vardoulakis, 1996b], the localisation condition depends only on the material drained properties [Loret and Preost, 1991].

8. Strain localisation modelling

It has been exposed so far that rupture in a localised mode is observed experimentally, and that theoretical tools are available to characterise this phenomenon when the conditions of occurrence are met. The next step is to define a robust modelling approach for strain localisation. In that purpose, this chapter tackles the general aspects related to the computational modelling of strain localisation in shear band mode.

The first part (Section 8.1) emphasises the practical implications behind the numerical implementation of such a process. The distinction between the continuous and discrete descriptions of fracture is briefly broached, with an emphasis on the former that is the one in use in the `LAGAMINE` FE code. The spatial discretisation dependency associated to the use of this approach with a classical finite element method is a major modelling issue that is also discussed. Some of the suitable regularisation techniques allowing to alleviate this mesh sensitivity are presented in the second part (Section 8.2). Finally, the last part (Section 8.3) of the chapter raises the question of the interactions between physical phenomena such as gas migration and the localisation process, and endorses the purpose of the numerical developments that will be presented in the next chapter.

8.1 Modelling issues

When it comes to the modelling of shear strain localisation, questions arise about how to represent discontinuities, either continuously or discontinuously, as well as how to mitigate mesh dependency, particularly if the former approach is used.

8.1.1 Continuous *vs* discontinuous approaches

An accurate numerical modelling of the entire failure process of a material subjected to strong solicitations has to account for the successive steps leading to material rupture, as described in section 7.2.3. The material first undergoes damage which subsequently generates strain localisation leading to the appearance of fractures with additional modifications of the properties inside, and *in fine* to the definitive rupture. The material damage by micro-cracking can be handled by a continuous approach corresponding to the progressive degradation of the elastic or plastic strength properties of the material, initiating a non-linear mechanical response. The large variety of computational techniques dedicated to the material damage in the context of continuum mechanics ensures the preservation of the description while reproducing the process of micro-cracking. They range from macroscopic and phenomenological methods [Kachanov, 1958, Lemaitre et al., 2009] to multi-scale or micro-mechanical methods, which include the microstructure effects on the solid properties [Budiansky and O'connell, 1976, Horii and Nemat-Nasser, 1983] or for which microcrack-induced damage can be produced [Zhu et al., 2008, Levasseur et al., 2013]. As a possible consequence of softening damage behaviour, the strain localisation phenomenon inducing discontinuities and fractures can occur. Among the existing models able to numerically represent the material discontinuities instigated by the fracturing process, the numerical analysis of strain localisation has traditionally fallen into two main categories:

- **Continuous approach**: The fracture is simulated presuming a smooth and continuous displace-

ment field everywhere in a material. As a result of the differentiability of this field, a strain field can also be specified at all positions within the body. From these assumptions, the material can be seen as a continuous medium and be investigated according to the continuum theory. This approach includes material damage without explicitly reproducing the fractures and their discontinuities.

- **Discontinuous approach**: The fracture is simulated assuming the development of jumps in the displacement field of the material, which translates into the creation of failure surfaces within the material. This approach is therefore dedicated to the physical replication of fractures.

Conceptually, the techniques pertaining to discontinuous failure models as *e.g.* [Armero and Garikipati, 1996, Larsson et al., 1999, Wells, 2001, Callari et al., 2010] that actually reproduce the appearance of failure surfaces within a material, exhibit a weak discontinuity (see Figure III–7a) or a strong discontinuity (see Figure III–7b) in the displacement field to model the strain localisation. On the other hand, the techniques related to continuous failure models as *e.g.* [Ortiz and Leroy, 1989, Chambon et al., 2001a, Collin et al., 2006, Salehnia et al., 2013, Pardoen et al., 2015b] consider continuous kinematic fields with a jump in the strain rate field involving potentially steep gradients across a small region to model the strain localisation (see Figure III–7c).

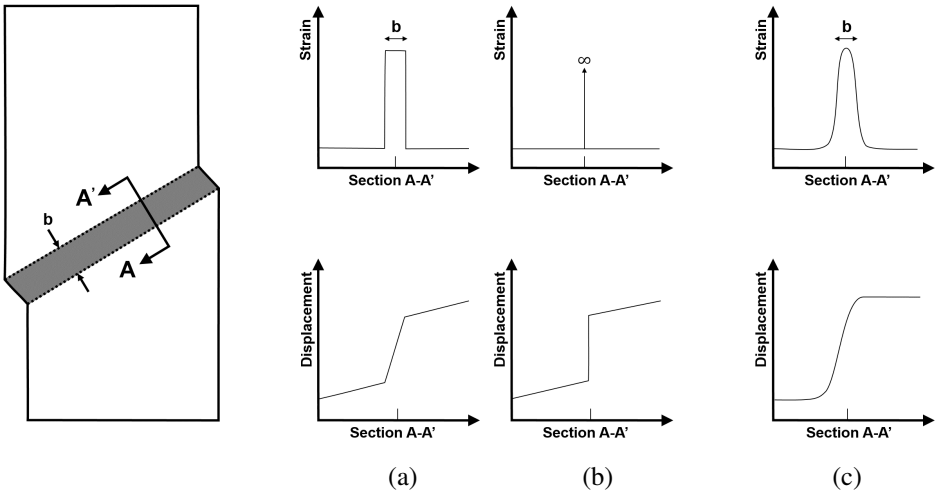

Figure III–7 – Conceptual representation of the displacement and strain fields for the numerical treatment of a localised zone (section A-A′): (a)-(b) discontinuous failure model applied for weak and strong discontinuities respectively, (c) continuous failure model . *After* [Wells, 2001].

From a physical standpoint, the choice between continuous and discontinuous models is rather dependent on the type of material that is studied. Discrete cracks (displacement jump) occur almost instantaneously while the yield strength of very brittle materials, like glass, is reached. By contrast, displacement jumps develop just at the last stage of failure, well past the peak load and just prior the ultimate collapse for highly ductile materials. As reported in [Wells, 2001], it becomes more difficult to opt for the most suitable approach when considering quasi-brittle materials that cover a large range of engineering materials, such as polymers, some metals, concrete or rocks, including those envisaged for deep geological disposals. For such materials, two main stages can be identified in the failure process, namely phases IV and V in Figure III–4. In the pre-peak phase dealing with the intensification and coalescence of microcracks, continuum formulations are more appropriate as the development of damage or plastic flow can be represented as a degradation of the continuum, *i.e.* strain softening. By contrast, discontinuous formulations are more suitable at the very last phase just before the destructive failure, when the displacement jumps across material surfaces may reach a critical point.

In this work, special attention is paid to clayey rocks likely to host underground waste repository, such as Boom Clay and Callovo-Oxfordian claystone, for which shear fracture in band mode is the pre-

dominant source of fracturing caused by the excavation process [Wileveau and Bernier, 2008, Armand et al., 2014]. Shear strain localisation can thus be seen as the predictive mechanism of the fracturing process leading up to failure. In light of these observations, it makes sense to opt for a continuous approach as it is implemented in the LAGAMINE code. The modelling of strain localisation in this framework will thus induce the development of shear bands with non-uniform strain distribution that may engender a displacement discontinuity between both sides of a shear band, but without explicitly reproducing the fractures.

8.1.2 Mesh dependency

Following the continuous approach, the strain localisation phenomenon is perceived as the appearance of a discontinuity in the strain rate, *i.e.* a localised shear band, which is a marker of the loss of uniqueness of the solution. Reaching the bifurcation criterion for continuum models applied to failure analysis is generally caused by some intrinsic features of the material behaviour, among which the strain softening is the driving mechanism [Lemaitre et al., 2009]. Material softening reflecting the decrease in load carrying capacity of a material under accumulated inelastic strains can be considered as the macroscopic reflection of the inhomogeneities propagation at the microscopic scale, such as micro-cracks, pre-existing defects, imperfections, *etc*. In that sense, the strain localisation response achieved by continuous models could be regarded as the degradation of continuum, that is, strain softening.

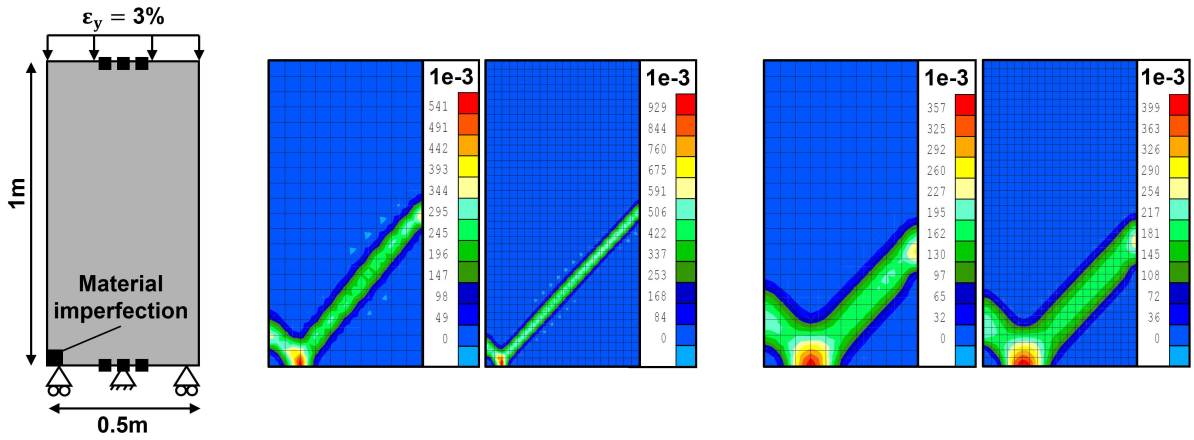

(a) Classical finite element method (b) Regulation technique

Figure III–8 – Modelling of a plane strain compression test with two distinct meshes of 10×20 and 20×40 elements: total deviatoric strain using (a) a classical finite element method and (b) a regularisation technique of second gradient type.

Nevertheless, classical finite element models are not capable of effectively predict the behaviour of a material as soon as highly heterogeneous deformations become involved, as it is the case in the post-bifurcation, or post-localisation regime. If one refer to the experimental observations presented in Section 7.2, these models do not take into account the microstructural mechanisms, such as the rearrangement of grains in granular materials or the development of micro-cracks in cohesive materials which lead to the sudden appearance of localisation bands and govern the width of these deformation zones. From a theoretical point of view, the governing equations in classical finite element methods do not provide any information on the band width, which is controlled by the intrinsic properties of the material at a lower scale and so, an infinity of solutions is possible. From a numerical point of view, the use of such kind of models to predict strain localisation upon softening leads to a mathematically ill-posed boundary value problem in the post-localisation regime suffering of a pathological dependency to the mesh size and orientation as widely reported in the literature [Pietruszczak and Mróz, 1981, De Borst and Mühlhaus, 1992, Zervos et al., 2001, Wu and Wang, 2010] and illustrated in Figure III–8a. This means that the

thickness of the shear band concentrates in a narrow band zone which is proportional to the element size of the mesh used to approximate the geometry of the problem. The physical implication gets reflected when a very refined finite element discretisation is considered with an element size tending towards zero [De Borst et al., 1993]. In this case, the localisation zone becomes vanishingly small, causing zero energy dissipation as far as it is entirely concentrated inside the zones of localised strains. It implies that the energy from the deformation of the material is totally conserved [Bažant and Belytschko, 1985] which is physically inadmissible.

In order to put in evidence the deficiency of classical tools, one can go back to simple compression tests as illustrated in Figure III–5b and modelled in Figure III–8. With these tools, the thickness of the shear band under softening plastic loading is a priori undetermined and a mesh-dependency of the model response is observed as far as the problem is ill-posed. For the most localised solution (strong discontinuity), the shear band thickness reduces to the size of the smallest element, and may theoretically cancel for an increasing number of elements [De Borst et al., 1993]. Another study [Kotronis et al., 2008] has exemplified that the situation is even worse, when solving the one-dimensional layer problem of thickness L subjected to shear loading. If the thickness l of the localised zone is larger than the overall thickness of the layer L, then it has been noticed that the solution of the shearing problem remains homogeneous, whereas if the thickness of the localised band l tend towards zero, the response of the material gets closer to its elastic regime. Such trivial examples evidence the need for an internal length scale in order to properly model the post-peak behaviour (Figure III–8b). Several regularisation techniques have been proposed to tackle the dependence to the finite element discretisation of such kind of problem, as listed in the next section.

8.2 Regularisation techniques

From previous observations, it appears that classical models require the introduction of one additional material parameter, defined as the internal length scale, in order to reflect the heterogeneous mechanisms at the microscopic scale and to control the width of the zone in which strains localise at the macroscopic level (the shear band thickness), in the post-localisation regime. By specifying the width of the failure zone, the non-physical case of complete collapse with zero energy dissipation is avoided, while setting the length scale to zero, classical continuum theory is recovered. This way, these adapted models - referred to as non-classical models - are capable to maintain well-posed governing equations for mode-II loading in the presence of strain softening [Pijaudier-Cabot and Bažant, 1987, De Borst, 1991], by restoring the mesh objectivity but not the uniqueness of the solution. They can be considered as enhancements of the classical models in the sense that they preserve the continuum concepts of continuous displacements and strains and are based on the same kinematic considerations.

In the literature, these enhanced approaches are basically gathered in two main categories described in the following: one consists in the enrichment of the constitutive law, and the other one consists in the enrichment of the continuum kinematics with microstructure effects.

Apart from that, some models propose to introduce the viscosity as a procedure to regularize the elastic-plastic solid [Needleman, 1988]. Other methods avoid the need to integrate an internal length scale by enriching the finite element formulation, and treat the localisation zone as a zero-thickness band [Simo and Rifai, 1990]. Even if these former techniques have difficulty controlling the band width and the latter ones relate more to a discontinuous-oriented approach which is not the one applied in this work, it seems coherent to give a few words about their potential applications dealing with shear band modelling.

8.2.1 Enrichment of the constitutive law

This kind of theory proposes to introduce the internal length scale at the level of the constitutive model, and constitutes a first solution to properly represent the experimental results involving strain

localised pattern. The constitutive law can be enriched with several types of strategies including the following.

The non-local approach

Originally formulated for elastic media [Kröner, 1967, Eringen, 1972], and later extended to the elasto-plasticity framework [Cemal Eringen, 1981], the classical non-local approach was then enhanced to handle strain softening in finite element analysis in a consistent manner, while at the same time avoiding spurious mesh sensitivity and precluding strain localisation to a vanishing volume [Bazant et al., 1984, Pijaudier-Cabot and Bažant, 1987]. Such a theory has proven to be applicable to concrete [Bazant et al., 1987] or to soils [Brinkgreve, 1994] and especially multiphase porous media [Lazari, 2016], regularising boundary value solutions when strain localisation takes place in the form of shear zones and cracks.

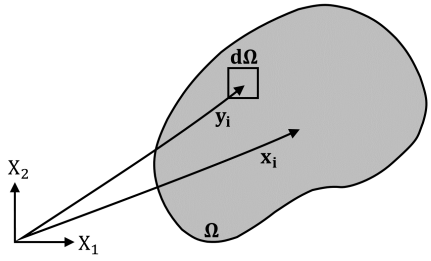

Figure III–9 – Non-local approach on a representative material volume.

The non-local integral theory states that the response of the material is determined not only by the corresponding state at the point under consideration but also by the state of its neighbouring points. The non-local variable $\mathring{v}$ at a material point x_i can be defined as an averaging value of the local variable v in a considered region Ω near that point (Figure III–9), and it is performed by a weighted spatial averaging function that contains the internal length used to regularise the numerical solution. For instance, the yield condition with isotropic hardening can be written as follows according to [De Borst et al., 2012]:

$$f(\mathring{\varepsilon}, \kappa) = \mathring{\varepsilon} - \kappa \tag{III–8}$$

where $\mathring{\varepsilon}$ is the non-local strain invariant that replaces the equivalent deviatoric strain, and κ is an internal variable.

Following the non-local theory, the non-local strain $\mathring{\varepsilon}$ is spatially averaged as follows:

$$\mathring{\varepsilon}(x_i) = \frac{1}{\psi(x_i)} \int_\Omega \Psi(y_i, x_i) \varepsilon_s(y_i) d\Omega \qquad \text{with} \qquad \psi(x_i) = \int_\Omega \Psi(y_i, x_i) d\Omega \tag{III–9}$$

where x_i is the coordinate vector of the material point where the non-local variable is considered and on which the representative volume Ω is centred, y_i is the coordinate vector of the infinitesimal volume $d\Omega$, and $\Psi(y_i, x_i)$ is a given non-local weight function scaling $\mathring{\varepsilon}$ to $\mathring{\varepsilon} = \varepsilon_s$ for a homogeneous and isotropic distribution of the variable. This distribution is usually defined in a Gaussian frame and depends on the distance $\|x_i - y_i\|$ and on a characteristic length parameter l_c that represents the internal length scale related to the microstructure.

The gradient plasticity approach

The gradient-dependent plasticity approach stems from pioneering works [Aifantis, 1984] that propose to incorporate the influence of gradients (of the first or higher orders) of internal variables in the yield condition [Mühlhaus, 1991] and in the flow-rule [Vardoulakis and Aifantis, 1991, Zervos et al., 2001]. This explicit gradient formulation can be derived from the non-local integral approach by introducing gradient of internal variable, expanding the local variable into a Taylor series [Bazant et al.,

1984, Lasry and Belytschko, 1988], using the weight function definition of Equation (III–9), and neglecting terms above the second order. It has been applied in the framework of multiphase porous media to analyse dynamic instabilities in fully and partially saturated granular materials [Zhang and Schrefler, 2000] and to derive an enhancement of the Cam-clay plasticity model [Stankiewicz and Pamin, 2006].

The explicit gradient formulation of the regularised variable can be derived explicitly from the local variable and its gradient. Getting back to the example of the equivalent deviatoric strain ε_s, the regularised expression of $\mathring{\varepsilon}$ comes from the Taylor expansion of ε_s and its truncation after the second-order terms, under the assumption of isotropy, as:

$$\mathring{\varepsilon} = \varepsilon_s + \bar{l}\frac{\partial^2 \varepsilon_s}{\partial x_i \partial x_i} \tag{III–10}$$

where $\bar{l}$ is the gradient parameter with a dimension of $[L^2]$ so $\sqrt{\bar{l}}$ can be related to the internal length scale l_c introduced to regularise the model.

The implicit gradient plasticity approach

The presence of second derivatives of the strain tensor in Equation (III–10) which involves first order derivatives of the displacements, leads to continuity requirements for the internal variable that has to be a continuously differentiable function [De Borst et al., 2012]. To overcome this necessity of class C_1 function (whose derivative is continuous) in the explicit gradient model, an alternative implicit gradient formulation close to the structure of the explicit non-local model has been proposed [Peerlings et al., 1996, Peerlings et al., 2001]. The non-local internal variable is an additional unknown of the problem and defined as the solution of the Helmholtz differential equation, which corresponds to an approximation of Equation (III–9) similar to Equation (III–10):

$$\mathring{\varepsilon} - \bar{l}\frac{\partial^2 \varepsilon_s}{\partial x_i \partial x_i} = \varepsilon_s \tag{III–11}$$

The solution of this Equation (III–11) is of the same form as the non-local Equation (III–9) [Zauderer, 1989], given that an additional boundary condition on $\mathring{\varepsilon}$ is provided, such as [Lasry and Belytschko, 1988]:

$$\frac{\partial \mathring{\varepsilon}}{\partial x_i} n_i = 0 \tag{III–12}$$

where n_i is the normal unit vector to the external boundary. Such formulations, initially proposed for gradient damage [Peerlings et al., 1996], have been also adapted for gradient plasticity [Engelen et al., 2002].

8.2.2 Enrichment of the kinematics

While the previous approaches with the enrichment of the constitutive law introduce the effect of the microstructure indirectly through non-local or gradient terms, this second kind of theory proposes to enrich the classical kinematics of the continuum medium with a proper description of the microstructure kinematics. Adding some mathematical constraints to general media with microstructure, also called micromorphic media [Eringen, 1970], yields a large panel of models including the following.

Macro-kinematic preliminaries

In the framework of classical continuum medium, the kinematics of a material particle of volume Ω is described at the macroscopic scale by its (macro) displacement field u_i, function of the coordinates denoted x_i. The classical kinematic fields and their related rate forms are then defined as:

- The (macro) deformation field corresponding to the gradient of the displacement field, and the related velocity gradient field:

$$F_{ij} = \frac{\partial u_i}{\partial x_j} \xrightarrow{\text{rate form}} L_{ij} = \frac{\partial \dot{u}_i}{\partial x_j} \tag{III–13}$$

- The (macro) strain field corresponding to the symmetric part of F_{ij}, and the related strain rate field:

$$\varepsilon_{ij} = \frac{1}{2}(F_{ij} + F_{ji}) \xrightarrow{\text{rate form}} \dot{\varepsilon}_{ij} = \frac{1}{2}(L_{ij} + L_{ji}) \tag{III–14}$$

- The (macro) rotation field corresponding to the antisymmetric part of F_{ij}, and the related spin rate field:

$$r_{ij} = \frac{1}{2}(F_{ij} - F_{ji}) \xrightarrow{\text{rate form}} \omega_{ij} = \frac{1}{2}(L_{ij} - L_{ji}) \tag{III–15}$$

Cosserat models

The most ancient model dealing with continua with microstructure that is reported can be traced back to Cosserat brother's seminal works [Cosserat and Cosserat, 1909]. In the Cosserat elastic theory, the displacements at each point of the classical continuum are enriched with local rotation degrees of freedom r_i^c, as presented in Figure III–10. Due to the particle rotation, additional kinematic fields are introduced [Vardoulakis and Sulem, 1995], and defined as:

- The micro-rotation fields (antisymmetric tensor):

$$r_{ij}^c = e_{ijk} r_k^c \tag{III–16}$$

  where e_{ijk} is the alternating tensor.

- The gradient of the particle rotation, or curvature:

$$K_{ij}^c = \frac{\partial r_i^c}{\partial x_j} \tag{III–17}$$

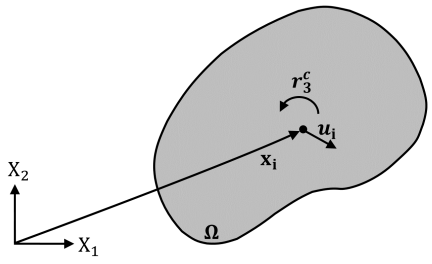

Figure III–10 – Cossert elastic continuum theory: Kinematic degrees of freedom.

It can be added that a relative strain $\bar{\varepsilon}_{ij} = F_{ij} - r_{ij}^c$ is deduced from the difference between the macro-deformations and the micro-rotations. Its symmetric part corresponds to the macro-strains ε_{ij}, while its antisymmetric part coincides with the difference between the macro- and micro-rotations $r_{ij} - r_{ij}^c$, and represents the relative rotation of a material point with regard to the rotation of its neighbourhood.

Furthermore, additional components are added to the stress and strain tensors. In particular, the couple of torques introduced in the former characterises bending and torsion at each material point. The kinematic and static components related to the micro-rotations are linked together by a bending modulus. The ratio between this latter and the Young modulus has the dimension of a length scale parameter

whose introduction in the constitutive equations makes it possible to regularise the numerical problem.

The Cosserat theory has been first applied to granular materials [Brown and Evans, 1972], to predict the state of bifurcation, the shear band orientation and the evolution of its thickness in sand specimens [Muhlhaus and Vardoulakis, 1987], to reproduce the elastoplastic behaviour of a sandstone sample under triaxial compression test [Sulem and Vardoulakis, 1990], or to study saturated and non-saturated conditions in the framework of multiphase porous media [Ehlers and Volk, 1998]. According to [Calvetti et al., 1997, Matsushima et al., 2003], it seems reasonable to assume that the mean value of the micro-rotations of the grains is comparable to the macro-rotation of the material in granular specimens. Localisation studies [de Borst and Sluys, 1991, Sluys and de Borst, 1992] have also been carried out with a Von Mises plasticity model formulated within the framework of the Cosserat continuum, highlighting that the regularisation effect is predominantly efficient when rupture occurs under high shearing deformation (mode II). Although the Cosserat continuum theory has existed for several decades [Papamichos, 2010], some questions still arise with regard to the direct measurement of the material moduli characterising the model or to the prescription of boundary conditions for the micro-rotations [Kunin, 1982, Kunin, 1983].

Toupin and Mindlin's principles

Other famous principles of materials with microstructure have been established in the 1960s by Toupin [Toupin, 1962] and Mindlin [Mindlin, 1964, Mindlin, 1965]. It is supposed that a marco-volume Ω includes smaller particles at the microscopic scale, which can be materialised by a micro-volume Ω^m embedded into the material volume Ω. A micro-displacement field u_i^m is specified independently of the macro-displacement u_i. Then, the kinematic fields at the microscopic scale are defined as:

- The micro-deformation field corresponding to the gradient of the micro-displacement field:

$$\nu_{ij} = \frac{\partial u_i^m}{\partial x_j} \tag{III–18}$$

  which is homogeneous in the micro-volume Ω^m but not in the macro-volume Ω.

- The micro-strain field corresponding to the symmetric part of ν_{ij}:

$$\varepsilon_{ij}^m = \frac{1}{2}(\nu_{ij} + \nu_{ji}) \tag{III–19}$$

- The micro-rotation field corresponding to the antisymmetric part of ν_{ij}:

$$r_{ij}^m = \frac{1}{2}(\nu_{ij} - \nu_{ji}) \tag{III–20}$$

  with the micro-rotation being the rotation components of the Cosserat model in Equation (III–16), *i.e.* $r_{ij}^m = r_{ij}^c$. The Cosserat theory can thus be seen as a particular case of the media with microstructure, in which the micro-deformations are assumed to be equal to zero.

- The micro second gradient field:

$$h_{ijk} = \frac{\partial \nu_{ij}}{\partial x_k} = \frac{\partial^2 u_i^m}{\partial x_j \partial x_k} \tag{III–21}$$

It can be added that the relative deformation of the microstructure $\bar{\varepsilon}_{ij} = F_{ij} - \nu_{ij}$ is deduced from the difference between the macro and the micro-deformations. Its symmetric part corresponds to the difference between the macro and the micro-strains $\varepsilon_{ij} - \varepsilon_{ij}^m$, while its antisymmetric part coincides with the difference between the macro and micro-rotations $r_{ij} - r_{ij}^m$.

Furthermore, additional stresses are introduced, namely the microstress τ_{ij} which is an additive stess field associated to the microstructure, and the double stress Σ_{ijk}. Following Toupin and Mindlin's framework, the constitutive law is computed from a potential, which implies to suppose a system with constant energy [Mindlin and Eshel, 1968].

(a) (b)

Figure III–11 – Kinematics of microstructure continuum: (a) initial configuration and (b) configuration after external solicitations with relative displacement of the microstructure.

Germain's general theory

A few years later, Germain's theory [Germain, 1973a, Germain, 1973b] proposes a more generalised version of the formulation based on the works of Toupin and Mindlin, where the kinematics of the microstructure is kept independent of the kinematics of the macrostructure. Rather than deriving the constitutive law from a potential energy-density which is a function of the strain and the rotation-gradient [Mindlin and Eshel, 1968], the virtual power principle is introduced to provide a global framework for the microstructure continuum formulation. This principle states that for any kinematically admissible virtual field, *i.e.* which respects the solid continuity and boundary conditions, the equality between the internal and external virtual power (produced by all stresses and forces acting on a mechanical system) ensures the local equilibrium at every point of the domain, and thus the global equilibrium of the solid. Since Germain's theory serves as basis for many enhanced models including the local second gradient model presented hereafter, the virtual work principle will be used for the formulation of a coupled finite element in Section 6.5.

Second gradient models

Among the wide class of constitutive models which account for materials microstructure, the second gradient models belonging to continuum models with higher deformation gradients (higher grade continuum) have been widely used over the last three decades [Fleck and Hutchinson, 1997, Chambon et al., 1998, Shu et al., 1999, Zervos et al., 2001, Collin et al., 2006]. This subclass includes the local second gradient model [1] developed in Grenoble [Chambon et al., 1998, Chambon et al., 2001a] and more particularly used in this work, which is briefly introduced in the following and whose entire numerical framework is set out in the next Section 9.

The contemporary formulation of such a model finds its roots in the successive evolutions of the theory of enhancement of the kinematics previously presented [Toupin, 1962, Mindlin, 1964, Germain, 1973a]. In particular, the local second gradient theory ensures that the material response at each point does not only depend on the first gradient of strain but also on the second gradient of strain. Moreover, it is based on the main assumption that there is no relative deformation of the microstructure, *i.e.* $\bar{\varepsilon}_{ij} = 0$, entailing the equalities between the (macro) deformation (Equation III–13) and micro-kinematic (Equation III–18) gradients and between the related virtual entities:

$$v_{ij} = F_{ij} = \frac{\partial u_i}{\partial x_j} \quad \text{implying} \quad v^*_{ij} = F^*_{ij} = \frac{\partial u^*_i}{\partial x_j} \tag{III–22}$$

This hypothesis allows to reformulate the principle of virtual work as further explained in Chapter 9.

Using this approach, it is possible to obtain mesh-independent numerical solutions thanks to the inclusion of an internal length represented by the constitutive parameter of the second gradient law

1. The term local refers to the constitutive equations which remain local.

(specified in the next chapter, Section 9.3). Following preliminaries one-dimensional applications on a bar in traction [Chambon et al., 1998, El-Hassan, 1997, Matsushima et al., 2002] or two-dimensional applications on a thick-walled cylinder under radial stress [Sieffert et al., 2009, Caillerie et al., 2011], several works during the last years have proved that the second gradient model is a competitive alternative to not only model strain localisation in monophasic media [Matsushima et al., 2002, Chambon and Moullet, 2004, Bésuelle et al., 2006] but also in multiphasic media [Collin et al., 2006, Pardoen et al., 2014].

8.2.3 Rate-dependent models

The adoption of rate-dependent models by substituting plasticity with visco-plasticity and by using the time-dependent viscosity parameter to tackle strain localisation has proven to be an effective technique especially in rate-dependent problems. Such an approach has been used in several works [Loret and Preost, 1991, Sluys and de Borst, 1992, Wang et al., 1997, Díez et al., 2000, Regueiro and Foster, 2011]. It is possible to demonstrate mathematically that the addition of this term implicitly introduces an internal length scale into the constitutive model, thus removing the pathological mesh dependency associated to strain localisation [Needleman, 1988]. Nevertheless, when the load velocity decreases, the visco-plastic solution tends towards the elasto-plastic one, vanishing the regularising effect for rate-independent or quasi-static problems. Therefore, one of the limitations of these models comes from the band width that is not exclusively determined by the material parameters but is mostly dependent on the load velocity.

8.2.4 Discontinuity approaches

The representation of a crack or a fracture in a discrete way dates back to the initial studies on fracture mechanics, first devoted to linear elastic behaviour of brittle materials [Griffith, 1921] and further enriched with the plastic considerations of ductile materials [Irwin, 1948, Orowan, 1949]. Numerically, discontinuous fracture modelling with elements techniques comprises the cohesive zone method [Dugdale, 1960, Barenblatt, 1962, Xu and Needleman, 1994], discontinuous mesh interface or contact elements [Zhong and Mackerle, 1992], the strong-discontinuity approach [Simo et al., 1993], remeshing methods [Bouchard et al., 2003], or extended finite element methods [Moës et al., 1999].

The so-called strong-discontinuity approach [Simo et al., 1993] is an efficient alternative when a shear band evolves as a fault, making it impossible for the material to support highly localised strains especially in the post-localisation regime. The principle is to model the crack growth implicitly by a jump in the displacement field [Simo and Rifai, 1990]. In that sense, discontinuity approaches provide a better kinematic description of highly discontinuous displacement fields than pure continuum models that smear the displacement jumps uniformly over the entire element as reported in Section 8.1.1. In particular, such approaches have been originally dedicated to solids, showing good results for deviatoric plasticity models with a constant post-localisation softening modulus [Armero and Garikipati, 1996, Simo et al., 1993], before being applied to geomechanics problems in the early 2000s [Borja, 2000, Regueiro and Borja, 2001, Borja, 2002], and especially to saturated porous media [Armero and Callari, 1999], later generalised to partially saturated conditions [Callari et al., 2010].

To overcome the dependency of the strain approximations on both parts of the element separated by a strong discontinuity [Jirásek, 2002], the Extended Finite Element Method (XFEM) [Belytschko and Black, 1999] propose to enrich only the nodal displacements surrounding the discontinuities and not the elements. Practically, XFEM has been employed for modelling shear bands as strong discontinuities within a continuum mechanics context [Samaniego and Belytschko, 2005, Areias and Belytschko, 2006], within a higher-order continuum model based on the Cosserat theory to simulate shear band localisation [Khoei and Karimi, 2008], or for modelling shear band localisation using non-associated plasticity models [Daneshyar and Mohammadi, 2013, Liu, 2015].

8.3 Hydro-mechanical couplings and model's raison d'être

The aim of numerically reproducing the phenomenon of gas migrations through the excavation damaged zone requires the extension of the employed regularisation techniques to multiphasic materials and multiphysics problems, which raises the question of the interactions between physical problems and localisation processes, and how to model them.

So far, the development of the EDZ has been only considered from a purely mechanical point of view. Considering that material rupture is generally preceded by localised deformations in shear band mode that can lead to material damage, micro-cracks and fractures, shear strain localisation is used as the precursor of fractures appearance numerically. This first step of numerical modelling can be undertaken via continuous or discontinuous methods provided that a suitable regularisation technique is implemented. Although some studies have highlighted the effects of permeability on shear band development and stability [Loret and Preost, 1991] and that permeability plays the role of an internal length parameter for a certain domain of values in dynamic coupled models [Zhang et al., 1999, Zhang and Schrefler, 2002], the irreversible impact of the fracturing process on flow characteristics is another aspect to address, particularly when it comes to gas transfers.

Indeed, besides the mechanical aspects discussed through continuous and discontinuous cracking, the fracturing process is also dominated by hydro-mechanical property changes, inducing significant modifications in the flow and transport behaviour of the studied zone [Wileveau and Bernier, 2008, Armand et al., 2014]. On the one hand, the intrinsic permeability can drastically vary of several orders of magnitude in the damaged zone, which impacts the potential gas transfers and must be taken into account numerically. The different methods aiming at modelling the influence of the fracturing on permeability range from classical approaches based on fracture aperture [Snow, 1969, Witherspoon et al., 1980] to more complex approaches based on hydraulic properties damage [Dormieux and Kondo, 2004, Barthélémy, 2009, Levasseur et al., 2013] or include a dependency of the permeability with a mechanical parameter, such as strain or plastic deformation for instance [Liu et al., 1999, Chen et al., 2007, Olivella and Alonso, 2008, Pardoen et al., 2016]. In this work, the latter approach is prescribed with a hydro-mechanical coupling involving a deformation-dependent evolution of the material intrinsic permeability based on a power formulation, as defined in the next chapter in Section 9.4. As far as the fractured rock is modelled as a continuous medium at the macro-scale, the evolution of the intrinsic permeability directly relies on the mechanical deformations. Such an evolution is responsible for the more important increase in permeability within the shear bands owing to the strain localisation effect. On the other hand, the retention behaviour is another property of the material that can evolve with the cracking and damage. In particular, the fracturing process in porous materials can induce modifications of the pore network morphology, thus affecting the water retention curve, the gas entry pressure (and the permeability) [Arson and Pereira, 2012, Pereira and Arson, 2013, M'Jahad et al., 2015]. Again, considering the fractured rock as a continuous medium at the macro-scale, this additional hydro-mechanical coupling can be implemented by assuming an evolution of the retention curve with the mechanical deformations [Olivella and Alonso, 2008, Gerard, 2011]. For such an evolution, an increase in the pore size under fracturing results in a decrease in the gas breakthrough pressure as highlighted in Section 5.4 of the literature review, which tends to amplify the desaturation of the damaged zone for a given capillary pressure.

In short, numerical models that can properly handle strain localisation phenomena in rocks considering HM [Plassart et al., 2013, Marinelli et al., 2015, Pardoen et al., 2016] or THM [Sieffert et al., 2011, Rattez et al., 2018] couplings have already been proposed, but without focussing explicitly on the presence of gas. The effect of the EDZ on the hydro-mechanical properties evolution is well captured [Pardoen et al., 2016] but direct interactions with gas migrations has only been briefly investigated by means of a simplified model of gas pressure evolution [Autio et al., 2006] or with a coupled HM-damaged model [Xue et al., 2018]. Yet in both cases, the rigorous and representative development of

the EDZ is eluded. This lack of numerical modelling which combines all the aspects inherent to gas migrations in damaged clay rock materials at once has stimulated the undertaking of the present numerical developments. This contribution aims thence at developing a second gradient H^2M model (standing for two-phase flow hydro-mechanical model) in order to simultaneously capture the multi-physics couplings related to gas transfers in partially saturated clay formations and the strain localisation aspects associated with the creation of the EDZ. More specifically, this model pays special attention to the modelling of HM couplings prone to occur in the EDZ and susceptible to affect the kinetics of gas transfers.

In practise, the second gradient H^2M model implemented in the `LAGAMINE` code following a number of serial contributions [Collin et al., 2006, Pardoen et al., 2015a] constitutes the basis of the developments described hereafter. With respect to these previous works, the presence of gas implies its proper degree of freedom. In particular, the following main axes of novelties are proposed:

- Introduction of an additional degree of freedom for variable gas pressure.
- Implementation of the stiffness matrix terms capturing the coupling of the mechanics on the fluids.
- Definition of appropriate retention models and relative permeability curves to simultaneously deal with variable water and gas pressures.
- Formulation of the hydro-mechanical couplings linking the fluid transfer properties to the deformations, to refine the modelling of the gas transport kinetics.
- Creation of suitable FE meshes to deals with gas propagation in different clay materials at different scales.

9. A second gradient H^{2}M model

This chapter focusses on the second gradient model originally elaborated by [Chambon et al., 1998, Chambon et al., 2001a] that is integrated in the LAGAMINE code, on the successive improvements made to this technique over the past decades, and on the novelties that the present work aims to provide. In particular, this chapter addresses the adaptations to the balance equations (Section 9.2) and the specific constitutive laws (Section 9.3) that are required when using a regularisation method with microstructure enriched medium in the finite element code. Some advanced hydro-mechanical couplings essential for a better representation of the hydraulic properties modifications induced by fracturation in the EDZ are also defined (Section 9.4). Finally, the theoretical developments leading to the formulation of the second gradient H^{2}M coupled finite element SGRT, including the linearisation of the field equations and the finite element discretisation are proposed (Section 9.5).

9.1 Review of the local second gradient model

As emphasised in previous Chapter 8, the proper reproduction of strain localisation in geomaterials with finite element methods requires an appropriate enhanced model. Among the extensive collection of available tools, the local second gradient model elaborated within the framework of microstructure continuum theory is the one that is chosen in the present work. This section aims to review the existing literature related to this model, by detailing the successive computational developments and advances regarding the implementation of this regularisation technique.

The origins of the local second gradient model can be traced back to the early 2000s in Grenoble, following innovative works of [Chambon et al., 1998, Chambon et al., 2001a], which aimed at providing a general framework to deal with local second gradient methods within theories with microstructure, keeping in mind future applications for geomaterials. The starting point of these numerical developments was that specific elasto-plastic local models with microstructure, such as Cosserat second gradient and local second gradient models, had promising features to model granular materials and cohesive geomaterials respectively. In the framework of microstructure continuum theory, a microkinematic gradient field ν_{ij} is introduced to describe strain and rotation at the micro-scale, and additional stresses are integrated, namely the micro-stress τ which is an additive stress field associated to the microstructure, and the double stress Σ_{ijk}. The local second gradient model is based on the main assumption that the micro-kinematic gradient is equal to the deformation gradient, as recalled from Equation (III–22):

$$v_{ij} = F_{ij} = \frac{\partial u_i}{\partial x_j} \quad \text{implying} \quad v^*_{ij} = F^*_{ij} = \frac{\partial u^*_i}{\partial x_j} \tag{III–23}$$

Concretely, this technique introduces an implicit internal length scale in the model that removes the pathological mesh dependency when strain localisation occurs. In elasticity, this parameter is proportional to the ratio of the two constitutive moduli defined by the first and second gradient constitutive laws as it will be specified in Section 9.3.

A variational formulation of the general expression of the second gradient model has been first derived from the virtual power principle [Germain, 1973a], for monophasic media in one dimensional

configurations [Chambon et al., 1998]. Second order derivatives of displacements are included in the virtual power principle. It means that the kinematically admissible field u^* as well as the displacement field u have to be two times differentiable implying the necessity of C_1 finite elements to be implemented in a FE code. This can be avoided by making use of Lagrange multipliers to enforce the relation between the micro-kinematic gradient and the spatial derivatives of the corresponding displacements. At that time, this first version of the second gradient theory was also extended to two dimensional cases, within the framework of either small deformations, that is to say all the configurations of equilibrium of a solid body remain infinitely close, or large deformations [Matsushima et al., 2000, Chambon et al., 2001a, Matsushima et al., 2002].

Later on, the second gradient theory was extended from monophasic to biphasic medium in order to model saturated and partially saturated porous media [Collin et al., 2006]. As specified in Chapter 6.1, the medium includes incompressible solid grains, under isothermal and quasi-static conditions. The solid and fluid phases are assumed as immiscible and phase changes, like evaporation and dissolution, are not taken into account. According to the more general formulation in which the second gradient effects are also associated to the fluid phase [Sciarra et al., 2007], the pore fluid equation could eventually introduce its own internal length scale in the system. Yet it is assumed that the pore fluid does not have an influence at the microstructure level, entailing that pore water pressure variations do not generate micro-kinematic gradient. This additional hypothesis was first formulated on a Cosserat model for biphasic medium [Ehlers and Volk, 1998]. Similarly to classical poromechanics, the effect of water on the total stress is defined according to Terzaghi's effective stress postulate [Terzaghi, 1936], contrary to the double stress Σ_{ijk} that is only related to the solid phase and is independent of the pore water pressure.

On the basis of the second gradient model was derived a simplified theory within the framework of constrained micromorphic models involving only the micro-volumetric strain [Fernandes et al., 2008]. Provided the use of an additional penalty term in the numerical treatment, this hydro-mechanical second gradient dilation model turns out to be quite efficient to regularise problems capturing behaviours with plastic volumetric strain such as the ones of geomaterials. This model is characterised by a reduction of the number of degree of freedoms which makes it less time consuming than the more general ones. It has thus been put into practise for 2D problems such as the biaxial compression test [Fernandes et al., 2008] or the drilling of a borehole, as well as for a very simple 3D problem dealing with a triaxial test [Fernandes et al., 2011].

Other important advances have been carried out to enrich the second gradient model with coupled and multiphysics phenomena. In order to take into account the potential heat exchanges occurring within geomaterials, the thermal effects were added to the initial HM model developed by [Collin et al., 2006], to come up with a local second gradient model involving thermo-hydro-mechanical couplings [Sieffert et al., 2011]. With this extension of the model implemented, it was more specifically possible to deal with the important topic of the evolution of an excavation damage zone under thermal load in the design of nuclear waste disposals. For this study, the analysis was restricted to saturated conditions, with a dependence of the solid grain density, of the liquid density and of the viscosity of the fluid on the temperature. Subsequently, the second gradient model has also been adapted for partially saturated conditions with constant gas pressure and permeability evolution [Pardoen et al., 2014]. Considering the fractured rock as a continuous medium at the macroscale, the intrinsic hydraulic permeability evolution is reproduced through a strain-dependent relation [Pardoen et al., 2016]. Some applications dedicated to the modelling of the excavation of a nuclear waste storage gallery in the Callovo-Oxfordian claystone have been performed, showing good agreement with *in situ* large-scale measurements and observations of the excavation damaged zone evolution.

Finally, other major efforts have been undertaken more recently to extent the local second gradient model to the multi-scale approach, by replacing the classical constitutive law by finite element simula-

tions performed at the micro-scale. Some contributions [Marinelli, 2014, van den Eijnden, 2015] have implemented the finite element squared (FE^2) framework, in which the finite element method is run at both scales, *i.e.* micro and macro [van den Eijnden et al., 2016]. In particular, this model is applied for modelling hydro-mechanical coupling in the Callovo-Oxfordian claystone during the simulation of gallery excavation in the context of radioactive waste repositories [van den Eijnden et al., 2017]. An alternative was also proposed based on a FEM × DEM multi-scale approach [Argilaga, 2016], namely a method that couples Discrete Elements at the micro-scale and Finite Elements at the macro-scale, with with applications to mechanical problems [Desrues et al., 2019]. Finally, some works [Plúa, 2018] have attempted to exploit the characteristics of Isogeometric Analysis (IGA) for the numerical solution of coupled hydro-mechanical problems in saturated and partially saturated second gradient poro-elastoplastic geomaterials. Among the most relevant features of IGA, its smoothness, its convergence rate and particularly its intrinsic higher-order continuity between elements represent a definite improvement over the standard FEM, with advantages in terms of computational efficiency.

9.2 Balance equations

As for classical continuum framework presented in chapter 6, the material is considered as a porous medium and the balance equations are based on averaging theories. In the proposed developments, the local second gradient model is extended from a biphasic to a multiphasic medium (solid particles, gas and water), with a view of taking variable gas pressure into account (H^2M). Then, starting from the balance equations of the multiphasic problem in classical poromechanics presented in Section 6.2, a micro-kinematic gradient field ν_{ij} is introduced in the framework of microstructure continuum theory in order to describe strain and rotation at the micro-scale, under the assumption of no relative deformation of the microstructure ($\nu_{ij} = F_{ij}$ and $\nu^*_{ij} = F^*_{ij}$). Moreover, when dealing with the second gradient theory in multiphasic context, the hypothesis of no pore fluids influence at micro-scale such that fluids pressure variations do not generate any micro-kinematic gradients generally holds [Ehlers and Volk, 1998]. It means that the second gradient effects are only taken into account for the solid phase. In the following, the balance equations of the second gradient H^2M model are presented in usual differential local form using an updated Lagrangian configuration which corresponds to the current material configuration (as stated in Subsection 6.1.3). These equations consist of the balance of momentum of the mixture, the solid mass balance equation and the fluids mass balance equations, both for the water and gas species.

9.2.1 Momentum balance equation

Starting from the general form of the balance of momentum of classical poromechanics, additional terms are incorporated in Equation (II–48) to account for microstructure effects. Consequently, the local momentum balance equation including both macro and micro quantities reads:

$$\frac{\partial \sigma_{ij}}{\partial x_j} - \frac{\partial^2 \Sigma_{ijk}}{\partial x_j \partial x_k} + \rho g_i = 0 \tag{III–24}$$

where Σ_{ijk} is the double stress dual of h^*_{ijk}, which needs an additional constitutive law introducing the internal length scale, $h^*_{ijk} = \frac{\partial \nu^*_{ij}}{\partial x_k}$ is the virtual micro second gradient. Developing the mixture homogenised density in this equation gives:

$$\rho = \rho_s(1-\phi) + \rho_w S_{r_w}\phi + \rho_g(1-S_{r_g})\phi \tag{III–25}$$

where $\phi = \frac{\Omega_v}{\Omega}$ is the porosity with Ω the current volume of a given mass of skeleton and Ω_v the corresponding porous volume, ρ_s is the solid grain density, ρ_w is the water density, ρ_g is the gas density, and S_{r_w} is the water degree of saturation.

9.2.2 Mass balance equations

The formulation of the mass balance equations follows the compositional approach of [Panday and Corapcioglu, 1989], which balances chemical species rather than phases, thence cancelling out the terms related to phase transfer. The model is elaborated for the solid particles, the water species and a single gas species corresponding to the predominant gas release in the case of a deep geological repository of high-level nuclear wastes. Finally, it is worth reminded that the different phases of the porous medium are assumed to be in thermodynamic equilibrium, following the restrictions (II–110) to (II–112) introduced in Section 6.4 and required to close the mass balance equations.

Solid mass balance equation

Thanks to a Lagrangian description (see Subsection 6.1.3), the reference system follows the solid phase and the conservation of the solid mass is necessarily met. For a given volume of mixture, the general form of the solid mass balance equation of classical poromechanics (Equation (II–55)) is conserved and reads:

$$\dot{M}_s = \frac{\partial}{\partial t}\left(\rho_s(1-\phi)\Omega\right) = 0 \tag{III–26}$$

where M_s is the solid mass inside the current porous material configuration Ω, and ρ_s is the density of solids, *i.e.* the clay rock matrix density.

Water mass balance equation

Following the particular hypothesis that second gradient effects are only assumed for the solid phase [Ehlers and Volk, 1998], it follows that the pore water pressure does not have an influence at the microstructure level so that pore water pressure variations do not generate micro-kinematic gradients. The water mass balance equation of classical poromechanics (Equation (II–60)) is thus conserved and reads for a unit porous medium ($\Omega = 1$):

$$\underbrace{\frac{\partial f_{w,i}}{\partial x_i} + \dot{M}_w}_{\text{Liquid water}} + \underbrace{\frac{\partial f_{v,i}}{\partial x_i} + \dot{M}_v}_{\text{Water vapour}} - Q_w = 0 \tag{III–27}$$

where $f_{w,i}$ and $f_{v,i}$ are the mass flows of liquid water and water vapour defined in the two-phase flow model in Section 6.3.1, Q_w is the water source/sink term, and M_w and M_v are the masses of liquid water and water vapour respectively, which are given in rate form to express the change in fluid storage:

$$\dot{M}_w = \frac{\partial}{\partial t}\left(\rho_w \phi S_{r_w} \Omega\right) \tag{III–28}$$

$$\dot{M}_v = \frac{\partial}{\partial t}\left(\rho_v \phi S_{r_g} \Omega\right) \tag{III–29}$$

where ρ_w and ρ_v are the densities of liquid water and water vapour respectively. In these expressions, the time partial derivatives express the change in fluid storage in the porous medium, while the divergence of fluxes corresponds to the difference between the input and output fluxes of a given volume of mixture.

Gas mass balance equation

Similarly, following the particular hypothesis that second gradient effects are only assumed for the solid phase [Ehlers and Volk, 1998], it follows that the gas pressure does not have an influence at the microstructure level so that gas pressure variations do not generate micro-kinematic gradients. The gas mass balance equation of classical poromechanics (Equation (II–60)) is thus conserved and reads for a unit porous medium ($\Omega = 1$):

$$\underbrace{\frac{\partial f_{g,i}}{\partial x_i} + \dot{M}_g}_{\text{Dry gas}} + \underbrace{\frac{\partial f_{dg,i}}{\partial x_i} + \dot{M}_{dg}}_{\text{Dissolved gas}} - Q_g = 0 \tag{III–30}$$

where $f_{g,i}$ and $f_{dg,i}$ are the mass flows of dry gas and dissolved gas defined in the two-phase flow model in Section 6.3.1, Q_g is the gas source/sink term, and M_g and M_{dg} are the masses of dry gas and dissolved gas respectively, which are given in rate form to express the change in fluid storage:

$$\dot{M}_g = \frac{\partial}{\partial t}\left(\rho_g \phi S_{r_g} \Omega\right) \qquad \text{(III–31)} \qquad \dot{M}_{dg} = \frac{\partial}{\partial t}\left(\rho_{dg} \phi S_{r_w} \Omega\right) \qquad \text{(III–32)}$$

where ρ_g and ρ_{dg} are the densities of dry gas and dissolved gas respectively. In these expressions, the time partial derivatives express the change in fluid storage in the porous medium, while the divergence of fluxes correspond to the difference between the input and output fluxes of a given volume of mixture.

9.3 Constitutive equations

A certain number of dependent variables such as the degree of saturation, fluid flows or densities are involved in the balance equations presented in the previous Section 9.2. All these variables are directly dependent on the main unknowns of the problem. They include the displacement fields u_i, the fluids pressure fields p_w and p_g, the micro-deformation field ν_{ij} describing the kinematics at micro-scale, and an additional unknown field of Lagrange multipliers λ_{ij} which will be introduced later for the FE method implementation. The constitutive equations are the specific relationships that make the link between these variables, in order to fully describe the behaviour of a multiphasic porous medium. The constitutive equations of the second gradient two-phase flow hydro-mechanical model include the multiphase flow model defined in Section 6.3.1 and the retention model of Section 6.3.2 which are not recalled in the present section. As for the mechanical model defined in Section 6.3.3, it remains applicable provided to define an additional relationship that accounts for the microstucture effects due to the presence of double stress in Equation (III–24).

With a view to extending the second gradient model to multiphasic materials, the balance equations remain valid as long as the total stress σ_{ij} is defined. In particular, the total Cauchy stress tensor introduced in the momentum balance Equation (III–24) must be related to the main unknowns of the problem. The mechanical behaviour of porous media is not entirely controlled by the total stress, but it is also influenced by the presence of fluids in the pore space. This behaviour is thus described by an alternative effective stress definition. Accounting for the partially saturated conditions with Biot's definition [Biot, 1941] to consider the solid phase compressibility, the Bishop's postulate introduced in Equation (II–92) can be written as:

$$\sigma'_{ij} = \sigma_{ij} - b_{ij}(S_{r_w} p_w \delta_{ij} + (1 - S_{r_w})\, p_g \delta_{ij}) \qquad \text{(III–33)}$$

where σ'_{ij} is the Bishop's effective stress, S_{r_w} is the water degree of saturation, p_w and p_g are the pore water and gas pressures respectively with $s = p_g - p_w$ the matrix suction, δ_{ij} is the Kronecker symbol, and b_{ij} is the Biot's tensor that represents more particularly the compressibility of the solid grain skeleton relative to the skeleton compressibility. Finally, it is worth reminded that in previous Equation (III–33), the stress field is defined under soil mechanics convention in which compressive stress is positive.

Second gradient constitutive equation

Similarly to classical media for which a constitutive equation relates σ'_{ij} to the kinematic history, the second gradient mechanical model requires an additional constitutive stress-strain relation between the kinematics and the double stress at micro-scale. Assuming that the latter is decoupled of the classical first gradient part and independent of fluid pressures, an isotropic linear elastic law has been initially proposed by [Mindlin, 1965]:

$$\tilde{\Sigma}_{ijk} = D_{ijklmn} \frac{\partial \dot{v}_{lm}}{\partial x_n} \qquad \text{(III–34)}$$

where $\tilde{\Sigma}_{ijk}$ is the Jaumann double stress rate expressed as a function of the micro second gradient rate $\dot{h}_{ijk}$:

$$\tilde{\Sigma}_{ijk} = \dot{\Sigma}_{ijk} + \Sigma_{ljk}\omega_{li} + \Sigma_{imk}\omega_{mj} + \Sigma_{ijp}\omega_{pk} \tag{III–35}$$

and D_{ijklmn} is the elastic constitutive tangent tensor for second gradient law, which depends on only one constitutive elastic parameter D in its simplified version derived in [Matsushima et al., 2002] and reads for two-dimensional problems:

$$\begin{bmatrix} \tilde{\Sigma}_{111} \\ \tilde{\Sigma}_{112} \\ \tilde{\Sigma}_{121} \\ \tilde{\Sigma}_{112} \\ \tilde{\Sigma}_{211} \\ \tilde{\Sigma}_{212} \\ \tilde{\Sigma}_{221} \\ \tilde{\Sigma}_{222} \end{bmatrix} = D \begin{bmatrix} 1 & 0 & 0 & 0 & 0 & \frac{1}{2} & \frac{1}{2} & 0 \\ 0 & \frac{1}{2} & \frac{1}{2} & 0 & -\frac{1}{2} & 0 & 0 & \frac{1}{2} \\ 0 & \frac{1}{2} & \frac{1}{2} & 0 & -\frac{1}{2} & 0 & 0 & \frac{1}{2} \\ 0 & 0 & 0 & 1 & 0 & -\frac{1}{2} & -\frac{1}{2} & 0 \\ 0 & -\frac{1}{2} & -\frac{1}{2} & 0 & 1 & 0 & 0 & 0 \\ \frac{1}{2} & 0 & 0 & -\frac{1}{2} & 0 & \frac{1}{2} & \frac{1}{2} & 0 \\ \frac{1}{2} & 0 & 0 & -\frac{1}{2} & 0 & \frac{1}{2} & \frac{1}{2} & 0 \\ 0 & \frac{1}{2} & \frac{1}{2} & 0 & 0 & 0 & 0 & 1 \end{bmatrix} \begin{bmatrix} \partial\dot{v}_{11}/\partial x_1 \\ \partial\dot{v}_{11}/\partial x_2 \\ \partial\dot{v}_{12}/\partial x_1 \\ \partial\dot{v}_{12}/\partial x_2 \\ \partial\dot{v}_{21}/\partial x_1 \\ \partial\dot{v}_{21}/\partial x_2 \\ \partial\dot{v}_{22}/\partial x_1 \\ \partial\dot{v}_{22}/\partial x_2 \end{bmatrix} \tag{III–36}$$

where D is the second gradient elastic modulus that symbolises the physical microstructure and is related to the internal length scale relevant for the shear band width [Chambon et al., 1998, Collin et al., 2009a].

It has been demonstrated from an identification procedure based on experimental triaxial tests [El Moustapha, 2014], that it is possible to determine the parameter D of the second gradient law just like the other parameters of an elasto-plastic law. Moreover, it is possible to show that continuous media of the second gradient type can integrate an internal length by carrying out the dimensional analysis of the internal virtual work as follows [Marinelli, 2014]:

$$W_I^* \quad \left[\frac{ML}{T^2}\frac{1}{L^2}\right] \quad \text{gives} \quad \begin{cases} \sigma_{ij}\varepsilon_{ij}^* & \left[\frac{ML}{T^2}\frac{1}{L^2}\right][-] & \text{First gradient} \\ \Sigma_{ijk}\dfrac{\partial u_i^*}{\partial x_j \partial x_k} & \left[\frac{ML}{T^2 L}\right]\left[\frac{1}{L}\right] & \text{Second gradient} \end{cases} \tag{III–37}$$

From a dimensional point of view, the constitutive parameter D has the dimensions of a force as making explicit in the following equation:

$$\begin{cases} \sigma_{ij} = C_{ijkl}\varepsilon_{kl} & \left[\frac{ML}{T^2}\frac{1}{L^2}\right] = \left[\frac{ML}{T^2}\frac{1}{L^2}\right][-] & \text{First gradient} \\ \Sigma_{ijk} = D_{ijklmn}\dfrac{\partial u_i^*}{\partial x_j \partial x_k} & \left[\frac{ML}{T^2}\frac{1}{L}\right] = \left[\frac{ML}{T^2}\right]\left[\frac{1}{L}\right] & \text{Second gradient} \end{cases} \tag{III–38}$$

Thence, from the ratio between the dimensions of the first and second gradient constitutive laws, it follows that an internal length parameter has been introduced into the formulation of the equilibrium. A rough estimation of the value of the band thickness can be extrapolated from the following square root expression:

$$\frac{|D|}{|C|} = \left[L^2\right] \qquad l_c = \sqrt{\frac{|D|}{|C|}} \tag{III–39}$$

9.4 Advanced hydro-mechanical couplings

Advanced hydro-mechanical couplings are added to the second gradient hydro-mechanical model in partial saturation, in order to reproduce the preferential propagation of gas within the excavation damage zone. The primary motivation behind these developments arises from experimental evidences that gas transport is mainly governed by the hydraulic properties modifications induced by fracturation [Tsang et al., 2005, Armand et al., 2014]. In particular, one can consider that gas propagation in

low-permeable clay materials is associated with the development of preferential paths along existing or pressure-dependent discontinuities. In these materials, the fracture opening can be induced by hydro-mechanical loadings, such as an increase of fluid pressure related to gas release or an effective unloading of the medium. For the clay host rock studied in this work, shearing can be relevantly considered as the predominant fracture mechanism around the storage galleries because of the high *in situ* stress state emphasised in Chapter 4. In the numerical model elaborated through this chapter, the shear fractures are represented at macro-scale by shear strain localisation in band mode using a second gradient regularisation technique. Knowing that the flow transfer properties are not homogeneous in the fractured zone, the basic idea consists in enriching the model with appropriate hydro-mechanical couplings that are established from a dependence with the deformations and are able to cause intense changes in the transfer properties inside the shear bands. More specifically, multiphysical interactions between pathways aperture and hydraulic properties, namely the permeability and the gas entry pressure are introduced on the basis of the intrinsic permeability based models [Pardoen et al., 2016] presented in Section 6.6.2.

9.4.1 Evolution of the intrinsic permeability with the deformations

On the one hand, the impact of fracturing on the flow transfer characteristics is captured by a strain-dependent isotropic evolution of the hydraulic permeability tensor based on a power (cubic) formulation, put forward in Equation (II–156):

$$k_{w,ij} = k_{w,ij,0}\left(1+\beta_{per}\langle\gamma_{per}\rangle^3\right) \tag{III–40}$$

where $k_{w,ij,0}$ is the initial intrinsic water permeability tensor, β_{per} is an evolution parameter, $\langle\rangle$ are the Macaulay brackets, and γ_{per} is a deformation parameter for which different expressions are envisaged hereafter. For such an Equation (III–40), the time derivative reads:

$$\dot{k}_{w,ij} = \frac{\partial k_{w,ij}}{\partial \varepsilon_{kl}}\dot{\varepsilon}_{kl} = \frac{\partial k_{w,ij}}{\partial \varepsilon_{kl}}\frac{\partial \dot{u}_k}{\partial u_l} \tag{III–41}$$

where

$$\frac{\partial k_{w,ij}}{\partial \varepsilon_{kl}} = \frac{\partial k_{w,ij}}{\partial \gamma_{per}}\frac{\partial \gamma_{per}}{\partial \varepsilon_{kl}} = k_{w,ij,0}\ 3\ \beta_{per}\gamma_{per}^2\frac{\partial \gamma_{per}}{\partial \varepsilon_{kl}} \tag{III–42}$$

with $\frac{\partial \gamma_{per}}{\partial \varepsilon_{kl}}$ depending on the expression of γ_{per}. The Equation (III–42) can be substituted in the Equations (III–83) and (III–84) to calculate the two sub-matrix terms involving the water and gas permeability evolution with strain in the FE computation process.

Among the different possible value of deformation that can be assigned to the parameter γ_{per} [Pardoen, 2015], a pertinent compromise to obtain a good agreement with the experimental permeability measurements for all the directions and with the permeability contrast between the intact rock and the fractured zone, is to slightly adapt the Equation (III–40) and account for the plastic deformations and a part of the elastic ones, as:

$$k_{w,ij} = k_{w,ij,0}\left(1+\beta_{per}\langle YI - YI^{thr}\rangle\hat{\varepsilon}_{eq}^3\right) \tag{III–43}$$

where the deformation parameter $\gamma_{per} = \hat{\varepsilon}_{eq}^p$ is taken as the Von Mises' equivalent deviatoric plastic strain to consider the plastic deformation in the permeability evolution, which rate form reads:

$$\dot{\hat{\varepsilon}}_{eq}^p = \sqrt{\frac{2}{3}\dot{\hat{\varepsilon}}_{ij}^p\dot{\hat{\varepsilon}}_{ij}^p} \tag{III–44}$$

where $\dot{\hat{\varepsilon}}_{eq}^p$ is the deviatoric part of the plastic strain rate tensor:

$$\dot{\hat{\varepsilon}}_{ij}^p = \dot{\varepsilon}_{ij}^p - \frac{\dot{\varepsilon}_{kk}^p}{3}\delta_{ij} \tag{III–45}$$

and YI and YI^{thr} are respectively the yield index and a threshold value below which the intrinsic permeability variation is not considered. The yield index is defined as the reduced second deviatoric stress invariant:

$$YI = \frac{II_{\hat{\sigma}'}}{II^{p}_{\hat{\sigma}'}} \tag{III–46}$$

with $YI < 1$ if the current state of the material is elastic and $YI = 1$ if it is plastic (on the yield surface). In addition, it is to mention that fracture closure or material sealing/healing under elastic unloading, leading to permeability decrease in the fracture zone is not treated in the present work. Permeability increases are thus assumed irreversible, which is implemented by keeping only the maximal estimation of permeability between the current and the last computed values, for every iterative step of the resolution process, that is to say:

$$k^{\tau}_{w,ij} = max\left(k^{t}_{w,ij}, k^{\tau}_{w,ij}\right) \tag{III–47}$$

9.4.2 Evolution of the gas entry pressure with the deformations

On the other hand, the water retention property is another aspect that can be influenced by the cracking and the material damage. The second enhanced HM coupling that is introduced in the model deals with the evolution of the water retention curve with strains and reproduces the effect of the modification of the pore network morphology on the water retention of the material [Olivella and Alonso, 2008, Gerard, 2011]. Concretely, the evolution of the parameter P_r, standing for the gas (Hydrogen) entry value in van Genuchten's model is correlated to the permeability evolution, and so to the deformations, as introduced in Equation (II–161):

$$P_r = P_{r,0}\frac{\sqrt[3]{k_{ij,0}}}{\sqrt[3]{k_{ij}}} \tag{III–48}$$

where P_r is the van Genuchten's parameter for the current gas entry pressure, $P_{r,0}$ is the van Genuchten's parameter for the initial value of gas entry pressure, k_{ij} is the current permeability, $k_{ij,0}$ is the initial permeability.

This expression of the gas entry pressure is then integrated in the retention curve formulation. It follows that the minimal capillary force needed to desaturate the material pores is lowered by the damage process, leading to an amplification of the desaturation of the medium for a given capillary pressure.

9.5 Finite element formulation

The local second gradient H^2M model described along this chapter is formulated as a set of balance equations derived in a strong form. In order to obtain a well-posed problem, initial and boundary conditions are also mandatory besides balance equations (Section 9.5.1). Furthermore, with a view to solving the problem with finite element analysis [Zienkiewicz and Taylor, 2000], the balance equations need to be expressed in a weak form (Section 9.5.2). It also requires to linearise the field equations (Section 9.5.4), and discretise continuous time and space into finite time steps and finite elements (Sections 9.5.3 and 9.5.5). Finally, solving the system of linear equations (Section 9.5.6) gives the global solution of the problem (Section 9.5.7). This section summarizes all these theoretical developments leading to the formulation of a second gradient H^2M coupled finite element.

9.5.1 Initial and boundary conditions

For a proper finite element implementation of the coupled hydro-mechanical problem, initial and boundary conditions are required to complete the balance equations. While these equations characterise the static equilibrium of an elementary volume, boundary conditions ensure the equilibrium at the external surface of the domain and initial conditions are needed for model closure.

The initial conditions describe the entire fields of displacement, water pressures, gas pressures, micro-deformations and Lagrange multipliers to start from at the beginning of the simulation ($t = t_0$):

$$\mathbf{u} = \mathbf{u_0} \qquad p_w = p_{w,0} \qquad p_g = p_{g,0} \qquad \nu_{ij} = \nu_{ij,0} \qquad \lambda_{ij} = \lambda_{ij,0} \qquad \text{on } \Omega \tag{III–49}$$

The boundary conditions of Dirichelet type correspond to imposed displacements, fluid pressures or second gradient variables at the boundary of the system (at all time $t > t_0$):

$$\mathbf{u} = \hat{\mathbf{u}} \ \text{ on } \delta\Gamma_{\mathbf{u}} \qquad p_w = \hat{p}_w \ \text{ on } \delta\Gamma_{p_w} \qquad p_g = \hat{p}_g \ \text{ on } \delta\Gamma_{p_g} \tag{III–50}$$

$$\nu_{ij} = \hat{\nu}_{ij} \ \text{ on } \delta\Gamma_{\nu_{ij}} \qquad \lambda_{ij} = \hat{\lambda}_{ij} \ \text{ on } \delta\Gamma_{\lambda_{ij}} \tag{III–51}$$

The boundary conditions of Neumann type correspond to imposed force or fluid flux. With respect to the classical poromechanics, the classical traction force per unit area acting on a part of the external surface and introduced in Equation (II–115) needs to be enriched with microstructure effects leading to non-classical conditions for a second gradient model:

$$\bar{t}_i = \sigma_{ij} n_j - n_k n_j D\Sigma_{ijk} - \frac{D\Sigma_{ijk}}{Dx_k} n_j - \frac{D\Sigma_{ijk}}{Dx_j} n_k + \frac{Dn_l}{Dx_l} \Sigma_{ijk} n_j n_k - \frac{Dn_j}{Dx_k} \Sigma_{ijk} \tag{III–52}$$

$$\bar{T}_i = \bar{P}_{ij} n_j = \Sigma_{ijk} n_j n_k \tag{III–53}$$

where n_i is the unit vector normal to the boundary Γ, σ_{ij} is the Cauchy total stress tensor, $\bar{t}_i$ is the (classical) imposed traction force per unit area and $\bar{T}_i$ is an additional external (double) force per unit area, both applied on a part Γ'_σ of the boundary of Ω, Σ_{ijk} is the double stress, $\bar{P}_{ij}$ is an additional external double surface traction acting on a part Γ_T of the boundary Γ, and $\Gamma_\sigma = \{\Gamma_t \bigcup \Gamma_T\}$ regroups the classical and additional external solicitations.

As for the boundary conditions for prescribed water and gas fluxes, the expressions of the classical poromechanics listed in Section 6.5.1 are conserved on the boundary, namely on a part Γ_{q_w} or Γ_{q_a} of Γ, and recalled hereafter:

$$\bar{q}_w + (f_{w,i} + f_{v,i}) \cdot n_i = 0 \ \text{ on } \delta\Gamma_{q_w} \qquad \bar{q}_a + (f_{a,i} + f_{da,i}) \cdot n_i = 0 \ \text{ on } \delta\Gamma_{q_g} \tag{III–54}$$

where $\bar{q}_w$ and $\bar{q}_g$ are the input water and gas masses (positive for inflow) per unit area imposed on $\bar{\Gamma}_{q_w}$ and $\bar{\Gamma}_{q_g}$ respectively and $f_{w,i}$ and $f_{g,i}$ are internal total fluxes of water and gas species in both liquid and gas phases, as defined in the constitutive equations in Section 6.3. The different boundary conditions of the material system in the current configuration Ω are represented schematically in Figure III–12.

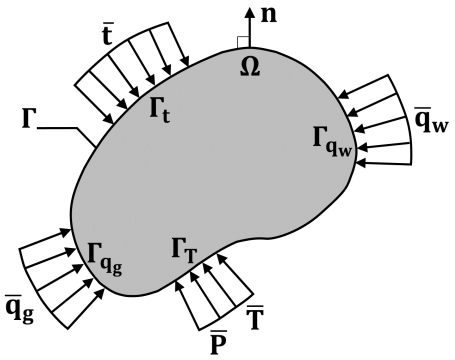

Figure III–12 – Current configuration of the material system with boundary conditions for the second gradient H^2M model.

9.5.2 Weak form of the balance equations

The governing Equations (III–24), (III–26), (III–27) and (III–30) presented in Section 9.2 are written in usual differential local form. However, a weak formulation of these equations is required in order to address boundary-value problems over large domains within a finite element framework.

Momentum balance equation

A weak form of the local momentum balance Equation (III–24) is obtained by using the principle of virtual work. As a reminder, it states that for any kinematically admissible virtual field, *i.e.* which respects the solid continuity and boundary conditions, the equality between the internal W_I^* and external W_E^* virtual power (produced by all stresses and forces acting on a mechanical system) ensures the local equilibrium at every point of the domain, and thus the global equilibrium of the solid.

Extending the scope of virtual work principle from classical kinematic theory of first gradient (see Equations (II–117) and (II–118)) to media with microstructure [Germain, 1973a] requires to adjoin a description of the kinematics at micro-scale to the classical (macro) displacement field. These microstructure effects are incorporated into the model by means of a micro-kinematic gradient field v_{ij}, which defines strain and rotation at micro-scale as defined in Equation (III–18) following Toupin and Mindlin's principles [Toupin, 1962, Mindlin, 1964]. With respect to the classical continuum mechanics, additional terms are thus added up in the internal virtual work of a given body whose expression reads for any virtual quantities:

$$W_I^* = \int_\Omega \left(\sigma_{ij} \frac{\partial u_i^*}{\partial x_j} - \tau_{ij}(F_{ij}^* - v_{ij}^*) + \Sigma_{ijk} h_{ijk}^* \right) d\Omega \tag{III–55}$$

where σ_{ij} is the Cauchy total stress field, v_{ij}^* is the virtual micro-kinematic gradient, F_{ij}^* is the virtual macro-deformation gradient, $\bar{\varepsilon}_{ij}^* = F_{ij}^* - v_{ij}^*$ is the virtual relative deformation of the microstructure, τ_{ij} is an additional stress associated to the microstructure, also called the micro-stress, $h_{ijk}^* = \frac{\partial v_{ij}^*}{\partial x_k}$ is the virtual micro second gradient, and Σ_{ijk} is the double stress dual of h_{ijk}^*, which needs an additional constitutive law introducing the internal length scale.

On the other hand, assuming that the boundary Ω is regular, the external virtual work W_{ext}^* of the classical kinematic theory defined in Equation (II–118) is enriched with contributions coming from the additional stresses associated to the microstructure, and reads:

$$W_{ext}^* = \int_\Omega \rho_{mix} g_i u_i^* d\Omega + \int_{\Gamma_\sigma} \left(\bar{t}_i u_i^* + \bar{P}_{n,i} v_{n,i}^* + \bar{P}_{t,ij} (v_{t,ij}^* - \nabla_t u_i^*) \right) d\Gamma \tag{III–56}$$

where ρ_{mix} is the mass density of the mixture defined in Equation (II–49), g_i is the gravity, $\bar{t}_i$ is the classical external traction force per unit area acting on a part Γ_t of the boundary Γ, $\bar{P}_{ij}$ is an additional external double force tensor per unit area acting on a part Γ_T of the boundary Γ, and $\Gamma_\sigma = \{\Gamma_t \bigcup \Gamma_T\}$ regroups the classical and additional external solicitations. It is assumed that $\bar{P}_{ij}$ and ν_{ij}^* can be decomposed into normal and tangential parts [Jouan et al., 2022]:

$$\underline{\underline{P}} = \underline{P}_n \otimes \underline{n} + \underline{\underline{P}}_t \tag{III–57}$$

$$\underline{\underline{v}}^* = \underline{v}_n^* \otimes \underline{n} + \underline{\underline{v}}_t^* \tag{III–58}$$

where,

$$\underline{P}_n = \underline{\underline{P}}.\underline{n} \quad \text{and} \quad \underline{\underline{P}}_t = \underline{\underline{P}} \circ Q_\perp \quad ; \quad \underline{v}_n^* = \underline{\underline{v}}^*.\underline{n} \quad \text{and} \quad \underline{\underline{v}}_t^* = \underline{\underline{v}}^* \circ Q_\perp \tag{III–59}$$

in which the symbol "$\circ$" denotes the composition product of two linear operators, $\underline{n}$ is the external normal at some smooth point of $\delta\Omega$ and $Q_\perp$ is the normal projection onto the tangential plane.

The principle of virtual works implies that the internal virtual work is equal to external one, which leads to the following weak form of the momentum balance equation:

$$\begin{aligned}&\underbrace{\int_\Omega \left(\sigma_{ij}\frac{\partial u_i^*}{\partial x_j} - \tau_{ij}(F_{ij}^* - v_{ij}^*) + \Sigma_{ijk}h_{ijk}^*\right) d\Omega}_{W_I^*} \\ &= \underbrace{\int_\Omega \rho_{mix} g_i u_i^* d\Omega + \int_{\Gamma_\sigma} \left(\bar{t}_i u_i^* + \overline{P}_{n,i} v_{n,i}^* + \overline{P}_{t,ij}(v_{t,ij}^* - \nabla_t u_i^*)\right) d\Gamma}_{W_E^*}\end{aligned} \tag{III–60}$$

However, the local second gradient model [Chambon et al., 2001a] integrates a kinematic constraint in order to obtain a local second gradient continuum medium. This hypothesis formulated in Equation (III–23) supposes no relative deformation of the microstructure, *i.e.* $\bar{\varepsilon}_{ij} = 0$, entailing the equalities between the micro-kinematic and macro-deformation gradients and between the related virtual entities which can be recalled as:

$$v_{ij} = F_{ij} = \frac{\partial u_i}{\partial x_j} \quad \text{implying} \quad v_{ij}^* = F_{ij}^* = \frac{\partial u_i^*}{\partial x_j} \tag{III–61}$$

Assuming that $\bar{T}_i = \bar{P}_{n,i}$, the principle of virtual work can be rewritten as follows:

$$\underbrace{\int_\Omega \left(\sigma_{ij}\frac{\partial u_i^*}{\partial x_j} + \Sigma_{ijk}\frac{\partial^2 u_i^*}{\partial x_j \partial x_k}\right) d\Omega}_{W_I^*} = \underbrace{\int_\Omega \rho_{mix} g_i u_i^* d\Omega + \int_{\Gamma_\sigma} \left(\bar{t}_i u_i^* + \bar{T}_i \frac{\partial u_i^*}{\partial x_j} n_k\right) d\Gamma}_{W_E^*} \tag{III–62}$$

Following the above assumption, the second derivative of the virtual displacement field is involved in the formulation. Hence, to implement the momentum balance Equation (III–62) in a finite element code, the displacement field has to be a continuously differentiable (C_1) function [Zervos et al., 2001]. To avoid such function while fulfilling the continuously differentiable requirement, the kinematic restrictions of Equation (III–61) are introduced in the momentum balance equation through a field of Lagrange multipliers λ_{ij} related to the weak form of the aforementioned constraint [Chambon et al., 1998]. Thence, the first two field equations of the coupled problem read for every kinematically admissible virtual displacement field u_i^*:

$$\int_\Omega \left(\sigma_{ij}\frac{\partial u_i^*}{\partial x_j} + \Sigma_{ijk}\frac{\partial v_{ij}^*}{\partial x_k} - \lambda_{ij}\left(\frac{\partial u_i^*}{\partial x_j} - v_{ij}^*\right)\right) d\Omega = \int_\Omega \rho_{mix} g_i u_i^* d\Omega + \int_{\Gamma_\sigma} (\bar{t}_i u_i^* + \bar{T}_i v_{ik}^* n_k) d\Gamma \tag{III–63}$$

$$\int_\Omega \lambda_{ij}^* \left(\frac{\partial u_i}{\partial x_j} - v_{ij}\right) d\Omega = 0 \tag{III–64}$$

With a view to extending the second gradient model to multiphasic materials, the previous equations remain valid provided to define the total stress σ_{ij} according to the Bishop's postulate [Bishop, 1959] as presented in Section 6.3.3.

Water mass balance equation

The water mass balance equation is written in a weak form in a similar way as the momentum balance equation. Nevertheless, assuming that the double stress Σ_{ijk} is independent of water pressures (second gradient effects occur solely for the solid phase) and that pore fluids have no influence at the micro-scale, the variations of water pressures do not generate any micro-kinematic gradient. According to this additional assumption formulated in [Ehlers and Volk, 1998], the weak form of the water mass balance equation of classical poromechanics (see Equation (II–120)) is conserved and reads for every kinematically admissible virtual pore water pressure field p_w^*:

$$\int_\Omega \left[\dot{M}_w p_w^* + \dot{M}_v p_w^* - f_{w,i}\frac{\partial p_w^*}{\partial x_i} - f_{v,i}\frac{\partial p_w^*}{\partial x_i}\right] d\Omega = \int_\Omega Q_w p_w^* d\Omega - \int_{\Gamma_q} \bar{q}_w p_w^* d\Gamma \tag{III–65}$$

where $\dot{M}_w$ and $\dot{M}_v$ are the mass variations of liquid water and water vapour respectively (see Section 6.2.2), $f_{w,i}$ and $f_{v,i}$ are the mass flows of liquid water and water vapour respectively (see Section 6.3.1), Q_w is the sink mass term of water, and Γ_q is the part of the boundary where the input water mass per unit area $\bar{q}_w$ is prescribed.

Gas mass balance equation

The gas mass balance equation is written in a weak form in a similar way as the momentum balance equation. Regarding the second gradient effects, the similar assumptions as for the water mass balance can be formulated, entailing that the weak form of the gas mass balance equation of classical poromechanics (see Equation (II–120)) is conserved and reads for every kinematically admissible virtual pore water pressure field p_g^*:

$$\int_\Omega \left[\dot{M}_g p_g^* + \dot{M}_{g^d} p_g^* - f_{g,i} \frac{\partial p_g^*}{\partial x_i} - f_{g^d,i} \frac{\partial p_g^*}{\partial x_i} \right] d\Omega = \int_\Omega Q_g p_g^* d\Omega - \int_{\Gamma_q} \bar{q}_g p_g^* d\Gamma \tag{III–66}$$

where $\dot{M}_g$ and $\dot{M}_{g^d}$ are the mass variations of dry gas and dissolved gas respectively (see Section 6.2.2), $f_{g,i}$ and $f_{gd,i}$ are the mass flows of dry gas and dissolved gas respectively (see Section 6.3.1), Q_g is the sink mass term of gas, and Γ_q is the part of the boundary where the input gas mass per unit area $\bar{q}_g$ is prescribed.

9.5.3 Time discretisation

The balance Equations (III–63) to (III–66) should be verified at any time t. Yet, the continuous loading process has to be discretised into finite time steps Δt to be able to numerically solve this non-linear problem. The time derivative of the problem unknown fields are defined using a fully implicit difference scheme, expressed in Equation (II–122) for the rate of any quantity a.

9.5.4 Linearisation

The second gradient two-phase flow hydromechanical model detailed here hinges on a series of balance Equations (III–63), (III–64), (III–65) and (III–66) expressed in a weak form in order to be implemented in a finite element code. Solving the loading process of a boundary condition problem consists in determining the unknown fields (u_i, p_w, p_g, ν_{ij}, λ_{ij}) for which the equilibrium equations are valid. However, since these governing equations include numerous hydro-mechanical couplings and advanced constitutive relationships, the whole system is characterised by high non-linearities which make the analytical resolution almost impossible. Since this system of highly non-linear relations is *a priori* not numerically satisfied at any instant t, an iterative procedure of Newton-Raphson type is employed. The aim of this section is to define an auxiliary linear problem deriving from the non-linear system following the approaches of [Borja and Alarcón, 1995, Chambon et al., 2001b], and to find a solution for the unknown fields for which equilibrium is achieved.

The main steps of the linearisation of such a system of equations have been described in Section 6.5.4 for classical hydro-mechanical two-phase flow models. The application of these steps to obtain a linearised system of field equations for the second gradient H^2M model and the analytical developments are reported in Appendix D.

9.5.5 Space discretisation

The classic finite element method lies on the spatial discretisation of the continuum medium Ω into n_e finite elements of volume Ω_e such that it is approximated by the Equation (II–133) and illustrated in Figure III–13b. In this part of the work, the coupled finite element developed to model the solid bodies is referred to as the SGRT element in the `LAGAMINE` code. This 2D isoparametric element is composed of eight nodes for the displacement fields u_i, the water pressure field p_w and the gas pressure field p_g,

four nodes for the microkinematic gradient field ν_{ij} and one node for the Lagrange multiplier field λ_{ij} as presented in Figure III–13c.

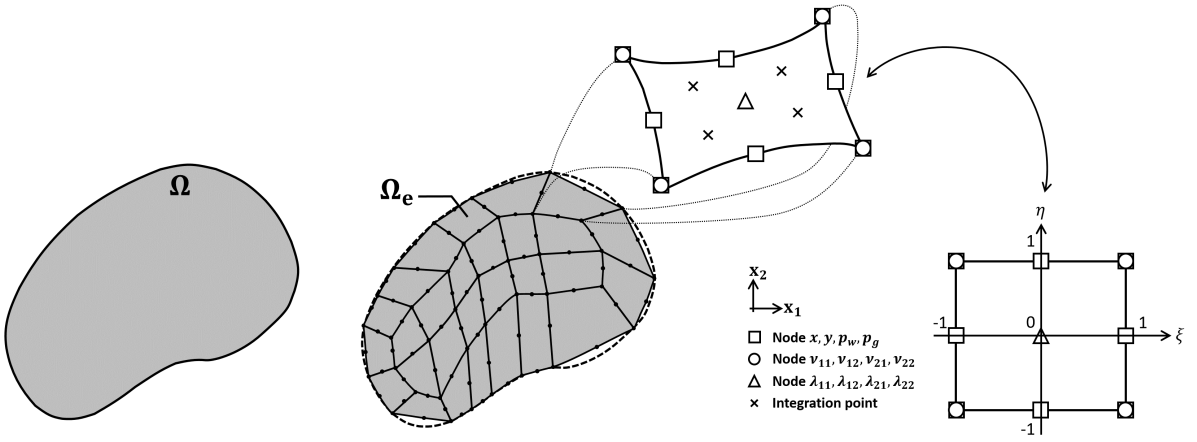

(a) Continuum (b) Discretisation (c) SGRT element

Figure III–13 – Spatial discretisation of the continuum: (a) continuum volume Ω, (b) discrete counterpart composed by n_e finite elements Ω_e, (c) 2D finite element SGRT (top left) and its corresponding parent element (right).

The Jacobian matrix J_{ij} of the transformation from the global (natural) coordinates (x_1, x_2) to the local (parent) coordinates (ξ, η) is defined in Equation (II–134). Let us specify the nodal unknowns coordinates u_{l_k}, each node k having l degrees of freedom, then the coordinates $u_l^e(\xi,\eta)$ and displacements $\Delta u_l^e(\xi,\eta)$ are interpolated over the parent element using the shape functions $\mathcal{F}^k(\xi,\eta)$:

$$u_l^e(\xi,\eta) = \sum_{k=1}^{n_e} \mathcal{F}^k(\xi,\eta) u_{l_k} \qquad \text{and} \qquad \Delta u_l^e(\xi,\eta) = \sum_{k=1}^{n_e} \mathcal{F}^k(\xi,\eta) \Delta u_{l_k} \tag{III–67}$$

where $n_e = 9$ is the number of nodes of the element Ω_e, and $l = 12$ since each node has 12 degrees of freedom: two global coordinates x_1, x_2, a pore water pressure p_w, a gas pressure p_g, a field of micro-displacement ν_{ij} and a field of Lagrange multipliers λ_{ij}.

Using Equation (III–60) to express the mechanical part of the virtual internal power of a single element Ω_e, together with a Gauss integration scheme and the Jacobian matrix of Equation (II–134), one can express the mechanical internal nodal forces of that element $\left[F_{I,i_k}^{\Omega_e}\right]^T$. Similary deriving hydraulic nodal forces from the expressions of internal virtual work of Equations (III–65) and (III–66), all these nodal forces can be gathered in a generalised equivalent vector $\left[F_{I,l_k}^{\Omega_e}\right]^T$. According to Equation (II–133), the global vector of internal energetically equivalent nodal forces is obtained by assembling the contributions of the n_e individual finite elements composing the continuous body:

$$F_{I,l_k} = \bigcup_{e=1}^{n_e} F_{I,l_k}^{\Omega_e} \tag{III–68}$$

It is worth notifying that the global vector of external energetically equivalent nodal forces is derived in the same way from external virtual power.

9.5.6 From the element computation to the global solution

Formulating the balance Equations (D–13) to (D–16) of the linear auxiliary problem in matrix form helps defining the stiffness (tangent) matrix of an element.

$$\int_{\Omega^t} \left[U^{*,t}_{(x_1,x_2)}\right]^T \left[E^t\right] \left[dU^t_{(x_1,x_2)}\right] d\Omega^t = -\Delta_1^t - \Delta_2^t - \Delta_3^t - \Delta_4^t \tag{III–69}$$

where $[E^t]$ is the stiffness matrix, $\left[dU^t_{(x_1,x_2)}\right]$ is the vector of the unknown increments of nodal variables, $\left[U^{*,t}_{(x_1,x_2)}\right]$ is a vector having the same structure with the corresponding virtual quantities. These two latter are defined as:

$$\begin{aligned}\left[dU^t_{(x_1,x_2)}\right]_{28\times1} = \Bigg[&\frac{\partial du^t_1}{\partial x^t_1}\frac{\partial du^t_1}{\partial x^t_2}\frac{\partial du^t_2}{\partial x^t_1}\frac{\partial du^t_2}{\partial x^t_2}du^t_1du^t_2\frac{\partial dp^t_w}{\partial x^t_1}\frac{\partial dp^t_w}{\partial x^t_2}dp^t_w\frac{\partial dp^t_g}{\partial x^t_1}\frac{\partial dp^t_g}{\partial x^t_2}dp^t_g\\ &\frac{\partial dv^t_{11}}{\partial x^t_1}\frac{\partial dv^t_{11}}{\partial x^t_2}\frac{\partial dv^t_{12}}{\partial x^t_1}\ldots\frac{\partial dv^t_{22}}{\partial x^t_2}dv^t_{11}dv^t_{12}dv^t_{21}dv^t_{22}d\lambda^t_{11}d\lambda^t_{12}d\lambda^t_{21}d\lambda^t_{22}\Bigg]^T\end{aligned} \tag{III–70}$$

$$\begin{aligned}\left[U^{*,t}_{(x_1,x_2)}\right]_{1\times28} = \Bigg[&\frac{\partial u^*_1}{\partial x^t_1}\frac{\partial u^*_1}{\partial x^t_2}\frac{\partial u^*_2}{\partial x^t_1}\frac{\partial u^*_2}{\partial x^t_2}u^*_1u^*_2\frac{\partial p^*_w}{\partial x^t_1}\frac{\partial p^*_w}{\partial x^t_2}p^*_w\frac{\partial p^*_g}{\partial x^t_1}\frac{\partial p^*_g}{\partial x^t_2}p^*_g\\ &\frac{\partial v^*_{11}}{\partial x^t_1}\frac{\partial v^*_{11}}{\partial x^t_2}\frac{\partial v^*_{12}}{\partial x^t_1}\ldots\frac{\partial v^*_{22}}{\partial x^t_1}v^*_{11}v^*_{12}v^*_{21}v^*_{22}\lambda^*_{11}\lambda^*_{12}\lambda^*_{21}\lambda^*_{22}\Bigg]\end{aligned} \tag{III–71}$$

The finite element spatial discretisation is introduced in Equation (III–69) using the transformation matrices $[T^t]$ and $[B]$ that connect the current element vector $\left[dU^t_{(x_1,x_2)}\right]$ to the parent element vector $\left[dU^t_{(\xi,\eta)}\right]$ and to the nodal variables $\left[dU^t_{(Node)}\right]$:

$$\left[dU^t_{(x_1,x_2)}\right] = \left[T^t\right]\left[dU^t_{(\xi,\eta)}\right] = \left[T^t\right]\left[B\right]\left[dU^t_{(Node)}\right] \tag{III–72}$$

Integrating Equation (III–69) on each parent element yields:

$$\int_{\Omega^t}\left[U^{*,t}_{(x_1,x_2)}\right]^T\left[E^t\right]\left[dU^t_{(x_1,x_2)}\right]d\Omega^t = \left[U^{*,t}_{(x_1,x_2)}\right]^T\underbrace{\int_{-1}^{1}\int_{-1}^{1}[B]^T\left[T^t\right]^T\left[E^t\right]\left[T^t\right][B]\,det(J^t)d\xi d\eta}_{[k^t]}\left[dU^t_{(x_1,x_2)}\right] \tag{III–73}$$

where $[k^t]$ is the local element stiffness matrix, $det(J^t)$ is the determinant of the Jacobian matrix of the transformation between the parent (ξ,η) and the current (x_1,x_2) elements, and $[E^t]$ is the stiffness matrix storing the different terms of the linearised balance equations, which reads:

$$\left[E^t\right] = \begin{bmatrix} E^t_{MM} & E^t_{WM} & E^t_{GM} & E^t_{\nu M} & E^t_{\lambda M}\\ E^t_{MW} & E^t_{WW} & E^t_{GW} & E^t_{\nu W} & E^t_{\lambda W}\\ E^t_{MG} & E^t_{WG} & E^t_{GG} & E^t_{\nu G} & E^t_{\lambda G}\\ E^t_{M\nu} & E^t_{W\nu} & E^t_{G\nu} & E^t_{\nu\nu} & E^t_{\lambda\nu}\\ E^t_{M\lambda} & E^t_{W\lambda} & E^t_{G\lambda} & E^t_{\nu\lambda} & E^t_{\lambda\lambda}\end{bmatrix} \tag{III–74}$$

where the matrices $[E^{\tau 1}_{MM}]$, $[E^{\tau 1}_{WW}]$, $[E^{\tau 1}_{GG}]$ are the classical stiffness matrices for mechanical, water flow and gas flow problems, while the off-diagonal matrices contain the multi-physical coupling terms. With a view to addressing the impact of fracturing on the rock transport properties, the stiffness matrices capturing the influence of mechanics on the fluids is of particular interest in the present study and are thus specifically detailed below, with a complete development available in Appendix D. The derivation of the other sub-matrices can be found in [Chambon and Moullet, 2004] for a monophasic medium further extended in [Collin et al., 2006, Sieffert et al., 2014] to account for a multiphasic system.

$$\left[E^t_{MW}\right] = \left[\begin{array}{c|c|c|c} A^{w,t}_{111}+L^{w,t}_j+N^{w,t}_1 & A^{w,t}_{121}+N^{w,t}_1+F^{w,t}_2 & A^{w,t}_{112}+N^{w,t}_2 & A^{w,t}_{122}+L^{w,t}_j+N^{w,t}_2-F^{w,t}_1\\ \hline A^{w,t}_{211}+L^{w,t}_j+N^{w,t}_1-F^{w,t}_2 & A^{w,t}_{221}+N^{w,t}_1 & A^{w,t}_{212}+N^{w,t}_2+F^{w,t}_1 & A^{w,t}_{222}+L^{w,t}_j+N^{w,t}_2\\ \hline C^{w,t}+M^{w,t} & 0 & 0 & C^{w,t}+M^{w,t}\end{array}\right] + \left[K^{w,t}\right] \tag{III–75}$$

$$\left[E^t_{MG}\right] = \left[\begin{array}{c|c|c|c} A^{g,t}_{111}+L^{g,t}_j & A^{g,t}_{121}+N^{g,t}_1 & A^{g,t}_{112}+N^{g,t}_2+N^{w,t}_2 & A^{g,t}_{122}-F^{g,t}_1 \\ +N^{g,t}_1 & +F^{g,t}_2 & & -L^{w,t}_j+L^{g,t}_j \\ & & & -N^{w,t}_2+N^{g,t}_2 \\ \hline A^{w,t}_{211}-F^{g,t}_2 & A^{w,t}_{221}+N^{g,t}_1 & A^{w,t}_{212}+N^{g,t}_2 & A^{w,t}_{222} \\ -L^{w,t}_j+L^{g,t}_j & -N^{w,t}_1 & -N^{w,t}_2+F^{g,t}_1 & +L^{g,t}_j-L^{w,t}_j \\ -N^{w,t}_1+N^{g,t}_1 & & & +N^{g,t}_2-N^{w,t}_2 \\ \hline C^{g,t}+M^{g,t} & 0 & 0 & C^{g,t}+M^{g,t} \end{array}\right] + \left[K^{g,t}\right] \tag{III–76}$$

where:

$$A^{w,t}_{ijk} = -\rho^t_w \frac{k^t_{r_w}}{\mu_w} k^{int}_{ij} \frac{\partial p^t_w}{\partial x^t_k} - \rho^t_v \frac{k^t_{r_g}}{\mu_g} k^{int}_{ij} \frac{\partial p^t_g}{\partial x^t_k} \quad \text{and} \quad A^{g,t}_{ijk} = -\rho^t_{H_2} \frac{k^t_{r_g}}{\mu_g} k^{int}_{ij} \frac{\partial p^t_g}{\partial x^t_k} - \rho^t_{H^d_2} \frac{k^t_{r_w}}{\mu_w} k^{int}_{ij} \frac{\partial p^t_w}{\partial x^t_k} \tag{III–77}$$

$$L^{w,t}_j = (b-\phi) S^t_{r_g} \bar{\tau} D_{v/H_2} \rho_g \frac{\partial\left(\frac{\rho_v}{\rho_g}\right)}{\partial x^t_j} \quad \text{and} \quad L^{g,t}_j = (b-\phi) S^t_{r_w} \bar{\tau} D_{H^d_2/w} \rho_w \frac{\partial\left(\frac{\rho_{H^d_2}}{\rho_w}\right)}{\partial x^t_j} \tag{III–78}$$

$$N^{w,t}_j = -\phi S^t_{r_g} \bar{\tau} D_{v/H_2} \rho_g \frac{\partial\left(\frac{\rho_v}{\rho_g}\right)}{\partial x^t_j} \quad \text{and} \quad N^{g,t}_j = -\phi S^t_{r_w} \bar{\tau} D_{H^d_2/w} \rho_w \frac{\partial\left(\frac{\rho_{H^d_2}}{\rho_w}\right)}{\partial x^t_j} \tag{III–79}$$

$$\begin{aligned} C^{w,t} &= \frac{\rho^B_w S^B_{r_w}}{\Delta t}\left(\phi^B + (b-\phi^A)\frac{V^B}{V^A}\right) + \frac{\rho^B_v S^B_{r_g}}{\Delta t}\left(\phi^B + (b-\phi^A)\frac{V^B}{V^A}\right) \\ C^{g,t} &= \frac{\rho^B_{H^d_2} S^B_{r_g}}{\Delta t}\left(\phi^B + (b-\phi^A)\frac{V^B}{V^A}\right) + \frac{\rho^B_{H^d_2} S^B_{r_w}}{\Delta t}\left(\phi^B + (b-\phi^A)\frac{V^B}{V^A}\right) \end{aligned} \tag{III–80}$$

$$F^{w,t}_i = f^t_{w,i} + f^t_{v,i} \qquad \text{and} \qquad F^{g,t}_i = f^t_{H_2,i} + f^t_{H^d_2,i} \tag{III–81}$$

$$M^{w,t} = \dot{M}_w + \dot{M}_v \qquad \text{and} \qquad M^{g,t} = \dot{M}_{H_2} + \dot{M}_{H^d_2} \tag{III–82}$$

Lastly, the two terms $[K^{w,t}]$ and $[K^{g,t}]$ are added in Equations (III–75) and (III–76) to consider the intrinsic permeability evolution. The constitutive Equations (III–47) and (III–48) of Section 9.4 are used to capture the effect of shear strain localisation on gas transport properties. For such a permeability evolution with the strain tensor, the two submatices are then described as follows:

$$\left[K^{w,t}\right] = \left(\rho^t_w \frac{k^t_{r,w}}{\mu_w}\left(\frac{\partial p^t_w}{\partial x^t_j} + \rho^t_w g_j\right) + \rho^t_v \frac{k^t_{r,g}}{\mu_g}\left(\frac{\partial p^t_g}{\partial x^t_j} + \rho^t_g g_j\right)\right) \begin{bmatrix} \frac{\partial k^{int}_{1j}}{\partial \varepsilon_{11}} & \frac{\partial k^{int}_{1j}}{\partial \varepsilon_{12}} & \frac{\partial k^{int}_{1j}}{\partial \varepsilon_{21}} & \frac{\partial k^{int}_{1j}}{\partial \varepsilon_{22}} \\ \frac{\partial k^{int}_{2j}}{\partial \varepsilon_{11}} & \frac{\partial k^{int}_{2j}}{\partial \varepsilon_{12}} & \frac{\partial k^{int}_{2j}}{\partial \varepsilon_{21}} & \frac{\partial k^{int}_{2j}}{\partial \varepsilon_{22}} \\ 0 & 0 & 0 & 0 \end{bmatrix} \tag{III–83}$$

$$\left[K^{g,t}\right] = \left(\rho^t_{H_2} \frac{k^t_{r,g}}{\mu_g}\left(\frac{\partial p^t_g}{\partial x^t_j} + \rho^t_g g_j\right) + \rho^t_{H^d_2} \frac{k^t_{r,w}}{\mu_w}\left(\frac{\partial p^t_w}{\partial x^t_j} + \rho^t_w g_j\right)\right) \begin{bmatrix} \frac{\partial k^{int}_{1j}}{\partial \varepsilon_{11}} & \frac{\partial k^{int}_{1j}}{\partial \varepsilon_{12}} & \frac{\partial k^{int}_{1j}}{\partial \varepsilon_{21}} & \frac{\partial k^{int}_{1j}}{\partial \varepsilon_{22}} \\ \frac{\partial k^{int}_{2j}}{\partial \varepsilon_{11}} & \frac{\partial k^{int}_{2j}}{\partial \varepsilon_{12}} & \frac{\partial k^{int}_{2j}}{\partial \varepsilon_{21}} & \frac{\partial k^{int}_{2j}}{\partial \varepsilon_{22}} \\ 0 & 0 & 0 & 0 \end{bmatrix} \tag{III–84}$$

In Equation (III–69), the residual terms are computed locally for each element from this relationship including the elementary out of balance force vector $[f^t_{OB}]$:

$$-\Delta^t_1 - \Delta^t_2 - \Delta^t_3 - \Delta^t_4 = \left[U^{*,t}_{Node}\right]^T \left[f^t_{OB}\right] \tag{III–85}$$

9.5.7 Global solution

Similarly to the developments presented in Section 6.5.7, a monolithic fully-coupled procedure is adopted, where the entire stiffness matrix is computed at each iteration of the Newton-Raphson strategy. The global solution is found by solving the global linear auxiliary system:

$$\left[K^t\right]\left[\delta U^t_{Node}\right] = -\left[F^t_{OB}\right] \tag{III–86}$$

where $\left[\delta U^t_{Node}\right]$ is the global correction vector of the nodal degrees of freedom, and the global stiffness matrix $\left[K^t\right]$ and the global out-of-balance force vector $\left[F^t_{OB}\right]$ of the whole continuum are obtained by assembling the elementary stiffness matrices and elementary out-of-balance force vectors, computed respectively from Equations (III–73) and (III–85).

After solving the system of linearised forms of equations (D–13) to (D–16), corrections are added to the generalised degrees of freedom to actualise the current configuration. The new configuration gets closer to the well-balanced configuration and its equilibrium is verified, leading to a new iteration or to the end of the loading step of the iterative procedure.

10. Applications

The objective of this chapter is to apply the numerical model elaborated in the previous Chapter 9 to practical cases in order to assess its ability to reproduce the creation of a damage zone in a clay host rock and to simulate gas transport processes through such a fractured zone.

On the one hand, numerical simulations are performed at the intermediate scale of *in situ* experiments to verify the good implementation of the model. The experimental set-up in question is the set of E4 and E5 gas injection experiments, introduced in Section 5.4.2 of Part II that was conducted in Boom Clay using Helium at the HADES URL, in Belgium, as part of the MEGAS EC project.

On the other hand, numerical simulations are performed at nuclear waste disposal scale from the excavation time and over a period long enough to cope with gas generation and migration. The selected case study is close to the current design of a storage drift for long-lived intermediate-level waste (MAVL) according to the French concept managed by the ANDRA.

10.1 Field-scale MEGAS experiment in Boom Clay

In the following section, a synthetic description of the two gas injection tests conducted in Boom Clay is first proposed on the basis of the relevant information and data collected in the final project reports [Volckaert et al., 1995, Ortiz et al., 1997]. Subsequently, all the ingredients required to establish a proper numerical framework for reproducing these experiments are detailed. Finally, the numerical results for the different phases of the simulations are provided and analysed.

10.1.1 Description of the experiments

Practically, the MEGAS project consists of two *in situ* experiments drilled in the low-permeable Boom Clay rock, and respectively referred to as E4 and E5 gas injection tests. This section covers in particular the design and course of the tests, the geometry of the problem, the mesh of the model, the initial boundary conditions as well as the successive steps of the simulations carried out by means of boundary conditions update.

10.1.1.1 Design

The design of the E4 *in situ* gas injection experiment consists of a vertical piezometer installed under the bottom of the first shaft at HADES URL, as sketched in Figure II–27 of the literature review. The diameter of the borehole is about 85 mm, while the diameter of the piezometer is 60 mm. This piezometer is about 17 m long and extends from the underside of the shaft at a depth of -229.3 m to a depth of -247 m. It is composed of eleven filters, including two injection filters (No.6 and No.9) and nine detection filters. The piezometer has only one connection tube to each filter, with an internal diameter of 2 mm.

The design of the E5 *in situ* gas injection experiment consists of four horizontally installed piezometers along the first meters of the test drift at the HADES URL, as sketched in Figure II–27 of the literature review. More precisely, the boreholes A, B, and D were drilled in the horizontal plane, while the borehole C was digged 3% upward inclined with respect to this horizontal plane. This configuration was chosen because the breakthrough is expected to occur more easily in the horizontal direction than in the vertical

one, on the basis of the anisotropy in the hydraulic conductivity. The drilling of these boreholes was performed in a destructive way, namely without core drill.

The central piezometer A is used for gas injections, and is geometrically characterized by a length of about 15.25 m, a borehole diameter of 102 mm, and an outer diameter of the inserted tubing equal to 88.9 mm. This piezometer is composed of 5 filters with a 10 mm wall thickness, and inner and outer diameters of 79 mm and 89 mm respectively. The filter No.19 has a length of 100 cm, while the other filters (No.17, No.18, No.20 and No.21) have a length of 9 cm. All these filters are equipped with twin tubing having a 2 mm internal diameter. More detailed information about the injection piezometer is attached in Appendix F. The three additional monitoring piezometers B, C and D used for the detection of pressure changes caused by gas or water injection, are not the subject of the numerical modelling.

10.1.1.2 Course

The E4 experiment was drilled and installed on the site of the URL during one day [1]. There is no available information about the imposed drilling rate, reason why, in the rest of this section, a drilling speed of 1 m/h will be assumed.

The drilling phase caused drainage of the interstitial water around the piezometer, leading to the decrease in the pore water pressure. After this step, time was thus let to the pore water pressures to re-establish and to stabilize in the surrounding zone, prior to any operation of injection [2].

In the next step running for about one month, gas was injected through the injection filters No.6 and No.9 at such a pressure that it could expel the water contained in the connection tube and in the dead volume of the filters into the clay massif, while remaining under the threshold pressure for gas flow.

Following this water expulsion phase from the system, a series of gas injections using Helium was performed through the piezometer. Without taking into account the modification of the geomechanical properties due to the drilling, the local total stress value was estimated to be in the range [2.5 MPa - 4.0 MPa], so that a pressure of 2.5 MPa was taken as the upper limit for the gas injection pressure in order to avoid any fracturation of the clay rock. The initial value for gas pressure was chosen at 2.25 MPa, *i.e.* between the local estimated total stress and the interstitial water pressure, established around 2.2 MPa.

As for the E5 experiment, the central injection piezometer was drilled up to 10 m depth the first day, assuming eight hours per day of working regime, completed up to 15.9 m the next day, considering the same drilling rate ($v = 1.25$ m/s), and it was finally let converge up to the casing. For the surrounding detection piezometers, the drilling and the installation were performed on the same day, assuming the same working regime. The pore water pressure evolution in the filters of the E5 experimental set-up has been monitored since its installation, in order to determine the moment when all the pressures would have reached equilibrium.

A hydraulic test was firstly performed to evaluate some hydraulic parameters. In a second time, the gas injection was started [3] after that the hydrostatic pressures of the piezometers had reached equilibrium. Helium injection pressure was first set at 0.1 MPa above the local pore water pressure, equal to 1.67 MPa, in the same filter No.20 and then increased weekly by an increment of 0.1 MPa until gas breakthrough was detected. It occurred 44 days after the beginning of the injection [4] through the 1m long filter No.19 located on the same piezometer, at a gas pressure of 2.36 MPa, *i.e.* 0.69 MPa above the original pore water pressure.

10.1.1.3 Initial conditions

At the level of the URL, 223m below the surface, the Boom Clay is assumed to be saturated and the total vertical stress and pore water pressure are respectively 4.5 MPa and 2.2 MPa, defining a verti-

1. On the 18th of December 1986.
2. Between the 3rd of December 1991 and the 3rd of November 1992.
3. On the 11th of April 1994.
4. On the 7th of June 1994.

cal effective stress of 2.3 MPa [Bernier et al., 2007a]. In Chapter 4, it has also been noted that Boom Clay presents an *in situ* stresses anisotropy, with an earth pressure coefficient at rest K_0 ranging from 0.8 to 1, on the basis of laboratory and *in situ* investigations [Bernier et al., 2002]. Boom Clay is also characterised by complex phenomena such as hardening/softening processes, and a strong anisotropy of the mechanical properties induced by the clay structure which displays horizontal bedding planes with alternating clay and silt layers.

Considering a studied section at the level of the injection filters No.6 (E4) and No.9 (E5) respectively, the initial conditions in the Boom Clay for the respective orientations of the piezometers are defined as:

$$\text{E4: } \sigma'_{x,0} = \sigma'_1 = 1.84 \text{ MPa}, \ \sigma'_{y,0} = \sigma'_3 = 1.84 \text{ MPa}, \ \sigma'_{z,0} = \sigma'_2 = 2.3 \text{ MPa}, \ p_{w,0} = 2.2 \text{ MPa} \quad \text{(III–87)}$$

$$\text{E5: } \sigma'_{x,0} = \sigma'_1 = 1.84 \text{ MPa}, \ \sigma'_{y,0} = \sigma'_2 = 2.3 \text{ MPa}, \ \sigma'_{z,0} = \sigma'_3 = 1.84 \text{ MPa}, \ p_{w,0} = 2.2 \text{ MPa} \quad \text{(III–88)}$$

where $\sigma'_{x,0}$, $\sigma'_{y,0}$, and $\sigma'_{z,0}$ are respectively the horizontal, vertical and out-of-plane (initial) effective stresses in the local coordinate system, and $p_{w,0}$ is the initial pore water pressure. In this configuration, the coefficient of earth pressure at rest K_0 takes a value of 0.8. In addition, the initial gas pressure is set to the atmospheric pressure of $p_{g,0} = 0.1$ MPa, while the temperature is maintained constant at $T_0 = 20°C$ throughout the simulations.

10.1.1.4 Geometry

The geometry of the E4 experiment corresponds to a 60 mm diameter piezometer that is numerically replicated for a specific cross-section located at the level of the injection filter No.6 [5] using a two-dimensional plane strain hydro-mechanical model. Similarly, the geometry of the E5 experiment corresponds to a 89 mm diameter piezometer that is numerically replicated for a specific cross-section located at the level of the injection filter No.9 [6] using a two-dimensional plane strain hydro-mechanical model. Infinitely rigid contact elements are employed to reproduce the casing of the piezometers, having a radius of 0.03 m and 0.0445 m in the E4 and E5 configurations respectively. A schematic representation of the numerical models involving the mesh and the different boundary conditions is illustrated in Figure III–14.

Assuming moreover symmetry along the x and y local axes, only a quarter of the studied cross-section is discretised in both cases. And so, the geometry extension covers a domain of 10 m $\times$ 10 m, thus establishing far-field boundary conditions in the `LAGAMINE` code.

For the built meshes, the boundary conditions consist in imposing the initial total stress, pore water pressure and gas pressure to a constant value at the mesh outer boundary. On the wall of the piezometer, the initial boundary conditions in terms of stresses and fluid pressures will be progressively adapted as a function of the successive phases of the simulation. Moreover, the symmetry condition is established along the symmetry axes by considering no normal displacements and impervious boundaries (water and gas flows blocked to zero).

Regarding the second gradient boundary conditions, a special attention must be dedicated to the kinematic boundary conditions required to establish the symmetry, as stipulated in [Zervos et al., 2001]. Due to the presence of gradient terms in the equilibrium Equations (III–63) to (III–66) of the H^2M second gradient model, higher order constraints have to be characterised in addition to the classical boundary conditions on the normal displacements. It implies that the radial displacement u_r must be symmetric on both sides of the symmetry axes, which means that the normal derivative of u_r with respect to the tangential direction θ, has to cancel:

$$\frac{\partial u_r}{\partial \theta} = 0, \quad \text{equivalent to} \quad \frac{\partial u_x}{\partial y} = 0 \ \text{ and } \ \frac{\partial u_x}{\partial y} = 0 \qquad \text{(III–89)}$$

5. At about 6.70 m underneath the shaft of the URL.
6. At about 15.70 m away from the main tunnel of the URL.

Finally, natural boundary conditions for the double force $\dot{T}_i = 0$ are assumed on the different boundaries and gravity is not taken into account. Schematic representations of the numerical models of the E4 and E5 boreholes involving the mesh and the boundary conditions are detailed in Figure III–14b.

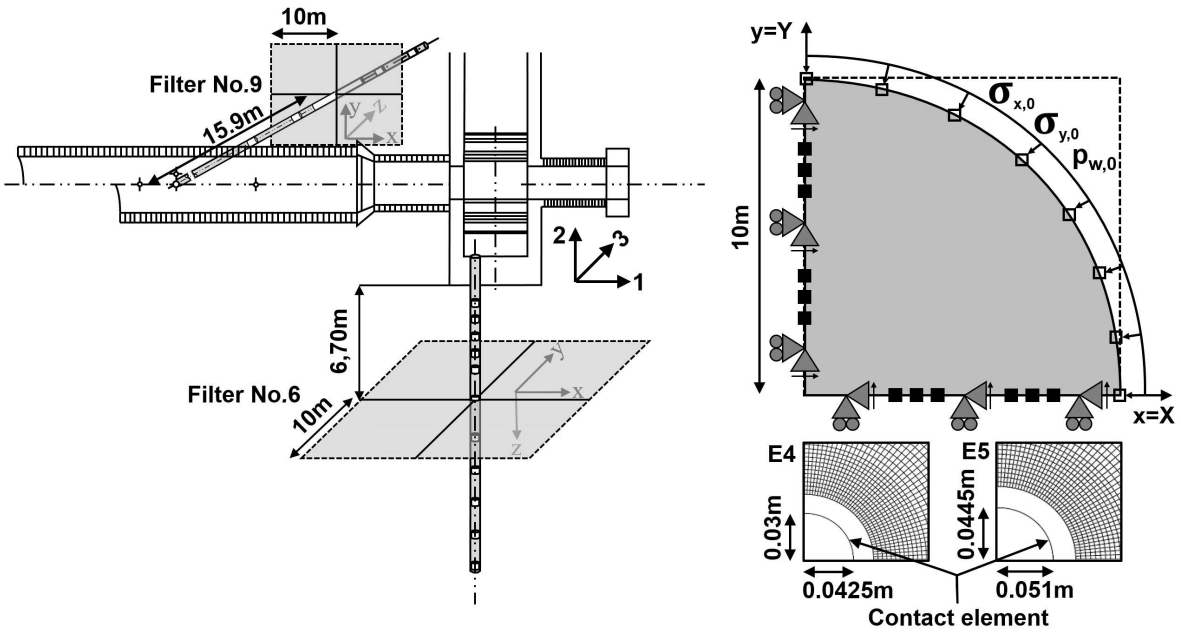

(a) (b)

Figure III–14 – (a) Location of the studied cross-sections in the E4 and E5 configurations. (b) Geometry and boundary conditions of the 2D plane strain models with a zoom on the refined zone of the mesh.

10.1.1.5 Boundary condition evolution

Now that the initial states, the geometries and the boundary conditions have been defined in the two cases, the piezometers installation and the subsequent gas pressure variations on the domains can be characterised. This sequential evolution of the problem is translated into a boundary value problem which is conducted by progressively adjusting the boundary conditions along the inner walls of the E4 and E5 boreholes using the `LAGAMINE` code.

Excavation phase

The drilling of the piezometer boreholes is performed with the convergence-confinement method which is an approximation method for tunnelling that allows transforming a whole 3D study of tunnel excavation into a 2D analysis in plane strain state, based on an identical gallery convergence assumption [Bernaud and Rousset, 1992]. The effect of the excavation front progress is taken into account by applying a fictive pressure σ_r^{Γ} on the borehole wall that depends on the vicinity of the excavation front to the studied borehole section through a deconfinement rate ζ (Figure III–15a):

$$\sigma_r^{\Gamma} = (1-\zeta)\sigma_{r,0} \tag{III–90}$$

where σ_r^{Γ} is the total radial stress, $\sigma_{r,0}$ is the initial mechanical pressure on the borehole wall that corresponds to the initial stress in the material, and ζ is the deconfinement rate ranging from 0 to 1.

The expression of the deconfinement rate $1-\zeta$ depends on the ratio of the distance between the excavation front and the studied cross-section z, and the borehole radius r. In the present work, a rate of 1 m/h is considered for both E4 and E5 *in situ* experiments, implying that the excavation front crosses the studied section after $\sim$ 6h42min and $\sim$ 10h36min, and that the excavation is fully completed after $\sim$

6h48min and $\sim$ 10h42min in the E4 and E5 configurations respectively. The evolution of the deconfinement rates with time are detailed in Figure III–15b, top and bottom.

The pore water pressure at the borehole wall p_w^{Γ} is also affected during the excavation phase and starts to decrease quickly and linearly from its initial value towards the atmospheric pressure when the deconfinement starts. A pore water pressure rate ζ_w can thus be defined in the same manner as for the total radial stress:

$$p_w^{\Gamma} = (1 - \zeta_w) p_{w,0} \tag{III–91}$$

where p_w^{Γ} is the pore water pressure at gallery wall, $p_{w,0}$ is the initial water pressure on the borehole wall, and ζ_w is the deconfinement rate ranging from 0 to 1.

In addition, this stress imposition is also conditioned by the support of the borehole. Concretely, the borehole wall is supposed to stop converging once the contact with the support, namely the steel casing of the inserted piezometer (modelled by an interface element and assumed to be in infinitely rigid) is reached. This first step is simulated during 24 hours.

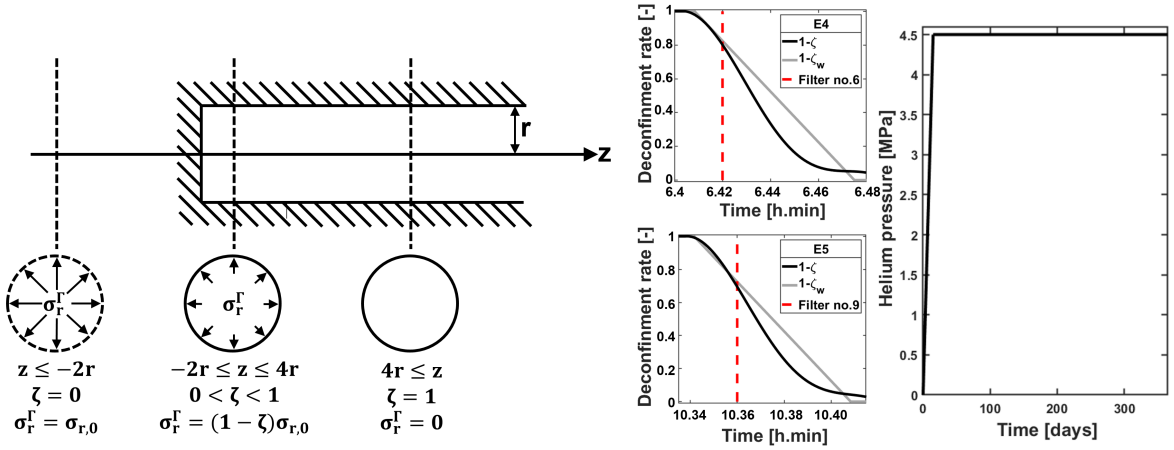

(a) (b) (c)

Figure III–15 – (a) Theory of deconfinement rate during tunnel excavation. (b) Applied deconfinement curves for the total radial stress and for the pore water pressure during E4 and E5 boreholes excavation. (c) Profile of gas pressures during Helium injection.

Phase of stabilisation of the pore water pressure

After the excavation of the borehole, and the convergence of the circumferential wall to the casing of the piezometer, the system is supposed to be impervious. From this time, a period of pore water pressures stabilisation initiates since there is no more drainage of these water pressure through the excavated profile. It is numerically simulated by considering an impervious inner wall of the borehole as updated boundary condition. This second phase ranges from 1 day to 1 year.

Phase of gas migration

After the excavation of the borehole and a one-year phase of water pressure re-establishment, a last phase of gas migration is considered. It is simulated by imposing a variation of the gas pressures at the interface between the outer face of the E4 (or E5) piezometer and the rock according to the profile given in Figure III–15c, while keeping the rest of the boundary conditions similar to those imposed during the previous phase. In practise, gas starts to be injected in the system in the form of Helium pressure change,

starting from the atmospheric pressure at 0.1 MPa to a peak of gas pressure at around 4.5 MPa. This last step is simulated for one additional year, during which the pressure ramp is imposed for one hour and then the maximum pressure is maintained constant for the rest of the year.

10.1.2 Constitutive models and parameters

The constitutive models of the Boom Clay and the piezometer casing and their related parameters required to study the E4 and E5 numerical applications are presented in this section. The hydro-mechanical description of the Boom Clay behaviour includes a mechanical model for the classical first gradient part related to the macrostructure, a mechanical model for the second gradient part related to the microstructure, and a hydraulic model to reproduce the water and gas flows in the partially saturated porous media.

Since the E4 piezometer is vertically installed, while the E5 piezometer is horizontally installed, the studied cross-section for the E4 experiment is characterised by isotropic conditions (parallel to the bedding), while anisotropy is prevailing in the plane of the E5 experiment (perpendicular to the bedding). This is the origin of the differences in the constitutive laws between the two experiments.

10.1.2.1 First gradient mechanical model

An elasto-plastic internal friction model with cross-anisotropy and horizontal isotropic bedding planes is considered for the mechanical behaviour of the Boom Clay, which can be decomposed into an elastic and a plastic components, as introduced in section 6.3.3:

$$\dot{\varepsilon}_{ij} = \dot{\varepsilon}^e_{ij} + \dot{\varepsilon}^p_{ij} \tag{III–92}$$

where ε^e_{ij} and ε^p_{ij} are the elastic and plastic components of the total strain rate.

Elastic component

The linear elastic behaviour of the rock is based on the classical Hooke's law (Equation (II–96)), where the elastic compliance tensor is expressed as a function of only two parameters (ν and E or G and K) for an isotropic material which is the case in the E4 orientation. However, the Boom Clay is also characterised by a strong anisotropy of its mechanical properties between the directions parallel and perpendicular to the bedding planes as it is the case for the E5 orientation. Switching to such a configuration with anisotropic elasticity increases the total number of required independent parameters. In cross-anisotropic materials, such as the Boom Clay formation [Chen et al., 2011], the behaviour remains isotropic in the parallel bedding planes which requires only 5 independent parameters [Amadei, 1983], as stipulated in Equation (II–99).

Plastic component

The elasto-plastic behaviour of the Boom Clay is characterised by an internal friction model with a non-associated plasticity and a Van Eekelen yield surface [Van Eekelen, 1980] (under soil mechanics convention with positive compressive stress) defined in Equation (II–102). Furthermore, the model reproduces isotropic hardening or softening of the cohesion and of the friction angles upon loading.

The elasto-plastic geomechanical parameters used in the mechanical law of the Boom Clay for the E4 and E5 modelling are taken from [Ortiz et al., 1997, François, 2014] and reported in Tables III–1 and III–2 respectively.

10.1.2.2 Second gradient mechanical model

In the context of microstructure media, the second gradient mechanical model gives an additional constitutive stress-strain relation between the kinematics and the stress at microscale. Based on reference works [Mindlin, 1965], it is an isotropic linear elastic law which relates the double stress to the rate of micro second gradient as defined in Equation (III–34) exposed in Section 9.3, and depends on one constitutive elastic parameter D in its simplified version proposed by [Matsushima et al., 2002]. This elastic modulus symbolises the physical microstructure of the material and is directly related to the internal length scale introduced to regularise the problem and which is suitable for shear band width [Chambon et al., 1998, Collin et al., 2009b].

The value of this modulus has been selected on the basis of the results of specific numerical modelling of biaxial compression tests, detailed in the next Section 10.1.3.

10.1.2.3 Hydraulic model

The hydraulic model used for the Boom Clay is based on the water-gas seepage and water diffusion constitutive law for partially saturated porous media, introduced in Section 6.3.1. The transfer of the liquid phase (water and gas) by advection is thus defined by the generalised Darcy's law [Darcy, 1856] introduced in Equations (II–70) and (II–71):

$$q_{w,i} = -\frac{k_{ij}^{int} k_{r_w}}{\mu_w}\left(\frac{\partial p_w}{\partial x_j} + \rho_w g_j\right) \qquad \text{(III–93)} \qquad q_{g,i} = -\frac{k_{ij}^{int} k_{r_g}}{\mu_g}\left(\frac{\partial p_g}{\partial x_j} + \rho_g g_j\right) \qquad \text{(III–94)}$$

where k_{r_w} and k_{r_g} are the water and gas relative permeabilities, μ_w and μ_g are the dynamic viscosities of water and gas respectively, and k_{ij}^{int} is the anisotropic tensor of intrinsic permeability of the material, defined by two components $k_{\parallel}$ and $k_{\perp}$ respectively parallel and perpendicular to the isotropic planes:

$$k_{w,ij} = \begin{bmatrix} k_{w\parallel} & 0 & 0 \\ 0 & k_{w\perp} & 0 \\ 0 & 0 & k_{w\parallel} \end{bmatrix} \qquad \text{(III–95)}$$

Note that in the present simulations, the hydraulic permeabilities are isotropic in the horizontal plane considered for the E4 experiment, while it exists a ratio of about 2 between the components of the intrinsic permeability in the direction parallel and perpendicular to the bedding in the vertical plane defined for the E5 experiment, *i.e.* $k_{w\parallel}/k_{w\perp} = 2$.

The material retention behaviour is represented by a retention curve of van Genuchten's type [van Genuchten, 1980] introduced in Equation (II–82) of Section 6.3.2, linking the capillary pressure to the degree of water saturation (Figure III–16b):

$$S_{r_w} = S_{r_w,res} + (S_{r,max} - S_{r_w,res})\left(1 + \left(\frac{s}{P_r}\right)^{\mathcal{N}}\right)^{\frac{1}{\mathcal{N}}-1} \qquad \text{(III–96)}$$

where $P_r = 12.5$ MPa is the parameter of gas entry pressure taken as a mean value between those proposed in [Prime et al., 2016, Gonzalez-Blanco et al., 2016] as detailed in Section 5.3.4 of the literature review, $S_{r,max} = 1$ and $S_{r_w,res} = 0.2$ are the maximum and residual degrees of water saturation, s is the suction, and $\mathcal{N} = \frac{1}{1-\mathcal{F}} = 2.5$ is a model parameter, fitted to obtain a good agreement with the experimental data in Figure III–16b.

Moreover, the Mualem - van Genuchten's model [Mualem, 1976] introduced in Equation (II–83) of Section 6.3.2 is used to express the water relative permeability, while the cubic law [Charlier et al., 2013] introduced in Equation (II–86) of Section 6.3.2 is adopted to describe the gas relative permeability:

$$k_{r_w} = \sqrt{S_{r_w}} \left(1 - \left(1 - S_{r_w}^{\frac{1}{\mathcal{M}}} \right)^{\mathcal{M}} \right)^2 \qquad \text{(III–97)} \qquad k_{r_g} = (1 - S_e)^{\mathcal{L}} \qquad \text{(III–98)}$$

where $S_e = \frac{S_{r_w} - S_{r_w,res}}{1 - S_{r_w,res} - S_{r_g,res}}$, with S_{r_w} the degree of water saturation, $S_{r_w,res}$ the residual degree of water saturation, $S_{r_g,res}$ the residual degree of gas saturation, and $\mathcal{M} = 1.1$ and $\mathcal{L} = 3$ are model parameters, is a model parameter, fitted to obtain a good agreement with the experimental data in Figure III–16a.

On top of that, enhanced hydro-mechanical couplings are integrated into the model in the form of a strain-dependent isotropic evolution of the hydraulic permeability tensor introduced in Equation (III–43), together with an evolution of the water retention curve with strain introduced in Equation (III–48):

$$k_{w,ij} = k_{w,ij,0} \left(1 + \beta_{per} \langle YI - YI^{thr} \rangle \hat{\varepsilon}_{eq}^3 \right) \qquad \text{(III–99)} \qquad P_r = P_{r,0} \frac{\sqrt[3]{k_0}}{\sqrt[3]{k}} \qquad \text{(III–100)}$$

where $k_{w,ij,0}$ is the initial intrinsic water permeability tensor, β_{per} is an evolution parameter, $\hat{\varepsilon}_{eq}^p$ is taken as the Von Mises' equivalent deviatoric plastic strain, YI is the yield index, YI^{thr} is a threshold value below which there is no intrinsic permeability variation, P_r is the current gas entry pressure, $P_{r,0}$ is the initial value of gas entry pressure, k is the current permeability and k_0 is the initial permeability.

All the parameters governing the hydraulic behaviour of Boom Clay are collected from the literature [Ortiz et al., 1997, Prime et al., 2016, Gonzalez-Blanco et al., 2016], and summarized in Table III–1 and Table III–2, for the E4 and E5 configurations respectively. More specifically, the value of the parameter β_{per} which controls the permeability evolution is established from the results of the numerical modelling of biaxial compression tests, detailed in the next Section 10.1.3, in such a way as to obtain a variation of about one order of magnitude of the value of the permeability.

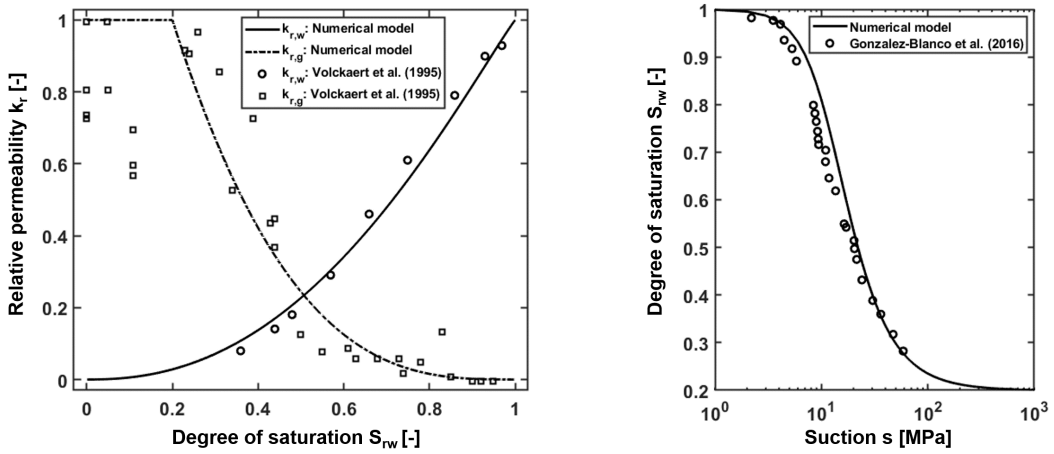

(a) (b)

Figure III–16 – Hydraulic model for the E4 and E5 numerical simulations: (a) experimental data for relative permeability in Boom Clay, *after* [Volckaert et al., 1995] together with model fitting, (b) experimental data for water retention curve in Boom Clay, *after* [Gonzalez-Blanco et al., 2016] with van Genuchten's numerical fitting.

10.1.2.4 Interface model

As exposed in Section 10.1.1, E4 and E5 boreholes are supported by the casings of the piezometers, which avoids the potential collapse of the hole during the drilling operations and ensures a limited

convergence of the surrounding rock mass. Two-dimensional interface elements having their own mechanical and flow constitutive laws are employed to model these rigid supports.

The mechanical contact behaviour of the interface elements can be established based on the Coulomb's yield criterion, as it is widely used in soil and rock mechanics to deal with contact problems [Charlier and Cescotto, 1988, Laursen and Simo, 1993, Wriggers and Zavarise, 2004]. Since the two sides of the interface never match perfectly, the global behaviour of this zone is characterised by a normal contact constraint and a tangential contact constraint. Given that the regularisation of the contact condition is mathematically enforced via a penalty method, a linear elastic relation is assumed between the variations of stresses and gap function, which yields:

$$\begin{bmatrix} \dot{p}_N \\ \dot{\tau}_T \end{bmatrix} = \begin{bmatrix} K_N & 0 \\ 0 & K_T \end{bmatrix} \begin{bmatrix} \dot{g}_N \\ \dot{g}_T \end{bmatrix} \tag{III–101}$$

where the normal contact constraint p_N is the component related to the interpenetration of the two bodies in the contact zone, and the tangential contact constraint τ_T describes the shear behaviour of the interface.

In case of sticking, there is no relative tangential displacement of the two faces of the contact zone in the plane of the interface, developing a non-zero shear stress. In case of sliding, a relative tangential displacement occurs and the shear stress is limited by a Coulomb's criterion:

$$\tau_{max} = \mu p'_N \tag{III–102}$$

where μ is the Coulomb's friction coefficient.

To fully characterize the hydro-mechanical behaviour of the contact elements, fluid flows through ($f_{w,N}$) and along ($f_{w,L}$) the interface are also considered since these zones constitute a preferential path for the groundwater. The transversal fluid flow includes flows from the surrounding rock mass to the inside of the interface and a second one from the inside to the foundation, while the longitudinal flow is given by the well-known Darcy's equation, where the minus sign stands for a flow from high to low pressures:

$$f_{w,N} = \rho_w \, T_w \, \Delta p_w \tag{III–103}$$

$$f_{w,L} = -\rho_w \, \frac{k_l}{\mu_w} \, \nabla p_w \, + \, \rho_w g \nabla z \tag{III–104}$$

where T_w is the transmissivity. Pratically, the longitudinal and transverse transmissivities are set to zero in order to symbolise the impervious nature of the casing.

Further details about the contact element are available in [Cerfontaine et al., 2015]. All the parameters of the contact laws are reported in Table III–1 and Table III–2 for the E4 and E5 configurations respectively.

Table III–1 – Set of Boom Clay parameters used in the E4 configuration, from [François, 2014].

	Parameter	Symbol	Value	Unit
Geomechanical	Young's elastic modulus	E	300	[MPa]
	Poisson's ratio	ν	0.125	$[-]$
	Shear modulus	G	133	$[MPa]$
	Initial cohesion	c_i	300	$[kPa]$
	Final cohesion	c_f	100	$[kPa]$
	Cohesion softening parameter	B_c	0.01	$[-]$
	Initial friction angle	φ_i	5	$[^\circ]$
	Final friction angle	φ_f	18	$[^\circ]$
	Friction angle hardening parameter	B_φ	0.01	$[-]$
	Dilatancy angle	ψ	0	$[^\circ]$
	Solid grain density	ρ_s	2650	$[kg/m^3]$
Microstructure	Second gradient elastic modulus	D	1.0	$[kN]$
Hydraulic	Initial porosity	n	0.39	$[-]$
	Intrinsic permeability	k	4.6×10^{-19}	$[m^2]$
	Water density	ρ_w	1000	$[kg/m^3]$
	Gas density (He)	ρ_g	0.1663	$[kg/m^3]$
	Water dynamic viscosity	μ_w	0.001	$[Pa.s]$
	Gas dynamic viscosity (He)	μ_g	2.0×10^{-6}	$[Pa.s]$
	Water compressibility	χ_w^{-1}	5×10^{-10}	$[Pa^{-1}]$
	Henry coefficient (He)	H_i	0.0091	$[-]$
	Gas entry pressure (1^{st} coeff. of S_{r_w})	P_r	12.5	$[MPa]$
	Parameter (2^{nd} coeff. of S_{r_w})	$\mathcal{N}$	2.5	$[-]$
	Parameter (1^{st} coeff. of k_{r_w})	$\mathcal{M}$	1.1	$[-]$
	Parameter (1^{st} coeff. of k_{r_g})	$\mathcal{K}$	3	$[-]$
	Max. degree of water saturation	$S_{r,max}$	1	$[-]$
	Residual degree of water saturation	$S_{r_w,res}$	0.2	$[-]$
	Evolution parameter	β_{per}	1×10^4	$[-]$
	Tortuosity	τ	0.6	$[-]$
Contact	Friction coefficient	μ	0.5	$[-]$
	Normal penalty coefficient	K_N	5×10^9	$[Pa/m]$
	Tangential penalty coefficient	K_T	5×10^9	$[Pa/m]$
	Transmissivity	T_w	0.0	$[m/Pa/s]$

Table III–2 – Set of Boom Clay parameters used in the E5 configuration, from [François, 2014].

	Parameter	Symbol	Value	Unit
Geomechanical	Parallel Young's modulus	$E_{\parallel}$	400	$[MPa]$
	Perpendicular Young's modulus	$E_{\perp}$	200	$[MPa]$
	Poisson's ratio	$\nu_{\parallel\parallel}$	0.125	$[-]$
	Poisson's ratio	$\nu_{\parallel\perp}$	0.125	$[-]$
	Poisson's ratio	$\nu_{\perp\parallel}$	0.0625	$[-]$
	Shear modulus	$G_{\parallel\perp} = G_{\perp\parallel}$	178	$[MPa]$
	Shear modulus	$G_{\parallel\parallel}$	178	$[MPa]$
	Solid grain density	ρ_s	2650	$[kg/m^3]$
	Initial cohesion	c_i	255 (0°)	$[kPa]$
			240 (45°)	$[kPa]$
			330 (90°)	$[kPa]$
	Ratio of cohesion softening	ξ_c	3	$[-]$
	Cohesion softening parameter	B_c	0.01	$[-]$
	Cohesion softening shifting	dec_c	0	$[-]$
	Initial compressive friction angle	$\varphi_{c,0}$	5	$[°]$
	Final compressive friction angle	$\varphi_{c,f}$	18	$[°]$
	Friction angle hardening parameter	B_φ	0.01	$[-]$
	Friction angle hardening shifting	dec_φ	0	$[-]$
	Dilatancy angle	ψ_c	0	$[°]$
Microstructure	Second gradient elastic modulus	D	1.0	$[kN]$
Hydraulic	Initial porosity	n	0.39	$[-]$
	Initial parallel intrinsic permeability	$k_{w,\parallel,0}$	4×10^{-20}	$[m^2]$
	Initial perp. intrinsic permeability	$k_{w,\perp,0}$	1.33×10^{-20}	$[m^2]$
	Water density	ρ_w	1000	$[kg/m^3]$
	Gas density (He)	ρ_g	0.1663	$[kg/m^3]$
	Water dynamic viscosity	μ_w	0.001	$[Pa.s]$
	Gas dynamic viscosity (He)	μ_g	2.0×10^{-5}	$[Pa.s]$
	Water compressibility	χ_w^{-1}	5×10^{-10}	$[Pa^{-1}]$
	Henry coefficient (He)	H_i	0.0091	$[-]$
	Gas entry pressure (1^{st} coeff. of S_{r_w})	P_r	12.5	$[MPa]$
	Parameter (2^{nd} coeff. of S_{r_w})	$\mathcal{N}$	2.5	$[-]$
	Parameter (1^{st} coeff. of k_{r_w})	$\mathcal{M}$	1.1	$[-]$
	Parameter (1^{st} coeff. of k_{r_g})	$\mathcal{K}$	3	$[-]$
	Max. degree of water saturation	$S_{r,max}$	1	$[-]$
	Residual degree of water saturation	$S_{r_w,res}$	0.2	$[-]$
	Evolution parameter	β_{per}	1×10^4	$[-]$
	Tortuosity	τ	0.6	$[-]$
Contact	Friction coefficient	μ	0.5	$[-]$
	Normal penalty coefficient	K_N	5×10^9	$[Pa/m]$
	Tangential penalty coefficient	K_T	5×10^9	$[Pa/m]$
	Transmissivity	T_w	0.0	$[m/Pa/s]$

10.1.3 Modelling of biaxial compression tests

Plane strain biaxial compression tests are numerically modelled in order to evaluate the constitutive elastic modulus D associated to the second gradient mechanical law on the one hand, and the evolution parameter β_{per} involved in the strain-dependent evolution of the permeability on the other hand. A good assessment of these values is of paramount importance since they have an influence on the fractured zone extent and on the fluid flows through this zone, that will directly impact the gas migrations in the EDZ.

Figure III–17 gives a sketch of the hydro-mechanical model in plane strain state, with all the boundary conditions. The considered sample has a height H of 1 m and a width H/2 of 0.5 m, and is meshed by a variable number of finite elements, i.e. 200 FEs (10×20), 450 FEs (15×30) and 800 FEs (20×40). To model the vertical compression of the 2D specimen, the vertical displacement u of all the nodes of the sample upper surface (smooth and rigid boundary) is increased during the test with a constant loading strain rate of $5.10^{-7}\ \frac{m}{s}$ up to a total vertical strain ε_y of 3%. The vertical displacement of all the nodes of the bottom surface is blocked (rigid boundary) and the displacement of the central node is blocked in the horizontal and vertical directions in order to avoid rigid body motion. The constitutive laws and parameters assigned to the model are those which are used for the E4 and the E5 models (see Section 10.1.2). Strain localisation can be triggered through the introduction of an imperfection in the specimen, which consists of a weaker element, located at the bottom left of the sample.

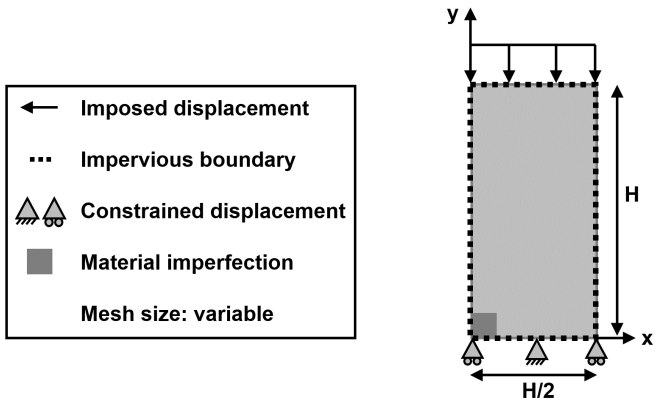

Figure III–17 – Geometry and boundary conditions of the numerical model used for the simulations of a plane strain biaxial compression test.

10.1.3.1 Evaluation of the second gradient elastic modulus D

As previously mentioned, the second gradient mechanical law depends on one constitutive elastic modulus D which characterises the internal length scale of the second gradient model and controls the width of the localised shear bands.

First, the biaxial compression test is simulated for the 10×20 mesh with different values of D, to examine the dependency of the shear band thickness to the choice of the second gradient elastic modulus. The results are presented at the end of the computation time to highlight the localised shear band that appears across the sample. The strain localisation patterns induced by the imperfection can be visualised through the Gauss integration points under softening plastic loading (red squares) and the contour of total deviatoric strain. The Figure III–18 shows the development of strain localisation for a value of D ranging from 1 N to 1000 N, and by considering the E4 (top) or the E5 (bottom) set of parameters.

With regard to the four different values of D that are represented, which implicitly signifies four different material internal length, the obtained results demonstrate that the higher the value of D, *i.e.* the larger the internal length scale, the larger the width of the shear bands. Several graphical observations make it possible to converge to an adequate value of the modulus. For $D \geq 1000$ N, there are so many

Gauss integration points falling into the plastic domain compared to the size of the mesh, that it is not possible to discern the precise location of the shear bands. For $D \leq 100$ N, less than three elements compose the shear band width, which might be problematic from a modelling point of view, regarding the numerical precision of the post-localisation plastic behaviour within the bands [Bésuelle et al., 2006]. This last remark is corroborated by the scattering of some plastic points with regards to the zone where these points are concentrated. In light of this, the suitable value of the D modulus for the studied model belongs to the range [100 N - 1000 N]. The same conclusions can be drawn for both biaxial compression tests, either it is the E4 parameters (Figures III–18a to III–18d) or the E5 parameters (Figures III–18e to III–18h) that are considered. In the end, to fix the scattered plastic points and to properly describe the shear band width, a suitable value of $D = 300$ N is selected, and kept constant in the following simulations of the biaxial compression test.

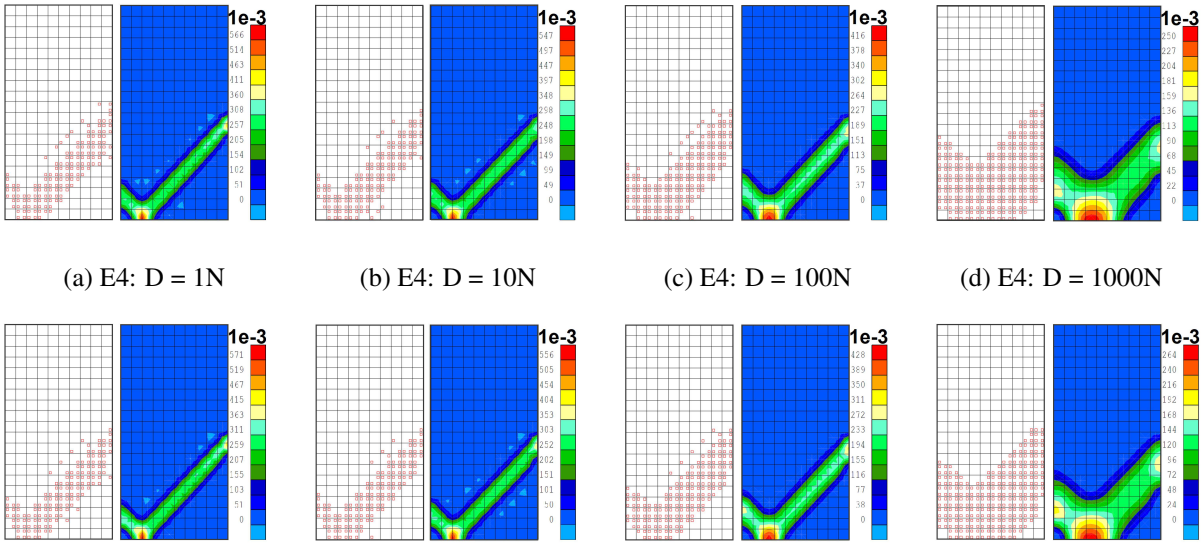

(a) E4: D = 1N (b) E4: D = 10N (c) E4: D = 100N (d) E4: D = 1000N

(e) E5: D = 1N (f) E5: D = 10N (g) E5: D = 100N (h) E5: D = 1000N

Figure III–18 – Localisation patterns represented by the plastic zone (left) and the total deviatoric strain (right) for different values of the D modulus: (a)-(d) E4 set of parameters, (e)-(h) E5 set of parameters.

To ensure the consistency of these results, the biaxial compression test is subsequently simulated for two finer meshes of 15×30 elements and 20×40 elements. From Figure III–19a to III–19f related to the E4 and E5 configurations, one can notice that the representation of the shear band is constant no matter the element size, implying that the shear strain localisation is well mesh-independent and that the chosen value of D is consistent.

However, the sizes of the elements in the different meshes simulated for the biaxial compression tests are of the order of the *cm*, while the size of the finite elements around the borehole in the E4 and E5 meshes of Figure III–14 are of the order of magnitude of the *mm*, as reported in Table III–3. Therefore, the value of the second gradient elastic modulus which has been established on the basis of the simulations of the biaxial compression tests needs to be scaled down to the sizes of the E4 and E5 models.

To this end, a rough estimation of the band thickness is first of all evaluated on the basis of the formula introduced in Equation (III–39):

$$l_c = \sqrt{\frac{|D|}{|E|}} \tag{III–105}$$

Where l_c is the estimation of the fracture thickness, D is the second gradient elastic modulus, and E is the Young's elastic modulus.

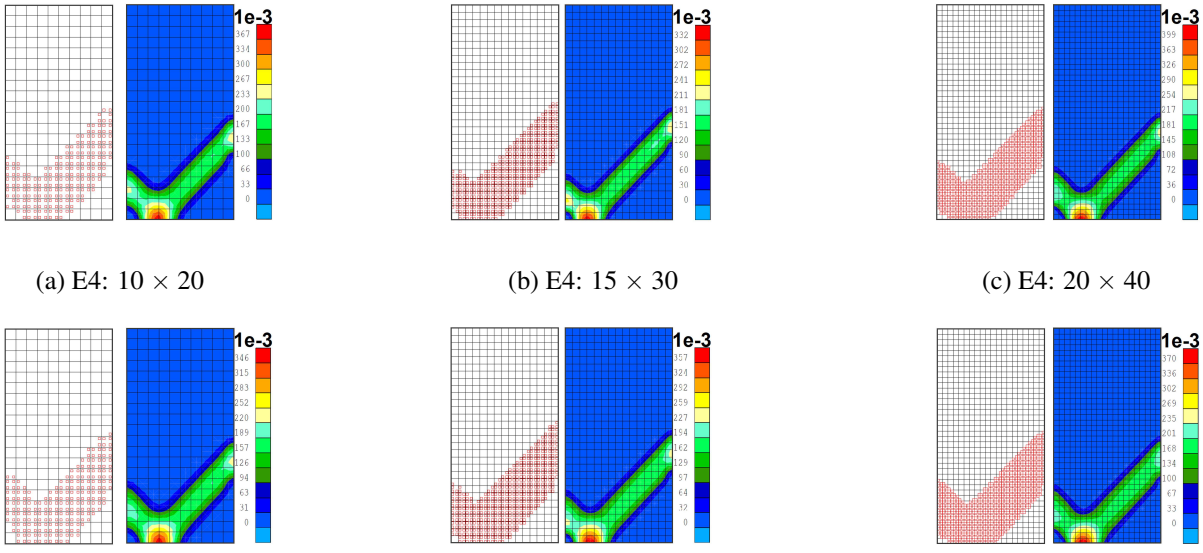

(a) E4: 10 × 20 (b) E4: 15 × 30 (c) E4: 20 × 40

(d) E5: 10 × 20 (e) E5: 15 × 30 (f) E5: 20 × 40

Figure III–19 – Localisation patterns represented by the plastic zone (left) and the total deviatoric strain (right) for different mesh sizes and a value of D=300 N: (a)-(c) E4 set of parameters, (d)-(f) E5 set of parameters.

The ratio R of this band thickness value to the size of the mesh net x can then be assessed for the different meshes of the biaxial compression test, and must be kept constant for the meshes of the *in situ* experiments. Considering a mean value of $E = 300$ MPa for the Boom Clay, it is thus possible to determine an estimation of the band thickness in the E4 and E5 configurations, knowing the size of the thinnest mesh net in these domains. From then on, the adapted value of the D modulus is computed by going back to Equation (III–105), and following the procedure proposed in Table III–4. From the deduced values, a second gradient modulus D of 1 N is chosen.

Table III–3 – Size of the thinnest mesh elements.

Model	Biaxial test			E4	E5
	10×20	15×30	20×40		
Element size [m]	0.05	0.033	0.025	0.0035	0.0035

Table III–4 – Evaluation of the second gradient modulus D for the E4 and E5 meshes.

Model		D_b [N]	$l_{c_b} = \sqrt{\frac{D_b}{E_b}}$ [m]	x_b [m]	$\frac{l_{c_b}}{x_b} = R = \frac{l_c}{x}$	x [m]	l_c [m]	D [N]
	10×20	300	1×10^{-3}	0.05	$\frac{1}{50}$	0.0035	7.0×10^{-5}	1.47
Biaxial	15×35	300	1×10^{-3}	0.033	$\frac{1}{33}$	0.0035	1.06×10^{-4}	3.37
	20×40	300	1×10^{-3}	0.025	$\frac{1}{25}$	0.0035	1.40×10^{-4}	5.88

10.1.3.2 Evaluation of the parameter β_{per}

As exposed in Section 10.1.2.3, a strain-dependant evolution of the hydraulic permeability is implemented in order to capture its increase in the fractured zones. Practically, it has been established from the state-of-the-art description in Section 4.3.6 that this rise in permeability should be about one order

of magnitude in the damaged zone around the excavation in Boom Clay. It is controlled by the evolution parameter β_{per}. In Figures III–20b and III–20c and Figures III–20e and III–20f, the evolutions of the permeability and of the entry pressure parameter along the height of the sample is sketched for different values of the β_{per} parameter, and for the E4 and E5 sets of parameters respectively. In order to reproduce the desired permeability modification, the selected value of β_{per} is 1×10^4 for both sets of parameters.

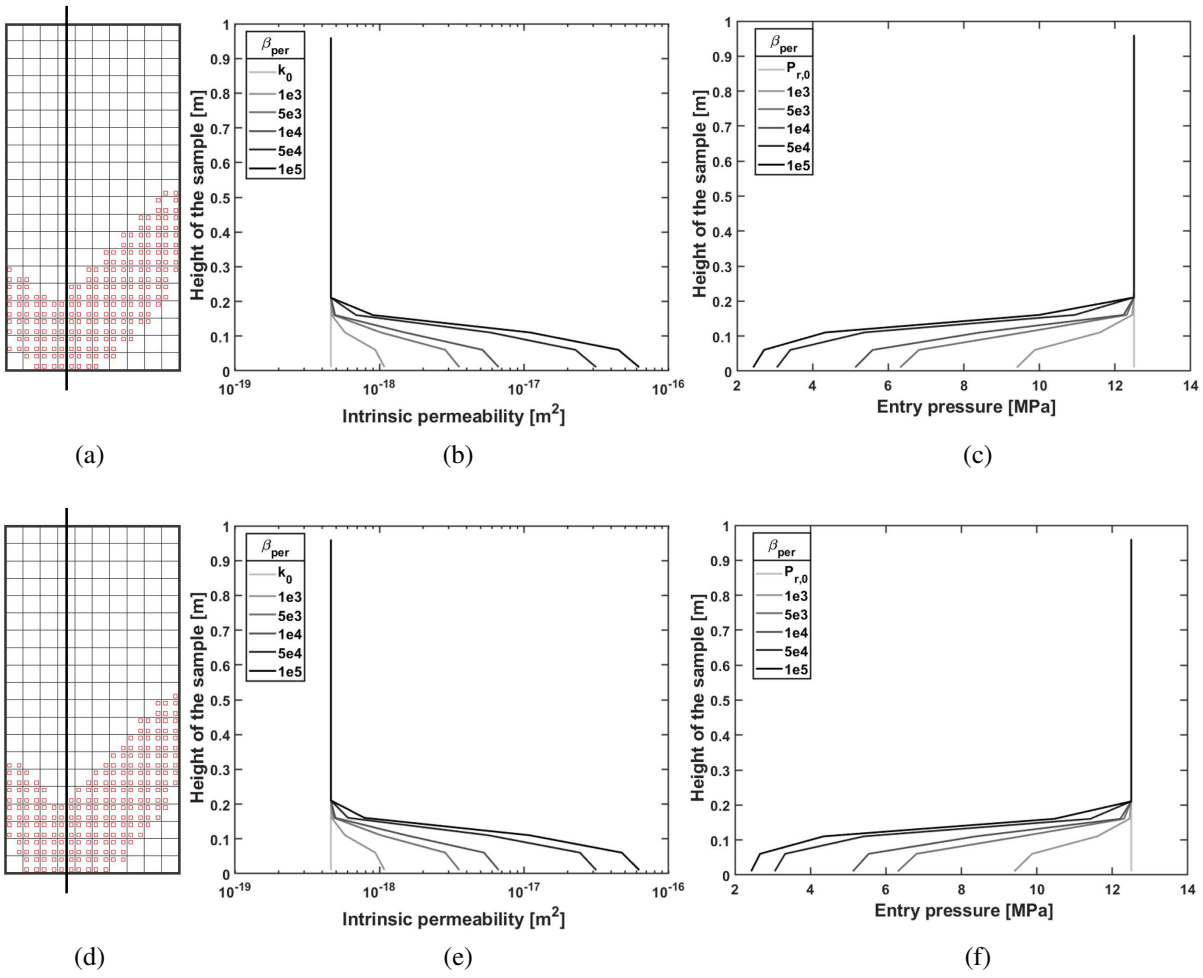

Figure III–20 – Location of the studied cross-section (left), variations of the permeability (centre) and of the entry pressure (right) along the sample: (a)-(c) E4 set of parameters, (d)-(f) E5 set of parameters.

10.1.4 Results and discussion

In this section, various numerical results, computed with the finite element code LAGAMINE for the E4 and E5 models are presented and discussed, for the three steps of the problem. In addition, three modelling cases are investigated to emphasise the effect of the EDZ on gas migrations. In the first reference simulation, the development of the EDZ is supposed to induce no alteration of the hydraulic properties in this zone. In the two subsequent simulations, the enhanced couplings between fluids transfers (water and Helium) and the mechanical behaviour of the fractured zone are taken into account.

10.1.4.1 Reference simulation

The first performed simulation focuses on the development of the EDZ following the drilling process of the different boreholes. The main purpose is to characterise the extent of fractures induced by rock deconfinement during the excavation phase. These fractures are reproduced by shear banding and no

modification of the hydraulic properties in the damaged zone is taken into account at this point.

By analysing first the results in terms of convergence, it can be deduced from Figure III–21a that for the considered parameters of the E4 configuration, the total convergence of the unsupported borehole is in the same order of magnitude as the other boreholes drilled in the vicinity. The radial convergence of Boom Clay during the excavation phase of the E4 and E5 boreholes is presented in Figure III–21b. In each configuration, the borehole wall is assumed to be supported when it enters in contact with the casing of the piezometer, which means that the borehole wall converges from 0.0425 m to 0.03 m in the E4 scenario, and from 0.051 m to 0.0445 m in the E5 scenario. Once the first contact is established, there is almost no residual convergence . Moreover, regarding the two studied nodes A and B in the horizontal and vertical directions respectively, the isotropic stress state in the E4 configuration induces an isotropic convergence. As for the E5 configuration, the initial anisotropic stress state and the subsequent stress redistribution leads to a higher convergence in the horizontal direction than in the vertical one.

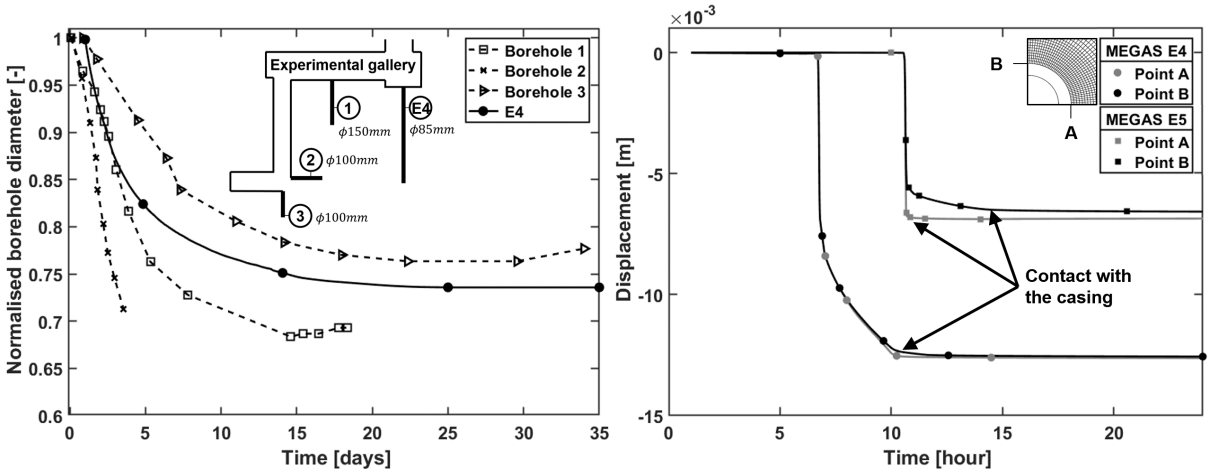

(a) (b)

Figure III–21 – (a) Comparison of the convergence without support for different boreholes, *modified after* [Rousset, 1988]. (b) Evolution of the convergence of a borehole drilled in the E4 and E5 configurations.

The creation and evolution of the fractured zone can be observed through the development of shear strain localisation. The numerical results are presented in terms of the Von Mises' equivalent deviatoric total strain (total deviatoric strain), the plastic zone, i.e. the plastic loading integration points (red squares), and the deviatoric strain increment, which represents the band activity:

$$\kappa_{eq} = \frac{\dot{\hat{\varepsilon}}_{eq} dt}{\int \dot{\hat{\varepsilon}}_{eq} dt} \tag{III–106}$$

where κ_{eq} is the deviatoric strain increment, $\hat{\varepsilon}_{eq} = \sqrt{\frac{2}{3}\hat{\varepsilon}_{ij}\hat{\varepsilon}_{ij}}$ is the total deviatoric strain, and $\hat{\varepsilon}_{ij} = \varepsilon_{ij} - \frac{\varepsilon_{kk}}{3}\delta_{ij}$ is the deviatoric part of the strain tensor.
Provided that the specific second gradient boundary condition is well implemented [Zervos et al., 2001], the results from a quarter of a drift can be extrapolated to the full section of the borehole. Hence, Figures III–22 and III–23 illustrate the creation of the damaged zone through the evolution of the strain localisation around the studied boreholes in the course of the drilling process. In both cases, the modelling exhibits a symmetric shear band pattern, whose onset and shape can be attributed to the anisotropy of the material and of the initial stress state. Therefore, the shear banding zone is more concentrated all around the borehole in the E4 configuration presenting an isotropic stress state, while it develops preferentially in the direction of the minor principal stress, *i.e.* horizontal, in the E5 configuration with an anisotropic stress state. By the end of the drilling process, the plastic zone has expanded over about 0.015 m to

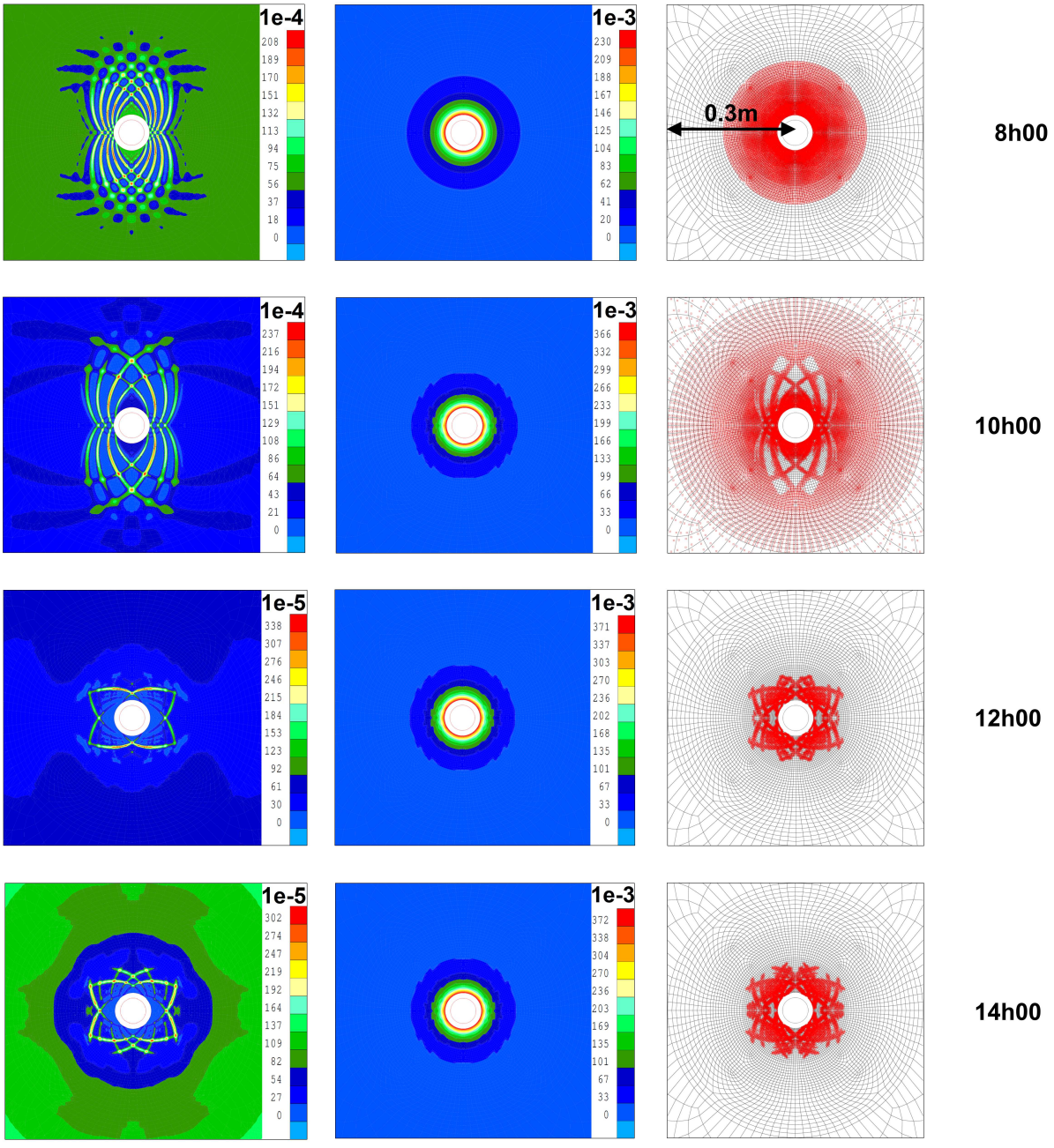

Figure III–22 – Development of shear bands during the drilling process of the E4 borehole: (a) deviatoric strain increment, (b) total deviatoric strain and (c) plastic loading points.

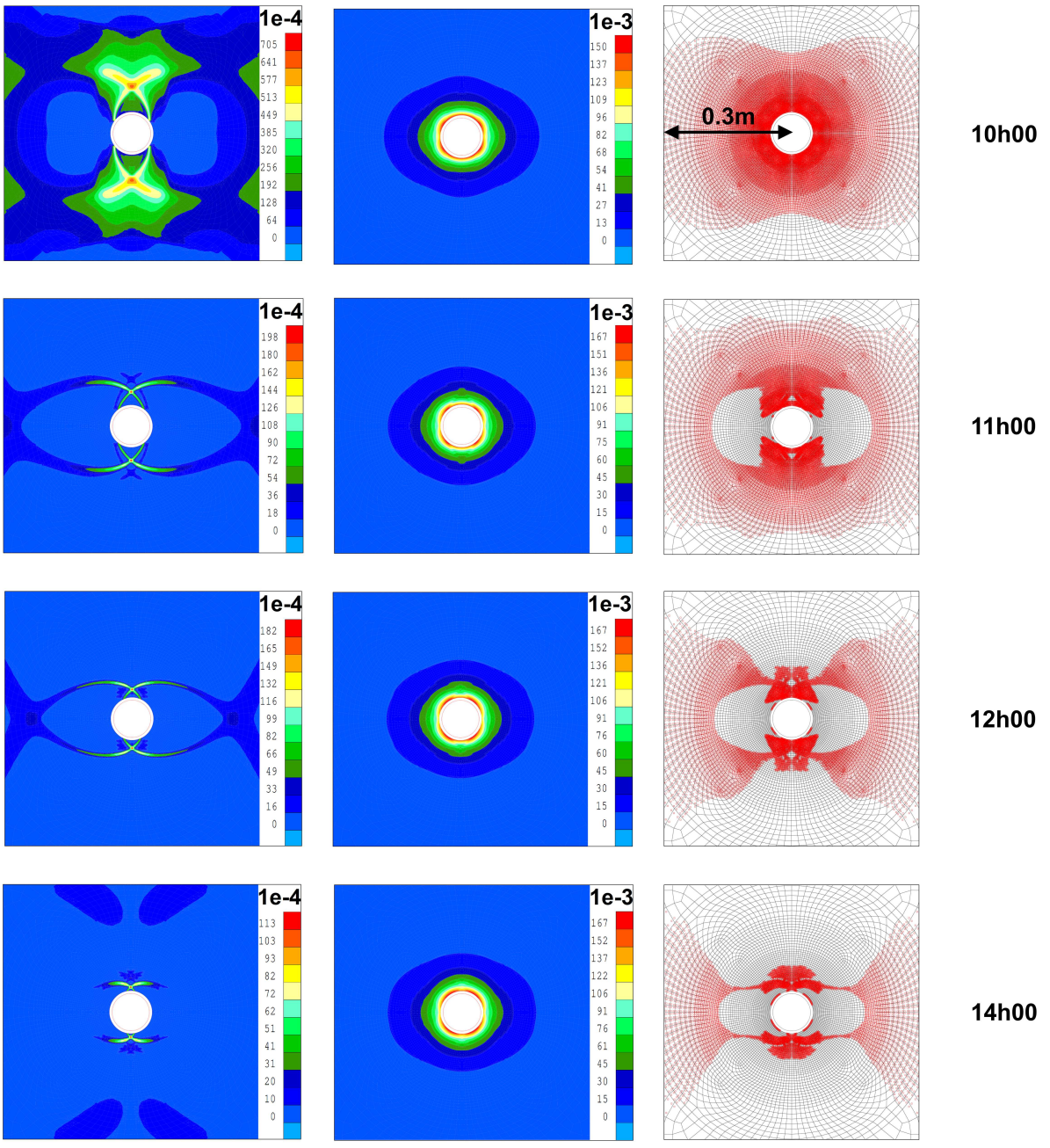

Figure III–23 – Development of shear bands during the drilling process of the E5 borehole: (a) deviatoric strain increment, (b) total deviatoric strain and (c) plastic loading points.

0.020 m in the horizontal and vertical directions. Yet, compared to the case of an unsupported excavation process, the installation of the piezometer has the consequences of limiting additional convergence of the borehole wall, thus limiting the points in plastic charge in the surrounding rock mass and inhibiting any further development of localisation.

The time evolution of pore water pressure at the borehole wall in the E4 and E5 configurations is exhibited in Figure III–24a. These curves detail the progressive update in water pressures from the initial condition of $p_w = 2.2$ MPa to the atmospheric pressure imposed by the deconfinement during the drilling and then back to the reference pressure during a phase of pressure stabilisation. However, this decrease in water pressure propagates further in the rock mass around the E5 set-up (up to $\sim$ 1 m) than around the E4 one (up to $\sim$ 0.6 m), as it is shown in Figures III–24b and III–24c respectively. Generation of overpressures is also apparent in the latter Figure III–24c which can be attributed to the hydro-mechanical couplings linked to the anisotropy of the initial stress state and permeability in the orientation of the E5 test. The effect of strain localisation on these pressure profiles is mostly observed when the band activity is intense which is reflected by a localised decrease in the pore water pressure located in the near vicinity of the borehole.

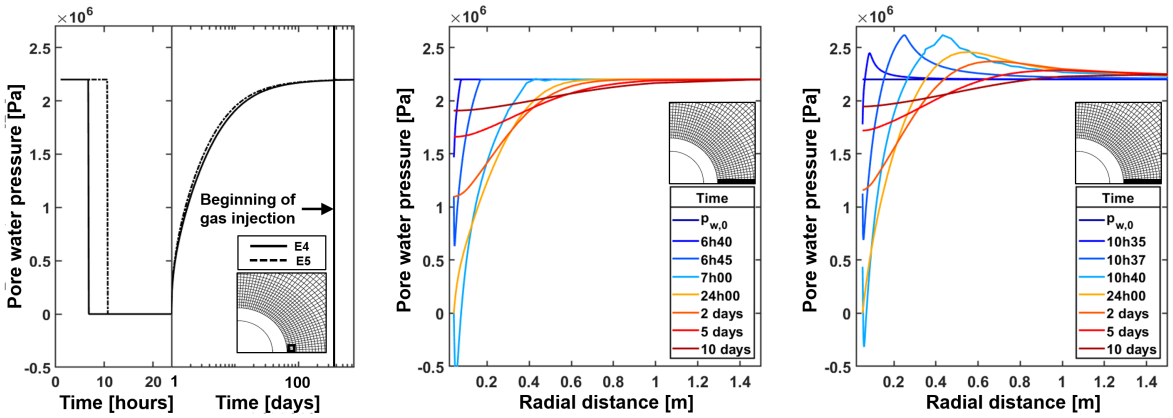

(a) Time evolution (b) E4 (c) E5

Figure III–24 – (a) Time evolution of pore water pressure during the successive phases of the simulation. (b)-(c) Evolution of pore water pressure along the domain for the E4 and E5 configurations.

The evolution of the effective stresses can be visualised by plotting the stress paths in the drift wall zone, as shown in Figure III–25a where the first stress invariant and the second deviatoric stress invariant are respectively defined as:

$$I_{\sigma'} = \sigma'_{ij}\delta_{ij} = \sigma'_{ii} \quad \text{and} \quad II'_{\hat{\sigma}} = \sqrt{0.5\hat{\sigma}'_{ij}\hat{\sigma}'_{ij}} \tag{III–107}$$

where $\hat{\sigma}'_{ij} = \sigma'_{ij} - \frac{\sigma'_{kk}}{3}\delta_{ij}$ is the deviatoric part of the effective stress tensor.
The evolution of the radial and orthoradial effective stresses with time during the excavation of the E4 and E5 boreholes are displayed along the domain in Figures III–25b and III–25c. It appears that the radial stress tends to decrease and vanish at the gallery wall while the orthoradial stress is increased. This results in an overall increase in the deviatoric stress invariant until the stress state reaches the plastic criterion.

Finally, gas transfers in the form of Helium are taken into account in the long-term part of the simulation, according to the evolution profile given in Figure III–15c of section 10.1.1. In Figures III–26a and III–26b (solid lines), gas pressure profiles are displayed along the horizontal section of the domain, highlighting the progressive propagation of Helium over a thin zone of about 1m across the rock mass.

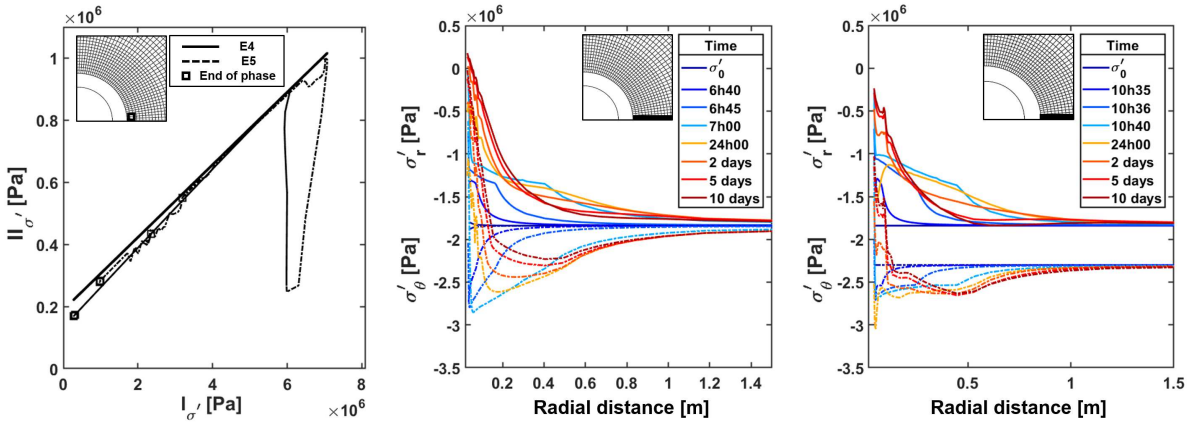

(a) Stress path (b) E4 (c) E5

Figure III–25 – (a) Evolution of the stress paths at the drift wall throughout the simulation. (b)-(c) Evolution of the radial (dashed line) and orthoradial (solid line) effective stresses along the domain for the E4 and E5 configurations.

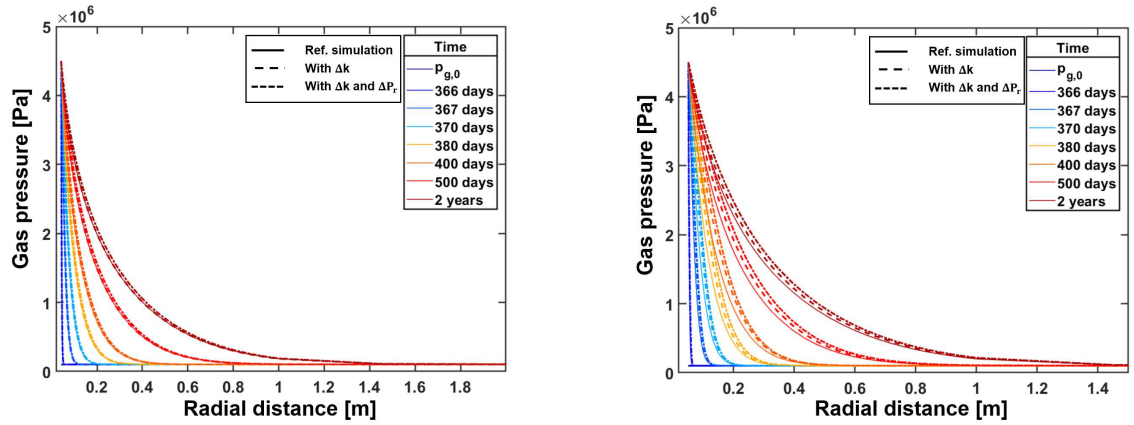

(a) E4

(b) E5

Figure III–26 – Evolution of gas (Helium) pressures as a function of the radial distance for different time steps for the (a) E4 and (b) E5 configurations: reference case (solid line), evolution of the permeability (dashed line) and of the retention curve (dash-dotted line) with strain.

Once the maximum gas pressure of about 4.5 MPa is reached at the piezometer wall, a slight desaturation of a few percent associated to this peak of Helium pressure can be seen in both configurations in Figures III–29b and III–29d. These desaturation profiles can be put into perspective with the dissolved and total Hydrogen flows profiles displayed in Figures III–29a and III–29c respectively. Close to the injection zone, it appears that dissolved gas in the water phase is not sufficient enough to ensure transfers of Helium in the Boom Clay under the largest gas production sequences. This quantity of dissolved Helium is indeed physically limited by Henry's law, which leads to the creation of a gaseous phase, and the desaturation of the rock over a certain radial distance. Since total Helium fluxes decrease with the radial distance, dissolved Helium becomes predominant again at the transition between saturated and partially saturated zones.

10.1.4.2 Influence of the HM couplings

So far, the behaviour of the EDZ has been limited to the development of fractures in the form of shear strain localisation bands. However, this process of fracture generation tends to substantially affect the flow properties of the *in situ* material. In this second part of the simulations, the hydro-mechanical behaviour of the EDZ is considered in order to end up with a more accurate representation of the phenomena related to gas migration. As detailed in Section 10.1.2, the impact of fracturing on the transfer characteristics is addressed by relating the evolutions of the intrinsic permeability and of the water retention curve with the mechanical deformations according to expressions recalled in Equations (III–99) and (III–100).

The variations in parallel (solid line) and perpendicular (dashed line) intrinsic water permeabilities around the boreholes are presented during the drilling process in Figures III–27b (E4) and III–28b (E5) respectively, and put into perspective with the creation of the plastic zone in Figures III–27a (E4) and III–28a (E5). Include a strain-dependent evolution of the intrinsic permeability in the simulation gives rise to additional hydro-mechanical couplings slightly interfering with the initiation of localisation, while leading to the same extent of the EDZ. Permeability variations are well visible in the part of the damaged zone which is the closest to the boreholes wall, and more particularly inside the strain localisation discontinuities where an increase of one order of magnitude (E4) or a bit less (E5) is obtained. This slight discrepancy directly results from the more important convergence of the E4 borehole, with respect to the E5 one.

From these observations, it follows that Helium tends to enter the damaged zone more easily, which is reflected by a slight horizontal offset of the dashed lines in Figures III–26a (E4) and III–26b (E5). Like in the reference case, the analysis of the Helium fluxes shown in Figures III–29e (E4) and III–29g (E5) reveals that for the largest amount of Helium, a distinct gas phase appears which desaturates the rock mass in the vicinity of the piezometers as displayed in Figures III–29f (E4) and III–29h (E5).

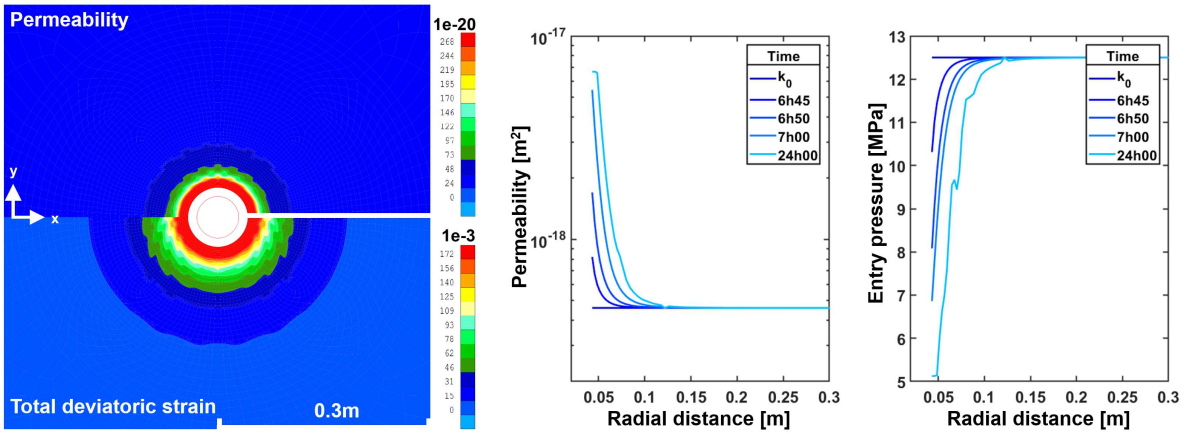

(a) (b) (c)

Figure III–27 – E4 configuration: (a) evolution of the intrinsic permeability in relation to the development of the plastic zone by the end of the drilling stage. Variations of (b) intrinsic permeability and (c) entry pressure as a function of the radial distance.

Next to the increase in the hydraulic permeability with strains, the evolution of the water retention curve with strain is also considered in order to obtain a more faithful representation of the influence of the EDZ on the hydraulic kinetics. The variations of the entry pressure parameter P_r in the horizontal (solid line) and vertical (dashed line) directions during the drilling process are given in Figures III–27c (E4) and III–28c (E5). These results attest to the global drop in P_r in the EDZ, correlated to the evolution of intrinsic permeability previously observed, which means that the minimum capillary pressure required

to desaturate the rock mass is lowered by the cracking process. As for the evolution of the intrinsic permeability displayed in Figures III–27b (E4) and III–27b (E5), the influence of shear bands on P_r is also clearly visible.

Regarding the gas migration phase, it emerges from the horizontal offset of the dash-dotted lines in Figures III–26a and III–26b that the evolution of the retention curve with the deformations has a clear effect on Helium migrations. The reduction of the gas entry pressure in the EDZ facilitates even more the penetration of gas into the Boom Clay. Once the Helium pressure reaches the maximum value set at 4.5 MPa, gas progresses in the form of a front through the zone affected by a reduction of the gas entry value. The distinct gas phase that emerges when the largest amounts of Helium are released is clearly discernible in Figures III–29i (E4) and III–29k (E5). In the EDZ, Helium is no longer dissolved in water but is almost only transferred in the gaseous state, which contributes to a more rapid and important decrease in the degree of water saturation around the boreholes than in the previous simulations, as reported in Figures III–29j (E4) and III–29l (E5).

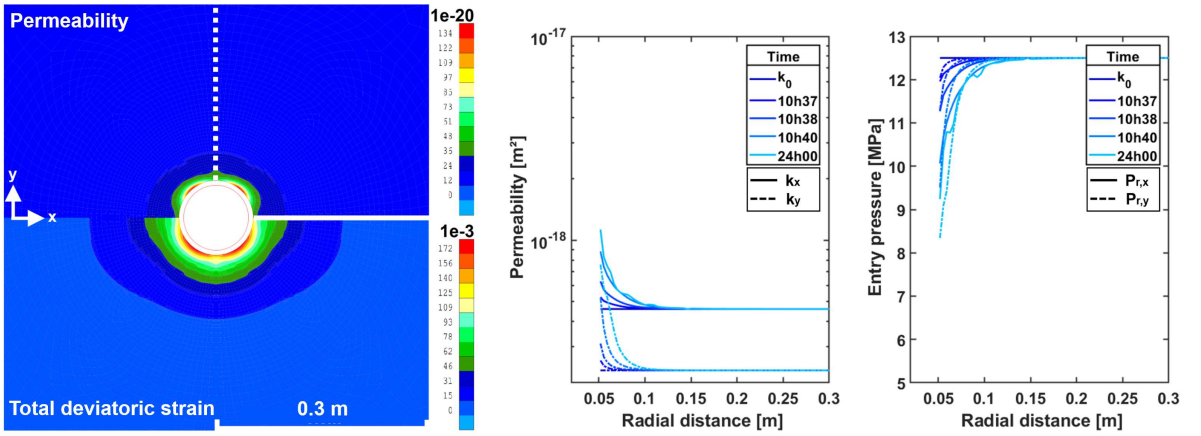

(a) (b) (c)

Figure III–28 – E5 configuration: (a) evolution of the intrinsic permeability in relation to the development of the plastic zone by the end of the drilling stage. Variations of (b) parallel (solid line) and perpendicular (dashed line) intrinsic permeability and (c) entry pressure as a function of the radial distance.

10.1.5 Conclusions

The performed numerical simulations provide a representative characterisation of rock fracturing within the EDZ of Boom Clay during the drilling phase. Under gas injection sequences, it appears that dissolved gas is not sufficient enough to transport Helium under large production of gas, which leads to the creation of a gaseous phase along with the desaturation of the first centimetres of the rock mass. Incorporate the HM effects of strain on permeability and retention behaviour in the modelling leads to a permeability increase of about one order of magnitude and an amplification of the desaturation of the rock mass. It consequently results in an even more rapid progression of Helium in the form of a gaseous front, which is limited to the EDZ close to the drift wall and tends to attenuate deeper in the rock mass.

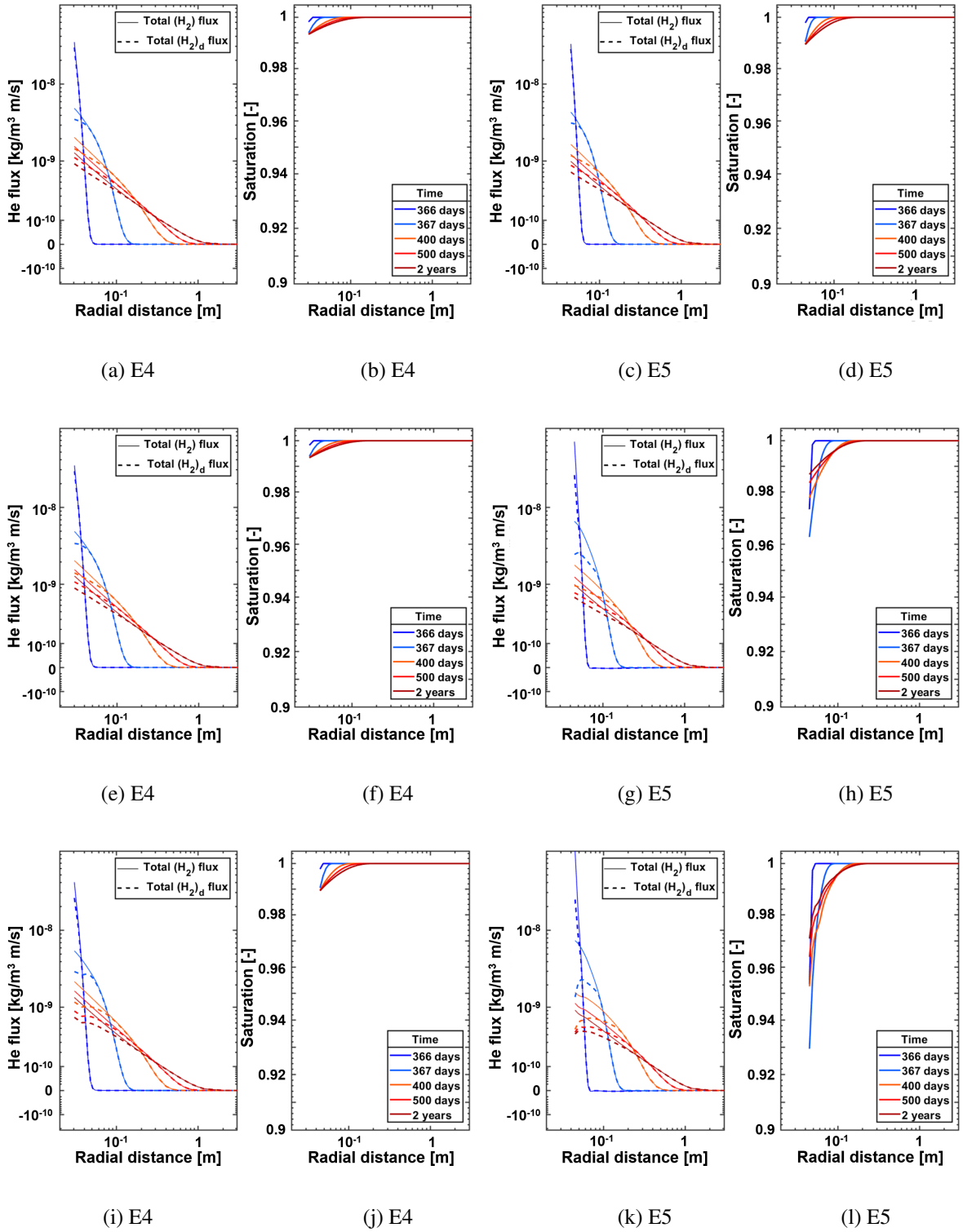

(a) E4 (b) E4 (c) E5 (d) E5

(e) E4 (f) E4 (g) E5 (h) E5

(i) E4 (j) E4 (k) E5 (l) E5

Figure III–29 – Comparison between dissolved Helium and total Helium flux (log scale along the Y-axis [Webber, 2013]), and corresponding saturation profiles as a function of the radial distance for the E4 and E5 configurations: (a)-(d) reference case, (e)-(h) evolution of the permeability with strains and (i)-(l) evolution of the retention curve with strains.

10.2 Large-scale MAVL drift in COx claystone

After having successfully demonstrated the ability of the model to reproduce the interactions between the fluids transfers and the damage at the scale of *in situ* experiments, the next step is to progress to the larger scale of a storage gallery. The first part of this section deals with the description of the numerical simulations of the MAVL storage drift drilled in the COx claystone, focussing particularly on the geometry and on the evolution of the boundary conditions. Three phases are specifically reproduced: the excavation of the gallery, the ventilation process when the storage drift is in operation and the generation and migration of Hydrogen on the long term. Then, the constitutive models and the associated parameters used for the simulations are given. Finally, the numerical results for the different phases of the simulations are provided and analysed in the last part of this section.

10.2.1 Description of the application

Concretely, MAVL galleries are made up of several hundred metres in length, 10.4 m in excavated diameter, and of concrete structural support ensuring stability, and are drilled in the low-permeable Callovo-Oxfordian claystone. In this section, the ingredients of the numerical simulations are described, covering in particular the geometry of the problem, the mesh of the model, the initial boundary conditions as well as the successive steps of the simulations carried out by means of boundary conditions update.

10.2.1.1 Initial conditions

The configuration of the MAVL storage gallery consists in a circular section drift of radius $R = 5.2$ m, parallel to the major *in situ* principal stress. From Chapter 4, it is known that the level of the Meuse/Haute-Marne URL is characterised by an anisotropic stress regime, with a major principal stress in the horizontal direction, a vertical stress more or less equal to the minor principal horizontal stress and a homogeneous water pressure [Wileveau et al., 2007], such that:

$$\sigma_{x,0} = 12.4 \text{ MPa}, \quad \sigma_{y,0} = 12.7 \text{ MPa}, \quad \sigma_{z,0} = \sigma_H = 16.1 \text{ MPa}, \quad p_{w,0} = 4.7 \text{ MPa} \tag{III–108}$$

where $\sigma_{x,0}$ is the minor horizontal principal total stress, $\sigma_{y,0}$ is the vertical principal total stress and $\sigma_{z,0}$ corresponds to the major horizontal principal total stress, while $p_{w,0}$ is the initial pore water pressure. In this confiduration, the coefficient of earth pressure at rest K_0 takes a value of about 0.7. In addition, the initial gas pressure is set to the atmospheric pressure of $p_{g,0} = 0.1$ MPa, while the temperature is maintained constant at $T_0 = 20°C$ throughout the simulations.

10.2.1.2 Geometry

As presented in Figure III–30b, MAVL galleries are reinforced by structural concrete support ensuing stability, namely stuffing layers and precast arch segments. It is worth noted that these latter are modelled as a continuous shell, without considering the joints between the segments. This gives a final usable circular cross-section with a radius of $R = 4.35$ m.

In the treated problem, the HM modelling of the tunnel is performed in two-dimensional plane strain state. A schematic representation of the numerical model involving the mesh and the different boundary conditions is illustrated in Figure III–30a. Assuming symmetries of the problem along the $x-$ and $y-$axes, only a quarter of the gallery cross-section is discretised. The geometry extension covers a domain of 300 m $\times$ 300 m in the horizontal and vertical directions, establishing two far field boundary conditions, and integrates a more refined discretisation close to the tunnel.

Concerning the boundary conditions, the initial stresses, pore water pressure and gas pressure are imposed constant at the mesh external boundaries. On the wall of the tunnel, the initial boundary conditions in terms of stresses and fluid pressures will be progressively adapted as a function of the successive phases of the simulation. Moreover, the symmetry condition is established along the symmetry axes by

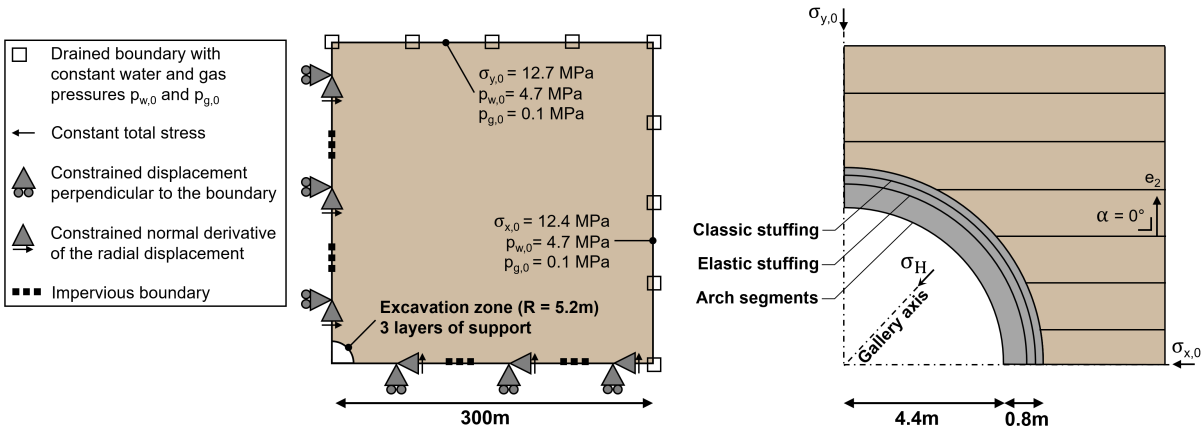

Figure III–30 – (a) Geometry and boundary conditions of the 2D plane strain model. (b) Zoom on the refined support zone, with stress state and bedding plane orientation.

considering no normal displacements and impervious boundaries (water and gas flows blocked to zero). Regarding the second gradient boundary conditions, a special attention must be dedicated to the kinematic boundary conditions required to establish the symmetry, as stipulated in [Zervos et al., 2001]. The presence of gradient terms in the equilibrium Equations (III–63) to (III–66) of the H^2M second gradient model requires that the radial displacement u_r must be symmetric on both sides of the symmetry axes. This supplementary kinematic condition implies that the normal derivative of u_r has to cancel with respect to the tangential direction θ, i.e. $\frac{\partial u_r}{\partial \theta} = 0$. Finally, natural boundary conditions for the double force $\dot{T}_i = 0$ are assumed on the different boundaries and gravity is not taken into account.

10.2.1.3 Boundary condition evolution

In practice, the three-step application discussed in this section is divided into the storage gallery excavation, the tunnel ventilation and finally the gas generation and migrations. This sequential evolution of the problem is translated into a boundary value problem which is carried out by progressively adjusting the boundary conditions using the `LAGAMINE` code.

Excavation phase

The drilling of the tunnel is performed with the convergence-confinement method which is an approximation method for tunnelling that allows transforming a whole three dimensional study of tunnel excavation into a two dimensional analysis in plane strain conditions, based on an identical gallery convergence assumption [Bernaud and Rousset, 1992]. The effect of the excavation front progress is taken into account by applying a fictive pressure σ_r^Γ on the drift wall that depends on the vicinity of the excavation front to the studied drift section through a deconfinement rate ζ (Figure III–31):

$$\sigma_r^\Gamma = (1-\zeta)\sigma_{r,0} \tag{III–109}$$

where σ_r^Γ is the total radial stress, $\sigma_{r,0}$ is the initial mechanical pressure on the gallery wall that corresponds to the initial stress in the material, and ζ is the deconfinement rate ranging from 0 to 1.

An excavation rate of 18 m per day is considered here, implying that the excavation front crosses the studied section after about 10 hours and that the excavation is fully completed after about 24 hours. The evolution of the deconfinement rate with time is detailed in Figure III–32a where the origin of the time axis corresponds to the moment when the studied section starts to be influenced by excavation of the previous sections of the tunnel. Pore water pressure at drift wall p_w^Γ is also affected during the excavation

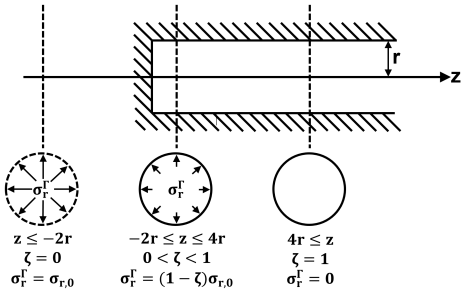

Figure III–31 – Theory of deconfinement rate during drift excavation.

phase and starts to decrease quickly and linearly from its initial value towards the atmospheric pressure when the deconfinement starts. In addition, the stress imposition at the gallery wall is also conditioned by the support structure. Practically, the three layers of support are supposed to be applied simultaneously at 96% deconfining as depicted in Figure III–32a.

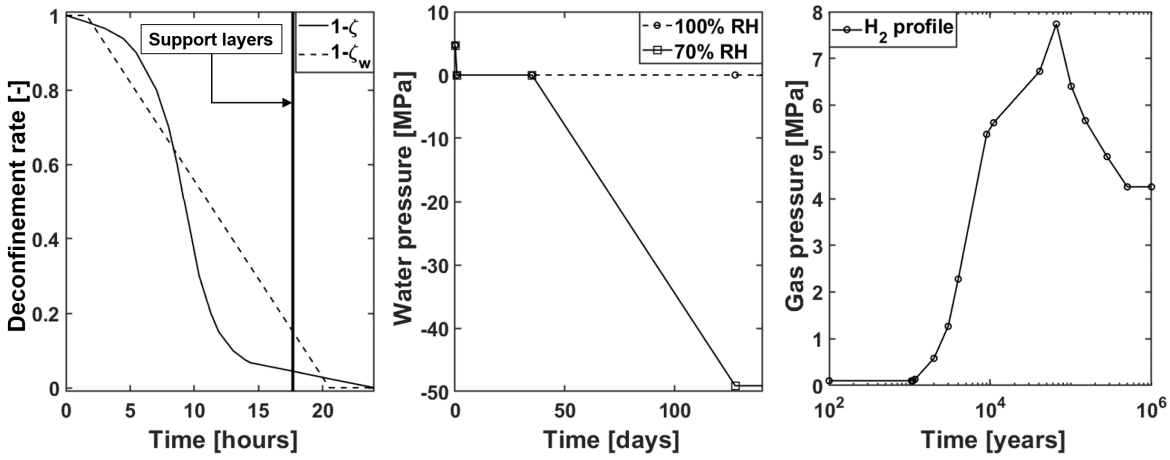

Figure III–32 – (a) Applied deconfinement curves for the total stress and for the pore water pressure during drift excavation. (b) Profile of pore water pressures during ventilation. (c) Profile of gas pressures during Hydrogen injection.

Ventilation phase

So far, there is no ventilation inside the gallery, which means that the air is fully saturated with water vapour. This maximum concentration corresponds to air with 100% of Relative Humidity (RH) according to Kelvin's law:

$$RH = \frac{p_v}{p_v^0} = \frac{\rho_v}{\rho_v^0} = exp\left(\frac{-p_c M_v}{\rho_w RT}\right) \tag{III–110}$$

where p_v is the partial pressure of water vapour, p_v^0 is the pressure of saturated water vapour, and ρ_v^0 is the saturated vapour concentration, M_v is the molar mass of water vapour, $R = 8.314$ [J/molK] is the gas constant and $T = 298.15$ [K] is the absolute temperature.

Afterwards, the drift is ventilated during the operation phase in order to regulate the temperature according to workers needs. The ventilation imposes a RH of about 70% which modifies the hydraulic boundary condition at the drift wall by reducing the pore water pressure from 0.1 MPa to -49.1 MPa. This process is initiated 35 days after the excavation starts, the RH is progressively decreased during a period of 3 months to reach the planned value of P_w after 125 days as exposed in Figure III–32b.

Ventilation is then maintained constant in the tunnel during an exploitation period of about 100 years. Modelling this ventilation phase is of particular interest since the generated suction may drain the water from the rock through the support, desaturate it, and thence modify the fracturing pattern as well as the size of the fractured zone.

Phase of gas migration

Finally, after the 100-year phase of ventilation, the storage gallery is supposed to be entirely filled with waste packages, properly sealed and closed. From this time, the system becomes impervious to water and a period of pore water pressures stabilisation initiates since there is no more drainage imposed by the ventilation of the drift. It is worth noting that concurrently to the installation of the canisters, a significant rise in temperature would normally occur around the storage but this effect falls beyond the scope of the present study. Subsequently, gas starts to be generated in the form of Hydrogen arising from steel corrosion. Hydrogen migrations are simulated by imposing a variation of gas pressures at the intrados of the support structure according to the H_2-profile given in Figure III–32c [Talandier, 2005]. This last phase ranges from 100 years to a million years, with peak value of gas pressures reached around 66000 years.

10.2.2 Constitutive models and parameters

The constitutive models of the Callovo-Oxfordian claystone and the support, and their related parameters required for the numerical application are presented in this section. The hydro-mechanical description of the COx behaviour includes a mechanical model for the classical first gradient part related to the macrostructure, a mechanical model for the second gradient part related to the microstructure and a hydraulic model to reproduce water and gas flows in the partially saturated porous medium.

10.2.2.1 First gradient mechanical model of the COx claystone

An elasto-visco-plastic model with cross-anisotropy and horizontal isotropic bedding planes is considered for the mechanical behaviour of the rock, which can be decomposed into an elastic, a plastic and a viscous component, as introduced in section 6.3.3:

$$\dot{\varepsilon}_{ij} = \dot{\varepsilon}^e_{ij} + \dot{\varepsilon}^p_{ij} + \dot{\varepsilon}^{vp}_{ij} \tag{III–111}$$

where ε^e_{ij}, ε^p_{ij} and ε^{vp}_{ij} are the elastic, plastic and viscous components of the total strain rate.

Elastic component

The linear elastic behaviour of the rock is based on the classical Hooke's law (Equation (II–96)). For cross-anisotropic materials such as the COx formation, the behaviour remains isotropic in the parallel bedding planes which requires 5 independent parameters to express the elastic compliance tensor [Amadei, 1983], as stipulated in Equation (II–99).

Plastic component

The elasto-plastic behaviour of the COx claystone is characterised by an internal friction model with a non-associated plasticity and a Van Eekelen yield surface [Van Eekelen, 1980] (under soil mechanics convention with positive compressive stress) defined in Equation (II–102). Furthermore, the model is able to generate isotropic hardening or softening of the cohesion and of the friction angles upon loading.

The elasto-plastic geomechanical parameters used in the mechanical law of the COx claystone, reported in Table III–5 are taken from [Argilaga et al., 2019] after [Pardoen and Collin, 2017] where calibration is realised based on experimental data.

Viscoplastic component

Viscoplasticity is also taken into account to reproduce the creep deformations characterising the long term behaviour of the claystone [Shao et al., 2003]. A single viscoplastic flow mechanism decoupled from elastoplasticity is considered, with the viscoplastic loading surface f^{vp} defined in Equation (II–108) controlled by the delayed viscoplastic hardening function α^{vp} defined in Equation (II–109).

A complete description of this viscoplastic model is available in [Jia et al., 2008, Zhou et al., 2008] and details about its implementation in the gallery excavation can be found in [Pardoen and Collin, 2017]. The viscoplastic parameters of the COx claystone, detailed in Table III–6, are taken from [Argilaga et al., 2019], after [Pardoen and Collin, 2017] and calibrated against laboratory tests.

10.2.2.2 Second gradient mechanical model of the COx claystone

The second gradient mechanical model gives an additional constitutive stress-strain relation between the kinematics and the stress at micro-scale. Based on [Mindlin, 1965], it is an isotropic linear elastic law which relates the double stress to the rate of micro second gradient as defined in Equation (III–34) exposed in Section 9.3, and depends on one constitutive elastic parameter D in its simplified version proposed by [Matsushima et al., 2002]. This elastic modulus symbolises the physical microstructure of the material and is directly linked to the internal length scale relevant for the shear band width [Chambon et al., 1998, Collin et al., 2009b].

The value of this modulus selected to suitably regularise the problem is reported in Table III–5.

10.2.2.3 Hydraulic model of the COx claystone

In the hydraulic model used for the COx claystone and introduced in Section 6.3.1, the transfer of the liquid phase (water and gas) by advection in an unsaturated porous medium is defined by the generalised Darcy's law [Darcy, 1856]:

$$q_{w,i} = -\frac{k_{ij}^{int} k_{r_w}}{\mu_w}\left(\frac{\partial p_w}{\partial x_j} + \rho_w g_j\right) \qquad \text{(III–112)} \qquad q_{g,i} = -\frac{k_{ij}^{int} k_{r_g}}{\mu_g}\left(\frac{\partial p_g}{\partial x_j} + \rho_g g_j\right) \qquad \text{(III–113)}$$

where k_{r_w} and k_{r_g} are the water and gas relative permeabilities, μ_w and μ_g are the dynamic viscosities of water and gas respectively, and k_{ij}^{int} is the anisotropic tensor of intrinsic permeability of the material, defined by two components $k_{\parallel}$ and $k_{\perp}$ respectively parallel and perpendicular to the isotropic planes:

$$k_{w,ij} = \begin{bmatrix} k_{w\parallel} & 0 & 0 \\ 0 & k_{w\perp} & 0 \\ 0 & 0 & k_{w\parallel} \end{bmatrix} \qquad \text{(III–114)}$$

The material retention behaviour is represented by a retention curve of van Genuchten's type [van Genuchten, 1980] introduced in Equation (II–82) of Section 6.3.2, linking the capillary pressure to the degree of water saturation (Figure III–33a):

$$S_{r_w} = S_{r_w,res} + (S_{r,max} - S_{r_w,res})\left(1 + \left(\frac{s}{P_r}\right)^{\mathcal{N}}\right)^{\frac{1}{\mathcal{N}}-1} \qquad \text{(III–115)}$$

where $P_r = 15$ MPa is the parameter of gas entry pressure taken from [Gerard et al., 2014, Pardoen et al., 2015b] as detailed in Section 5.3.4 of the literature review, $S_{r,max} = 1$ and $S_{r_w,res} = 0.01$ are the maximum and residual degrees of water saturation, s is the suction, and $\mathcal{N} = \frac{1}{1-\mathcal{F}} = 1.49$ is a model parameter, fitted to obtain a good agreement with the experimental data in Figure II–21b of the state of the art.

Moreover, the Mualem - van Genuchten's model [Mualem, 1976] introduced in Equation (II–83) of Section 6.3.2 is used to express the water relative permeability in Figure III–33b, while the cubic law [Charlier et al., 2013] introduced in Equation (II–86) of Section 6.3.2 is adopted to describe the gas relative permeability in Figure III–33c:

$$k_{r_w} = \sqrt{S_{r_w}} \left(1 - \left(1 - S_{r_w}^{\frac{1}{\mathcal{M}}} \right)^{\mathcal{M}} \right)^2 \qquad \text{(III–116)} \qquad k_{r_g} = (1 - S_e)^{\mathcal{L}} \qquad \text{(III–117)}$$

where $S_e = \frac{S_{r_w} - S_{r_w,res}}{1 - S_{r_w,res} - S_{r_g,res}}$, with S_{r_w} the degree of water saturation, $S_{r_w,res}$ the residual degree of water saturation, $S_{r_g,res}$ the residual degree of gas saturation, and $\mathcal{M} = 0.33$ and $\mathcal{L} = 3$ are model parameters, fitted to obtain a good agreement with the experimental data in Figure II–23b of the state of the art.

On top of that, enhanced hydro-mechanical couplings are integrated into the model and include the strain-dependent isotropic evolution of the hydraulic permeability tensor and of the water retention property introduced in Equations (III–43) and (III–48) respectively:

$$k_{w,ij} = k_{w,ij,0} \left(1 + \beta_{per} \langle YI - YI^{thr} \rangle \hat{\varepsilon}_{eq}^3 \right) \qquad \text{(III–118)} \qquad P_r = P_{r,0} \frac{\sqrt[3]{k_0}}{\sqrt[3]{k}} \qquad \text{(III–119)}$$

where $k_{w,ij,0}$ is the initial intrinsic water permeability tensor, β_{per} is an evolution parameter, $\hat{\varepsilon}_{eq}^p$ is taken as the Von Mises' equivalent deviatoric plastic strain, YI is the yield index, YI^{thr} is a threshold value below which there is no intrinsic permeability variation, P_r is the current gas entry pressure, $P_{r,0}$ is the initial value of gas entry pressure, k is the current permeability and k_0 is the initial permeability.

The hydraulic parameters of the COx claystone, reported in Table III–7, are taken from [Pardoen and Collin, 2017], after [Charlier et al., 2013] where a synthesis of the claystone parameters is detailed. The calibration is obtained from laboratory experiments and results, available in the literature.

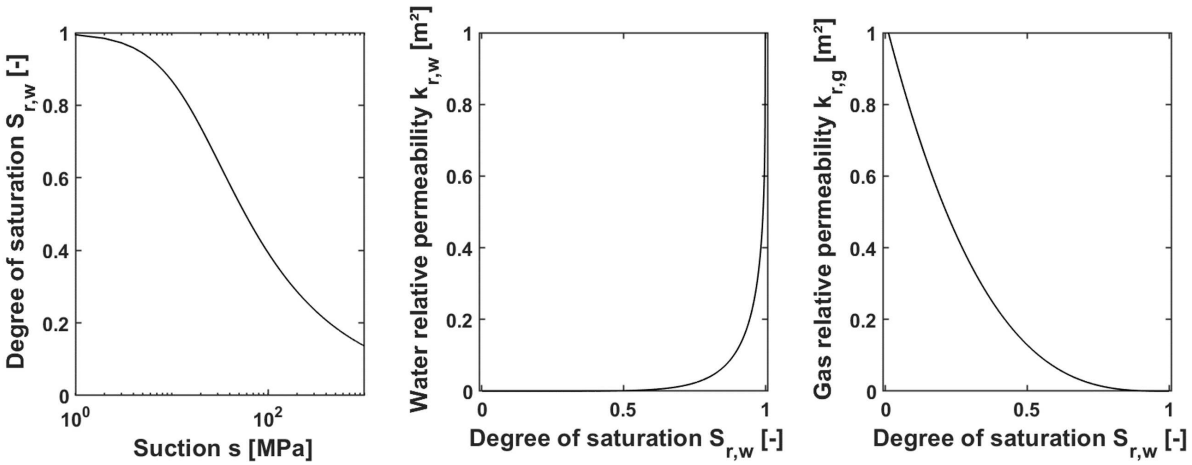

(a) (b) (c)

Figure III–33 – Definition of (a) water retention curve, (b) water relative permeability and (c) gas relative permeability.

10.2.2.4 Effective stress definition

In the context of unsaturated and anisotropic material dealing with water and gas, Bishop's formulation of effective stresses presented in Equation (II–92) is used. In this expression, the Biot's tensor is expressed in orthotropic axes according to Equation (II–93). The prescribed values of parallel and perpendicular Biot's coefficients for the COx claystone are respectively given by $b_{\parallel} = 0.6$ and $b_{\perp} = 0.64$.

10.2.2.5 Support behaviour

As exposed in Section 10.2.1, MAVL drifts are reinforced by different layers of support with the aim of avoiding partial collapse of the tunnel during drilling operations and limiting convergence of the surrounding rock. Practically, the classic and compressible stuffing layers have a thickness of 0.15 m and 0.2 m respectively while the arch segments are 0.5 m thick. The concrete arch segments and the classic stuffing layer are characterised by an elasto-plastic mechanical behaviour while the compressible stuffing layer is assumed to have a linear elastic behaviour. The mechanical parameters of the support layers are retrieved from [Andra, 2016, Gerard et al., 2008] and gathered in the first part of Table III–8.

Hydraulically, the same model as for the COx claystone (described in Equations (III–112) to (III–116)) is used for the support, without considering any evolution of hydraulic properties with strain. The specific hydraulic parameters assigned to each layer of the support structure are gathered in the second part of Table III–8.

Table III–5 – Set of COx elasto-plastic mechanical parameters.

	Parameter	Symbol	Value	Unit
Geomechanical	Parallel Young's modulus	$E_{\parallel}$	5	$[GPa]$
	Perpendicular Young's modulus	$E_{\perp}$	4	$[GPa]$
	Poisson's ratio	$\nu_{\parallel\parallel}$	0.24	$[-]$
	Poisson's ratio	$\nu_{\parallel\perp}$	0.325	$[-]$
	Poisson's ratio	$\nu_{\perp\parallel}$	0.26	$[-]$
	Shear modulus	$G_{\parallel\perp} = G_{\perp\parallel}$	1.63	$[GPa]$
	Shear modulus	$G_{\parallel\parallel}$	2.016	$[GPa]$
	Parallel Biot's coefficient	$b_{\parallel}$	0.6	$[-]$
	Perpendicular Biot's coefficient	$b_{\perp}$	0.64	$[-]$
	Solid grain density	ρ_s	2750	$[kg/m^3]$
	Initial cohesion	c_i	4.1 (0°)	$[MPa]$
	Cohesion parameter	A_{11}	0.117	$[-]$
	Cohesion parameter	b_1	14.236	$[-]$
	Ratio of cohesion softening	ξ_c	5	$[-]$
	Cohesion softening parameter	B_c	0.003	$[-]$
	Initial compressive friction angle	$\varphi_{c,0}$	10	[°]
	Final compressive friction angle	$\varphi_{c,f}$	23	[°]
	Initial extensive friction angle	$\varphi_{e,0}$	7	[°]
	Final extensive friction angle	$\varphi_{e,f}$	23	[°]
	Friction angle hardening parameter	B_{φ}	0.001	$[-]$
	Dilatancy angles	$\psi_c = \psi_e$	0.5	[°]
Microstructure	Second gradient elastic modulus	D	14.016	$[kN]$

Table III–6 – Set of COx visco-plastic mechanical parameters.

	Parameter	Symbol	Value	Unit
Viscoplastic	Uniaxial compressive strength	R_c	21	$[MPa]$
	Internal friction coefficient	A^{vp}	2.62	$[-]$
	Cohesion coefficient	C^{vp}	0.03	$[-]$
	Visco-plastic potential parameter	β^{vp}	1.1	$[-]$
	Initial threshold for the VP flow	α_0^{vp}	0.142	$[-]$
	Reference fluidity	γ_0	700	$[s^{-1}]$
	Temperature parameter	γ_1	57×10^3	$[J/mol]$
	Creep curve shape parameter	$\mathcal{N}$	5.0	$[-]$
	VP hardening function parameter	B^{vp}	7.5×10^{-2}	$[-]$

Table III–7 – Set of COx hydraulic parameters.

	Parameter	Symbol	Value	Unit
Hydraulic	Initial porosity	n	0.173	$[-]$
	Initial parallel intrinsic permeability	$k_{w,\parallel,0}$	4×10^{-20}	$[m^2]$
	Initial perp. intrinsic permeability	$k_{w,\perp,0}$	1.33×10^{-20}	$[m^2]$
	Water density	ρ_w	1000	$[kg/m^3]$
	H_2 density	ρ_{H2}	0.0794	$[kg/m^3]$
	Water dynamic viscosity	μ_w	0.001	$[Pa.s]$
	H_2 dynamic viscosity	μ_{H2}	9×10^{-6}	$[Pa.s]$
	Water compressibility	χ_w^{-1}	5×10^{-10}	$[Pa^{-1}]$
	H_2 Henry coefficient	H_i	0.0193	$[-]$
	Air entry pressure (1^{st} coeff. of S_r^w)	P_r	15	$[MPa]$
	Parameter (2^{nd} coeff. of S_r^w)	$\mathcal{F}$	1.49	$[-]$
	Parameter (1^{st} coeff. of $k_{r,w}$)	$\mathcal{M}$	0.32886	$[-]$
	Max. degree of water saturation	S_{max}	1	$[-]$
	Residual degree of water saturation	S_{res}	0.01	$[-]$
	Evolution parameter	β_{perm}	10^{10}	$[-]$
	Permeability variation threshold	ε_{eq}^{thr}	0.01	$[-]$
	Tortuosity	τ	0.25	$[-]$

Table III–8 – Set of parameters used in the different constitutive laws of the sustaining structure: classic stuffing, compressible stuffing and arch segments.

	Parameter	Symbol	Value	Unit
Classic Stuffing	Elastic Young's modulus	E	17.5	$[GPa]$
	Poisson'ratio	ν	0.25	$[-]$
	Friction angle	φ	30	$[°]$
	Cohesion	c	2.94	$[MPa]$
	Density	ρ	2300	$[\frac{kg}{m^3}]$
Compressible stuffing	Elastic Young's modulus	E	0.1	$[GPa]$
	Poisson's ratio	ν	0.0	$[-]$
	Density	ρ	2300	$[\frac{kg}{m^3}]$
Arch segments	Elastic Young's modulus	E	39	$[GPa]$
	Poisson's ratio	ν	0.2	$[-]$
	Friction angle	φ	38	$[°]$
	Cohesion	c	14.6	$[MPa]$
	Density	ρ	2650	$[\frac{kg}{m^3}]$
Classic Stuffing	Initial porosity	n	0.25	$[-]$
	Initial parallel intrinsic permeability	$k_{w,\parallel,0}$	10^{-15}	$[m^2]$
	Initial perp. intrinsic permeability	$k_{w,\perp,0}$	10^{-15}	$[m^2]$
	Air entry pressure (1^{st} coeff. of S_r^w)	P_r	1	$[MPa]$
	Parameter (2^{nd} coeff. of S_r^w)	$\mathcal{G}$	1.54	$[-]$
	Parameter (1^{st} coeff. of $k_{r,w}$)	$\mathcal{F}$	0.3507	$[-]$
	Max. degree of water saturation	S_{max}	1	$[-]$
	Residual degree of water saturation	S_{res}	0.01	$[-]$
	Tortuosity	τ	0.25	$[-]$
Compressible Stuffing	Initial porosity	n	0.5	$[-]$
	Initial parallel intrinsic permeability	$k_{w,\parallel,0}$	10^{-10}	$[m^2]$
	Initial perp. intrinsic permeability	$k_{w,\perp,0}$	10^{-10}	$[m^2]$
	Air entry pressure (1^{st} coeff. of S_r^w)	P_r	0.2	$[MPa]$
	Parameter (2^{nd} coeff. of S_r^w)	$\mathcal{G}$	1.54	$[-]$
	Parameter (1^{st} coeff. of $k_{r,w}$)	$\mathcal{F}$	0.3507	$[-]$
	Max. degree of water saturation	S_{max}	1	$[-]$
	Residual degree of water saturation	S_{res}	0.01	$[-]$
	Tortuosity	τ	0.25	$[-]$
Arch Segments	Initial porosity	n	0.15	$[-]$
	Initial parallel intrinsic permeability	$k_{w,\parallel,0}$	10^{-18}	$[m^2]$
	Initial perp. intrinsic permeability	$k_{w,\perp,0}$	10^{-18}	$[m^2]$
	Air entry pressure (1^{st} coeff. of S_r^w)	P_r	5	$[MPa]$
	Parameter (2^{nd} coeff. of S_r^w)	$\mathcal{G}$	1.54	$[-]$
	Parameter (1^{st} coeff. of $k_{r,w}$)	$\mathcal{F}$	0.3507	$[-]$
	Max. degree of water saturation	S_{max}	1	$[-]$
	Residual degree of water saturation	S_{res}	0.01	$[-]$
	Tortuosity	τ	0.25	$[-]$

10.2.3 Results and discussion

To emphasize the effect of the EDZ on gas migrations, three modelling cases are investigated. In the first reference simulation, the development of the EDZ is supposed to induce no alteration of the hydraulic properties in this zone. In the two subsequent simulations, the enhanced couplings between fluids transfers (water and gas) and the mechanical behaviour of the fractured zone are progressively activated. First, a strain-dependent evolution of the material intrinsic permeability is envisaged, subsequently enriched by the modification of the water retention property with the deformation.

Various numerical results computed with the LAGAMINE code are presented and analysed hereafter for the studied section and in terms of temporal evolutions in selected points of this section (Figure III–34).

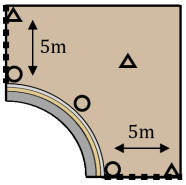

Figure III–34 – Definition of cross-section and observation points for the results.

10.2.3.1 Reference simulation

The first performed simulation focuses on the development of the EDZ following the drilling process. The main purpose is to characterise the extent of fractures induced by rock deconfinement during the excavation phase. These fractures are reproduced by shear banding and no modification of the hydraulic properties in the damaged zone is taken into account in this preliminary simulation. Analysing first the results in terms of convergence in Figure III–35 offers a good overview of the drift behaviour throughout the simulations. For the considered drift, most part of the short-term radial displacement is due to the excavation process and the remainder of the displacement comes from the initiation of the ventilation phase. Viscosity is responsible of the long-term convergence of the system in Figure III–35b. Once the stress imposed by ventilation is released and gas starts to be injected, the system progressively reconfines, leaving a residual radial displacement. This displacement is not uniform over the circumference because of inherent anisotropies and stress redistribution. Time captures of the increments of vertical and horizontal displacements at the end of the excavation are given in Figure III–36, which confirms a slightly more important convergence vertically.

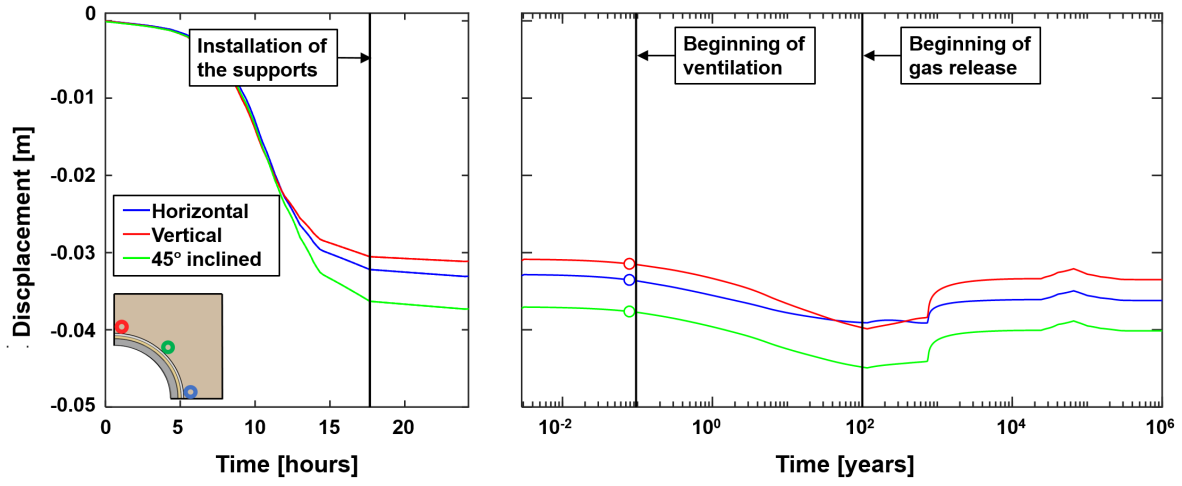

(a) Excavation phase

(b) Ventilation and gas migration phases

Figure III–35 – Long-term convergence induced by the successive phases of the simulation.

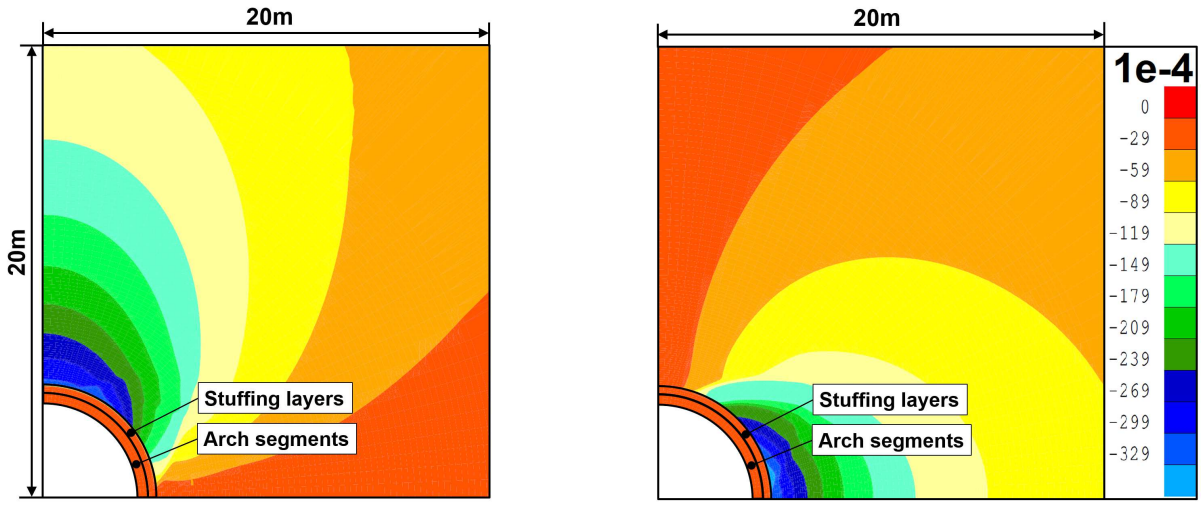

(a) Δy (b) Δx

Figure III–36 – Variation of (a) vertical and (b) horizontal displacements at the end of the excavation.

The creation and evolution of the fractured zone can then be observed through the evolution of the shear strain localisation. The numerical results are presented in terms of Von Mises' equivalent deviatoric total strain (total deviatoric strain), the plastic zone, i.e. the plastic loading integration points (red squares), and the deviatoric strain increment, which represents the shear band activity:

$$\kappa_{eq} = \frac{\dot{\hat{\varepsilon}}_{eq} dt}{\int \dot{\hat{\varepsilon}}_{eq} dt} \tag{III–120}$$

where κ_{eq} is the deviatoric strain increment, $\hat{\varepsilon}_{eq} = \sqrt{\frac{2}{3}\hat{\varepsilon}_{ij}\hat{\varepsilon}_{ij}}$ is the total deviatoric strain, and $\hat{\varepsilon}_{ij} = \varepsilon_{ij} - \frac{\varepsilon_{kk}}{3}\delta_{ij}$ is the deviatoric part of the strain tensor.

As previously exposed in this chapter, a second gradient model is used to guarantee the mesh-independence of the strain localisation process. In particular, the second gradient mechanical law (III–34) incorporates one constitutive elastic modulus D which represents the microstructure and characterises the internal length scale. This aspect is highlighted in Figures III–37b and III–37c which represent the development of the damaged zone considering the selected value of $D = 15000N$ and a value ten times higher. These results give a good insight into the role of the second gradient elastic modulus in the proper representation of the shear bands and in the control of the band width. In addition, Figures III–37a and III–37b show good agreement in the development of the fracture pattern, whether the coupled local second gradient model [Pardoen et al., 2015b] is used or the H^2M upgrade accounting for variable gas pressure. If an overestimated value of D is considered, there are so many Gauss integration points falling into the plastic domain compared to the discretisation of the mesh that it is not possible to precisely discern the location of the shear bands. On the contrary, for the selected value of D it appears that at least three elements compose the shear band width, which is somehow recommended from a modelling point of view, to obtain a good numerical precision of the post-plastic behaviour within the band [Bésuelle et al., 2006].

From previous analyses [Pardoen et al., 2015b], it has been demonstrated that results from a quarter of a drift can be extrapolated to the full section drift provided that the specific second gradient boundary condition is well used [Zervos et al., 2001]. Hence, Figure III–39 illustrates the creation of the fractured zone through the evolution of strain localisation around a full storage drift in the course of the excavation process. During the first part of the drilling, the deformation develops homogeneously around the drift. Then, the growth of a clear and well-constructed shear band pattern starts by the end of the deconfine-

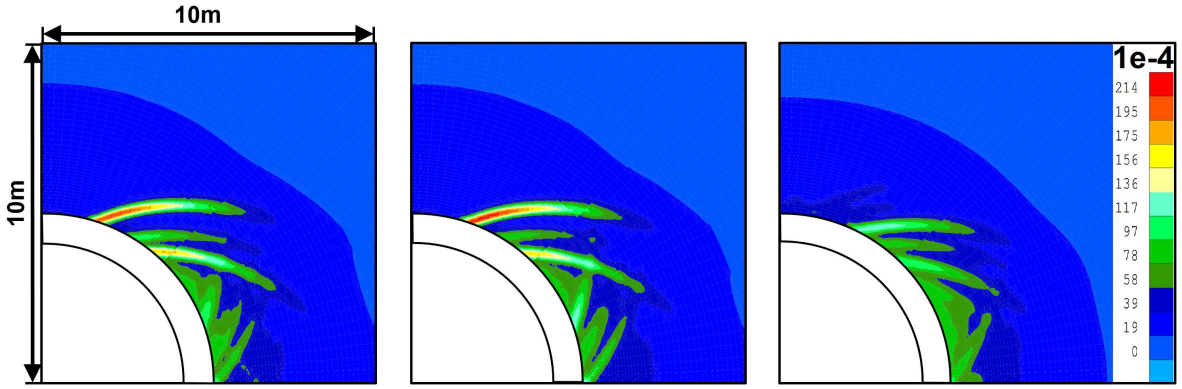

(a) HM model (b) H^2M model (c) H^2M model (10 × D)

Figure III–37 – Development of the damaged zone by the end of the excavation considering (a) HM model and (b)-(c) H^2M model with different values of the second gradient elastic modulus D.

ment. The complete formation of the shear bands happens at about 96% deconfining, just before the installation of the support layers. The strain localisation initiates in the zone under plastic loading that appears in the vicinity of the storage drift. The onset and shape of this strain localisation zone can be attributed to the anisotropy of the material as well as of the initial stress state [Pardoen et al., 2015b]. Since this initial stress state is not perfectly isotropic, the plastic zone appears to extent preferentially in the direction of the minor principal stress, namely horizontally. Within this fractured zone, shear bands initiate primarily from lateral edges of the tunnel. This preferential development of shear bands can be related to the evolution of cohesion around the drift [Pardoen and Collin, 2017], as presented in Figure III–38. Due to the loading evolution engendered by the drilling, cohesion softening occurs at the drift wall. This decrease in cohesion is more pronounced in the horizontal direction than in the vertical one. It tends to trigger the appearance of shear bands in this direction since the strength of the material is the lowest in this zone. By the end of the excavation process, the plastic zone has expanded over 7 m in the horizontal direction and 5m in the vertical direction. Compared to the case of an unsupported drilling process, the installation of the support has the consequences of limiting the points in plastic charge and inhibiting any further development of localisation.

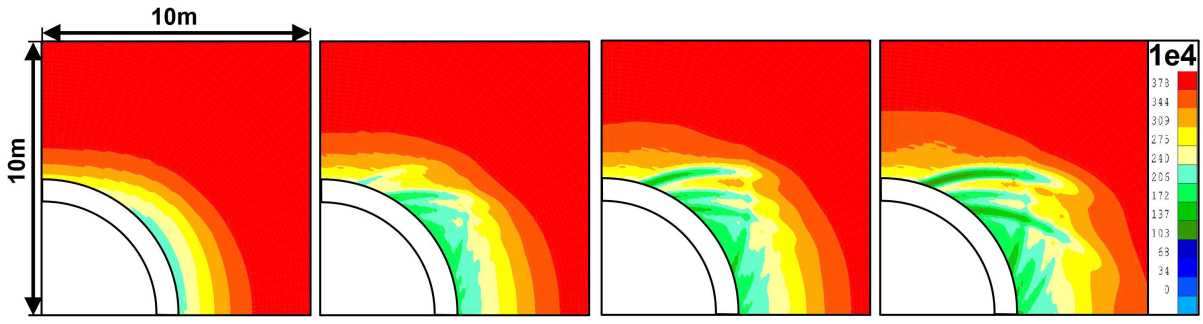

(a) 80% (b) 90% (c) 92.5% (d) 95.5%

Figure III–38 – Evolution of cohesion during the excavation process.

In the following, various numerical results are presented to emphasize the influence of the drift air ventilation. First, the time evolution of pore water pressure close to the drift wall is exhibited in Figure III–40. These curves details the progressive update in water pressures from the initial condition of p_w = 4.7 MPa to the atmospheric pressure imposed by the deconfinement during the excavation and then up to p_w = -35 MPa during the ventilation. As expected, the effect of the suction imposed at the intrados of the

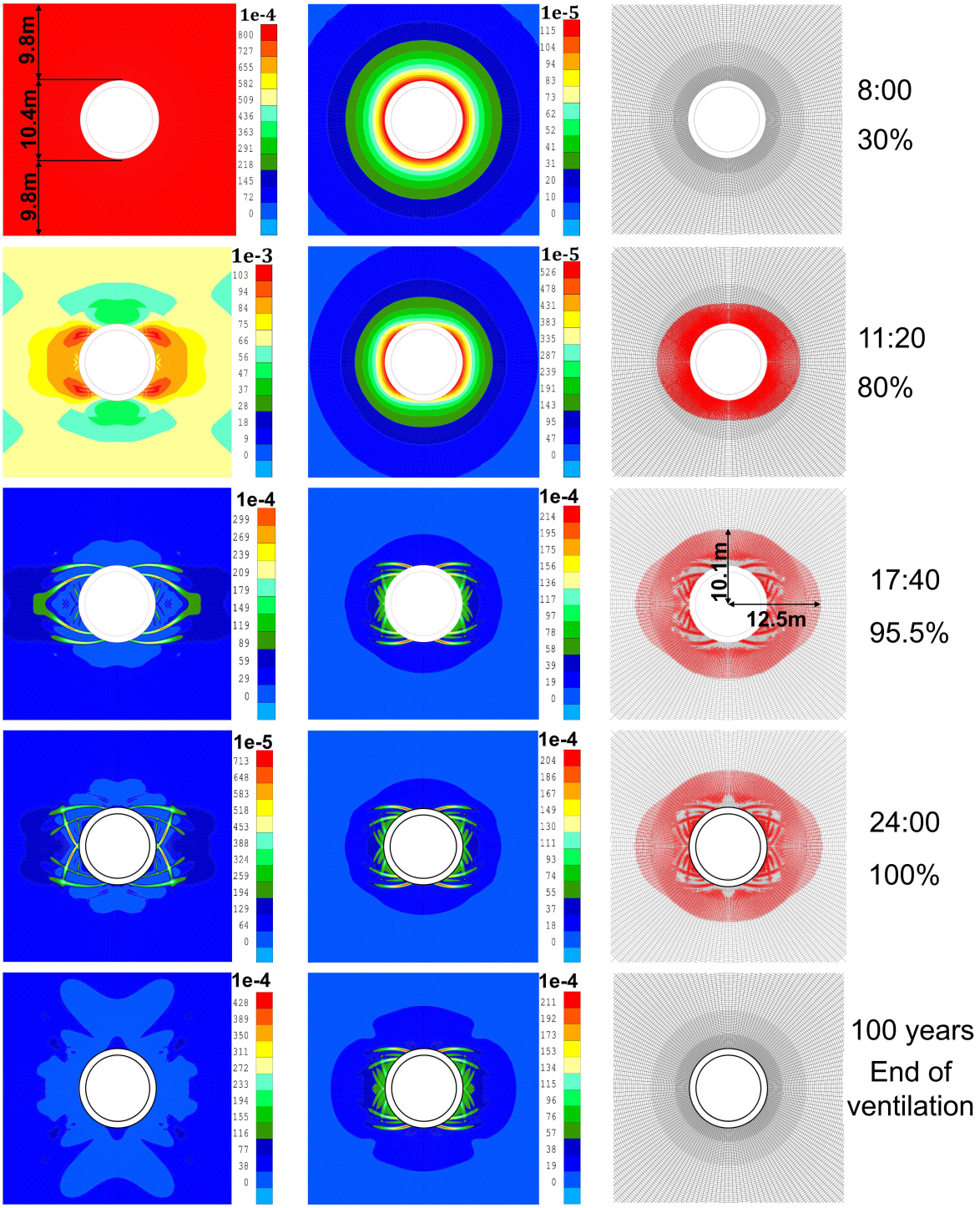

Figure III–39 – Development of shear bands during the excavation process: (a) deviatoric strain increment, (b) total deviatoric strain and (c) plastic loading points.

drift is highlighted by the progressive drainage of the rock mass, which tends to propagate further in the horizontal direction due to the anisotropy of permeability ($k_{w,\parallel,0} > k_{w,\perp,0}$ in Table III–7). This drainage is delayed by the concrete layer that acts as a buffer because of its low transfer properties.

In parallel, the time evolution of the water degree of saturation in the vicinity of the drift wall is illustrated in Figure III–41. During the excavation, the claystone remains almost fully saturated, while a

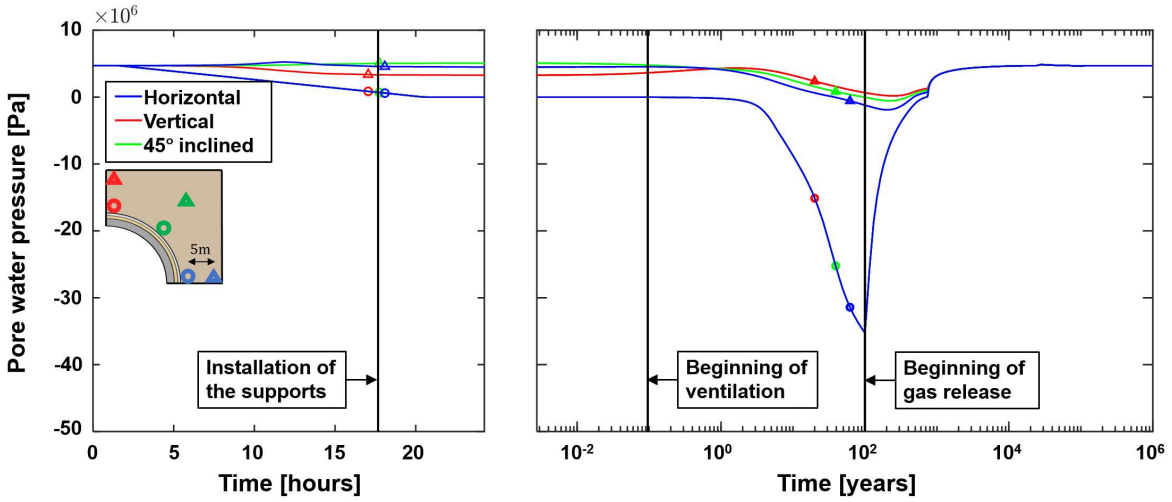

(a) Excavation phase (b) Ventilation and gas migration phases

Figure III–40 – Time evolution of pore water pressure during the successive phases of the simulation, for the reference simulation.

significant reduction of the saturation appears throughout the phase of ventilation, resulting in a partially saturated zone over a distance of approximately 5 m in the rock. This strong desaturation observed close to the support is also consistent with the values of saturation given by the water retention curve III–33a for the evolution of suction displayed in Figure III–40b.

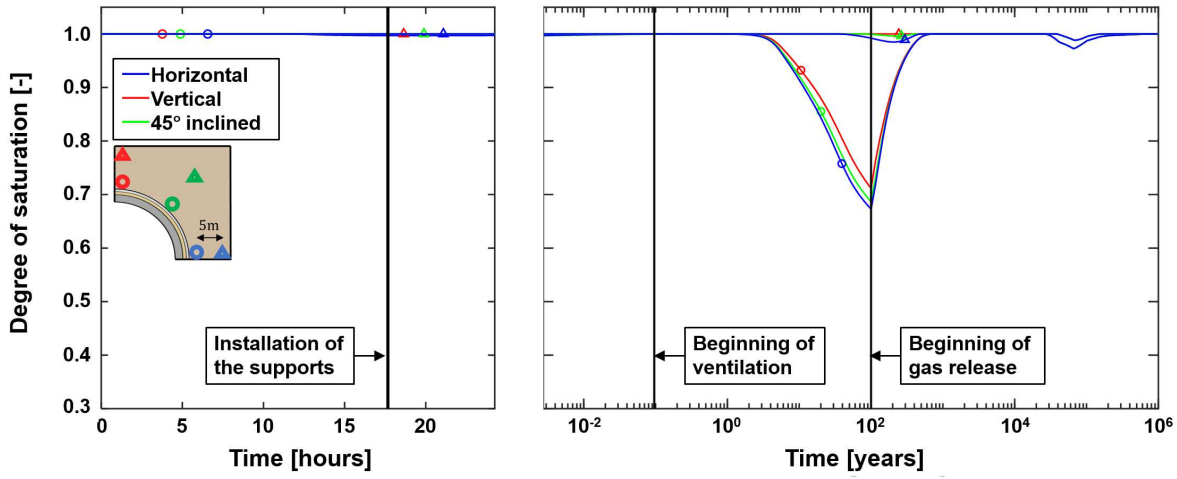

(a) Excavation phase (b) Ventilation and gas migration phases

Figure III–41 – Time evolution of the degree of saturation during the successive phases of the simulation, for the reference case.

Moreover, the drainage of the rock together with the related desaturation around the drift causes the plastic zone to progressively become elastic again as highlighted in Figure III–39 (between 1 day and the end of excavation). Integration points that were under plastic loading are now subjected to elastic unloading. It actually stems from the hydro-mechanical coupling inherent to Bishop's effective stress definition of Equation (II–92). Considering this expression under constant total stress, any decrease in pore water pressure intrinsically implies an increase in the effective stress, which consequently engenders an enhancement of the material strength, *i.e.* a consolidation.

The evolution of effective stresses can be visualised by plotting the stress paths in the drift wall zone, as shown in Figure III–42 where $I_{\sigma'} = \sigma'_{ij}\delta_{ij} = \sigma'_{ii}$ is the first invariant of stresses, $II_{\hat{\sigma}'} = \sqrt{0.5\hat{\sigma}'_{ij}\hat{\sigma}'_{ij}}$ is the second invariant of deviatoric stresses, $\hat{\sigma}'_{ij}$ is the deviatoric part of the effective stress tensor.

In the course of the excavation phase, the radial stress tends to decrease and vanish at the gallery wall while the orthoradial stress is increased. This results in an overall increase in the deviatoric stress invariant until the stress state reaches the plastic criterion. In case of ventilation, an increase in effective stresses and consequently in the first stress invariant is noted around the drift owing to the imposed negative pore water pressure. This coupled response is well reflected in the corresponding stress path at the drift wall but is less discernible further away in the rock mass.

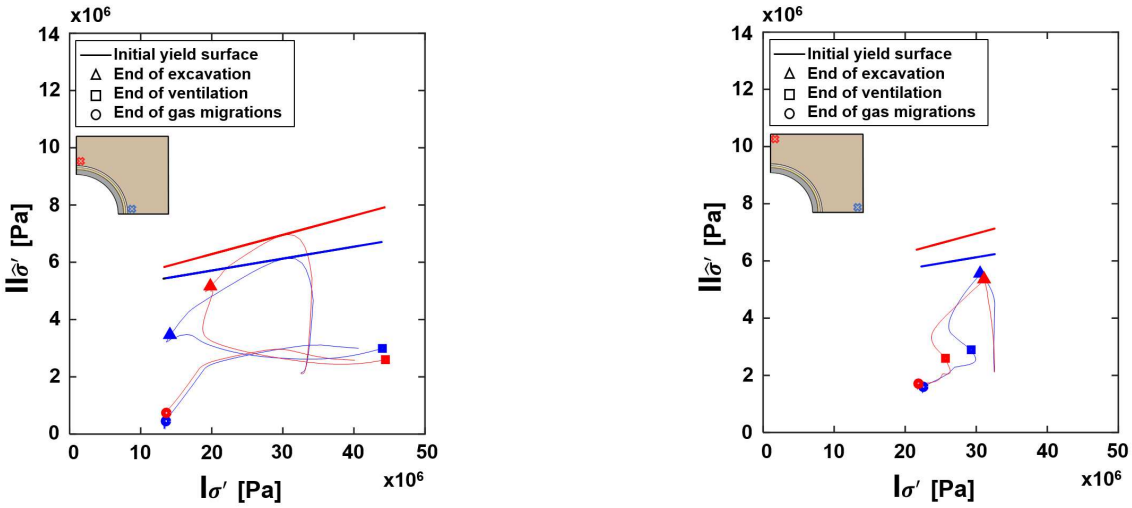

Figure III–42 – Evolution of the stress paths during the simulation: (a) at the drift wall, (b) at a distance of 5m from the drift wall.

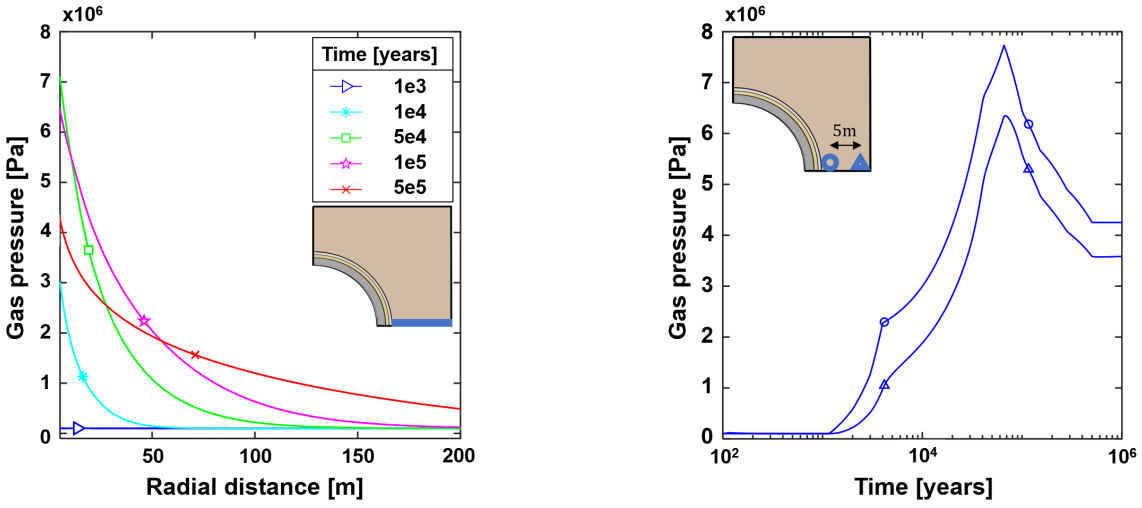

Figure III–43 – Evolution of gas (Hydrogen) pressures (a) over the domain and (b) with time.

Finally, gas transfers in the form of Hydrogen take place in the long-term part of the simulation,

according to the evolution profile given in Section 10.2.1.3. In Figure III–43a, gas pressure profiles are displayed along the horizontal section of the domain, highlighting the progressive propagation of Hydrogen across the rock mass. The temporal evolution of gas pressures in the zone adjacent to the drift wall is presented in Figure III–43b. By referring to the time evolution of water pressure (Figure III–40b), it comes out that the release of Hydrogen materialized by an increase in gas pressure starts after a period of approximately 1000 years when the pore water pressure has almost recovered the initial value of 4.7 MPa. No water overpressure is observed subsequently as a result of this rise in gas pressure.

A maximum gas pressure of about 7.5 MPa is reached at the drift wall after a period of around 60000 years. Referring to the temporal evolution of the water degree of saturation in Figure III–41b points out that a desaturation of a few percent is associated to this peak of Hydrogen pressure. Desaturation profiles in the rock mass are illustrated in Figure III–44b and put into perspective with the dissolved and total Hydrogen flows profiles displayed in Figure III–44a in log scale [Webber, 2013]. Close to the injection zone, it appears that dissolved gas in the water phase is not sufficient enough to ensure transfers of Hydrogen in the claystone rock under the largest Hydrogen production sequences. This quantity of dissolved Hydrogen is indeed physically limited by Henry's law, which leads to the creation of a gaseous phase, and to the desaturation of argillite over a certain radial distance. Since total Hydrogen fluxes decrease with the radial distance, dissolved hydrogen becomes predominant again at the transition between saturated and partially saturated zones.

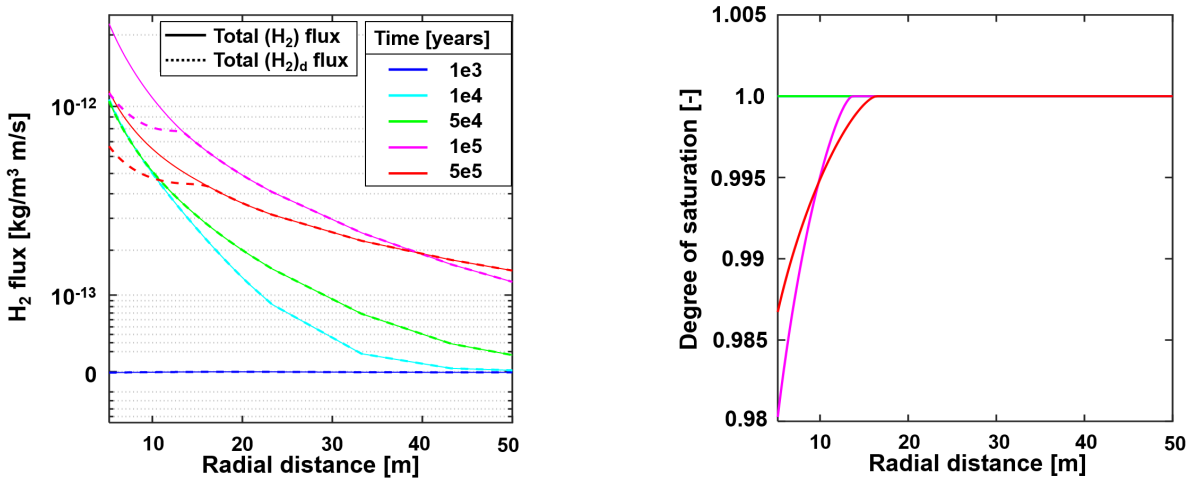

(a) (b)

Figure III–44 – (a) Comparison between dissolved Hydrogen and total Hydrogen flux (log scale along *y*-axis [Webber, 2013]) and (b) corresponding saturation profiles.

10.2.3.2 Evolution of the intrinsic permeability with the deformations

So far, the behaviour of the EDZ has been limited to the development of fractures in the form of shear strain localisation bands. However, this process of fracture generation tends also to substantially affect the flow properties of the *in situ* material. In this second part of the simulations, an advanced coupled hydro-mechanical behaviour of the EDZ is considered in order to end up with a more accurate representation of the phenomena related to gas migration. As detailed in Section 10.2.1, the impact of fracturing on the flow transfer characteristics is addressed by relating the intrinsic permeability evolution with the mechanical deformations according to expression (III–43).

The variations in (parallel and perpendicular) intrinsic water permeabilities around the drift are presented at the end of the excavation process in Figures III–45c and III–45d respectively, and put into perspective with the creation of the plastic zone in Figures III–45a and III–45b. Compared to the results

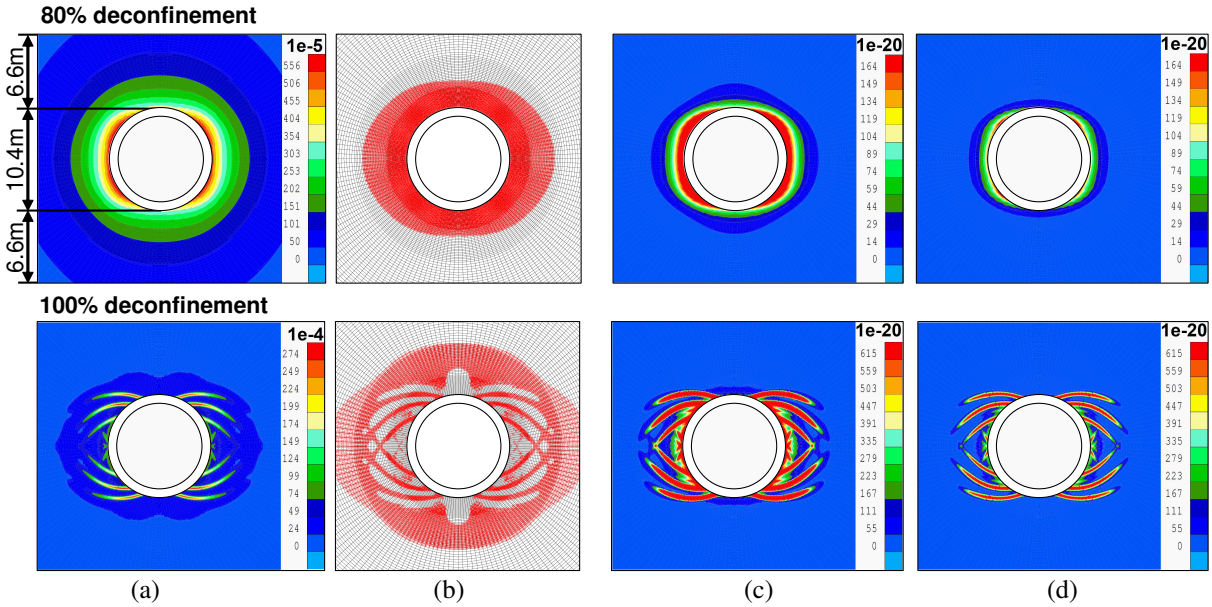

Figure III–45 – Development of shear bands and evolution of water permeability at the end of excavation: (a) total deviatoric strain, (b) plastic loading points, and intrinsic water permeability in the (c) horizontal and (d) vertical directions.

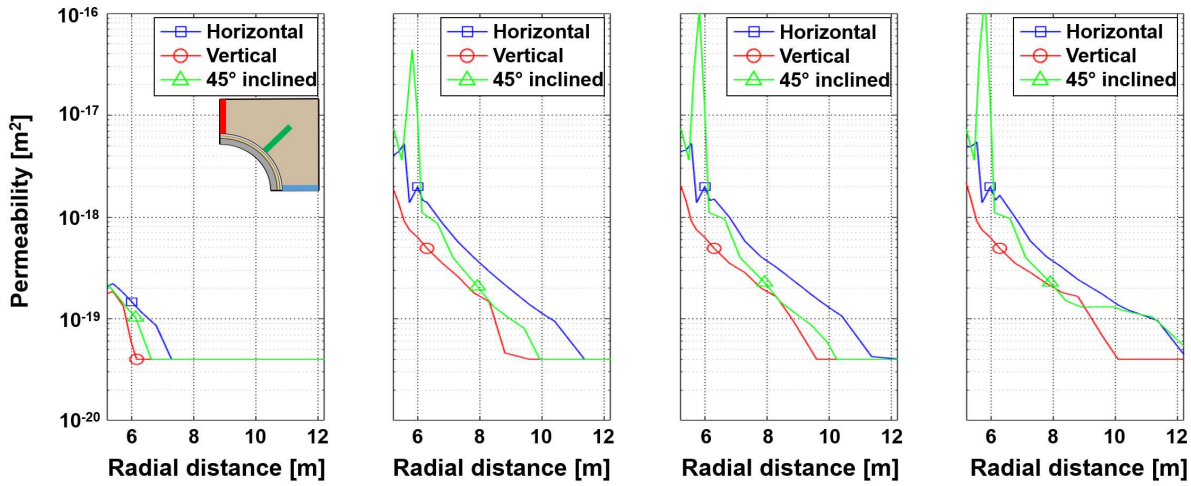

Figure III–46 – Variation of parallel intrinsic permeability $k_{w,\|}$ as a function of the radial distance for different time steps.

obtained for the reference case in Figure III–39, minor differences are noticed in the overall development of the plastic zone. Include a strain-dependent evolution of the intrinsic permeability in the simulation gives rise to additional hydro-mechanical couplings slightly interfering with the initiation of localisation bands that tend to grow preferentially in the horizontal direction. However, the total extent of the EDZ remains all in all identical. Permeability variations are well visible in the part of this damaged zone which is the closest to the drift wall, and more particularly inside the strain localisation discontinuities where a significant increase of several orders of magnitude is obtained. A closer look at the distribution of the parallel intrinsic permeability provided in Figure III–46 confirms a global permeability increase of about two orders of magnitude between the initial and final states of excavation, with permeability peaks

along the diagonal and horizontal profiles because of the presence of shear bands in these directions. It is worth noting that a symmetrical evolution of the perpendicular intrinsic permeability would be obtained since the strain-dependent isotropic expression (III–43) conserves the initial directions of anisotropy and the imposed permeability ratio $\frac{k_{w,\parallel}}{k_{w,\perp}} = 3$.

The effect of permeability variation on the ventilation phase can then be investigated through the temporal evolution of the pore water pressure and of the water degree of saturation close to the drift wall which are depicted in Figures III–47 and III–48. Due to the fact that the water transfer capacity through

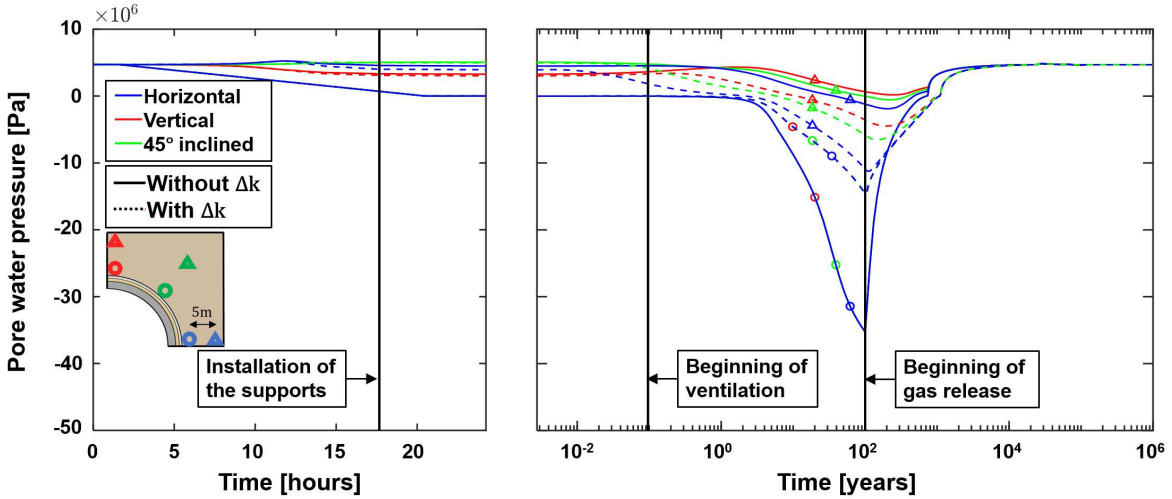

(a) Excavation phase (b) Ventilation and gas migration phases

Figure III–47 – Time evolution of pore water pressure during the successive phases of the simulation, considering a permeability evolution with strain.

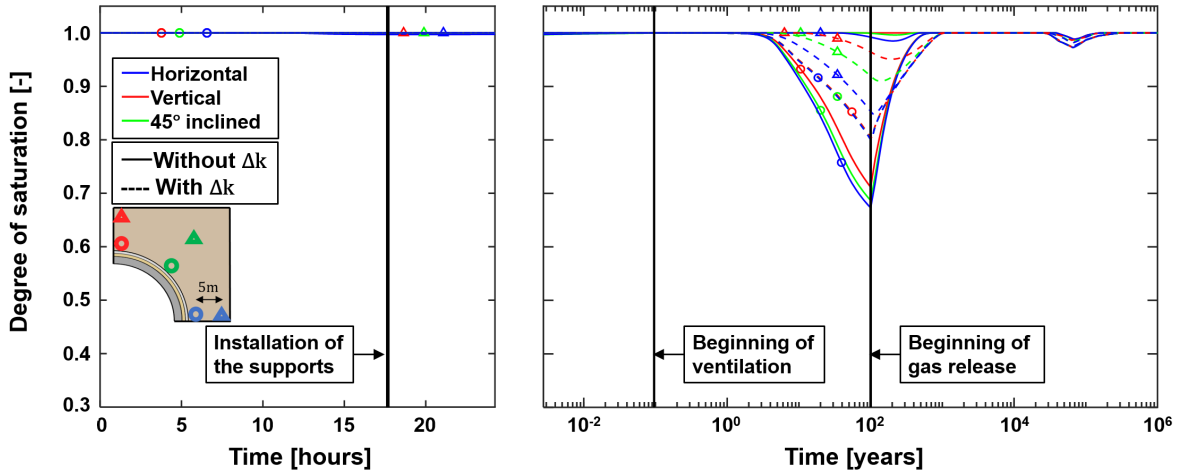

(a) Excavation phase (b) Ventilation and gas migration phases

Figure III–48 – Time evolution of water degree of saturation during the successive phases of the simulation, considering a permeability evolution with strain.

the EDZ has increased, the drainage of the rock mass becomes more gradual in this zone. The diminution of pore water pressures is slower in the vicinity of the drift due to more water inflows. In parallel the effect of the imposed suction is all the more marked further in the EDZ, especially along the horizontal

section given that the plastic zone is more developed in this direction.

With respect to the gas migration phase, the re-establishement of the pore water pressures is also made more progressive, extending the period necessary for the resaturation of the claystone. As a consequence, pore water pressure in the EDZ has not fully returned to its initial state prior to the beginning of gas injection (Figure III–47b). From these first observations, it follows that Hydrogen tends to enter

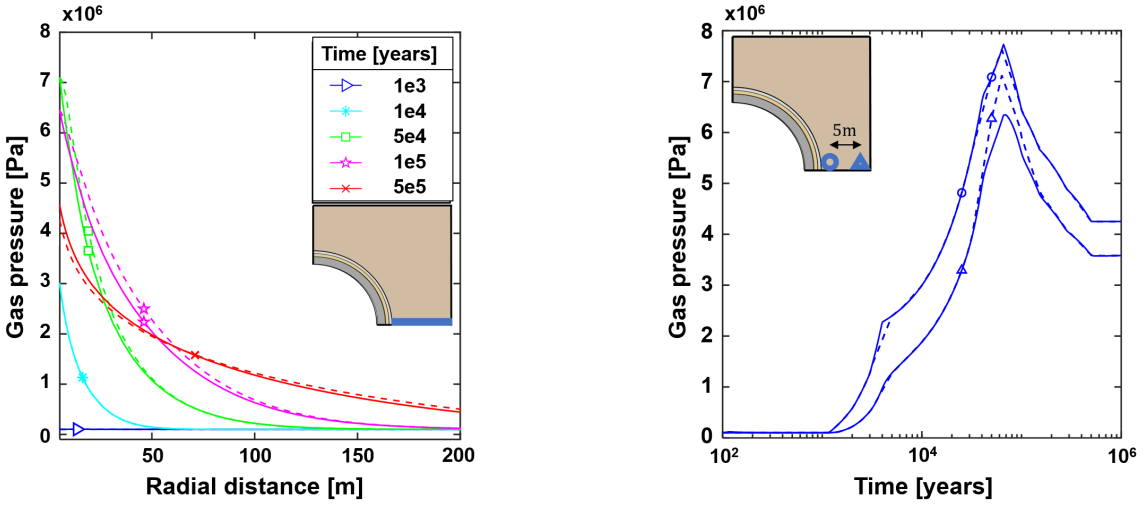

(a) (b)

Figure III–49 – Evolution of gas (Hydrogen) pressures (a) over the domain and (b) over time, considering a permeability evolution with strain.

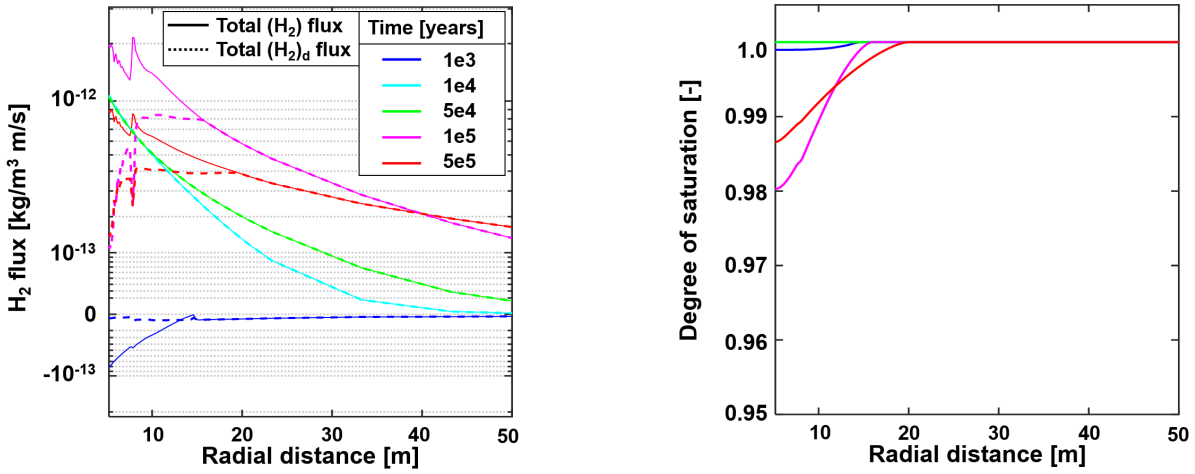

(a) (b)

Figure III–50 – (a) Comparison between dissolved Hydrogen and total Hydrogen flux (log scale along *y*-axis [Webber, 2013]) and (b) corresponding saturation profiles, considering permeability evolution with strain.

the first meters of the rock mass more easily, which is highlighted by a slight horizontal offset of the curves in Figure III–49a and by a rise in the maximum gas pressure reached beyond the EDZ in Figure III–49b. As in the reference case, the analysis of the Hydrogen fluxes shown in Figure III–50 reveals that for the largest amount of Hydrogen, a distinct gas phase appears which desaturates the argillite in

the vicinity of the support. The maps of gas pressures in Figure III–51 corroborate these aspects and show that Hydrogen propagates more efficiently in the EDZ. More specifically, preferential flow paths corresponding to the localised shear bands seem to initiate around the drift due to the high increase in permeability within these discontinuities where the deformation is concentrated.

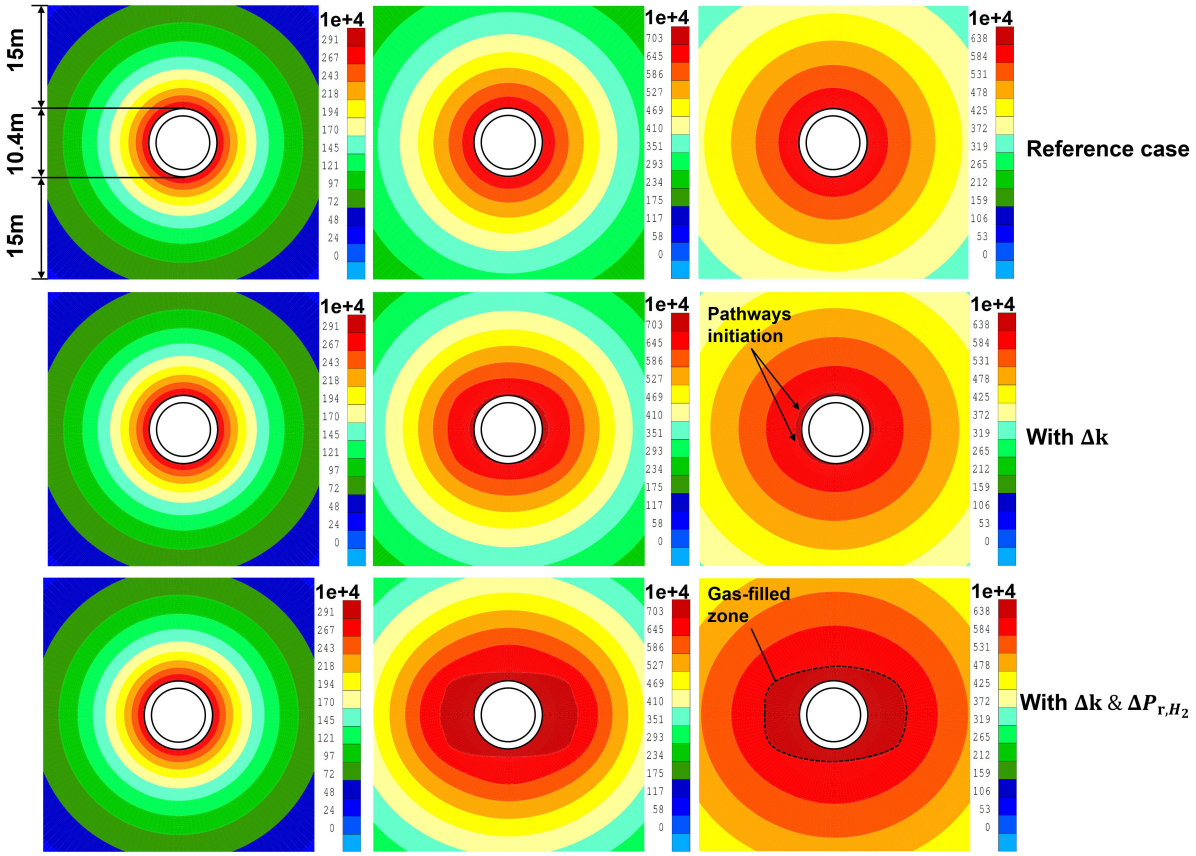

(a) 10 000 years (b) 50 000 years (c) 100 000 years

Figure III–51 – Evolution of gas (Hydrogen) pressure in the vicinity of the gallery wall, for the reference case and considering the HM couplings.

10.2.3.3 Evolution of the retention curve with the deformations

Next to the increase in the hydraulic permeability with strain, an additional HM mechanism is considered in order to obtain a more faithful representation of the influence of the EDZ on the hydraulic kinetics. This second advanced HM coupling concerns the evolution of the water retention curve with strain [Olivella and Alonso, 2008, Gerard et al., 2012]. Indeed, the water retention property of the rock is susceptible to be affected by the modification of the pore network morphology induced by cracking and damage processes. In particular, the increase in pore size following the opening of discontinuities is correlated to the reduction of the gas entry pressure. This feature is integrated into the model thanks to the expression (III–48) given in Section 9.

The evolution of the entry pressure parameter for the Hydrogen P_r is given in Figures III–52 by the end of the excavation and ventilation phases. These results attest of a global drop in P_r in the EDZ, correlated to the evolution of intrinsic permeability previously observed. As for the evolution of the intrinsic permeability displayed in Figure III–46, the influence of shear bands on P_r is also clearly visible.

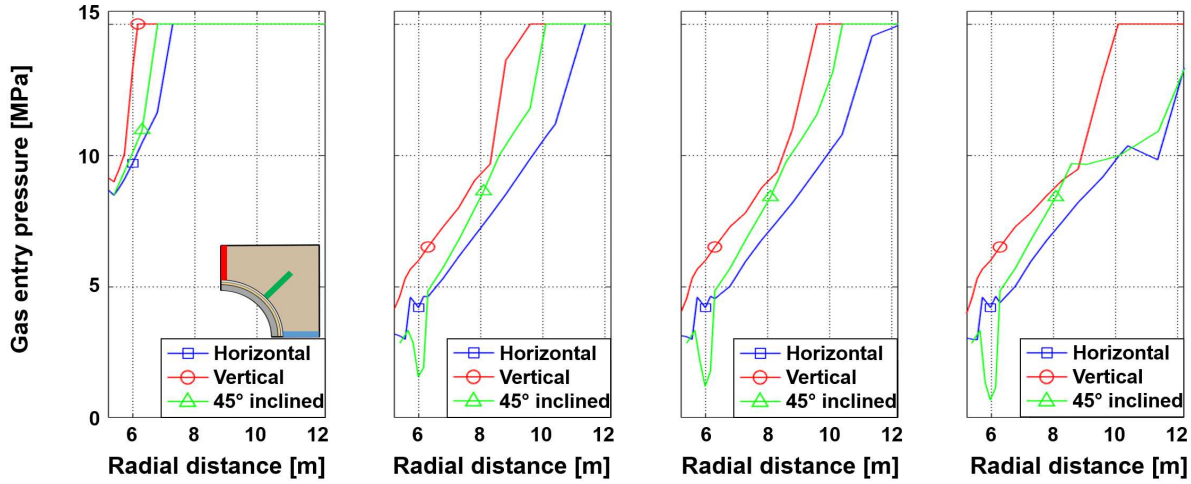

(a) 10h15 (65%) (b) 11h20 (80%) (c) 1 day (100%) (d) 100 years (100%)

Figure III–52 – Variation of gas (Hydrogen) entry pressure P_r as a function of the radial distance for different time steps.

Then, the effect of the evolution of the entry pressure on the ventilation phase is investigated through the temporal evolution of the pore water pressure and of the water degree of saturation close to the drift wall, which are depicted in Figures III–53 and III–54. The Hydrogen entry pressure reduces significantly after damage, which means that the minimum capillary pressure required to desaturate the rock mass is lowered by the cracking process. Under imposed ventilation, a rapid decrease in the water degree of saturation is thus noted. However, the overall water transfer capacity has been enhanced in the EDZ considering the advanced hydro-mechanical couplings, which leads to a more continuous and gradual drainage of the pore water pressure over the entire EDZ compared to the reference case.

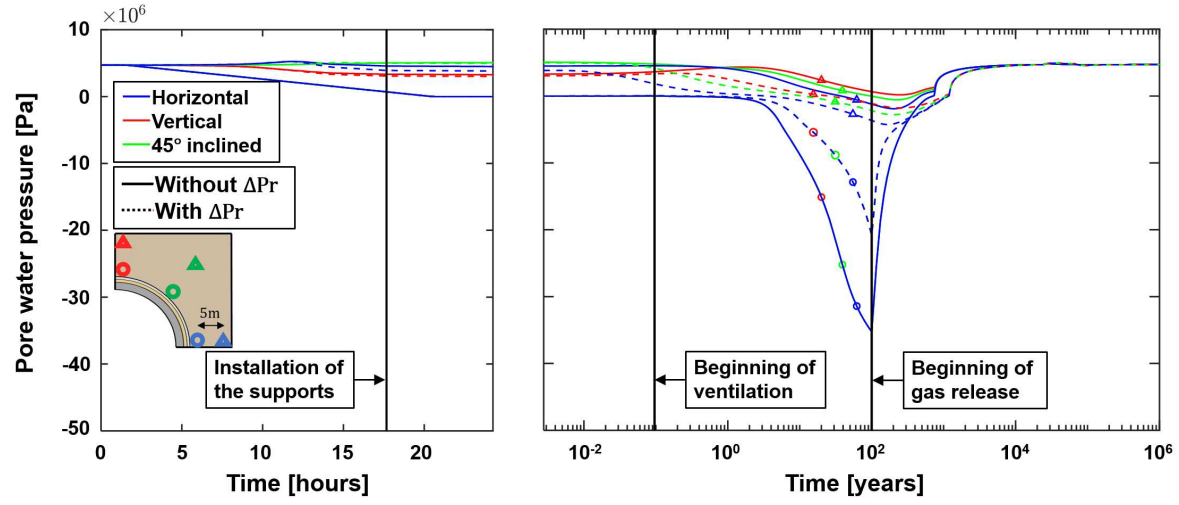

(a) Excavation phase (b) Ventilation and gas migration phases

Figure III–53 – Time evolution of pore water pressure during the successive phases of the simulation, considering an evolution of the retention curve with strain.

Regarding the gas migration phase, it emerges from Figure III–54b that the pore water pressure has almost returned to its initial value, restablishing a fully saturated state in the EDZ (Figure III–53b), prior to the beginning of gas injection. The evolution of the retention curve with the deformations has a clear

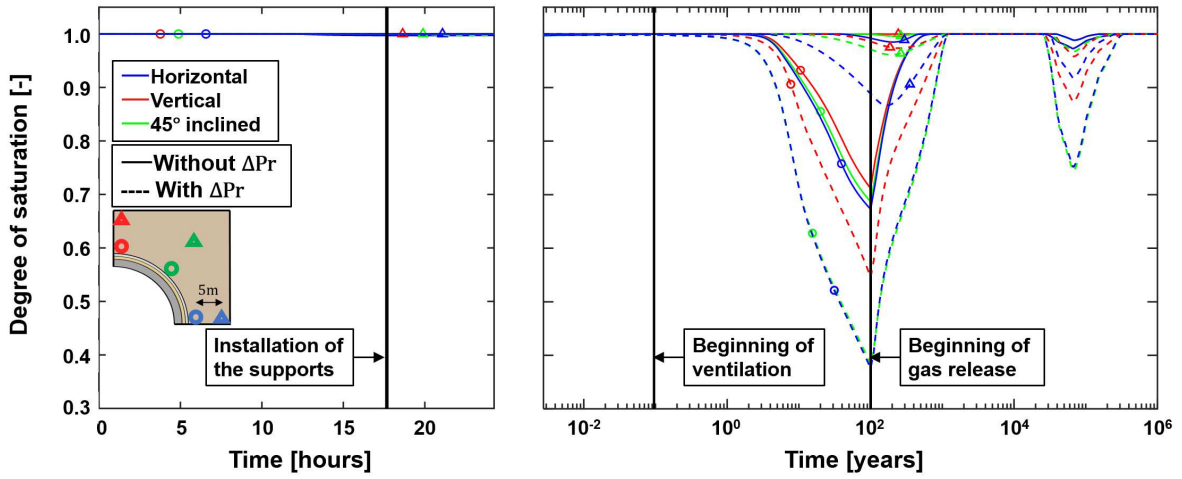

(a) Excavation phase (b) Ventilation and gas migration phases

Figure III–54 – Time evolution of water degree of saturation during the successive phases of the simulation, considering an evolution of the retention curve with strain.

influence on the Hydrogen migrations. The reduction of Hydrogen entry pressure in the EDZ facilitates even more the penetration of gas into the claystone. Once the Hydrogen pressure reaches and exceeds the water pressure set at 4.7 MPa (in the time window between 3×10^4 and 3×10^5 years), gas progresses in the form of a front through the zone affected by a reduction of the gas entry value (Figure III–55a). The maximum gas pressure reached at the limit of the EDZ is then drastically increased as shown in Figure III–55b. The distinct gas phase that emerges when the largest amounts of Hydrogen are released is clearly discernible in Figure III–56a. In the EDZ, Hydrogen is no longer dissolved in water but is almost only transferred in the gaseous state, which contributes to a more rapid and important decrease in the degree of water saturation around the drift than in the previous simulations, as reported in Figure III–56b. All these observations can be further supported with the maps of gas pressures in the vicinity of the drift presented in Figure III–51. The first foreseeable point that can be raised is that Hydrogen propagates

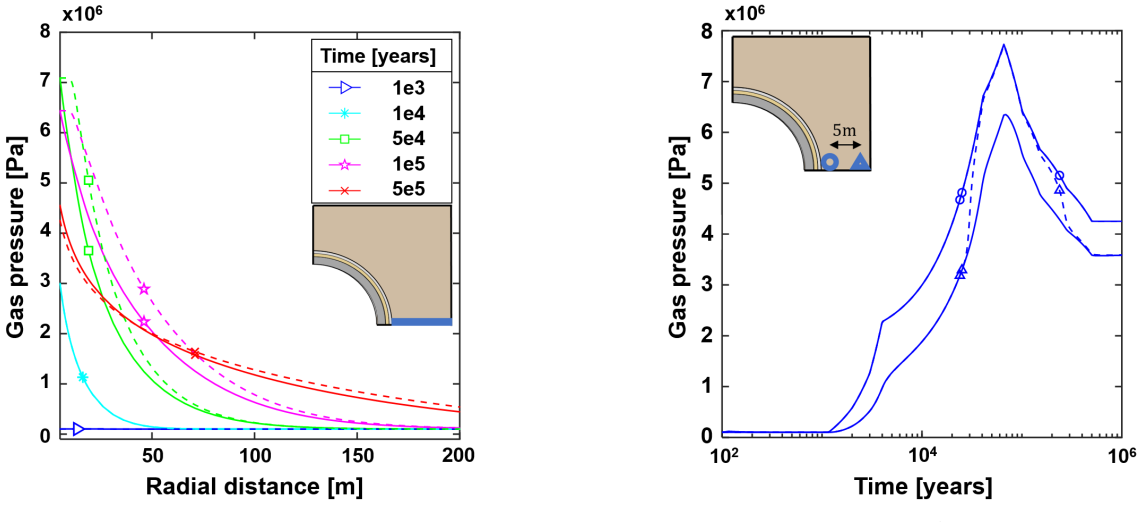

(a) (b)

Figure III–55 – Evolution of gas (Hydrogen) pressures (a) over the domain and (b) over time, considering an evolution of the retention curve with strain.

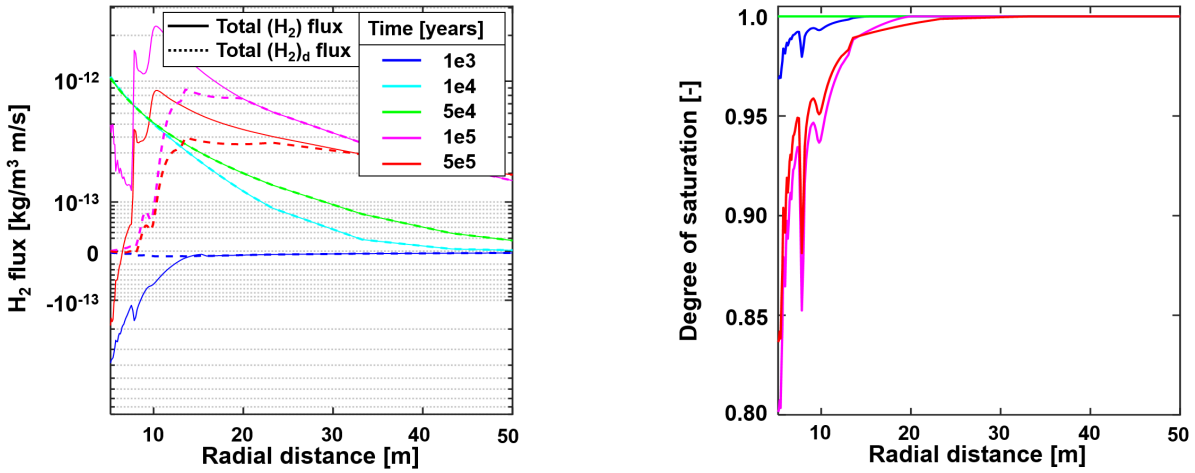

(a) (b)

Figure III–56 – (a) Comparison between dissolved Hydrogen and total Hydrogen flux (log scale along Y-axis [Webber, 2013]) and (b) corresponding saturation profiles, considering an evolution of the retention curve with strain.

easier and faster in that zone compared to the reference case. Moreover, since the cracking process in the EDZ amplifies the desaturation as made explicit in Figure III–54b, one can notice a uniform and rapid increase in gas pressure across the whole EDZ. This gas front propagation attenuates the preferential flow paths along the localised shear bands highlighted in Section 10.2.3.2, as well as band activity reactivation by the end of gas migration phase.

10.2.4 Conclusions

The modelling of a large-scale storage drift has been carried out from excavation stage to gas migration stage, for three configurations including increasing complexity with respect to the HM couplings. The numerical results of these distinct simulations have then been investigated and compared in terms of desaturation and fluid transfers in the excavation damaged zone.

First, a representative characterisation of rock fracturing within the EDZ during the excavation phase has been provided. An important rock desaturation is noted in the fractured zone surrounding the drift during the pore water drainage imposed by the ventilation phase. During the phase of gas injection, it appears that dissolved gas is not sufficient enough to transport Hydrogen under large production of gas. This leads to the creation of a gaseous phase along with the desaturation of the first metres of the rock mass. Concerning the hydro-mechanical couplings that take place in the damaged zone, a permeability increase of several orders of magnitude can be obtained within the shear bands by imposing permeability variations with the localisation effect. This way, faster Hydrogen propagation is observed in the EDZ with evidence of preferential pathway initiation for gas flows within the bands. Introducing the second hydro-mechanical effect in the simulation, which couples water retention property of the rock and damage process, significantly amplifies the desaturation of the rock mass. It consequently results in an even more rapid progression of Hydrogen across the EDZ in the form of a gaseous front. It is worth noting that these coupled effects are globally limited to the EDZ close to the drift wall and tend to attenuate deeper in the rock mass. The conclusion of the performed analysis demonstrates the non-negligible impact of the hydro-mechanical couplings inherent to the EDZ on gas migrations. Incorporate these couplings in the modelling should therefore lead to more realistic and accurate predictions of the long-term behaviour of a deep geological disposal.

Conclusion Part III

The work presented in this part of the thesis is devoted to the numerical analysis of gas transport processes in clay materials and their specific interaction with damaged rock. To that end, a second gradient two-phase flow hydro-mechanical (H^2M) model has been implemented. On the one hand, this model integrates the second gradient theory to properly reproduce the fractures around underground structures with strain localisation in shear band mode. On the other hand, the model incorporates the features of an extended two-phase flow transfer approach in order to deal with the mechanisms inherent to gas migrations. On top of that, specific coupled effects of the mechanical deformations on fluids transport properties like the intrinsic permeability and the retention behaviour have been taken into account, to better apprehend the impact of the excavation damaged zone on gas transport.

After the description of the equations implemented in the finite element code, the model has been applied to a set of field-scale gas injection tests conducted in Boom Clay and to a large-scale case study, dealing with a MAVL storage drift drilled in the Callovo-Oxfordian claystone. Complete constitutive hydro-mechanical models encompassing (visco-)plastic effects have been employed to reproduce the behaviour of these low-permeable rocks. The use of the second gradient strategy makes it possible to obtain a proper and representative reproduction of the pattern and extent of the fractures surrounding the excavations in the different cases. The real emphasis of these simulations is on the non-negligible

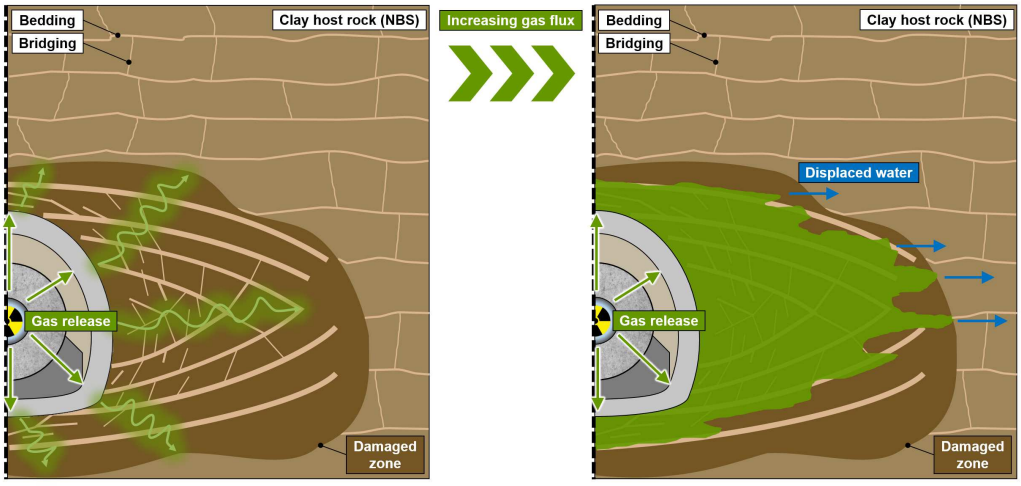

(a) (b)

Figure III–57 – Schematic representation of the expected gas flow regimes from a disposal gallery to the EDZ: (a) Advection and diffusion of dissolved gas, (b) Visco-capillary two-phase flow. *Inspired from* [Levasseur et al., 2024].

impact of the hydro-mechanical couplings inherent to this damaged zone on gas transport processes. For this purpose, two HM interactions, which aim at coupling the intrinsic permeability and the retention property of the rock to the deformations have been introduced in the numerical modelling. In this way,

the model has demonstrated the ability to replicate not only the slow background process of gas transport by diffusion, but also the faster propagation of gas in the form of a gaseous front throughout the entire EDZ for the largest gas production sequences (Figure III–51). This transition between the two modes of gas transfer is all the more operating in the large-scale modelling of a storage drift, where a larger EDZ develops with much more affected transfer properties than in the case of smaller *in situ* piezometers with a limited damaged zone. In both cases, these mechanisms are restricted to the EDZ and tend to attenuate deeper in the undisturbed rock mass.

In this way, the performed numerical analysis is in line with the current state of knowledge of gas impact at repository scale. Indeed, it is accepted that the diffusion of dissolved gas in water-saturated clay is certain to occur but with a limited capacity of gas transfer. In parallel, it is also expected that visco-capillary two-phase flow of water and gas will be mainly located within the EDZ and its discontinuities. Since the developed numerical tool is able to replicate these two mechanisms of gas flow from a storage gallery to a clayey host rock with an EDZ (Figures III–57a and III–57b respectively), it should therefore help converging to more realistic and accurate predictions of the long-term integrity of the geological barrier. Nevetheless, some uncertainties remain in the simulations and are reflected in the ranges adopted for the values of the leading parameters, namely permeability and gas entry pressure, in the visco-capillary two-phase flow model [Corman et al., 2022].

With respect to the mechanically undisturbed host formation, there is no clear evidence for significant visco-capillary two-phase flow, and gas transport will primarily occur through the creation of gas-specific pathways. Attempting to numerically reproduce the activation and development of such a mechanism is the objective of the next Part IV of the work.

Part IV

Modelling gas transport in sound rocks

Introduction Part IV

It is now well established that local gas-specific pathway can form in clay-rich materials when the initially water-saturated clay barrier is exposed to pressurised gas that cannot migrate by the visco-capillary two-phase flow mechanism. The initiation and propagation of these preferential gas pathways exploit the weakest zones of the system, at the interfaces between the engineered and natural components, caused by previously damaged zones of increased permeability around excavations, or inherent to the rock, such as bedding planes, low-density zones, or rock discontinuities. Such zones are characterised by abrupt changes in stiffness and material strength together with localised changes in microstructure, and represent a very small, but well connected fraction of the total pore volume. The process of opening discrete pathways is therefore very sensitive to the HM couplings between the deformation response and the gas pressure build-up, and can lead to undesired variations in the favourable containment properties of the host rock, which could alter the overall integrity of the barrier.

This part of the thesis presents a multi-scale HM model that combines the advantages of both small-scale and large-scale modelling strategies to reproduce macroscopic gas flow mechanisms in sound rock layers that could be enhanced by hydro-mechanical interactions affecting the microstructural constituents of the medium. This approach is based on the concept of Representative Element Volume (REV), which is introduced to computationally decouple the large-scale medium from the small-scale phenomena [Smit et al., 1998]. In the model, the definition of the REV is supported by experimental data [Gonzalez-Blanco et al., 2016] as exemplified in Figure IV–1, and provides a faithful representation of the behaviour of the microstructural components. This micro-scale HM constitutive model for partially saturated clay materials is integrated into a multi-scale scheme using homogenisation and localisation equations for the transition from one scale to the other [Kouznetsova et al., 2001], thus avoiding the use of some macro-scale constitutive equations, while ensuring the modelling of lab-scale gas injection tests and pathway propagation at intermediate scales.

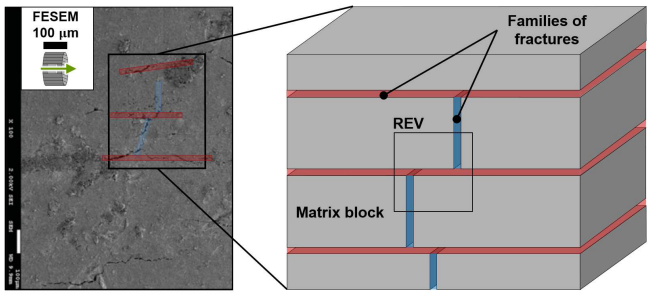

Figure IV–1 – Idealisation of the material microstructure and definition of the REV from experimental data, *from* [Gonzalez-Blanco et al., 2016].

This part is divided into three main sections. The first one describes the main steps of a multi-scale modelling approach in a general way, and how it is applicable to the study of gas transport processes. The second section presents the development and the implementation of the hydro-mechanical double-scale model. The final chapter deals with applications of this model to specific gas injection tests in Boom Clay, and to more general and up-scaled configurations.

11. Multi-scale modelling approach

The aim of this chapter is to summarise the multi-scale modelling approach that is used to elaborate a multi-scale HM model in the following chapter. Firstly, a general description of the principle and key steps involved in this method are provided. Then, the advantages of selecting such an approach when dealing with gas flows in clay materials is outlined. Finally, this section reviews the current status of multi-scale modelling strategies to establish the starting point of the proposed numerical tool.

11.1 Description of the multi-scale approach

Argillaceous rocks, such as the Boom Clay and the Callovo-Oxfordian claystone belong to materials with microstructure, which means that the macroscopic behaviour has its origin notably in the interaction of its micro-mechanical constituents, such as sheets, particles or grains. For the type of multi-physics problems involving gas flows that is under study, different scaling approaches can be envisaged to couple the modelling of the macroscopic behaviour of the rock with the microscopic effects:

- **The microscopic approach**: The modelling is performed at the scale of the material microstructure ($< \mu m$). At this side of the spectrum, the adopted numerical approach would ideally detail the material microstructure with separate descriptions of each of its constituents with their own constitutive equations [Yu et al., 2019]. Although this direct modelling of the entire (micro-)structure using sub-scale models shows some usefulness to study fundamental processes like for instance the physico-chemical properties of dissolved gases in hydrated clay systems [Owusu et al., 2022], modelling sizeable problems at the scale of a repository is excluded due to the high computational expense it would require.
- **The macroscopic approach**: The modelling is performed at the scale of geological and geotechnical structures ($> cm - dm$), considering homogeneous and uniformly distributed properties for the rock. This other side of the spectrum is usually phenomenological in nature, which means that it is characterised by indirect modelling of the behaviour of all constituents using collective closed-form macroscopic constitutive equations, as presented in Sections 6.1 to 6.5 of the state of the art for the classical HM two-phase flow model [Olivella et al., 1996, Collin et al., 2002]. Despite its apparent simplicity, improving such large-scale models with more and more micro-mechanical effects, as it is the case for the majority of the advanced HM models inventoried in Section 6.6 [Olivella and Alonso, 2008, Gerard et al., 2014, Gonzalez-Blanco et al., 2016], implies modelling limits because the simplification of the complexity of the material behaviour is often done at the cost of a number of additional assumptions and onerous identification of parameters.
- **The multi-scale approach**: It constitutes an alternative description that proposes to insert the microscopic constitutive model at the macroscopic level ($\mu m \leftrightarrow dm$), using homogenisation techniques. The principle is thus to model the micro-mechanical effects explicitly on their specific length scale through a direct modelling and then to couple their homogenised effects to the macro-scale. It is practically based on the concept of Representative Element Volume (REV), which is somehow introduced to decouple the macro-scale medium from the micro-scale in a computational way [Smit et al., 1998]. The material behaviour and properties are therefore not valid for the whole macrostructure, but rather at some macroscopic points where relevant estimations are

acquired from direct computations on the REV assigned to those integration points of the discretised macroscopic medium. The macroscopic quantities are then converted into specific boundary conditions applied to the REV. Once the analysis on the REV level has been carried out, a homogenisation technique is used to bridge the gap between the micro- and macro-levels, in such a way that the global response of the REV serves as a numerical constitutive law for the macro-scale.

The numerical double-scale procedure is built on a series of sequential steps, illustrated in Figure IV–2, and repeated for each Gauss point of the mesh until convergence is obtained on both scales. Of course, such a procedure is only possible thanks to the periodicity assumption of the microstructure in the vicinity of each integration point of the mesh.

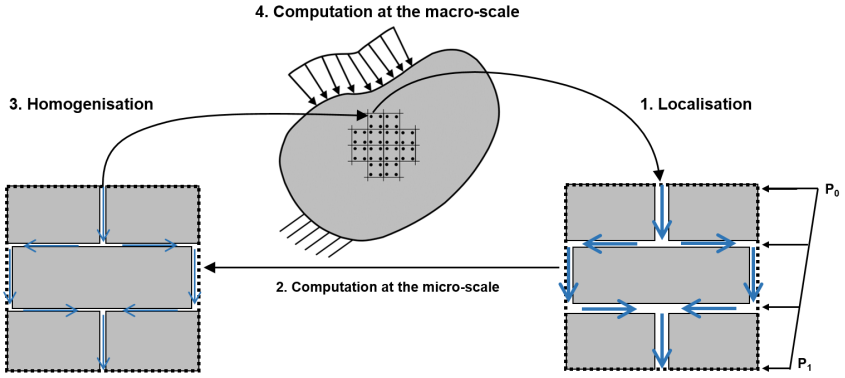

Figure IV–2 – Conceptual scheme of the iterative process for the multi-scale modelling approach.

11.1.1 Macro-to-micro scale transition (Localisation)

The first step consists in specifying how the transition from the large to the small scale is managed, through the localisation of the macro-scale scalar fields to the micro-scale.

11.1.1.1 Decomposition of the micro-kinematics

The distinction between a micro-scale denoted by the superscript m and a macro-scale, labelled by the superscript M is the basic principle of a multi-scale modelling approach. From this basis, it must be ensured that for any point $\hat{P}$ of the material, every scalar field ϖ is identical to the micro-quantities, such that:

$$\varpi^M(\hat{P}) = \varpi^m(\hat{P}) \tag{IV–1}$$

Then, for a point P close to $\hat{P}$, the scalar field can be written following a Taylor expansion, such that:

$$\varpi(P) = \varpi(\hat{P}) + \frac{\partial \varpi(\hat{P})}{\partial x_j}(x_j - \hat{x}_j) + \frac{1}{2}\frac{\partial^2 \varpi(\hat{P})}{\partial x_j \partial x_k}(x_j - \hat{x}_j)(x_k - \hat{x}_k) \tag{IV–2}$$

where x_j and $\hat{x}_j$ are the j^{th} coordinates of P and $\hat{P}$ respectively.

In the macro-scale continuum, it is limited to the first-order so that the macro-scale scalar fields can be approximated by:

$$\varpi^M(P) \approx \varpi^M(\hat{P}) + \frac{\partial \varpi^M(\hat{P})}{\partial x_j}(x_j - \hat{x}_j) \tag{IV–3}$$

In the micro-scale, a fluctuation field is added to replace the higher-order terms of the expansion, which cannot be neglected because the continuity is not ensured, so that the micro-scale scalar fields can be approximated by:

$$\varpi^m(P) \approx \varpi^M(\hat{P}) + \frac{\partial \varpi^M(\hat{P})}{\partial x_j}(x_j - \hat{x}_j) + \varpi^f(\hat{P}) \tag{IV–4}$$

where $\varpi^f(\hat{P})$ is the fluctuation field, which results from the variations in material properties within the REV, and represents therefore the fine scale deviations with respect to the average pressure fields.

11.1.1.2 Separation of scales

As the statement in Equation (IV–1) has to hold for any point of the macro-scale, it follows from Equation (IV–3) and (IV–4) that:

$$\frac{\partial \varpi^M(\hat{P})}{\partial x_j}(x_j - \hat{x}_j) + \varpi^f(\hat{P}) \ll \varpi^M(\hat{P}) \tag{IV–5}$$

which corresponds to the concept of separation of scales [Kouznetsova et al., 2002]. The validity of the approach is therefore theoretically restricted to situations in which the scale of variation of the macroscopic fields is large compared to the variation of the microscopic fields. In other words, it means that the characteristic length l_c of the microstructure and its REV is negligible compared to the characteristic fluctuation length L_c of the macroscopic fields:

$$l_c \ll L_c \tag{IV–6}$$

If this assumption holds, the boundary conditions of the micro-scale Boundary Value Problem (BVP) can be properly dictated by the local macro-scale deformation gradient.

Conversely, the hypothesis of scale separation may not hold if the macroscopic fields vary considerably in critical regions of high gradients as in the case of strain localisation problems like those treated in Part III. It follows that the Taylor expansion of the scalar fields can not be truncated before the second-order term, meaning that a higher-order homogenisation technique must be applied [Schröder, 2014]. The present part of the work is limited to application of first-order computational homogenisation, which implies the validity of the separation of scales.

11.1.2 Micro-scale boundary value problem

The resolution of the boundary value problem at the microscopic scale requires to generate a relevant REV, and to define the boundary conditions through which the macroscopic quantities will be transferred to the REV. In addition, it is also necessary to formulate the balance and constitutive equations specific to the microstructure and its constituents in order to numerically solve the micro-scale BVP.

11.1.2.1 REV generation

The definition of a REV requires the assumption that the microstructure is locally formed by the spatial repetition of a suitable very small part of the whole microstructure. The physical and geometrical properties of this microstructure can then be embedded on the REV providing that it is selected large enough to represent the microstructure and small enough so that the principle of scale separation is not violated. Identifying such an elementary volume that is well representative is not an easy task, as it is emphasised in Figure IV–3, for the case of the porosity [Bear, 1972, Lake and Srinivasan, 2004].

Practically, the REV must encompass enough constituents of the microstructure to offer a relevant statistical representation of any random area of the micro-scale. In the case of materials with a specifically built periodic microstructure such as masonry walls or other human-made materials [Anthoine, 1995, Massart, 2003], the type of REV most often goes to a periodic unit cell with a rectangular framework despite this choice is not unique, as illustrated in Figure IV–3b. Although the use of such a periodic REV seems questionable for natural materials which are heterogeneous in essence, it will be demonstrated in Section 12.3.1 that clay rocks can still be approximated as homogeneous materials with a periodic microstructure.

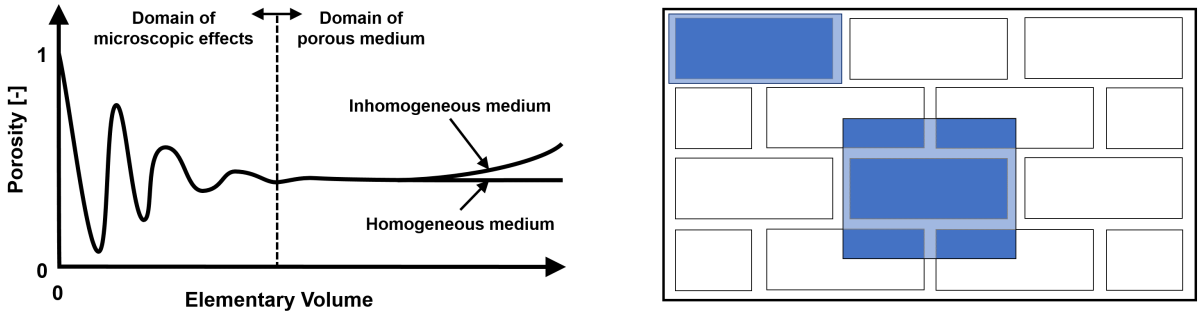

(a) (b)

Figure IV–3 – (a) Representativeness of an elementary volume applied to the concept of porosity. *From* [Lake and Srinivasan, 2004], *adapted from* [Bear, 1972]. (b) Examples of two rectangular unit cells. *Modified from* [Anthoine, 1995].

A last point to mention is that it is not necessary to define a proper REV size for the micro-scale computations, which is by default one by one. A factor defining the length unit of the REV is therefore used for the conversion of all the quantities going to (localisation step) or coming from (homogenisation step) the micro-scale.

11.1.2.2 Boundary conditions

The macroscopic scalar fields are translated to the micro-scale BVP through the boundary conditions applied to the REV [Geers et al., 2010]. The three main types of boundary conditions that can be chosen are:

- **Dirichlet boundary conditions**: equal displacements of the boundaries are enforced to apply the macro-scale deformation, which corresponds to uniform strain boundary conditions.
- **Neumann boundary conditions**: equal traction is applied on the boundaries, which corresponds to uniform stress boundary conditions.
- **Periodic boundary conditions**: relative displacements between opposite boundaries are enforced and boundary traction on opposite boundaries is antisymmetric.

Actually, it is well known that Neumann and Dirichlet boundary conditions provide a lower and upper bound solution respectively, as the former tend to underestimate and the latter to overestimate the equivalent material strength when the REV is not large enough to be fully representative [Suquet, 1987]. Since the periodic boundary conditions give a result bounded by these two limits, it is more efficient to converge towards a representative response with increasing REV sample size, as justified by [Van Der Sluis et al., 2000, Terada et al., 2000]. Although a periodic material is not strictly necessary for the application of periodic boundary conditions, as illustrated by [Nguyen et al., 2012] or [Fanara et al., 2022] for granular materials, it remains a natural course of action for periodic media such as those treated in this work (see next Section 11.2) since these boundary conditions enforce the local periodicity of the behaviour of the material at the microscopic scale [van den Eijnden, 2015].

Among the different periodic frames that can be chosen for the definition of the BVP on the REV [Anthoine, 1995], it is appropriate to select a simple geometry, for which a regular frame aligned along the coordinate axes is the most straightforward. For such a periodic frame with finite dimensions illustrated in Figure IV–4, the boundary Γ enclosing the domain Ω can be splitted into two parts: the lead part Γ^L and the follow part Γ^F. Note that one point on the lead boundary must be fixed to prevent rigid body motion, for instance the lower left corner. Then, the kinematics of any point x^F on the follow boundary Γ^F depends on the kinematics of its homologous point x^L on the lead boundary Γ^L, so that the periodicity

condition for the microstructural REV is written as:

$$x_i^F = x_i^L + \frac{\partial x_i^M}{\partial X_j}\left(X_j^F - X_j^L\right) \tag{IV–7}$$

where the capital letter X_j refers to the vector of coordinates in the reference configuration of the REV, and $F_{ij}^M = \frac{\partial x_i^M}{\partial X_j}$ is the global deformation gradient tensor.

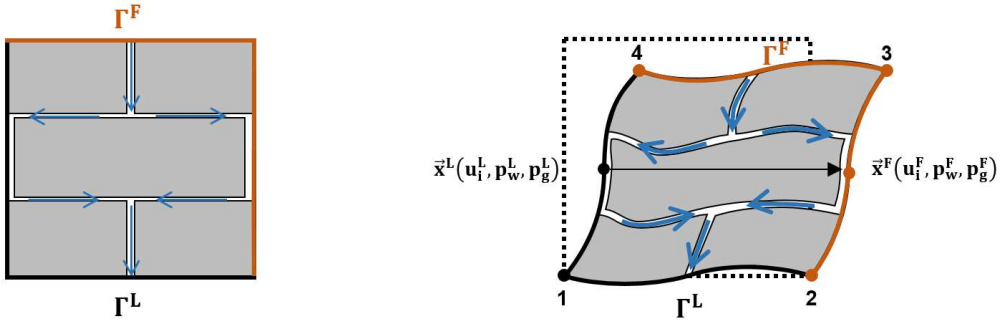

(a) (b)

Figure IV–4 – (a) Schematic representation of the REV in (a) initial state and (b) deformed state, with the periodic boundary conditions.

In terms of displacements, the mechanical part of the periodic boundary conditions for the REV reads:

$$u_i^F = u_i^L + \frac{\partial u_i^M}{\partial X_j}\left(X_j^F - X_j^L\right) \tag{IV–8}$$

where $\varepsilon_{ij}^M = \frac{\partial u_i^M}{\partial X_j}$ is the macroscopic Cauchy strain.

Similarly, the hydraulic part of the periodic boundary conditions for the REV is defined through the following relations for water and gas pressures respectively:

$$p_w^F = p_w^L + \frac{\partial p_w^M}{\partial x_j}\left(x_j^F - x_j^L\right) \tag{IV–9}$$

$$p_g^F = p_g^L + \frac{\partial p_g^M}{\partial x_j}\left(x_j^F - x_j^L\right) \tag{IV–10}$$

Moreover, the periodic boundary conditions stipulate that the boundary traction $\bar{t}_i$ on opposite boundaries must be antisymmetric, such that:

$$\bar{t}_i^F + \bar{t}_i^L = 0 \tag{IV–11}$$

In a similar way for the hydraulic part, anti-symmetric boundary (water and gas) fluxes $\bar{q}_w$ and $\bar{q}_g$ must be ensured,which respectively reads:

$$\bar{q}_w^F + \bar{q}_w^L = 0 \tag{IV–12}$$

$$\bar{q}_g^F + \bar{q}_g^L = 0 \tag{IV–13}$$

11.1.2.3 Balance equations

The REV must be in equilibrium, which is mechanically ensured through the general momentum balance equation. In addition, the REV must also be hydraulically equilibrated, through a pair of mass balance equations for water and gas.

11.1.2.4 Constitutive equations

The balance equations over the REV involve a number of dependent variables, which should be related to the main unknowns of the problem, *i.e.* displacement u_i, water pressure p_w and gas pressure p_g, in order to fully describe the behaviour of the microstructure. Thence, each microstructural constituent present in the REV is characterised by constitutive laws specifying these relationships.

11.1.2.5 Numerical solution of the problem

The resolution of the problem in the REV can be conducted via several methods, from the finite element method [Terada and Kikuchi, 1995, Smit et al., 1998, Feyel and Chaboche, 2000, Kouznetsova et al., 2001, Massart and Selvadurai, 2014, Larsson et al., 2010, Frey et al., 2013, van den Eijnden et al., 2016, Bertrand et al., 2020], to the discrete element method [Nitka et al., 2011, Nguyen et al., 2014], by way of the Voronoi cell method [Ghosh et al., 1995] or the Fourier series approach [Moulinec and Suquet, 1998]. Note that in the case where finite element analysis is carried out at both scales, the term Finite Element Square (FE^2) method is commonly employed.

11.1.3 Micro-to-macro scale transition (Homogenisation)

Once the equilibrium is obtained for the micro-scale boundary value problem, the next step consists in specifying how the transition from the small to the large scale is managed, through the homogenisation of the microscopic fields to compute the microscopic quantities.

Among the different homogenisation frameworks for the solving of two-scale problems, one of the most suited is the mathematical homogenisation theory documented in [Bensoussan et al., 1978, Sanchez-Palencia and Zaoui, 1987], which is based on a double-scale asymptotic expansion of the variable fields following the ratio l/L. Then, resulting partial differences are used to bridge the gap between the two scales, provided that the microstructure is periodic, *i.e.* locally formed by the spatial repetition of unit cells and that the material properties are periodic functions of the microscopic special parametrisation [Fish and Wagiman, 1993], reasons why this method is usually restricted to very simple microscopic geometries.

The numerical homogenisation theory [Kouznetsova et al., 2001] is an alternative method, where the macroscopic phenomenological constitutive law is replaced by suitable averages of the global response of the REV to the perturbation fields dictated by the macro-scale.

It is practically achieved by ensuring that the volume average of the variation of work on the REV is equal to the local variation of the work on the macro-scale, according to the Hill-Mandel macro-homogeneity condition [Hill, 1965]:

$$\delta W^M = \frac{1}{\Omega_0}\int_{\Omega_0} \delta W^m d\Omega_0 \tag{IV–14}$$

Formulating the micro-scale problem under a small strain assumption, the macro-homogeneity condition in a virtual work formulation for the microscopic Cauchy stress tensor σ_{ij} reads:

$$\sigma_{ij}^M \frac{\partial u_i^{*,M}}{\partial x_j} = \frac{1}{\Omega}\int_{\Omega} \sigma_{ij}^m \frac{\partial u_i^{*,m}}{\partial x_j} d\Omega \tag{IV–15}$$

Applying the Gauss theorem and using the periodic boundary conditions, this Equation (IV–15) is reduced to:

$$\sigma_{ij}^M \frac{\partial u_i^{*,M}}{\partial x_j} = \frac{1}{\Omega}\frac{\partial u_i^{*,m}}{\partial x_j}\int_{\Gamma} \bar{t}_i x_j d\Gamma \tag{IV–16}$$

which results in volume averaging from the REV:

$$\sigma_{ij}^M = \frac{1}{\Omega}\int_{\Gamma} \bar{t}_i x_j d\Gamma = \frac{1}{\Omega}\int_{\Omega} \sigma_{ij}^m d\Omega \tag{IV–17}$$

By following the same approach for the homogenisation of the fluid [Massart and Selvadurai, 2014] or thermal [Ozdemir, 2009] fluxes, it is possible to obtain the macro-scale water and gas fluxes as integrals of the micro-scale boundary fluxes.

Regarding the macroscopic fluid contents of water and gas, it is directly defined as the total amounts of fluid stored in the microstructural constituents of the REV.

11.1.4 Macro-scale boundary value problem

Considering a general HM two-phase flow problem, the resolution of the boundary value problem at the macro-scale can be formulated in a matrix form:

$$\begin{bmatrix} \left[K^M_{mm}\right] & \left[K^M_{mw}\right] & \left[K^M_{mg}\right] \\ \left[K^M_{wm}\right] & \left[K^M_{ww}\right] & \left[K^M_{wg}\right] \\ \left[K^M_{gm}\right] & \left[K^M_{gw}\right] & \left[K^M_{gg}\right] \end{bmatrix} \begin{Bmatrix} \{\delta\varepsilon^M\} \\ \{\delta\nabla p^M_w\} \\ \{\delta p^M_w\} \\ \{\delta\nabla p^M_g\} \\ \{\delta p^M_g\} \end{Bmatrix} = \begin{Bmatrix} \{\delta\sigma^M\} \\ \{\delta f^M_w\} \\ \{\delta \dot{M}^M_w\} \\ \{\delta f^M_g\} \\ \{\delta \dot{M}^M_g\} \end{Bmatrix} \tag{IV–18}$$

which can be summarised as follows:

$$\left[A^M\right]\left\{\delta U^M\right\} = \left\{\delta \Sigma^M\right\} \tag{IV–19}$$

where $\left[A^M\right]$ is the macro-scale stiffness matrix obtained by perturbations, $\left\{\delta U^M\right\}$ contains the infinitesimal variations of the macro-scale variables, and $\left\{\delta \Sigma^M\right\}$ is the responses of these variables.

11.2 Multi-scale modelling's raison d'être

In this part of the thesis, a multi-scale modelling approach is adopted to reproduce gas flow mechanisms in sound rock layers. This specific choice lays its foundations on the experimental findings associated to the creation of gas-filled pathways in argillaceous rocks. As mentioned in Section 5.4 of the state-of-the-art Part II, gas transport by pathway dilation is a flow mechanism of particular significance for low-strength clayey rocks less conductive to visco-capillary two-phase flow [Horseman et al., 1996]. In such materials, there is no transport of gas phase until gas pressure has sufficiently built up, which induces localised consolidation and/or micro-fractrures in the clay-rich rocks that cannot withstand long-term gas pressures with a magnitude greater than the minimum principal stress. Since this gas breakthrough event is a major indication revealing the development of preferential pathways, laboratory campaigns have thus been traditionally focused on determining the gas breakthrough pressure and gas outflow rate [Ortiz et al., 1997, Harrington and Horseman, 1999, Senger et al., 2006, Cuss and Harrington, 2011, Jacops et al., 2014, de La Vaissière et al., 2014a]. More recently, the tracking of the gas-induced micro-fracturing has brought clear evidences [Harrington et al., 2012b, Cuss et al., 2014a, Gonzalez-Blanco et al., 2016, Harrington et al., 2017b, Gonzalez-Blanco and Romero, 2022] that natural heterogeneities and anisotropy inherent to the clay-rich formations such as bedding planes, or pre-existing fractures in disturbed portions around excavations represent preferred weaknesses exploited by the gas to flow. As a result, the propagation of gas is not uniformly distributed across the specimen but concentrates on some discrete gas-filled pathways [Volckaert et al., 1995, Harrington et al., 2012a]. Such a gas transport mode emphasises the fundamental role played by the HM couplings between the deformational response and the gas pressure [Cuss et al., 2014a, Liu et al., 2016b, Harrington et al., 2017a], as well as the ensuing impact on the host rock properties [Harrington et al., 2012b, Gonzalez-Blanco et al., 2016, Gonzalez-Blanco et al., 2022].

In that sense, the microstructural information before and after gas injection tests such as those obtained with MIP visualisation technique on Boom Clay samples in Figure IV–5 [Gonzalez-Blanco and Romero, 2022] allows for corroborating the changes in transport properties due to the mechanical degradation of the clayey material under gas-induced loading. Under micro-fracture creation, the porosity is locally enhanced, leading to important increase in permeability and reduction in gas entry pressure [Cuss et al., 2014a]. This kind of microstructural study capturing the geometric properties of the gas pathways, *i.e.* aperture, separation and volume of fissures, proves to be essential to the development and validation of advanced coupled numerical models for predicting gas flow processes through low-permeability rock formations.

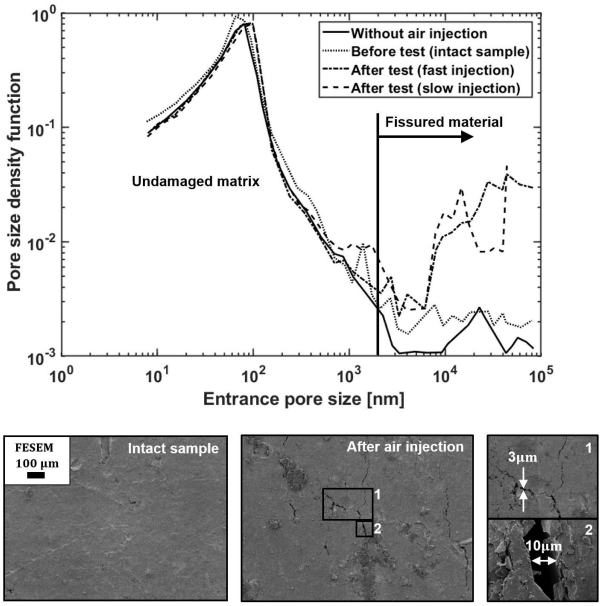

Figure IV–5 – Changes in Boom Clay pore size distribution after air injection tests, and corresponding FESEM scans with zooms on the detected fissures in the horizontal and vertical directions. *Modified after* [Gonzalez-Blanco and Romero, 2022].

Therefore, with a view to reproducing gas flow mechanisms whose activation threshold is linked to the spatial distribution of the hydro-mechanical properties of the clay microstructure and the variability inherent to it, combining the benefits from both large- and small-scale modelling strategies through a multi-scale approach proves to be appropriate.

11.3 Review of the multi-scale modelling

As exposed in Section 6.6.4 of the state of the art, different types of numerical multi-scale approaches have already been developed to study the macroscopic response of a rock material initiated from microscopic heterogeneities and phenomena. It is proposed here to browse some of these models that contribute to capture the macroscopic damage mechanisms induced by micro-cracking, to which belongs the gas transport by discrete pathway creation. One can thus better apprehend the relevance of the numerical developments introduced in the rest of this Part IV of the work.

11.3.1 Background

A homogenisation technique has been elaborated by [Dormieux and Kondo, 2004, Dormieux et al., 2006] in the micro-mechanical framework in order to estimate the permeability of a porous medium with dense networks of micro-fractures. It has been showed that the modification of the geometry of a fluids-saturated crack induced by the mechanical loading, following Terzaghi's effective stress results in an evolution of the permeability. In particular, the existence of a damage threshold beyond which the permeability of a cracked porous medium is likely to change by several orders of magnitude, especially for low values of the permeability of the uncracked porous matrix has been proved.

Such a micro-macro approach of a damage-induced permeability evolution has been extended to media containing families of both micro-fractures and long fractures cross-cutting the REV by [Barthélémy, 2009], and further applied to the qualitative prediction of damage processes induced by micro-cracks and of subsequent modifications in permeability around an excavation in an indurated clay candidate for radioactive waste repository by [Levasseur et al., 2013].

Other significant contributions such as the rate dependent damage models for brittle rocks developed by [Bhat et al., 2012] and [Wang et al., 2015] remain limited to the mechanical cases, but account for the micro-cracks propagation and are based on the analytical or numerical up-scaling method starting from micro-structural considerations.

By following a similar up-scaling procedure based on periodicity assumption and asymptotic homogenisation, a similar class of two-scale damage models has been developed by [Dascalu and Bilbie, 2007, Dascalu, 2009] to obtain macroscopic damage law from the propagation of micro-fractures in a microstructure that contains an explicit distance between neighbouring micro-cracks. This model has been successfully used and extended to represent brittle failure [Dascalu et al., 2010], the sub-critical damage propagation [François and Dascalu, 2010] or the dynamic fracture propagation with branching instabilities [Atiezo and Dascalu, 2017].

This latter dynamic micro-crack criterion has more recently been adapted to cover coupled thermo-mechanical problem induced by micro-cracking [Dascalu and Gbetchi, 2019]. Similarly, there are some other multi-scale models considering the HM coupling from microscopic phenomena. For instance, a multi-scale computational homogenisation method for the modelling of hydro-mechanical coupling problem for quasi-brittle materials has been developed by [Zhuang et al., 2017] to simulate the hydraulic fracturing phenomenon. Inspired by this multi-scale framework of HM coupled formulation [Zhuang et al., 2017] combined with the micro-scale analysis of permeability change on the interface element [van den Eijnden et al., 2016] and with the homogenised poro-elastic analysis on the crack characteristics [Argilaga et al., 2016], a two-scale time-dependent damage model under single [Yang and Fall, 2021b] and two-phase flow conditions [Yang and Fall, 2021a] has been constructed from the multi-physics framework introduced in [Dascalu and Gbetchi, 2019] in order to explicitly simulate the gas induced micro-fracturing in clayey rock materials. Specifically applied to gas injection experiments, this model allows to simulate the gas induced fracturing process, in which the damage propagation and the dilatant gas pathways are rather well captured.

In the context of multi-physics problems, there are other numerical models capable of incorporating the HM couplings in the multi-scale framework, such as the FE^2 method. Originally presented for the modelling of mechanical problems by [Kouznetsova et al., 2001], the computational homogenisation included in the FE^2 method was then applied to deal with heat conduction problems by [Ozdemir et al., 2008]. Building upon this theory, a hydro-mechanical double-scale model has been implemented following the successive works of [Marinelli et al., 2016, van den Eijnden et al., 2016, Pardoen et al., 2018], preceded by [Bilbie, 2007, Frey et al., 2013], in order to simulate the coupled hydro-mechanical behaviour of a saturated porous medium, and to analyse the cracking-induced localisation phenomena. This coupled HM double-scale model was the starting point of the developments carried out by [Bertrand et al., 2020] to account for partially saturated conditions, and reproduce the coupled phenomena associated with multiphase flows in fractured reservoirs.

11.3.2 Proposed developments

From the previous review of existing models, it appears that the only tool that explicitly reproduces the dominant process of gas migration by preferential pathways initiated from the microscopic phenomena, is the two-scale time-dependent damage model under two-phase flow conditions developed by [Yang and Fall, 2021a]. And yet, the microstructure incorporated in this model is only confined to unidirectional fractures for the initiation of the damage and flows at the macroscopic scale, while the consideration of the joint effects of the key constituents of the microstructure is eluded. This lack of numerical modelling which integrates the complexity of the microstructure, *i.e.* pore network morphology, bedding planes and other fissures, and accounts for the hydro-mechanical effects of each of these constituents on the macroscopic gas flow has stimulated the undertaking of the present work.

This contribution aims thence at developing a detailed micro-scale HM constitutive model for partially saturated clay materials, and integrating this microstructure into a multi-scale scheme using ho-

mogenisation techniques for the transition from one scale to the other. More specifically, this multi-scale model pays special attention to the modelling of the emergence of gas fracturing mechanisms while simulating advection–diffusion of dissolved gas and visco-capillary two-phase flow as background processes.

In practise, the hydro-mechanical double-scale model implemented in the `LAGAMINE` code by [Bertrand, 2020] arising from a number of serial contributions [Bilbie, 2007, Frey, 2010, Marinelli, 2014, van den Eijnden, 2015] constitutes the basis of the developments described hereafter. With respect to these previous works, the presence of gas implies its proper degree of freedom and requires the implementation of a specific hydraulic constitutive model at the microscopic scale. In particular, the following novelties are proposed:

- Implementation of the tube elements in addition to the interface elements (bedding and bridging planes) of the microstructure, in order to substitute the hydraulic behaviour of the solid matrix.
- Possibility to simulate a variable number of tubes with an associated tortuosity parameter, in order to numerically approach the void volume of the studied material.
- Definition of different retention models (Brooks-Corey, van Genuchten) for the microstructure constituents (fracture and tube).
- Introduction of the hydraulic transmissivity function and the relative permeability curve to compute fluxes through the tubes.
- Implementation of the mechanism of diffusion of dissolved gas within the liquid phase for the microstructure constituents, in addition to advective fluxes.
- Formulation of the hydro-mechanical coupling linking the fracture/tube opening to the variation of fluids pressure, to account for the gas propagation kinetics under gas injection.
- Possibility to simulate interface elements with different properties, in order to represent random zones of weakness in the mesh, propitious for the development of preferential pathways.
- Parallelisation of the micro-level routine, in order to solve multiple REV boundary value problems in parallel and obtain an important gain in time and efficiency.

12. Hydro-mechanical multi-scale model

This chapter gives an overview of the hydro-mechanical double-scale model built on the basis of the key steps of the multi-scale approach presented in the previous Sections 11.1.1 to 11.1.4.

The proposed numerical tool can be seen as hybrid, in the sense that a complete hydraulic system is explicitly implemented and solved at the micro-scale, while the effects of the mechanical problem are addressed at the macroscopic scale and implicitly integrated at the lower level by means of hydro-mechanical couplings. The coupled finite element elaborated to mesh the macro-scale in the LAGAMINE code is the EHMIC element and the related law to be used for the double-scale computations is the HMIC law.

In the proposed developments, the complex structure of the clay material is treated as a porous medium commonly assimilated as the superposition of several continua, relying on the mixture theory introduced in Section 6.1 of Part II. In order to cope with multiphase flows through such a clay medium, a binary fluid mixture is considered, which includes a liquid and a gaseous phase. The former phase is a combination of two species, namely liquid water and dissolved gas, while the latter is solely made of dry gas, assuming water vapour is negligible. In the proposed formulation, it is also assumed that the mineral species and the solid phase coincide, and that solid and fluid phases are immiscible.

12.1 Model formulation at the macroscopic scale

Given the concepts introduced above, the state of the material is therefore described by its displacement field u_i, liquid pressure field p_w, and gas pressure field p_g, while being restricted to isothermal conditions. In the following, the required balance equations for the coupled hydro-mechanical problem under study are presented in usual differential local form using the current porous material configuration, and in a weak form necessary to address boundary value problems over large domains within a finite element framework. Since the multi-scale model is implemented in way as to treat the mechanical problem directly at the macroscopic scale, while solving the hydraulic flows from the definition of a microstructure at a lower scale, only the solid phase behaviour is specified in this section. As for the hydraulic constitutive model, it will be presented later in Section 12.3.

12.1.1 Balance equations

The general momentum balance equation in differential form reads:

$$\frac{\partial \sigma_{ij}}{\partial x_j} + \rho g_i = 0 \tag{IV–20}$$

where σ_{ij} is the Cauchy total stress field, g_i is the gravity force, and ρ is the mixture homogenised density, which can be defined as:

$$\rho = \rho_s(1-\phi) + \rho_w S_{r_w}\phi + \rho_g(1-S_{r_w})\phi \tag{IV–21}$$

where $\phi = \frac{\Omega_v}{\Omega}$ is the porosity with Ω the current volume of a given mass of skeleton and Ω_v the corresponding porous volume, ρ_s is the solid grain density, ρ_w is the water density, ρ_g is the gas density, and S_{r_w} is the water degree of saturation.

The weak form of the local momentum balance Equation (IV–20) is obtained by applying the principle of virtual works considering the admissible virtual displacement field u_i^*, it reads:

$$\int_\Omega \sigma_{ij} \frac{\partial u_i^*}{\partial x_j} d\Omega = \int_\Omega \rho g_i u_i^* d\Omega + \int_{\Gamma_\sigma} \bar{t}_i u_i^* d\Gamma \tag{IV–22}$$

where $\bar{t}_i$ is the classical external traction force per unit area acting on a part Γ_t of the boundary Γ.

In addition to the mechanical equilibrium, the mass balance equations for water and gas in a strong form respectively read, for a unit porous medium ($\Omega = 1$):

$$\underbrace{\dot{M}_w + \frac{\partial f_{w,i}}{\partial x_i}}_{\text{Liquid water}} - Q_w = 0 \tag{IV–23}$$

$$\underbrace{\dot{M}_g + \frac{\partial f_{g,i}}{\partial x_i}}_{\text{Dry gas}} + \underbrace{\dot{M}_{dg} + \frac{\partial f_{dg,i}}{\partial x_i}}_{\text{Dissolved gas}} - Q_g = 0 \tag{IV–24}$$

where $\dot{M}_w$, $\dot{M}_g$ and $\dot{M}_{dg}$ are the mass variations of liquid water, dry gas and dissolved gas respectively, $f_{w,i}$, $f_{g,i}$ and $f_{dg,i}$ are the mass flows of liquid water, dry gas and dissolved gas respectively, and Q_w and Q_g are the sink mass terms of water and gas.

The weak forms of the water and gas balance Equations (IV–23)-(IV–24) are obtained in a similar way as the momentum balance equation, and read for every kinematically admissible virtual water pressure field p_w^* and gas pressure field p_g^*:

$$\int_\Omega \left[\dot{M}_w p_w^* - f_{w,i} \frac{\partial p_w^*}{\partial x_i} \right] d\Omega = \int_\Omega Q_w p_w^* d\Omega - \int_{\Gamma_q} \bar{q}_w p_w^* d\Gamma \tag{IV–25}$$

$$\int_\Omega \left[\dot{M}_g p_g^* + \dot{M}_{dg} p_g^* - f_{g,i} \frac{\partial p_g^*}{\partial x_i} - f_{dg,i} \frac{\partial p_g^*}{\partial x_i} \right] d\Omega = \int_\Omega Q_g p_g^* d\Omega - \int_{\Gamma_q} \bar{q}_g p_g^* d\Gamma \tag{IV–26}$$

where Γ_q and is the part of the boundary where the input water/gas mass per unit area $\bar{q}_w$ or $\bar{q}_g$ is prescribed.

12.1.2 Constitutive equations

With a view to represent multiphasic materials in the model, the previous Equation (IV–20) remains valid provided to define the total stress σ_{ij}. Accounting for the partially saturated conditions with Biot's definition [Biot, 1941] to consider the solid phase compressibility, the Bishop's postulate [Bishop, 1959] can be written as:

$$\sigma_{ij} = \sigma'_{ij} + b_{ij} \left[S_{r_w} p_w^M + (1 - S_{r_w}) p_g^M \right] \delta_{ij} \tag{IV–27}$$

where δ_{ij} is the Kronecker symbol, b_{ij} is Biot's tensor, and σ'_{ij} is the Bishop's effective stress. This concept, corresponding to the total stress reduced by the fluid pressures weighted by the degree of saturation of each phase represents a first important hydro-mechanical coupling that connects the two levels of the model. Note that in previous Equation (IV–27), the stress field is defined under soil mechanics convention in which compressive stress is positive.

The Biot tensor introduced in Equation (IV–27) represents more particularly the compressibility of the solid grain skeleton relative to the skeleton compressibility, expressed in orthotropic axes as [Cheng, 1997]:

$$b_{ij} = \delta_{ij} - \frac{C^e_{ijkl}}{3K_s} \tag{IV–28}$$

where K_s is the isotropic bulk modulus of the solid grains, and C^e_{ijkl} is the elastic stiffness tensor of the material. It is worth noting that including the plastic material behaviour in case the medium is not assumed elastic requires an extension to poroplasticity, as proposed by [Coussy and Ulm, 1995]. Yet, these developments are not included in the present work.

On top of that, the isotropic variation of solid density can be linked to the variations of pore water pressure, gas pressure and mean effective stress according to [Detournay and Cheng, 1993]:

$$\frac{\dot{\rho}_s}{\rho_s} = \frac{(b_{ij} - \phi)(S_{r_w}\dot{p}_w + S_{r_g}\dot{p}_g) + \dot{\sigma}'}{(1-\phi)K_s} \tag{IV–29}$$

where ρ_s is the solid grain density, ϕ is the porosity and σ' is Bishop's mean effective stress.

As for the fluid phase behaviour, it will be described in the hydraulic constitutive model presented in Section 12.3.4.

12.2 Macro-to-micro scale transition

Now that the governing equations of the model have been presented at the macro-scale, the next step is to specify how the transition between the macroscopic scale and the microscopic scale is handled.

12.2.1 Decomposition of the microkinematics

With respect to the theory introduced in Section 11.1.1 for a purely mechanical problem, water and gas pressures must be added to address hydro-mechanical problems under partially saturated conditions. In particular, it must be ensured that for any point $\hat{P}$ of the material, the macro-pressure fields of water and gas are identical to the micro-quantities, such that:

$$p^M_w(\hat{P}) = p^m_w(\hat{P}) \tag{IV–30}$$

$$p^M_g(\hat{P}) = p^m_g(\hat{P}) \tag{IV–31}$$

Then, in a similar way as in Equation (IV–2), the water pressure p_w and the gas pressure p_g of any point P close to $\hat{P}$ can be written following a Taylor expansion. In the macro-scale continuum, it is limited to the first order so that the macro-scale pressure fields of water and gas can be approximated by:

$$p^M_w(P) \approx p^M_w(\hat{P}) + \frac{\partial p^M_w(\hat{P})}{\partial x_j}(x_j - \hat{x}_j) \tag{IV–32}$$

$$p^M_g(P) \approx p^M_g(\hat{P}) + \frac{\partial p^M_g(\hat{P})}{\partial x_j}(x_j - \hat{x}_j) \tag{IV–33}$$

where x_j and $\hat{x}_j$ are respectively the j^{th} coordinates of P and $\hat{P}$.

In the micro-scale, a fluctuation field is added to replace the higher-order terms of the expansion which can not be neglected because of the uncertain continuity, so that the micro-scale pressure fields of water and gas are approximated by:

$$p^m_w(P) \approx p^M_w(\hat{P}) + \frac{\partial p^M_w(\hat{P})}{\partial x_j}(x_j - \hat{x}_j) + p^f_w(\hat{P}) \tag{IV–34}$$

$$p^m_g(P) \approx p^M_g(\hat{P}) + \frac{\partial p^M_g(\hat{P})}{\partial x_j}(x_j - \hat{x}_j) + p^f_g(\hat{P}) \tag{IV–35}$$

where $p^f_w(\hat{P})$ and $p^f_g(\hat{P})$ are the fluctuation fields, which result of the variations in material properties within the REV, and represent therefore the fine scale deviations with respect to the average pressure fields.

12.2.2 Separation of scales

Together with Equation (IV–1), Equations (IV–30) and (IV–31) have to hold for any point of the macro-scale. Thence, it follows from Equations (IV–34) and (IV–35) that:

$$\frac{\partial p_w^M(\hat{P})}{\partial x_j}(x_j - \hat{x}_j) + p_w^f(\hat{P}) \ll p_w^M(\hat{P}) \tag{IV–36}$$

$$\frac{\partial p_g^M(\hat{P})}{\partial x_j}(x_j - \hat{x}_j) + p_g^f(\hat{P}) \ll p_g^M(\hat{P}) \tag{IV–37}$$

which corresponds to the concept of separation of scales [Kouznetsova et al., 2002] introduced in Section 12.2.

Applying the macroscopic fields on the boundaries, the microscopic characteristic length is reasonably assimilated to the size of the REV l_{REV}, while the macroscopic length can be defined as the ratio of the macroscopic pressure over the load applied on the REV, *i.e.* the macroscopic gradient of fluids pressure $\nabla p^M = \frac{\partial p^M}{\partial x_j}$, such that Equation (IV–6) can be specifically reformulated for the hydraulic quantities as:

$$l_{REV} \ll \frac{p^M}{\nabla p^M} \tag{IV–38}$$

which is expressed as a function of fluids (water and gas) pressures and gradients given that the aim here is to simulate a gas pressure increase through the modelled clay rock.

Moreover, for such a separation of scales, the assumption of steady-state conditions that supposes that the hydraulic flow at the micro-scale is insensitive to the time variation of the fluid storage at this level is generally valid. Finally, given that the present work is limited to the application of the first-order computational homogenisation for which the assumption of separation of scales holds, it means that the boundary conditions of the micro-scale boundary value problem can be properly determined by the local macro-scale pressure gradient.

12.3 Micro-scale boundary value problem

The resolution of the boundary problem at the microscopic scale requires to built a REV which provides a good representation of the clay microstructure. The boundary conditions through which the macroscopic hydraulic quantities are transferred to the REV must also be defined. It is finally necessary to formulate the balance equations and the hydraulic constitutive model specific to the microstructure and its constituents in order to numerically solve the microscopic hydraulic system.

12.3.1 REV generation

Although the use of a REV seems questionable for natural materials which are heterogeneous in essence, clay rocks such as the Boom Clay or the Callovo-Oxfordian claystone are generally characterised by a horizontal layered structure owing to their process of deposition [Vandenberghe, 1978, Wenk et al., 2008] as highlighted in Section 4.2. Opting for the multi-scale method to model microstructure-induced processes in clay rocks is thus convenient, which eludes a complex description of the matrix blocks separated by pore and fracture networks over the entire domain.

In the proposed modelling of a Boom Clay material, the size and structure of the REV comes from experimental data acquired for instance from Field-Emission Scanning Electron Microscopy (FESEM) images like the one given in Figure IV–5 [Gonzalez-Blanco et al., 2016]. Such a scan reveals the opening of large-aperture fissures with a repeated distance in-between after the passage of gas, as shown in Figure IV–6a.

It is then possible to extrapolate a physical idealisation of the microstructure in Figure IV–6b, which includes matrix blocks of Boom Clay separated by dominant horizontal fractures, corresponding to the bedding planes. In the vertical direction, secondary narrow-aperture fissures connecting the bedding planes were also detected experimentally as contributors to the flow normal to the bedding. Through this simplification of the studied material, it is possible to identify the main constituents responsible for the flow through the microstructure, and which should therefore be included in the REV.

Considering first the repeated separation distance w between the horizontal fractures, one of these bedding planes (red element) is integrated as the central element of the REV, as depicted in Figure IV–6c. Another fracture element prone to develop in the vertical direction is added to the REV, and is referred to as a bridging plane (blue element). Finally, the matrix block is substituted by an assembly of tubes with specific diameters and tortuosities, in the different directions, so as to match the pore size distribution curve. In the REV, this bundle of tubes is gathered into one equivalent tube (grey elements) in the three guiding directions of the micro-scale problem. In this way, a complete hydraulic volume to calculate fluid flows at the microscopic scale has been generated, which is coupled to the mechanics through the definition of effective stresses in the media, as described in Section 12.1.2. In the model, the pore network is also supposed to be the same in all directions, and the anisotropy thus comes from the different separation planes, *i.e.* the bedding planes and the bridging planes.

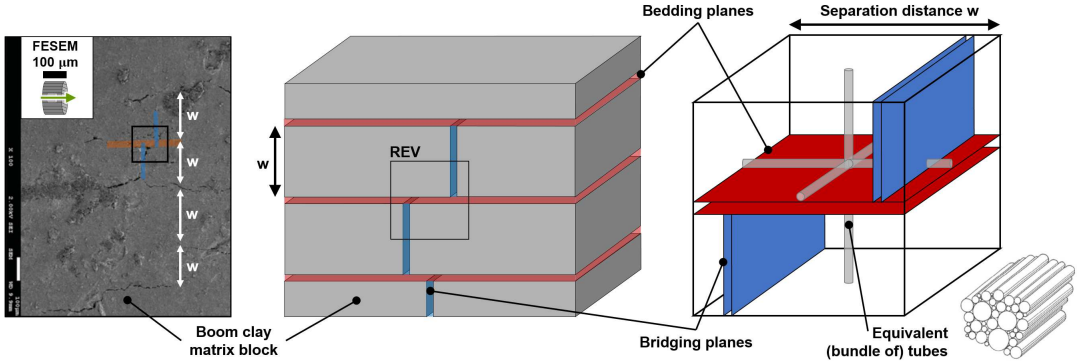

Figure IV–6 – (a) Internal visualisation of a Boom Clay sample using FESEM, *after* [Gonzalez-Blanco and Romero, 2022]. (b) Physical idealisation of the microstructure. (c) Definition of the REV.

12.3.2 Periodic boundary conditions

The macroscopic fluid pressure gradients enter the micro-scale BVP through the periodic boundary conditions applied to the REV [Geers et al., 2010]. In a practical way, the REV is enclosed in the boundary Γ, which is divided into a lead part Γ^L and a follow part Γ^F owing to its periodic nature. Then in terms of fluid pressure fields, any point on the follow boundary x^F is naturally dependent on its homologous on the lead boundary x^L. In this way, the hydraulic part of the periodic boundary conditions for the REV is reformulated according to Equations (IV–9) and (IV–10):

$$p_w^F = p_w^L + \frac{\partial p_w^M}{\partial x_j}\left(x_j^F - x_j^L\right) \qquad \text{(IV–39)} \qquad\qquad p_g^F = p_g^L + \frac{\partial p_g^M}{\partial x_j}\left(x_j^F - x_j^L\right) \qquad \text{(IV–40)}$$

Moreover, the periodic boundary conditions stipulate that the boundary fluxes of water q_w and gas q_g on opposite boundaries must be anti-symmetric, following Equations (IV–12) and (IV–13):

$$\bar{q}_w^F + \bar{q}_w^L = 0 \qquad \text{(IV–41)} \qquad\qquad \bar{q}_g^F + \bar{q}_g^L = 0 \qquad \text{(IV–42)}$$

12.3.3 Balance equations

Since the mechanical problem is exclusively solved at the macroscopic scale, only mass balance equations for water and gas are required at the microscopic scale, which reads from Equations (IV–23) and (IV–24):

$$\dot{M}_w^m + \frac{\partial f_{w_i}^m}{\partial x_i} = 0 \qquad \text{(IV–43)} \qquad\qquad \dot{M}_g^m + \frac{\partial f_{g_i}^m}{\partial x_i} + \dot{M}_{dg}^m + \frac{\partial f_{dg_i}^m}{\partial x_i} = 0 \qquad \text{(IV–44)}$$

where $\dot{M}_w^m$, $\dot{M}_g^m$ and $\dot{M}_{dg}^m$ represent the variations of the fluid contents, namely water, gas and dissolved gas, that vanish out under the assumption of steady state at the microscale, and $f_{w_i}^m$, $f_{g_i}^m$ and $f_{dg_i}^m$ are the total mass flows of water gas, and dissolved gas respectively.

As stated in the introductory part of this Chapter 12, the description of the fluid transport processes in a partially saturated porous medium relies on a biphasic fluid flow model consisting of a liquid phase made up of liquid water and dissolved gas, and a gaseous phase comprising dry gas. Thus the mass flows included in Equations (IV–43) and (IV–44) take into account the advection of each phase using the generalised Darcy's law [Darcy, 1856] and the diffusion of the components within each phase by Fick's law [Fick, 1855], as follows:

$$f_{w_i}^m = \rho_w q_{w_i} \qquad \text{(IV–45)} \qquad\qquad f_{g_i}^m = \rho_g q_{g_i} \qquad \text{(IV–46)} \qquad\qquad f_{dg_i}^m = \rho_{dg} q_{w_i} + i_{dg_i} \qquad \text{(IV–47)}$$

where ρ_w, ρ_g and ρ_{dg} are the densities of water, gas and dissolved gas respectively, q_{w_i} and q_{g_i} are the advective fluxes respectively of the liquid and gaseous phases, i_{dg_i} is the diffusion flux for dissolved gas in the liquid phase. It is worth noting that the liquid water diffusion within the liquid phase and the dry gas diffusion within the gaseous phase are both neglected in the model. All these fluxes will be defined in detail in the next Section 12.3.4.

Considering some kinematically admissible virtual fluid pressure fields $p_w^{*,m}$ and $p_g^{*,m}$, the weak forms of the mass balance equations for water and gas derive from Equations (IV–25) and (IV–26), and read, assuming steady state flow conditions at the microscale:

$$\int_\Omega \left[\cancel{\dot{M}_w^m p_w^{*,m}} - f_{w_i}^m \frac{\partial p_w^{*,m}}{\partial x_i} \right] d\Omega = -\int_\Gamma \bar{q}_w^m p_w^{*,m} d\Gamma \qquad \text{(IV–48)}$$

$$\int_\Omega \left[\cancel{\dot{M}_g^m p_g^{*,m}} + \cancel{\dot{M}_{dg}^m p_g^{*,m}} - f_{g_i}^m \frac{\partial p_g^{*,m}}{\partial x_i} - f_{dg_i}^m \frac{\partial p_g^{*,m}}{\partial x_i} \right] d\Omega = -\int_\Gamma \bar{q}_g^m p_g^{*,m} d\Gamma \qquad \text{(IV–49)}$$

where Ω is the volume of the REV, and Γ stands for the periodic REV boundaries.

12.3.4 Constitutive laws

The hydraulic constitutive model is written at the scale of the microstructural constituents, namely the bedding and bridging planes (fractures), and the matrix blocks (tubes), which are described by a multiphase flow model and variation laws for the fluids density. To account for the mechanical effects coming from the macro-scale, additional hydro-mechanical couplings are considered at this level of the numerical model.

Hydraulic problem

The hydraulic problem is solved by considering a channel flow model extended to unsaturated conditions to simultaneously consider gas and water flows at the micro-scale.

The longitudinal multiphase flow directly derives from the motion of compressible fluids between two closely-space parallel plates or inside a cylinder described by the Navier-Stokes equations, which gives the expressions of the hydraulic transmissivity function for such geometries, as detailed in [Marinelli, 2014] and reported in Appendix E:

$$\kappa_{frac} = -\frac{h_b^2}{12} h_b \cdot w \qquad \text{(IV–50)} \qquad\qquad \kappa_{tube} = -\pi \frac{D^4}{128} \qquad \text{(IV–51)}$$

where h_b and D are the hydraulic aperture of the fracture and the opening diameter of the tube respectively, and w is the separation distance between the bedding planes, which corresponds to the size of the REV.

So, the longitudinal advective component of the multiphase flow along a fracture embedded in a REV of section $A = (w + h_b)^2 \simeq w^2$ assuming $w \gg h_b$, is expressed as:

$$q_{\alpha,i} = -\frac{k_{r_\alpha}}{\mu_\alpha} \frac{1}{A} \kappa_{frac} \frac{\partial p_\alpha}{\partial x_i} = -\frac{k_{r_\alpha}}{\mu_\alpha} \frac{h_b^3}{12w} \frac{\partial p_\alpha}{\partial x_i} \qquad \text{(IV–52)}$$

where the subscript $\alpha = w, g$ represents the liquid or gaseous phase respectively, p is the applied pressure, either of water or gas, and k_{r_α} is the relative permeability, introduced as a measure of the reduction in permeability to a given phase α, that occurs between partially and fully saturated conditions. In porous media, these relative permeabilities of water k_{r_w} and gas k_{r_g} phases are often expressed as power functions of the saturation, according to [Corey, 1954], which reads for a single fracture (see Appendix E for further developments [Fourar and Lenormand, 1998]):

$$k_{r_w} = \frac{S_r^{*2}}{2}(3 - S_r^*) \qquad \text{(IV–53)} \qquad\qquad k_{r_g} = (1 - S_r^*)^3 \qquad \text{(IV–54)}$$

where $S_r^* = \frac{S_{rw} - S_{rw,res}}{1 - S_{rw,res} - S_{rg,res}}$ is the normalised saturation.

In the same way, the longitudinal advective component of the multiphase flow along a tube embedded in the REV of section A, is expressed as:

$$q_{\alpha,i} = -\frac{k_{r_\alpha}}{\mu_\alpha} \frac{1}{A} \kappa_{tube} \frac{\partial p}{\partial x_i} = -\frac{k_{r_\alpha}}{\mu_\alpha} \pi \frac{D^4}{128 w^2} \frac{\partial p}{\partial x_i} \qquad \text{(IV–55)}$$

where the relative permeabilities of water ($k_{r_{\alpha_w}}$) and gas ($k_{r_{\alpha_g}}$) are similarly formulated as power functions of the saturation, according to [Corey, 1954], which reads for a single capillary (see Appendix E for further developments [Yuster, 1951]):

$$k_{r_w} = S_r^{*2} \qquad \text{(IV–56)} \qquad\qquad k_{r_g} = (1 - S_r^*)^2 \qquad \text{(IV–57)}$$

As for the longitudinal diffusive component of the multiphase flow along a fracture or a tube, it is defined by Fick's law [Fick, 1855], which states that the flux in the direction i for a diffusing species is directly proportional to the concentration gradient in that direction. Thence, the diffusion flux of dissolved gas within the liquid phase reads:

$$i_{dg_i} = -S_{r_w}\, \bar{\tau}\, D_{dg/w}\, \rho_w \frac{\partial}{\partial x_i} \left(\frac{\rho_{dg}}{\rho_w} \right) \qquad \text{(IV–58)}$$

where $D_{dg/w}$ is the diffusion coefficient for the dissolved gas in liquid water, and $\bar{\tau}$ is the tortuosity of the REV constituent, which characterises the path followed by the dissolved gas particles across the REV in the direction i. It is supposed that $\bar{\tau} = 1$ for the fractures.

Density variations

If the fluids are supposed to be compressible, it implies variations of liquid and gas densities. And yet, considering the scale separability, it is assumed that the fluids pressure variation remains very small compared to the REV size and has a negligible effect on the fluids densities. As proposed by [van den

Eijnden, 2015] to be in line with the separation of scales, the fluid densities are considered to be constant throughout the REV.

Under isothermal conditions, the isotropic compressibility of water is thus assumed to respect the following relationship, which predicts an increase in water density as a function of the macro-scale water pressure:

$$\rho_w = \rho_{w_0}\left(1 + \frac{p_w^M - p_{w_0}^M}{\chi_w}\right) \tag{IV–59}$$

where ρ_{w_0} is the liquid density at the pressure $p_{w_0}^M$ and $\frac{1}{\chi_w}$ is the liquid compressibility.

The density of dry gas phase in a fracture or a tube is expressed according to the classical ideal gas equation of state [Clapeyron, 1834] as a function of the macro-scale gas pressure, which yields:

$$\rho_g = \frac{m_g}{RT} p_g^M \tag{IV–60}$$

where m_g is the molar mass of dry gas, R is the universal gas constant and T is the absolute temperature, and p_g^M is the macro-scale gas pressure.

Based on this Equation (IV–60) and considering a constant mass of dry air between two states of pressure and temperature noted respectively (T, p_g^M) and $(T_0, p_{g,0}^M)$, the following relation is obtained:

$$\rho_g(T, p_g^M) = \rho_{g,0} \frac{p_g^M}{p_{g,0}^M} \frac{T_0}{T} \tag{IV–61}$$

where $\rho_{g,0}$ is the dry gas density at reference pressure and temperature. Under isothermal conditions, it reduces to:

$$\rho_g(p_g^M) = \rho_{g,0} \frac{p_g^M}{p_{g,0}^M} \tag{IV–62}$$

Thermodynamic equilibrium

The density of the dissolved gas is obtained with the Henry's law [Weast, 1987], which states that the amount of dissolved gas in the liquid phase is always in thermodynamic equilibrium and proportional with the quantity of dry gas, such that:

$$\rho_g^d = H_g \rho_g \tag{IV–63}$$

where H_g is the so-called Henry's coefficient.

Hydro-mechanical couplings

Following the concept of effective stress introduced at the macro-scale in Equation (IV–27), and transferred to the microscopic scale, it is possible to relate the evolution of fracture aperture and tube opening at the micro-scale to the variation in fluids pressure at the macro-scale, without any change in the total stress. Specific HM laws are therefore formulated to express the fracture and tube apertures as a function of the effective stress.

The interface HM law used for the fractures relates the displacement of the facing edges to the stress state via the normal stiffness K_n. A hyperbolic law [Goodman, 1976, Bandis et al., 1983] is generally used to account for the deforming asperities in the evolution of the normal stiffness with the fracture closure [Gens et al., 1990] as depicted in Figure IV–7a, such that the relation between the normal effective stress rate and the fracture aperture reads:

$$\dot{\sigma}' = K_n \dot{h} \tag{IV–64}$$

with the normal stiffness being defined as:

$$K_n = \frac{K_n^0}{\left(1 + \frac{\Delta h}{h_0}\right)^2} \tag{IV–65}$$

where K_n^0 is the stiffness corresponding to the the initial aperture h_0, defined for a null stress. Thus, when considering some initial stresses and that $\Delta h = h - h_0$, the initial normal closure is given by:

$$\Delta h_0 = \frac{-\sigma_0' \, h_0}{K_n^0 \, h_0 + \sigma_0'} \tag{IV–66}$$

where σ_0' is the effective stress normal to the fracture wall.

As a result, the relation between effective stresses and displacements for the fractures governing the bedding and bridging planes is given by:

$$\sigma_0' + \Delta\sigma' = \frac{K_n^0 h_0}{h}(\Delta h_0 + \Delta h) \tag{IV–67}$$

The HM law used for the tubes representing the matrix blocks relates the circumference closure to the normal effective stresses via a linear relation derived from the convergence-confinement theory [Panet and Guenot, 1982]:

$$\Delta\sigma' = K \, \Delta D_b \tag{IV–68}$$

with the stiffness K being defined as:

$$K = \frac{2G}{D_0} \tag{IV–69}$$

where D_0 is the tube diameter defined for a null stress, and G is the shear modulus of the clay rock.

Given the initial stress state of the material σ_{xx_0} and σ_{yy_0}, and the orientation θ of the fractures and the tubes with the horizontal, the normal effective stresses of the studied configuration can be computed as:

$$\sigma_0 = \sigma_{xx_0} \cos^2(\theta) + \sigma_{yy_0} \sin^2(\theta) \tag{IV–70}$$

Introducing effective stresses in the aforementioned formulations allows to initiate variations of the fracture aperture and tube opening with the fluid pressure without changing the total stress owing to the hydro-mechanical coupling defined in Equation (IV–27).

A second implicit coupling is the dependency of the intrinsic permeability on the fracture and tube apertures, which are stress-dependent as formulated in Equations (IV–52) and (IV–55). Furthermore, as the gas entry pressure is likely to decrease with the progressive opening of fractures and tubes, the respective aperture or diameter of each of these micro-elements can be used to scale the entry value of each specific element as:

$$p_e = p_{e_0} \left(\frac{h_{b_0}}{h_b}\right)^m \tag{IV–71}$$

$$p_e = p_{e_0} \left(\frac{D_{b_0}}{D_b}\right)^m \tag{IV–72}$$

where m is a material parameter of the power law, which is assigned a value of 0 for a constant entry pressure, and a value of 3.3 in [Dieudonné, 2016] based on experimental results on bentonite, and p_{e_0} is the initial entry pressure defined for the aperture h_{b_0} of a fracture or the diameter D_{b_0} of a tube, and is directly derived from the Young-Laplace equilibrium introduced in Equation (II–8), which defines the mechanical balance between the capillary pressure p_c and the surface tensions σ_{GL} in a fracture and a tube respectively:

$$p_e = \frac{2\sigma_{GL} cos\theta}{D_b/2} \tag{IV–73}$$

$$p_e = \frac{2\sigma_{GL} cos\theta}{h_b} \tag{IV–74}$$

Note that hydraulic apertures h_b and D_b are considered in order to take into account the non-smoothness of the fracture and tube edges, which respectively reads:

$$h_b = h_0 + h \qquad \text{(IV–75)} \qquad\qquad D_b = D_0 + D \qquad \text{(IV–76)}$$

It means that a mechanically closed fracture/tube $(h = D = 0)$ still allows a residual flow to circulate between the asperities as long as a non-zero minimal hydraulic opening is defined, as exemplified in Figure IV–7b.

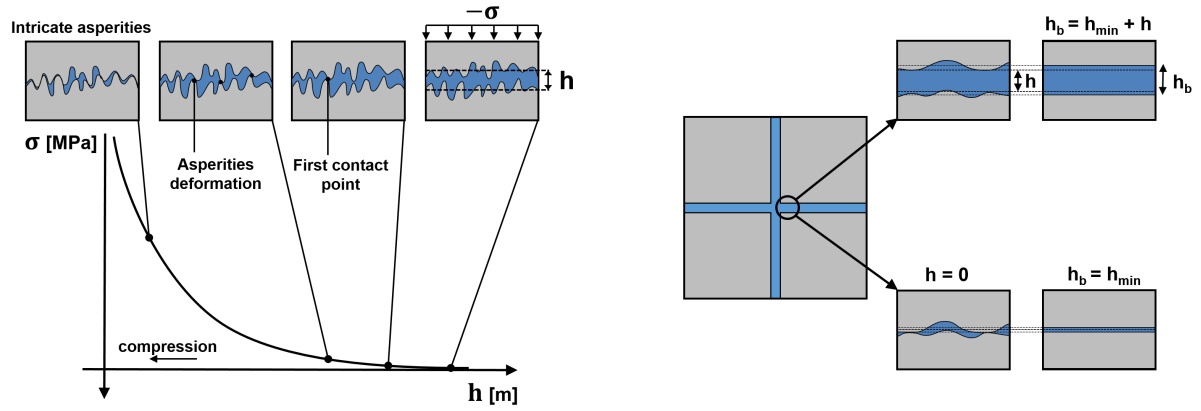

(a) (b)

Figure IV–7 – (a) Constitutive law describing the normal behaviour of a rough rock joint, *modified from* [Cerfontaine et al., 2015]. (b) Definitions of the hydraulic and the mechanical aperture in reality (left) and in the modelling (right), *modified from* [Marinelli et al., 2016].

12.3.5 Numerical solution of the problem

Given that the mechanical problem is solved separately at the macro-scale, the resolution at the microscopic scale consists in finding the different flows for the given openings of fractures and tubes. To that end, the explicit description of the fluid network is resolved over the REV in order to find the profiles of the gas and water pressures that respect the boundary conditions and, at the same time, have some average values of the pressure fields equal to the macroscopic water and gas pressures.

From the constitutive micro-scale model of Section 12.3.4, the general expressions for the channel (fracture or tube) mass fluxes of water and gas are respectively expressed as a function of the water or gas pressure gradient along this channel, such that:

$$\omega_w = \underbrace{-\frac{\rho_w k_{r_w}}{\mu_w}\kappa\frac{\partial p_w^m}{\partial s}}_{\text{Advection of liquid water}} \qquad \text{(IV–77)}$$

$$\omega_g = \underbrace{-\frac{\rho_g k_{r_g}}{\mu_g}\kappa\frac{\partial p_g^m}{\partial s}}_{\text{Advection of gaseous gas}} \underbrace{-H_g\frac{\rho_g k_{r_w}}{\mu_w}\kappa\frac{\partial p_w^m}{\partial s}}_{\text{Advection of dissolved gas}} \underbrace{-S_{r_w}\bar{\tau}D_{dg/w}\frac{H_g}{\rho_w}\left(\frac{\rho_w\rho_{g,0}}{p_{g,0}}\frac{\partial p_g^m}{\partial s}-\frac{\rho_g\rho_{w,0}}{\chi_w}\frac{\partial p_w^m}{\partial s}\right)}_{\text{Diffusion of dissolved gas}} \qquad \text{(IV–78)}$$

where κ is the hydraulic transmissivity function along the fractures and the tubes defined in Equations IV–50 and IV–51 respectively, with s the coordinate along these channels.

These two mass fluxes of water ω_w and gas ω_g are constant over the length of the channel, as implied by the steady state flow conditions at the microscopic scale. Then, accounting for the variations of

fluids densities defined in Equations (IV–59) and (IV–62), and considering in addition that the saturation S_{r_w}, and the relative permeabilities of each channel k_{r_w} and k_{r_g} are dependent on the macroscopic fluids pressures and the respective opening of the channel, the Equations (IV–77) and (IV–78) can be rewritten over the channel between s_1 and s_2 such that:

$$\omega_w = [p_w^m(s_2) - p_w^m(s_1)] \frac{\rho_w(p_w^M)}{\mu_w} \left(\int_{s_1}^{s_2} \frac{1}{k_{r_w}(p_w^M, p_g^M, s)\kappa(s)} ds \right)^{-1} \tag{IV–79}$$

$$\begin{aligned} \omega_g = & \left[p_g^m(s_2) - p_g^m(s_1)\right] \frac{\rho_g(p_g^M)}{\mu_g} \left(\int_{s_1}^{s_2} \frac{1}{k_{r_g}(p_w^M, p_g^M, s)\kappa(s)} ds \right)^{-1} \\ & + [p_w^m(s_2) - p_w^m(s_1)] H_g \frac{\rho_g(p_g^M)}{\mu_w} \left(\int_{s_1}^{s_2} \frac{1}{k_{r_w}(p_w^M, p_g^M, s)\kappa(s)} ds \right)^{-1} \\ & + \left[p_g^m(s_2) - p_g^m(s_1)\right] D_{dg/w} \frac{H_g}{\rho_w(p_w^M)} \frac{\rho_w(p_w^M)\rho_{g,0}}{p_{g,0}} \left(\int_{s_1}^{s_2} \frac{1}{S_{r_w}(p_w^M, p_g^M, s)\bar{\tau}(s)} ds \right)^{-1} \\ & - [p_w^m(s_2) - p_w^m(s_1)] D_{dg/w} \frac{H_g}{\rho_w(p_w^M)} \frac{\rho_g(p_g^M)\rho_{w,0}}{\chi_w} \left(\int_{s_1}^{s_2} \frac{1}{S_{r_w}(p_w^M, p_g^M, s)\bar{\tau}(s)} ds \right)^{-1} \end{aligned} \tag{IV–80}$$

where the following substitution variables can be used, knowing that κ is the hydraulic transmissivity function along the fracture or the tube and that s is the coordinate along these channels:

$$\phi_w = \left(\int_{s_1}^{s_2} \frac{1}{k_{r_w}(p_w^M, p_g^M, s)\kappa(s)} ds \right)^{-1} \tag{IV–81}$$

$$\phi_g = \left(\int_{s_1}^{s_2} \frac{1}{k_{r_g}(p_w^M, p_g^M, s)\kappa(s)} ds \right)^{-1} \tag{IV–82}$$

$$\lambda = \left(\int_{s_1}^{s_2} \frac{1}{S_{r_w}(p_w^M, p_g^M, s)\bar{\tau}(s)} ds \right)^{-1} \tag{IV–83}$$

Given the channel network in Figure IV–8 as basic example, the fluid mass balance equations along each channel can be applied to calculate the pressure profiles of the fluid network. This mass conservation principle introduced in Equation (II–51) can be easily formulated in terms of mass flows in a fluid network, implying that the mass flow is constant along a given channel in such a way that for each node of the hydraulic network, the sum of the input flows is equal to the sum of the output flows:

$$\frac{d\omega_\alpha^i}{ds^i} = 0 \qquad \Leftrightarrow \qquad \omega_\alpha^{i-1} + \omega_\alpha^i + \omega_\alpha^{i+1} = 0 \tag{IV–84}$$

where $\alpha = w, g$ represents the liquid or gaseous phase respectively, with $\omega_w^i \propto \phi_w^i$ and $\omega_g^i \propto \phi_w^i + \phi_g^i + \lambda^i$.

For water, the mass balance equations written at each intersection give the following system of equations:

$$[E_{WW}] \left\{ p_w^m \right\} = 0 \tag{IV–85}$$

For the proposed configuration, taking into account the homologous connectivity of lead and follow node couples over the periodic boundaries and the conditions given by the macroscopic pressure gradient in Equation (IV–39), the system to solve is given by Equation (IV–86), supposing that $\phi_w^i \propto k_{r_w}^i \kappa^i$ is the term encompassing the variable quantities of the channel i.

$$\frac{\rho_w}{\mu_w} \begin{bmatrix} \phi_w^A & 0 & -\phi_w^A - \phi_w^C & \phi_w^C & 0 \\ 0 & \phi_w^B & -\phi_w^B - \phi_w^D & 0 & \phi_w^D \\ -\phi_w^A & -\phi_w^B & \phi_w^A + \phi_w^B + \phi_w^C + \phi_w^D & -\phi_w^C & -\phi_w^D \\ -1 & 0 & 0 & 1 & 0 \\ 0 & -1 & 0 & 0 & 1 \end{bmatrix} \begin{pmatrix} p_w^1 \\ p_w^2 \\ p_w^3 \\ p_w^4 \\ p_w^5 \end{pmatrix} = \begin{pmatrix} 0 \\ 0 \\ 0 \\ (\Delta p_w)_x^M \\ (\Delta p_w)_y^M \end{pmatrix} \tag{IV–86}$$

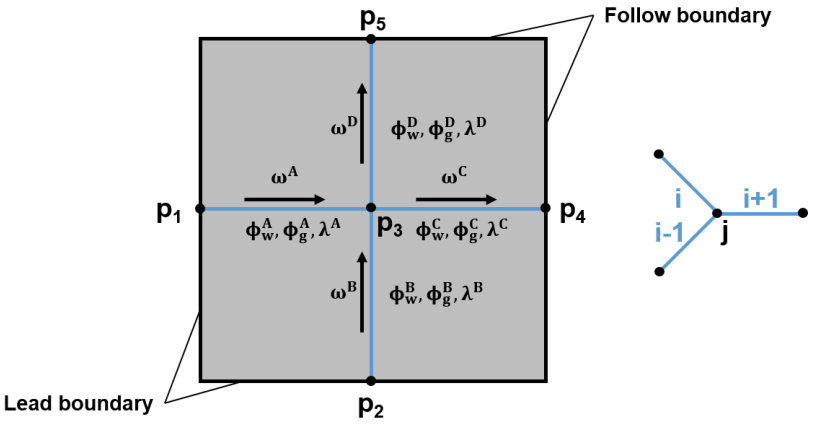

Figure IV–8 – Example of a channel network with the mass balance on node j.

To overcome the ill-posed nature of this system, where the third equation is a linear combination of the first and second ones, the macroscopic water pressure is applied at one of the nodes of the hydraulic network, *i.e.* the second, which leads to:

$$\frac{\rho_w}{\mu_w}\begin{bmatrix} \phi_w^A & 0 & -\phi_w^A-\phi_w^C & \phi_w^C & 0 \\ 0 & 1 & 0 & 0 & 0 \\ -\phi_w^A & -\phi_w^B & \phi_w^A+\phi_w^B+\phi_w^C+\phi_w^D & -\phi_w^C & -\phi_w^D \\ -1 & 0 & 0 & 1 & 0 \\ 0 & -1 & 0 & 0 & 1 \end{bmatrix}\begin{pmatrix} p_w^1 \\ p_w^2 \\ p_w^3 \\ p_w^4 \\ p_w^5 \end{pmatrix} = \begin{pmatrix} 0 \\ p_w^M \\ 0 \\ (\Delta p_w)_x^M \\ (\Delta p_w)_y^M \end{pmatrix} \tag{IV–87}$$

For gas, the presence of dissolved gas in the water leads to additional gas mass fluxes associated to the advective component of water flows and the diffusive component of gas flow, which gives the following system of equations:

$$[E_{GG}]\left\{p_g^m\right\} + [E_{GW}]\left\{p_w^m\right\} = 0 \tag{IV–88}$$

In the same way as for water, considering the configuration proposed in Figure IV–8, the well-posed system to solve is given in Equation (IV–89), supposing that $\phi_g^i \propto k_{r_g}^i \kappa^i$ and $\lambda^i \propto S_{r_w}^i \bar{\tau}^i \Omega^i$ represent terms encompassing the variable quantities of the channel i, with $S_{r_w}^i$, $\bar{\tau}^i$ and Ω^i being the saturation, the tortuosity and the section of element i. Since the system of Equations (IV–87) is solved independently from the microscopic gas pressures, the microscopic water pressures appearing in Equation (IV–88) are therefore already known before solving the system for gas and it may be written as an independent term on the right side of the equation. Applying the conditions given by the macroscopic pressure gradient in Equation (IV–40) together with the macroscopic gas pressure at one of the nodes, it leads to the following system of equations:

$$\begin{aligned} &\frac{\rho_g}{\mu_g}\begin{bmatrix} \phi_g^A & 0 & -\phi_g^A-\phi_g^C & \phi_g^C & 0 \\ 0 & 1 & 0 & 0 & 0 \\ -\phi_g^A & -\phi_g^B & \phi_g^A+\phi_g^B+\phi_g^C+\phi_g^D & -\phi_g^C & -\phi_g^D \\ -1 & 0 & 0 & 1 & 0 \\ 0 & -1 & 0 & 0 & 1 \end{bmatrix}\begin{pmatrix} p_g^1 \\ p_g^2 \\ p_g^3 \\ p_g^4 \\ p_g^5 \end{pmatrix} \\ &+ D_{dg/w}\frac{H_g}{\rho_w}\left(\frac{\rho_w \rho_{g,0}}{p_{g,0}}\right)\begin{bmatrix} \lambda^A & 0 & -\lambda^A-\lambda^C & \lambda^C & 0 \\ 0 & 1 & 0 & 0 & 0 \\ -\lambda^A & -\lambda^B & \lambda^A+\lambda^B+\lambda^C+\lambda^D & -\lambda^C & -\lambda^D \\ -1 & 0 & 0 & 1 & 0 \\ 0 & -1 & 0 & 0 & 1 \end{bmatrix}\begin{pmatrix} p_g^1 \\ p_g^2 \\ p_g^3 \\ p_g^4 \\ p_g^5 \end{pmatrix} \end{aligned} \tag{IV–89}$$

$$+D_{dg/w}\frac{H_g}{\rho_w}\left(\frac{\rho_g\rho_{w,0}}{\chi_w}\right)\begin{bmatrix}\lambda^A & 0 & -\lambda^A-\lambda^C & \lambda^C & 0\\ 0 & 1 & 0 & 0 & 0\\ -\lambda^A & -\lambda^B & \lambda^A+\lambda^B+\lambda^C+\lambda^D & -\lambda^C & -\lambda^D\\ -1 & 0 & 0 & 1 & 0\\ 0 & -1 & 0 & 0 & 1\end{bmatrix}\begin{pmatrix}p_w^1\\ p_w^2\\ p_w^3\\ p_w^4\\ p_w^5\end{pmatrix}$$

$$=-\frac{H_g\rho_g}{\mu_w}\begin{bmatrix}\phi_w^A & 0 & -\phi_w^A-\phi_w^C & \phi_w^C & 0\\ 0 & 1 & 0 & 0 & 0\\ -\phi_w^A & -\phi_w^B & \phi_w^A+\phi_w^B+\phi_w^C+\phi_w^D & -\phi_w^C & -\phi_w^D\\ -1 & 0 & 0 & 1 & 0\\ 0 & -1 & 0 & 0 & 1\end{bmatrix}\begin{pmatrix}p_w^1\\ p_w^2\\ p_w^3\\ p_w^4\\ p_w^5\end{pmatrix}+\begin{pmatrix}0\\ p_g^M\\ 0\\ (\Delta p_g)_x^M\\ (\Delta p_g)_y^M\end{pmatrix}$$

12.4 Micro-to-macro scale transition

Once the equilibrium is obtained for the micro-scale boundary value problem, the micro-to-macro scale transition is achieved by ensuring that the average micro-scale work is equal to the macro-scale work according to the Hill-Mandel macro-homogeneity condition [Hill, 1965]. In this way, the macro-scale response for the (water and gas) fluxes and fluids masses is computed by homogenisation.

12.4.1 Fluid fluxes

For the water fluxes, the macro-homogeneity condition in a virtual work formulation reads:

$$\dot{M}_w^M p_w^{*,M}-f_{w_i}^M\frac{\partial p_w^{*,M}}{\partial x_i}=\frac{1}{\Omega}\int_\Omega\left(\dot{M}_w^m p_w^{*,M}-f_{w_i}^m\frac{\partial p_w^{*,M}}{\partial x_i}\right)d\Omega \tag{IV–90}$$

Given the steady state conditions at the micro-level and the applied boundary conditions, the macro-scale fluxes in Equation (IV–90) reduces to:

$$\begin{aligned}f_{w_i}^M\frac{\partial p_w^{*,M}}{\partial x_i}&=\frac{1}{\Omega}\int_\Omega f_{w_i}^m\frac{\partial p_w^{*,M}}{\partial x_i}d\Omega=\frac{1}{\Omega}\int_\Gamma\bar{q}_w^m p_w^{*,M}d\Gamma\\ &=\frac{1}{\Omega}\frac{\partial p_w^{*,M}}{\partial x_i}\int_\Gamma\bar{q}_w^m x_i d\Gamma\end{aligned} \tag{IV–91}$$

Thence, the macro-scale fluxes reduce to the integrals of the micro-scale boundary fluxes that corresponds to the sum of the fluxes on the nodes belonging to the follow boundary in Figure IV–8:

$$f_{w_i}^M=\frac{1}{\Omega}\int_\Gamma\bar{q}_w^m x_i d\Gamma \tag{IV–92}$$

For the gas fluxes, similar considerations can be made, so that the macro-scale fluxes read:

$$f_{g_i}^M+f_{dg_i}^M=\frac{1}{\Omega}\int_\Gamma\bar{q}_g^m x_i d\Gamma \tag{IV–93}$$

More specifically, the homogenised horizontal flow corresponds to the flows on the vertical border of the REV while the vertical one is determined from the flows on the horizontal border.

12.4.2 Fluid masses

The macroscopic fluid contents M_w^M and M_g^M are directly defined as the total amounts of fluid, *i.e.* liquid water, dry gas and dissolved gas in the water phase, inside the fractures and tubes included in the REV, such that:

$$M_w^M = \frac{1}{\Omega}\int_{\Omega_w^{int}} \rho_w d\Omega = \rho_w S_{r_w} \phi_n \qquad \text{(IV–94)}$$

$$\begin{aligned} M_g^M &= M_g^m + M_{dg}^m \\ &= \frac{1}{\Omega}\left(\int_{\Omega_g^{int}} \rho_g d\Omega + \int_{\Omega_w^{int}} \rho_{dg} d\Omega\right) \\ &= \rho_g \left(1 - S_{r_w}\right)\phi_n + \rho_{dg} S_{r_w} \phi_n \end{aligned} \qquad \text{(IV–95)}$$

where ρ_w and ρ_g are constant over the REV, $S_{r_w} = \frac{\Omega_w^{int}}{\Omega^{int}}$ is the water saturation, and $\phi_n = \frac{\Omega^{int}}{\Omega}$ is the porosity from the network of fractures and tubes within the REV.

The macroscopic fluid mass storage terms $\dot{M}_w^{M,t}$ and $\dot{M}_g^{M,t}$ are then computed using some finite difference approximations over the time interval Δt:

$$\dot{M}_w^{M,t} \approx \frac{M_w^{M,t} - M_w^{M,t-\Delta t}}{\Delta t} \qquad \text{(IV–96)}$$

$$\dot{M}_g^{M,t} \approx \frac{M_g^{M,t} - M_g^{M,t-\Delta t}}{\Delta t} \qquad \text{(IV–97)}$$

which corresponds to the time variations of the fluid densities and the saturation of each phase on the one hand, and of the opening/closure of the fractures and the tubes on the other hand.

12.5 Macro-scale boundary value problem

The resolution of the boundary value problem at the macroscopic scale is governed by a coupled system encompassing the mechanical response computed at the macro-scale and the hydraulic effects of the fluid mixture evaluated from micro-scale calculations:

$$\begin{bmatrix} \left[E_{MM}^M\right]_{(4\times4)} & \left[E_{MW}^M\right]_{(4\times3)} & \left[E_{MG}^M\right]_{(4\times3)} \\ \left[E_{WM}^M\right]_{(3\times4)} & \left[E_{WW}^M\right]_{(3\times3)} & \left[E_{WG}^M\right]_{(3\times3)} \\ \left[E_{GM}^M\right]_{(3\times4)} & \left[E_{GW}^M\right]_{(3\times3)} & \left[E_{GG}^M\right]_{(3\times3)} \end{bmatrix} \begin{Bmatrix} \left\{\delta\varepsilon^M\right\}_{(4)} \\ \begin{Bmatrix} \delta\nabla p_w^M \\ \delta p_w^M \end{Bmatrix}_{(3)} \\ \begin{Bmatrix} \delta\nabla p_g^M \\ \delta p_g^M \end{Bmatrix}_{(3)} \end{Bmatrix} = \begin{Bmatrix} \left\{\delta\sigma^M\right\}_{(4)} \\ \begin{Bmatrix} \delta f_w^M \\ \delta\dot{M}_w^M \end{Bmatrix}_{(3)} \\ \begin{Bmatrix} \delta f_g^M \\ \delta\dot{M}_g^M \end{Bmatrix}_{(3)} \end{Bmatrix} \qquad \text{(IV–98)}$$

which can be summarised as follows:

$$\left[E^M\right]_{(10\times10)} \left\{\delta U^M\right\}_{(10)} = \left\{\delta\Sigma^M\right\}_{(10)} \qquad \text{(IV–99)}$$

where $\left[E^M\right]$ is the macro-scale stiffness matrix obtained by numerical perturbations as presented in Section 6.5.7, $\left\{\delta U^M\right\}$ contains the infinitesimal variations of the macro-scale variables, and $\left\{\delta\Sigma^M\right\}$ is the responses of these variables. The matrices $[E_{mm}]$, $[E_{ww}]$, $[E_{gg}]$ are the classical stiffness matrices for mechanical, water flow and gas flow problems, while the off-diagonal matrices contain the multi-physical coupling terms. The stiffness matrices capturing the influence of the mechanics on the fluids are computed in a similar way as in Equations (III–75) and (III–76) for the second gradient H^2M model, while the simplified versions of the terms reflecting the influence of the fluids on the mechanics are considered, which reads:

$$\left[E_{MW}\right] = \left[\begin{array}{c|c|c|c} A_{111}^w + L_j^w + N_1^w & A_{121}^w + N_1^w + F_2^w & A_{112}^w + N_2^w & A_{122}^w + L_j^w + N_2^w - F_1^w \\ \hline A_{211}^w + L_j^w + N_1^w - F_2^w & A_{221}^w + N_1^w & A_{212}^w + N_2^w + F_1^w & A_{222}^w + L_j^w + N_2^w \\ \hline C^w + M^w & 0 & 0 & C^w + M^w \end{array}\right] \qquad \text{(IV–100)}$$

$$\left[E_{MG}\right] = \left[\begin{array}{c|c|c|c} A^g_{111} + L^g_j + N^g_1 & A^g_{121} + N^g_1 + F^g_2 & A^g_{112} + N^g_2 + N^w_2 & A^g_{122} - F^g_1 - L^w_j + L^g_j - N^w_2 + N^g_2 \\ \hline A^w_{211} - F^g_2 - L^w_j + L^g_j - N^w_1 + N^g_1 & A^w_{221} + N^g_1 - N^w_1 & A^w_{212} + N^g_2 - N^w_2 + F^g_1 & A^w_{222} + L^g_j - L^w_j + N^g_2 - N^w_2 \\ \hline C^g + M^g & 0 & 0 & C^g + M^g \end{array}\right] \tag{IV–101}$$

$$\left[E_{WM}\right] = \left[\begin{array}{c|c|c|c} 0 & 0 & 0 & 0 \\ \hline 0 & 0 & 0 & 0 \\ \hline -bS_{r_w} & 0 & 0 & -bS_{r_w} \end{array}\right] \tag{IV–102}$$

$$\left[E_{GM}\right] = \left[\begin{array}{c|c|c|c} 0 & 0 & 0 & 0 \\ \hline 0 & 0 & 0 & 0 \\ \hline -b\left(1 - S_{r_w}\right) & 0 & 0 & -b\left(1 - S_{r_w}\right) \end{array}\right] \tag{IV–103}$$

where the expressions of the different sub-matrices have been given in Chapter 9 of Part III, and further developed in Appendix D. The detailed derivation of the other sub-matrices can be found in [Collin et al., 2006] for a multiphasic medium.

13. Applications

In this last chapter of Part IV, the multi-scale HM model is applied to the numerical modelling of gas injection tests conducted in Boom Clay. The study considers two gas flow orientations, either parallel or perpendicular to the primary bedding planes of the rock. The modelling task is then extended to focus on the representation of gas-filled pathways in more general configurations, with the aim of tackling the issues of heterogeneity and tortuosity inherent to the rock structure, as well as the questions raised by the up-scaling of such phenomena.

13.1 Numerical modelling of gas injection tests

This section covers the experimental design of the gas injection tests and its translation into numerical modelling. The constitutive models and their associated parameters are carefully determined for both the Boom Clay and the experimental set-up. Preliminary model verifications are conducted prior to presenting and examining the key numerical findings from the various simulations, with an emphasis on the emergence of gas-specific pathways.

13.1.1 Experimental design

The experimental design reported in [Gonzalez-Blanco et al., 2016] consists of air injection tests under oedometer conditions on initially saturated samples of Boom Clay. These samples were retrieved from the HADES underground research laboratory, at a depth of 223 m, under a total vertical stress and water pressure of $\sigma_v = 4.6$ MPa and $p_w = 2.2$ MPa respectively, with $K_0 = 1$.

The experimental set-up, described in [Gonzalez-Blanco et al., 2016, Gonzalez-Blanco and Romero, 2022] and presented in Figure IV–9, features an instrumented high-pressure and high-stiffness oedometer cell for cylindrical samples of 50 mm in diameter and 25 mm in height. It is designed in such a way as to investigate water and gas flow through intact and disturbed samples of clayey rocks.

The protocol for air injection tests starts by following a pre-conditioning path, *i.e.* a water undrained loading path, to approximately restore the *in situ* effective stress of the material. Boom Clay samples are vertically loaded to an initial total vertical stress of $\sigma_v = 3$ MPa in the oedometer cell, and put in contact with synthetic water at atmospheric pressure afterwards. It is high enough to avoid a large swelling during saturation, and it enables to reach the *in situ* effective stress after imposing water pressure and keeping the stress level within the working range of the equipment. Then, the water permeability of the sample is determined under different pressure gradients and at constant total vertical/isotropic stress, before performing a drained loading stage to a total vertical stress of $\sigma_v = 6$ MPa. Just before the air injection phase, a fast drainage of the bottom line is performed to replace water by air, with an initial air pressure of $p_g = 0.5$ MPa applied at the upstream boundary.

Air injection tests at two different injection rates (*slow:* 2 mL/min and *fast:* 100 mL/min) are performed to analyse their influence on the coupled hydro-mechanical response. The selected rates are relatively fast to minimise air diffusion mechanisms through the matrix and to enhance single-phase air flow mechanisms through discontinuities [Marschall et al., 2005]. The air injection piston is stopped

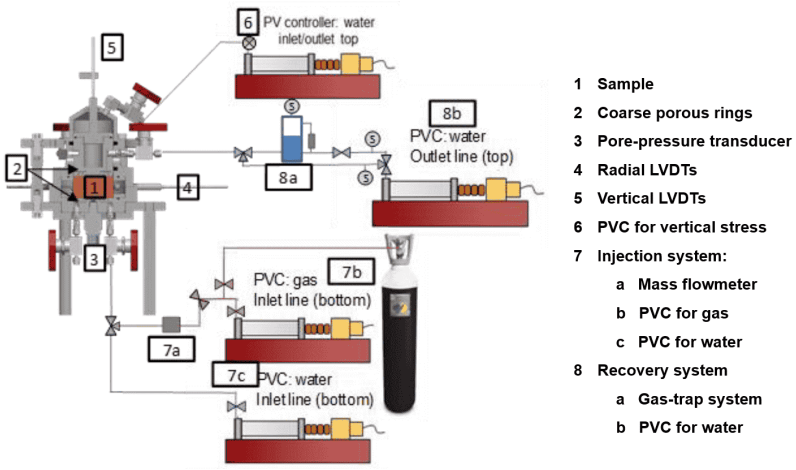

Figure IV–9 – Scheme of the experimental set-up, *after* [Gonzalez-Blanco et al., 2016].

(shutoff) when air pressure reaches a maximum of $p_g = 4$ MPa, close to the air-entry value. At this stress state, the air pressure is let decaying at constant air volume of the inlet line. The recovery lines are initially full of water and the controller is kept at a constant pressure of 0.5 MPa in both set-ups. However, the Pressure/Volume Controller (PVC) of the recovery system is not able to keep this constant pressure condition when the air flow is very high, so that an increase in the downstream pressure occurs, up to a maximum pressure of 1.8 MPa controlled by a pressure release valve. Finally, samples are unloaded under undrained conditions.

13.1.2 Modelling design

In this section, the ingredients required to convert the experimental design into a numerical model are described, covering especially the geometry of the problem, the mesh of the model, the initial boundary conditions as well as the successive steps of the simulations carried out by means of boundary conditions update.

13.1.2.1 Geometry

Taking advantage of the radial symmetry of the oedometer sample, the modelling design of the air injection tests consists of a 2D axisymmetric representation of the Boom Clay sample using the multi-scale model developed in previous Chapter 12 and implemented in the `LAGAMINE` code. Thence, null vertical displacements at the bottom of the system and null radial displacement on the sample lateral wall are imposed by the oedometer conditions. To properly simulate the stages of the gas injection tests, injection (bottom) and recovery (top) reservoirs surrounding the sample are also included in the model as illustrated in Figure IV–10, which materialise the injection and recovery pistons, lines and coarse porous rings of the experimental set-up.

In order to investigate the consequences of the development of gas-filled preferential pathways, the sample is divided into two zones having different hydraulic properties as depicted in Figure IV–10c: the matrix (undisturbed clay, coloured in grey) and a Zone of Fracture Development (ZFD), including either disturbed bedding planes in red or disturbed bridging planes in blue, depending on the orientation of the sample. This latter part located in a single predefined central band with a thickness of 2 mm, represents a zone where cracks will preferentially open and is characterised by weaker properties for the rock corresponding to the ones obtained after the injection test. Such an imposed arrangement makes it possible to reproduce the global effect of the preferential pathways activation on the global sample response but does not account for the local distribution of the fractures.

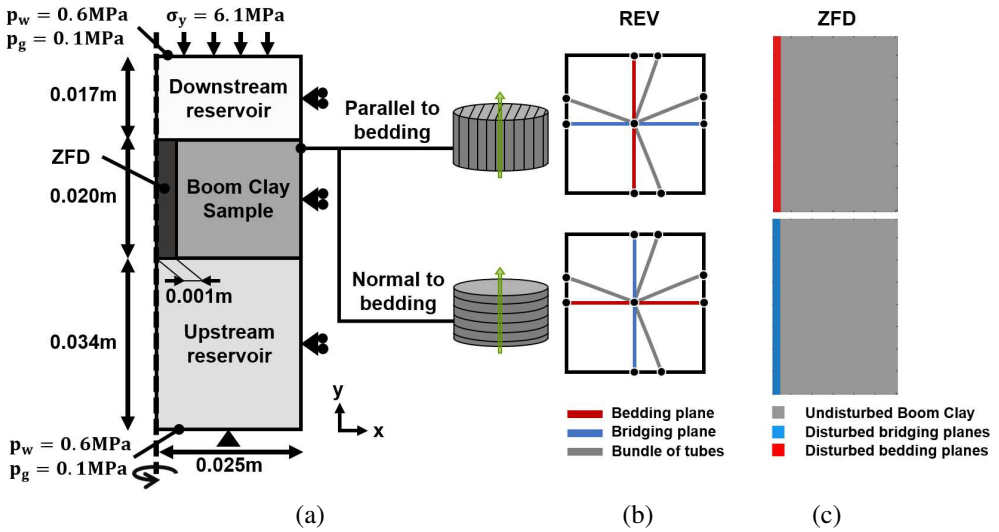

Figure IV–10 – (a) Geometry and initial boundary conditions, with (b) the REV idealisation showing the two orientations of the studied sample, and (c) the two configurations of the ZFD.

13.1.2.2 Initial conditions

The initial conditions in the Boom Clay sample following the initial pre-conditioning phase and whatever the orientation of the sample are defined by an isotropic stress state and homogeneous water and air pressures as:

$$\sigma_{x,0} = \sigma_{y,0} = 6\ \text{MPa},\ p_{w,0} = 0.6\ \text{MPa},\ p_{g,0} = 0.1\ \text{MPa} \tag{IV–104}$$

where $\sigma_{x,0}$ and $\sigma_{y,0}$ are the horizontal and vertical principal total stress respectively, while $p_{w,0}$ and $p_{g,0}$ correspond to the initial pore water and gas pressures respectively.

13.1.2.3 Boundary condition evolution

Since the numerical simulations focus solely on the slow gas injection tests carried out parallel and perpendicular to the bedding planes of the sample, it should be first mentioned that the initial pre-conditioning and final unloading stages are neglected.

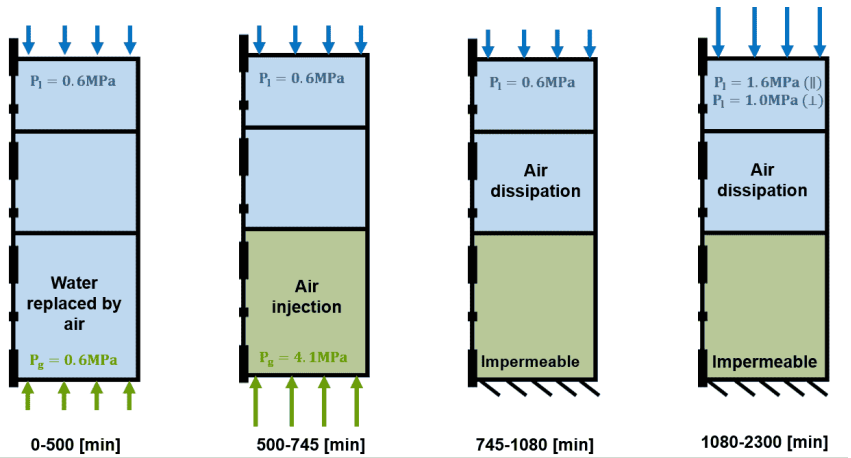

Figure IV–11 – Evolution of the boundary conditions in terms of water and gas pressures during the successive steps of the numerical simulation.

The sequential evolution of the experiment is translated into a boundary value problem which is conducted by progressively adjusting the boundary conditions at the two sides of the geometry, as highlighted in Figure IV–11. Before the air injection starts, the sample was fully saturated, as well as both reservoirs. First, water is replaced by air in the upstream reservoir with an upstream air pressure increasing up to 0.6 MPa. Then the air injection phase is performed with a pressure ramp applied at the bottom of the injection reservoir, which follows the data recorded experimentally up to a pressure of 4.1 MPa. Once the injection pressure reaches this maximum pressure, the dissipation phase starts, during which the bottom boundary becomes impermeable forcing the accumulated air in the upstream reservoir to flow upwards. As for the downstream reservoir, the pressure there is kept constant at 0.6 MPa throughout the tests. In practise, this device is capable of maintaining the pressure constant by adjusting the volume. However, once the tank of the controller is full and the air continues to flow through the sample, the device is not longer able to maintain the pressure. Accordingly, the pressure boundary condition in the recovery system is increased up to 1.6 MPa and 1.0 MPa in a second part of the dissipation stage for injection parallel and perpendicular to the bedding respectively. A schematic picture of the boundary conditions evolution is shown in Figure IV–11.

13.1.3 Constitutive models and parameters

The constitutive models of the Boom Clay, the injection and recovery systems and their related parameters required for the numerical application are presented in this section.

13.1.3.1 Mechanical model

An elasto-plastic internal friction model with cross-anisotropy and horizontal isotropic bedding planes is considered for the mechanical behaviour of the Boom Clay, which can be decomposed into an elastic and a plastic component, such that:

$$\dot{\varepsilon}_{ij} = \dot{\varepsilon}^e_{ij} + \dot{\varepsilon}^p_{ij} \tag{IV–105}$$

where ε^e_{ij} and ε^p_{ij} are the elastic and plastic components of the total strain rate.

Elastic component

The linear elastic behaviour of the rock is based on the classical Hooke's law (Equation (II–96)), where the elastic compliance tensor is expressed as a function of only five independent parameters as stipulated in Equation (II–99) for cross-anisotropic materials [Amadei, 1983]. The Boom Clay formation is indeed characterised by a strong anisotropy of its mechanical properties between the directions parallel and perpendicular to the bedding planes [Chen et al., 2011], but the behaviour remains isotropic in the parallel bedding planes.

Plastic component

The elasto-plastic behaviour of the Boom Clay is characterised by an internal friction model with a non-associated plasticity and a van Eekelen yield surface [Van Eekelen, 1980] (under soil mechanics convention with positive compressive stress) defined in Equation (II–102). Furthermore, the model is able to produce isotropic hardening or softening of the cohesion and of the friction angles upon loading. Further details about the elasto-plastic model are available in [Pardoen, 2015].

The elasto-plastic parameters of the Boom Clay, reported in Table IV–1, are taken from [François, 2014] where calibration is realised based on experimental data.

13.1.3.2 Hydraulic model

The hydraulic model used for the Boom Clay is based on the multi-scale HM model presented in previous Chapter 12. At this point, all the parameters characterising the microstructural components of

Table IV–1 – Set of elasto-plastic parameters of the Boom Clay, *from* [François, 2014].

Parameter	Symbol	Value	Unit
Parallel Young's modulus	$E_{\parallel}$	400	$[MPa]$
Perpendicular Young's modulus	$E_{\perp}$	200	$[MPa]$
Poisson's ratio	$\nu_{\parallel\parallel}$	0.125	$[-]$
Poisson's ratio	$\nu_{\parallel\perp}$	0.125	$[-]$
Poisson's ratio	$\nu_{\perp\parallel}$	0.0625	$[-]$
Shear modulus	$G_{\parallel\perp}$	178	$[MPa]$
Shear modulus	$G_{\parallel\parallel}$	178	$[MPa]$
Solid grain density	ρ_s	2650	$[kg/m^3]$
Initial cohesion	c_i	255 (0°)	$[kPa]$
		240 (45°)	$[kPa]$
		330 (90°)	$[kPa]$
Ratio of cohesion softening	ξ_c	3	$[-]$
Cohesion softening parameter	B_c	0.01	$[-]$
Cohesion softening shifting	dec_c	0	$[-]$
Initial compressive friction angle	$\varphi_{c,0}$	5	[°]
Final compressive friction angle	$\varphi_{c,f}$	18	[°]
Friction angle hardening param.	B_φ	0.01	$[-]$
Friction angle hardening shifting	dec_φ	0	$[-]$
Dilatancy angle	ψ_c	0	[°]

Table IV–2 – Initial apertures and separation values obtained from different techniques by [Gonzalez-Blanco and Romero, 2022].

Geometric property	Unit	MIP	FESEM	μCT
Aperture h	μm	> 2	$3-10$	$90^{\parallel}-153^{\perp}$
Separation w	μm	–	$150-270$	$410^{\parallel}-558^{\perp}$

the REV described in Section 12.3.1 must be defined, in order to approach as closely as possible the *in situ* behaviour of the studied host rock.

Separation value

First of all, a physical value of the bedding plane separation is selected so that it is in the range of the averaged data for Boom Clay, obtained experimentally with different techniques by [Gonzalez-Blanco, 2017] and summarized in Table IV–2. This value constitutes the reference size w of the REV. In the present case, a value of $w = 3 \cdot 10^{-4}$m is chosen.

Macro-porosity

Then, a specific calibration parameter value is assigned to each individual tube within the bundle which represents the micro-scale porous matrix. This latter can be assimilated to a tortuosity parameter in the sense that it is used to artificially increase the volume of each individual straight tube. This way, it is possible to fit the experimental pore size distribution curve [Lima, 2011, Gonzalez-Blanco, 2017] as highlighted in Figure IV–12a, and get the correct value of the macro-porosity of Boom Clay, *i.e.* around $n = 0.38$. Of course, increasing the number of tubes included in the REV, especially the smaller ones, should make the value of the calibration parameter to gradually converge towards the estimates of the natural equivalent tortuosity of the Boom Clay established around $\bar{\tau} = 0.6$ [Wiseall et al., 2015a]. Nevertheless, to keep reasonable computation times during simulations, a limited number of tubes is integrated in the implemented REV.

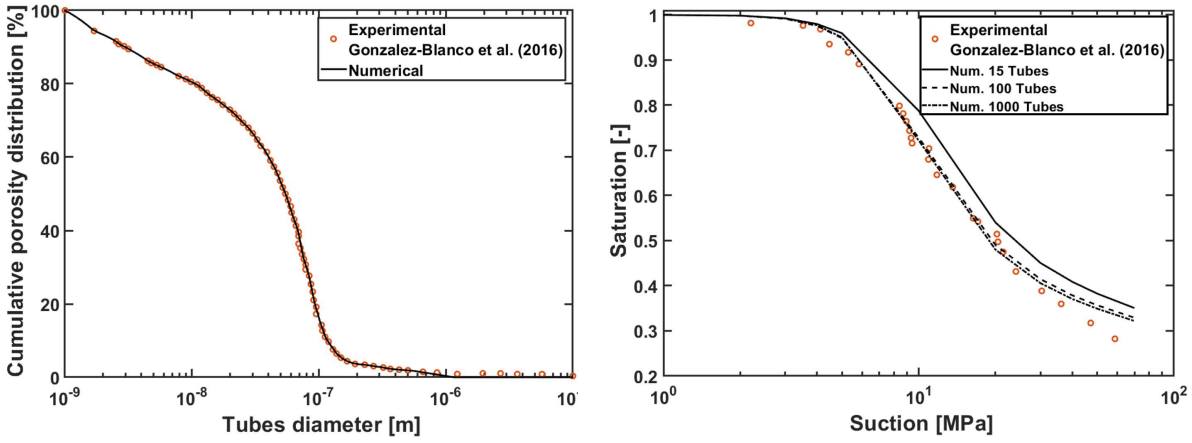

(a) (b)

Figure IV–12 – (a) Experimental data for the cumulative porosity distribution of the Boom Clay [Gonzalez-Blanco et al., 2016], with respective fitted numerical results. (b) Experimental data for the water retention curve of intact Boom Clay [Gonzalez-Blanco et al., 2016], together with van Genuchten's model fitting for an increased numbre of tubes.

Retention curves

To characterise the Boom Clay retention behaviour, a retention curve of van Genuchten's type [van Genuchten, 1980] linking the capillary pressure to the degree of water saturation is assigned to each microstructural constituent, *i.e.* tubes and fractures:

$$S_{r_w} = S_{r_{res}} + (S_{max} - S_{r_{res}}) \left(1 + \left(\frac{p_c}{P_r}\right)^{\mathcal{N}}\right)^{\frac{1}{\mathcal{N}}-1} \tag{IV–106}$$

where P_r is a parameter identified as the gas entry pressure, S_{max} and $S_{r_{res}}$ are the maximum and residual degrees of water saturation, $\mathcal{N}$ is a model parameter controlling the curve shape, and $p_c = s$ is the capillary pressure or suction.

Hence, the global retention response of the material is not computed at the macroscopic scale but results from the integration of the whole individual retention curves of the microstructure elements, which allows to reasonably capture the experimental data [Gonzalez-Blanco, 2017] as the number of tubes is increased.

Intrinsic permeability of the microstructural constituents

In addition, knowing that the permeability in Boom Clay is anisotropic with a ratio of more or less two between the horizontal and vertical directions, the initial aperture of the bedding planes is chosen so that it contributes to half of the permeability in this principal direction:

$$k_{x,0} = \underbrace{\frac{\pi}{8}\left(\frac{D_{b,0}}{2}\right)^4 \left(\frac{1}{w^2}\right)}_{\sum k_{tube,0}} + \underbrace{\frac{h_{b,0}^2}{12}\frac{h_{b,0}\cdot w}{w^2}}_{k_{frac,0}} \longrightarrow h_{b,0} = \sqrt[3]{12\, w\, k_{frac,0}} \tag{IV–107}$$

where $k_{x,0}$ is the intrinsic permeability in the horizontal direction, $k_{frac,0}$ and $k_{tube,0}$ are the initial permeability of the bedding plane and each tube. In practise, bedding and bridging plane apertures of $h_{b0,\parallel} = 0.060\ \mu m$ and $h_{b0,\perp} = 0.035\ \mu m$ are respectively found for an intact sample of Boom Clay. This corroborates experimental results [Lima, 2011, Gonzalez-Blanco et al., 2016] that assimilate the dominant entrance pore size of the statistical distribution of apertures as representative of the initial bedding or bridging apertures, with values of the order of $0.1\ \mu m$.

The other fraction of the permeability is obviously provided by the macro-pores which are responsible for the majority of the permeability in the vertical direction, such that:

$$k_{y,0} = \underbrace{\frac{\pi}{8}\left(\frac{D_{b,0}}{2}\right)^4\left(\frac{1}{w^2}\right)}_{\sum k_{tube,0}} \tag{IV–108}$$

where $k_{y,0}$ is the intrinsic permeability in the vertical direction.

Relative permeability of the microstructural constituents

On top of that, relative permeability coefficients for the liquid and gas phases are expressed as functions of the effective degree of saturation S_r^*, according to the power law Equations (IV–53)-(IV–54) for the fracture, and (IV–56)-(IV–57) for the tube respectively. These expressions provide a rather good fitting of the experimental data for bulk Boom Clay reported by [Volckaert et al., 1995] despite the dispersion, as highlighted in Figure IV–13a.

Normal stiffness of the families of fractures

Given the hydro-mechanical coupling in Equation (IV–66) which relates the stress state to the fracture aperture and thus implicitly to its permeability, it is possible to estimate the initial stiffness of the bedding plane K_n^0. Practically, this value is obtained by fitting the experimental compilation of the permeability evolution as a function of the isotropic effective stress given in Figure IV–13b [Coll, 2005, Bésuelle et al., 2014], considering that the rest of the permeability (shaded area) arises from the porosity related to the bundle of tubes.

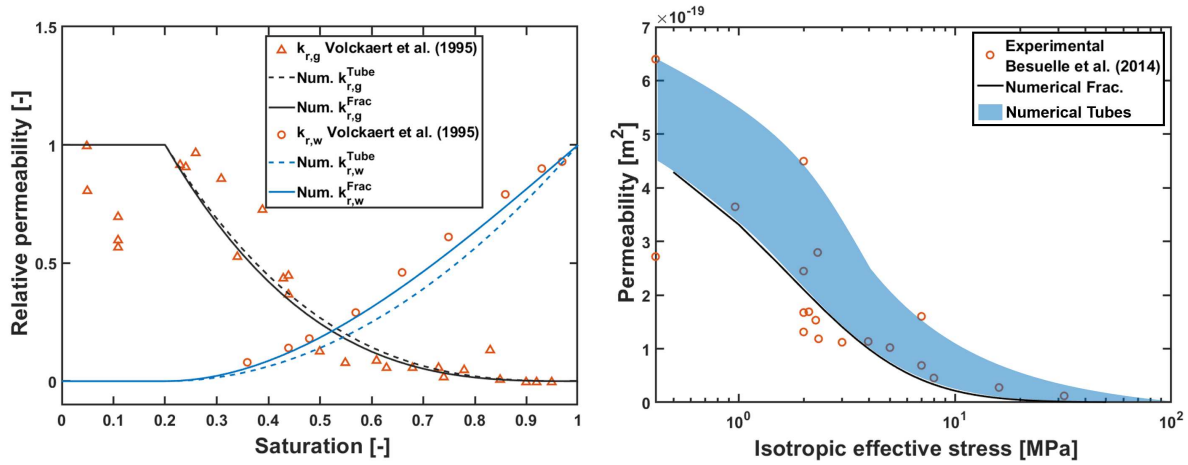

(a) (b)

Figure IV–13 – (a) Experimental data for the water and gas relative permeability curves [Volckaert et al., 1995], with fitted numerical formulation for fractures and tubes. (b) Experimental data for he water permeability of Boom Clay as a function of isotropic effective stress [Coll, 2005, Bésuelle et al., 2014], with fitted numerical results.

Zone of fracture development

Regarding the zone of fracture development, it is assumed to be characterised by weaker properties corresponding to the ones experimentally obtained at the end of the air injection tests. More specifically, it is supposed that the measured fissure opening are in between the initial and the maximum aperture of the generated pathways during gas migrations [Gonzalez-Blanco, 2017], as it is expected that the fissures close up during the air pressure dissipation when the sample undergoes compression. Therefore, in the

ZFD, the bedding and bridging plane take initial values of aperture of respectively $b_{0,\parallel} = 0.200\ \mu m$ and $b_{0,\perp} = 0.095\ \mu m$. Moreover, it is also assumed that the initial stiffness of any fissure belonging to one of these two families of fractures in this zone is reduced due to the damage compared to the intact stiffness deduced from Figure IV–13b. It means that for a given evolution of the stress state, the bedding and bridging planes are prone to open/close in a more important way in this zone of the sample, compared to the intact portions of the material, as depicted in Figures IV–14a and IV–14b. Preliminary analysis has suggested that assigning those affected parameters to fractures in the ZFD from the start of the simulation was necessary to replicate the experimental response through the initiation of preferential pathways.

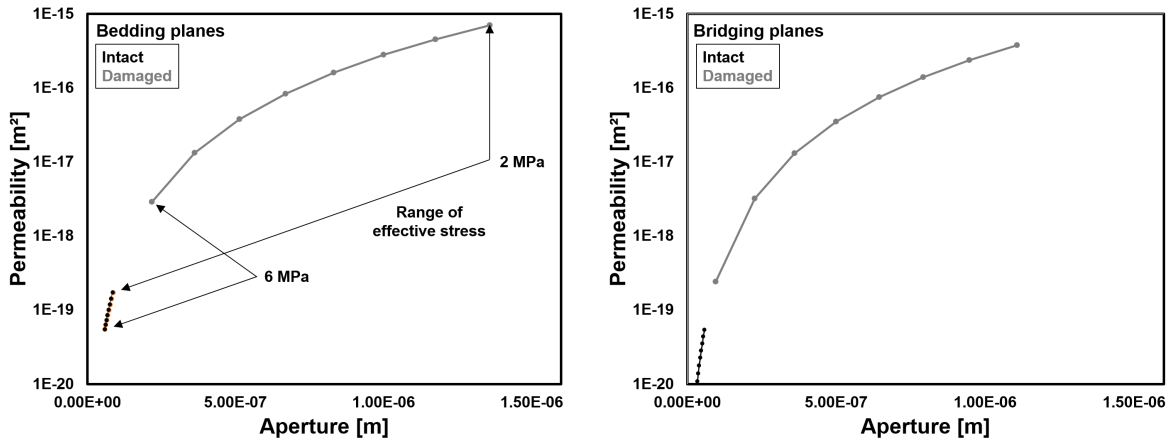

(a) (b)

Figure IV–14 – Evolution of the fracture permeability with the fracture aperture for a given stress state evolution: (a) bedding planes and (b) bridging planes.

All the hydraulic parameters of the Boom Clay are summarised in Table IV–3, which also gathers the parameters related to the zone of fracture development in the last part.

Table IV–3 – Set of hydraulic parameters of the Boom Clay, *from* [Gonzalez-Blanco et al., 2016].

Parameter	Symbol	Value		Unit
		Bedding ($\parallel$)	*Bridging* ($\perp$)	
Initial porosity	n	0.38	0.36	$[-]$
Initial parallel intrinsic permeability	$k_{w,0}$	4.2×10^{-19}	2.1×10^{-19}	$[m^2]$
Water density	ρ_w	1000		$[kg/m^3]$
Gas density (*Air*)	ρ_g	1.205		$[kg/m^3]$
Water dynamic viscosity	μ_w	0.001		$[Pa.s]$
Gas dynamic viscosity (*He*)	μ_g	1.86×10^{-5}		$[Pa.s]$
Water compressibility	χ_w^{-1}	5×10^{-10}		$[Pa^{-1}]$
Henry coefficient (*He*)	H_i	0.0234		$[-]$
Gas entry pressure (1^{st} coeff. of S_{r_w})	P_r	10.0		$[MPa]$
Parameter (2^{nd} coeff. of S_{r_w})	$\mathcal{N}$	2.5		$[-]$
Max. degree of water saturation	$S_{r,max}$	1		$[-]$
Residual degree of water saturation	$S_{r_w,res}$	0.2		$[-]$
Bedding plane separation	w	4×10^{-4}		$[m]$
Initial aperture	h_{b0}	0.060	0.035	$[\mu m]$
Initial fracture stiffness	K_n^0	4×10^{13}	$1 \times 1 \times 10^{14}$	$[Pa/m]$
Zone of fracture development (ZFD)				
Initial aperture	h_{b0}^{ZFD}	0.20	0.095	$[\mu m]$
Initial fracture stiffness	$K_n^{0,ZFD}$	2.15×10^{12}	$1 \times 2.55 \times 10^{12}$	$[Pa/m]$
Gas entry pressure (1^{st} coeff. of S_{r_w})	P_r^{ZFD}	1.0		$[MPa]$

13.1.3.3 Injection and recovery systems

These two reservoirs are idealised as very stiff elements having a linear elastic mechanical law with a very high Young modulus. The total volume of each system corresponds to the dead volumes obtained from calibration tests of the equipment [Gonzalez-Blanco et al., 2016]. Hydraulically, they are characterised by a porosity of 0.5 since the code does not model non-porous materials, with a high conductivity and a flat retention curve including a very low air entry value. All the hydro-mechanical parameters of the injection and recovery systems, retrieved from [Gonzalez-Blanco et al., 2016], are gathered in Table IV–4.

Table IV–4 – Set of hydromechanical parameters of the injection and recovery systems, *from* [Gonzalez-Blanco et al., 2016].

Parameter	Symbol	Value	Unit
Young's modulus	E	1×10^5	$[MPa]$
Poisson coefficient	ν	0.3	$[-]$
Porosity	n	0.5	$[-]$
Intrinsic permeability	k	10^{-10}	$[m^2]$
Entry pressure parameter	P_r	0.001	$[MPa]$

13.1.4 Preliminary model verification

Before applying the multi-scale model to the analysis of the laboratory experiments, a preliminary verification of the implementation of the different processes as well as the constituents of the microstructure is performed.

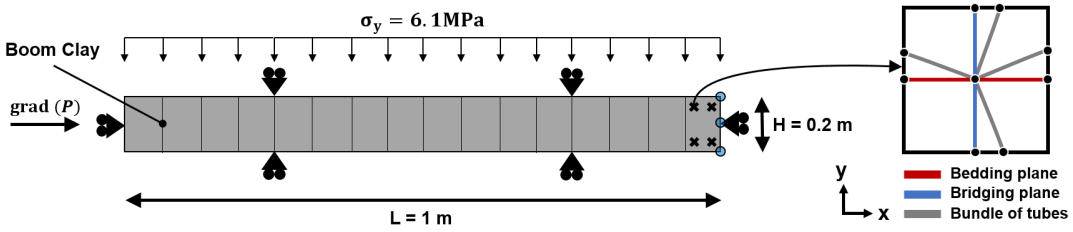

(a) (b)

Figure IV–15 – (a) Sketch of the mesh used for the model verification, representing a horizontal column of Boom Clay, with (b) the REV idealisation.

To that end, injection simulations are carried out on a poro-elastic column of Boom Clay of $L = 1$ m $\times$ $H = 0.2$ m, with a variation of fluid pressure applied at the left boundary of the mesh, while fluid pressures remain fixed at the right boundary as depicted in Figure IV–15. This column is initially saturated with liquid water at a constant pressure of $p_{w,0} = 0.6$ MPa, assuming a constant temperature of $T = 293$ °K throughout the simulation, and neglecting the gravity forces. The Boom Clay microstructure and parameters used for the model verification are identical to those characterising the modelling of the gas injection tests, introduced earlier in this Section 13.1.3. Treating more particularly the mechanisms inherent to gas migration, a gas pressure increase from $p_g = 0.1$ MPa to $p_g = 1.0$ MPa is imposed over a period of 10 days, and then it is supposed to remain constant for the rest of the simulation.

Total number of tubes

At the microscopic scale, the porous matrix of the rock mass is substituted by an assembly of tubes. Each of these straight capillaries is assigned a tortuosity-like calibration parameter to increase the total pore volume so that the macroscopic porosity is respected. Of course, the total number of tubes included

in the REV is not *a priori* fixed, as it is likely to vary as a function of the size of the problem. The larger the mesh to be modelled, the smaller the number of tubes taken into account in the REV, in order to keep calculation times acceptable. And in this case, the volume of each remaining tube will be even increased, by adjusting the value of the associated calibration parameter.

In these conditions, it is important to ensure that the responses obtained for a variable quantity of tubes remain consistent. To that end, the gas injection simulation into the column is simulated supposing a REV made of 10, 100, and 1000 tubes respectively. Results in terms of evolution profiles of gas pressures and gas fluxes are given in Figure IV–16a and IV–16b respectively. It appears that by increasing the number of tubes, the gas tends to propagate slightly faster through the column. But overall, the results obtained for the different configurations are very similar, which attests to the correct representation of the pore space by the bundle of tubes.

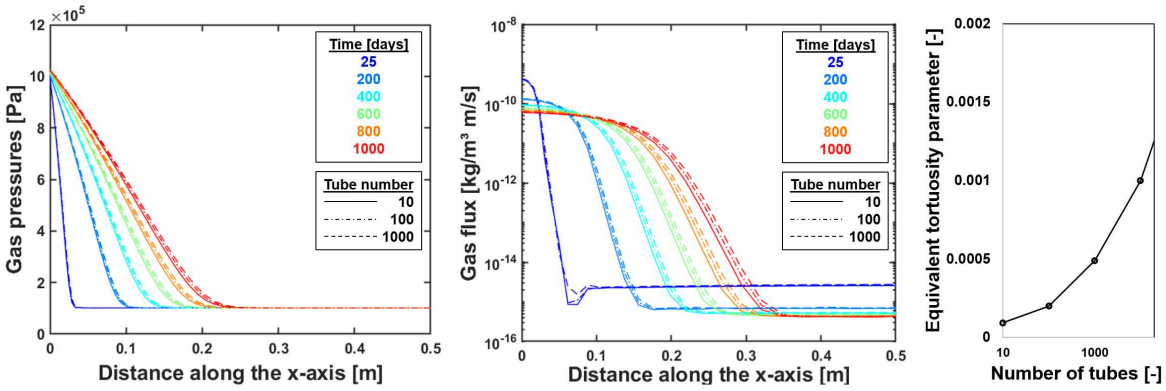

(a) (b) (c)

Figure IV–16 – Comparisons of the profiles of (a) gas pressures and (b) gas flux, for a REV including 10 tubes (solid line), 100 tubes (dotted-dashed line), and 1000 tubes (dotted line).

It is also possible to calculate an equivalent calibration coefficient for the assembly of tubes by summing the tortuosity parameter of each individual capillary, normalised by its contribution to the total pore volume. The results presented in Figure IV–16c show the evolution of this equivalent calibration parameter as a function of the number of tubes, which should theoretically tend towards the natural value of tortuosity in Boom Clay, for an infinite number of tubes.

Coupled processes

The verification of the multi-scale model capabilities with regard to the coupled processes modelling is performed by comparing the responses in terms of fluid pressures and fluxes against a well established and documented macro-scale THM coupled model. This latter constitutes the backbone of the `LAGAMINE` code with respect to coupled processes encountered in the field of geo-mechanics, and has itself been verified through a large set of benchmark exercises [Alonso and Alcoverro, 1999a, Alonso and Alcoverro, 1999b, Collin, 2003]. This multi-scale model verification is performed through a careful step-by-step procedure, where each dual coupled process is checked by progressively adding complexity and releasing the desired degrees of freedom.

At first, results in terms of water pressures, water flux and water storage are depicted in Figures IV–17a, IV–17b and IV–17c respectively. As the gas penetrates the medium and replaces water over the first meters of the column, it appears that the magnitude of the water flux just like the water storage decreases. All in all, a rather good agreement between the results of the two models are observed for these curves related to water quantities.

Similarly, Figures IV–18a, IV–18b and IV–18c provides some results in terms of gas pressure, gas

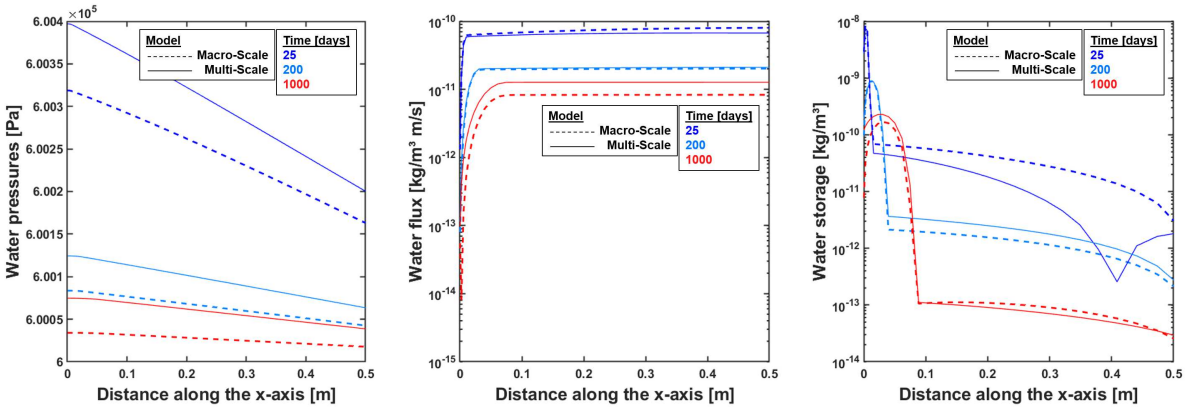

(a) (b) (c)

Figure IV–17 – Comparisons between the multi-scale model (solid line) with respect to a macro-scale model (dashed line): (a) water pressure, (b) water flux, and (c) water storage.

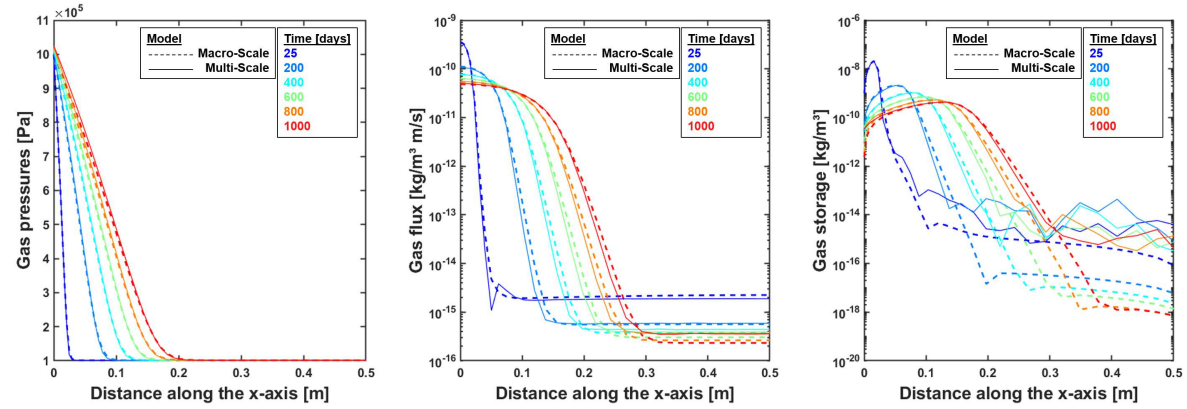

(a) (b) (c)

Figure IV–18 – Comparisons between the multi-scale model (solid line) with respect to a macro-scale model (dashed line): (a) gas pressure, (b) gas flux, and (c) gas storage.

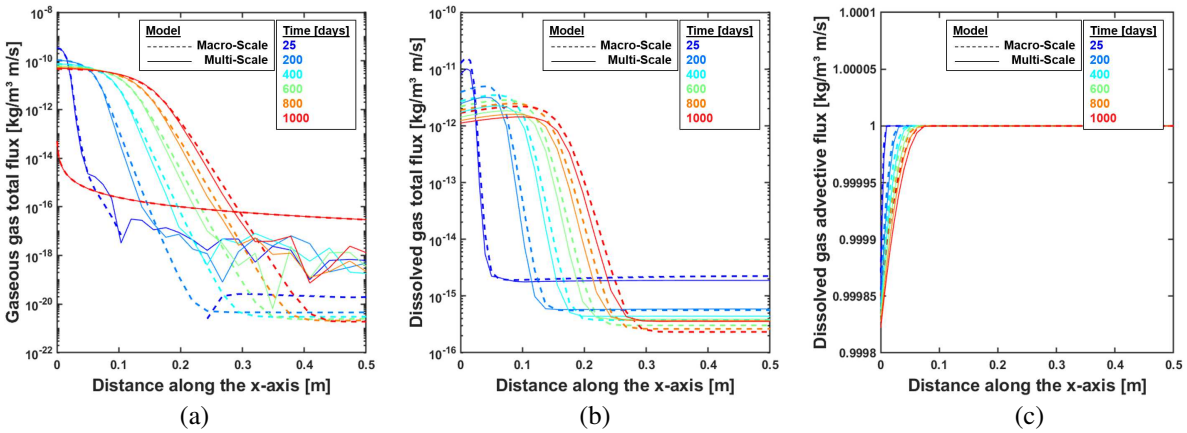

(a) (b) (c)

Figure IV–19 – Comparisons between the multi-scale model (solid line) with respect to a macro-scale model (dashed line): total flux of (a) gaseous gas, and (b) dissolved gas. (c) Saturation.

flux and gas storage respectively. The progressive propagation of gas inside the domain reveals through the increase in gas pressures, which results in the augmentation of the gas flux and gas storage. Again, the overlapping of the curves generated by the two models is really fine, and only a few oscillations are noted for the latter two quantities with the multi-scale model, when the gas pressure gets close to its initial value over the domain.

To complete this verification of the multi-scale model, two components of the gas flux are plotted in Figures IV–19a and IV–19b, namely the flux of gaseous gas and of dissolved gas respectively. These results attest to the capability of the multi-scale model to reproduce the mechanisms of gas flows both dissolved in solution and transferred in the gaseous state associated with the emergence of a distinct gas phase. Finally, a slight desaturation is observed in Figure IV–19c as gas invades the rock. Here again, the desaturation process occurs over a similar distance and amplitude with both models.

13.1.5 Results and discussion

Numerical simulations are performed by implementing the predefined geometry of the Boom Clay sample surrounded by the injection and outflow systems, with the corresponding boundary conditions applied on these two sides. The numerical results are computed for a specimen oriented parallel and perpendicular to the air flow, at a slow injection rate of 2 mL/min.

It is first proposed to observe how the system behaves mechanically under the effect of gas injection and propagation through the Boom Clay material. To that end, the evolution of the average axial strain along the sample height as a function of time is represented in Figures IV–20a and IV–20b for bedding planes oriented parallel and perpendicular to the air flow respectively. Whatever the orientation, it appears that the sample undergoes expansion under the increasing pressure of injected gas, before being subjected to contraction during the air dissipation phases. All in all, the sample volume change is reasonably well reproduced during gas injection, in the sense that the computed results show the same expansion as the experimental measurements in both cases of Figure IV–20. Over the phase of air dissipation however, the empirical data seem to be underestimated for injection parallel to bedding and overestimated in the other case.

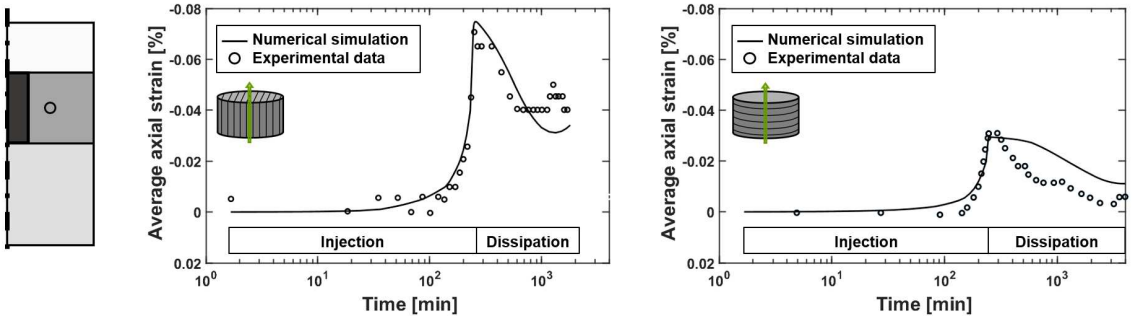

Figure IV–20 – Computed versus measured [Gonzalez-Blanco et al., 2016] average axial strain for slow injection (a) parallel and (b) normal to bedding.

Then, the evolution of the outflow volume over time, computed as the sum of water and air volumes in the downstream reservoir is represented in Figure IV–21a and IV–21b for bedding planes oriented parallel and perpendicular to the air flow respectively. These result show that the time in which the outflow takes place is relatively well captured by the model compared with the measurements, but it tends to increase faster than the estimations, once the gas breakthrough occurs in both directions.

At this point, it is good to analyse the fractures behaviour under gas pressure variations throughout the simulation. The time evolution of the normalised apertures of the bedding and bridging planes are

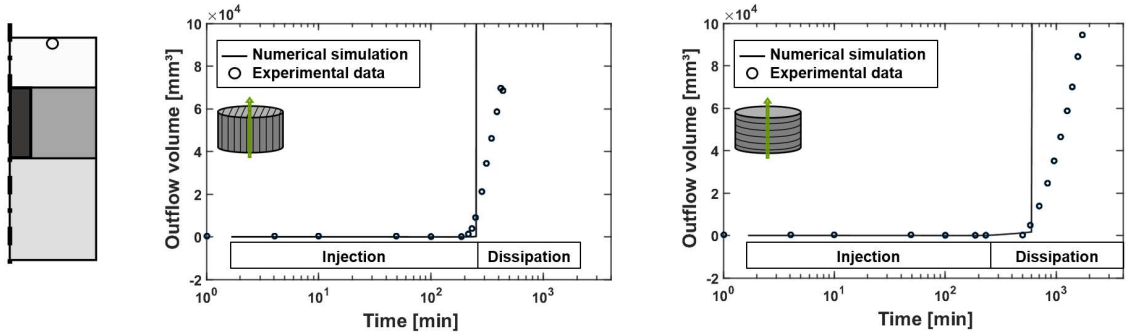

Figure IV–21 – Computed versus measured [Gonzalez-Blanco et al., 2016] outflow volumes for slow injection (a) parallel and (b) normal to bedding.

depicted in Figures IV–22a and IV–22b respectively. An important fracture opening is first noted during the injection phase, which tends to partially close once the maximum pressure has been reached and the gas starts to dissipate through the sample. However, the order of magnitude of variation is much more pronounced in the ZFD compared to the undisturbed clay matrix, given the properties assigned to the fissures of these two zones from experimental observations in Section 13.1.3. Moreover, microstructural observations from the laboratory tests [Gonzalez-Blanco, 2017] have attested that the different families of fractures remain open after the passage of the gas, as it has been exposed in Figure IV–5. Therefore, it appears reasonable to assume that both bedding and the bridging planes, which attract most of the gas during injection in the ZFD, could maintain a partially open aperture during the dissipation phase. Accounting for such a rough hypothesis of constant fracture aperture to refine the numerical modelling leads to the dotted grey lines in Figure IV–22.

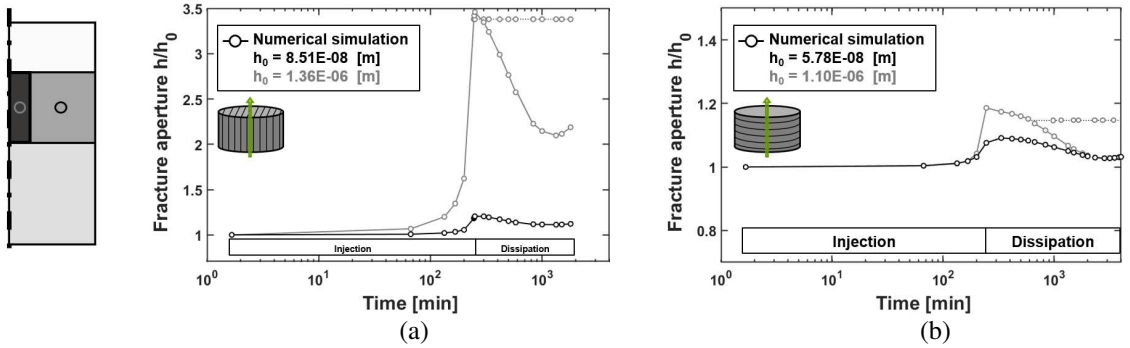

Figure IV–22 – Computed versus measured [Gonzalez-Blanco et al., 2016] outflow volumes for slow injection (a) parallel and (b) normal to bedding.

Finally, Figures IV–23a and IV–23b display the results of the numerically computed injection and outflow pressure response as a function of time for bedding planes oriented parallel and perpendicular to the air flow respectively. These results are expressed as relative pressure, namely it is zero-referenced against atmospheric pressure. It appears that the air pressure decay at the bottom of the sample during the dissipation stages (triangle marker) is rather well fitted. Accounting for a constant fracture opening in the ZFD after the peak of gas pressure allows to slightly improve the pressure drop, as illustrated by the dashed lines in Figure IV–22. Good agreement is also found on the fluid pressures at the top of the system for both orientations of the sample (circle marker), which is computed as the maximum between air and water pressures.

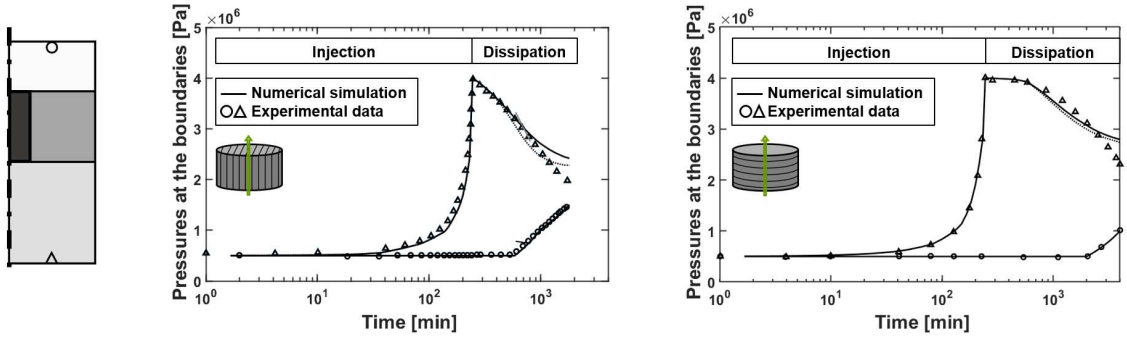

Figure IV–23 – Computed versus measured [Gonzalez-Blanco et al., 2016] injection and recovery pressures for slow injection (a) parallel and (b) normal to bedding.

In order to better apprehend the influence of the zone of fractures development in the overall sample response to gas migration, the gas pressure variations at different time steps are displayed in the form of contour plots in Figure IV–24, for gas injection parallel (top) and perpendicular to the bedding planes (bottom).

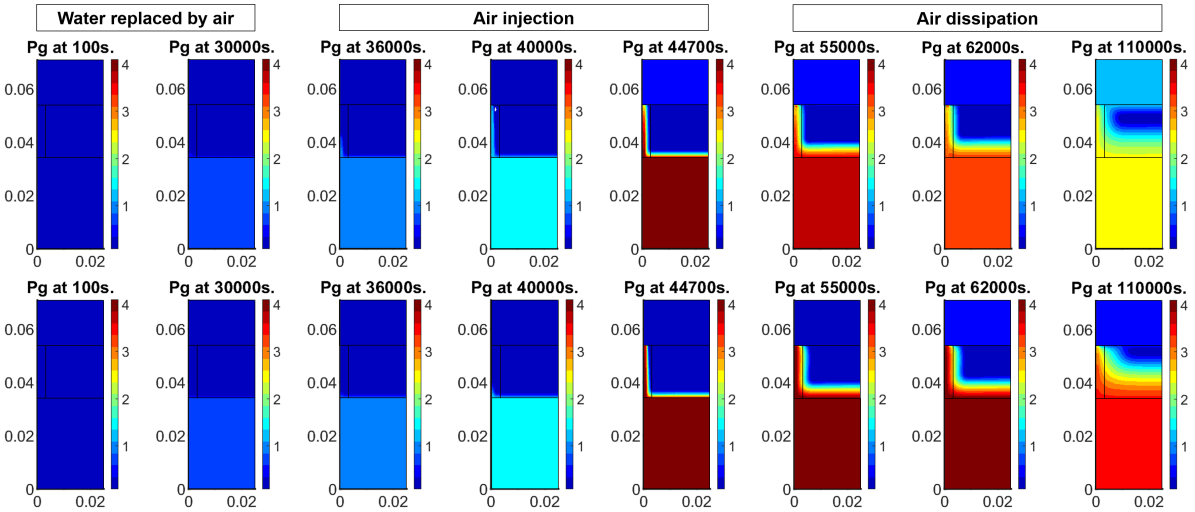

Figure IV–24 – Maps of gas pressures throughout the simulation for slow injection parallel (top) and normal (bottom) to the bedding.

In both cases, it appears that the prevailing fractures in the ZFD tend to significantly open up when the air has sufficiently raised in pressure during the air injection phase. Once this pressure threshold has been exceeded, it follows that the fractured zone progressively desaturates, which creates a preferred outlet to allow the air to flow. On the contrary, the matrix of Boom Clay remains in a state close to the full saturation. Thus, the primary means of gas entry into the sample corresponds to the rapid transport mode by preferential gas-filled pathways development in the ZFD on the one hand, and to the slow transport mode by gradual diffusion of dissolved air within the undisturbed clay matrix on the other hand.

Due to the fast propagation of gas by pathway initiation, a clear breakthrough event occurs by the end of the injection phase if the sample is oriented parallel to air injection flow, and a couple of minutes later once the air dissipation has already started, if the sample is tested in the other direction. This time delay is directly related to the different fracture behaviours that are attributed to the bedding and the bridging planes, on the basis of the experimental observations as presented in Figure IV–14.

As a result of this gas outflow at the top of the sample, the gas pressure gradually decreases during the dissipation phase. This leads to the progressive closure of the different fractures, as the global effective stress gets back to its initial value, following the hydro-mechanical coupling given in Equations (IV–66).

In consequence, the diffusion of dissolved gas takes over to transport the air through the sample until the end of the simulation.

The analysis of the gas transport mode involved can be further detailed on the basis of Figure IV–25, which shows the contribution of the diffusive and advective flows in the matrix and in the ZFD for gas injection parallel (left) and perpendicular (right) to the bedding planes. It appears that the diffusion of dissolved air within the liquid phase prevails in the intact matrix of Boom Clay, even if advective flows progressively develop as the gas front enters the sample. In the ZFD on the contrary, a dominant advective flow is observed and amplifies as the preferential path initiates along the height of the sample.

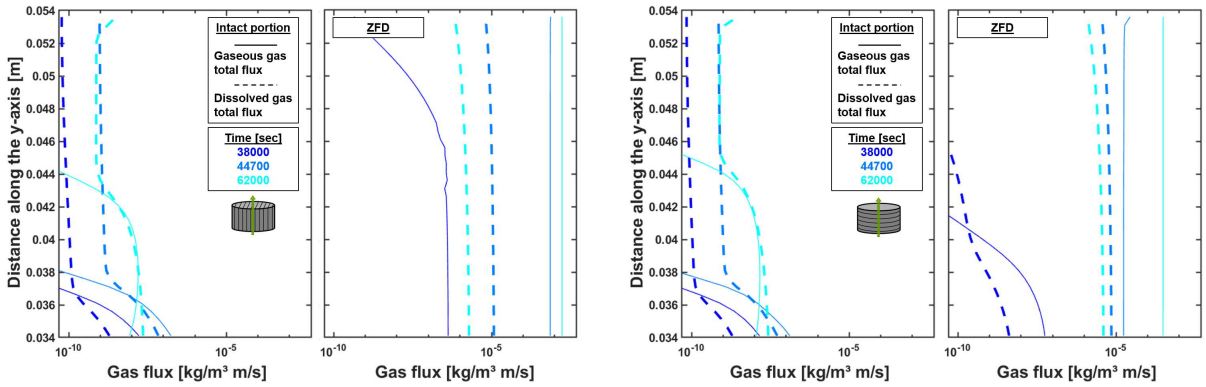

Figure IV–25 – Profiles of the gaseous gas and dissolved gas total fluxes along the sample height in the intact matrix (left) and in the ZFD (right) for slow injection (a) parallel and (b) normal to bedding.

13.2 Numerical modelling of gas-filled pathways

The HM multi-scale model implemented for the analysis of the oedometer tests in the previous section provides a suitable reproduction of the key features of the Boom Clay response under gas pressurisation and migration, including the evolution of the gas pressure fields and the coupling with the material deformation. These encouraging numerical predictions of the main outcomes of the air injection tests attest in some ways of a good implementation of the constituents of the microstructure, *i.e.* the two families of fractures and the bundle of tubes.

And yet, with a straight zone of fracture development representing the easiest path for gas to flow, the heterogeneous aspect of natural materials is avoided in this preliminary application of the model. Also, the possibility to extrapolate the phenomena associated with gas-induced damage evolution in clayey materials at a scale closer to the repository size still needs to be demonstrated.

The ensuing objective is therefore twofold:

- Propose a more general and random configuration for modelling the development of the gas-induced pathways.
- Up-scale the laboratory scale to a behaviour closer to the *in situ* scale, with an amplification of at least one order of magnitude.

To perform such simulations, the same modelling design and parameters as the ones used for the gas injection tests are adopted, except that the axisymmetric geometry is now converted to plane strain conditions, as shown in Figures IV–26 and IV–28. Orientations of the bedding planes parallel and normal to the gas seepage are both investigated, as illustrated in Figures IV–26b and IV–28b. In addition, a similar three-step procedure is envisaged comprising first the replacement of water by air in the upstream reservoir followed by the injection of air up to an inlet pressure of 4.1 MPa (44700 s) that is kept constant until breakthrough, and completed by a final phase of air dissipation.

13.2.1 More general pathway configuration

The axisymmetric configurations discussed in the previous Section 13.1 can be seen as an over-simplification of the ZFD, which was assumed to be straight and located at the centre of the sample. Nevertheless, the computed responses yielded results that were quite accurate in approximating the experimental behaviour. Therefore, it is not unreasonable to conclude that the ZFD remains continuous over the height of the specimen.

In order to propose a more general configuration for the evolution of the gas-filled pathway, it was decided to introduce some kind of heterogeneity in the numerical model by making some adjustments to the zone of fracture development, while keeping it continuous. For the two orientations of the bedding planes, the idea is to propose a representation of the ZDF closer to the gas flow sequences that have been observed experimentally and conceptualised in Figure IV–26c, according to [Gonzalez-Blanco and Romero, 2022]. Therefore, a more tortuous pattern of affected micro-elements is delineated in the central part of the Boom Clay material. This specific ZFD remains continuous at the scale of the sample and includes both damaged bedding planes illustrated by the elements coloured in red, and bridging planes highlighted by the elements coloured in blue, which are more heterogeneously distributed. In the case of flow parallel to the bedding planes (top), a rather simple and direct pathway geometry is assumed, whereas in the other case (bottom), the activation of low-aperture fissures connecting the bedding planes is necessary to allow the gas to jump from one bedding plane to the other, resulting in a more complex pathway geometry.

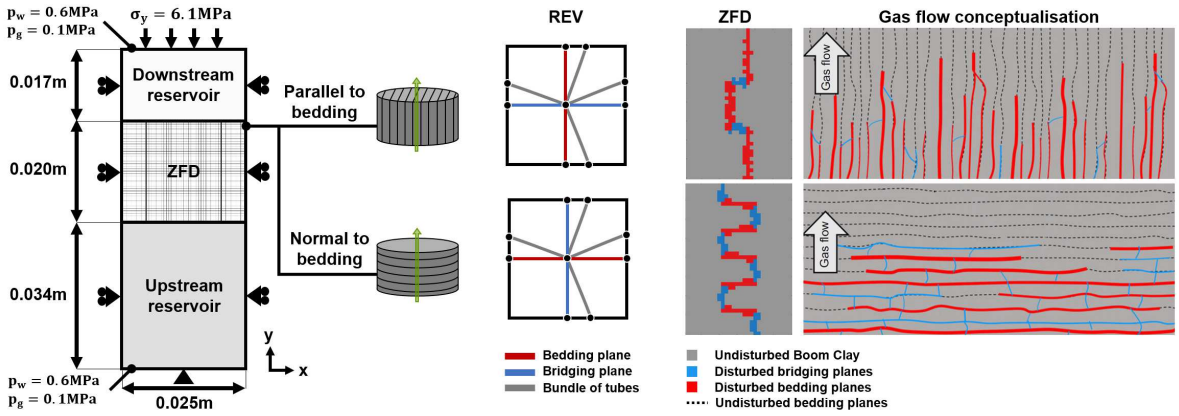

Figure IV–26 – (a) Geometry and initial boundary conditions, with (b) the REV idealisation for the two orientations of the sample, and (c) the two configurations of the ZFD regarding the schematic representation of expected gas flow, conceptualised by [Gonzalez-Blanco and Romero, 2022].

Figure IV–27 shows the contour plots of gas phase pressure at different characteristic times, for a continuous pattern of damaged elements in the zone of fractures development, considering a sample oriented parallel (top) and perpendicular (bottom) to the gas flow. It is thus possible to examine the influence of the fractures connectivity and the twisted aspect of the ZFD on the gas migration behaviour. As soon as the air rises in pressure, there is a quick and tangible opening of the bedding and bridging planes in the disturbed elements initiating the creation of a clear preferential pathway as the primary gas transport mechanism. Provided that the air pressure keeps increasing, there is a rapid activation of all disturbed elements by domino effect, leading to the development of a fully-connected air-filled pathway through the whole Boom Clay sample. During this phase, the advection of air via the predefined families of damaged planes governs the gas flow. The propagation rate of the air through the material remains in the same proportions as in the previous reference cases, so that the breakthrough event occurs shortly after the air pressure has reached its maximum of 4.1 MPa, at around 47000 s for injection parallel to the bedding and at 51600 s for injection perpendicular to the bedding. This delay is mainly due to the

tortuosity of the implemented pathway pattern. The most winding the geometry, the longer the gas takes to flow through the material. This is well corroborated by experimental observations that gas has to jump from one bedding plane to another via the bridging planes when gas is injected normally to the bedding planes. During the subsequent dissipation phase, the air transport by the mechanism of diffusion takes hold as slow background process throughout the sample, and gradually supplants the prevailing advective flows in the ZFD. Despite this, the preferential direction of air flow towards the downstream reservoir is maintained, which tends to reduce gas pressure in the overall system until the end of the simulation.

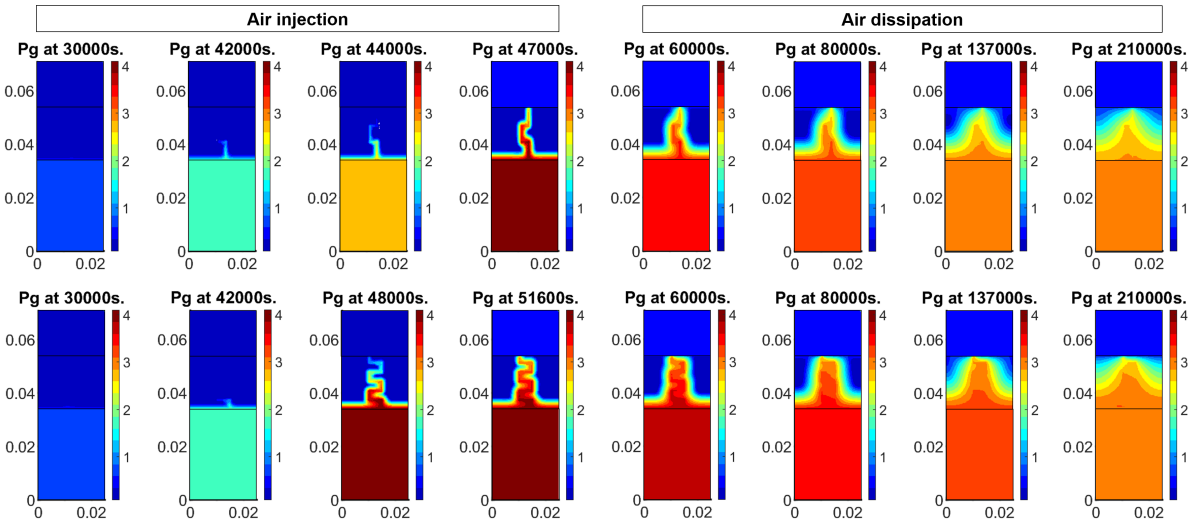

Figure IV–27 – Maps of gas pressures throughout the simulation for slow injection (top) parallel and (bottom) perpendicular to the bedding planes.

13.2.2 Up-scaled pathway configuration

Understanding the potential propagation of gas through pathway development on a larger scale is still an open key issue that must be addressed to ensure a safe ultimate repository for nuclear waste. However, extrapolating the interpretations of preferential pathway development to the field scale is not

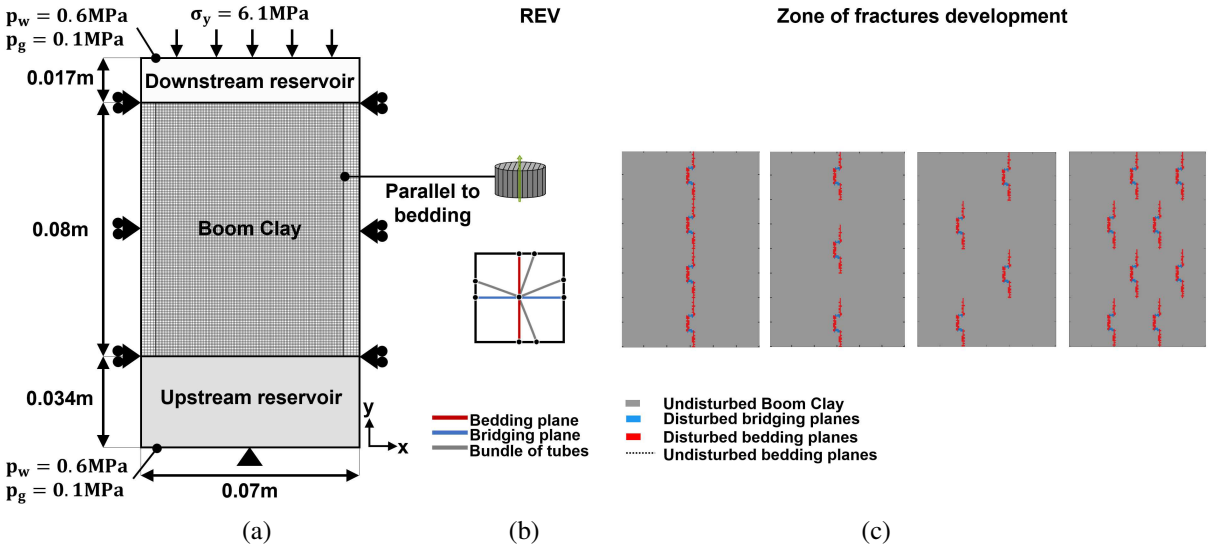

Figure IV–28 – (a) Geometry and initial boundary conditions, with (b) the REV idealisation for the two orientations of the sample, and (c) the two configurations of the ZFD regarding the schematic representation of expected gas flow, conceptualised by [Gonzalez-Blanco and Romero, 2022].

an easy task because it is not yet possible to rely on experimental data, as it is the case at the laboratory scale. While it seems reasonable to consider a continuous ZFD at the scale of the sample, this hypothesis is more questionable when it comes to zooming out on the problem. For this reason, a four times larger mesh has been implemented for injection parallel to bedding in Figure IV–28a, integrating different ZFDs ranging from continuous patterns to increasingly disconnected and heterogeneous patterns, as shown in Figure IV–28c. These ZFD configurations remain tortuous with both damaged bedding planes captured by red elements and bridging planes captured by blue elements, while the intact portions of the rock are represented in grey. For this analysis, a bedding orientation parallel to gas flow is more specifically investigated.

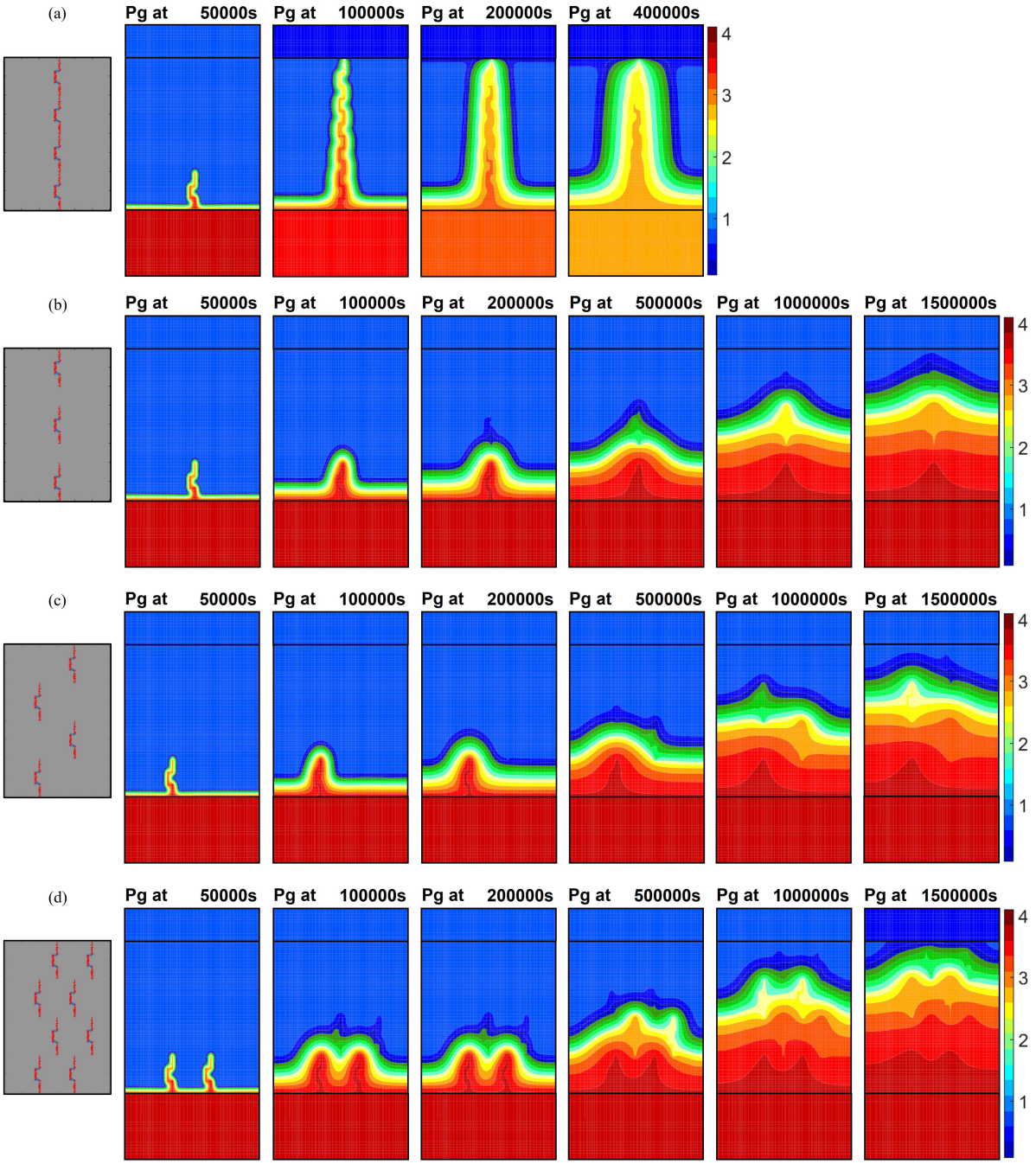

Figure IV–29 – Maps of gas pressure showing the evolution of the gas propagation for (a) a continuous configuration of the ZFD, and for (b)-(d) the different discontinuous configurations of the ZFD.

The results for the different configurations of ZFD are proposed in Figure IV–29. It appears from these maps of gas pressure evolution, that the connectivity of the weakest zones of the material is a key driving factor for gas flows. As long as the continuity of these zones is ensured as depicted in Figure IV–29a, the propagation of the gas through the material remains very fast by advection of gas through the creation of a preferential pathway, giving rise to a breakthrough after 100.000 s. Nevertheless, while this continuity between the weakest zones of the material could be assumed at the scale of the laboratory, it seems however less probable at the *in situ* or the repository scale given the heterogeneity of the clay rock. As soon as the ZFD is not continuous, one can observe in Figure IV–29b-d that the propagation of gas is significantly slowed down. In this case, the migration of gas is mainly governed by the density of the weak and heterogeneous parts in the material. In fact, the gas tends to flow rapidly through the first ZFD by the advection process but then has to reach the next one to keep propagating very fast. This gives the gas time to slowly diffuse and invade the rest of the material. The mechanism of gas transfer by pathway development tends therefore to be supplanted by the slow background process of gas diffusion. Thus, despite some local acceleration of the gas propagation in the heterogeneously distributed ZFDs, it appears that the global gas migration through the material takes place in the form of a rather homogeneous gaseous front, which is a much slower mode of gas propagation.

Conclusions Part IV

The work presented in this part of the thesis is devoted to the numerical analysis of the gas transport processes in the mechanically undisturbed parts of the host rock, and their interactions with the material microstructure leading to the emergence of gas-specific pathways. To that end, a multi-scale modelling approach has been adopted because of the role played by the rock structure at a micro-level in the initiation and propagation of such a macro-scale gas transport mechanism. Based on experimental data, a suitable REV has been defined to idealise the material microstructure with different families of discontinuities, and an assembly of tubes substituting the flow behaviour of the porous matrix blocks. This complete hydraulic constitutive model is solved at the scale of the microstructural constituents, and is directly affected by the mechanical effects addressed at the macroscopic scale, which makes the whole model hydro-mechanically coupled in an implicit way. The transition between the two scales is achieved by means of homogenisation and localisation techniques. With these developments, the proposed model configures a robust tool to explore and assess the impact of the weakest zones, whether inherent to the heterogeneous nature of the rock or induced by previously disturbed portions, on the propagation of localised gas flows in clay-rich materials.

After the description of the multi-scale equations implemented in the `LAGAMINE` code, this model has been applied to a lab-scale case study, dealing with gas injection tests conducted parallel and normal to the bedding orientation in the Boom Clay. A full characterisation of the microstructure components has been performed to reproduce the macro-scale behaviour of this low-permeable host rock. Hydraulically, a model of advection-diffusion of a multiphase flow along the fractures and tubes embedded in the REV is used to simulate the flow response, with specific retention behaviour and relative permeability curves assigned to each micro-element. To stimulate the development of preferential pathway, the sample is modelled with two zones having different hydraulic properties, namely an intact matrix block and a zone of fractures development characterised by the properties of the fissures experimentally detected after the gas injection. For both orientations of the specimen, the comparison between the experimental results and the model predictions provides encouraging agreement, especially in terms of gas pressure evolution, volume change and outflow volume computation.

The application of the multi-scale HM model has also been extended to a more general and random configuration, which has been up-scaled in order to evaluate the possibility to extrapolate the lab observations of gas-induced damage processes on a larger scale. These simulations highlight two essential aspects in the development of preferential pathways. One the one hand, the more continuous the connectivity between the disturbed planes, the faster the gas flow through this discrete zone. On the other hand, the density of these well-connected weaker zones must be sufficiently important and distributed over extended portions of the rock to ensure a rapid gas propagation at a larger scale. Otherwise, the fast mechanism of gas transport by advective fluxes through the pathways development is supplanted by the diffusion of dissolved gas in the liquid phase, which is a slower and less damaging mode of gas transfer.

In this way, the performed numerical analysis corroborates the current state of knowledge of gas impact at repository scale. Contrary to what has been conceptualised in the EDZ, there is no clear evidence of significant visco-capillary two-phase flow through the mechanically undisturbed host formation. As long as gas release from the repository system and the adjacent EDZ remains low, the transport of gas in solution is the governing mechanism that causes a slow gas penetration in the water-saturated clay

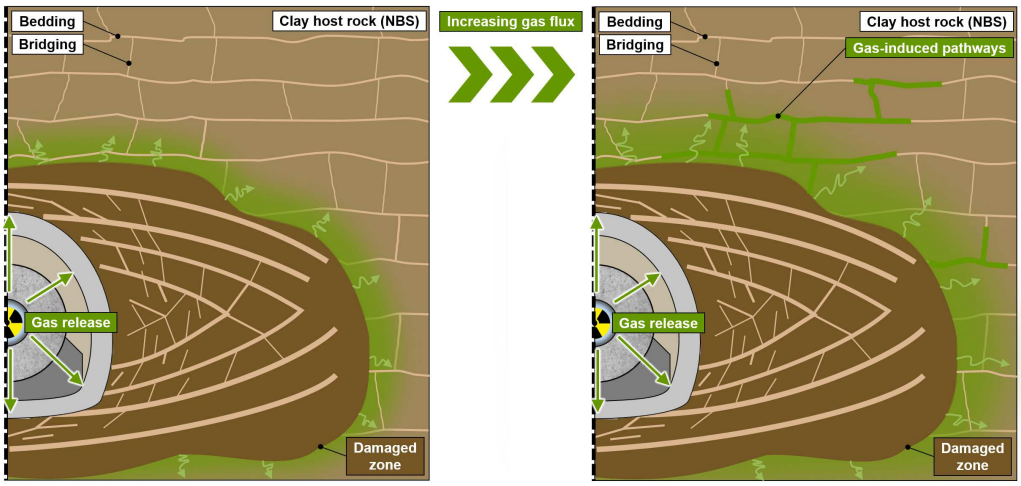

(a) (b)

Figure IV–30 – Schematic representation of the expected gas flow regimes from a disposal gallery and the adjacent EDZ to an undisturbed clayey host rock: (a) diffusion of dissolved gas, (b) creation of gas-specific pathways. *Inspired from* [Levasseur et al., 2024].

barrier. For the low-permeable media under study, there are very little water flows and so the diffusion of dissolved gas tends to supplant the advection in the liquid phase as dominant background process (Figure IV–30a), although the gas transport capacity of this mechanism is limited. However, when a saturated low-strength clay rock is exposed to pressurised gas, this latter cannot displace pore water by visco-capillary two-phase flow like in the EDZ. As a result, there is no transport of gas phase until gas pressure has sufficiently built up to get close or exceed the strength of the material. Once this pressure threshold is reached, the weakest zones in the rock are step by step activated leading to micro-fracture creation and the coalescence of larger pores as a consequence of local, gas-induced, stress redistribution. Locally, the porosity and permeability are increased while the gas entry pressure is reduced, creating conditions for gas flow to concentrate in some discrete gas-filled pathways, as shown in Figure IV–30b. Although the activation threshold of this mechanism is associated with the spatial distribution of the hydro-mechanical clay properties at a smaller scale, and its inherent variability, it is worth mentioning that the process of gas-driven pathway opening processes could remain intermittent in some materials, owing to the self-sealing capacity of these rocks over the long term.

Part V

Conclusions

14. Summary

Today, nuclear power plays a leading role in the global electricity supply. Tomorrow, it could hold an even more prominent position in supporting the decarbonisation of energy-based sectors, with a view of mitigating climate change. However, this sector faces the immense challenge to permanently and safely dispose of the high-level radioactive waste it generates, which could persist in the environment for up to one hundred thousand years. Burying this waste in a deep geological repository is the preferred approach at present as it incorporates a multi-layered confinement system, consisting of both engineered and natural barriers. Clay-based host materials are commonly envisaged in design due to their excellent insulation properties. Among the various multi-physics perturbations that could affect the long-term behaviour of the clay barrier, the release of large amounts of gas, induced by the corrosion of the metal components of the system is a major issue. Implementing advanced numerical models is therefore required to enhance comprehension of gas transport processes in clayey materials, and their interactions with mechanical behaviour. The first part of the thesis provided a general introduction to this research topic.

At this stage, it was appropriate to firstly characterise the clay-based materials to be modelled, *i.e.* Boom Clay and Callovo-Oxfordian claystone, to secondly determine the state of knowledge regarding gas transport through clayey materials in the specific context of geological disposal, and to thirdly identify numerical tools capable of replicating such processes. Thence, the second part of the thesis provided an extensive literature review on these aspects to lay the physical, phenomenological, and numerical foundations of the research. In addition to the basic geotechnical properties of clay rocks, a particular attention was paid to the features dictating the gas movement within these formations, and how these are affected in disturbed zones. In fact, the low values of permeability and porosity measured at the macro-scale are related to the specific clay microstructure reflected by the fine-grained distribution of pore size. Due to this specific behaviour of low-permeable clay-based materials, four basic gas transport modes can be gradually stimulated as a function of the gas pressures build-up. If the amount of gas remains marginal, the gas is dissolved in solution and primarily transported via diffusion within the liquid phase. Once the gas entry pressure is exceeded, gas transfer via visco-capillary two-phase flows takes over. Above the breakthrough pressure, gas-specific pathways develop within the rock formation, which could even lead to gas fracturing under certain conditions. From experimental findings in the clay rocks, the key parameters governing each mechanism can be identified and quantified for integration into the models. From a numerical point of view, the classical two-phase flow models are usually able to reproduce the gas transport modes before preferential pathway development using weak hydro-mechanical couplings. However, modelling the entire range of gas flow processes in clay materials requires alternative numerical methods introducing stronger couplings between gas transfers and the rock behaviour. This thesis aimed to elaborate some of these advanced numerical models capable of properly replicating hydro-mechanical features of gas migrations observed experimentally, such as the impact of a damaged host rock on gas flow, and the creation of gas-filled pathways in the intact rock layers.

The drilling process in clay rocks inevitably generates a zone of cracks and fractures in the close vicinity of the storage cell. This excavation damaged zone is characterised by significant and irreversible modifications of the hydraulic properties, which could interfere with the gas flows occurring in the long term. The aim of the third part of the thesis was to enhance understanding of gas transport processes in that particular zone and their implications on practical applications. To that end, a second gradient two-

phase flow hydro-mechanical (H^2M) model was developed. On the one hand, it integrates the second gradient theory to properly reproduce the fractures in the material with strain localisation in shear band mode. On the other hand, it incorporates the features of an extended two-phase flow approach to address the mechanisms inherent to gas migrations. On top of that, specific coupled effects of the mechanical deformations on fluids transport properties like the intrinsic permeability and the retention behaviour are taken into account. The model showed capabilities of replicating a rapid gas propagation in the form of a gaseous front across the EDZ, that tends to attenuate deeper in the intact rock mass (first three images in Figure V–1b). These results are in line with the expected gas transport process in the vicinity of the storage drifts, involving first slow diffusion of dissolved gas with a limited capacity of transfer, subsequently supplanted by visco-capillary two-phase flows of water and gas located within the discontinuities of the damaged zone, as illustrated in the first two images in Figure V–1c.

Beyond the EDZ, the mechanically undisturbed parts of the rock mass under pressurised gas can be subjected to the emergence of gas-specific pathway from the weakest zones of the rock microstructure, which can lead to undesirable changes in the favourable containment properties of the host rock. The aim of the fourth part of the thesis was to contribute to the conceptualisation of gas transport processes in that particular zone to assess their implications on the integrity of the geological barrier. Because of the role played by the microstructure constituents such as heterogeneities, discontinuities or bedding planes in the propagation of the macroscopic gas flow mechanisms, a multi-scale modelling approach has been adopted. The definition of a relevant REV supported by experimental data makes it possible to idealise the flow behaviour of the material microstructure with different families of discontinuities, and an assembly of tubes substituting the porous matrix blocks. This complete hydraulic constitutive model is solved at the scale of the microstructural constituents, and is directly affected by the mechanical effects tackled at the macroscopic scale, which makes the whole model hydro-mechanically coupled in an implicit way. The transition between the two scales is achieved by means of homogenisation and localisation techniques. Specifically applied to simulate gas injection tests on clay-rich samples, this model showed capabilities of replicating the main markers associated to the development of gas-filled pathways (last three images in Figure V–1b). These results are in line with the expected gas transport processes through the intact host formation, involving first a slow penetration of gas in the water saturated clay-barrier by diffusion, supplemented by the initiation of discrete gas-induced pathways once gas pressure has sufficiently built up to get close or exceed the strength of the material, as illustrated in the last two images of Figure V–1c.

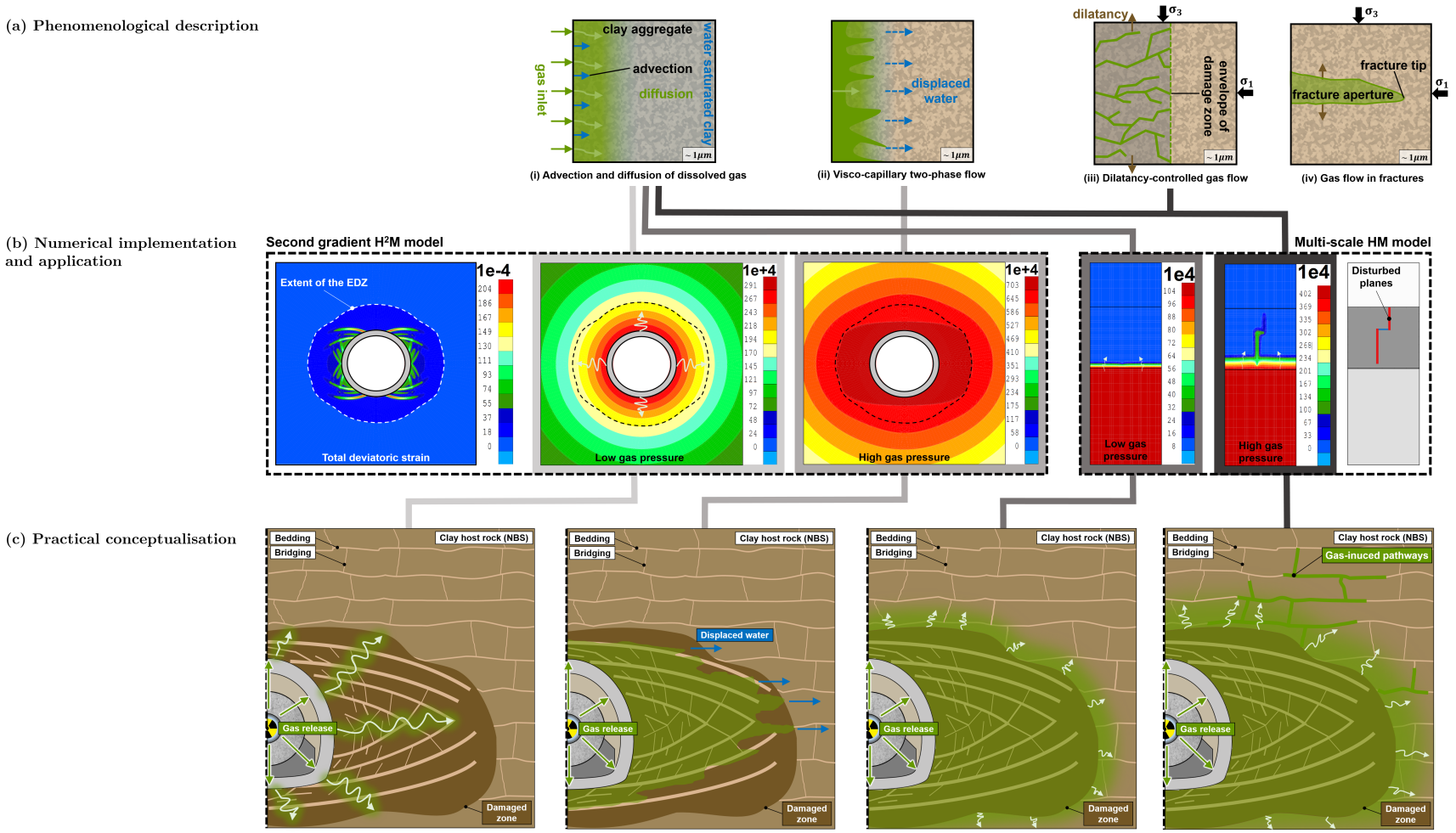

Figure V–1 – Illustrative summary of the thesis, showing how the basic modes of gas transport in low-permeable clayey rocks (top, (a)) are integrated into the second gradient H^2M model and the multi-scale HM model (middle, (b)), in order to propose a schematic representation of the expected gas flow regimes from a disposal gallery to a clay host formation with an EDZ (bottom, (c)). *Inspired from* [Levasseur et al., 2024].

15. Original contributions

Whatever the topic, a thesis always takes its firm roots from previous researches, to initiate new contributions. Accordingly, the objective of this Ph.D thesis was to extend a pre-existing constitutive framework implemented in the LAGAMINE code by developing new constitutive models in order to address hydro-mechanical modelling of gas transport processes in clay host rocks. In particular, the present work has drawn strength from the unsaturated and coupled models from [Collin, 2003, Gerard, 2011] as basis for the general hydro-mechanical aspects behind fluids transfers in geomaterials, from the coupled local second gradient model from [Pardoen, 2015] to investigate gas flows in the excavation damaged zone, and from the hydro-mechanical double-scale models from [Marinelli, 2014, van den Eijnden, 2015, Bertrand, 2020] to study gas flows in the sound rock layers.

For the different parts of the research, the main original contributions include:

- Basics of multiphase flows in clay materials
  - An overview of the current state of knowledge regarding the basic geotechnical properties and their typical ranges of values for the Boom Clay and the COx claystone.
  - An overview of the current state of knowledge regarding the experimental characterisation of gas transport processes in low-permeable clay materials, including the key governing parameters and their typical ranges of values for the Boom Clay and the COx claystone.
  - An overview of the current modelling capabilities concerning gas transport processes in low-permeable clay materials, with an emphasis on the advanced hydro-mechanical models.
- Modelling gas migrations in the EDZ
  - The implementation of a new degree of freedom for gas in the second gradient framework.
  - The integration of a biphasic fluid transfer model into the second gradient framework.
  - The introduction of an advanced HM coupling between the gas entry pressure and the deformations into the second gradient framework.
  - The numerical modelling of an *in situ* experiment in the Boom Clay, namely the MEGAS gas injection tests, which provides a refined characterisation of rock fracturing around the boreholes and a representative propagation of gas in the EDZ.
  - The numerical modelling of a large-scale storage drift in the COx claystone, which demonstrates the non-negligible impact of the HM couplings inherent to the EDZ on gas flows, and contributes to refine predictions of the long-term behaviour of storage cells.
- Modelling gas migrations in sound rocks
  - The integration of tube elements in the multi-scale framework, with *ad hoc* parameters of tortuosity, retention and transmissivity, in order to substitute the flow behaviour of the clay solid matrix.
  - The Implementation of the mechanism of diffusion of dissolved gas within the liquid phase in addition to advective fluxes for the fracture and tube elements of the microstructure.
  - The introduction of advanced HM couplings between the transmissivity and entry pressure of the REV constituents and their opening, through the variation of the fluids pressure.

— The numerical modelling of lab-scale gas injection tests in the Boom Clay, which provides a fine reproduction of the gas transport mechanisms involved.

— The numerical modelling of up-scaled configurations, which contributes to refine predictions of the impacts of gas migrations at a larger scale.

All these original contributions in terms of numerical modelling of gas transport processes in clay materials open new perspectives for achieving the Work Package objectives outlined in Chapter 2.

- Conceptualise the transport mechanisms both at micro- and macro-scale (sub-task 2.2).

Under large quantities of gas produced within the repository, it is anticipated that dissolution and diffusion of gas would most probably not be sufficient to prevent the creation of a distinct gas phase in the EBS and the EDZ, and to avoid the formation of gas-specific pathways in the intact host formation. As highlighted in Figure V–1, the developed numerical models are capable of reproducing these transitions from one mode of gas transport to another as a function of the gas pressure increase. In the EDZ, the activation of visco-capillary two-phase flows in the wake of diffusion of dissolved gas is well handled by the second gradient H^2M model, which can thus replicate the rapid invasion of the disturbed zone by a gaseous front. In the intact rock, the multi-scale model incorporates a description of the microstructure, which makes it possible to capture the sudden development of gas-specific pathways from the micro-scale heterogeneity of the material.

- Improve understanding of the observed gas transport modes and their main control (sub-task 2.2) - Gain a mechanistic understanding of the hydro-mechanical phenomena associated with gas-induced failure, within the EDZ and the host rock (sub-task 3.1).

The work carried out in this thesis provides some elements of interpretation regarding which transport mechanism prevails under specific HM conditions, from a numerical perspective. Besides the mechanical aspects behind the development of the EDZ, the second gradient H^2M model is also able to capture the experimentally measured changes in the transport properties (permeability and gas entry pressure), by means of effective HM couplings. The higher permeability and lower gas entry pressure induced by the rock deformations allow to sufficiently amplify the desaturation of the disturbed zone. Such HM interactions facilitate the movement of gas to the point of readily activating visco-capillary two-phase flows in the EDZ, without the need for a substantial pressure build-up. As for gas flows in the mechanically undisturbed rock, the HM multi-scale model is able to replicate the development of preferential pathways from weaker parts in the material microstructure. The activation of this mechanism requires sufficient gas pressure build-up in an initially water-saturated clay layer which cannot displace enough pore water by visco-capillary two-phase flow, and leans on the HM couplings arising from the small scale. To simulate the formation of pathways in the model, the rapid gas pressure build-up induces stress redistribution, which leads to significant micro-fractures opening in zones where the material strength is lower. As a result, there is a local rise in permeability and drop in the entry pressure causing a discrete breach in the uniform gaseous front. However, it seems likely that this mechanism would remain transient in nature on a larger scale without long-lasting effects on the global gas propagation, given that it requires a high gas production rate concurrent to a certain continuity in the micro-scale disturbed portions of the material.

- Evaluate achievements by the application of the newly developed modelling tools on *in situ* experiments (sub-task 3.3).

The application of the second gradient H^2M model on MEGAS *in situ* gas injection tests has evidence the importance of strong HM interactions between the transfer properties and the damage to suitably reproduce gas transport processes in the EDZ. In the intact rock layers, the application of the multi-scale model has demonstrated encouraging modelling capabilities to reproduce gas injection tests at the scale of the laboratory. Yet, the extrapolations at a larger *in situ* scale still need to be substantiated by empirical evidences.

16. Limitations and perspectives

Whatever the topic, a thesis always sows the seeds of following ones. Indeed, this doctoral thesis introduced new constitutive models in the LAGAMINE code to pave the way for the hydro-mechanical modelling of gas transport processes in clay host rocks. Yet, various assumptions were formulated, and limitations were encountered, forming the main axes of improvements and perspectives of this work.

- Modelling gas transport in the EDZ

The proposed approach is based on a continuous description of the fractures in the material, instigated from strain localisation in shear band mode. Overall, such a description correctly reproduces the shape of the EDZ, but even if shearing is the predominant fracture mechanism in clay materials, the fracturing pattern could still be improved by considering other types of fractures that have been experimentally detected in the EDZ. For instance, the representation of the EDZ could be refined with a large number of thinner bands and tensile fractures, which would require other rupture mechanisms in the modelling strategy. Adapting the structure of the EDZ towards a more representative configuration would also affect the hydraulic aspects governing the gas transport mechanisms in that zone. For the strain localisation approach, one way to proceed could be to link the rock transfer properties with the tensile strain in the normal direction to the shear bands.

In order to enhance the modelling of the EDZ, it would also be worth investigating the onset of strain localisation as it depends on various numerical aspects, among which the rock properties and its anisotropy, the material imperfections, the geometry of the tunnel, the imposed drainage and excavation rates as well as the elastic modulus of the second gradient model with respect to the size of the finite elements. An in-depth sensitivity analysis would provide a better understanding of how these different parameters influence the development and extent of localisation bands.

Finally, the second gradient H^2M model that has been elaborated to study the impact of the damaged on gas transport processes could be extended to other coupled processes prone to occur in the context of a deep geological repository. In particular, it could involve the short-term thermal effects [Song et al., 2023] in order to study how the generated heat could induce water overpressures and affect the favourable properties of the clay host rock, especially its transport characteristics. Since clayey materials exhibit a strong capacity for self-sealing of discontinuities after sustaining mechanical perturbations, the transfer properties of the undisturbed rock could be restored over time in the EDZ. Accounting for such a mechanism in the modelling could have an influence on the very long-term behaviour of the geological barrier subjected to an uninterrupted gas production.

- Modelling gas transport in sound rocks

The proposed multi-scale HM model has shown capabilities to reproduce the first mode of gas transport by diffusion of dissolved gas within the liquid phase, and the two primary modes for gas transport as a separate phase, namely two-phase flow, in which gas displaces pore water through the pre-existing porosity, and the propagation of gas-specific pathways, in which the gas production rate is balanced steadily by the newly created pore volume at the pathway tips. However, this model is not able to reproduce the last mode of gas transport by sudden fracture propagation, *i.e.* gas fracturing, which relates

to fracture mechanics [Liaudat et al., 2023]. While the formation of gas-specific pathways is associated to local damage of the material of a clay barrier, which does not imply the structural failure of the component, gas fracturing is associated to the sudden and energetic relief of accumulated pressure, which could induce cascading effects through the multi-barrier system. Furthermore, the self-sealing capacity of the rock after gas transport is another mechanism that could be integrated into the conceptual model [Bernier et al., 2007b] to capture the closure and sealing of the pathways once the gas pressure is released.

Another challenge lies in up-scaling the promising laboratory-scale results to the *in situ*-scale behaviour. Since the mineralogical variability, the microstructural heterogeneity of the clay properties (stiffness and strength), and the connectivity of the macro-pores and micro-fractures are all driven factors for gas-specific pathway initiation that cannot be easily anticipated at a large scale, further experimental work is still required. In that sense, building a clear mechanistic understanding of the gas flow processes using simple and robust descriptions requires continuous interactions between modellers and experimentalists. On the one hand, the progress of the numerical models remains tributary of a correct experimental characterisation and understanding of the processes. On the other hand, process-level models allow to test some of the hypotheses, contributing to gain additional comprehension of the phenomena.

Investigating the gas-induced pathways that could develop along interfaces between clay barriers and other components at an *in situ* scale is another axis of possible developments.

- Integration of the models

By introducing advanced HM couplings pertaining to the gas-induced physical phenomena, the two numerical models proposed in this thesis contribute to advancements in the modelling of gas transfer in saturated clayey materials. To go further and gain a unified and comprehensive vision of gas transport processes in the clay host rock surrounding a storage cell, integrating both models in one single simulation of gas release from the system would be beneficial. Nonetheless, such a modelling task would be restricted to a process-level investigation in the close vicinity of the storage drift because of the high computational costs of both approaches. Building an efficient and exhaustive model that describes the complex physical processes involved in the gas transport modes at the scale of the repository is of course still missing at present.

The transition between the laboratory scale, where process-level models prove their efficiency and the *in situ* scale, which is the perspective of end-users is still an open key question. Small-scale models, such as those elaborated in this study, aim to assess the threshold pressure for the activation of different gas transport mechanisms and the capacity for gas evacuation form the different components of the system through each of these modes. The knowledge acquired at that level intends to provide relationships between gas pressure evolution and fluxes that must in turn be integrated into repository-scale models. At that larger scale, classical two-phase flow models appear to reproduce reasonably well the observed rock mass response in terms of gas pressure and gas fluxes. Therefore, the models built at the scale of the system components must be designed in order to support large-scale simplified methods, by validating some simplification hypotheses, by assessing the impact of each of the couplings, and by providing some applicable sets of values for the governing parameters. For instance, the main outcomes of the two developed models can be taken into account in the modelling of *in situ* gas injection experiments such as PGZ3 in the COx claystone [de La Vaissière, 2021]. In that case, affected transfer properties will be incorporated in different portions of the mesh around the borehole from preliminary simulations of second gradient type, and the necessity to integrate specific zones of heterogeneity for the initiation of preferential pathways will be assessed from the former application of the multi-scale model.

Since the problems related to gas migrations in rocks are characterised by a multi-directional propagation, extending the modelling developments to the 3D framework is another perspective of the present

work.

Numerical models play an important role in the assessment of long-term repository safety, as they allow *e.g.* for parameter identification based on experiments, for fundamental process understanding and for prediction of repository evolution in the future. Although the advanced HM models proposed in this work have shown the ability to qualitatively reproduce the experimental response, they however still fail being predictive, as some model parameters are tuned in order to mimic the data, which is another shortcoming to tackle.

The numerical modelling of physical processes in the earth science field also involves inherent uncertainties, arising from the variable nature of geological properties and the simplification of the conceptual models. Rather than using strictly deterministic models where the output relies on a single set of parameters values and initial conditions, introducing ranges of values in the form of probability distributions for each parameter of the material and applying a stochastic approach would be appropriate.

Finally, the developed numerical approach could be extended to other materials and other applications. With respect to the topic of nuclear waste repository, different types of geological formations including salt or granite rock formations are under study in Europe, which would require an adaptation of the different couplings to the considered materials. Moreover, the knowledge gained on gas invasion processes in clay rocks could be easily transposed to other geoscientific disciplines like oil and gas industry, geothermal exploration and CO_2 sequestration.

In conclusion, the newly developed and implemented modelling tools within the `LAGAMINE` code are capable of accurately capturing the primary gas-induced HM processes in clay rocks. Although there is a room for further improvement, these models are certain to demonstrate their utility in and beyond the scope of a deep geological repository for nuclear waste.

"There is a rapidly closing window of opportunity to secure a liveable and sustainable future for all (very high confidence).
The choices and actions implemented in this decade will have impacts now and for thousands of years (high confidence)."

— IPCC (2023)

Bibliography

[Abdullah et al., 1999] Abdullah, W. S., Alshibli, K. A., and Al-Zou'Bi, M. S. (1999). Influence of pore water chemistry on the swelling behavior of compacted clays. *Applied Clay Science*, 15(5-6):447–462.

[Adamantiades and Kessides, 2009] Adamantiades, A. and Kessides, I. (2009). Nuclear power for sustainable development: Current status and future prospects. *Energy Policy*, 37(12):5149–5166.

[Aertsens et al., 2009] Aertsens, M., De Cannière, P., Moors, H., and Van Gompel, M. (2009). Effect of ionic strength on the transport parameters of tritiated water, iodide and H14CO3- in Boom Clay. In *Scientific Basis for Nuclear Waste Management XXXIII. Symposium Proceedings*, volume 1193, pages 497–504, Warrendale, The United States.

[Aertsens et al., 2005] Aertsens, M., Dierckx, A., Put, M., Moors, H., Janssen, K., Van, Ravestyn, L., Van Gompel, M., Van Gompel, M., and De Cannière, P. (2005). Determination of the hydraulic conductivity, the product ηR of the porosity η and the retardation factor R and the apparent diffusion coefficient Dp on Boom Clay cores from the Mol-1 drilling. Technical report, Restricted contract report of the Belgian Nuclear Research Centre SCK•CEN R-3503, Mol, Belgium.

[Aertsens et al., 2013] Aertsens, M., Maes, N., and Ravestyn, L. V. A. N. (2013). Overview of radionuclide migration experiments in the HADES Underground Research Facility at Mol (Belgium). *Clay Minerals*, 48:153–166.

[Aertsens et al., 2008] Aertsens, M., Van Gompel, M., De Cannière, P., Maes, N., and Dierckx, A. (2008). Vertical distribution of H14 CO3- transport parameters in Boom Clay in the Mol-1 borehole (Mol, Belgium). *Physics and Chemistry of the Earth*, 33(SUPPL. 1).

[Aertsens et al., 2004] Aertsens, M., Wemaere, I., and Wouters, L. (2004). Spatial variability of transport parameters in the Boom Clay. *Applied Clay Science*, 26(1-4 SPEC. ISS.):37–45.

[Aifantis, 1984] Aifantis, E. C. (1984). On the Microstructural Origin of Certain Inelastic Models. *Journal of Engineering Materials and Technology*, 106(4):326–330.

[Aitchison, 1965] Aitchison, G. (1965). Soil properties, shear strength and consolidation. In *Proceedings of the Sixth International Conference on Soil Mechanics and Foundation Engineering*, pages 318–321, Montreal, Canada.

[Alonso and Alcoverro, 1999a] Alonso, E. E. and Alcoverro, J. (1999a). Catsius clay project: Calculation and testing of behaviour of unsaturated clay as barrier in radioactive waste repositories. Stage 1: Validation exercises. (Publication Technica Num. 10/99 ENRESA).

[Alonso and Alcoverro, 1999b] Alonso, E. E. and Alcoverro, J. (1999b). Catsius clay project: Calculation and testing of behaviour of unsaturated clay as barrier in radioactive waste repositories. Stage 2: Validation exercises at laboratory scale. Technical Report Publication Technica Num. 11/99 ENRESA, ENRESA, Madrid, Spain.

[Alonso et al., 2006] Alonso, E. E., Olivella, S., and Arnedo, D. (2006). Mechanisms of gas transport in clay barriers. *Journal of Iberian Geology*, 32(2):175–196.

[Amadei, 1983] Amadei, B. (1983). *Rock anisotropy and the theory of stress measurements*. Springer-Verlag. Lecture Notes in Engineering Series., New-York, The United States.

[Amarasiri and Kodikara, 2013] Amarasiri, A. L. and Kodikara, J. K. (2013). Numerical Modeling of Desiccation Cracking Using the Cohesive Crack Method. *International Journal of Geomechanics*, 13(3):213–221.

[Andra, 2005] Andra (2005). Dossier 2005 Argile – Synthèse: Evaluation de la faisabilité du stockage géologique en formation argileuse, Meuse/Haute Marne site. Technical report, Agence nationale pour la gestion des déchets radioactifs, Paris, France.

[Andra, 2016] Andra (2016). Analyse de l'interaction (thermo-)hydro-mécanique des alvéoles MAVL - Approche milieu continu. Technical report, Agence natioanle pour la gestion des déchets radioactifs, Châtenay-Malabry, France.

[ANDRA, 2020] ANDRA (2020). Inventaire national des déchets radioactifs. *Les essentiels*, page 26.

[Andra, 2023] Andra (2023). Concevoir des centres de stockage, Retrieved February 10, 2023 from https://www.andra.fr/nos-expertises/concevoir-des-centres-de-stockage.

[Andrews-Speed, 2022] Andrews-Speed, P. (2022). The governance of civil nuclear power in France. Advantages and disadvantages of deep state involvement.pdf. *The Journal of World Energy Law & Business*, 15(2):151–166.

[Anthoine, 1995] Anthoine, A. (1995). Derivation of the in-plane elastic characteristics of masonry through homogenization theory. *International Journal of Solids and Structures*, 32(2):137–163.

[Areias and Belytschko, 2006] Areias, P. M. and Belytschko, T. (2006). Two-scale shear band evolution by local partition of unity. *International Journal for Numerical Methods in Engineering*, 66(5):878–910.

[Argilaga, 2016] Argilaga, A. (2016). FEMxDEM double scale approach with second gradient regularization applied to granular materials modelization.

[Argilaga et al., 2019] Argilaga, A., Collin, F., Lacarrière, L., Charlier, R., Armand, G., and Cerfontaine, B. (2019). Modelling of Short-Term Interactions Between Concrete Support and the Excavated Damage Zone Around Galleries Drilled in Callovo–Oxfordian Claystone. *International Journal of Civil Engineering*, 17(1).

[Argilaga et al., 2016] Argilaga, A., Papachristos, E., Caillerie, D., and Dal Pont, S. (2016). Homogenization of a cracked saturated porous medium: Theoretical aspects and numerical implementation. *International Journal of Solids and Structures*, 94-95:222–237.

[Armand et al., 2016] Armand, G., Conil, N., Talandier, J., and Seyedi, D. M. (2016). Fundamental aspects of the hydromechanical behaviour of Callovo-Oxfordian claystone: From experimental studies to model calibration and validation. *Computers and Geotechnics*, 85:277–286.

[Armand et al., 2015] Armand, G., Dewonck, S., Bosgiraud, J.-M., and Richard-Panot, L. (2015). Development and New Research Program in the Meuse Haute-Marne Underground Research Laboratory (France). In *13th ISRM International Congress of Rock Mechanics*, Montreal, Canada.

[Armand et al., 2014] Armand, G., Leveau, F., Nussbaum, C., de La Vaissiere, R., Noiret, A., Jaeggi, D., Landrein, P., and Righini, C. (2014). Geometry and properties of the excavation-induced fractures at the Meuse/Haute-Marne URL drifts. *Rock Mechanics and Rock Engineering*, 47(1):21–41.

[Armand et al., 2013] Armand, G., Noiret, A., Zghondi, J., and Seyedi, D. M. (2013). Short- and long-term behaviors of drifts in the Callovo-Oxfordian claystone at the Meuse/Haute-Marne Underground Research Laboratory. *Journal of Rock Mechanics and Geotechnical Engineering*, 5(3):221–230.

[Armand et al., 2007] Armand, G., Wileveau, Y., Morel, J., Cruchaudet, M., and Rebours, H. (2007). Excavation Damaged Zone (EDZ) In the Meuse Haute Marne Underground Research Laboratory. In *Proceedings of the 11th Congress of the ISRM*, pages 33–36, Lisbon, Portugal.

[Armero and Callari, 1999] Armero, F. and Callari, C. (1999). An analysis of strong discontinuities in a saturated poro-plastic solid. *International Journal for Numerical Methods in Engineering*, 46(10):1673–1698.

[Armero and Garikipati, 1996] Armero, F. and Garikipati, K. (1996). An analysis of strong discontinuities in multiplicative finite strain plasticity and their relation with the numerical simulation of strain localization in solids. *International Journal of Solids and Structures*, 33(20-22):2863–2885.

[Arnedo et al., 2013] Arnedo, D., Alonso, E. E., and Olivella, S. (2013). Gas flow in anisotropic claystone: modelling triaxial experiments. *International Journal for Numerical and Analytical Methods in Geomechanics*, 37(14):2239–2256.

[Arson and Pereira, 2012] Arson, C. and Pereira, J. M. (2012). Influence of damage on pore size distribution and permeability of rocks. *International Journal for Numerical and Analytical Methods in Geomechanics*, 37(8):810–831.

[Arthur et al., 1977] Arthur, J. R., Chua, K. S., and Dunstan, T. (1977). Induced anisotropy in a sand. *Geotechnique*, 27(1):13–30.

[Asem and Gardoni, 2022] Asem, P. and Gardoni, P. (2022). A probabilistic, empirical model for permeability of mudstone. *Probabilistic Engineering Mechanics*, 69(July):103262.

[Atiezo and Dascalu, 2017] Atiezo, M. K. and Dascalu, C. (2017). Antiplane two-scale model for dynamic failure. *International Journal of Fracture*, 206(2):195–214.

[Autio et al., 2006] Autio, J., Gribi, P., Johnson, L., and Marschall, P. (2006). Effect of excavation damaged zone on gas migration in a KBS-3H type repository at Olkiluoto. *Physics and Chemistry of the Earth*, 31(10-14):649–653.

[Bäckblom, 1991] Bäckblom, G. (1991). The Äspö Hard Rock Laboratory-a step toward the Swedish final repository for high-level radioactive waste. *Tunnelling and Underground Space Technology*, 6(4):463–467.

[Baker and Frydman, 2009] Baker, R. and Frydman, S. (2009). Unsaturated soil mechanics. Critical review of physical foundations. *Engineering Geology*, 106(1-2):26–39.

[Baldi et al., 1988] Baldi, G., Hueckel, T., and Pellegrini, R. (1988). Thermal volume changes of the mineral-water system in low-porosity clay soils. *Canadian Geotechnical Journal*, 25(4):807–825.

[Bandis et al., 1983] Bandis, S. C., Lumsden, A. C., and Barton, N. R. (1983). Fundamentals of rock joint deformation. *International Journal of Rock Mechanics and Mining Sciences & Geomechanics Abstracts*, 20(6):249–268.

[Barenblatt, 1962] Barenblatt, G. I. (1962). The Mathematical Thsory of Equilibrium Cracks in Brittle Fracture. *Advances in Applied Mechanics*, 7:55–129.

[Barnichon, 1998] Barnichon, J.-D. (1998). *Finite Element Modelling in Structural and Petroleum Geology*. PhD thesis, University of Liège.

[Barnichon and Volckaert, 2003] Barnichon, J. D. and Volckaert, G. (2003). Observations and predictions of hydromechanical coupling effects in the Boom clay, Mol Underground Research Laboratory, Belgium. *Hydrogeology Journal*, 11(1):193–202.

[Barthélémy, 2009] Barthélémy, J. F. (2009). Effective permeability of media with a dense network of long and micro fractures. *Transport in Porous Media*, 76(1):153–178.

[Baruchel et al., 2000] Baruchel, J., Buffière, J.-Y., Maire, E., Merle, P., and Peix, G. (2000). *X-ray tomography in Materials Science*. HERMES Science Publications, Paris, France.

[Bastiaens and Bernier, 2006] Bastiaens, W. and Bernier, F. (2006). 25 years of underground engineering in a plastic clay formation: the HADES underground research laboratory. In Bakker, K. J., Bezuijen, A., Broere, W., and Kwast, E. A., editors, *Geotechnical aspects of under- ground construction in soft ground*, pages 795–801. Taylor & Francis, London, The United Kingdom.

[Bastiaens et al., 2003] Bastiaens, W., Bernier, F., Buyens, M., Demarche, M., Li, X. L., Linotte, J. M., and Verstricht, J. (2003). The connecting gallery-the extension of the HADES underground research facility at Mol, Belgium. Technical report, European Underground Research Infrastructure for Disposal of nuclear waste in Clay Environment (EURIDICE), Mol, Belgium.

[Bastiaens et al., 2007] Bastiaens, W., Bernier, F., and Li, X. L. (2007). SELFRAC: Experiments and conclusions on fracturing, self-healing and self-sealing processes in clays. *Physics and Chemistry of the Earth*, 32(8-14):600–615.

[Bastiaens et al., 2006] Bastiaens, W., Bernier, F., and Ling Li, X. (2006). An overview of long-term HM measurements around HADES URF. *Proceedings of the International Symposium on Multiphysics Coupling and Long Term Behaviour in Rock Mechanics*, pages 15–26.

[Bažant and Belytschko, 1985] Bažant, Z. P. and Belytschko, T. B. (1985). Wave Propagation in a Strain-Softening Bar: Exact Solution. *Journal of Engineering Mechanics*, 111(3):381–389.

[Bazant et al., 1984] Bazant, Z. P., Belytschko, T. B., and Chang, T.-P. (1984). Continuum Theory for Strain-Softening. *Journal of Engineering MEchanics*, 110(12):1666–1692.

[Bazant et al., 1987] Bazant, Z. P., Lin, F., and Pijaudier-Cabot, G. (1987). Yield limit degradation: non-local continuum model with local strain. In *Proceedings of the International Conference on Computational Plasticity*, pages 1757–1780, Barcelona, Spain.

[Bear, 1972] Bear, J. (1972). *Dynamics of fluids in porous media*. Elsevier Pub., New-York, The United States.

[Bear et al., 1993] Bear, J., Tsang, C.-F., and De Marsily, G. (1993). *Flow and Contaminant Transport in Fractured Rock*. Academic Press.

[Beaufays et al., 1994] Beaufays, R., Blommaert, W., Bronders, J., De Cannière, P., Del Marmol, P., Henrion, P., Monsecour, M., Patyn, J., and Put, M. (1994). Characterisation of the Boom Clay and its multilayeres hydrogeological environment. European Commission Report EUR14961. Technical report, European Commission, Brussels, Belgium.

[Behlau and Mingerzahn, 2001] Behlau, J. and Mingerzahn, G. (2001). Geological and tectonic investigations in the former Morsleben salt mine (Germany) as a basis for the safety assessment of a radioactive waste repository. *Engineering Geology*, 61(2-3):83–97.

[Belanteur et al., 1997] Belanteur, N., Tacherifet, S., and Pakzad, M. (1997). Etude des comportements mécanique, thermomécanique et hydro-mécanique des argiles gonflantes et non gonflantes fortement compactées. *Revue française de géotechnique*, 78(1er trimestre):229–237.

[BelGov, 2003] BelGov (2003). Loi sur la sortie progressive de l'énergie nucléaire à des fins de production industrielle d'électricité. Arrêt n°30/2003 du 26 février 2003, p9845, Moniteur Belge. In *Moniteur Belge*, volume 3, pages 9879–9880. Belgian Government, Brussels, Belgium.

[Belytschko and Black, 1999] Belytschko, T. and Black, T. (1999). Elastic crack growth in finite elements with minimal remeshing. *International Journal for Numerical Methods in Engineering*, 45:601–620.

[Bensenouci et al., 2011] Bensenouci, F., Michelot, J. L., Matray, J. M., Savoye, S., Lavielle, B., Thomas, B., and Dick, P. (2011). A profile of helium-4 concentration in pore-water for assessing the transport phenomena through an argillaceous formation (Tournemire, France). *Physics and Chemistry of the Earth*, 36(17-18):1521–1530.

[Bensoussan et al., 1978] Bensoussan, A., Lions, J.-L., and Papanicolaou, G. (1978). *Asymptotic analysis for periodic structures*. North-Holland Publishing Company, Amsterdam, The Nederland.

[Bernaud and Rousset, 1992] Bernaud, D. and Rousset, G. (1992). La « nouvelle méthode implicite » pour l'étude du dimensionnement des tunnels. *Revue Française de Géotechnique*, 60:5–26.

[Bernier et al., 2007a] Bernier, F., Li, X.-L., and Bastiaens, W. (2007a). Twenty-five years' geotechnical observation and testing in the Tertiary Boom Clay format. *Géotechnique*, 57(2):229–237.

[Bernier et al., 2007b] Bernier, F., Li, X. L., Bastiaens, W., Ortiz, L., Van Geet, M., Wouters, L., Frieg, B., Blümling, P., Desrues, J., Viaggiani, G., Coll, C., Chanchole, S., De Greef, V., Hamza, R., Malinsky, L., Vervoort, A., Vanbrabant, Y., Debecker, B., Verstraelen, J., Govaerts, A., Wevers, M., Labiouse, V., Escoffier, S., Mathier, J.-F., Gastaldo, L., and Bühler, C. (2007b). Fractures and Self-healing

within the Excavation Disturbed Zone in Clays (SELFFRAC). Technical report, Work performed as part of the European Atomic Energy Community's R&T specific programme Nuclear Energy 1998-2002, key action Nuclear Fission Safety.

[Bernier et al., 2002] Bernier, F., Li, X. L., Verstricht, J., Barnichon, J. D., Labiouse, V., Bastiaens, W., Palut, J. M., Ben Slimane, J. K., Ghoreychi, M., Gaombalet, J., Huertas, F., Galera, J. M., Merrien, K., Elorza, F. J., and Davies, C. (2002). CLIPEX: Clay Instrumentation Programme for the Extension of an Underground Research Laboratory. Technical report, Commission of the European Communities, EUR20619, Luxembourg.

[Bertrand, 2020] Bertrand, F. (2020). *Hydro-mechanical modelling of multiphase flow in naturally fractured coalbeds applied to CBM recovery or CO2 storage*. PhD thesis, Faculty of Engineering and Built Environment Priority, University of Newcastle.

[Bertrand et al., 2020] Bertrand, F., Buzzi, O., Bésuelle, P., and Collin, F. (2020). Hydro-mechanical modelling of multiphase flowin naturally fractured coalbed using a multiscale approach. *Journal of Natural Gas Science and Engineering*, 78.

[Bertrand et al., 2017] Bertrand, F., Cerfontaine, B., and Collin, F. (2017). A fully coupled hydro-mechanical model for the modeling of coalbed methane recovery. *Journal of Natural Gas Science and Engineering*, 46:307–325.

[Bésuelle, 1999] Bésuelle, P. (1999). *Déformation et rupture dans les roches tendres et les sols indurés: comportement homogène et localisation*. PhD thesis, Universié Joseph-Fourier - Grenoble I.

[Bésuelle, 2001] Bésuelle, P. (2001). Compacting and dilating shear bands in porous rock: Theoretical and experimental conditions. *Journal of Geophysical Research: Solid Earth*, 106(B7):13435–13442.

[Bésuelle, 2021] Bésuelle, P. (2021). Experimental Investigation of the Emergence of Strain Localization in Geomaterials. In Sulem, J. and Stefanou, I., editors, *Instabilities Modeling in Geomechanics*, chapter 4, pages 95–140. ISTE Ltd and John Wiley & Sons, Inc., London, The United Kingdom and Hoboken, The United States.

[Bésuelle et al., 2006] Bésuelle, P., Chambon, R., and Collin, F. (2006). Switching deformation modes in post-localization solutions with a quasibrittle material. *Journal of Mechanics of Materials and Structures*, 1:1115–1134.

[Bésuelle et al., 2000] Bésuelle, P., Desrues, J., and Raynaud, S. (2000). Experimental characterisation of the localisation phenomenon inside a Vosges sandstone in a triaxial cell. *International Journal of Rock Mechanics and Mining Sciences*, 37(8):1223–1237.

[Bésuelle and Lanatà, 2016] Bésuelle, P. and Lanatà, P. (2016). A new true triaxial cell for field measurements on rock specimens and its use in the characterization of strain localization on a vosges sandstone during a plane strain comprebion test. *Geotechnical Testing Journal*, 39(5):879–890.

[Bésuelle et al., 2014] Bésuelle, P., Viggiani, G., Desrues, J., Coll, C., and Charrier, P. (2014). A laboratory experimental study of the hydromechanical behavior of boom clay. *Rock Mechanics and Rock Engineering*, 47(1):143–155.

[Bhat et al., 2012] Bhat, H. S., Rosakis, A. J., and Sammis, C. G. (2012). A micromechanics based constitutive model for brittle failure at high strain rates. *Journal of Applied Mechanics, Transactions ASME*, 79(3):1–13.

[Bigler et al., 2005] Bigler, T., Ilhy, B., Lehmann, B., and Waber, H. (2005). Helium Production and Transport in the Low-Permeability Callovo-Oxfordian Shale at the Site Meuse/Haute Marne, France. Nagra Arbeitsbericht NAB 05-07. Technical report, National Cooperative for the Disposal of Radioactive Waste (NAGRA).

[Bigoni and Hueckel, 1991a] Bigoni, D. and Hueckel, T. (1991a). Uniqueness and localization-I. Associative and non-associative elastoplasticity. *International Journal of Solids and Structures*, 28(2):197–213.

[Bigoni and Hueckel, 1991b] Bigoni, D. and Hueckel, T. (1991b). Uniqueness and localization-II. Coupled elastoplasticity. *International Journal of Solids and Structures*, 28(2):215–224.

[Bilbie, 2007] Bilbie, G. (2007). *Modélisation multi-échelle de l'endommagement et de la rupture dans les milieux (quasi-) fragiles*. PhD thesis, University Joseph Fourier - Grenoble 1.

[Biot, 1941] Biot, M. A. (1941). General theory for three-dimensional consolidation. *Journal of Applied Physics*, 12(2):155–164.

[Biot, 1956] Biot, M. A. (1956). Theory of Propagation of Elastic Waves in a Fluid-Saturated Porous Solid. I. Low-Frequency Range. *Journal of the Acoustical Society of America*, 28(2):168–178.

[Biot, 1962] Biot, M. A. (1962). Mechanics of deformation and acoustic propagation in porous media. *Journal of Applied Physics*, 33(4):1482–1498.

[Birkholzer et al., 2012] Birkholzer, J., Houseworth, J., and Tsang, C. F. (2012). Geologic disposal of high-level radioactive waste: Status, key issues, and trends. *Annual Review of Environment and Resources*, 37:79–106.

[Birkholzer et al., 2019] Birkholzer, J., Tsang, C. F., Bond, A. E., Hudson, J. A., Jing, L., and Stephansson, O. (2019). 25 years of DECOVALEX - Scientific advances and lessons learned from an international research collaboration in coupled subsurface processes. *International Journal of Rock Mechanics and Mining Sciences*, 122(August):103995.

[Bishop, 1959] Bishop, A. W. (1959). The principle of effective stress. *Teknisk Ukeblad*, 39:859–863.

[Blechschmidt and Vomvoris, 2010] Blechschmidt, I. and Vomvoris, S. (2010). Underground research facilities and rock laboratories for the development of geological disposal concepts and repository systems. Part I: Part I Introduction to geological disposal of spent nuclear fuels and radioactive waste. In Ahn, J. and Apted, M., editors, *Geological Repository Systems for Safe Disposal of Spent Nuclear Fuels and Radioactive Waste*, chapter 4, pages 82–118. Woodhead Publishing Limited.

[Blümling et al., 2007] Blümling, P., Bernier, F., Lebon, P., and Derek Martin, C. (2007). The excavation damaged zone in clay formations time-dependent behaviour and influence on performance assessment. *Physics and Chemistry of the Earth*, 32(8-14):588–599.

[Borja, 2000] Borja, R. I. (2000). Finite element model for strain localization analysis of strongly discontinuous fields based on standard Galerkin approximation. *Computer Methods in Applied Mechanics and Engineering*, 190(11-12):1529–1549.

[Borja, 2002] Borja, R. I. (2002). Finite element simulation of strain localization with large deformation: Capturing strong discontinuity using a Petrov-Galerkin multiscale formulation. *Computer Methods in Applied Mechanics and Engineering*, 191(27-28):2949–2978.

[Borja and Alarcón, 1995] Borja, R. I. and Alarcón, E. (1995). A mathematical framework for finite strain elastoplastic consolidation Part 1: Balance laws, variational formulation, and linearization. *Computer Methods in Applied Mechanics and Engineering*, 122(1-2):145–171.

[Bornert et al., 2008] Bornert, M., Brémand, F., Doumalin, P., Dupré, J.-C., Fazzini, M., Grédiac, M., Hild, F., Mistou, S., Molimard, J., Orteu, J.-J., Robert, L., Surrel, Y., Vacher, P., and Wattrisse, B. (2008). Assessment of digital image correlation measurement errors: Methodology and results. *Experim. Mech.*, 3:353–370.

[Bouchard et al., 2003] Bouchard, P. O., Bay, F., and Chastel, Y. (2003). Numerical modelling of crack propagation: Automatic remeshing and comparison of different criteria. *Computer Methods in Applied Mechanics and Engineering*, 192(35-36):3887–3908.

[Boudreau, 1997] Boudreau, B. (1997). *Diagenetic models and their implementation : modelling transport and reactions in aquatic sediments*. Springer, Berlin, Germany.

[Boulin, 2008] Boulin, P. (2008). *Expérimentation et Modélisation du Transfert d'hydrogène à travers des argiles de centre de stockage de déchets radioactifs*. PhD thesis, Polytechnique de Grenoble, Grenoble, France.

[Boulin et al., 2008a] Boulin, P. F., Angulo-Jaramillo, R., Daian, J. F., Talandier, J., and Berne, P. (2008a). Experiments to estimate gas intrusion in Callovo-oxfordian argillites. *Physics and Chemistry of the Earth*, 33:225–230.

[Boulin et al., 2008b] Boulin, P. F., Angulo-Jaramillo, R., Daian, J. F., Talandier, J., and Berne, P. (2008b). Pore gas connectivity analysis in Callovo-Oxfordian argillite. *Applied Clay Science*, 42(1-2):276–283.

[Bowen, 1980] Bowen, R. (1980). Incompressible porous media models by use of the theory of mixtures. *International Journal of Engineering Science*, 18(9):1129–1148.

[BP, 2022] BP (2022). BP Statistical Review of World Energy 2022. Technical report, BP, London, The United Kingdom.

[Bredehoeft et al., 1978] Bredehoeft, J., England, A., Steward, D., Trask, N., and Winograd, I. (1978). Geologic Disposal of High-Level Radioactive Wastes, Earth-Science Perspectives. Technical report, U.S. Geological Survey.

[Brinkgreve, 1994] Brinkgreve, R. (1994). *Geomaterials Models and Numerical Analysis of Softening*. PhD thesis, Technische Universiteit Delft.

[Brooks and Corey, 1964] Brooks, R. H. and Corey, A. (1964). Hydraulic properties of porous media and their relation to drainage design. *Transactions of the ASAE*, 7(1):26–28.

[Brown and Evans, 1972] Brown, C. B. and Evans, R. J. (1972). On the application of couple-stress theories to granular media. *Geotechnique*, 22(2):356–361.

[Bruggeman and De Craen, 2012] Bruggeman, C. and De Craen, M. (2012). Boom Clay natural organic matter. Technical report, SCK•CEN, Mol, Belgium.

[Bruggeman et al., 2015] Bruggeman, C., Maes, N., Aertsens, M., Salah, S., and Cen, S. C. K. (2015). Tritiated water retention and migration behaviour in Boom Clay. Status 2015. Technical report, SCK•CEN, Mol, Belgium.

[Budiansky and O'connell, 1976] Budiansky, B. and O'connell, R. J. (1976). Elastic moduli of a cracked solid. *International Journal of Solids and Structures*, 12(2):81–97.

[Buscarnera, 2012] Buscarnera, G. (2012). A conceptual model for the chemo-mechanical degradation of granular geomaterials. *Geotechnique Letters*, 2(7-9):149–154.

[Busch and Amann-Hildenbrand, 2013] Busch, A. and Amann-Hildenbrand, A. (2013). Predicting capillarity of mudrocks. *Marine and Petroleum Geology*, 45:208–223.

[Butterfield et al., 1970] Butterfield, R., Harkness, R. M., and Andrawes, K. Z. (1970). a Stereo-Photogrammetric Method for Measuring Displacement Fields. *Géotechnique*, 20(3):308–314.

[Caillerie et al., 2011] Caillerie, D., Chambon, R., and Collin, F. (2011). Analytical Evidence of Shear Band Bifurcations for Softening Materials. *Springer Series in Geomechanics and Geoengineering*, pages 277–283.

[Callari et al., 2010] Callari, C., Armero, F., and Abati, A. (2010). Strong discontinuities in partially saturated poroplastic solids. *Computer Methods in Applied Mechanics and Engineering*, 199(23-24):1513–1535.

[Calvetti et al., 1997] Calvetti, F., Combe, G., and Lanier, J. (1997). Experimental micromechanical analysis of a 2D granular material: relation between structure evolution and loading path. *Mechanics of Cohesive-frictional Materials*, 2(2):121–163.

[Carman, 1937] Carman, P. G. (1937). Fluid flow through granular beds. *Chemical Engineering Research and Design*, 15:150–166.

[Carrier and Granet, 2012] Carrier, B. and Granet, S. (2012). Numerical modeling of hydraulic fracture problem in permeable medium using cohesive zone model. *Engineering Fracture Mechanics*, 79:312–328.

[Cauchy, 1823] Cauchy, A.-L. (1823). Recherches sur l'équilibre et le mouvement intérieur des corps solides ou fluides. élastiques ou non élastiques. *Bulletin de la société philomatique*.

[Cemal Eringen, 1981] Cemal Eringen, A. (1981). On nonlocal plasticity. *International Journal of Engineering Science*, 19(12):1461–1474.

[Cerfontaine et al., 2015] Cerfontaine, B., Dieudonné, A. C., Radu, J. P., Collin, F., and Charlier, R. (2015). 3D zero-thickness coupled interface finite element: Formulation and application. *Computers and Geotechnics*, 69:124–140.

[Chambon, 1986] Chambon, R. (1986). Bifurcation par localisation en bande de cisaillement, une approche avec des lois incrémentalement nonlinéaires. *Journal de Mécanique théorique et appliquée*, 5(2):277–298.

[Chambon, 2000] Chambon, R. (2000). Uniqueness, second order work and bifurcation in hypoplasticity. *Constitutive Modelling of Granular Materials*, pages 147–165.

[Chambon and Caillerie, 1999] Chambon, R. and Caillerie, D. (1999). Existence and uniqueness theorems for boundaryvalue problems involving incrementally non linear models. *International Journal of Solids and Structures*, 36(33):5089–5099.

[Chambon et al., 1998] Chambon, R., Caillerie, D., and El Hassan, N. (1998). One-dimensional localisation studied with a second grade model. *European Journal of Mechanics, A/Solids*, 17(4):637–656.

[Chambon et al., 2001a] Chambon, R., Caillerie, D., and Matsushima, T. (2001a). Plastic continuum with microstructure, local second gradient theories for geomaterials: Localization studies. *International Journal of Solids and Structures*, 38(46-47):8503–8527.

[Chambon et al., 2001b] Chambon, R., Crochepeyre, S., and Charlier, R. (2001b). An algorithm and a method to search bifurcation points in non-linear problems. *International Journal for Numerical Methods in Engineering*, 51(3):315–332.

[Chambon and Moullet, 2004] Chambon, R. and Moullet, J. (2004). Uniqueness studies in boundary value problems involving some second gradient models. *Computer Methods in Applied Mechanics and Engineering*, 193(27-29):2771–2796.

[Chapman and Hooper, 2012] Chapman, N. and Hooper, A. (2012). The disposal of radioactive wastes underground. *Proceedings of the Geologists' Association*, 123(1):46–63.

[Chapman and McKinley, 1987] Chapman, N. and McKinley, I. G. (1987). *The geological disposal of nuclear waste*. John Wiley & Sons, United States.

[Char and Csik, 1987] Char, N. L. and Csik, B. J. (1987). Nuclear Power Development: History and Outlook. *International Atomic Energy Agency bulletin*, 29(3):19–23.

[Charlier, 1987] Charlier, R. (1987). *Approche unifiée de quelques problèmes non linéaires de mécanique des milieux continus par la méthode des éléments finis (grandes déformations des métaux et des sols, contact unilatéral de solides, conduction thermique et écoulements en milieux poreux).* PhD thesis, Faculty of Applied Sciences, University of Liège, Belgium.

[Charlier and Cescotto, 1988] Charlier, R. and Cescotto, S. (1988). Modélisation du phénomène de contact unilatéral avec frottement dans un contexte de grandes déformations.

[Charlier et al., 2013] Charlier, R., Collin, F., Pardoen, B., Talandier, J., Radu, J. P., and Gerard, P. (2013). An unsaturated hydro-mechanical modelling of two in-situ experiments in Callovo-Oxfordian argillite. *Engineering Geology*, 165:46–63.

[Chavant and Fernandes, 2005] Chavant, C. and Fernandes, R. (2005). Fernandes_R - Evaluating the reliability of HM simulation.pdf. In Andra, editor, *2nd International Meeting Clays in Natural and Engineering Barriers for Radioactive Waste Confinement*, pages 14–18. Tours, France.

[Chen et al., 2011] Chen, G. J., Sillen, X., Verstricht, J., and Li, X. L. (2011). ATLAS III in situ heating test in boom clay: Field data, observation and interpretation. *Computers and Geotechnics*, 38(5):683–696.

[Chen et al., 2012] Chen, W., Jia, S., Yu, H., Li, X. L., and Chen, G. (2012). Back analysis of permeability parameters in Boom Clay. In *Impact of thermo-hydro-mechanical chemical (THMC) processes on the safety of underground radioactive waste repositories. Proceedings of the European Commission TIMODAZ-THERESA International Conference*, pages 489–494, Luxembourg. European Commission.

[Chen et al., 2007] Chen, Y., Zhou, C., and Sheng, Y. (2007). Formulation of strain-dependent hydraulic conductivity for a fractured rock mass. *International Journal of Rock Mechanics and Mining Sciences*, 44(7):981–996.

[Cheng, 1997] Cheng, A.-D. (1997). Material coefficients of anisotropic poroelasticity. *International Journal of Rock Mechanics and Mining Sciences*, 34(2):199–205.

[Christensen and Larsen, 2004] Christensen, N. P. and Larsen, M. (2004). Assessing the European potential for geological storage of CO2: The GESTCO project. *Geological Survey of Denmark and Greenland Bulletin*, 16(4):13–16.

[Clapeyron, 1834] Clapeyron, E. (1834). Mémoire sur la Puissance Motrice de la Chaleur. *Journal de l'École polytechnique*, 23:153–191.

[Clayton and Hay, 1994] Clayton, C. J. and Hay, S. J. (1994). Gas migration mechanisms from accumulation to surface. *Bulletin of the Geological Society of Denmark*, 41:12–23.

[Cnudde and Boone, 2013] Cnudde, V. and Boone, M. N. (2013). High-resolution X-ray computed tomography in geosciences: A review of the current technology and applications. *Earth-Science Reviews*, 123:1–17.

[Coll, 2005] Coll, C. (2005). *Endommagement des Roches Argileuses et Perméabilité Induite au Voisinage d'Ouvrages Souterrains*. PhD thesis, Université Joseph Fourier, Grenoble, France.

[Collin, 2003] Collin, F. (2003). *Couplages thermo-hydro-mécaniques dans les sols et les roches tendres partiellement saturés*. Phd thesis, Faculty of Applied Sciences, University of Liège, Belgium.

[Collin et al., 2009a] Collin, F., Caillerie, D., and Chambon, R. (2009a). Analytical solutions for the thick-walled cylinder problem modeled with an isotropic elastic second gradient constitutive equation. *International Journal of Solids and Structures*, 46(22-23):3927–3937.

[Collin et al., 2006] Collin, F., Chambon, R., and Charlier, R. (2006). A finite element method for poro mechanical modelling of geotechnical problems using local second gradient models. *International Journal for Numerical Methods in Engineering*, 65(11):1749–1772.

[Collin et al., 2009b] Collin, F., Levasseur, S., and Chambon, R. (2009b). Numerical post failure methods in multiphysical problems. *European Journal of Environmental and Civil Engineering*, 13(7-8):983–1004.

[Collin et al., 2002] Collin, F., Li, X. L., Radu, J. P., and Charlier, R. (2002). Thermo-hydro-mechanical coupling in clay barriers. *Engineering Geology*, 64:179–193.

[Conil et al., 2018] Conil, N., Talandier, J., Djizanne, H., de La Vaissière, R., Righini-Waz, C., Auvray, C., Morlot, C., and Armand, G. (2018). How rock samples can be representative of in situ condition: A case study of Callovo-Oxfordian claystones. *Journal of Rock Mechanics and Geotechnical Engineering*, 10(4):613–623.

[Cook and Hodgson, 1965] Cook, N. G. W. and Hodgson, K. (1965). Some Detailed Stress-Strain Curves for Rock. *Journal of Geophysical Research*, 70(12).

[Corey, 1954] Corey, A. T. (1954). The Interrelation Between Gas and Oil Relative Permeabilites. *Producers Monthly*, 19(1):38–41.

[Corman et al., 2022] Corman, G., Vu, M., and Collin, F. (2022). Numerical investigation of the couplings between strain localisation processes and gas migrations in clay materials. *International Journal of Solids and Structures*, 256(June):111974.

[Cosserat and Cosserat, 1909] Cosserat, E. and Cosserat, F. (1909). *Théorie des corps déformables*. A Hermann et fils. Library of the John Hopkins University, Paris, France, a hermann edition.

[Coste et al., 2000] Coste, F., Bounenni, A., Chanchole, S., and Su, K. (2000). A method for measuring mechanical, hydraulic and hydromechanical properties during damaging in materials with low permeability. In Hoteit, N., Shao, J., Su, K., and Tijani, M., editors, *Int. Workshop on THM Modeling of Argillaceous Rocks*, pages 109–116, Ecole des Mines de Paris, France. Balkema Publishers.

[Coulomb, 1773] Coulomb, C. A. (1773). Essai sur une application des règles de maximis et minimis à quelques problèmes de statique à l'architecture (Essay on maximums and minimums of rules to some static problems relating to architecture). *Académie Royale des Sciences*, 7:343–382.

[Coussy, 1991] Coussy, O. (1991). Mécanique des milieux poreux (Mechanics of porous media). *The Journal of the Acoustical Society of America*, 91(536):437.

[Coussy and Ulm, 1995] Coussy, O. and Ulm, F. (1995). *Mechanics of Porous Continua*. John Wiley & Sons, Ltd, New-York, The United States.

[Cruchaudet et al., 2010a] Cruchaudet, M., Noiret, A., and Talandier, J. (2010a). OHZ en GED: EDZ initiale et évolution. Technical report, D.RP.AMFS.11.0016, Agence Nationale pour la gestion des Déchets RAdioactifs., Châtenay-Malabry, France.

[Cruchaudet et al., 2010b] Cruchaudet, M., Noiret, A., Talandier, J., and Armand, G. (2010b). Expérimentation SDZ - Bilan de la mise en place de l'instrumentation et des premières mesures à fin mars 2010 - Centre de Meuse/Haute-Marne. Technical report, D.RP.AMFS.09.0087, Agence Nationale pour la gestion des Déchets RAdioactifs., Châtenay-Malabry, France.

[Cuss et al., 2014a] Cuss, R., Harrington, J., Giot, R., and Auvray, C. (2014a). Experimental observations of mechanical dilation at the onset of gas flow in Callovo-Oxfordian claystone. *Geological Society Special Publication*, 400(1):507–519.

[Cuss and Harrington, 2011] Cuss, R. J. and Harrington, J. F. (2011). Update on dilatancy associated with onset of gas flow in Callovo-Oxfordian claystone. Progress report on test SPP_COx-2 Minerals and Waste Programme. Technical report, British Geological Survey, Keyworth, Nottingham.

[Cuss et al., 2014b] Cuss, R. J., Harrington, J. F., Noy, D. J., Graham, C. C., and Sellin, P. (2014b). Evidence of localised gas propagation pathways in a field-scale bentonite engineered barrier system; results from three gas injection tests in the large scale gas injection test (Lasgit). *Applied Clay Science*, 102:81–92.

[Dagher et al., 2019] Dagher, E. E., Nguyen, T. S., and Infante Sedano, J. A. (2019). Development of a mathematical model for gas migration (Two-phase flow) in natural and engineered barriers for radioactive waste disposal. *Geological Society Special Publication*, 482(1):115–148.

[Dalton, 1802] Dalton, J. (1802). Essay IV. On the expansion of elastic fluids by heat. *Memoirs of the Literary and Philosophical Society of Manchester*, 5(2):595–602.

[Damians et al., 2019] Damians, I. P., Olivella, S., and Gens, A. (2019). Modelling a gas flow experiment in Mx80 bentonite. In *17th European Conference on Soil Mechanics and Geotechnical Engineering, ECSMGE 2019 - Proceedings*, pages 1–8.

[Daneshyar and Mohammadi, 2013] Daneshyar, A. and Mohammadi, S. (2013). Strong tangential discontinuity modeling of shear bands using the extended finite element method. *Computational Mechanics*, 52(5):1023–1038.

[Daouadji et al., 2011] Daouadji, A., Darve, F., Al Gali, H., Hicher, P. Y., Laouafa, F., Lignon, S., Nicot, F., Nova, R., Pinheiro, M., Prunier, F., Sibille, L., and Wan, R. (2011). Diffuse failure in geomaterials: Experiments, theory and modelling. *International Journal for Numerical and Analytical Methods in Geomechanics*, 35(16):1731–1773.

[Darcy, 1856] Darcy, H. (1856). *Les fontaines publiques de la ville de Dijon*. Librairie des Corps Impériaux des Ponts et Chaussées et des Mines, Paris, France.

[Darda et al., 2021] Darda, S. A., Gabbar, H. A., Damideh, V., Aboughaly, M., and Hassen, I. (2021). A comprehensive review on radioactive waste cycle from generation to disposal. *Journal of Radioanalytical and Nuclear Chemistry*, 329(1):15–31.

[Das et al., 2011] Das, A., Nguyen, G. D., and Einav, I. (2011). Compaction bands due to grain crushing in porous rocks: A theoretical approach based on breakage mechanics. *Journal of Geophysical Research: Solid Earth*, 116(8).

[Dascalu, 2009] Dascalu, C. (2009). A two-scale damage model with material length. *Comptes Rendus - Mecanique*, 337(9-10):645–652.

[Dascalu and Bilbie, 2007] Dascalu, C. and Bilbie, G. (2007). A multiscale approach to damage configurational forces. *International Journal of Fracture*, 147(1-4):285–294.

[Dascalu et al., 2010] Dascalu, C., Dobrovat, A. M., and Tricarico, M. (2010). On a 3D micromechanical damage model. *International Journal of Fracture*, 166(1-2):153–162.

[Dascalu and Gbetchi, 2019] Dascalu, C. and Gbetchi, K. (2019). Dynamic evolution of damage by microcracking with heat dissipation. *International Journal of Solids and Structures*, 174-175:128–144.

[Davies, 1991] Davies, P. B. (1991). Evaluation of the Role of Threshold Pressure in Controlling Flow of Waste-Generated Gas into Bedded Salt at the Waste Isolation Pilot Plant. Sandia Report SAND90-3246 for the United States Department of Energy. Technical report, Sandia National Laboratories.

[Davy et al., 2007] Davy, C. A., Skoczylas, F., Barnichon, J. D., and Lebon, P. (2007). Permeability of macro-cracked argillite under confinement: Gas and water testing. *Physics and Chemistry of the Earth*, 32(8-14):667–680.

[Davy et al., 2009] Davy, C. A., Skoczylas, F., Lebon, P., and Dubois, T. (2009). Gas migration properties through a bentonite/argillite interface. *Applied Clay Science*, 42(3-4):639–648.

[De Borst, 1991] De Borst, R. (1991). Simulation of strain localization: A reappraisal of the cosserat continuum. *Engineering Computations*, 8(4):317–332.

[De Borst et al., 2012] De Borst, R., Crisfield, M., and Remmers, J. (2012). *Nonlinear Finite Element Analysis of Solids and Structures*. Wiley, 2nd edition.

[De Borst and Mühlhaus, 1992] De Borst, R. and Mühlhaus, H.-B. (1992). Gradient-Dependent Plasticity: Formulation and Algorithmic Aspects. *International Journal for Numerical Methods in Engineering*, 35(3):521–539.

[de Borst and Sluys, 1991] de Borst, R. and Sluys, L. J. (1991). Localisation in a Cosserat continuum under static and dynamic loading conditions. *Computer Methods in Applied Mechanics and Engineering*, 90(1-3):805–827.

[De Borst et al., 1993] De Borst, R., Sluys, L. J., Mühlhaus, H.-B., and Pamin, J. (1993). Fundamental issues in finite element analyses of localization of deformation. *Engineering Computations*, 10(2):99–121.

[De Bruyn et al., 1988] De Bruyn, D., Meynendonckx, P., Neerdael, B., Noynaert, L., Voet, M., Volckaert, G., and Bonne, A. (1988). The HADES demonstration and pilot project. Technical report, Commission of the European Communities, nuclear science and technology, EUR11499, Brussels, Belgium.

[De Craen, 1998] De Craen, M. (1998). *The formation of septarian carbonate concretions in organic-rich argillaceous sediments*. PhD thesis, KULeuven.

[De Greef et al., 2004] De Greef, V., Giraud, A., and Su, K. (2004). Mesures de la perméabilité des argilites saturées et non saturées. Technical report, Agence nationale pour la gestion des déchets radioactifs, Châtenay-Malabry, France.

[de La Vaissière, 2013] de La Vaissière, R. (2013). Hydration versus gas percolation in bentonite. In-situ experiment PGZ2. Experimental borehole results. FORGE Report D3.17- D3.18. Technical report, European Commision.

[de La Vaissière, 2021] de La Vaissière, R. (2021). PGZ3 experiment, preliminary technical note. Technical Report February, ANDRA.

[de La Vaissière et al., 2015] de La Vaissière, R., Armand, G., and Talandier, J. (2015). Gas and water flow in an excavation-induced fracture network around an underground drift: A case study for a radioactive waste repository in clay rock. *Journal of Hydrology*, 521:141–156.

[de La Vaissière et al., 2019] de La Vaissière, R., Armand, G., Vu, M., Talandier, J., and Cornet, F. (2019). Effect of Gas Flow Rate on Gas Fracturing in Callovo-Oxfordian Claystone. In *14th ISRM Congress*, Foz do Iguaçu, Brazil.

[de La Vaissière et al., 2014a] de La Vaissière, R., Gerard, P., Radu, J. P., Charlier, R., Collin, F., Granet, S., Talandier, J., Piedevache, M., and Helmlinger, B. (2014a). Gas injection test in the Callovo-Oxfordian claystone: Data analysis and numerical modelling. *Geological Society Special Publication*, 400(1):427–441.

[de La Vaissière et al., 2014b] de La Vaissière, R., Noiret, A., Côte, P., Helmlinger, B., Sohrabi, R., Lavanchy, J. M., Leveau, F., Nussbaum, C., and Morel, J. (2014b). Excavation-induced fractures network surrounding tunnel: Properties and evolution under loading. In Norris, S., Bruno, J., Cathelineau, M., Delage, P., Fairhurst, C., Gaucher, E. C., Höhn, E. H., Kalinichev, A., Lalieux, P., and Sellin, P., editors, *Clays in Natural and Engineered Barriers for Radioactive Waste Confinement*, volume 400, pages 279–291. Geological Society, London, Special Publications, London, The United Kingdom.

[de La Vaissiere and Vinsot, 2019] de La Vaissiere, R. and Vinsot, A. (2019). Current research in LS-Andra Underground Lab about gas transfer. In *ECCSEL workshop Nancy*, Nancy, France.

[Decamps and Dujacquier, 1997] Decamps, F. and Dujacquier, L. (1997). Overview of European practices and facilities for waste management and disposal. *Nuclear Engineering and Design*, 176(1-2):1–7.

[DeCraen et al., 2004] DeCraen, M., Wang, L., Van Geet, M., and Moors, H. (2004). Geochemistry of Boom Clay pore water at Mol site. Technical report, SCK·CEN, Mol, Belgium.

[Dehandschutter et al., 2004] Dehandschutter, B., Vandycke, S., Sintubin, M., Vandenberghe, N., Gaviglio, P., Sizun, J. P., and Wouters, L. (2004). Microfabric of fractured Boom Clay at depth: A case study of brittle-ductile transitional clay behaviour. *Applied Clay Science*, 26(1-4 SPEC. ISS.):389–401.

[Dehandschutter et al., 2005] Dehandschutter, B., Vandycke, S., Sintubin, M., Vandenberghe, N., and Wouters, L. (2005). Brittle fractures and ductile shear bands in argillaceous sediments: Inferences from Oligocene Boom Clay (Belgium). *Journal of Structural Geology*, 27(6):1095–1112.

[Delage, 1987] Delage, P. (1987). Aspects du comportement des sols non saturés - Some aspects of the behaviour of non-saturated soils. *Revue Française de Géotechnique*, 40:33–43.

[Delage et al., 2014] Delage, P., Menaceur, H., Tang, A. M., and Talandier, J. (2014). Suction effects in deep callovo-oxfordian claystone. *Geotechnique Letters*, 4:267–271.

[Delage et al., 2016] Delage, P., Menaceur, H., Tang, A. M., and Talandier, J. (2016). Stress release and suction generation in the Callovo-Oxfordian claystone. *E3S Web of Conferences*, 9.

[Delahaye and Alonso, 2002] Delahaye, C. H. and Alonso, E. E. (2002). Soil heterogeneity and preferential paths for gas migration. *Engineering Geology*, 64(2-3):251–271.

[Delay et al., 2014] Delay, J., Bossart, P., Ling, L. X., Blechschmidt, I., Ohlsson, M., Vinsot, A., Nussbaum, C., and Maes, N. (2014). Three decades of underground research laboratories: What have we learned? *Geological Society Special Publication*, 400(1):7–32.

[Delay et al., 2005] Delay, J., Krîeguer, J.-M., Vinsot, A., Rebours, H., and Armand, G. (2005). Underground Experimental Program at the Meuse/Haute-Marne Underground Research Laboratory, Northeastern France. In *International meeting on clays in natural and engineered barriers for radioactive waste confinement*, pages 57–58, Tours, France.

[Delay et al., 2006] Delay, J., Trouiller, A., and Lavanchy, J. M. (2006). Propriétés hydrodynamiques du Callovo-Oxfordien dans l'Est du bassin de Paris : comparaison des résultats obtenus selon différentes approches. *Comptes Rendus - Geoscience*, 338(12-13):892–907.

[Delay et al., 2007] Delay, J., Vinsot, A., Krieguer, J. M., Rebours, H., and Armand, G. (2007). Making of the underground scientific experimental programme at the Meuse/Haute-Marne underground research laboratory, North Eastern France. *Physics and Chemistry of the Earth*, 32(1-7):2–18.

[Dellano-Paz et al., 2015] Dellano-Paz, F., Calvo-Silvosa, A., Iglesias Antelo, S., and Soares, I. (2015). The European low-carbon mix for 2030: The role of renewable energy sources in an environmentally and socially efficient approach. *Renewable and Sustainable Energy Reviews*, 48:49–61.

[Desbois et al., 2010] Desbois, G., Urai, J. L., and De Craen, M. (2010). In-situ and direct characterization of porosity in Boom Clay (Mol site, Belgium) by using novel combination of ion beam cross-sectioning, SEM and cryogenic methods Motivations, first results and perspectives. Technical Report External Report 124, SCK•CEN, Belgian Nuclear Research Centre, Mol, Belgium.

[Descostes et al., 2008] Descostes, M., Blin, V., Bazer-Bachi, F., Meier, P., Grenut, B., Radwan, J., Schlegel, M. L., Buschaert, S., Coelho, D., and Tevissen, E. (2008). Diffusion of anionic species in Callovo-Oxfordian argillites and Oxfordian limestones (Meuse/Haute-Marne, France). *Applied Geochemistry*, 23(4):655–677.

[Desrues, 1984] Desrues, J. (1984). *La localisation de la déformation dans les milieux granulaires*. PhD thesis, Université Joseph Fourier, Institut National Polytechnique, Grenobre, France.

[Desrues, 1989] Desrues, J. (1989). Shear band analysis for granular materials: the question of incremental non-linearity. *Archive of Applied Mechanics*, 59(3):187–196.

[Desrues, 1990] Desrues, J. (1990). Shear band initiation in granular materials. Experimentation and theory.pdf. In *Geomaterials - Constitutive Equations and Modelling*, chapter 13, pages 283–310. Elsevier, Amsterdam, The Nederland, 1 edition.

[Desrues, 2005] Desrues, J. (2005). Hydro-mechanical coupling and strain localization in saturated porous media. *Revue Européenne de Génie Civil*, 9(5-6):619–634.

[Desrues et al., 2019] Desrues, J., Argilaga, A., Caillerie, D., Combe, G., Nguyen, T. K., Richefeu, V., and Dal Pont, S. (2019). From discrete to continuum modelling of boundary value problems in geomechanics: An integrated FEM-DEM approach. *International Journal for Numerical and Analytical Methods in Geomechanics*, 43(5):919–955.

[Desrues and Chambon, 2002] Desrues, J. and Chambon, R. (2002). Shear band analysis and shear moduli calibration. *International Journal of Solids and Structures*, 39(13-14):3757–3776.

[Desrues et al., 1996] Desrues, J., Chambon, R., Mokni, M., and Mazerolle, F. (1996). Void ratio evolution inside shear bands in triaxial sand specimens studied by computed tomography. *Geotechnique*, 46(3):529–546.

[Desrues and Viggiani, 2004] Desrues, J. and Viggiani, G. (2004). Strain localization in sand: An overview of the experimental results obtained in Grenoble using stereophotogrammetry. *International Journal for Numerical and Analytical Methods in Geomechanics*, 28(4):279–321.

[Detournay and Cheng, 1993] Detournay, E. and Cheng, A. (1993). Fundamentals of Poroelasticity. In *Comprehensive Rock Engineering: Principles, Practice and Projects.*, volume 2, chapter 5, pages 113–171. Pergamon Press, Oxford.

[Dewhurst et al., 1999] Dewhurst, D. N., Aplin, A. C., and Sarda, J. P. (1999). Influence of clay fraction on pore-scale properties and hydraulic conductivity of experimentally compacted mudstones. *Journal of Geophysical Research: Solid Earth*, 104(B12):29261–29274.

[Didier, 2012] Didier, M. (2012). Étude Du Transfert Réactif De L'Hydrogène Au Sein De L'Argilite.

[Diederichs, 2003] Diederichs, M. S. (2003). Rock Fracture and Collapse Under Low Confinement Conditions. *Rock Mechanics and Rock Engineering*, 36(5):339–381.

[Dieudonné, 2016] Dieudonné, A.-C. (2016). *Hydromechanical behaviour of compacted bentonite : from micro-scale analysis to macro-scale modelling*. PhD thesis, University of Liège.

[Díez et al., 2000] Díez, P., Arroyo, M., and Huerta, A. (2000). Adaptivity based on error estimation for viscoplastic softening materials. *Mechanics of Cohesive-Frictional Materials*, 5(2):87–112.

[Distinguin and Lavanchy, 2007] Distinguin, M. and Lavanchy, J. M. (2007). Determination of hydraulic properties of the Callovo-Oxfordian argillite at the bure site: Synthesis of the results obtained in deep boreholes using several in situ investigation techniques. *Physics and Chemistry of the Earth*, 32(1-7):379–392.

[Dizier, 2011] Dizier, A. (2011). *Caractérisation des effets de température dans la zone endommagée autour de tunnels de stockage de déchets nucléaires dans des roches argileuses*. PhD thesis, University of Liège.

[Dizier et al., 2018] Dizier, A., Chen, G., and Li, X.-l. (2018). State of the art : Thermo-hydro- mechanical behavior of the Boom Clay. Technical report, EURIDICE report.

[Dormieux et al., 1995] Dormieux, L., Barboux, P., Coussy, O., and Dangla, P. (1995). A macroscopic model of the swelling phenomenon of a saturated clay. *European Journal of Mechanics and Solids*, 14(6):981–1004.

[Dormieux and Kondo, 2004] Dormieux, L. and Kondo, D. (2004). Approche micromécanique du couplage perméabilité- endommagement. *Comptes Rendus - Mecanique*, 332(2):135–140.

[Dormieux et al., 2006] Dormieux, L., Kondo, D., and Ulm, F. J. (2006). A micromechanical analysis of damage propagation in fluid-saturated cracked media. *Comptes Rendus - Mecanique*, 334(7):440–446.

[Doyi et al., 2015] Doyi, I., Essumang, D. K., and Dampare, S. (2015). Technologically Enhanced Naturally Occurring Radioactive Materials (TENORM) in the Oil and Gas Industry : A Review. *Reviews of Environmental Contamination and Toxicology*, 238.

[Du Bernard et al., 2002] Du Bernard, X., Eichhubl, P., and Aydin, A. (2002). Dilation bands: A new form of localized failure in granular media. *Geophysical Research Letters*, 29(24).

[Dugdale, 1960] Dugdale, D. S. (1960). Yielding of steel sheets containing slits. *J. Mech. Phys. Solids*, 8(2):100–104.

[Dumont, 1849] Dumont, M. (1849). Rapport sur la carte géologique du Royaume. *Bulletins de l'Académie Royale des Sciences, des Lettres et des Beaux-Arts de Belgique*, 16(11):351–373.

[Dupré and Dupré, 1869] Dupré, M. and Dupré, M. (1869). *Théorie mécanique de la chaleur*. Gauthier-Villars, Paris, France.

[Duveau et al., 2011] Duveau, G., M'Jahad, S., Davy, C., Skoczylas, F., Shao, J., Talandier, J., and Granet, S. (2011). Gas entry through water-saturated argillite: Experimental and numerical approaches. In *45th US Rock Mechanics / Geomechanics Symposium*, San Fransisco, The United States. American Rock Mechanics Association.

[Dvorkin et al., 1990] Dvorkin, E. N., Cuitiño, A. M., and Gioia, G. (1990). Finite elements with displacement interpolated embedded localization lines insensitive to mesh size and distortions. *International Journal for Numerical Methods in Engineering*, 30(3):541–564.

[Dymitrowska et al., 2014] Dymitrowska, M., Olivella, S., Arnedo, D., Alcoverro, J., Alonso, E. E., and Shaw, R. P. (2014). Final modelling results and progress in gas transport modelling. In *FORGE Report D3.31 71pp.*

[EC, 2000] EC (2000). Euradwaste '99: Radioactive Waste Management Strategies and Issues (Proc. 5th EC Conf. Luxembourg, 1999). Technical Report EUR 19143 EN, European Commission, Brussels, Belgium.

[EC, 2005a] EC (2005a). Impact of the excavation disturbed or damaged zone (EDZ) on the performance of radioactive waste geological repositories. In Davies, C. and Bernier, F., editors, *Proceedings of a European Commission Cluster Conference and Workshop*, pages 3–4, Luxembourg. Office for Official Publications of the European Communities.

[EC, 2005b] EC (2005b). Ventilation experiment in Opalinus Clay for the disposal of radioactive waste in underground repositories (Project funded by the European Community under the 'EURATOM' Programme 1998–2002 under contract No. FIKWCT-2001-00126). Technical Report Nuclear science and technology, Office for Official Publications of the European Communities, Luxembourg.

[EC, 2019] EC (2019). *Report from the Commission to the Council and the European Parliament on progress of implementation of Council Directive 2011/70/EURATOM and an inventory of radioactive waste and spent fuel present in the Community's territory and the future prospects*. Second Report. COM(2019) 632 Final. European Parliament, Brussels, Belgium.

[Ehlers and Volk, 1998] Ehlers, W. and Volk, W. (1998). On theoretical and numerical methods in the theory of porous media based on polar and non-polar elasto-plastic solid materials. *Int J Solids Struct*, 35(34-35):4597–4617.

[El-Hassan, 1997] El-Hassan, N. (1997). *Modélisation théorique et numérique de la localisation de la déformation dans les géomateriaux*. PhD thesis, Université Joseph Fourier - Grenoble I.

[El Moustapha, 2014] El Moustapha, K. (2014). *Identification de lois de comportement enrichie pour les géomatériaux en présence d'une localisation de la déformation*. PhD thesis, Université de Grenoble, Grenoble, France.

[Engelen et al., 2002] Engelen, R. A., Geers, M. G., and Baaijens, F. P. (2002). Nonlocal implicit gradient-enhanced elasto-plasticity for the modelling of softening behaviour. *International Journal of Plasticity*, 19(4):403–433.

[Enssle et al., 2011] Enssle, C. P., Cruchaudet, M., Croisé, J., and Brommundt, J. (2011). Determination of the permeability of the Callovo-Oxfordian clay at the metre to decametre scale. *Physics and Chemistry of the Earth*, 36(17-18):1669–1678.

[Eringen, 1970] Eringen, A. C. (1970). Balance laws of micromorphic mechanics. *International Journal of Engineering Science*, 8(10):819–828.

[Eringen, 1972] Eringen, A. C. (1972). Nonlocal polar elastic continua. *International Journal of Engineering Science*, 10(1):1–16.

[Escoffier, 2002] Escoffier, S. (2002). *Caractérisation expérimentale du comportement hydromécanique des argilites de Meuse/Haute-Marne*. PhD thesis, Institut national polytechnique de Lorraine, Nancy, France.

[Escoffier et al., 2005] Escoffier, S., Homand, F., Giraud, A., Hoteit, N., and Su, K. (2005). Under stress permeability determination of the Meuse/Haute-Marne mudstone. *Engineering Geology*, 81(3):329–340.

[Esteban, 2006] Esteban, L. (2006). *Anisotropies magnétique et de porosité des argilites du Callovo-Oxfordien du laboratoire souterrain de l'Andra (Meuse/Haute-Marne, Bassin de Paris)*. PhD thesis, University of Toulouse III.

[Euler, 1749] Euler, L. (1749). *Scientia navalis seu tractatus de construendis ac dirigendis navibus, 2 vols*, volume 2 vols. Paris, St. Petersbourg, Russia.

[Ewen and Thomas, 1989] Ewen, J. and Thomas, H. R. (1989). Heating unsaturated medium sand. *Géotechnique*, 39(3):455–470.

[Ewing et al., 2016] Ewing, R., Whittleston, R., and Yardley, B. (2016). Geological disposal of nuclear waste: A primer. *Elements*, 12(4):233–237.

[Faivre et al., 2016] Faivre, M., Paul, B., Golfier, F., Giot, R., Massin, P., and Colombo, D. (2016). 2D coupled HM-XFEM modeling with cohesive zone model and applications to fluid-driven fracture network. *Engineering Fracture Mechanics*, 159:115–143.

[Fall et al., 2014] Fall, M., Nasir, O., and Nguyen, T. S. (2014). A coupled hydro-mechanical model for simulation of gas migration in host sedimentary rocks for nuclear waste repositories. *Engineering Geology*, 176:24–44.

[Fanara et al., 2022] Fanara, A., Courard, L., and Collin, F. (2022). FE2 multiscale modelling of chloride ions transport in recycled aggregates concrete. *Computational Modelling of Concrete and Concrete Structures*, pages 66–75.

[Fatt, 1956] Fatt, I. (1956). The Network Model of Porous Media. *Transactions of the AIME*, 207(01):144–181.

[Félix et al., 1996] Félix, B., Lebon, P., Miguez, R., and Plas, F. (1996). A review of the ANDRA's research programmes on the thermo-hydromechanical behavior of clay in connection with the radioactive waste disposal project in deep geological formations. *Engineering Geology*, 41:35–50.

[Fernandes et al., 2008] Fernandes, R., Chavant, C., and Chambon, R. (2008). A simplified second gradient model for dilatant materials: Theory and numerical implementation. *International Journal of Solids and Structures*, 45(20):5289–5307.

[Fernandes et al., 2011] Fernandes, R., Ducoin, B., and Chambon, R. (2011). 2D and 3D Modelling of Geomaterials Using a Second Gradient Dilation Model. In *Advances in Bifurcation and Degradation in Geomaterials*, pages 209–2018. Springer Series in Geomechanics and Geoengineering, Springer, Dordrecht.

[Feyel and Chaboche, 2000] Feyel, F. and Chaboche, J. L. (2000). FE 2 multiscale approach for modelling the elastoviscoplastic behaviour of long fibre SiC/Ti composite materials. *Computer Methods in Applied Mechanics and Engineering*, 183(3-4):309–330.

[Fick, 1855] Fick, A. (1855). Über Diffusion [Translated: On liquid diffusion]. *Poggendorff's Annalen der Physik und Chemie*, 170(1):59–86.

[Finno et al., 1997] Finno, R. J., Harris, W. W., Mooney, M. A., and Viggiani, G. (1997). Shear bands in plane strain compression of loose sand. *Geotechnique*, 47(1):149–165.

[Finno et al., 1996] Finno, R. J., Wendell, W. H., Mooney, M., and Viggiani, G. (1996). Strain Localization and Undrained Steady State of Sand. *Journal of Geotechnical and Geoenvironmental Engineering*, 122(6):462–473.

[Fish and Wagiman, 1993] Fish, J. and Wagiman, A. (1993). Multiscale finite element method for a locally nonperiodic heterogeneous medium. *Computational Mechanics*, 12(3):164–180.

[Fleck and Hutchinson, 1997] Fleck, N. A. and Hutchinson, J. W. (1997). Strain Gradient Plasticity.

[Fossen et al., 2007] Fossen, H., Schultz, R. A., Shipton, Z. K., and Mair, K. (2007). Deformation bands in sandstone: A review. *Journal of the Geological Society*, 164(4):755–769.

[Fourar and Lenormand, 1998] Fourar, M. and Lenormand, R. (1998). A Viscous Coupling Model for Relative Permeabilities in Fractures. In *SPE Annual Technical Conference and Exhibition*, pages 253–258. Society of Petroleum Engineers.

[Francis et al., 1997] Francis, A. J., Gillow, J. B., and Giles, M. R. (1997). Microbial Gas Generation Under Expected Waste Isolation Pilot Plant Repository Conditions (iEl Sandia National laboratories. Technical Report SAND96- 2582, Sandia National Laboratory, Albuquerque, The United States.

[François, 2014] François, B. (2014). Hollow Cylinder Tests on Boom Clay : Modelling of Strain Localization in the Anisotropic Excavation Damaged Zone. *Rock Mech Rock Eng*, 47:71–86.

[François and Dascalu, 2010] François, B. and Dascalu, C. (2010). A two-scale time-dependent damage model based on non-planar growth of micro-cracks. *Journal of the Mechanics and Physics of Solids*, 58(11):1928–1946.

[Frankenbach et al., 2021] Frankenbach, P., Kruck, A., and Zangl, B. (2021). India's recognition as a nuclear power: A case of strategic cooptation. *Contemporary Security Policy*, 42(4):530–553.

[Frederickx, 2019] Frederickx, L. (2019). *An advanced mineralogical study of the clay mineral fraction of the Boom Clay*. PhD thesis, KULeuven.

[Frey, 2010] Frey, J. (2010). *Modélisation multi-échelle de l'endommagement hydromécanique des roches argileuses*. PhD thesis, INPG, Grenoble, France.

[Frey et al., 2013] Frey, J., Chambon, R., and Dascalu, C. (2013). A two-scale poromechanical model for cohesive rocks. *Acta Geotechnica*, 8(2):107–124.

[Galindo, 2022] Galindo, A. (2022). What is Nuclear Energy? The Science of Nuclear Power | IAEA (Accessed 29 July 2022), www.iaea.org. https://www.iaea.org/newscenter/news/what-is-nuclear-energy-the-science-of-nuclear-power.

[Garamszeghy, 2011] Garamszeghy, M. (2011). Compaction processes and technology for treatment and conditioning of radioactive waste. In Ojovan, M., editor, *Handbook of Advanced Radioactive Waste Conditioning Technologies. Part I: Radioactive waste treatment processes and conditioning technologies*, chapter 2, pages 19–42. Woodhead Publishing Limited.

[Garcia et al., 2020] Garcia, M., Beattie, T., and Schumacher, S. (2020). EURAD: the European Joint Programme for research on radioactive waste management between EU members states national programmes. *EPJ Nuclear Sciences & Technologies*, 6:21.

[Garrels and Christ, 1965] Garrels, R. and Christ, C. (1965). *Solutions, minerals, and equilibria*. Harper & Row, San Fransisco.

[Gatabin et al., 2016] Gatabin, C., Talandier, J., Collin, F., Charlier, R., and Dieudonné, A. C. (2016). Competing effects of volume change and water uptake on the water retention behaviour of a compacted MX-80 bentonite/sand mixture. *Applied Clay Science*, 121-122:57–62.

[Gawin and Sanavia, 2009] Gawin, D. and Sanavia, L. (2009). A unified approach to numerical modeling of fully and partially saturated porous materials by considering air dissolved in water. *CMES - Computer Modeling in Engineering and Sciences*, 53(3):255–302.

[Geers et al., 2010] Geers, M. G., Kouznetsova, V. G., and Brekelmans, W. A. (2010). Multi-scale computational homogenization: Trends and challenges. *Journal of Computational and Applied Mathematics*, 234(7):2175–2182.

[Gens, 2010] Gens, A. (2010). Soil-environment interactions in geotechnical engineering. *Geotechnique*, 60(1):3–74.

[Gens, 2013] Gens, A. (2013). On the hydromechanical behaviour of argillaceous hard soils-weak rocks Au sujet du comportement hydromécanique des sols indurés- roches tendres argileux. In Anagnostopoulos, A., Pachakis, M., and Tsatsanifos, C., editors, *Proceedings of the 15th European Conference on Soil Mechanics and Geotechnical Engineering – Geotechnics of Hard Soils – Weak Rocks*, pages 71–118, Athens, Greece. IOS Press.

[Gens et al., 1990] Gens, A., Carol, I., and Alonso, E. E. (1990). A constitutive model for rock joints formulation and numerical implementation. *Computers and Geotechnics*, 9(1-2):3–20.

[Gens et al., 1998] Gens, A., Garcia-Molina, A. J., Olivella, S., Alonso, E. E., and Huertas, F. (1998). Analysis of a full scale in situ testing simulating repository conditions. *International Journal for Numerical and Analytical Methods in Geomechanics*, 22(7):515–548.

[Gens and Olivella, 2001] Gens, A. and Olivella, S. (2001). Clay barriers in radioactive waste disposal. *Revue Française de Génie Civil*, 5(6):845–856.

[Gens et al., 2007] Gens, A., Vaunat, J., Garitte, B., and Wileveau, Y. (2007). In situ behaviour of a stiff layered clay subject to thermal loading: Observations and interpretation. *Stiff Sedimentary Clays: Genesis and Engineering Behaviour - Geotechnique Symposium in Print 2007*, 57(2):123–144.

[Gensterblum et al., 2015] Gensterblum, Y., Ghanizadeh, A., Cuss, R. J., Amann-Hildenbrand, A., Krooss, B. M., Clarkson, C. R., Harrington, J. F., and Zoback, M. D. (2015). Gas transport and storage capacity in shale gas reservoirs - A review. Part A: Transport processes. *Journal of Unconventional Oil and Gas Resources*, 12:87–122.

[Gerard, 2011] Gerard, P. (2011). *Impact des transferts de gaz sur le comportement poro-mécanique des matériaux argileux Thèse présentée par*. Thèse de doctorat, University of Liège.

[Gerard et al., 2008] Gerard, P., Charlier, R., Su, K., Duveau, G., Giot, R., Chavant, C., and Collin, F. (2008). Numerical modelling of coupled mechanics and gas tansfer around radioactive waste in long-term storage. *Journal of Theoretical and Applied Mechanics*, 38:25–44.

[Gerard et al., 2012] Gerard, P., Harrington, J., Charlier, R., and Collin, F. (2012). Hydro-Mechanical Modelling of the Development of Preferential Gas Pathways in Claystone. *Unsaturated Soils: Research and Applications*, pages 175–180.

[Gerard et al., 2014] Gerard, P., Harrington, J., Charlier, R., and Collin, F. (2014). Modelling of localised gas preferential pathways in claystone. *International Journal of Rock Mechanics and Mining Sciences*, 67:104–114.

[Gerard et al., 2011] Gerard, P., Radu, J. P., Talandier, J., De La Vaissière, R., Charlier, R., and Collin, F. (2011). Numerical modelling of the resaturation of swelling clay with gas injection. *Unsaturated Soils - Proceedings of the 5th International Conference on Unsaturated Soils*, 2(section 5):1383–1388.

[Germain, 1973a] Germain, P. (1973a). The method of virtual power in continuum mechanics. Part 1: Second-gradient theory. *Journal de Mécanique*, 12(2):235–274.

[Germain, 1973b] Germain, P. (1973b). The method of virtual power in continuum mechanics. Part 2: Microstructure. *Society for Industrial and Applied Mathematics*, 25(3):556–575.

[Ghosh et al., 1995] Ghosh, S., Lee, K., and Moorthy, S. (1995). Multiple scale analysis of heterogeneous elastic structures using homogeneisation theory and Voronoi cell finite element method. *International Journal of Solids and Structures*, 32(1):27–65.

[Giddings et al., 2002] Giddings, B., Hopwood, B., and O'Brien, G. (2002). Environment, economy and society: fitting them together into sustainable development. *Sustainable Development*, 10:187–196.

[Gilman and Beckie, 2000] Gilman, A. and Beckie, R. (2000). Flow of coal-bed methane to a gallery. *Transport in Porous Media*, 41(1):1–16.

[Golshani et al., 2007] Golshani, A., Oda, M., Okui, Y., Takemura, T., and Munkhtogoo, E. (2007). Numerical simulation of the excavation damaged zone around an opening in brittle rock. *International Journal of Rock Mechanics and Mining Sciences*, 44(6):835–845.

[Gómez-Hernández, 2000] Gómez-Hernández, J. (2000). Flow Mechanism (FM-C) Experiment: Part A) Effective diffusivity and accessible porosity derived from in-situ He-4 tests - Part B) Prediction of HE-3 concentration in a cross-hole experiment. Technical Report 2000-40. Technical Report September, Technical University of Valencia – Spain.

[Gonzalez-Blanco and Romero, 2022] Gonzalez-Blanco, L. and Romero, E. (2022). A multi-scale insight into gas transport in a deep Cenozoic clay. *Geotechnique*.

[Gonzalez-Blanco et al., 2016] Gonzalez-Blanco, L., Romero, E., Jommi, C., Li, X., and Sillen, X. (2016). Gas migration in a Cenozoic clay: Experimental results and numerical modelling. *Geomechanics for Energy and the Environment*, 6:81–100.

[Gonzalez-Blanco et al., 2022] Gonzalez-Blanco, L., Romero, E., Marschall, P., and Levasseur, S. (2022). Hydro - mechanical Response to Gas Transfer of Deep Argillaceous Host Rocks for Radioactive Waste Disposal. *Rock Mechanics and Rock Engineering*, 55(3):1159–1177.

[Gonzalez-Blanco, 2017] Gonzalez-Blanco, L. (2017). *Gas migration in deep argillaceous formations : Boom Clay and indurated clays*. PhD thesis, Universitat Politècnica de Catalunya (UPC).

[Goodman, 1976] Goodman, R. (1976). *Methods of geological engineering in Discontinuous Rocks*. West Publishing Co.

[Graham et al., 2002] Graham, J., Halayko, K. G., Hume, H., Kirkham, T., Gray, M., and Oscarson, D. (2002). A capillarity-advective model for gas break-through in clays. *Engineering Geology*, 64(2-3):273–286.

[Gramegna, 2021] Gramegna, L. (2021). *Hydromechanical behaviour of bentonite seals in the context of nuclear waste disposals : contributions for engineered barriers evaluation*. PhD thesis, University of Liège.

[Gray, 1987] Gray, I. (1987). Reservoir Engineering in Coal Seams: Part 1 - the Physical Process of Gas Storage and Movement in Coal Seams. *SPE Reservoir Engineering (Society of Petroleum Engineers)*, 2(1):28–34.

[Griffith, 1921] Griffith, A. A. (1921). The phenomena of rupture and flow in solids. *Phil. Trans. R. Soc. Lond*, 221(582-593):163–198.

[Grindrod et al., 1994] Grindrod, P., Impey, M., Saddique, S., and Takase, H. (1994). Saturation and gas migration within clay buffers. In *Proceedings of Conference on High Level Radioactive Waste Management*, Las Vegas, The United States.

[GSL, 2020] GSL (2020). Geological disposal of Radioactive Waste. In *A policy briefing note from the Geological Society of London*. London, The United Kingdom.

[Gui et al., 2016] Gui, Y. L., Zhao, Z. Y., Kodikara, J., Bui, H. H., and Yang, S. Q. (2016). Numerical modelling of laboratory soil desiccation cracking using UDEC with a mix-mode cohesive fracture model. *Engineering Geology*, 202:14–23.

[Guillocheau et al., 2000] Guillocheau, F., Robin, C., Allemand, P., Bourquin, S., Brault, N., Dromart, G., Friedenberg, R., Garcia, J. P., Gaulier, J. M., Gaumet, F., Grosdoy, B., Hanot, F., Le Strat, P., Mettraux, M., Nalpas, T., Prijac, C., Rigollet, C., Serrano, O., and Grandjean, G. (2000). Meso-Cenozoic geodynamic evolution of the Paris Basin: 3D stratigraphic constraints. *Geodinamica Acta*, 13(4):189–245.

[Guo and Fall, 2018] Guo, G. and Fall, M. (2018). Modelling of dilatancy-controlled gas flow in saturated bentonite with double porosity and double effective stress concepts. *Engineering Geology*, 243(July):253–271.

[Guo and Fall, 2019] Guo, G. and Fall, M. (2019). Modelling of preferential gas flow in heterogeneous and saturated bentonite based on phase field method. *Computers and Geotechnics*, 116(August).

[Guo and Fall, 2021] Guo, G. and Fall, M. (2021). Advances in modelling of hydro-mechanical processes in gas migration within saturated bentonite: A state-of-art review. *Engineering Geology*, 287(July 2020):106123.

[Habraken, 1989] Habraken, A. (1989). *Contribution à la modélisation du formage des métaux par la méthode des éléments finis*. PhD thesis, University of Liège.

[Hadamard, 1903] Hadamard, J. (1903). *Leçons sur la Propagation des Ondes et les Equations de l'Hydrodynamique.* Paris : A. Hermann, Paris, France.

[Haïed, 1995] Haïed, A. (1995). *Etude expérimentale de la rupture en mode localisé dans un gré*. PhD thesis, Université de Lille I.

[Haijtink and Rodwell, 1995] Haijtink, B. and Rodwell, W. (1995). Project on Effects of GAS in Underground Storage facilities for radioactive waste (PEGASUS project). Proceedings of a progress meeting held in Rapolano Terme, Italy on 14 and 15 June 1995. Technical Report Nuclear Science and Technology EUR 16746 EN, European Commission, Luxembourg.

[Hall, 2012] Hall, S. A. (2012). Digital image correlation in experimental geomechanics. In Viggiani, G., Hall, S., and Romero, E., editors, *ALERT Doctoral School 2012 – Advanced experimental techniques in geomechanics,*, chapter 2, pages 69–112. ALERT Geomaterials.

[Hall et al., 2010] Hall, S. A., Bornert, M., Desrues, J., Pannier, Y., Lenoir, N., Viggiani, G., and Bésuelle, P. (2010). Discrete and continuum analysis of localised deformation in sand using X-ray μCT and volumetric digital image correlation. *Geotechnique*, 60(5):315–322.

[Hall et al., 2009] Hall, S. A., Lenoir, N., Viggiani, G., Desrues, J., and Bésuelle, P. (2009). Strain localisation in sand under triaxial loading: Characterisation by x-ray micro tomography and 3D Digital Image Correlation. *Computational Geomechanics, COMGEO I - Proceedings of the 1st International Symposium on Computational Geomechanics*, pages 239–247.

[Han and Vardoulakis, 1991] Han, C. and Vardoulakis, I. (1991). Plane-strain compression experiments on water-saturated fine-grained sand. *Géotechnique*, 47(1):49–78.

[Han et al., 1997] Han, K. W., Heinonen, J., and Bonne, A. (1997). Radioactive waste disposal : Global experience and challenges. *IAEA Bulletin*, pages 33–41.

[Harrington et al., 2017a] Harrington, J. F., Cuss, R. J., and Talandier, J. (2017a). Gas transport properties through intact and fractured Callovo-Oxfordian mudstones. In Rutter, E. H., Mecklenburgh, J., and Taylor, K. G., editors, *Geomechanical and Petrophysical Properties of Mudrock*, volume 454, pages 131–154. Geological Society, London, Special Publications.

[Harrington et al., 2017b] Harrington, J. F., Cuss, R. J., Wiseall, A. C., Daniels, K. A., Graham, C. C., and Tamayo-Mas, E. (2017b). Scoping study examining the behaviour of Boom Clay at disposal depths investigated in OPERA. COVRA Report OPERA-PU-BGS523 and 616. Technical report, British Geological Survey.

[Harrington et al., 2012a] Harrington, J. F., de La Vaissière, R., Noy, D. J., Cuss, R. J., and Talandier, J. (2012a). Gas flow in Callovo-Oxfordian claystone (COx): results from laboratory and field-scale measurements. *Mineralogical Magazine*, 76(8):3303–3318.

[Harrington and Horseman, 1999] Harrington, J. F. and Horseman, S. T. (1999). Gas transport properties of clays and mudrocks. *Geological Society Special Publication*, 158(c):107–124.

[Harrington et al., 2012b] Harrington, J. F., Milodowski, A. E., Graham, C. C., Rushton, J. C., and Cuss, R. J. (2012b). Evidence for gas-induced pathways in clay using a nanoparticle injection technique. *Mineralogical Magazine*, 76(8):3327–3336.

[Harrington et al., 2013] Harrington, J. F., Volckaert, G., Jacobs, E., Maes, N., Areias, L., Charlier, R., Collin, F., Gerard, P., Levasseur, S., Radu, J.-P., Svoboda, J., Granet, S., Alcoverro, J., Arnedo, D., Olivella, S., Alonso, E., Marschall, P., Gaus, I., Rüedi, J., Cuss, R., Sathar, S., and Noy, D. (2013). FORGE Milestone D4 . 24-R. Summary report : Experiments and modelling of excavation damage zone (EDZ) behaviour in argillaceous and crystalline rocks (Work Package 4). Technical report, European Commision.

[Hassanizadeh and Gray, 1979a] Hassanizadeh, M. and Gray, W. G. (1979a). General conservation equations for multi-phase systems: 1. Averaging procedure. *Advances in Water Resources*, 2:131–144.

[Hassanizadeh and Gray, 1979b] Hassanizadeh, M. and Gray, W. G. (1979b). General conservation equations for multiphase systems: 2. Mass, momenta, energy, and entropy equations. *Advances in Water Resources*, 2:191–203.

[Hassanizadeh and Gray, 1980] Hassanizadeh, M. and Gray, W. G. (1980). General conservation equations for multi-phase systems: 3. Constitutive theory for porous media flow. *Advances in Water Resources*, 3(1):25–40.

[Heider and Sun, 2020] Heider, Y. and Sun, W. C. (2020). A phase field framework for capillary-induced fracture in unsaturated porous media: Drying-induced vs. hydraulic cracking. *Computer Methods in Applied Mechanics and Engineering*, 359:112647.

[Heitz and Hicher, 2002] Heitz, J.-F. and Hicher, P.-Y. (2002). The mechanical behaviour of argillaceous rocks – Some questions from laboratory experiments. In Hoteit, N., Shao, J., Su, K., and Tijani, M., editors, *Proceedings of International Symposium on Hydromechanical and Thermohydromechanical Behaviour of Deep Argillaceous Rock*, pages 99–108. Swets & Zeitlinger.

[Helmig, 1997] Helmig, R. (1997). *Multiphase Flow and Transport Processes in the Subsurface*. Springer Publ., Berlin, Germany.

[Hemes et al., 2011] Hemes, S., Desbois, G., Urai, J. L., De Craen, M., and Honty, M. (2011). Comparative study on porosity in fine- and coarse-grained Boom Clay samples (Mol-Dessel reference site, Belgium) External report (SCK-CEN-ER-157). Technical Report External Report 157, SCK•CEN, Belgian Nuclear Research Centre, Mol, Belgium.

[Henry, 1803] Henry, W. (1803). Experiments on the quantity of gases absorbed by water, at different temperatures, and under different pressures. *Society*, 93:29–274.

[Heremans et al., 1977] Heremans, R., de Beer, E., Carpentier, R., and Manfroy, P. (1977). Preliminary studies of an underground facility for nuclear waste burial in a tertiary clay formation. In Bergman, M., editor, *Proceedings of the First International Symposium*, pages 771–780, Stockholm, Sweden. Pergamon.

[Hicher et al., 1994] Hicher, P. Y., Wahyudi, H., and Tessier, D. (1994). Microstructural analysis of strain localisation in clay. *Computers and Geotechnics*, 16(3):205–222.

[Hicks et al., 2008] Hicks, T. W., Baldwin, T. D., Hooker, P. J., Richardson, P. J., Chapman, N. A., McKinley, I. G., and Neall, F. B. (2008). Concepts for the Geological Disposal of Intermediate-Level Radioactive Waste. Technical Report NDA Report 0736-1, Nuclear Decommissioning Authority.

[Hill, 1958] Hill, R. (1958). General Stability Theory of uniqueness and stability in elasto-plastic solids. *Journal of the Mechanics and Physics of Solids*, 6:239–249.

[Hill, 1962] Hill, R. (1962). Acceleration Waves in Solids. *Journal of the Mechanics and Physics of Solids*, 10(1):1–16.

[Hill, 1965] Hill, R. (1965). A self-consistent mechanics of composite materials. *Journal of the Mechanics and Physics of Solids*, 13(4):213–222.

[Hill and Hutchinson, 1975] Hill, R. and Hutchinson, J. W. (1975). Bifurcation phenomena in the plane tension test. *Journal of the Mechanics and Physics of Solids*, 23(4-5):239–264.

[Hirschfelder et al., 1964] Hirschfelder, J., Curtiss, C., and Bird, R. (1964). *The Molecular Theory of Gases and Liquids*. Wiley, New-York, The United States.

[Högberg, 2013] Högberg, L. (2013). Root causes and impacts of severe accidents at large nuclear power plants. *Ambio*, 42(3):267–284.

[Homand et al., 2004] Homand, F., Giraud, A., Escoffier, S., Koriche, A., and Hoxha, D. (2004). Permeability determination of a deep argillite in saturated and partially saturated conditions. *International Journal of Heat and Mass Transfer*, 47(14-16):3517–3531.

[Honty and De Craen, 2012] Honty, M. and De Craen, M. (2012). Boom Clay mineralogy – qualitative and quantitative aspects. Technical report, SCK•CEN, Mol, Belgium.

[Honty et al., 2010] Honty, M., De Craen, M., Wang, L., Madejová, J., Czímerová, A., Pentrák, M., Stríček, I., and Van Geet, M. (2010). The effect of high pH alkaline solutions on the mineral stability of the Boom Clay - Batch experiments at 60°C. *Applied Geochemistry*, 25(6):825–840.

[Horii and Nemat-Nasser, 1983] Horii, H. and Nemat-Nasser, S. (1983). Overall moduli of solids with microcracks: Load-induced anisotropy. *Journal of the Mechanics and Physics of Solids*, 31(2):155–171.

[Horseman and Harrington, 1994] Horseman, S. T. and Harrington, J. (1994). Migration of repository gases in an overconsolidated clay.

[Horseman et al., 1999] Horseman, S. T., Harrington, J. F., and Sellin, P. (1999). Gas migration in clay barriers. *Engineering Geology*, 54(1-2):139–149.

[Horseman et al., 1996] Horseman, S. T., Higgo, J. J. W., Alexander, J., and Harrington, J. F. (1996). Water, Gas and Solute Movement Through Argillaceous Media. Nuclear Energy Agency Report CC-91/1 OECD. Technical report, Organisation for Economic Co-operation and Development (OECD), Paris, France.

[Horseman et al., 1987] Horseman, S. T., Winter, M. G., and Entwistle, D. (1987). Geotechnical characterization of Boom Clay in relation to the disposal of radioactive waste. Publications of the European Communities, EUR 1087 EN. Technical report, European Commission, Luxembourg.

[Horvath and Rachlew, 2016] Horvath, A. and Rachlew, E. (2016). Nuclear power in the 21st century: Challenges and possibilities. *Ambio*, 45(1):38–49.

[Hoteit et al., 1999] Hoteit, N., Ozanam, O., Su, K., François, O., Heitz, J., and Nguyen, M. (1999). Geomechanical research for radwaste disposal in deep clays - First results and prospects. *WM'99 Conference*.

[Hou et al., 2011] Hou, J., Tan, Z., Wang, J., and Xie, P. (2011). Government Policy and Future Projection for Nuclear Power in China. *Journal of Energy Engineering*, 137(3):151–158.

[Hounsfield, 1975] Hounsfield, G. (1975). Method of and apparatus for examining a body by radiation such as x or gamma radiation. United-States Patent. US 3919552.

[Hoxha and Auvray, 2005] Hoxha, D. and Auvray, D. (2005). Effet de la désaturation et de la resaturation sur l'argilite dans les ouvrages souterrains. Technical report, Agence Nationale pour la gestion des Déchets RAdioactifs., Châtenay-Malabry, France.

[Hu and Hueckel, 2007] Hu, L. B. and Hueckel, T. (2007). Coupled chemo-mechanics of intergranular contact: Toward a three-scale model. *Computers and Geotechnics*, 34(4):306–327.

[Hubert, 2018] Hubert, J. (2018). *Experimental and Numerical Study of Cracking During the Drying of Porous Materials: Application To the Fields of Chemical Engineering and Geomechanics*. PhD thesis, University of Liège.

[Hudson et al., 2001] Hudson, J. A., Stephansson, O., Andersson, J., Tsang, C. F., and Jing, L. (2001). Coupled T-H-M issues relating to radioactive waste repository design and performance. *International Journal of Rock Mechanics and Mining Sciences*, 38(1):143–161.

[Hueckel, 2021] Hueckel, T. (2021). Multiphysics Role in Instabilities in Geomaterials: a Review. In Sulem, J. and Stefanou, I., editors, *Instabilities Modeling in Geomechanics*, chapter 1, pages 1–30. ISTE Ltd and John Wiley & Sons, Inc., London, The United Kingdom and Hoboken, The United States.

[Hueckel et al., 2011] Hueckel, T., Francois, B., and Laloui, L. (2011). Temperature-dependent internal friction of clay in a cylindrical heat source problem. *Geotechnique*, 61(10):831–844.

[Hueckel and Pellegrini, 1991] Hueckel, T. and Pellegrini, R. (1991). Thermoplastic modeling of undrained failure of saturated clay due to heating. *Soils and Foundations*, 31(3):1–16.

[IAEA, 1993] IAEA (1993). Report on Radioactive Waste Disposal. Technical Report Specific Safety Guide No. SSG-14 S, International Atomic Energy Agency, Vienna, Austria.

[IAEA, 2001] IAEA (2001). Handling and Processing of Radioactive Waste from Nuclear Applications. Technical Reports Series No. 402. Technical report, International Atomic Energy Agency, Vienna, Austria.

[IAEA, 2002] IAEA (2002). Management of Radioactive Waste from the Mining and Milling of Ores. Safety guide No. WS-G-1.2. Technical report, International Atomic Energy Agency, Vienna, Austria.

[IAEA, 2003] IAEA (2003). Scientific and Technical Basis for the Geological Disposal of Radioactive Wastes. Technical Report 4, International Atomic Energy Agency, New-York, The United States.

[IAEA, 2008] IAEA (2008). INES - the international nuclear and radiological event scale. User's manual 2008 edition. Technical report, International Atomic Energy Agency, Vienna, Austria.

[IAEA, 2009a] IAEA (2009a). Classification of Radioactive Waste. General Safety Guide No. GSG-1. Technical report, International Atomic Energy Agency, Vienna, Austria.

[IAEA, 2009b] IAEA (2009b). Status and Trends of Nuclear Technologies. Report of the International Project on Innovative Nuclear Reactors and Fuel Cycles (INPRO). Technical report, International Atomic Energy Agency, Vienna, Austria.

[IAEA, 2011a] IAEA (2011a). Disposal of radioactive waste. Specific Safety Requirements No. SSR-5. Technical report, International Atomic Energy Agency, Vienna, Austria.

[IAEA, 2011b] IAEA (2011b). Geological Disposal Facilities for Radioactive Waste. Technical report, International Atomic Energy Agency, Vienna, Austria.

[IAEA, 2018a] IAEA (2018a). Decommissioning of Nuclear Power Plants, Research Reactors and Other Nuclear Fuel Cycle Facilities. Specific Safety Guide No. SSG-47. Technical report, International Atomic Energy Agency, Vienna, Austria.

[IAEA, 2018b] IAEA (2018b). Status and Trends in Spent Fuel and Radioactive Waste Management. Nuclear Energy Series No. NW-T-1.14 (Rev. 1). Technical report, International Atomic Energy Agency, Vienna, Austria.

[IAEA, 2020a] IAEA (2020a). Climate Change and Nuclear Power 2020. Technical report, International Atomic Energy Agency, Vienna, Austria.

[IAEA, 2020b] IAEA (2020b). Design and operation of radioactive waste incineration facilities. Safety Series No. 108. Technical Report 2, International Atomic Energy Agency, Vienna, Austria.

[IAEA, 2021] IAEA (2021). Energy, Electricity and Nuclear Power Estimates for the Period up to 2050. Reference data series No. 1, 2021 Edition. Technical report, International Atomic Energy Agency, Vienna, Austria.

[ICRP, 1985] ICRP (1985). Radiation Protection Principles for the Disposal of Solid Radioactive Waste. *Annals of the ICRP*, 15(4).

[IEA, 2019] IEA (2019). Nuclear Power in a Clean Energy System. Technical report, International Energy Agency, Paris, France.

[IEA, 2021] IEA (2021). Key World Energy Statistics 2021. Technical report, International Energy Agency, Paris, France.

[Impey et al., 1997] Impey, M. D., Grindrod, P., Takase, H., and Worgan, K. J. (1997). A capillary network model for gas migration in low-permeability media. *SIAM Journal on Applied Mathematics*, 57(3):597–608.

[IPCC, 2014] IPCC (2014). *Climate Change 2014: Mitigation of Climate Change. Contribution of Working Group III to the fifth Assessment Report of the Intergovernmental Panel on Climate Change*, volume In Press. Cambridge University Press, Cambridge, United Kingdom and New York, NY, USA.

[IPCC, 2021] IPCC (2021). *Climate Change 2021: The Physical Science Basis. Contribution of Working Group I to the Sixth Assessment Report of the Intergovernmental Panel on Climate Change*, volume In Press. Cambridge University Press, Cambridge, United Kingdom and New York, NY, USA.

[IPCC, 2022] IPCC (2022). *Climate Change 2022: Impacts, Adaptation, and Vulnerability. Contribution of Working Group II to the Sixth Assessment Report of the Intergovernmental Panel on Climate Change*, volume In Press. Cambridge University Press, Cambridge, United Kingdom and New York, NY, USA.

[Irwin, 1948] Irwin, G. (1948). Fracture dynamics. In *Fracturing of Metals*, pages 147–166. American Society for Metals, Cleveland, The United States.

[Issen and Rudnicki, 2000] Issen, K. A. and Rudnicki, J. W. (2000). Conditions for compaction bands in porous rock. *Journal of geophysical research*, 105(9):21529–21536.

[Jacops et al., 2014] Jacops, B. E., Volckaert, G., Maes SCK, N., Charlier, B. R., Collin, F., Gerard, P., Levasseur, S., Delavaissière, F. R., Talandier Granet, J. S., Navarro Spain M Villar, G. M., Romero, F., Martin Zandarin, P. M., Olivella, S., Alonso, E., and Marschall, S. P. (2014). WP5 Final Report: Experiments and modelling of gas migration processes in undisturbed rocks. *FORGE Report D5.19. 146pp.*, page 146.

[Jacops et al., 2017a] Jacops, E., Aertsens, M., Maes, N., Bruggeman, C., Krooss, B. M., Amann-Hildenbrand, A., Swennen, R., and Littke, R. (2017a). Interplay of molecular size and pore network geometry on the diffusion of dissolved gases and HTO in Boom Clay. *Applied Geochemistry*, 76:182–195.

[Jacops et al., 2017b] Jacops, E., Aertsens, M., Maes, N., Bruggeman, C., Swennen, R., Krooss, B., Amann-Hildenbrand, A., and Littke, R. (2017b). The Dependency of Diffusion Coefficients and Geometric Factor on the Size of the Diffusing Molecule: Observations for Different Clay-Based Materials. *Geofluids*, 2017:1–17.

[Jacops and Maes, 2015] Jacops, E. and Maes, N. (2015). Measuring the diffusion coefficient for He and Ar in Callovo-Oxfordian Clay. Technical report, SCK•CEN, Mol, Belgium.

[Jacops et al., 2016] Jacops, E., Maes, N., Bruggeman, C., and Grade, A. (2016). Measuring diffusion coefficients of dissolved He and Ar in three potential clay host formations: Boom Clay, Callovo-Oxfordian Clay and Opalinus Clay. *Geological Society Special Publication*, 443(1):349–360.

[Jacops et al., 2020a] Jacops, E., Rogiers, B., Frederickx, L., Swennen, R., Littke, R., Krooss, B. M., and Bruggeman, C. (2020a). The relation between petrophysical and transport properties of the Boom Clay and Eigenbilzen Sands. *Applied Geochemistry*, page 104527.

[Jacops et al., 2020b] Jacops, E., Swennen, R., Janssens, N., Seemann, T., Amann-hildenbrand, A., and Krooss, B. M. (2020b). Applied Clay Science Linking petrographical and petrophysical properties to transport characteristics : A case from Boom Clay and Eigenbilzen Sands. *Applied Clay Science*, 190(August 2019):105568.

[Jacops et al., 2013] Jacops, E., Volckaert, G., Maes, N., Weetjens, E., and Govaerts, J. (2013). Applied Clay Science Determination of gas diffusion coef fi cients in saturated porous media : He and CH 4 diffusion in Boom Clay. *Applied Clay Science*, 83-84:217–223.

[Jacops et al., 2015] Jacops, E., Wouters, K., Volckaert, G., Moors, H., Maes, N., Bruggeman, C., Swennen, R., and Littke, R. (2015). Measuring the effective diffusion coefficient of dissolved hydrogen in saturated Boom Clay. *Applied Geochemistry*, 61:175–184.

[Jain and Juanes, 2009] Jain, A. K. and Juanes, R. (2009). Preferential mode of gas invasion in sediments: Grain-scale mechanistic model of coupled multiphase fluid flow and sediment mechanics. *Journal of Geophysical Research: Solid Earth*, 114(8):1–19.

[Jaumann, 1911] Jaumann, G. (1911). Geschlossenes system physikalischer und chemischer differentialgesetze. *Sitz.Ber. d.Akad.d.Wiss.,Math.-Nat.Kl. Wien, Abt.2a; Bd.120, Heft 4*, pages 385–530.

[Jia et al., 2008] Jia, Y., Bian, H. B., Duveau, G., Su, K., and Shao, J. F. (2008). Hydromechanical modelling of shaft excavation in Meuse/Haute-Marne laboratory. *Physics and Chemistry of the Earth*, 33:422–435.

[Jiang and Shen, 1998] Jiang, M. and Shen, Z. (1998). Microscopic analysis of shear band in structured clay. *Chinese J. Geot. Eng.*, 20(2):102–108.

[Jirásek, 2000] Jirásek, M. (2000). Comparative study on finite elements with embedded discontinuities. *Computer Methods in Applied Mechanics and Engineering*, 188(1):307–330.

[Jirásek, 2002] Jirásek, M. (2002). Numerical modeling of strong discontinuities. *Revue Française de Génie Civil*, 6(6):1133–1146.

[Jouan et al., 2022] Jouan, G., Kotronis, P., Caillerie, D., and Collin, F. (2022). A second gradient cohesive element for mode I crack propagation. *Finite Elements in Analysis and Design*, 204(30):103732.

[Kachanov, 1958] Kachanov, L. M. (1958). Time of the rupture process under creep conditions. *Otdelenie tekhnicheskich nauk*, 8:26–31.

[Kampan and Tanielian, 2016] Kampan, P. and Tanielian, A. R. (2016). Nuclear power: Irreplaceable before and after Fukushima. *International Journal of Global Energy Issues*, 39(6):394–412.

[Kano et al., 2020] Kano, Y., Sato, T., and Oyama, H. (2020). Numerical study on the formations of gas channels and subsequent bubbles in unconsolidated sandy seabed sediment using a coupled LBM-DEM method. *Journal of Natural Gas Science and Engineering*, 74:103101.

[KASAM, 1998] KASAM (1998). Nuclear Waste. State-of-the-art reports 1998. Technical report, Report from the Swedish National Council for Nuclear Waste, Stockholm, Sweden.

[Katsube, 2000] Katsube, T. (2000). *Shale permeability and pore-structure evolution characteristics*. Geological Survey of Canada,, Ottawa, Canada.

[Kernenergie, 2022] Kernenergie (2022). L'énergie nucléaire dans le monde (Accessed 5 August 2022), https://www.kernenergie.ch/fr/l-energie-nucleaire-dans-le-monde-_content—1–1071.html.

[Ketcham and Carlson, 2001] Ketcham, R. A. and Carlson, W. D. (2001). Acquisition, optimization and interpretation of x-ray computed tomographic imagery: Applications to the geosciences. *Computers and Geosciences*, 27(4):381–400.

[Khoei and Karimi, 2008] Khoei, A. R. and Karimi, K. (2008). An enriched-FEM model for simulation of localization phenomenon in Cosserat continuum theory. *Computational Materials Science*, 44(2):733–749.

[Kickmaier and McKinley, 1997] Kickmaier, W. and McKinley, I. (1997). A review of research carried out in European rock laboratories. *Nuclear Engineering and Design*, 176(1-2):75–81.

[Kleppe et al., 1997] Kleppe, J., Delaplace, P., Lenormand, R., Hamon, G., and Chaput, E. (1997). Representation of capillary pressure hysteresis in reservoir simulation. In *Proceedings - SPE Annual Technical Conference and Exhibition Sigma*, pages 597–604, San Antonio, The United States.

[Klinkenberg, 1941] Klinkenberg, L. J. (1941). The permeability of porous media to liquids and gases. *Drilling and Production Practice 1941*, pages 200–213.

[Kohl et al., 1995] Kohl, T., Evansi, K. F., Hopkirk, R. J., and Rybach, L. (1995). Coupled hydraulic, thermal and mechanical considerations for the simulation of hot dry rock reservoirs. *Geothermics*, 24(3):345–359.

[Kolymbas, 1981] Kolymbas, D. (1981). Bifurcation analysis for sand samples with a non-linear constitutive equation. *Archive of Applied Mechanics*, 50(2):131–140.

[Koriche, 2004] Koriche, A. (2004). Caractérisation du comportement couplé des argilites de Meuse/Haute-Marne aux états saturé et partiellement saturé.

[Kotronis et al., 2008] Kotronis, P., Al Holo, S., Bésuelle, P., and Chambon, R. (2008). Shear softening and localization: Modelling the evolution of the width of the shear zone. *Acta Geotechnica*, 3(2):85–97.

[Kouznetsova et al., 2001] Kouznetsova, V., Brekelmans, W. A., and Baaijens, F. P. (2001). Approach to micro-macro modeling of heterogeneous materials. *Computational Mechanics*, 27(1):37–48.

[Kouznetsova et al., 2002] Kouznetsova, V., Geers, M. G., and Brekelmans, W. A. (2002). Multi-scale constitutive modelling of heterogeneous materials with a gradient-enhanced computational homogenization scheme. *International Journal for Numerical Methods in Engineering*, 54(8):1235–1260.

[Kramer, 2018] Kramer, D. (2018). US nuclear industry fights for survival. *Physics Today*, 71(12):26–27.

[Kröner, 1967] Kröner, E. (1967). Elasticity theory of materials with long range cohesive forces. *International Journal of Solids and Structures*, 3(5):731–742.

[Krooss et al., 1992] Krooss, B. M., Leythaeuser, D., and Schaefer, R. G. (1992). The quantification of diffusive hydrocarbon losses through cap rocks of natural gas reservoirs.pdf. *The American Association of Petroleum Geologists Bulletin*, 76(3):403–406.

[Kunin, 1982] Kunin, I. (1982). Elastic media with microstructure I: One-dimensional models. In Cardona, M., Fuld, e. P., Queisser, H.-J., and Kröner, E., editors, *Springer Series in Solid State Sciences*. Springer-Verlag.

[Kunin, 1983] Kunin, I. (1983). Elastic media with microstructure II: Three-dimensional models. In Cardona, M., Fuld, e. P., Queisser, H.-J., and Kröner, E., editors, *Springer Series in Solid State Sciences*, volume 26. Springer-Verlag.

[Labalette et al., 2011] Labalette, T., Harman, A., and Dupuis, M.-C. (2011). The Cigéo Industrial Geological Repository Project. In *ASME 2011 14th International Conference on Environmental Remediation and Radioactive Waste Management*, pages 1069–1075, Reims, France.

[Lade and Tsai, 1985] Lade, P. and Tsai, J. (1985). Effect of localisation in triaxial tests on clay. In *Proceedings of the Eleventh international Conference on Soil Mechanics and Foundation Engineering*, pages 549–552, San Fransisco, The USA. AA. Balkema.

[Laego, 2005] Laego (2005). Essai de perméabilité – Ouvrage EST 212. Technical report, Agence Nationale pour la gestion des Déchets RAdioactifs., Châtenay-Malabry, France.

[Lagny, 1996] Lagny, C. (1996). *Comportement mécanique des sols fins sous fortes contraintes et fortes pressions négatives*. PhD thesis, Ecole centrale de Paris, Châtenay-Malabry, France.

[Lake and Srinivasan, 2004] Lake, L. W. and Srinivasan, S. (2004). Statistical scale-up of reservoir properties: Concepts and applications. *Journal of Petroleum Science and Engineering*, 44(1-2):27–39.

[Lanata, 2015] Lanata, P. (2015). *Full-field experimental characterization of mechanical behaviour and failure in a porous rock in plane strain compression : homogeneous deformation and strain localization*. Theses, Université Grenoble Alpes.

[Langer, 1999] Langer, M. (1999). Principles of geomechanical safety assessment for radioactive waste disposal in salt structures. *Engineering Geology*, 59(3-4):257–269.

[Larsson et al., 2010] Larsson, F., Runesson, K., and Su, F. (2010). Directional response of a reconstituted fine-grained soil - Part II : Performance of different constitutive models. *International Journal for Numerical and Analytical Methods in Geomechanics*, 34(13):1431–1458.

[Larsson et al., 1999] Larsson, R., Steinmann, P., and Runesson, K. (1999). Finite element embedded localization band for finite strain plasticity based on a regularized strong discontinuity. *Mechanics of Cohesive-Frictional Materials*, 4(2):171–194.

[Lasry and Belytschko, 1988] Lasry, D. and Belytschko, T. (1988). Localization limiters in transient problems. *International Journal of Solids and Structures*, 24(6):581–597.

[Laursen and Simo, 1993] Laursen, T. A. and Simo, J. C. (1993). A continuum-based finite element formulation for the implicit solution of multibody, large deformation-frictional contact problems. *International Journal for Numerical Methods in Engineering*, 36(20):3451–3485.

[Lazari, 2016] Lazari, M. (2016). *Finite Element Regularisation for Post Localized Bifurcation in Variably Saturated Media*. PhD thesis, Universita degli studi di Padova.

[Le and Nguyen, 2014] Le, A. D. and Nguyen, T. S. (2014). Hydromechanical response of a bedded argillaceous rock formation to excavation and water injection. 52:1–17.

[Le, 2007] Le, T. (2007). *Comportement thermo-hydro-mécanique de l'argile de Boom*. PhD thesis, Ecole Nationale des Ponts et Chaussées.

[Lee et al., 2016] Lee, S., Wheeler, M. F., and Wick, T. (2016). Pressure and fluid-driven fracture propagation in porous media using an adaptive finite element phase field model. *Computer Methods in Applied Mechanics and Engineering*, 305:111–132.

[Lekhnitskii, 1963] Lekhnitskii, S. G. (1963). *Theory of Elasticity of an Anisotropic elastic body*. Holden-Day, San Fransisco, The USA.

[Lelieveld et al., 2012] Lelieveld, J., Kunkel, D., and Lawrence, M. G. (2012). Global risk of radioactive fallout after major nuclear reactor accidents. *Atmospheric Chemistry and Physics*, 12(9):4245–4258.

[Lemaitre et al., 2009] Lemaitre, J., Chaboche, J.-L., Benallal, A., and Desmorat, R. (2009). *Mécanique des matériaux solides*. Dunod, Dunod, 3rd edition.

[Lenoir et al., 2007] Lenoir, N., Bornert, M., Desrues, J., Bésuelle, P., and Viggiani, G. (2007). Volumetric digital image correlation applied to x-ray microtomography images from triaxial compression tests on argillaceous rock. *Strain*, 43(3):193–205.

[Lenormand et al., 1988] Lenormand, R., Touboul, E., and Zarcone, C. (1988). Numerical models and experiments on immiscible displacements in porous media. *Journal of Fluid Mechanics*, 189(1988):165–187.

[Lerouge et al., 2011] Lerouge, C., Grangeon, S., Gaucher, E. C., Tournassat, C., Agrinier, P., Guerrot, C., Widory, D., Fléhoc, C., Wille, G., Ramboz, C., Vinsot, A., and Buschaert, S. (2011). Mineralogical and isotopic record of biotic and abiotic diagenesis of the Callovian-Oxfordian clayey formation of Bure (France). *Geochimica et Cosmochimica Acta*, 75(10):2633–2663.

[Levasseur et al., 2010] Levasseur, S., Charlier, R., Frieg, B., and Collin, F. (2010). Hydro-mechanical modelling of the excavation damaged zone around an underground excavation at Mont Terri Rock Laboratory. *International Journal of Rock Mechanics and Mining Sciences*, 47(3):414–425.

[Levasseur et al., 2013] Levasseur, S., Collin, F., Charlier, R., and Kondo, D. (2013). A micro-macro approach of permeability evolution in rocks excavation damaged zones. *Computers and Geotechnics*, 49:245–252.

[Levasseur et al., 2021] Levasseur, S., Collin, F., Daniels, K., Dymitrowska, M., Harrington, J., Jacops, E., Kolditz, O., Marschall, P., Norris, S., Sillen, X., Talandier, J., Truche, L., and Wendling, J. (2021). Initial State of the Art on Gas Transport in Clayey Materials. Deliverable D6.1 of HORIZON 2020 project EURAD, Work Package Gas. EC Grant agreement no: 847593. Technical report, European commission.

[Levasseur et al., 2024] Levasseur, S., Collin, F., Daniels, K., Dymitrowska, M., Harrington, J., Jacops, E., Kolditz, O., Marschall, P., Norris, S., Sillen, X., Talandier, J., Truche, L., and Wendling, J. (2024). State of the Art on Gas Transport in Clayey Materials II. Deliverable D6.2 of HORIZON 2020 project EURAD, Work Package Gas. EC Grant agreement no: 847593. Technical report, European commission.

[Levasseur et al., 2022] Levasseur, S., Sillen, X., Marschall, P., Wendling, J., Olin, M., Grgic, D., and Svoboda, J. (2022). EURADWASTE ' 22 Paper – Host rocks and THMC processes in DGR. *EPJ Nuclear Sci. Technol.*, 21(8).

[Lewis and Schrefler, 1998] Lewis, R. and Schrefler, B. (1998). The Finite Element Method in the Static and Dynamic Deformation and Consolidation of Porous Media. Second Edition. *Communications in Numerical Methods in Engineering*, 34.

[Li et al., 2022] Li, T., Du, D., Wang, X., and Qin, X. (2022). Can Nuclear Power Products Mitigate Greenhouse Gas Emissions? Evidence from Global Trade Network. *International Journal of Environmental Research and Public Health*, 19(13):7808.

[Li et al., 2007] Li, X., Bernier, F., Vietor, T., and Lebon, P. (2007). Thermal impact on the damaged zone around a radioactive waste disposal in clay host rocks. Deliverable 2. Technical report, TIMODAZ, FI6W-CT-036449, European Commision Project,, Luxembourg.

[Liaudat et al., 2023] Liaudat, J., Dieudonné, A.-c., and Vardon, P. J. (2023). Computers and Geotechnics Modelling gas fracturing in saturated clay samples using triple-node zero-thickness interface elements. *Computers and Geotechnics*, 154(October 2022):105128.

[Lima, 2011] Lima, A. (2011). *Thermo-Hydro-Mechanical Behaviour of two deep Belgian formations: Boom and Ypresian Clays*. PhD thesis, Universitat Politècnica de Catalunya (UPC).

[Lima et al., 2012] Lima, A., Romero, E., and Pina, Y. (2012). Water retention properties of two deep Tertiary clay formations within the context of radioactive waste disposal. In *Simpósio Brasileiro de Solos Nao Saturados. "VII Brazilian Symposium on Unsaturated Soil"*, pages 315–321, Pirenópolis, Goiania, Brazil.

[Linard et al., 2011] Linard, Y., Vinsot, A., Vincent, B., Delay, J., Wechner, S., de La Vaissière, R., Scholz, E., Garry, B., Lundy, M., Cruchaudet, M., Dewonck, S., and Vigneron, G. (2011). Water flow in the Oxfordian and Dogger limestone around the Meuse/Haute-Marne Underground Research Laboratory. *Physics and Chemistry of the Earth*, 36(17-18):1450–1468.

[Lisjak et al., 2015] Lisjak, A., Garitte, B., Grasselli, G., Müller, H. R., and Vietor, T. (2015). The excavation of a circular tunnel in a bedded argillaceous rock (Opalinus Clay): Short-term rock mass response and FDEM numerical analysis. *Tunnelling and Underground Space Technology*, 45(February 2019):227–248.

[Liu et al., 2016a] Liu, H., Kang, Q., Leonardi, C. R., Schmieschek, S., Narváez, A., Jones, B. D., Williams, J. R., Valocchi, A. J., and Harting, J. (2016a). Multiphase lattice Boltzmann simulations for porous media applications: A review. *Computational Geosciences*, 20(4):777–805.

[Liu et al., 2009] Liu, H. H., Rutqvist, J., and Berryman, J. G. (2009). On the relationship between stress and elastic strain for porous and fractured rock. *International Journal of Rock Mechanics and Mining Sciences*, 46(2):289–296.

[Liu et al., 2011] Liu, H. H., Rutqvist, J., and Birkholzer, J. T. (2011). Constitutive relationships for elastic deformation of clay rock: Data analysis. *Rock Mechanics and Rock Engineering*, 44(4):463–468.

[Liu et al., 1999] Liu, J., Elsworth, D., and Brady, B. H. (1999). Linking stress-dependent effective porosity and hydraulic conductivity fields to RMR. *International Journal of Rock Mechanics and Mining Sciences*, 36(5):581–596.

[Liu, 2015] Liu, P. (2015). Extended finite element method for strong discontinuity analysis of strain localization of non-associative plasticity materials. *International Journal of Solids and Structures*, 72:174–189.

[Liu et al., 2016b] Liu, Z. B., Shao, J. F., Liu, T. G., Xie, S. Y., and Conil, N. (2016b). Gas permeability evolution mechanism during creep of a low permeable claystone. *Applied Clay Science*, 129:47–53.

[Loret and Preost, 1991] Loret, B. and Preost, J. (1991). Dynamic strain localization in fluid-saturated porous media. *Journal of Engineering Mechanics*, 117(4):907–922.

[Lyapunov, 1892] Lyapunov, A. (1892). *The General Problem of the Stability of Motion*. Taylor & Francis (1992), translated edition.

[Mahjoub et al., 2018] Mahjoub, M., Rouabhi, A., Tijani, M., Granet, S., M'Jahad, S., and Talandier, J. (2018). Numerical Study of Callovo-Oxfordian Argillite Expansion due to Gas Injection. *International Journal of Geomechanics*, 18(1).

[Malinsky, 2009] Malinsky, L. (2009). *Etude expérimentale et modélisation du comportement hydro-mécanique et de transfert de matériaux argileux saturés et non-saturés*. PhD thesis, Ecole Polytechnique, Paris, France.

[Malvern, 1969] Malvern, L. E. (1969). *Introduction to the Mechanics of a Continuous Medium*. Prentice-Hall, Inc., Englewood Cliffs, New-Jersey, The USA.

[Manai, 1997] Manai, T. (1997). EVEGAS: Eureopean validation exercise of gas migration models through geological media (Phase 3). Technical Report EUR 17557EN, European Commission, Luxembourg.

[Mandel, 1966] Mandel, J. (1966). Conditions de Stabilite et Postulat de Drucker. In Kravtchenko, J. and Sirieys, P., editors, *Rheology and Soil Mechanics / Rhéologie et Mécanique des Sols*, pages 58–68. International Union of Theoretical and Applied Mechanics. Springer, Berlin, Germany.

[Marinelli, 2014] Marinelli, F. (2014). *Comportement couplé des géo-matériaux : deux approches de modélisation numérique*. PhD thesis, Université de Grenoble, Grenoble, France.

[Marinelli et al., 2015] Marinelli, F., Sieffert, Y., and Chambon, R. (2015). Hydromechanical modeling of an initial boundary value problem: Studies of non-uniqueness with a second gradient continuum. *International Journal of Solids and Structures*, 54:238–257.

[Marinelli et al., 2016] Marinelli, F., Van Den Eijnden, A. P., Sieffert, Y., Chambon, R., and Collin, F. (2016). Modeling of granular solids with computational homogenization: Comparison with Biot's theory. *Finite Elements in Analysis and Design*, 119:45–62.

[Marschall et al., 2005] Marschall, P., Horseman, S., and Gimmi, T. (2005). Characterisation of Gas Transport Properties of the Opalinus Clay, a Potential Host Rock Formation for Radioactive Waste Disposal. *Oil & Gas Science and Technology – Rev. IFP*, 60(1):121–139.

[Martinez et al., 2013] Martinez, M. J., Newell, P., Bishop, J. E., and Turner, D. Z. (2013). Coupled multiphase flow and geomechanics model for analysis of joint reactivation during CO2 sequestration operations. *International Journal of Greenhouse Gas Control*, 17:148–160.

[Massart, 2003] Massart, T. (2003). *Multi-scale modeling of damage in masonry structures*. PhD thesis, Technische Universiteit Eindhoven.

[Massart and Selvadurai, 2014] Massart, T. J. and Selvadurai, A. P. (2014). Computational modelling of crack-induced permeability evolution in granite with dilatant cracks. *International Journal of Rock Mechanics and Mining Sciences*, 70:593–604.

[Mathew, 2022] Mathew, M. D. (2022). Nuclear energy: A pathway towards mitigation of global warming. *Progress in Nuclear Energy*, 143(August 2021):104080.

[Matsushima et al., 2000] Matsushima, T., Chambon, R., and Caillerie, D. (2000). Second gradient models as a particular case of microstructured models: A large strain finite elements analysis. *Comptes Rendus de l'Academie de Sciences - Serie IIb: Mecanique, Physique, Chimie, Astronomie*, 328(2):179–186.

[Matsushima et al., 2002] Matsushima, T., Chambon, R., and Caillerie, D. (2002). Large strain finite element analysis of a local second gradient model: application to localisation. *International Journal for Numerical Methods in Engineering*, 54(4):499–521.

[Matsushima et al., 2003] Matsushima, T., Saomoto, H., Tsubokawa, Y., and Yamada, Y. (2003). Grain rotation versus continuum rotation during shear deformation of granular assembly. *Soils and foundations*, 43(4):95–106.

[McKinley et al., 2007] McKinley, I. G., Russell Alexander, W., and Blaser, P. C. (2007). Development of geological disposal concepts. In Alexander, L. and McKinley, I. G., editors, *Deep Geological Disposal of Radioactive Wastes*, volume 9, chapter 6, pages 41–76. Elsvier, Amsterdam, The Nederland.

[Meadows et al., 1972] Meadows, D. H., Meadows, D. L., Randers, J., and Behrens, W. W. (1972). *Limits to growth. A Report for the Club of Rome's Project on the Predicament of Mankind*. Universe Books, New-York, The United States.

[Mégnien et al., 1980] Mégnien, C., Mégnien, F., and Debrand-Passard, S. (1980). *Synthèse géologique du Bassin de Paris*. Memoires du B.R.G.M., Orléans.

[Méheust et al., 2002] Méheust, Y., Løvoll, G., Måløy, K. J., and Schmittbuhl, J. (2002). Interface scaling in a two-dimensional porous medium under combined viscous, gravity, and capillary effects. *Physical Review E - Statistical Physics, Plasmas, Fluids, and Related Interdisciplinary Topics*, 66(5):12.

[Mertens et al., 2004] Mertens, J., Bastiaens, W., and Dehandschutter, B. (2004). Characterisation of induced discontinuities in the Boom Clay around the underground excavations (URF, Mol, Belgium). *Applied Clay Science*, 26:413–428.

[Mertens et al., 2003] Mertens, J., Vandenberghe, N., Wouters, L., and Sintubin, M. (2003). The origin and development of joints in the Boom Clay Formation (Rupelian) in Belgium. *Geological Society Special Publication*, 216:309–321.

[Metzger, 1977] Metzger, N. (1977). *Energy: The continuing crisis*. Crowell Company, New-York, The United States.

[Miller et al., 1994] Miller, W., Alexander, R., Chapman, N., McKinley, I. G., and Smellie, J. (1994). *Natural Analogue Studies in the Geological Disposal of Radioactive Wastes*. Number Studies in Environmental Science 57. Elsevier, Amsterdam, The Nederland.

[Mindlin, 1964] Mindlin, R. D. (1964). Micro-structure in linear elasticity. *Archive for Rational Mechanics and Analysis*, 16(1):51–78.

[Mindlin, 1965] Mindlin, R. D. (1965). Second gradient of strain and surface-tension in linear elasticity. *International Journal of Solids and Structures*, 1(4):417–438.

[Mindlin and Eshel, 1968] Mindlin, R. D. and Eshel, N. N. (1968). On first strain-gradient theories in linear elasticity. *International Journal of Solids and Structures*, 4(1):109–124.

[M'Jahad, 2012] M'Jahad, S. (2012). *Impact de la fissuration sur les propriétés de rétention d'eau et de transport de gaz des géomatériaux : Application au stockage géologique des déchets radioactifs.* PhD thesis, Ecole Centrale de Lille.

[M'Jahad et al., 2015] M'Jahad, S., Davy, C. A., Bourbon, X., and Skoczylas, F. (2015). Water Retention and Gas Migration of Two High-Performance Concretes after Damage. *Journal of Materials in Civil Engineering*, 27(2):1–11.

[Moës et al., 1999] Moës, N., Dolbow, J., and Belytschko, T. (1999). A finite element method for crack growth without remeshing. *International Journal for Numerical Methods in Engineering*, 46(1):131–150.

[Mohajerani et al., 2011] Mohajerani, M., Delage, P., Monfared, M., Tang, A. M., Sulem, J., and Gatmiri, B. (2011). Oedometric compression and swelling behaviour of the Callovo-Oxfordian argillite. *International Journal of Rock Mechanics and Mining Sciences*, 48(4):606–615.

[Mokni and Desrues, 1999] Mokni, M. and Desrues, J. (1999). Strain localization measurements in undrained plane-strain biaxial tests on Hostun RF sand. *Mechanics of Cohesive-frictional Materials*, 4(4):419–441.

[Moulinec and Suquet, 1998] Moulinec, H. and Suquet, P. (1998). A numerical method for computing the overall response of nonlinear composites with complex microstructure. *Computer Methods in Applied Mechanics and Engineering*, 157(1-2):69–94.

[Mualem, 1976] Mualem, J. (1976). A new model for predicting the hydraulic conductivity of unsaturated porous media. *Water Resources Research*, 12(3):513–522.

[Mualem, 1978] Mualem, Y. (1978). Hydraulic conductivity of unsaturated porous media: Generalized macroscopic approach. *Water Resources Research*, 14(2):325–334.

[Mühlhaus, 1991] Mühlhaus, H.-B. (1991). A variational principle for gradient plasticity. *International Journal of Solids and Structures*, 28(7):845–857.

[Muhlhaus and Vardoulakis, 1987] Muhlhaus, H. B. and Vardoulakis, I. (1987). The thickness of shear bands in granular materials. *Geotechnique*, 37(3):271–283.

[NEA, 1999] NEA (1999). Geological disposal of radioactive waste : review of developments in the last decade. Technical report, Nuclear Energy Agency of the Organisation for Economic Co-operation and Development, Paris, France.

[NEA, 2001a] NEA (2001a). Going underground for testing, characterisation and demonstration. Technical report, Nuclear Energy Agency. Radioactive waste management committee, Paris, France.

[NEA, 2001b] NEA (2001b). Radioactive Waste Management Gas Generation and Migration in Radioactive Waste Disposal: Safety-relevant Issues. Technical Report Workshop Proceedings Reims, France, 26-28 June, Nuclear Energy Agency of the Organisation for Economic Co-operation and Development, Reims, France.

[NEA, 2001c] NEA (2001c). The Role of Underground Laboratories in Nuclear Waste Disposal Programmes. Technical report, Nuclear Energy Agency of the Organisation for Economic Co-operation and Development, Paris.

[Neaupane et al., 1999] Neaupane, K. M., Yamabe, T., and Yoshinaka, R. (1999). Simulation of a fully coupled thermo-hydro-mechanical system in freezing and thawing rock. *International Journal of Rock Mechanics and Mining Sciences*, 36(5):563–580.

[Needleman, 1988] Needleman, A. (1988). Material rate dependence and mesh sensitivity in localization problems. *Computer Methods in Applied Mechanics and Engineering*, 67(1):69–85.

[Neerdael and Boyazis, 1997] Neerdael, B. and Boyazis, J. P. (1997). The Belgium underground research facility: Status on the demonstration issues for radioactive waste disposal in clay. *Nuclear Engineering and Design*, 176(1-2):89–96.

[Nelson, 2009] Nelson, P. H. (2009). Pore-throat sizes in sandstones, tight sandstones, and shales. *AAPG Bulletin*, 93(3):329–340.

[Neuzil, 1994] Neuzil, C. E. (1994). by Bethke permeability , measurements in Figure. *Water Resources*, 30(2):145–150.

[Neuzil, 2019] Neuzil, C. E. (2019). Permeability of clays and shales. *Annual Review of Earth and Planetary Sciences*, 47(May 2019):247–273.

[Newton, 1687] Newton, I. (1687). *Philosophiae naturalis principia mathematica*. London.

[Nguyen et al., 2014] Nguyen, T. K., Combe, G., Caillerie, D., and Desrues, J. (2014). FEM × DEM modelling of cohesive granular materials: Numerical homogenisation and multi-scale simulations. *Acta Geophysica*, 62(5):1109–1126.

[Nguyen and Le, 2015] Nguyen, T. S. and Le, A. D. (2015). Simultaneous gas and water flow in a damage-susceptible bedded argillaceous rock. *Canadian Geotechnical Journal*, 52(1):18–32.

[Nguyen et al., 2012] Nguyen, V. D., Béchet, E., Geuzaine, C., and Noels, L. (2012). Imposing periodic boundary condition on arbitrary meshes by polynomial interpolation. *Computational Materials Science*, 55:390–406.

[Nguyen et al., 2017] Nguyen, V. P., Lian, H., Rabczuk, T., and Bordas, S. (2017). Modelling hydraulic fractures in porous media using flow cohesive interface elements. *Engineering Geology*, 225:68–82.

[Nitka et al., 2011] Nitka, M., Combe, G., Dascalu, C., and Desrues, J. (2011). Two-scale modeling of granular materials: A DEM-FEM approach. *Granular Matter*, 13(3):277–281.

[Norris, 2017] Norris, S. (2017). Radioactive waste confinement: Clays in natural and engineered barriers - introduction. *Geological Society Special Publication*, 443(1):1–8.

[Nova et al., 2003] Nova, R., Castellanza, R., and Tamagnini, C. (2003). A constitutive model for bonded geomaterials subject to mechanical and/or chemical degradation. *International Journal for Numerical and Analytical Methods in Geomechanics*, 27(9):705–732.

[Nuth and Laloui, 2008] Nuth, M. and Laloui, L. (2008). Advances in modelling hysteretic water retention curve in deformable soils. *Computers and Geotechnics*, 35(6):835–844.

[Oda et al., 2004] Oda, M., Takemura, T., and Takahashi, M. (2004). Microstructure in shear band observed by microfocus X-ray computed tomography. *Géotechnique*, 54(8):539–542.

[Ojovan and Steinmetz, 2022] Ojovan, M. I. and Steinmetz, H. J. (2022). Approaches to Disposal of Nuclear Waste. *Energies*, 15(20).

[Olivella and Alonso, 2008] Olivella, S. and Alonso, E. E. (2008). Gas flow through clay barriers. *Géotechnique*, 58(3):157–176.

[Olivella et al., 1996] Olivella, S., Gens, A., Carrera, J., and Alonso, E. E. (1996). Numerical formulation for a simulator (CODE_BRIGHT) for the coupled analysis of saline media. *Engineering Computations (Swansea, Wales)*, 13(7):87–112.

[Olsson, 1974] Olsson, W. A. (1974). Microfracturing and faulting in a limestone. *Tectonophysics*, 24(3):277–285.

[Omoto, 2005] Omoto, A. (2005). Nuclear power for sustainable development and relevant IAEA activities for the future. *Progress in Nuclear Energy*, 47(1-4):16–26.

[ONDRAF, 1989] ONDRAF (1989). SAFIR 1, Safety Assessment and Feasibility Interim Report. Technical report, NIRAS/ ONDRAF, Belgian Agency for Radioactive Waste and Enriched Fissile Materials, Brussels, Belgium.

[ONDRAF, 2001] ONDRAF (2001). Safir-2, Safety Assessment and Feasibility Interim Report 2. Technical report, NIRAS/ ONDRAF, Belgian Agency for Radioactive Waste and Enriched Fissile Materials, Brussels, Belgium.

[ONDRAF, 2012] ONDRAF (2012). ONDRAF/NIRAS Research, Development and Demonstration (RD&D) Plan for the geological disposal of high-level and/or long-lived radioactive waste including irradiated fuel if considered as waste. State-of-the-art report as of December 2012. Technical Report December 2012, NIRAS/ ONDRAF, Belgian Agency for Radioactive Waste and Enriched Fissile Materials.

[ONDRAF, 2018] ONDRAF (2018). *Rapport d'inventaire des passifs nucléaires de l'ONDRAF à sa tutelle (période 2013 – 2017)*, volume 4. ONDRAF, Brussels, Belgium.

[ONDRAF, 2020] ONDRAF (2020). Design and Construction of the Geological Disposal Facility for Category B and Category C Wastes (V3). Technical Report NIROND-TR 2017-12 E V3, NIRAS/ ONDRAF, Belgian Agency for Radioactive Waste and Enriched Fissile Materials, Brussels, Belgium.

[ONDRAF, 2021] ONDRAF (2021). *Rapport annuel 2021. Pour une gestion sûre des déchets radioactifs en Belgique*. ONDRAF, Brussels, Belgium.

[ORG, 2007] ORG (2007). Secure Energy ? Civil Nuclear Power, Security and Global Warming. Technical report, Oxford Research Group, London, The United Kingdom.

[Orowan, 1949] Orowan, E. (1949). Fracture and strength of solids. *Reports on Progress in Physics*, 12(1):185–232.

[Ortiz et al., 1996] Ortiz, L., Impey, M., and Einchcomb, S. (1996). Characterization of Gas Flow in Boom Clay, a Low Permeability Plastic Rock. In *Proceedings of the Fluid Flow through Faults and Fractures in Argillaceous Formations – Joint NEA/EC Workshop*, pages 287–298, Berne, Switzerland.

[Ortiz et al., 1997] Ortiz, L., Volckaert, G., De Cannière, P., Put, M., Sen, M., Horseman, S.T., Harrington, J., Impey, M., and Einchcomb, S. (1997). MEGAS: modelling and experiments on GAS migration in repository host rocks. Final report phase 2. Technical report, Eur. Comm., [Rep.] EUR 17453 EN.

[Ortiz et al., 2002] Ortiz, L., Volckaert, G., and Mallants, D. (2002). Gas generation and migration in Boom Clay, a potential host rock formation for nuclear waste storage. *Engineering Geology*, 64(2-3):287–296.

[Ortiz and Leroy, 1989] Ortiz, M. and Leroy, Y. (1989). Finite Element Analysis of Strain Localization. *International Journal for Numerical and Analytical Methods in Geomechanics*, 13(June 1988):53–74.

[Owusu et al., 2022] Owusu, J. P., Karalis, K., Prasianakis, N. I., and Churakov, S. V. (2022). Mobility of Dissolved Gases in Smectites under Saturated Conditions: Effects of Pore Size, Gas Types, Temperature, and Surface Interaction. *Journal of Physical Chemistry C*, 126(40):17441–17455.

[Ozdemir, 2009] Ozdemir, I. (2009). *Multi-scale Modelling of Thermal Shock Damage in Refractory Materials Izzet*, volume 1.

[Ozdemir et al., 2008] Ozdemir, I., Brekelmans, W. A., and Geers, M. G. (2008). Computational homogenization for heat conduction in heterogeneous solids. *International Journal for Numerical Methods in Engineering*, 73:185–204.

[Panday and Corapcioglu, 1989] Panday, S. and Corapcioglu, M. Y. (1989). Reservoir transport equations by compositional approach. *Transport in Porous Media*, 4(4):369–393.

[Panet and Guenot, 1982] Panet, M. and Guenot, A. (1982). Analysis of convergence behind the face of a tunnel. *proceedings of the 3rd international symposium: Tunnelling 82*.

[Papamichos, 2010] Papamichos, E. (2010). Continua with microstructure: Cosserat theory. *European Journal of Environmental and Civil Engineering*, 14(8-9):1011–1029.

[Pardoen, 2015] Pardoen, B. (2015). *Hydro-mechanical analysis of the fracturing induced by the excavation of nuclear waste repository galleries using shear banding*. PhD thesis, University of Liège.

[Pardoen and Collin, 2017] Pardoen, B. and Collin, F. (2017). Modelling the influence of strain localisation and viscosity on the behaviour of underground drifts drilled in claystone. *Computers and Geotechnics*, 85:351–367.

[Pardoen et al., 2014] Pardoen, B., Levasseur, S., and Collin, F. (2014). Excavation damaged zone modelling including hydraulic permeability evolution in unsaturated argilaceous rock. *Unsaturated Soils: Research and Applications - Proceedings of the 6th International Conference on Unsaturated Soils, UNSAT 2014*, 2(Desrues):1387–1393.

[Pardoen et al., 2015a] Pardoen, B., Levasseur, S., and Collin, F. (2015a). Using Local Second Gradient Model and Shear Strain Localisation to Model the Excavation Damaged Zone in Unsaturated Claystone. *Rock Mechanics and Rock Engineering*, 48(2):691–714.

[Pardoen et al., 2018] Pardoen, B., Pont, S. D., Desrues, J., Bésuelle, P., Prêt, D., and Cosenza, P. (2018). Heterogeneity and Variability of Clay Rock Microstructure in a Hydro-Mechanical Double Scale FEM × FEM Analysis. In Giovine, P., Mariano, P., and Mortara, G., editors, *Micro to MACRO Mathematical Modelling in Soil Mechanics. Trends in Mathematics*, number May, pages 247–256, University Mediterranea of Reggio Calabria - DICEAM. Springer.

[Pardoen et al., 2015b] Pardoen, B., Seyedi, D. M., and Collin, F. (2015b). Shear banding modelling in cross-anisotropic rocks. *International Journal of Solids and Structures*, 72:63–87.

[Pardoen et al., 2016] Pardoen, B., Talandier, J., and Collin, F. (2016). Permeability evolution and water transfer in the excavation damaged zone of a ventilated gallery. *International Journal of Rock Mechanics and Mining Sciences*, 85:192–208.

[Peerlings et al., 1996] Peerlings, R. H., De Borst, R., Brekelmans, W. A., and De Vree, J. H. (1996). Gradient enhanced damage for quasi-brittle materials. *International Journal for Numerical Methods in Engineering*, 39(19):3391–3403.

[Peerlings et al., 2001] Peerlings, R. H., Geers, M. G., De Borst, R., and Brekelmans, W. A. (2001). A critical comparison of nonlocal and gradient-enhanced softening continua. *International Journal of Solids and Structures*, 38(44-45):7723–7746.

[Pellet et al., 2009] Pellet, F., Roosefid, M., and Deleruyelle, F. (2009). On the 3D numerical modelling of the time-dependent development of the damage zone around underground galleries during and after excavation. *Tunnelling and Underground Space Technology*, 24(6):665–674.

[Peng and Johnson, 1972] Peng, S. and Johnson, A. M. (1972). Crack growth and faulting in cylindrical specimens of chelmsford granite. *International Journal of Rock Mechanics and Mining Sciences and*, 9(1):37–86.

[Pereira and Arson, 2013] Pereira, J. M. and Arson, C. (2013). Retention and permeability properties of damaged porous rocks. *Computers and Geotechnics*, 48:272–282.

[Perzyna, 1966] Perzyna, P. (1966). Fundamental Problems in Viscoplasticity. volume 9 of *Advances in Applied Mechanics*, pages 243–377. Elsevier.

[Peters and Ranson, 1982] Peters, W. and Ranson, W. (1982). Digital imaging techniques in experimental stress analysis. *Optical Engineering*, 21(3):427–431.

[Pham, 2010] Pham, Q. T. (2010). *Effet de la désaturation et de la resaturation sur l'argilite dans les ouvrages souterrains*. PhD thesis, Ecole Polytechnique, Paris, France.

[Pham et al., 2007] Pham, Q. T., Vales, F., Malinsky, L., Nguyen Minh, D., and Gharbi, H. (2007). Effects of desaturation-resaturation on mudstone. *Physics and Chemistry of the Earth*, 32(8-14):646–655.

[Philip and de Vries, 1957] Philip, J. R. and de Vries, D. A. (1957). Moisture movement in porous materials under temperature gradients. *Eos, Trans Amer Geophys Union*, 38(2):222–232.

[Phoon and Kulhawy, 1999] Phoon, K. K. and Kulhawy, F. H. (1999). Characterization of geotechnical variability. *Canadian Geotechnical Journal*, 36(4):612–624.

[Pietruszczak and Mróz, 1981] Pietruszczak, S. and Mróz, Z. (1981). Finite element analysis of deformation of strain-softening materials. *International Journal for Numerical Methods in Engineering*, 17(3):327–334.

[Piguet, 2001] Piguet, J.-P. (2001). French Underground Research Laboratory: Construction and Experimental Programme. In *ASME 2001 8th International Conference on Radioactive Waste Management and Environmental Remediation*, pages 269–274, Bruges, Belgium.

[Pijaudier-Cabot and Bažant, 1987] Pijaudier-Cabot, G. and Bažant, Z. P. (1987). Nonlocal damage theory. *Journal of Engineering Mechanics*, 113(10):1512–1533.

[Plassart et al., 2013] Plassart, R., Fernandes, R., Giraud, A., Hoxha, D., and Laigle, F. (2013). Hydromechanical modelling of an excavation in an underground research laboratory with an elastoviscoplastic behaviour law and regularization by second gradient of dilation. *International Journal of Rock Mechanics and Mining Sciences*, 58:23–33.

[Plúa, 2018] Plúa, C. (2018). *Development of a Numerical Strategy for 2nd Gradient Continuum Porous Media based on Iso-Geometric Finite Element . Application to Partially Saturated Media*. PhD thesis, Université Grenoble Alpes, Grenoble, France.

[Pollock, 1986] Pollock, D. (1986). Simulation of fluid flow and energy transport processes associated with high-level radioactive waste disposal in unsaturated alluvium. *Water Resources Research*, 22(5):765–775.

[Ponthot, 2002] Ponthot, J. P. (2002). Unified stress update algorithms for the numerical simulation of large deformation elasto-plastic and elasto-viscoplastic processes. *International Journal of Plasticity*, 18(1):91–126.

[Prime et al., 2016] Prime, N., Levasseur, S., Miny, L., Charlier, R., Léonard, A., and Collin, F. (2016). Drying-induced shrinkage of boom clay: An experimental investigation. *Canadian Geotechnical Journal*, 53(3):396–409.

[Prăvălie and Bandoc, 2018] Prăvălie, R. and Bandoc, G. (2018). Nuclear energy: Between global electricity demand, worldwide decarbonisation imperativeness, and planetary environmental implications. *Journal of Environmental Management*, 209:81–92.

[Raniecki and Bruhns, 1981] Raniecki, B. and Bruhns, O. T. (1981). Bounds to bifurcation stresses in solids with non-associated plastic flow law at finite strain. *Journal of the Mechanics and Physics of Solids*, 29(2):153–172.

[Rattez et al., 2018] Rattez, H., Stefanou, I., Sulem, J., Veveakis, M., and Poulet, T. (2018). Numerical Analysis of Strain Localization in Rocks with Thermo-hydro-mechanical Couplings Using Cosserat Continuum. *Rock Mechanics and Rock Engineering*, 51(10):3295–3311.

[Rebour et al., 1997] Rebour, V., Billiotte, J., Deveughele, M., Jambon, A., and Guen, C. L. (1997). Molecular diffusion in water-saturated rocks: A new experimental method. *Journal of Contaminant Hydrology*, 28(1-2):71–93.

[Regueiro and Borja, 2001] Regueiro, R. A. and Borja, R. I. (2001). Plane strain finite element analysis of pressure sensitive plasticity with strong discontinuity. *International Journal of Solids and Structures*, 38(21):3647–3672.

[Regueiro and Foster, 2011] Regueiro, R. A. and Foster, C. D. (2011). Bifurcation analysis for a rate-sensitive, non-associative, three-invariant, isotropic/kinematic hardening cap plasticity model for geomaterials: Part I. Small strain. *International Journal for Numerical and Analytical Methods in Geomechanics*, 35(2):201–225.

[Réthoré et al., 2008] Réthoré, J., De Borst, R., and Abellan, M. A. (2008). A two-scale model for fluid flow in an unsaturated porous medium with cohesive cracks. *Computational Mechanics*, 42(2):227–238.

[Reynolds et al., 1903] Reynolds, O., Brightmore, A., and Moorby, W. (1903). Papers on Mechanical and Physical Subjects: The sub-mechanics of the universe. In *Proceedings of the Royal Society of London*, volume 3, pages 425–433. The University Press.

[Rhattas, 1994] Rhattas, A. (1994). *Transfert de masse dans les matériaux argileux à faible porosité: Analyse théorique et résultats expérimentaux.pdf*. PhD thesis, Université d'Orléans.

[Rice, 1976] Rice, J. (1976). Localization of Plastic Deformation. In Koiter, W., editor, *Theoretical and Applied Mechanics*, volume 1, pages 207–220. North-Holland Publishing Company.

[Rice and Rudnicki, 1980] Rice, J. R. and Rudnicki, J. W. (1980). A note on some features of the theory of localization of deformation. *International Journal of Solids and Structures*, 16(7):597–605.

[Rimstidt and Barnes, 1980] Rimstidt, J. D. and Barnes, H. L. (1980). The kinetics of silica-water reactions. *Geochimica et Cosmochimica Acta*, 44(11):1683–1699.

[Robinet, 2008] Robinet, J. C. (2008). Mineralogie, porosité et diffusion des solutes dans l'argilite du Callovo- Oxfordien de Bure (Meuse/Haute-Marne, France) de l'échelle centimétrique à micrométrique.

[Robinet et al., 2012] Robinet, J. C., Sardini, P., Coelho, D., Parneix, J. C., Prt, D., Sammartino, S., Boller, E., and Altmann, S. (2012). Effects of mineral distribution at mesoscopic scale on solute diffusion in a clay-rich rock: Example of the Callovo-Oxfordian mudstone (Bure, France). *Water Resources Research*, 48(5):1–17.

[Robinet et al., 2015] Robinet, J. C., Sardini, P., Siitari-Kauppi, M., Prêt, D., and Yven, B. (2015). Upscaling the porosity of the Callovo-Oxfordian mudstone from the pore scale to the formation scale; insights from the 3H-PMMA autoradiography technique and SEM BSE imaging. *Sedimentary Geology*, 321:1–10.

[Rodwell and Nash, 1992] Rodwell, W. and Nash, P. (1992). Mechanisms and Modelling of Gas Migration from Deep Radioactive Waste Repositories. Nirex Safety Study Report NSS/R250. Technical report.

[Rodwell, 2000] Rodwell, W. R. (2000). Research into gas generation and migration in radioactive waste repository systems (PROGRESS Project). (Nuclear science and technology):337.

[Rodwell et al., 1999] Rodwell, W. R., Harris, A. W., Horseman, S. T., Lalieux, P., Müller, W., Ortiz Amaya, L., and Pruess, K. (1999). Gas migration and two-phase flow through engineered and geological barriers for a deep repository for radioctive waste. A Joint EC/NEA Status Report. Technical report, European Commission, Brussels, Belgium.

[Rodwell et al., 2003] Rodwell, W. R., Norris, S., Cool, W., Cuñado, M., Johnson, L., Mäntynen, M., Müller, W., Sellin, P., Snellman, M., Talandier, J., Vieno, T., and Vines, S. (2003). GASNET - A thematic network on gas issues in safety assessment of deep repositories for radioactive waste. Technical Report Final Report on the Treatment in Safety Assessments of Issues Arising from Gas Generation, European Commission, Luxembourg.

[Roger et al., 1998] Roger, V., Desrues, J., and Viggiani, C. (1998). Experiments on strain localisation in dense sand underisochoric conditions. In Adachi, T., Oka, F., and Yashima, A., editors, *Localization and Bifurcation Theory for Soils and Rocks*, pages 239–248. 4th Workshop on Localization and Bifurcation Theory for soils and Rocks, Gifu (Japan) 28 septembre- 2 octobre 1997. Balkema, Rotterdam, The Nederland.

[Rogner, 2013] Rogner, H. H. (2013). World outlook for nuclear power. *Energy Strategy Reviews*, 1(4):291–295.

[Romero, 1999] Romero, E. (1999). *Charaterisation and Thermo-Hydro-Mechanical Behaviour of Unsaturated Boom Clay - An Experimental Study*. PhD thesis, Universitat Politècnica de Catalunya (UPC), Barcelona, Spain.

[Roth and Jaramillo, 2017] Roth, M. B. and Jaramillo, P. (2017). Going nuclear for climate mitigation: An analysis of the cost effectiveness of preserving existing U.S. nuclear power plants as a carbon avoidance strategy. *Energy*, 131:67–77.

[Rousset, 1988] Rousset, G. (1988). *Comportement mecanique des argiles profondes : application au stockage de dechets radioactifs*. PhD thesis, Ecole Nationale des Ponts et Chaussées.

[Rudnicki and Rice, 1975] Rudnicki, J. W. and Rice, J. R. (1975). Conditions for the localization of deformation in pressure-sensitive dilatant materials. *Journal of the Mechanics and Physics of Solids*, 23(6):371–394.

[Rutqvist et al., 2009] Rutqvist, J., Bäckström, A., Chijimatsu, M., Feng, X., Pan, P. Z., Hudson, J., Jing, L., Kobayashi, A., Koyama, T., Lee, H., Huang, X. H., Rinne, M., and Shen, B. (2009). A multiple-code simulation study of the long-term EDZ evolution of geological nuclear waste repositories. *Environmental Geology*, 57(6):1313–1324.

[Rutqvist et al., 2020] Rutqvist, J., Guglielmi, Y., Xu, H., Tian, Y., Zarzycki, P., Deng, H., Li, P., Hu, M., Nico, P., Borglin, S., Fox, P., Sasaki, T., and Birkholzer, J. (2020). Investigation of Coupled Processes in Argillite Rock: FY20 Progress. Technical report, Lawrence Berkeley National Laboratory, Berkeley, California (The United States).

[Rutqvist et al., 2002] Rutqvist, J., Wu, Y., Tsang, C., and Bodvarsson, G. (2002). A modeling approach for analysis of coupled multiphase fluid flow , heat transfer , and deformation in fractured porous rock. 39:429–442.

[Salager et al., 2011] Salager, S., Rizzi, M., and Laloui, L. (2011). An innovative device for determining the soil water retention curve under high suction at different temperatures. *Acta Geotechnica*, 6(3):135–142.

[Salah and Wang, 2014] Salah, S. and Wang, L. (2014). Speciation and solubility calculations for waste relevant radionuclides in Boom Clay. External Report of the Belgian Nuclear Research Centre. Technical report, SCK•CEN, Mol, Belgium.

[Salehnia, 2015] Salehnia, F. (2015). *From some obscurity to clarity in Boom Clay behavior : Analysis of its coupled hydro-mechanical response in the presence of strain localization*. PhD thesis, University of Liège.

[Salehnia et al., 2013] Salehnia, F., Charlier, R., and Levasseur, S. (2013). Modeling of strain localization around the radioactive waste disposal galleries. In Manassero, M., Dominijanni, A., Foti, S., and Musso, G., editors, *Coupled Phenomena in Environmental Geotechnics: From theoretical and experimental research to practical applications.*, pages 443–450. Taylor & Francis Group, London, The United Kingdom.

[Salimzadeh and Khalili, 2015] Salimzadeh, S. and Khalili, N. (2015). A three-phase XFEM model for hydraulic fracturing with cohesive crack propagation. *Computers and Geotechnics*, 69:82–92.

[Samaniego and Belytschko, 2005] Samaniego, E. and Belytschko, T. (2005). Continuum-discontinuum modelling of shear bands. *International Journal for Numerical Methods in Engineering*, 62(13):1857–1872.

[Sammartino et al., 2003] Sammartino, S., Bouchet, A., Prêt, D., Parneix, J. C., and Tevissen, E. (2003). Spatial distribution of porosity and minerals in clay rocks from the Callovo-Oxfordian formation (Meuse/Haute-Marne, Eastern France) - Implications on ionic species diffusion and rock sorption capability. *Applied Clay Science*, 23(1-4):157–166.

[Sanchez-Palencia and Zaoui, 1987] Sanchez-Palencia, E. and Zaoui, A. (1987). Homogenization Techniques for Composite Media. In *CISM International Center for Mechanical Sciences*, Udine, Italy.

[Sanders and Sanders, 2016] Sanders, M. C. and Sanders, C. E. (2016). A world's dilemma 'upon which the sun never sets' - The nuclear waste management strategy (part I): Western European Nation States and the United States of America. *Progress in Nuclear Energy*, 90(2016):69–97.

[Santillán et al., 2017] Santillán, D., Mosquera, J. C., and Cueto-Felgueroso, L. (2017). Fluid-driven fracture propagation in heterogeneous media: Probability distributions of fracture trajectories. *Physical Review E*, 96(5):1–10.

[Savage, 1996] Savage, D. (1996). *The Scientific and Regulatory Basis for the Geological Disposal of Radioactive Waste*. Wiley, New-York, The United States.

[Schaffer, 2007] Schaffer, M. B. (2007). Nuclear power for clean, safe and secure energy independence. *Foresight*, 9(6):47–60.

[Schlömer and Krooss, 1997] Schlömer, S. and Krooss, B. M. (1997). Experimental characterisation of the hydrocarbon sealing efficiency of cap rocks. *Marine and Petroleum Geology*, 14(5):565–580.

[Schneider et al., 2021] Schneider, M., Froggatt, A., Hazemann, J., Sakiyama, H., and Ahmda, A. (2021). The World Nuclear Industry Status Report 2021. Technical report, World Nuclear Industry, Paris, France.

[Schrefler, 1984] Schrefler, B. A. (1984). *The finite element method in soil consolidation (with applications to surface subsidence)*. University College of Swansea.

[Schröder, 2014] Schröder, J. (2014). A numerical two-scale homogenisation scheme: The FE2 method. In Schröder, J. and Hackl, K., editors, *Plasticity and Beyond*, pages 1–64. Springer, Vienna, Austria.

[Sciarra et al., 2007] Sciarra, G., Dell'Isola, F., and Coussy, O. (2007). Second gradient poromechanics. *International Journal of Solids and Structures*, 44(20):6607–6629.

[Segura and Carol, 2008a] Segura, J. and Carol, I. (2008a). Coupled HM analysis using zero-thickness interface elements with double nodes. Part I: Theoretical model. *Int. J. Numer. Anal. Meth. Geomech.*, 32:1303–1336.

[Segura and Carol, 2008b] Segura, J. and Carol, I. (2008b). Coupled HM analysis using zero-thickness interface elements with double nodes—Part II: Verification and application. *Int. J. Numer. Anal. Meth. Geomech.*, 32:2103–2123.

[Semete et al., 2008] Semete, P., Imbert, C., Desgree, P., Février, B., Courtois, A., and Touzé, G. (2008). Experimental study of the water permeability of a partially saturated argillite. In Shao, J. and Burlion, N., editors, *Proceedings of 3rd International Symposium GeoProc'2008. Thermo-Hydromechanical and Chemical Coupling in Geomaterials and Applications*, pages 219–230, Polytech-Lille, France.

[Senger et al., 2006] Senger, R., Enachescu, C., Doe, T., Distinguin, M., Delay, J., and Frieg, B. (2006). Design and analysis of a gas threshold pressure test in a low-permeability clay formation at ANDRA's underground research laboratory, Bure (France). In *Proceedings TOUGH Symposium '06*, pages 1–9, Berkeley, California.

[Senger et al., 2014] Senger, R., Romero, E., Ferrari, A., and Marschall, P. (2014). Characterization of gas flow through low-permeability claystone: Laboratory experiments and two-phase flow analyses. *Geological Society Special Publication*, 400(1):531–543.

[Senger et al., 2018] Senger, R., Romero, E., and Marschall, P. (2018). Modeling of Gas Migration Through Low-Permeability Clay Rock Using Information on Pressure and Deformation from Fast Air Injection Tests. *Transport in Porous Media*, 123(3):563–579.

[Shao et al., 2006] Shao, J. F., Duveau, G., Bourgeois, F., and Chen, W. Z. (2006). Elastoplastic Damage Modeling in Unsaturated Rocks. (April):119–130.

[Shao et al., 2003] Shao, J. F., Zhu, Q. Z., and Su, K. (2003). Modeling of creep in rock materials in terms of material degradation. *Computers and Geotechnics*, 30(7):549–555.

[Shaw, 2015] Shaw, R. P. (2015). The Fate of Repository Gases (FORGE) project. *Geological Society Special Publication*, 415(1):1–7.

[Shu et al., 1999] Shu, J. Y., King, W. E., and Fleck, N. A. (1999). Finite elements for materials with strain gradient effects. *International Journal for Numerical Methods in Engineering*, 44(3):373–391.

[Sieffert et al., 2009] Sieffert, Y., Al Holo, S., and Chambon, R. (2009). Loss of uniqueness of numerical solutions of the borehole problem modelled with enhanced media. *International Journal of Solids and Structures*, 46(17):3173–3197.

[Sieffert et al., 2014] Sieffert, Y., Buzzi, O., and Collin, F. (2014). Numerical study of shear band instability and effect of cavitation on the response of a specimen under undrained biaxial loading. *International Journal of Solids and Structures*, 51(9):1686–1696.

[Sieffert et al., 2011] Sieffert, Y., Marinelli, F., and Chambon, R. (2011). Local Second Gradient Models for Thermo-Hydro-Mechanical Coupling in Rock Like Materials. In Bonelli, S., Dascalu, C., and Nicot, F., editors, *Advances in Bifurcation and Degradation in Geomaterials. Proceedings of the 9th International Workshop on Bifurcation and Degradation in Geomaterials.*, pages 219–226.

[Sillen, 2012] Sillen, X. (2012). Keynote on repository-induced perturbations of the host rock, in the context of the safety case for the geological disposal of VHLW and SF in clay formations. In *Proceedings of the European Commission TIMODAZ-THERESA International Conference*, pages 159–171, Brussels, Belgium. European Commission.

[Simo et al., 1993] Simo, J., Olivier, J., and Armero, F. (1993). An analysis of strong discontinuities induced by strain-softening in rate-independent inelastic solids. *Computatlonal Mechanics*, 12:277–296.

[Simo and Rifai, 1990] Simo, J. C. and Rifai, M. S. (1990). A class of mixed assumed strain methods and the method of incompatible modes. *International Journal for Numerical Methods in Engineering*, 29(8):1595–1638.

[Siqueira et al., 2019] Siqueira, D. S., de Almeida Meystre, J., Hilário, M. Q., Rocha, D. H. D., Menon, G. J., and da Silva, R. J. (2019). Current perspectives on nuclear energy as a global climate change mitigation option. *Mitigation and Adaptation Strategies for Global Change*, 24(5):749–777.

[Sluys and de Borst, 1992] Sluys, L. J. and de Borst, R. (1992). Wave propagation and localization in a rate-dependent cracked medium-model formulation and one-dimensional examples. *International Journal of Solids and Structures*, 29(23):2945–2958.

[Smil, 2016] Smil, V. (2016). *Energy Transitions: Global and National Perspectives, 2nd Edition*. Online, praeger edition.

[Smit et al., 1998] Smit, R. J., Brekelmans, W. A., and Meijer, H. E. (1998). Prediction of the mechanical behavior of nonlinear heterogeneous systems by multi-level finite element modeling. *Computer Methods in Applied Mechanics and Engineering*, 155(1-2):181–192.

[Snow, 1969] Snow, D. (1969). Anisotropic Permeability of Fractured Media. *Water Resources Research*, 5(6):1273–1289.

[Song et al., 2023] Song, H., Corman, G., and Collin, F. (2023). Thermal Impact on the Excavation Damage Zone Around a Supported Drift Using the 2nd Gradient Model. *Rock Mechanics and Rock Engineering*, (0123456789).

[Song, 2014] Song, Y. (2014). *Water retention and fine microstructure of Bure argillite*. PhD thesis, . Ecole Centrale de Lille.

[Song et al., 2016] Song, Y., Davy, C. A., and Troadec, D. (2016). Gas Breakthrough Pressure (GBP) through Claystones: Correlation with FIB/SEM Imaging of the Pore Volume. *Oil & Gas Science and Technology – Revue d'IFP Energies nouvelles*, 71(4):51.

[Song et al., 2015] Song, Y., Davy, C. A., Troadec, D., Blanchenet, A. M., Skoczylas, F., Talandier, J., and Robinet, J. C. (2015). Multi-scale pore structure of COx claystone: Towards the prediction of fluid transport. *Marine and Petroleum Geology*, 65:63–82.

[Souley et al., 2022] Souley, M., Vu, M.-n., and Armand, G. (2022). 3D Modelling of Excavation-Induced Anisotropic Responses of Deep Drifts at the Meuse / Haute-Marne URL. *Rock Mechanics and Rock Engineering*, 55:4183–4207.

[Stankiewicz and Pamin, 2006] Stankiewicz, A. and Pamin, J. (2006). Gradient-Enhanced Cam-Clay Model in Simulation of Strain Localization in Soil. *Foundations of Civil and Environmental Engineering*, 7(7):293–318.

[Stefanou and Sulem, 2014] Stefanou, I. and Sulem, J. (2014). Chemically induced compaction bands: Triggering conditions and band thickness. *Journal of Geophysical Research: Solid Earth*, 119(2):880–899.

[Steffen et al., 2015] Steffen, W., Broadgate, W., Deutsch, L., Gaffney, O., and Ludwig, C. (2015). The trajectory of the anthropocene: The great acceleration. *Anthropocene Review*, 2(1):81–98.

[Stephansson et al., 1996] Stephansson, O., Jing, L., and Tsang, C.-F. (1996). *Coupled Thermo-Hydro-Mechanical Processes of Fractured Media: Mathematical and Experimental Studies*, volume 79. Elsevier Science B.V., Amsterdam, The Nederland.

[Su, 2007] Su, K. (2007). Development of Hydro-mechanical Models of the Callovo-Oxfordian Argillites for the Geological Disposal of Radioactive Waste (MODEX-REP). Technical report, Work performed as part of the European Atomic Energy Community's R&T specific programme Nuclear Energy 1998-2002, key action Nuclear Fission Safety Area: Safety of the fuel cycle.

[Sulem, 2010] Sulem, J. (2010). Bifurcation theory and localization phenomena. *European Journal of Environmental and Civil engineering*, 14(8-9):989–1009.

[Sulem and Vardoulakis, 1990] Sulem, J. and Vardoulakis, I. (1990). Bifurcation analysis of the triaxial test on rock specimens. A theoretical model for shape and size effect. *Acta Mechanica*, 83(3-4):195–212.

[Sulem et al., 1999] Sulem, J., Vardoulakis, I., Papamichos, E., Oulahna, A., and Tronvoll, J. (1999). Elasto-plastic modelling of Red Wildmoor sandstone. *Mechanics of Cohesive-Frictional Materials*, 4:215–245.

[Supko, 2016] Supko, E. (2016). Nuclear fuel fabrication. In Hore-Lacy, I., editor, *Uranium for Nuclear Power: Resources, Mining and Transformation to Fuel*, chapter 13, pages 353–382. Elsevier Ltd.

[Suquet, 1987] Suquet, P. (1987). Elements of homogenization for in solid mechanics. *Lecture Notes in Physics*, 272(January 1985):193–278.

[Sutton et al., 1983] Sutton, M., Wolters, W., Peters, W., Ranson, W., and McNeill, S. (1983). Determination of displacements using an improved digital correlation method. *Image and Vision Computing*, 1(3):133–139.

[Talandier, 2005] Talandier, J. (2005). La production et le transfert de gaz dans un stockage et dans la couche du Callovo-Oxfordien - Lien avec le transitoire hydraulique - Site de Meuse / Haute-Marne. Rapport Andra n° C.NT.ASCM.03.0042. Technical report, Andra.

[Tamagnini et al., 2000] Tamagnini, C., Viggiani, G., and Chambon, R. (2000). A review of two different approaches to hypoplasticity. In *Constitutive Modelling of Granular Materials*, pages 107–145. Springer Berlin Heidelberg, Berlin, Germany.

[Tamayo-Mas and Harrington, 2020] Tamayo-Mas, E. and Harrington, J. F. (2020). DECOVALEX-2019 Task A Final Report. Technical Report October, LBNL-2001262.

[Tatsuoka et al., 1990] Tatsuoka, F., Nakamura, S., Huang, C. C., and Tani, K. (1990). Strength anisotropy and shear band direction in plane strain tests of sand. *Soils and Foundations*, 30(1):35–54.

[Tatsuoka et al., 1986] Tatsuoka, F., Sakamoto, M., Kawamura, T., and Fukushima, S. (1986). Strength and Deformation Characteristics of Sand in Plane Strain Compression At Extremely Low Pressures. *Soils and Foundations*, 26(1):65–84.

[Taylor and Quinney, 1931] Taylor, G. I. and Quinney, H. (1931). The plastic distortion of metals. *Philosophical Transactions of the Royal Society of London. Series A, Containing Papers of a Mathematical or Physical Character*, 230(681-693):323–362.

[Terada et al., 2000] Terada, K., Hori, M., Kyoya, T., and Kikuchi, N. (2000). Simulation of the multi-scale convergence in computational homogenization approaches. *International Journal of Solids and Structures*, 37(16):2285–2311.

[Terada and Kikuchi, 1995] Terada, K. and Kikuchi, N. (1995). Nonlinear homogenization method for practical applications. *American Society of Mechanical Engineers, Applied Mechanics Division, AMD*, 212(January 1995):1–16.

[Terzaghi, 1936] Terzaghi, K. (1936). The Shearing Resistance of Saturated Soils and the Angle between the Planes of Shear. *First International Conference on Soil Mechanics*, 1:54–59.

[Thakur, 2007] Thakur, V. (2007). *Strain localization in sensitive soft clays*. PhD thesis, Norwegian University of Science and Technology, Trondheim, Norway.

[Thakur et al., 2018] Thakur, V., Nordal, S., Viggiani, G., and Charrier, P. (2018). Shear bands in undrained plane strain compression of Norwegian quick clays. *Canadian Geotechnical Journal*, 55(1):45–56.

[Thomas and He, 1995] Thomas, H. R. and He, Y. (1995). Discussion: Analysis of coupled heat, moisture and air transfer in a deformable unsaturated soil. *Géotechnique*, 47(1):197–198.

[Thomas, 1961] Thomas, T. Y. (1961). *Plastic Flow and Fracture in Solids*. Academic Press, New-York, The United States.

[Toupin, 1962] Toupin, R. A. (1962). Elastic materials with couple-stresses. *Archive for Rational Mechanics and Analysis*, 11(1):385–414.

[Triantafyllidis, 1980] Triantafyllidis, N. (1980). Bifurcation phenomena in pure bending. *Journal of the Mechanics and Physics of Solids*, 28(3-4):221–245.

[Truesdell and Noll, 1965] Truesdell, C. and Noll, W. (1965). *The Non-Linear Field Theories of Mechanics*. Springer-Verlag, Berlin, Germany, ed. s. flu edition.

[Tsang et al., 2005] Tsang, C., Bernier, F., and Davies, C. (2005). Geohydromechanical processes in the Excavation Damaged Zone in crystalline rock, rock salt, and indurated and plastic clays - In the context of radioactive waste disposal. *International Journal of Rock Mechanics and Mining Sciences*, 42(1):109–125.

[Tsang, 1987] Tsang, C. F. (1987). *Coupled Processes Associated with Nuclear Waste Geologic Repositories*. Academic Press, San Diego, California, The United States.

[Tsang et al., 2012] Tsang, C. F., Barnichon, J. D., Birkholzer, J., Li, X. L., Liu, H. H., and Sillen, X. (2012). Coupled thermo-hydro-mechanical processes in the near field of a high-level radioactive waste repository in clay formations. *International Journal of Rock Mechanics and Mining Sciences*, 49:31–44.

[Tsang et al., 2000] Tsang, C.-F., Stephansson, O., and Hudson, J. (2000). A discussion of thermo–hydro–mechanical (THM) processes associated with nuclear waste repositories. *International Journal of Rock Mechanics and Mining Sciences*, 37(1-2):397–402.

[UN, 2015] UN (2015). Transforming our World: The 2030 Agenda for Sustainable Development. Technical report, United Nations, New-York, The United States.

[Valko and Economides, 1997] Valko, P. and Economides, M. (1997). *Hydraulic fracture mechanics*. John Wiley & Sons, New-York, The United States.

[van den Eijnden et al., 2017] van den Eijnden, A., Bésuelle, P., Collin, F., Chambon, R., and Desrues, J. (2017). Modeling the strain localization around an underground gallery with a hydro-mechanical double scale model; effect of anisotropy. *Computers and Geotechnics*, 85:384–400.

[van den Eijnden et al., 2016] van den Eijnden, A. P., Bésuelle, P., Chambon, R., and Collin, F. (2016). A FE2 modelling approach to hydromechanical coupling in cracking-induced localization problems. *International Journal of Solids and Structures*, 97-98:475–488.

[van den Eijnden, 2015] van den Eijnden, B. (2015). *Multi-scale modelling of the hydromechanical behaviour of argillaceous rocks*. PhD thesis, Université Grenoble Alpes and Université de Liège.

[Van Der Sluis et al., 2000] Van Der Sluis, O., Schreurs, P. J., Brekelmans, W. A., and Meijer, H. E. (2000). Overall behaviour of heterogeneous elastoviscoplastic materials: Effect of microstructural modelling. *Mechanics of Materials*, 32(8):449–462.

[Van Der Zwaan, 2008] Van Der Zwaan, B. (2008). Prospects for nuclear energy in Europe. *International Journal of Global Energy Issues*, 30(1-4):102–121.

[Van Dorp et al., 1989] Van Dorp, F., Grogan, H., and McCombie, C. (1989). Disposal of radioactive waste. *International Journal of Radiation Applications and Instrumentation. Part*, 34(2):337–346.

[Van Eekelen, 1980] Van Eekelen, H. A. M. (1980). Isotropic yield surfaces in three dimensions for use in soil mechanics. *International Journal for Numerical and Analytical Methods in Geomechanics*, 4(1):89–101.

[Van Geet et al., 2003] Van Geet, M., Maes, N., and Dierckx, A. (2003). Characteristics of the Boom Clay organic matter, a review. *Geological survey of Belgium, Professional paper 2003/1 N. 298, Royal Belgian Institute of Natural Sciences,*.

[van Genuchten, 1980] van Genuchten, M. (1980). Predicting the hydraulic conductivity of unsaturated soils. *Soil. Sci. Soc. Am. J*, 44(5):892–898.

[Van Humbeeck et al., 2008] Van Humbeeck, H., Bastiaens, W., De Bock, C., and Van Cotthem, A. (2008). Experimental Programme to Demostrate the Viability of the Supercontainer Concept for HLW. In *International Conference on Underground Disposal Unit Design & Emplacement Processes for a Deep Geological Repository*, number June, pages 1–10, Prague, Czech Republic.

[Van Laer, 2018] Van Laer, L. (2018). Long-term laboratory and in-situ migration experiments in Boom Clay – status 2017. Technical report, SCK•CEN, Mol, Belgium.

[Van Marcke and Bastiaens, 2010] Van Marcke, P. and Bastiaens, W. (2010). Excavation induced fractures in a plastic clay formation: Observations at the HADES URF. *Journal of Structural Geology*, 32(11):1677–1684.

[Vandenberghe, 1978] Vandenberghe, N. (1978). Sedimentology of the Boom Clay (Rupelian) in Belgium. *Verhandeling Koninklijke Academie voor Wetenschappen, Letteren en Schone Kunsten van België, Klasse Wetenschappen, XL/147*, page 147.

[Vandenberghe et al., 2014] Vandenberghe, N., De Craen, M., and Wouters, L. (2014). The Boom Clay Geology from sedimentation to present-day occurrence - a review. *Memoirs of the Geological Survey of Belgium*, 60(3):76.

[Vandenberghe et al., 1997] Vandenberghe, N., Laenen, B., Van Echelpoel, E., and Lagrou, D. (1997). Cyclostratigraphy and climatic eustasy. Example of the Rupelian stratotype. *Comptes Rendus de l'Academie de Sciences - Serie IIa: Sciences de la Terre et des Planetes*, 325(5):305–315.

[Vardoulakis, 1979] Vardoulakis, I. (1979). Bifurcation analysis of the triaxial test on sand samples. *Acta Mechanica*, 32(1-3):35–54.

[Vardoulakis, 1980] Vardoulakis, I. (1980). Shear band inclination and shear modulus of sand in biaxial tests. *International Journal for Numerical and Analytical Methods in Geomechanics*, 4(2):103–119.

[Vardoulakis, 1981] Vardoulakis, I. (1981). Bifurcation analysis of the plane rectilinear deformation on dry sand samples. *International Journal of Solids and Structures*, 17(11):1085–1101.

[Vardoulakis, 1984] Vardoulakis, I. (1984). Rock bursting as a surface instability phenomenon. *International Journal of Rock Mechanics and Mining Sciences and*, 21(3):137–144.

[Vardoulakis, 1996a] Vardoulakis, I. (1996a). Deformation of water-saturated sand: I. uniform undrained deformation and shear banding. *Geotechnique*, 46(3):441–456.

[Vardoulakis, 1996b] Vardoulakis, I. (1996b). Deformation of water-saturated sand: II. effect of pore water flow and shear banding. *Geotechnique*, 46(3):457–472.

[Vardoulakis and Aifantis, 1991] Vardoulakis, I. and Aifantis, E. C. (1991). A gradient flow theory of plasticity for granular materials. *Acta Mechanica*, 87(3-4):197–217.

[Vardoulakis et al., 1978] Vardoulakis, I., Goldscheider, M., and Gudehus, G. (1978). Formation of shear bands in sand bodies as a bifurcation problem. *International Journal for Numerical and Analytical Methods in Geomechanics*, 2(2):99–128.

[Vardoulakis and Graf, 1985] Vardoulakis, I. and Graf, B. (1985). Calibration of constitutive models for granular materials using data from biaxial experiments. *Geotechnique*, 35(3):299–317.

[Vardoulakis and Sulem, 1995] Vardoulakis, I. and Sulem, J. (1995). *Bifurcation analysis in geomechanics*. Blackie Academic & Professional, London, The United Kingdom.

[Verbruggen, 2008] Verbruggen, A. (2008). Renewable and nuclear power: A common future? *Energy Policy*, 36(11):4036–4047.

[Verstricht, 2013] Verstricht, J. (2013). 30 years of monitoring experience in HADES. In *18th Exchange Meeting "Instrumentation and monitoring in radioactive waste repository research"*, Mol, Belgium. SCK•CEN.

[Vervoot et al., 2004] Vervoot, M., Wevers, M., Rudy, S., Roels, S., Van Geet, M., and Sellars (2004). Recent Advances of X-Ray CT and its application for rock material. In Otani, J. and Obara, Y., editors, *Proceedings of the international workshop on X-ray CT for Geomaterials. Soils, Concrete, Rocks.*, pages 79–91, Kumamoto, Japan. Balkema Publishers.

[Viggiani et al., 2010] Viggiani, G., Bésuelle, P., Desrues, J., and Hall, S. (2010). Sand Deformation at the Grain Scale Quantified Through X-Ray Imaging. In Alshibli, K. A. and Reed, A., editors, *Advances in Computed Tomography for Geomaterials: GeoX 2010*, pages 1–16. John Wiley & Sons, Ltd.

[Viggiani and Hall, 2008] Viggiani, G. and Hall, S. (2008). Full-field measurements, a new tool for laboratory experimental geomechanics. In Burns, S., Mayne, P., and Santamarina, J., editors, *n Proceedings of the 4th International Symposium on Deformation Characteristics of Geomaterials, Atlanta, The United-States*, pages 3–26, Amsterdam, The Nederland. IOS Press.

[Viggiani and Hall, 2012] Viggiani, G. and Hall, S. (2012). Full-field measurements in experimental geomechanics. In Viggiani, G., Hall, S., and Romero, E., editors, *ALERT Doctoral School 2012 – Advanced experimental techniques in geomechanics,*, chapter 1, pages 3–68. ALERT Geomaterials.

[Viggiani et al., 2004] Viggiani, G., Lenoir, N., Bésuelle, P., Di Michiel, M., Marello, S., Desrues, J., and Kretzschmer, M. (2004). Utilisation de la microtomographie rayon X pour l'étude de la localisation des déformations dans les géomatériaux argileux sous sollicitation axisymétrique. *Comptes Rendus - Mecanique*, 332(10):819–826.

[Villar et al., 2020] Villar, M., Armand, G., Conil, N., de Lesquen, C., Herold, P., Simo, E., Mayor, J., Dizier, A., Li, X., Chen, G., Leupin, O., Niskanen, M., Bailey, M., Thompson, S., Svensson, D., Sellin, P., and Hausmannova, L. (2020). Initial State-of-the-Art on THM behaviour of i) Buffer clay materials and of ii) Host clay materials. Deliverable D7.1 of HORIZON 2020 project EURAD, Work Package HITECH. EC Grant agreement no: 847593. Technical Report Deliverable D7.1 HITEC, European commission.

[Villar and Lloret, 2001] Villar, M. V. and Lloret, A. (2001). Variation of the intrinsic permeability of expansive clays upon saturation. Proceedings of the International Symposium on Suction, Swelling, Permeability and Structure of Clays. In *Clay Science for Engineering*, pages 259–266. Balkema, Rotterdam, The Nederland, adachi and edition.

[Vo et al., 2017] Vo, T. D., Pouya, A., Hemmati, S., and Tang, A. M. (2017). Numerical modelling of desiccation cracking of clayey soil using a cohesive fracture method. *Computers and Geotechnics*, 85:15–27.

[Voinis et al., 1997] Voinis, S., Plas, F., Vercoutère, G., Cuñado, M., Müller, W., Thellen, D., Kannen, H., Rodrigo, M., Breton, J., and Kunc, T. (1997). PEGASE: Study of Consequences Associated with the Production of Gas in a Geological Repository. Technical Report Nº INT RP ADAI 97-005, European Commision, Luxembourg.

[Volckaert et al., 2005] Volckaert, G., Bernier, F., Sillen, X., Van Geet, M., Mayor, J., Göbel, I., Blümling, P., Frieg, B., and Su, K. (2005). Similarities and Differences in the Behaviour of Plastic and Indurated Clays. In *Proceedings Euradwaste'04. Radioactive waste management community policy and research initiatives. EUR-21027*, pages 281–291.

[Volckaert et al., 1995] Volckaert, G., Ortiz, L., Canniere, P. D., Put, M., Horseman, S. T., Harrington, J. F., Fioravante, V., and Impey, M. (1995). MEGAS: modelling and experiments on GAS migration in repository host rocks. Final report phase 1. Technical report, Eur. Comm., [Rep.] EUR 16235 EN.

[Walsh, 1965] Walsh, J. B. (1965). The effect of cracks on the uniaxial elastic compression of rocks. *Journal of Geophysical Research*, 70(2):399–411.

[Wan, 1996] Wan, A. W. L. (1996). The use of thermocouple psychrometers to measure in situ suctions and water contents in compacted clays.

[Wang et al., 2011] Wang, L., Salah, S., and Soete, H. D. (2011). MOLDATA : A thermochemical data base for phenomenological and safety assessment studies for disposal of radioactive waste in Belgium – Data compilation strategy. External report ER-121. Technical report, SCK•CEN, Mol, Belgium.

[Wang et al., 2020] Wang, M., Feng, Y. T., Wang, Y., Qu, T. M., and He, W. (2020). A hybrid discrete bubble-lattice Boltzmann–discrete element model for gas-charged sediments. *Computational Particle Mechanics*, 7(3):509–522.

[Wang et al., 2015] Wang, W., Shao, J. F., Zhu, Q. Z., and Xu, W. Y. (2015). A discrete viscoplastic damage model for time-dependent behaviour of quasi-brittle rocks. *International Journal of Damage Mechanics*, 24(1):21–40.

[Wang et al., 1997] Wang, W. M., Sluys, L. J., and De Borst, R. (1997). Viscoplasticity for instabilities due to strain softening and strain-rate softening. *International Journal for Numerical Methods in Engineering*, 40(20):3839–3864.

[Wang, 1993] Wang, X. (1993). *Modélisation numérique des problèmes avec localisation de la déformation en bandes de cisaillement*. PhD thesis, University of Liège.

[Weast, 1987] Weast, R. (1987). *Handbook of Chemistry and Physics*, volume 51. CRC Press, Cleveland, The United States.

[Webber, 2013] Webber, J. B. W. (2013). A bi-symmetric log transformation for wide-range data. *Measurement Science and Technology*, 24(2).

[Weetjens et al., 2014] Weetjens, E., Maes, N., and Van Ravestyn, L. (2014). Model validation based on in situ radionuclide migration tests in Boom Clay : status of a large-scale migration experiment, 24 years after injection. In Norris, S., Bruno, J., Cathelineau, M., Delage, P., Fairhurst, C., Gaucher, E. C., Höhn, E. H., Kalinichev, A., Lalieux, P., and Sellin, P., editors, *Clays in Natural and Engineered Barriers for Radioactive Waste Confinement*, volume 400, pages 613–623. Geological Society, London, Special Publications.

[Wells, 2001] Wells, G. N. (2001). *Discontinuous modelling of strain localisation and failure*. PhD thesis, Technische Universiteit Delft.

[Wemaere et al., 2008] Wemaere, I., Marivoet, J., and Labat, S. (2008). Hydraulic conductivity variability of the Boom Clay in north-east Belgium based on four core drilled boreholes. *Physics and Chemistry of the Earth*, 33(SUPPL. 1):24–36.

[Wenk et al., 2008] Wenk, H. R., Voltolini, M., Mazurek, M., Van Loon, L. R., and Vinsot, A. (2008). Preferred orientations and anisotropy in shales: Callovo-oxfordian shale (France) and opalinus clay (Switzerland). *Clays and Clay Minerals*, 56(3):285–306.

[White et al., 2005] White, C. M., Smith, D. H., Jones, K. L., Goodman, A. L., Jikich, S. A., LaCount, R. B., DuBose, S. B., Ozdemir, E., Morsi, B. I., and Schroeder, K. T. (2005). Sequestration of carbon dioxide in coal with enhanced coalbed methane recovery - A review. *Energy and Fuels*, 19(3):659–724.

[Whittaker et al., 1992] Whittaker, B., Singh, R., and Sun, G. (1992). *Rock fracture mechanics: Principles, design and applications*. Elsvier, Amsterdam, The Nederland.

[WHO, 1999] WHO (1999). *Safe management of wastes from health-care activities*. Prüss, A. Giroult, E. Rushbrook, P., World Health Organisation. Geneva, Switzerland.

[Wileveau and Bernier, 2008] Wileveau, Y. and Bernier, F. (2008). Similarities in the hydromechanical response of Callovo-Oxfordian clay and Boom Clay during gallery excavation. *Physics and Chemistry of the Earth*, 33(SUPPL. 1):343–349.

[Wileveau et al., 2007] Wileveau, Y., Cornet, F. H., Desroches, J., and Blumling, P. (2007). Complete in situ stress determination in an argillite sedimentary formation. *Physics and Chemistry of the Earth*, 32(8-14):866–878.

[Wilhelmi and Somerton, 1967] Wilhelmi, N. and Somerton, W. (1967). Simultaneous Measurement of Pore and Elastic Properties of Rocks Under Triaxial Stress Conditions. *Society of Petroleum Engineers Journal*, 7(3):283–294.

[Wiliarty, 2013] Wiliarty, S. E. (2013). Nuclear power in Germany and France. *Polity*, 45(2):281–296.

[Wiseall et al., 2015a] Wiseall, A., Graham, C., Zihms, S., Harrington, J., Cuss, R., Gregory, S., and Shaw, R. (2015a). Properties and Behaviour of the Boom Clay Formation within a Dutch Repository Concept. OPERA-PU-BGS615. Technical report, British Geological Survey.

[Wiseall et al., 2015b] Wiseall, A. C., Cuss, R. J., Graham, C. C., and Harrington, J. F. (2015b). The visualization of flow paths in experimental studies of clay-rich materials. *Mineralogical Magazine*, 79(6):1335–1342.

[Witherspoon, 1991] Witherspoon, P. (1991). Geological Problems in Radioactive Waste Isolation: A World Wide Review. Technical report, Berkeley, California.

[Witherspoon et al., 1980] Witherspoon, P., Wang, J., Iwai, K., and Gale, J. (1980). Validity of Cubic Law for Fluid Flow in a Deformable Rock Fracture. *Water Resources Research*, 16(6):1016–1024.

[Wriggers and Zavarise, 2004] Wriggers, P. and Zavarise, G. (2004). Computational Contact Mechanics. In Stein, E., Borst, R., and Hughes, T., editors, *Encyclopedia of Computational Mechanics*, chapter 6. John Wiley & Sons, Ltd.

[Wu and Wang, 2010] Wu, S. and Wang, X. (2010). Mesh dependence and nonlocal regularization of one-dimensional strain softening plasticity. *Journal of Engineering Mechanics*, 136(11):1354–1365.

[X. Li et al, 2007] X. Li et al (2007). TIMODAZ: Thermal impact on the damaged zone around a radioactive waste disposal in clay host rocks. Deliverable 2. State of the art on THMC. Technical report, Euratom European Project.

[Xie et al., 2011] Xie, S. Y., Shao, J. F., and Xu, W. Y. (2011). Influences of chemical degradation on mechanical behaviour of a limestone. *International Journal of Rock Mechanics and Mining Sciences*, 48(5):741–747.

[Xu et al., 1997] Xu, K., Daian, J.-F., and Quenard, D. (1997). Multiscale Structures to Describe Porous Media Part I: Theoretical Background and Ivasion by Fluids. *Transport in Porous Media*, 26(1):51–73.

[Xu et al., 2013a] Xu, W., Shao, H., Marschall, P., Hesser, J., and Kolditz, O. (2013a). Analysis of flow path around the sealing section HG-A experiment in the Mont Terri Rock Laboratory. *Environmental Earth Sciences*, 70(7):3363–3380.

[Xu et al., 2013b] Xu, W. J., Shao, H., Hesser, J., Wang, W., Schuster, K., and Kolditz, O. (2013b). Coupled multiphase flow and elasto-plastic modelling of in-situ gas injection experiments in saturated claystone (Mont Terri Rock Laboratory). *Engineering Geology*, 157:55–68.

[Xu and Needleman, 1994] Xu, X. P. and Needleman, A. (1994). Numerical simulations of fast crack growth in brittle solids. *Journal of the Mechanics and Physics of Solids*, 42(9):1397–1434.

[Xue et al., 2018] Xue, Y., Dang, F., Shi, F., Li, R., and Cao, Z. (2018). Evaluation of Gas Migration and Rock Damage Characteristics for Underground Nuclear Waste Storage Based on a Coupled Model. *Science and Technology of Nuclear Installations*, 2018:1–11.

[Yang and Fall, 2021a] Yang, J. and Fall, M. (2021a). A two-scale hydro-mechanical-damage model for simulation of preferential gas flow in saturated clayey host rocks for nuclear repository. *Computers and Geotechnics*, 138(March):104365.

[Yang and Fall, 2021b] Yang, J. and Fall, M. (2021b). A two-scale time dependent damage model for preferential gas flow in clayey rock materials. *Mechanics of Materials*, 158(March):103853.

[Yang and Fall, 2021c] Yang, J. and Fall, M. (2021c). Hydro-mechanical modelling of gas transport in clayey host rocks for nuclear waste repositories. *International Journal of Rock Mechanics and Mining Sciences*, 148(June):104987.

[Yang et al., 2020] Yang, J., Fall, M., and Guo, G. (2020). A Three-Dimensional Hydro-mechanical Model for Simulation of Dilatancy Controlled Gas Flow in Anisotropic Claystone. *Rock Mechanics and Rock Engineering*, 53(9):4091–4116.

[Yu et al., 2019] Yu, H., Zhu, Y. B., Jin, X., Liu, H., and Wu, H. A. (2019). Multiscale simulations of shale gas transport in micro/nano-porous shale matrix considering pore structure influence. *Journal of Natural Gas Science and Engineering*, 64(October 2018):28–40.

[Yu et al., 2011] Yu, L., Gedeon, M., Wemaere, I., Marivoet, J., and De Craen, M. (2011). Boom Clay hydraulic conductivity - a synthesis of 30 years of research. External Report of Belgian Nuclear Research Centre. SCK•CEN-ER-122. Technical report, SCK•CEN, Belgian Nuclear Research Centre, Mol, Belgium.

[Yu et al., 2012] Yu, L., Rogiers, B., and Gedeon, M. (2012). Hydraulic conductivity of Boom Clay in north-east Belgium. In *Propriétés de transfert des géomatériaux TRANSFERT 2012*, pages 408–417, Lille, France.

[Yu et al., 2013] Yu, L., Rogiers, B., Gedeon, M., Marivoet, J., Craen, M. D., and Mallants, D. (2013). A critical review of laboratory and in-situ hydraulic conductivity measurements for the Boom Clay in Belgium. *Applied Clay Science*, 75-76:1–12.

[Yuster, 1951] Yuster, S. (1951). Theoretical considerations of multiphase flow in idealized capillary systems.pdf. *Proceedings of the 3rd World Petroleum Congress, Section II,The Hague*, 2:437–445.

[Zauderer, 1989] Zauderer, E. (1989). *Partial Differential Equations of Applied Mathematics*. Pure and applied mathematics. Wiley, Chichester, The UK, second edition.

[Zeelmaekers et al., 2015] Zeelmaekers, E., Honty, M., Derkowski, A., Środoń, J., De Craen, M., Vandenberghe, N., Adriaens, R., Ufer, K., and Wouters, L. (2015). Qualitative and quantitative mineralogical composition of the Rupelian Boom Clay in Belgium. *Clay Minerals*, 50(2):249–272.

[Zervos et al., 2001] Zervos, A., Papanastasiou, P., and Vardoulakis, I. (2001). A finite element displacement formulation for gradient elastoplasticity. *International Journal for Numerical Methods in Engineering*, 50(6):1369–1388.

[Zhang and Rothfuchs, 2004] Zhang, C. and Rothfuchs, T. (2004). Experimental study of the hydro-mechanical behaviour of the Callovo- Oxfordian argillite. *Applied Clay Science*, 26(1-4 SPEC. ISS.):325–336.

[Zhang, 2014] Zhang, C. L. (2014). Characterization of excavated claystone and claystone-bentonite mixtures as backfill/seal material. *Geological Society Special Publication*, 400(1):327–337.

[Zhang et al., 2019] Zhang, C. L., Armand, G., Conil, N., and Laurich, B. (2019). Investigation on anisotropy of mechanical properties of Callovo-Oxfordian claystone. *Engineering Geology*, 251(January):128–145.

[Zhang et al., 2010] Zhang, C. L., Czaikowski, O., and Rothfuchs, T. (2010). Thermo-Hydro- Mechanical Behaviour of the Callovo- Oxfordian Clay Rock. Technical report, Gesellschaft für Anlagen- und Reaktorsicherheit (GRS) within the Framework of GRS/ANDRA Cooperation Programme and the EC TIMODAZ Project.

[Zhang et al., 1999] Zhang, H. W., Sanavia, L., and Schrefler, B. A. (1999). Internal length scale in dynamic strain localization of multiphase porous media. *Mechanics of Cohesive-Frictional Materials*, 4(5):443–460.

[Zhang and Schrefler, 2000] Zhang, H. W. and Schrefler, B. A. (2000). Gradient-dependent plasticity model and dynamic strain localization analysis of saturated and partially saturated porous media: One dimensional model. *European Journal of Mechanics, A/Solids*, 19(3):503–524.

[Zhang and Schrefler, 2002] Zhang, H. W. and Schrefler, B. A. (2002). Analytical and numerical investigation of uniqueness and localization in saturated porous media. *International Journal for Numerical and Analytical Methods in Geomechanics*, 26(14):1429–1448.

[Zhong and Mackerle, 1992] Zhong, Z. and Mackerle, J. (1992). Static contact problems - a review. *Engineering Computations*, 9(1):3–37.

[Zhou et al., 2008] Zhou, H., Jia, Y., and Shao, J. F. (2008). A unified elastic–plastic and viscoplastic damage model for quasi-brittle rocks. *International Journal of Rock Mechanics and Mining Sciences*, 45(8):1237–1251.

[Zhu et al., 2008] Zhu, Q., Shao, J., and Kondo, D. (2008). A micromechanics-based non-local anisotropic model for unilateral damage in brittle materials. *Comptes Rendus - Mecanique*, 336(3):320–328.

[Zhuang et al., 2017] Zhuang, X., Wang, Q., and Zhu, H. (2017). Multiscale modelling of hydro-mechanical couplings in quasi-brittle materials. *International Journal of Fracture*, 204(1):1–27.

[Zienkiewicz and Taylor, 2000] Zienkiewicz, O. C. and Taylor, R. (2000). *The finite element method: solid mechanics*, volume 2. Butterworth-Heinemann, 5 edition.

[Zohuri, 2020] Zohuri, B. (2020). Nuclear fuel cycle and decommissioning. In *Nuclear Reactor Technology Development and Utilization*, chapter 2, pages 61–120. Woodhead Publishing.

Appendices

A List of Symbols

Acronyms

μ-CT	Micro-Computed Tomography
2D	Two-dimensional
3D	Three-dimensional
CO_2	Carbon dioxide
ANDRA	Agence Nationale pour la gestion des Déchets RAdioactifs (French national radioactive waste management agency)
BJH	Barrett, Joyner and Halenda method
COVRA	Centrale Organisatie Voor Radioactief Afval (Dutch central organisation for radioactive waste)
CZM	Cohesive Zone Model
DEM	Discrete Element Method
DIC	Digital Image Correlation
EBS	Engineered Barrier System
EU	European Union
EURAD	European Joint Programme on Radioactive Waste Management
EW	Exempt Waste
FE^2	Finite Element Square Method
FEM	Finite Element Method
FESEM	Field-Emission Scanning Electron Microscopy images
FRS	False Relief Stereophotogrammetry
GDF	Geological Disposal Facility
HADES	High-Activity Disposal Experimental Site
HLW	High Level Waste
IAEA	International Atomic Energy Agency
ICRP	International Commission on Radiological Protection
IEA	International Energy Agency
ILW	Intermediate Level Waste

ILW-LL	Intermediate Level Waste Long Lived (MA-VL in French)
INES	International Nuclear and radiological Event Scale
IPCC	Intergovernmental Panel on Climate Change
KASAM	Predecessor of the present-day Swedish National Council for Nuclear Waste
LILW-SL	Low and Intermediate Level Waste Short Lived (FMA-VC in French)
LLW	Low Level Waste
LLW-LL	Low Level Waste Long Lived (FA-VL in French)
MEGAS	Modelling and Experiments on GAS migration in repository host rocks
MIP	Mercury Intrusion Porosimetry
NBS	Natural (or geological) Barrier System
NEA	Nuclear Energy Agency
NMR	Nuclear Magnetic Resonance
ONDRAF/NIRAS	Organisme National des Déchets RAdioactifs et des matières Fissiles enrichies (Belgian National Agency for Radioactive Waste and enriched Fissile Material)
OPERA	OnderzoeksProgramma Eindberging Radioactief Afval (Dutch research programme on geological disposal of radioactive waste)
ORG	Oxford Research Group
PFM	Phase-Field Method
PSD	Pore Size Density function
REV	Representative Element Volume
SEM	Scanning Electron Microscopy
TENORM	Technologically Enhanced Naturally Occurring Radioactive Materials
THM	Thermo-Hydo-Mechanical
UN	United Nations
URL	Underground Research Laboratory
US	United States
USSR	Union of Soviet Socialist Republics
VLLW	Very Low Level Waste
VSLW	Very Short Lived Waste
WHO	World Health Organization
WNA	World Nuclear Association
WP	Work Package
X-ray CT	X-ray Computed Tomography
XFEM	eXtended Finite Element Method
ZFD	Zone of fractures developement

Greek Symbols

$\bar{\tau}$	Tortuosity	$[-]$
$\bar{\varepsilon}_{ij}$	Relative deformation of the microstructure	$[-]$
β_{per}	Evolution parameter for intrinsic water permeability	$[-]$
χ_w	Water tortuosity	$[ML^{-1}T^{-2}]$
$\delta\Gamma$	Infinitesimal boundary	$[L^2]$
$\Delta_1^t, \Delta_2^t, \Delta_3^t, \Delta_4^t$	Non-equilibrium forces (residuals) of balance equations in numerical iterative procedure	$[ML^2T^{-2}]$
δ_{ij}	Kronecker symbol	$[-]$
η	Second coordinate of the parent finite element	$[-]$
η_c	Yield surface convexity parameter	$[-]$
$\frac{1}{\chi_w}$	Liquid water isotropic bulk modulus	$[M^{-1}LT^2]$
Γ^F	Follow boundary	$[L^2]$
Γ^L	Lead boundary	$[L^2]$
Γ_σ	Part of Γ on which external traction forces $\bar{t}_i$ and $\bar{T}_i$ are applied	$[L^2]$
γ_{per}	Deformation parameter for the evolution of intrinsic water permeability	$[-]$
Γ_{q_g}	Part of Γ on which input water mass $\bar{q}_g$ is prescribed	$[L^2]$
Γ_{q_w}	Part of Γ on which input water mass $\bar{q}_w$ is prescribed	$[L^2]$
Γ_T	Part of Γ on which external double force $\bar{T}_i$ is applied	$[L^2]$
Γ_t	Part of Γ on which classical external traction force $\bar{t}_i$ is applied	$[L^2]$
$\hat{\sigma}_{ij}$	Deviatoric stress tensor	$[ML^{-1}T^{-2}]$
$\hat{\varepsilon}_{eq}$	Von Mises' equivalent deviatoric total strain	$[-]$
$\hat{\varepsilon}^p_{eq}$	Von Mises' equivalent deviatoric plastic strain	$[-]$
$\hat{\varepsilon}_{ij}$	Deviatoric total strain field	$[-]$
$\hat{\varepsilon}^p_{ij}$	Deviatoric plastic strain field	$[-]$
κ	Hydraulic transmissivity function along the channel (fracture or tube)	$[L^4]$
λ	Substitution parameter gathering the saturation and tortuosity of a micro-constituent	$[-]$
λ^p	Plastic multiplier	$[-]$
μ	Coulomb's friction coefficient	$[-]$
μ_g	Gas viscosity	$[ML^{-1}T^{-1}]$
μ_v	Water vapour viscosity	$[ML^{-1}T^{-1}]$
μ_w	Water viscosity	$[ML^{-1}T^{-1}]$
ν_{ij}	Microkinematic gradient field (micro-deformation field)	$[-]$
Ω	Volume of the control space	$[L^3]$
ω_α	Mass flux of the phase α in the channel (fracture or tube)	$[MT^{-1}]$

Ω_π	Volume of the phase π	$[L^3]$
ω_{ij}	Spin rate tensor	$[T^{-1}]$
Ω_s	Volume of the solid grains	$[L^3]$
Ω_v	Volume of voids	$[L^3]$
ϕ	Porosity	$[-]$
ϕ_g	Substitution parameter assimilated to an hydraulic conductivity (gas)	$[L^4]$
ϕ_w	Substitution parameter assimilated to an hydraulic conductivity (water)	$[L^4]$
π	Phase	$[-]$
ψ	Total water potential	$[L]$
$\Psi(y_i, x_i)$	Non-local weight function	$[-]$
ψ_g	Gravitational potential	$[L]$
ψ_m	Matrix potential	$[L]$
ψ_o	Osmotic potential	$[L]$
ψ_p	External pressure potential	$[L]$
ρ	Density	$[ML^{-3}]$
ρ_{dg}	Dissolved gas density	$[ML^{-3}]$
ρ_f	Fluid density	$[ML^{-3}]$
ρ_g	Gas density	$[ML^{-3}]$
ρ_s	Solid density	$[ML^{-3}]$
ρ_v	Water vapour density	$[ML^{-3}]$
ρ_w	Water density	$[ML^{-3}]$
σ_{GL}	Surface tension at the interface between gas G and liquid L	$[ML^{-1}T^{-2}]$
Σ_{ijk}	Double stress or second order stress	$[ML^{-1}T^{-2}]$
σ_{ij}	Cauchy stress tensor	$[ML^{-1}T^{-2}]$
σ'_{ij}	Effective stress tensor	$[ML^{-1}T^{-2}]$
$\sigma_{r,0}$	Initial mechanical pressure on the tunnel wall	$[ML^{-1}T^{-2}]$
σ_r^Γ	Fictive total radial stress on the tunnel wall	$[ML^{-1}T^{-2}]$
σ_{SG}	Surface tension at the interface between solid S and gas G	$[ML^{-1}T^{-2}]$
σ_{SG}	Surface tension between solid surface S and gas G	$[ML^{-1}T^{-2}]$
σ_{SL}	Surface tension at the interface between solid S and liquid L	$[ML^{-1}T^{-2}]$
σ_{SL}	Surface tension between solid surface S and liquid L	$[ML^{-1}T^{-2}]$
$\tau, \tau 1, \tau 2$	Times at the end of time steps in numerical iterative procedure	$[T]$
τ_{ij}	Microstructure stress field (microstress)	$[ML^{-1}T^{-2}]$
τ_N	Tangential component of the contact stress vector	$[ML^{-1}T^{-2}]$
θ	Contact angle	$[-]$

$\tilde{\Sigma}_{ijk}$	Jaumann double stress rate	$[MT^{-3}]$
$\tilde{\sigma}_{ij}$	Jaumann stress rate	$\left[ML^{-1}T^{-3}\right]$
ε_{ij}	Strain tensor	$[-]$
ε^{e}_{ij}	Elastic strain field	$[-]$
ε^{p}_{ij}	Plastic strain field	$[-]$
ε^{vp}_{ij}	Visco-plastic strain field	$[-]$
φ	Friction angle	[deg]
$\varphi_{c,0}, \varphi_{c,f}$	Initial and final compression friction angles	[deg]
φ_{c}	Compression friction angle	[deg]
$\varphi_{e,0}, \varphi_{e,f}$	Initial and final extension friction angles	[deg]
φ_{e}	Extension friction angle	[deg]
ϖ	Random scalar field	$[-]$
ς_{i}	Macro-velocity gradient field of a shear band	$\left[T^{-1}\right]$
Ξ	Volume fraction	$[-]$
ξ	First coordinate of the parent finite element	$[-]$
Ξ_{g}	Gas volume fraction	$[-]$
Ξ_{l}	Liquid volume fraction	$[-]$
Ξ_{s}	Solid volume fraction	$[-]$
ζ	Stress deconfinement rate	$[-]$
ζ_{w}	Pore water pressure deconfinement rate	$[-]$
$d\Omega$	Elementary volume	$\left[L^{3}\right]$
$W\Omega_{e}$	Volume of a finite element e	$[L^{3}]$

Roman Symbols

$\bar{l}$	Gradient parameter	$[L^{2}]$
$\bar{P}_{ij}$	External double traction force	$[MT^{-2}]$
$\bar{q}_{g}$	Input gas mass per unit area on the porous material boundary	$[ML^{-2}T^{-1}]$
$\bar{q}_{w}$	Input water mass per unit area on the porous material boundary	$[ML^{-2}T^{-1}]$
$\bar{T}_{i}$	External double force per unit area on the porous material boundary	$[MT^{-2}]$
$\bar{t}_{i}$	Classical external traction force per unit area on the porous material boundary	$[ML^{-1}T^{-2}]$
$\delta\left[U^{t}_{(Node)}\right]$	Global correction vector of the nodal variables	$[-]$
$\dot{E}^{g-dg}_{gas}$	Mass of dry gas transformed into vapour	$[ML^{-3}]$
$\dot{E}^{w-v}_{H_2O}$	Mass of liquid water transformed into vapour	$[ML^{-3}]$
$[B]$	Transformation matrix for finite element methods	$[-]$

$[E^t]$	Local stiffness matrix of the current finite element	$[-]$
$\left[E^t_{GG}\right]$	Classical stiffness matrix for gas flow problems	$[-]$
$[E^t_{MM}]$	Classical stiffness matrix for mechanical problems	$[-]$
$[E^t_{WW}]$	Classical stiffness matrix for water flow problems	$[-]$
$\left[F^t_{OB}\right]$	Vector of the global out of balance forces	$[-]$
$\left[f^t_{OB}\right]$	Vector of the elementary out of balance forces	$[-]$
$[K^t]$	Global stiffness matrix	$[-]$
$[k^t]$	Local element stiffness matrix	$[-]$
$\left[K^t_{MG}\right]$	Coupling matrix of the mechanics influence on the gas	$[-]$
$[K^t_{MW}]$	Coupling matrix of the mechanics influence on the liquid	$[-]$
$\left[K^t_{WG}\right]$	Coupling matrix of the gas influence on the mechanics	$[-]$
$[K^t_{WM}]$	Coupling matrix of the liquid influence on the mechanics	$[-]$
$[K^t_{WW}]$	Classical stiffness matrix of the flow problem	$[-]$
$[T^t]$	Transformation matrix for finite element methods	$[-]$
$\left[U^{*,t}_{(Node)}\right]$	Vector of the virtual nodal variables	$[-]$
$\left[U^{*,t}_{(x_1,x_2)}\right]$	Vector of the virtual nodal variables for the current finite element	$[-]$
$\mathcal{F}$	Interpolation function	
$\mathcal{K}$	Brooks and Corey's model parameter	$[-]$
$\mathcal{L}$	Cubic formulation coefficient	$[-]$
$\mathcal{M}$	Mualem-van Genuchten coefficient	$[-]$
$\mathcal{N}$	van Genuchten's model parameter	$[-]$
A	Area or boundary surface area	$\left[L^2\right]$
A_i	Empirical parameter in the intrinsic permeability based models	$[-]$
b	Fracture aperture	$[L]$
b_0	initial fracture aperture	$[L]$
B_1, B_2	Shear band boundaries	$[L]$
B_φ	Friction softening coefficient	$[-]$
B_c	Cohesion softening coefficient	$[-]$
c	Cohesion	$[ML^{-1}T^{-2}]$
c_0, c_f	Initial and final cohesions	$[ML^{-1}T^{-2}]$
C_{ijkl}	Elastoplastic constitutive tangent tensor for small strains and rotations	$\left[ML^{-1}T^{-2}\right]$
C^e_{ijkl}	Hooke elastic stiffness tensor	$\left[ML^{-1}T^{-2}\right]$
C^p_{ijkl}	Plastic constitutive tangent tensor	$\left[ML^{-1}T^{-2}\right]$
D	Second gradient elastic modulus	$[MLT^{-2}]$

$d\left[U^t_{(\xi,\eta)}\right]$	Vector of the unknown increments of nodal variables for the parent finite element	$[-]$
$d\left[U^t_{(Node)}\right]$	Vector of the unknown increments of nodal variables	$[-]$
$d\left[U^t_{(x_1,x_2)}\right]$	Vector of the unknown increments of nodal variables for the current finite element	$[-]$
d_1, d_2	Yield surface parameters	$[-]$
$D_{\alpha/\beta}$	Diffusion coefficient of the species α through the phase β	$[L^2T^{-1}]$
$D^*_{\alpha/\beta}$	Effective diffusion coefficient of the species α through the phase β	$[L^2T^{-1}]$
$D_{dg/w}$	Diffusion coefficient of the dissolved gas in the liquid phase	$[L^2T^{-1}]$
$D^*_{dg/w}$	Effective diffusion coefficient of the dissolved gas in the liquid phase	$[L^2T^{-1}]$
D_{ijklmn}	Elastic constitutive tangent tensor for second gradient law	$[MLT^{-2}]$
D^e_{ijkl}	Elastic compliance tensor	$[M^{-1}LT^2]$
d_{max}	Maximum damage variable	$[-]$
$D_{v/g}$	Diffusion coefficient of the water vapour in the gaseous phase	$[L^2T^{-1}]$
$D^*_{v/g}$	Effective diffusion coefficient of the water vapour in the gaseous phase	$[L^2T^{-1}]$
dec_φ	Friction angle hardening shifting	$[-]$
dec_c	Cohesion softening shifting	$[-]$
e_{ijk}	Alternating tensor	$[-]$
f	Yield surface	$[-]$
f^{vp}	Visco-plastic yield surface	$[-]$
F_i	Force vector	$[ML^{-2}T^{-2}]$
$f_{dg,i}$	Mass flow of dissolved gas	$[ML^{-2}T^{-1}]$
F_E	Energetically equivalent external force vector	$[-]$
$f_{g,i}$	Mass flow of dry gas	$[ML^{-2}T^{-1}]$
F_{ij}	Macro-deformation field	$[-]$
F_I	Energetically equivalent internal force vector	$[-]$
$f_{v,i}$	Mass flow of water vapour	$[ML^{-2}T^{-1}]$
$f_{w,i}$	Mass flow of liquid water	$[ML^{-2}T^{-1}]$
$f_{w,L}$	Longitudinal fluid flow in contact element	$[ML^{-2}T^{-1}]$
$f_{w,N}$	Transversal fluid flow in contact element	$[ML^{-2}T^{-1}]$
G	Shear modulus	$[ML^{-1}T^{-2}]$
g_i	Gravity acceleration vector	$[LT^{-2}]$
g_N	gap function	$[L]$
g_T	Tangential displacement on the contact interface	$[L]$
H	Height	$[L]$
H_g	Henry's coefficient for dissolved gas	$[-]$

h_{ijk}	Microkinematic second gradient field	$[L^{-1}]$
I_σ	First invariant of the stress tensor	$\left[ML^{-1}T^{-2}\right]$
$i_{dg,i}$	Diffusive flux of dissolved gas	$[ML^{-2}T^{-1}]$
$i_{g,i}$	Diffusive flux of dry gas	$[ML^{-2}T^{-1}]$
$i_{v,i}$	Diffusive flux of water vapour	$[ML^{-2}T^{-1}]$
$II_{\hat{\sigma}}$	Second invariant of the stress tensor	$\left[ML^{-1}T^{-2}\right]$
$II^p_{\hat{\sigma}}$	Second invariant of stress tensor at plastic state	$[ML^{-1}T^{-2}]$
$III_{\hat{\sigma}}$	Third invariant of the stress tensor	$\left[ML^{-1}T^{-2}\right]$
J_{ij}	Jacobian matrix	$[-]$
K	Bulk modulus	$[ML^{-1}T^{-2}]$
K^{eq}_{da}	Equilibrium constant for dissolved gas	$[ML^{-1}T^{-2}]$
$k_{g,ij,0}$	Initial intrinsic gas permeability tensor	$[L^2]$
$k_{g,ij}$	Gas permeability	$[L^2]$
$k_{ij,0}$	Initial intrinsic permeability tensor	$[L^2]$
$k_{ij,D}$	Damaged permeability tensor	$[L^2]$
$k_{ij,frac}$	Intrinsic permeability of the rock	$[L^2]$
$k_{ij,matrix}$	Intrinsic permeability of the matrix	$[L^2]$
$k_{ij,UD}$	Undamaged permeability tensor	$[L^2]$
K^c_{ij}	Cosserat's micro-rotation gradient field (curvature)	$[L^-]$
k^{int}_{ij}	Intrinsic water permeability tensor	$[L^2]$
K^{sat}_{ij}	Hydraulic conductivity	$[LT^{-1}]$
k_{max}	Maximum permeability corresponding to d_{max}	$[L^2]$
K_N, K_T	Normal and tangential penalty coefficients	$[ML^{-2}T^{-2}]$
k_{r_g}	Gas relative permeability	$[-]$
k_{r_w}	Water relative permeability	$[-]$
$k_{w,ij,0}$	Initial intrinsic water permeability tensor	$[L^2]$
$k_{w,ij}$	Water permeability	$[L^2]$
L_c	Characteristic length of the macro-scale	$[L]$
l_c	Characteristic length of the microstructure	$[L]$
L_e	Effective length	$[L]$
L_{ij}	Macro-velocity gradient field	$\left[T^{-1}\right]$
m	Yield surface parameter	$[-]$
M_{dg}	Dissolved gas mass inside unit volume Ω	$[ML^{-3}]$
M_g	Dry gas mass inside unit volume Ω	$[ML^{-3}]$
M_v	Water vapour mass inside unit volume Ω	$[ML^{-3}]$

M_w	Liquid water mass inside unit volume Ω	$[ML^{-3}]$
n_i	Unit vector normal to the boundary	$[-]$
p'	Mean effective stress	$\left[ML^{-1}T^{-2}\right]$
p_g	gas pressure	$[ML^{-1}T^{-2}]$
p_w	Pore water pressure	$[ML^{-1}T^{-2}]$
p_c	Capillary pressure	$[ML^{-1}T^{-2}]$
p_N	Normal component of the contact stress vector	$[ML^{-1}T^{-2}]$
$P_{r,0}$	Initial value of van Genuchten's gas entry pressure	$[ML^{-1}T^{-2}]$
P_r	van Genuchten gas entry pressure	$[ML^{-1}T^{-2}]$
p_{thr}	Gas threshold pressure	$[ML^{-1}T^{-2}]$
$p_{v,0}$	Pressure of saturated water vapour	$[ML^{-1}T^{-2}]$
p_v	Partial pressure of water vapour	$[ML^{-1}T^{-2}]$
$p_{w,0}$	Initial pore water pressure on the tunnel wall	$[ML^{-1}T^{-2}]$
p_w^{Γ}	Pore water pressure on the tunnel wall	$[ML^{-1}T^{-2}]$
Q	Source/sink term	$[ML^{-3}T^{-1}]$
q	Invariant of deviatoric stress tensor	$\left[ML^{-1}T^{-2}\right]$
Q_g^g	Dry gas source/sink term	$[ML^{-3}T^{-1}]$
Q_g^w	Water vapour source/sink term	$[ML^{-3}T^{-1}]$
Q_l^g	Dissolved gas source/sink term	$[ML^{-3}T^{-1}]$
Q_l^w	Liquid water source/sink term	$[ML^{-3}T^{-1}]$
$q_{\alpha,i}$	Advective flux (Darcy velocity vector) of phase α	$[ML^{-2}T^{-1}]$
$q_{g,i}$	Advective flow vector of the gas phase	$[LT^{-1}]$
Q_g	Total gas Source/sink term	$[ML^{-3}T^{-1}]$
$q_{l,i}$	Advective flow vector of the liquid phase	$[LT^{-1}]$
$q_{w,i}$	Advective flow vector of the liquid water	$[LT^{-1}]$
Q_w	Total water Source/sink term	$[ML^{-3}T^{-1}]$
R	Universal gas constant	$[ML^2N^{-1}\theta^{-1}T^{-2}]$
r	Radius	$[L]$
r_{ij}	Macro-rotation field	$[-]$
r_{ij}^c	Cosserat's micro-rotation field	$[-]$
r_i^c	Cosserat's local rotation (dof)	$[-]$
RH	Relative humidity	$[-]$
s	Matrix suction	$[ML^{-1}T^{-2}]$
S_r^*	Normalised saturation	$[-]$
s_{GE}	Gas-entry pressure	$[ML^{-1}T^{-2}]$

S_{max}	Maximum degree of water saturation	$[-]$
s_{osm}	Osmotic suction	$[ML^{-1}T^{-2}]$
S_{r_w}	Water saturation degree	$[-]$
S_{r_g}	Gas saturation degree	$[-]$
$S_{r_{res}}$	Residual saturation	$[-]$
S_r	Saturation degree	$[-]$
s_t	Total suction	$[ML^{-1}T^{-2}]$
T	Absolute temperature	$[\theta]$
t_i	Traction vector or stress vector	$\left[ML^{-1}T^{-2}\right]$
T_s	Surface tension	$[ML^{-1}T^{-2}]$
T_w	Transmissivity	$[M^{-1}L^2T]$
u_i	Displacement vector	$[L]$
u_i^m	Microscale displacement field	$[L]$
v_i	Velocity vector	$\left[LT^{-1}\right]$
w	Characteristic distance between adjacent fractures in a specific rock	$[L]$
W_E^*	Virtual work of external forces	$[ML^2T^{-2}]$
w_{ij}	Spin rate tensor	$\left[T^{-1}\right]$
W_I^*	Virtual work of internal forces	$[ML^2T^{-2}]$
x_{da}	Mole fraction of dissolved gas	$[-]$
X_i	Coordinates in the reference configuration	$[L]$
x_i	Coordinates in the current configuration	$[L]$
YI	Yield index	$[-]$
YI^{thr}	Yield index threshold for the evolution of intrinsic permeability	$[-]$

Superscripts

$[.]^0, [.]^1$	Quantity outside and inside a shear band
$[.]^*$	Virtual quantity
$[.]^\tau, [.]^{\tau 1}, [.]^{\tau 2}$	Quantity at the end of time step in numerical iterative procedure
$[.]^f$	Quantity related to the fluctuation field for micro-scale fields
$[.]^M$	Quantity related to the macroscopic scale
$[.]^m$	Quantity related to the microscopic scale
$[.]^t$	Current value of a quantity at a given time t
$\dot{[.]}$	Time derivative
$\hat{[.]}$	Boundary condition of Dirichelet type
$\mathring{[.]}$	Non-local variable

Subscripts

$[.]_{\parallel}$	Quantity in the direction parallel to te isotropic bedding plane
$[.]_{\perp}$	Quantity in the direction perpendicular to te isotropic bedding plane
$[.]_{dH_2}$	Quantity related to the dissolved Hydrogen species
$[.]_g$	Quantity related to the gas phase
$[.]_{H_2}$	Quantity related to the dry Hydrogen species
$[.]_l$	Quantity related to the liquid phase
$[.]_n$	Normal part of a quantity
$[.]_s$	Quantity related to the solid phase
$[.]_t$	Tangential part of a quantity
$[.]_v$	Quantity related to the water vapour species
$[.]_w$	Quantity related to the liquid water species

Operators

$\circ$	Composition product of two linear operators
$\Delta[.]$	Discrete variation of a quantity
$\delta[.]$	Infinitesimal variation of a quantity
$\langle[.]\rangle$	Macaulay brackets
$D[.]$	Normal derivative of a quantity
$d[.]$	Variation of a quantity in numerical iterative procedure t

B List of Figures

C List of Tables

D Linearisation of the field equations for the second gradient H^{2}M model

The linearisation of the field Equations (III–63), (III–64), (III–65), and (III–66) of the second gradient H^{2}M model presented in Section 9, leading to the linear auxiliary problem of Equation (III–69), is detailed hereafter.

D.1 Balance equations

First of all, the weak formulation of the governing Equations (III–24), (III–26), (III–27) and (III–30) required to address boundary-value problems over large domains within a finite element framework is recalled.

$$\int_\Omega \left(\sigma_{ij} \frac{\partial u_i^*}{\partial x_j} + \Sigma_{ijk} \frac{\partial v_{ij}^*}{\partial x_k} - \lambda_{ij} \left(\frac{\partial u_i^*}{\partial x_j} - v_{ij}^* \right) \right) d\Omega = \int_\Omega \rho_{mix} g_i u_i^* d\Omega + \int_{\Gamma_\sigma} \left(\bar{t}_i u_i^* + \bar{T}_i v_{ik}^* n_k \right) d\Gamma \tag{D–1}$$

$$\int_\Omega \lambda_{ij}^* \left(\frac{\partial u_i}{\partial x_j} - v_{ij} \right) d\Omega = 0 \tag{D–2}$$

$$\int_\Omega \left[\dot{M}_w p_w^* + \dot{M}_v p_w^* - f_{w,i} \frac{\partial p_w^*}{\partial x_i} - f_{v,i} \frac{\partial p_w^*}{\partial x_i} \right] d\Omega = \int_\Omega Q_w p_w^* d\Omega - \int_{\Gamma_q} \bar{q}_w p_w^* d\Gamma \tag{D–3}$$

$$\int_\Omega \left[\dot{M}_g p_g^* + \dot{M}_{g^d} p_g^* - f_{g,i} \frac{\partial p_g^*}{\partial x_i} - f_{g^d,i} \frac{\partial p_g^*}{\partial x_i} \right] d\Omega = \int_\Omega Q_g p_g^* d\Omega - \int_{\Gamma_q} \bar{q}_g p_g^* d\Gamma \tag{D–4}$$

Since this system of highly non-linear relations is a priori not numerically satisfied at any instant t, an iterative procedure of Newton–Raphson type is employed. To this end, time discretisation into finite time steps Δt (Section 9.5.3) is prerequisite which leads to two configurations. One configuration Ω^t is assumed to be known and in equilibrium with the boundary conditions at a given time t of the loading, while the other configuration Ω^τ is not at equilibrium at a time ($\tau = t + \Delta t$). The objective of the iterative procedure is to find a new configuration in equilibrium at the end of the time step. Consequently, a first guess of this new configuration close to the solution but for which the equilibrium is not met is proposed and denoted as $\Omega^{\tau 1}$. Both configurations at time t and $\tau 1$ are assumed to be known and non-equilibrium forces, *i.e.* residuals $\Delta_1^{\tau 1}$, $\Delta_2^{\tau 1}$, $\Delta_3^{\tau 1}$ and $\Delta_4^{\tau 1}$ appear in the four governing equations respectively:

$$\begin{aligned} &\int_{\Omega^{\tau 1}} \left(\sigma_{ij}^{\tau 1} \frac{\partial u_i^*}{\partial x_j^{\tau 1}} + \Sigma_{ijk}^{\tau 1} \frac{\partial v_{ij}^*}{\partial x_k^{\tau 1}} \right) d\Omega^{\tau 1} - \int_{\Omega^{\tau 1}} \lambda_{ij}^{\tau 1} \left(\frac{\partial u_i^*}{\partial x_j^{\tau 1}} - v_{ij}^* \right) d\Omega^{\tau 1} \\ &\quad - \int_{\Omega^{\tau 1}} \rho_{mix}^{\tau 1} g_i u_i^* d\Omega^{\tau 1} - \int_{\Gamma_\sigma^{\tau 1}} \left(\bar{t}_i^{\tau 1} u_i^* + \bar{T}_i^{\tau 1} v_{ik}^* n_k^{\tau 1} \right) d\Gamma^{\tau 1} = \Delta_1^{\tau 1} \end{aligned} \tag{D–5}$$

$$\int_{\Omega^{\tau 1}} \lambda_{ij}^* \left(\frac{\partial u_i^{\tau 1}}{\partial x_j^{\tau 1}} - v_{ij}^{\tau 1} \right) d\Omega^{\tau 1} = \Delta_2^{\tau 1} \tag{D–6}$$

$$\int_{\Omega^{\tau 1}} \left[\dot{M}_w^{\tau 1} p_w^* + \dot{M}_v^{\tau 1} p_w^* - f_{w,i}^{\tau 1} \frac{\partial p_w^*}{\partial x_i^{\tau 1}} - f_{v,i}^{\tau 1} \frac{\partial p_w^*}{\partial x_i^{\tau 1}} \right] d\Omega^{\tau 1} - \int_{\Omega^{\tau 1}} Q_w^{\tau 1} p_w^* d\Omega^{\tau 1} + \int_{\Gamma^{\tau 1}} \bar{q}_w^{\tau 1} p_w^* d\Gamma^{\tau 1} = \Delta_3^{\tau 1} \tag{D–7}$$

$$\int_{\Omega^{\tau 1}} \left[\dot{M}_g^{\tau 1} p_g^* + \dot{M}_{dg}^{\tau 1} p_g^* - f_{g,i}^{\tau 1} \frac{\partial p_g^*}{\partial x_i^{\tau 1}} - f_{dg,i}^{\tau 1} \frac{\partial p_g^*}{\partial x_i^{\tau 1}} \right] d\Omega^{\tau 1} - \int_{\Omega^{\tau 1}} Q_g^{\tau 1} p_g^* d\Omega^{\tau 1} + \int_{\Gamma^{\tau 1}} \bar{q}_g^{\tau 1} p_g^* d\Gamma^{\tau 1} = \Delta_4^{\tau 1} \tag{D–8}$$

The aim is now to find another configuration denoted $\Omega^{\tau 2}$ close to $\Omega^{\tau 1}$ for which the non-equilibrium forces (residuals) vanish:

$$\begin{aligned}&\int_{\Omega^{\tau 2}}\left(\sigma_{ij}^{\tau 2}\frac{\partial u_i^*}{\partial x_j^{\tau 2}}+\Sigma_{ijk}^{\tau 2}\frac{\partial v_{ij}^*}{\partial x_k^{\tau 2}}\right)d\Omega^{\tau 2}-\int_{\Omega^{\tau 2}}\lambda_{ij}^{\tau 2}\left(\frac{\partial u_i^*}{\partial x_j^{\tau 2}}-v_{ij}^*\right)d\Omega^{\tau 2}\\&-\int_{\Omega^{\tau 2}}\rho_{mix}^{\tau 2}g_i u_i^* d\Omega^{\tau 2}-\int_{\Gamma_\sigma^{\tau 2}}\left(\bar{t}_i^{\tau 2}u_i^*+\bar{T}_i^{\tau 2}v_{ik}^* n_k^{\tau 2}\right)d\Gamma^{\tau 2}=0\end{aligned}\tag{D–9}$$

$$\int_{\Omega^{\tau 2}}\lambda_{ij}^*\left(\frac{\partial u_i^{\tau 2}}{\partial x_j^{\tau 2}}-v_{ij}^{\tau 2}\right)d\Omega^{\tau 2}=0\tag{D–10}$$

$$\int_{\Omega^{\tau 2}}\left[\dot{M}_w^{\tau 2}p_w^*+\dot{M}_v^{\tau 2}p_w^*-f_{w,i}^{\tau 2}\frac{\partial p_w^*}{\partial x_i^{\tau 2}}-f_{v,i}^{\tau 2}\frac{\partial p_w^*}{\partial x_i^{\tau 2}}\right]d\Omega^{\tau 2}-\int_{\Omega^{\tau 2}}Q_w^{\tau 2}p_w^* d\Omega^{\tau 2}+\int_{\Gamma^{\tau 2}}\bar{q}_w^{\tau 2}p_w^* d\Gamma^{\tau 2}=0\tag{D–11}$$

$$\int_{\Omega^{\tau 2}}\left[\dot{M}_g^{\tau 2}p_g^*+\dot{M}_{dg}^{\tau 2}p_g^*-f_{g,i}^{\tau 2}\frac{\partial p_g^*}{\partial x_i^{\tau 2}}-f_{dg,i}^{\tau 2}\frac{\partial p_g^*}{\partial x_i^{\tau 2}}\right]d\Omega^{\tau 2}-\int_{\Omega^{\tau 2}}Q_g^{\tau 2}p_g^* d\Omega^{\tau 2}+\int_{\Gamma^{\tau 2}}\bar{q}_g^{\tau 2}p_g^* d\Gamma^{\tau 2}=0\tag{D–12}$$

Rewriting the field equations related to $\Omega^{\tau 2}$ in configuration $\Omega^{\tau 1}$ (using the Jacobian transformation), assuming in addition that g_i, $\bar{t}_i$, $\bar{q}_w$, $\bar{q}_g$, Q_w, Q_g are independent of the different unknown fields, and that $\overline{T}_i$ vanishes, and subtracting after all the balance equations for the two configurations yields:

$$\begin{aligned}&\int_{\Omega^{\tau 1}}\frac{\partial u_i^*}{\partial x_l^{\tau 1}}\left(\sigma_{ij}^{\tau 2}\frac{\partial x_l^{\tau 1}}{\partial x_j^{\tau 2}}det(F)-\sigma_{il}^{\tau 1}\right)+\frac{\partial v_{ij}^*}{\partial x_l^{\tau 1}}\left(\Sigma_{ijk}^{\tau 2}\frac{\partial x_l^{\tau 1}}{\partial x_k^{\tau 2}}det(F)-\Sigma_{ijl}^{\tau 1}\right)d\Omega^{\tau 1}\\&-\frac{\partial u_i^*}{\partial x_l^{\tau 1}}\left(\lambda_{ij}^{\tau 2}\frac{\partial x_l^{\tau 1}}{\partial x_j^{\tau 2}}det(F)-\lambda_{il}^{\tau 1}\right)-v_{ij}^*\left(\lambda_{ij}^{\tau 2}det(F)-\lambda_{ij}^{\tau 1}\right)\\&-u_i^*\left(\rho_{mix}^{\tau 2}det(F)-\rho_{mix}^{\tau 1}\right)g_i d\Omega^{\tau 1}=-\Delta_1^{\tau 1}\end{aligned}\tag{D–13}$$

$$\int_{\Omega^{\tau 1}}\lambda_{ij}^*\left(\frac{\partial u_i^{\tau 2}}{\partial x_k^{\tau 1}}\frac{\partial x_k^{\tau 1}}{\partial x_j^{\tau 2}}det(F)-\frac{\partial u_i^{\tau 1}}{\partial x_1^{\tau 1}}\right)-\lambda_{ij}^*\left(v_{ij}^{\tau 2}det(F)-v_{ij}^{\tau 1}\right)d\Omega^{\tau 1}=-\Delta_2^{\tau 1}\tag{D–14}$$

$$\begin{aligned}&\int_{\Omega^{\tau 1}}p_w^*\left(\dot{M}_w^{\tau 2}det(F)+\dot{M}_v^{\tau 2}det(F)-\dot{M}_w^{\tau 1}-\dot{M}_v^{\tau 1}\right)\\&-\frac{\partial p_w^*}{\partial x_k^{\tau 1}}\left(f_{w,i}^{\tau 2}\frac{\partial x_k^{\tau 1}}{\partial x_j^{\tau 2}}det(F)+f_{v,i}^{\tau 2}\frac{\partial x_k^{\tau 1}}{\partial x_j^{\tau 2}}det(F)-f_{w,k}^{\tau 1}-f_{v,k}^{\tau 1}\right)d\Omega^{\tau 1}=-\Delta_3^{\tau 1}\end{aligned}\tag{D–15}$$

$$\begin{aligned}&\int_{\Omega^{\tau 1}}p_g^*\left(\dot{M}_g^{\tau 2}det(F)+\dot{M}_{dg}^{\tau 2}det(F)-\dot{M}_g^{\tau 1}-\dot{M}_{dg}^{\tau 1}\right)\\&-\frac{\partial p_g^*}{\partial x_k^{\tau 1}}\left(f_{g,i}^{\tau 2}\frac{\partial x_k^{\tau 1}}{\partial x_j^{\tau 2}}det(F)+f_{dg,i}^{\tau 2}\frac{\partial x_k^{\tau 1}}{\partial x_j^{\tau 2}}det(F)-f_{g,k}^{\tau 1}-f_{dg,k}^{\tau 1}\right)d\Omega^{\tau 1}=-\Delta_4^{\tau 1}\end{aligned}\tag{D–16}$$

where $\frac{\partial x_i^{\tau 2}}{\partial x_j^{\tau 1}}$ is the Jacobian matrix of the transformation between the two configurations, and $det(F)=\left|\frac{\partial x_i^{\tau 2}}{\partial x_j^{\tau 1}}\right|$ is the Jacobian determinant.

D.2 Variations

By making the two configurations tend towards each other, which leads to the limit $\tau 2 = \tau 1$ the variations of the quantities of the problem can be defined as:

$$du_i^t = x_i^{\tau 2} - x_i^{\tau 1} \quad \text{(D–17)} \qquad d\nu_{ij}^t = \nu_{ij}^{\tau 2} - \nu_{ij}^{\tau 1} \quad \text{(D–18)} \qquad d\lambda_{ij}^t = \lambda_{ij}^{\tau 2} - \lambda_{ij}^{\tau 1} \quad \text{(D–19)}$$

$$d\sigma_{ij}^t = \sigma_{ij}^{\tau 2} - \sigma_{ij}^{\tau 1} = d\sigma_{ij}'^t + bS_{r_w}^t dp_w^t \delta_{ij} + b(1 - S_{r_w}^t) dp_g^t \delta_{ij} \quad \text{(D–20)} \quad d\Sigma_{ijk}^t = \Sigma_{ijk}^{\tau 2} - \Sigma_{ijk}^{\tau 1} \quad \text{(D–21)}$$

$$d\rho_w^t = \rho_w^{\tau 2} - \rho_w^{\tau 1} = \rho_w^t \frac{dp_w^t}{\chi_w} \quad \text{(D–22)} \qquad d\rho_g^t = \rho_g^{\tau 2} - \rho_g^{\tau 1} = \frac{m_{H_2}}{RT} p_{H_2}^t + \frac{m_v}{RT} p_v^t \quad \text{(D–23)}$$

$$d\rho_s^t = \rho_s^{\tau 2} - \rho_s^{\tau 1} = \frac{(b - \phi^t)(S_r^{w,t} dp_w^t + (1 - S_r^{w,t}) dp_g^t) + d\sigma'^t}{(1 - \phi^t) K_s} \quad \text{(D–24)}$$

$$d\phi^t = \phi^{\tau 2} - \phi^{\tau 1} = (b - \phi^t) \left[\frac{S_r^{w,t}}{K_s} dp_w^t + \frac{1 - S_r^{w,t}}{K_s} dp_g^t + d\varepsilon_v^t \right] \quad \text{(D–25)}$$

$$d\varepsilon_v^t = \frac{d\Omega^t}{\Omega^t} = \frac{\partial du_i^t}{\partial x_i^t} \quad \text{(D–26)}$$

$$d\sigma_{il}^{\tau 1} = \sigma_{il}^{\tau 2} - \sigma_{ij}^{\tau 1} = d\sigma_{ij}'^{\tau 1} - bS_r^{w,\tau 1} dp_w^{\tau 1} \delta_{ij} - bS_r^{g,\tau 1} dp_g^{\tau 1} \delta_{ij} \quad \text{(D–27)}$$

Moreover, the Jacobian matrix $\bar{F}_{ij}$ of the transformation between the two configurations $\Omega^{\tau 1}$ and $\Omega^{\tau 2}$ is approximated by using a Taylor expansion and by retaining only the linear approximation [Chambon and Moullet, 2004], meaning that the terms of degree greater than one are discarded:

$$\bar{F}_{ij} = \frac{\partial x_i^{\tau 2}}{\partial x_j^{\tau 1}} = \frac{\partial (x_i^{\tau 1} + du_i^{\tau 1})}{\partial x_j^{\tau 1}} \approx \delta_{ij} + \frac{\partial du_i^{\tau 1}}{\partial x_j^{\tau 1}} \quad \text{(D–28)}$$

The Jacobian determinant becomes:

$$\det(F) = \left| \frac{\partial x_i^{\tau 2}}{\partial x_j^{\tau 1}} \right| \approx 1 + \frac{\partial du_i^{\tau 1}}{\partial x_j^{\tau 1}} \quad \text{(D–29)}$$

Similarly and by applying the limit $\tau 2 = \tau 1$, the inverse relation yields:

$$\frac{\partial x_i^{\tau 1}}{\partial x_j^{\tau 2}} = \frac{\partial (x_i^{\tau 2} - du_i^{\tau 1})}{\partial x_j^{\tau 2}} \approx \delta_{ij} + \frac{\partial du_i^{\tau 1}}{\partial x_j^{\tau 2}} \approx \delta_{ij} - \frac{\partial du_i^{\tau 1}}{\partial x_j^{\tau 1}} \quad \text{(D–30)}$$

D.3 Linearisation

D.3.1 Balance of momentum of the mixture

The developments relative to the momentum balance equation of the mixture (D–13) are firstly considered.

The first term can be rewritten as:

$$\begin{aligned}
\sigma_{ij}^{\tau 2}\frac{\partial x_l^{\tau 1}}{\partial x_j^{\tau 2}}det(F)-\sigma_{il}^{\tau 1} &= \sigma_{ij}^{\tau 2}\left(\delta_{jl}-\frac{\partial(x_l^{\tau 2}-x_l^{\tau 1})}{\partial x_j^{\tau 2}}\right)\det(F)-\sigma_{il}^{\tau 1}\\
&= \sigma_{il}^{\tau 2}\det(F)-\sigma_{ij}^{\tau 2}\frac{\partial(x_l^{\tau 2}-x_l^{\tau 1})}{\partial x_j^{\tau 2}}\det(F)-\sigma_{il}^{\tau 1}\\
&= \underbrace{\sigma_{il}^{\tau 2}\det(F)-\sigma_{il}^{\tau 2}}-\sigma_{ij}^{\tau 2}\frac{\partial(x_l^{\tau 2}-x_l^{\tau 1})}{\partial x_j^{\tau 2}}\det(F)\underbrace{-\sigma_{il}^{\tau 1}+\sigma_{il}^{\tau 2}}\\
&= (\sigma_{il}^{\tau 2}-\sigma_{il}^{\tau 1})-\sigma_{ij}^{\tau 2}\frac{\partial(x_l^{\tau 2}-x_l^{\tau 1})}{\partial x_j^{\tau 2}}\det(F)+\sigma_{il}^{\tau 2}(\det(F)-1)\\
&= d\sigma_{il}^{\tau 1}-\sigma_{ij}^{\tau 1}\underbrace{\frac{\partial du_l^{\tau 1}}{\partial x_j^{\tau 1}}\left(1+\frac{\partial du_l^{\tau 1}}{\partial x_j^{\tau 1}}\right)}_{\frac{\partial_{du_l^{\tau 1}}}{\partial_{x_j^{\tau 1}}}}+\sigma_{il}^{\tau 1}\underbrace{\left(1+\frac{\partial du_m^{\tau 1}}{\partial x_m^{\tau 1}}-1\right)}_{\frac{\partial_{du_m^{\tau 1}}}{\partial_{x_m^{\tau 1}}}}\\
&= d\sigma_{il}^{\tau 1}-\sigma_{ij}^{\tau 1}\frac{\partial du_l^{\tau 1}}{\partial x_j^{\tau 1}}+\sigma_{il}^{\tau 1}\frac{\partial du_m^{\tau 1}}{\partial x_m^{\tau 1}}
\end{aligned} \tag{D–31}$$

Where the terms of order higher than one are neglected.

The second term of equation (D–13) is obtained with similar developments, including the densities and porosity variations:

$$\begin{aligned}
&\rho_{mix}^{\tau 2}det(F)-\rho_{mix}^{\tau 1}=\rho_{mix}^{\tau 2}\left(1+\frac{\partial du_i^{\tau 1}}{\partial x_j^{\tau 1}}\right)-\rho_{mix}^{\tau 1}=d\rho_{mix}^{\tau 1}+\rho_{mix}^{\tau 1}\frac{\partial du_m^{\tau 1}}{\partial x_m^{\tau 1}}\\
&=d\rho_s^{\tau 1}(1-\phi^{\tau 1})-\rho_s^{\tau 1}d\phi^{\tau 1}+\ d\rho_w^{\tau 1}S_r^{w,\tau 1}\phi^{\tau 1}+\rho_w^{\tau 1}dS_r^{w,\tau 1}\phi^{\tau 1}+\rho_w^{\tau 1}S_r^{w,\tau 1}d\phi^{\tau 1}\\
&+d\rho_g^{\tau 1}(1-S_r^{w,\tau 1})\phi^{\tau 1}-\rho_g^{\tau 1}dS_r^{w,\tau 1}\phi^{\tau 1}+\rho_g^{\tau 1}(1-S_r^{w,\tau 1})d\phi^{\tau 1}\\
&+\ \left(\rho_s^{\tau 1}(1-\phi^{\tau 1})+\rho_w^{\tau 1}S_r^{w,\tau 1}\phi^{\tau 1}+\rho_g^{\tau 1}(1-S_r^{w,\tau 1})\phi^{\tau 1}\right)\frac{\partial du_m^{\tau 1}}{\partial x_m^{\tau 1}}\\
&=\rho_s^{\tau 1}\frac{(b-\phi^{\tau 1})(S_r^{w,\tau 1}dp_w^{\tau 1}+S_r^{g,\tau 1}dp_g)-d\sigma'^{\tau 1}}{\cancel{(1-\phi^{\tau 1})}K_s}\cancel{(1-\phi^{\tau 1})}\\
&-\ \left(\rho_s^{\tau 1}-\rho_w^{\tau 1}S_r^{w,\tau 1}-\rho_g^{\tau 1}(1-S_r^{w,\tau 1})\right)(1-\phi^{\tau 1})\left(\frac{(b-\phi^{\tau 1})(S_r^{w,\tau 1}dp_w^{\tau 1}+S_r^{g,\tau 1}dp_g)-d\sigma'^{\tau 1}}{(1-\phi^{\tau 1})K_s}+d\varepsilon_v^{\tau 1}\right)\\
&+\rho_w^{\tau 1}dS_r^{w,\tau 1}\phi^{\tau 1}+\rho_g^{\tau 1}(1-S_r^{w,\tau 1})\phi^{\tau 1}\\
&+\rho_w^{\tau 1}\frac{p_w^{\tau 1}}{\chi_w}S_r^{w,\tau 1}\phi^{\tau 1}+\left(d\rho_g^{\tau 1}+d\rho_v^{\tau 1}\right)(1-S_r^{w,\tau 1})\phi^{\tau 1}\\
&+\ \left(\rho_s^{\tau 1}(1-\phi^{\tau 1})+\rho_w^{\tau 1}S_r^{w,\tau 1}\phi^{\tau 1}+\rho_g^{\tau 1}(1-S_r^{w,\tau 1})\phi^{\tau 1}\right)\frac{\partial du_m^{\tau 1}}{\partial x_m^{\tau 1}}
\end{aligned} \tag{D–32}$$

Taking the following developments into account:

$$\sigma_{ij}^{\tau 2}\frac{\partial x_l^{\tau 1}}{\partial x_j^{\tau 2}}det(F)-\sigma_{il}^{\tau 1}=C_{ilnp}\frac{\partial du_n^{\tau 1}}{\partial x_p^{\tau 1}}-bS_r^{w,\tau 1}dp_w^{\tau 1}\delta_{ij}^{\tau 1}-\sigma_{ij}^{\tau 1}\frac{\partial du_l^{\tau 1}}{\partial x_j^{\tau 1}}+\sigma_{il}^{\tau 1}\frac{\partial du_m^{\tau 1}}{\partial x_m^{\tau 1}} \tag{D–33}$$

$$\Sigma_{ijk}^{\tau 2}\frac{\partial x_l^{\tau 1}}{\partial x_k^{\tau 2}}det(F)-\Sigma_{ijl}^{\tau 1}=d\Sigma_{ijl}^{\tau 1}-\Sigma_{ijk}^{\tau 1}\frac{\partial du_l^{\tau 1}}{\partial x_k^{\tau 1}}+\Sigma_{ijl}^{\tau 1}\frac{\partial du_m^{\tau 1}}{\partial x_m^{\tau 1}} \tag{D–34}$$

$$\lambda_{ij}^{\tau 2}\frac{\partial x_l^{\tau 1}}{\partial x_j^{\tau 2}}det(F)-\lambda_{il}^{\tau 1}=d\lambda_{il}^{\tau 1}-\lambda_{ij}^{\tau 1}\frac{\partial du_l^{\tau 1}}{\partial x_j^{\tau 1}}+\lambda_{il}^{\tau 1}\frac{\partial du_m^{\tau 1}}{\partial x_m^{\tau 1}} \tag{D–35}$$

$$\lambda_{ij}^{\tau 2}det(F)-\lambda_{ij}^{\tau 1}=d\lambda_{ij}^{\tau 1}+\lambda_{ij}^{\tau 1}\frac{\partial du_m^{\tau 1}}{\partial x_m^{\tau 1}} \tag{D–36}$$

The balance of momentum of the mixture can be written as:

$$\begin{aligned}
&\int_{\Omega^{\tau 1}}\frac{\partial u_l^*}{\partial x_k^{\tau 1}}\left(C_{ilnp}\frac{\partial du_n^{\tau 1}}{\partial x_p^{\tau 1}}-bS_r^{w,\tau 1}dp_w^{\tau 1}\delta_{ij}^{\tau 1}-\sigma_{ij}^{\tau 1}\frac{\partial du_l^{\tau 1}}{\partial x_j^{\tau 1}}+\sigma_{il}^{\tau 1}\frac{\partial du_m^{\tau 1}}{\partial x_m^{\tau 1}}\right)\\
&+\frac{\partial \nu_{ij}^*}{\partial x_l^{\tau 1}}\left(d\Sigma_{ijl}^{\tau 1}-\Sigma_{ijk}^{\tau 1}\frac{\partial du_l^{\tau 1}}{\partial x_k^{\tau 1}}+\Sigma_{ijl}^{\tau 1}\frac{\partial du_m^{\tau 1}}{\partial x_m^{\tau 1}}\right)d\Omega^{\tau 1}\\
&-\int_{\Omega^{\tau 1}}\frac{\partial u_i^*}{\partial x_l^{\tau 1}}\left(d\lambda_{il}^{\tau 1}-\lambda_{ij}^{\tau 1}\frac{\partial du_l^{\tau 1}}{\partial x_j^{\tau 1}}+\lambda_{il}^{\tau 1}\frac{\partial du_m^{\tau 1}}{\partial x_m^{\tau 1}}\right)-\nu_{ij}^*\left(d\lambda_{ij}^{\tau 1}+\lambda_{ij}^{\tau 1}\frac{\partial du_m^{\tau 1}}{\partial x_m^{\tau 1}}\right)d\Omega^{\tau 1}\\
&-\int_{\Omega^{\tau 1}}u_i^*\Bigg\{\rho_s^{\tau 1}\frac{(b-\phi^{\tau 1})(S_r^{w,\tau 1}dp_w^{\tau 1}+S_r^{g,\tau 1}dp_g^{\tau 1})-d\sigma'^{\tau 1}}{K_s}\\
&-\left(\rho_s^{\tau 1}-\rho_w^{\tau 1}S_r^{w,\tau 1}-\rho_g^{\tau 1}(1-S_r^{w,\tau 1})\right)(1-\phi^{\tau 1})\left(\frac{(b-\phi^{\tau 1})(S_r^{w,\tau 1}dp_w^{\tau 1}+S_r^{w,\tau 1}dp_w^{\tau 1})-d\sigma'^{\tau 1}}{(1-\phi^{\tau 1})K_s}+d\varepsilon_v^{\tau 1}\right)\\
&+\rho_w^{\tau 1}dS_r^{w,\tau 1}\phi^{\tau 1}+\rho_g^{\tau 1}(1-S_r^{w,\tau 1})\phi^{\tau 1}+\rho_w^{\tau 1}\frac{dp_w^{\tau 1}}{\chi_w}S_r^{w,\tau 1}\phi^{\tau 1}+(d\rho_g^{\tau 1}+d\rho_v^{\tau 1})(1-S_r^{w,\tau 1})\phi^{\tau 1}\\
&+\left(\rho_s^{\tau 1}(1-\phi^{\tau 1})+\rho_w^{\tau 1}S_r^{w,\tau 1}\phi^{\tau 1}+\rho_g^{\tau 1}(1-S_r^{w,\tau 1})\phi^{\tau 1}\right)\frac{\partial du_m^{\tau 1}}{\partial x_m^{\tau 1}}\Bigg\}g_i d\Omega^{\tau 1}\\
&=-\Delta_1^{\tau 1}
\end{aligned} \tag{D–37}$$

D.3.2 Kinematic constraint

The kinematic constraint corresponding to micro-macro continuity of the deformation gradient fields is given by Equation (D–14).

The first term of this equation is written:

$$\begin{aligned}
\frac{\partial u_i^{\tau 2}}{\partial x_k^{\tau 1}}\frac{\partial x_k^{\tau 1}}{\partial x_j^{\tau 2}}det(F)-\frac{\partial u_i^{\tau 1}}{\partial x_1^{\tau 1}}&=\left(\frac{\partial u_i^{\tau 1}}{\partial x_k^{\tau 1}}+\frac{\partial du_i^{\tau 1}}{\partial x_k^{\tau 1}}\right)\left(\delta_{jk}-\frac{\partial du_k^{\tau 1}}{\partial x_j^{\tau 2}}\right)det(F)-\frac{\partial u_i^{\tau 1}}{\partial x_j^{\tau 1}}\\
&=\frac{\partial u_i^{\tau 1}}{\partial x_j^{\tau 1}}det(F)+\frac{\partial du_i^{\tau 1}}{\partial x_j^{\tau 1}}det(F)-\frac{\partial u_i^{\tau 1}}{\partial x_k^{\tau 1}}\frac{\partial du_k^{\tau 1}}{\partial x_j^{\tau 2}}det(F)\\
&-\frac{\partial du_i^{\tau 1}}{\partial x_k^{\tau 1}}\frac{\partial du_k^{\tau 1}}{\partial x_j^{\tau 2}}det(F)-\frac{\partial u_i^{\tau 1}}{\partial x_j^{\tau 1}}
\end{aligned} \tag{D–38}$$

As previously, by making the two configurations tend towards each other ($\tau 2=\tau 1$) and by neglecting terms of order higher than one, it becomes:

$$\frac{\partial u_i^{\tau 2}}{\partial x_k^{\tau 1}}\frac{\partial x_k^{\tau 1}}{\partial x_j^{\tau 2}}det(F)-\frac{\partial u_i^{\tau 1}}{\partial x_1^{\tau 1}}=\frac{\partial u_i^{\tau 1}}{\partial x_j^{\tau 1}}+\frac{\partial u_i^{\tau 1}}{\partial x_j^{\tau 1}}\frac{\partial du_m^{\tau 1}}{\partial x_m^{\tau 1}}-\frac{\partial u_i^{\tau 1}}{\partial x_k^{\tau 1}}\frac{\partial du_k^{\tau 1}}{\partial x_j^{\tau 1}} \tag{D–39}$$

The second term of the equation reads:

$$v_{ij}^{\tau 2}det(F)-v_{ij}^{\tau 1}=d\nu_{ij}^{\tau 1}+\nu_{ij}\frac{\partial du_m^{\tau 1}}{\partial x_m^{\tau 1}} \tag{D–40}$$

Thus the equation becomes:

$$\int_{\Omega^{\tau 1}}\lambda_{ij}^*\left(\left(\frac{\partial u_i^{\tau 1}}{\partial x_j^{\tau 1}}-\nu_{ij}^{\tau 1}\right)\frac{\partial du_m^{\tau 1}}{\partial x_m^{\tau 1}}+\frac{\partial du_i^{\tau 1}}{\partial x_j^{\tau 1}}-\frac{\partial u_i^{\tau 1}}{\partial x_k^{\tau 1}}\frac{\partial du_k^{\tau 1}}{\partial x_j^{\tau 1}}-d\nu_{ij}^{\tau 1}\right)d\Omega^{\tau 1}=-\Delta_2^{\tau 1} \tag{D–41}$$

D.3.3 Water mass balance equation

The developments relative to the mass balance Equation (D–15) are now treated.
The first term of this equation is written as:

$$\dot{M}_w^{\tau 2} det(F) + \dot{M}_v^{\tau 2} det(F) - \dot{M}_w^{\tau 1} - \dot{M}_v^{\tau 1} = \dot{M}_w^{\tau 2}\left(1+\frac{\partial du_i^{\tau 1}}{\partial x_j^{\tau 1}}\right) + \dot{M}_v^{\tau 2}\left(1+\frac{\partial du_i^{\tau 1}}{\partial x_j^{\tau 1}}\right) - \dot{M}_w^{\tau 1} - \dot{M}_v^{\tau 1}$$

$$= \underbrace{d\dot{M}_w^{\tau 1}}_{\textbf{(1)}} + \underbrace{\dot{M}_w^{\tau 1}\frac{\partial du_m^{\tau 1}}{\partial x_m^{\tau 1}}}_{\textbf{(3)}} + \underbrace{d\dot{M}_v^{\tau 1}}_{\textbf{(2)}} + \underbrace{\dot{M}_v^{\tau 1}\frac{\partial du_m^{\tau 1}}{\partial x_m^{\tau 1}}}_{\textbf{(4)}}$$

$$= \underbrace{\underbrace{\dot{\rho}_w^{\tau 1}\phi^{\tau 1}S_r^{w,\tau 1}}_{\textbf{(1.1)}} + \underbrace{\rho_w^{\tau 1}\dot{\phi}^{\tau 1}S_r^{w,\tau 1}}_{\textbf{(1.2)}} + \underbrace{\rho_w^{\tau 1}\phi^{\tau 1}\dot{S}_r^{w,\tau 1}}_{\textbf{(1.3)}}}_{\textbf{(1)}} + \underbrace{\underbrace{\dot{\rho}_v^{\tau 1}\phi^{\tau 1}S_r^{g,\tau 1}}_{\textbf{(2.1)}} + \underbrace{\rho_v^{\tau 1}\dot{\phi}^{\tau 1}S_r^{g,\tau 1}}_{\textbf{(2.2)}} + \underbrace{\rho_v^{\tau 1}\phi^{\tau 1}\dot{S}_r^{g,\tau 1}}_{\textbf{(2.3)}}}_{\textbf{(2)}} + \underbrace{\dot{M}_w^{\tau 1}\frac{\partial du_m^{\tau 1}}{\partial x_m^{\tau 1}}}_{\textbf{(3)}} + \underbrace{\dot{M}_v^{\tau 1}\frac{\partial du_m^{\tau 1}}{\partial x_m^{\tau 1}}}_{\textbf{(4)}}$$

$$= \underbrace{d\rho_w^{\tau 1}\frac{\dot{p}_w^{\tau 1}}{\chi_w}\phi^{\tau 1}S_{r_w}^{\tau 1} + \rho_{w^{\tau 1}}\frac{d\dot{p}_w^{\tau 1}}{\chi_w}\phi^{\tau 1}S_{r_w}^{\tau 1} + \rho_w^{\tau 1}\frac{\dot{p}_w^{\tau 1}}{\chi_w}d\phi^{\tau 1}S_{r_w}^{\tau 1} + \rho_w^{\tau 1}\frac{\dot{p}_w^{\tau 1}}{\chi_w}\phi^{\tau 1}dS_{r_w}^{\tau 1}}_{\textbf{(1.1)}}$$

$$+ d\rho_w^{\tau 1}\cancel{(1-\phi^{\tau 1})}\frac{(b-\phi^{\tau 1})(S_{r_w}^{\tau 1}\dot{p}_w^{\tau 1} + S_{r_g}^{\tau 1}\dot{p}_g^{\tau 1})}{\cancel{(1-\phi^{\tau 1})}K_s}S_{r_w}^{\tau 1} - \rho_w^{\tau 1}\cancel{(1-\phi^{\tau 1})}\frac{d\phi^{\tau 1}(S_{r_w}^{\tau 1}\dot{p}_w^{\tau 1} + S_{r_g}^{\tau 1}\dot{p}_g^{\tau 1})}{\cancel{(1-\phi^{\tau 1})}K_s}S_{r_w}^{\tau 1}$$

$$+ \rho_w^{\tau 1}\cancel{(1-\phi^{\tau 1})}\frac{(b-\phi^{\tau 1})(2S_{r_w}^{\tau 1}dS_{r_w}^{\tau 1}\dot{p}_w^{\tau 1} + dS_{r_w}^{\tau 1}S_{r_w}^{\tau 1}\dot{p}_g^{\tau 1})}{\cancel{(1-\phi^{\tau 1})}K_s} + \rho_w^{\tau 1}\cancel{(1-\phi^{\tau 1})}\frac{(b-\phi^{\tau 1})(S_{r_w}^{\tau 1}d\dot{p}_w^{\tau 1} + S_{r_w}^{\tau 1}d\dot{p}_g^{\tau 1})}{\cancel{(1-\phi^{\tau 1})}K_s}S_{r_g}^{\tau 1}$$

$$+ \rho_w^{\tau 1}\cancel{(1-\phi^{\tau 1})}\frac{(b-\phi^{\tau 1})(dS_{r_g}^{\tau 1}\dot{p}_g^{\tau 1})}{\cancel{(1-\phi^{\tau 1})}K_s}S_{r_w}^{\tau 1}$$

$$+ \underbrace{d\rho_w^{\tau 1}\left((1-\phi^{\tau 1})\dot{\varepsilon}_v^{\tau 1} - \frac{\dot{\sigma}'^{\tau 1}}{K_s}\right)S_{r_w}^{\tau 1} + \rho_w^{\tau 1}\left((1-\phi^{\tau 1})d\dot{\varepsilon}_v^{\tau 1} - \frac{d\dot{\sigma}'^{\tau 1}}{K_s}\right)S_{r_w}^{\tau 1} + \rho_w^{\tau 1}\left((1-\phi^{\tau 1})\dot{\varepsilon}_v^{\tau 1} - \frac{\dot{\sigma}'^{\tau 1}}{K_s}\right)dS_{r_w}^{\tau 1}}_{\textbf{(1.2)}}$$

$$+ \underbrace{d\rho_w^{\tau 1}\phi^{\tau 1}\dot{S}_{r_w}^{\tau 1} + \rho_w^{\tau 1}d\phi^{\tau 1}\dot{S}_{r_w}^{\tau 1} + \rho_w^{\tau 1}\phi^{\tau 1}d\dot{S}_{r_w}^{\tau 1}}_{\textbf{(1.3)}} + \underbrace{\frac{m_v}{RT}d\dot{p}_v^{\tau 1}\phi^{\tau 1}S_r^{g,\tau 1} + \frac{m_v}{RT}\dot{p}_v^{\tau 1}d\phi^{\tau 1}S_r^{g,\tau 1} + \frac{m_v}{RT}\dot{p}_v^{\tau 1}\phi^{\tau 1}dS_r^{g,\tau 1}}_{\textbf{(2.1)}}$$

$$+ d\rho_v^{\tau 1}\cancel{(1-\phi^{\tau 1})}\frac{(b-\phi^{\tau 1})(S_r^{w,\tau 1}\dot{p}_w^{\tau 1} + S_r^{g,\tau 1}\dot{p}_g^{\tau 1})}{\cancel{(1-\phi^{\tau 1})}K_s}S_r^{g,\tau 1} - \rho_v^{\tau 1}\cancel{(1-\phi^{\tau 1})}\frac{d\phi^{\tau 1}(S_r^{w,\tau 1}\dot{p}_w^{\tau 1} + S_r^{g,\tau 1}\dot{p}_g^{\tau 1})}{\cancel{(1-\phi^{\tau 1})}K_s}S_g^{w,\tau 1}$$

$$+ \rho_v^{\tau 1}\cancel{(1-\phi^{\tau 1})}\frac{(b-\phi^{\tau 1})(dS_r^{w,\tau 1}\dot{p}_w^{\tau 1})}{\cancel{(1-\phi^{\tau 1})}K_s}S_g^{w,\tau 1} + \rho_v^{\tau 1}\cancel{(1-\phi^{\tau 1})}\frac{(b-\phi^{\tau 1})(S_r^{w,\tau 1}d\dot{p}_w^{\tau 1} + S_r^{g,\tau 1}d\dot{p}_g^{\tau 1})}{\cancel{(1-\phi^{\tau 1})}K_s}S_r^{g,\tau 1}$$

$$+ \rho_v^{\tau 1}\cancel{(1-\phi^{\tau 1})}\frac{(b-\phi^{\tau 1})(S_r^{w,\tau 1}dS_r^{g,\tau 1}\dot{p}_w^{\tau 1} + 2S_r^{g,\tau 1}dS_r^{g,\tau 1}\dot{p}_g^{\tau 1})}{\cancel{(1-\phi^{\tau 1})}K_s}$$

$$+ \underbrace{d\rho_v^{\tau 1}\left((1-\phi^{\tau 1})\dot{\varepsilon}_v^{\tau 1} - \frac{\dot{\sigma}'^{\tau 1}}{K_s}\right)S_r^{g,\tau 1} + \rho_v^{\tau 1}\left((1-\phi^{\tau 1})d\dot{\varepsilon}_v^{\tau 1} - \frac{d\dot{\sigma}'^{\tau 1}}{K_s}\right)S_r^{g,\tau 1} + \rho_v^{\tau 1}\left((1-\phi^{\tau 1})\dot{\varepsilon}_v^{\tau 1} - \frac{\dot{\sigma}'^{\tau 1}}{K_s}\right)dS_r^{g,\tau 1}}_{\textbf{(2.2)}}$$

$$+ \underbrace{d\rho_v^{\tau 1}\phi^{\tau 1}\dot{S}_r^{g,\tau 1} + \rho_v^{\tau 1}d\phi^{\tau 1}\dot{S}_r^{g,\tau 1} + \rho_v^{\tau 1}\phi^{\tau 1}d\dot{S}_r^{g,\tau 1}}_{\textbf{(2.3)}} + \underbrace{\dot{M}_w^{\tau 1}\frac{\partial du_m^{\tau 1}}{\partial x_m^{\tau 1}}}_{\textbf{(3)}} + \underbrace{\dot{M}_v^{\tau 1}\frac{\partial du_m^{\tau 1}}{\partial x_m^{\tau 1}}}_{\textbf{(4)}}$$

(D–42)

Where:

$$d\dot{p}_w^{\tau 1} = \frac{dp_w^{\tau 1}}{\Delta t}, \quad d\dot{S}_{r_w}^{\tau 1} = \frac{dS_{r_w}^{\tau 1}}{\Delta t}, \quad d\dot{p}_v^{\tau 1} = \frac{dp_v^{\tau 1}}{\Delta t}, \quad d\dot{S}_{r_g}^{\tau 1} = \frac{dS_{r_g}^{\tau 1}}{\Delta t}, \quad d\dot{\sigma}'^{\tau 1} = \frac{d\sigma'^{\tau 1}}{\Delta t} \tag{D–43}$$

$$\begin{aligned} d\dot{\varepsilon}_v^{\tau 1} &= d\left(\frac{\dot{\Omega}^{\tau 1}}{\Omega^{\tau 1}}\right) = \frac{\dot{\Omega}^{\tau 2}}{\Omega^{\tau 2}} - \frac{\dot{\Omega}^{\tau 1}}{\Omega^{\tau 1}} = \frac{\dot{\Omega}^{\tau 2}}{\Omega^{\tau 2}} - \frac{\dot{\Omega}^{\tau 1}}{\Omega^{\tau 2}} + \frac{\dot{\Omega}^{\tau 1}}{\Omega^{\tau 2}} - \frac{\dot{\Omega}^{\tau 1}}{\Omega^{\tau 1}} = \frac{\dot{\Omega}^{\tau 2} - \dot{\Omega}^{\tau 1}}{\Omega^{\tau 2}} + \frac{\dot{\Omega}^{\tau 1}}{\Omega^{\tau 1}} \frac{-\left(\Omega^{\tau 2} - \Omega^{\tau 1}\right)}{\Omega^{\tau 2}} \\ &= \frac{\Omega^{\tau 2} - \Omega^{\tau 1}}{\Omega^{\tau 2}\Delta t} + \frac{\dot{\Omega}^{\tau 1}}{\Omega^{\tau 1}} \frac{-\left(\Omega^{\tau 2} - \Omega^{\tau 1}\right)}{\Omega^{\tau 2}} \\ &= \frac{d\Omega^{\tau 1}}{\Omega^{\tau 1}\Delta t} - \frac{\dot{\Omega}^{\tau 1}}{\Omega^{\tau 1}} \frac{d\Omega^{\tau 1}}{\Omega^{\tau 1}} = \frac{d\Omega^{\tau 1}}{\Omega^{\tau 1}} \left(\frac{1}{\Delta t} - \frac{\dot{\Omega}^{\tau 1}}{\Omega^{\tau 1}}\right) = \frac{\partial du_m^{\tau 1}}{\partial x_m^{\tau 1}} \left(\frac{1}{\Delta t} - \dot{\varepsilon}_v^{\tau 1}\right) \qquad \text{for } \Omega^1 \to \Omega^2 \end{aligned} \tag{D–44}$$

With Δt being the time step and $dS_r^{w,\tau 1}$ and $dS_r^{g,\tau 1}$ depending on the choice of the retention curve.

After including all the different variations, the first term (D–42) of the water mass balance equation can finally be expressed as:

$$\begin{aligned} &\dot{M}_w^{\tau 2} det(F) + \dot{M}_v^{\tau 2} det(F) - \dot{M}_w^{\tau 1} - \dot{M}_v^{\tau 1} \\ &= \rho_w^{\tau 1} \frac{dp_w^{\tau 1}}{\chi_w} \frac{\dot{p}_w^{\tau 1}}{\chi_w} \phi^{\tau 1} S_{r_w}^{\tau 1} + \rho_{w^{\tau 1}} \frac{dp_w^{\tau 1}}{\Delta t \chi_w} \phi^{\tau 1} S_{r_w}^{\tau 1} + \rho_w^{\tau 1} \frac{\dot{p}_w^{\tau 1}}{\chi_w} (1-\phi^{\tau 1}) \left(\frac{(b-\phi^{\tau 1})(S_{r_w}^{\tau 1} dp_w^{\tau 1} + S_{r_g}^{\tau 1} dp_g) - d\sigma'^{\tau 1}}{(1-\phi^{\tau 1}) K_s} + \frac{\partial du_m^{\tau 1}}{\partial x_m^{\tau 1}} \right) S_{r_w}^{\tau 1} \\ &+ \rho_w^{\tau 1} \frac{\dot{p}_w^{\tau 1}}{\chi_w} \phi^{\tau 1} dS_{r_w}^{\tau 1} + \rho_w^{\tau 1} \frac{dp_w^{\tau 1}}{\chi_w} \frac{(b-\phi^{\tau 1})(S_{r_w}^{\tau 1} \dot{p}_w^{\tau 1} + S_{r_g}^{\tau 1} \dot{p}_g^{\tau 1})}{K_s} S_{r_w}^{\tau 1} \\ &- \rho_w^{\tau 1} \frac{(S_{r_w}^{\tau 1} \dot{p}_w^{\tau 1} + S_{r_g}^{\tau 1} \dot{p}_g^{\tau 1})}{K_s} S_{r_w}^{\tau 1} (1-\phi^{\tau 1}) \left(\frac{(b-\phi^{\tau 1})(S_{r_w}^{\tau 1} dp_w^{\tau 1} + S_{r_g}^{\tau 1} dp_g) - d\sigma'^{\tau 1}}{(1-\phi^{\tau 1}) K_s} + \frac{\partial du_m^{\tau 1}}{\partial x_m^{\tau 1}} \right) \\ &+ \rho_w^{\tau 1} \frac{(b-\phi^{\tau 1})(2 S_{r_w}^{\tau 1} dS_{r_w}^{\tau 1} \dot{p}_w^{\tau 1} + dS_{r_w}^{\tau 1} S_{r_g}^{\tau 1} \dot{p}_g^{\tau 1})}{K_s} + \rho_w^{\tau 1} \frac{(b-\phi^{\tau 1})(S_{r_w}^{\tau 1} dp_w^{\tau 1} + S_{r_g}^{\tau 1} dp_g^{\tau 1})}{K_s \Delta t} S_{r_w}^{\tau 1} \\ &+ \rho_w^{\tau 1} \frac{(b-\phi^{\tau 1})(dS_{r_g}^{\tau 1} \dot{p}_g^{\tau 1})}{K_s} S_{r_w}^{\tau 1} + \rho_w^{\tau 1} \frac{dp_w^{\tau 1}}{\chi_w} \left((1-\phi^{\tau 1}) \dot{\varepsilon}_v^{\tau 1} - \frac{\dot{\sigma}'^{\tau 1}}{K_s} \right) S_{r_w}^{\tau 1} + \rho_w^{\tau 1} \left((1-\phi) \frac{\partial du_m^{\tau 1}}{\partial x_m^{\tau 1}} \left(\frac{1}{\Delta t} - \dot{\varepsilon}_v^{\tau 1} \right) - \frac{d\sigma'^{\tau 1}}{K_s \Delta t} \right) S_{r_w}^{\tau 1} \\ &+ \rho_w^{\tau 1} \left((1-\phi^{\tau 1}) \dot{\varepsilon}_v^{\tau 1} - \frac{\dot{\sigma}'^{\tau 1}}{K_s} \right) dS_{r_w}^{\tau 1} + \rho_w^{\tau 1} (1-\phi^{\tau 1}) \left(\frac{(b-\phi^{\tau 1})(S_{r_w}^{\tau 1} dp_w^{\tau 1} + S_{r_g}^{\tau 1} dp_g) - d\sigma'^{\tau 1}}{(1-\phi^{\tau 1}) K_s} + \frac{\partial du_m^{\tau 1}}{\partial x_m^{\tau 1}} \right) \dot{S}_{r_w}^{\tau 1} \\ &+ \rho_w^{\tau 1} \frac{dp_w^{\tau 1}}{\chi_w} \phi^{\tau 1} \dot{S}_{r_w}^{\tau 1} + \rho_w^{\tau 1} \phi^{\tau 1} \frac{dS_{r_w}^{\tau 1}}{\Delta t} + \frac{m_v}{RT} \frac{dp_v^{\tau 1}}{\Delta t} \phi^{\tau 1} S_{r_g}^{\tau 1} + \frac{m_v}{RT} \dot{p}_v^{\tau 1} \phi^{\tau 1} dS_{r_g}^{\tau 1} + \frac{m_v}{RT} dp_v^{\tau 1} \frac{(b-\phi^{\tau 1})(S_{r_w}^{\tau 1} \dot{p}_w^{\tau 1} + S_{r_g}^{\tau 1} \dot{p}_g^{\tau 1})}{K_s} S_{r_g}^{\tau 1} \\ &+ \frac{m_v}{RT} \dot{p}_v^{\tau 1} (1-\phi^{\tau 1}) \left(\frac{(b-\phi^{\tau 1})(S_{r_w}^{\tau 1} dp_w^{\tau 1} + S_{r_w}^{\tau 1} dp_g) - d\sigma'^{\tau 1}}{(1-\phi^{\tau 1}) K_s} + \frac{\partial du_m^{\tau 1}}{\partial x_m^{\tau 1}} \right) S_{r_g}^{\tau 1} \\ &- \rho_v^{\tau 1} \frac{(S_{r_w}^{\tau 1} \dot{p}_w^{\tau 1} + S_{r_g}^{\tau 1} \dot{p}_g^{\tau 1})}{K_s} S_g^{w,\tau 1} (1-\phi^{\tau 1}) \left(\frac{(b-\phi^{\tau 1})(S_{r_w}^{\tau 1} dp_w^{\tau 1} + S_{r_g}^{\tau 1} dp_g) - d\sigma'^{\tau 1}}{(1-\phi^{\tau 1}) K_s} + \frac{\partial du_m^{\tau 1}}{\partial x_m^{\tau 1}} \right) \\ &+ \rho_v^{\tau 1} \frac{(b-\phi^{\tau 1})(dS_{r_w}^{\tau 1} \dot{p}_w^{\tau 1})}{K_s} S_g^{w,\tau 1} + \rho_v^{\tau 1} \frac{(b-\phi^{\tau 1})(S_{r_w}^{\tau 1} dp_w^{\tau 1} + S_{r_g}^{\tau 1} dp_g^{\tau 1})}{K_s \Delta t} S_{r_g}^{\tau 1} \\ &+ \rho_v^{\tau 1} \frac{(b-\phi^{\tau 1})(S_{r_w}^{\tau 1} dS_{r_g}^{\tau 1} \dot{p}_w^{\tau 1} + 2 S_{r_g}^{\tau 1} dS_{r_g}^{\tau 1} \dot{p}_g^{\tau 1})}{K_s} + \frac{m_v}{RT} dp_v^{\tau 1} \left((1-\phi^{\tau 1}) \dot{\varepsilon}_v^{\tau 1} - \frac{\dot{\sigma}'^{\tau 1}}{K_s} \right) S_{r_g}^{\tau 1} \end{aligned}$$

(continued on next page)

$$
\begin{aligned}
&+\ \rho_v^{\tau 1}\left((1-\phi^{\tau 1})\frac{\partial du_m^{\tau 1}}{\partial x_m^{\tau 1}}\left(\frac{1}{\Delta t}-\dot{\varepsilon}_v^{\tau 1}\right)-\frac{d\sigma'^{\tau 1}}{K_s\Delta t}\right)S_{r_g}^{\tau 1}+\ \rho_v^{\tau 1}\left((1-\phi^{\tau 1})\dot{\varepsilon}_v^{\tau 1}-\frac{\dot{\sigma}'^{\tau 1}}{K_s}\right)dS_{r_g}^{\tau 1}+\ \frac{m_v}{RT}dp_v^{\tau 1}\phi^{\tau 1}\dot{S}_r^{g,\tau 1}\\
&+\ \rho_v^{\tau 1}(1-\phi^{\tau 1})\left(\frac{(b-\phi^{\tau 1})(S_{r_w}^{\tau 1}dp_w^{\tau 1}+S_{r_g}^{\tau 1}dp_g)-d\sigma'^{\tau 1}}{(1-\phi^{\tau 1})K_s}+\frac{\partial du_m^{\tau 1}}{\partial x_m^{\tau 1}}\right)\dot{S}_r^{g,\tau 1}\\
&+\ \rho_v^{\tau 1}\phi^{\tau 1}\frac{dS_{r_g}^{\tau 1}}{\Delta t}+\ \dot{M}_w^{\tau 1}\frac{\partial du_m^{\tau 1}}{\partial x_m^{\tau 1}}+\ \dot{M}_v^{\tau 1}\frac{\partial du_m^{\tau 1}}{\partial x_m^{\tau 1}}
\end{aligned}
\tag{D–45}
$$

The second term of the water mass balance equation is written as:

$$
\begin{aligned}
&f_{w,i}^{\tau 2}\frac{\partial x_k^{\tau 1}}{\partial x_j^{\tau 2}}det(F)+f_{v,i}^{\tau 2}\frac{\partial x_k^{\tau 1}}{\partial x_j^{\tau 2}}det(F)-f_{w,k}^{\tau 1}-f_{v,k}^{\tau 1}\\
&\qquad=f_{w,i}^{\tau 2}\frac{\partial x_k^{\tau 1}}{\partial x_j^{\tau 2}}\left(1+\frac{\partial du_i^{\tau 1}}{\partial x_j^{\tau 1}}\right)+f_{v,i}^{\tau 2}\frac{\partial x_k^{\tau 1}}{\partial x_j^{\tau 2}}\left(1+\frac{\partial du_i^{\tau 1}}{\partial x_j^{\tau 1}}\right)-f_{w,k}^{\tau 1}-f_{v,k}^{\tau 1}\\
&\qquad=\underbrace{df_{w,l}^{\tau 1}}_{(1)}-\underbrace{f_{w,i}^{\tau 1}\frac{\partial du_l^{\tau 1}}{\partial x_i^{\tau 1}}}_{(3)}+\underbrace{f_{w,l}^{\tau 1}\frac{\partial du_m^{\tau 1}}{\partial x_m^{\tau 1}}}_{(4)}+\underbrace{df_{v,l}^{\tau 1}}_{(2)}-\underbrace{f_{v,i}^{\tau 1}\frac{\partial du_l^{\tau 1}}{\partial x_i^{\tau 1}}}_{(5)}+\underbrace{f_{v,l}^{\tau 1}\frac{\partial du_m^{\tau 1}}{\partial x_m^{\tau 1}}}_{(6)}
\end{aligned}
\tag{D–46}
$$

Considering the variation of the liquid water advective flow and of the water vapour advective flow, as well as the diffusion in the gaseous mixture dry air-water vapour, the equation (D–46) can be re-expressed by developing the different terms (1) to (6) as:

$$
\begin{aligned}
&f_{w,i}^{\tau 2}\frac{\partial x_k^{\tau 1}}{\partial x_j^{\tau 2}}det(F)+f_{v,i}^{\tau 2}\frac{\partial x_k^{\tau 1}}{\partial x_j^{\tau 2}}det(F)-f_{w,k}^{\tau 1}-f_{v,k}^{\tau 1}\\
&\quad=-d\rho_w^{\tau 1}\frac{k_{ij}^{int}k_{r,w}^{\tau 1}}{\mu_w}\left(\frac{\partial p_w^{\tau 1}}{\partial x_j^{\tau 1}}+\rho_w^{\tau 1}g_j\right)-\rho_w^{\tau 1}\frac{dk_{ij}^{int}k_{r,w}^{\tau 1}}{\mu_w}\left(\frac{\partial p_w^{\tau 1}}{\partial x_j^{\tau 1}}+\rho_w^{\tau 1}g_j\right)\\
&\quad\underbrace{-\rho_w^{\tau 1}\frac{k_{ij}^{int}dk_{r,w}^{\tau 1}}{\mu_w}\left(\frac{\partial p_w^{\tau 1}}{\partial x_j^{\tau 1}}+\rho_w^{\tau 1}g_j\right)-\rho_w^{\tau 1}\frac{k_{ij}^{int}k_{r,w}^{\tau 1}}{\mu_w}\left(d\left(\frac{\partial p_w^{\tau 1}}{\partial x_j^{\tau 1}}\right)+d\rho_w^{\tau 1}g_j\right)}_{(1)}\\
&\quad-d\rho_v^{\tau 1}\frac{k_{ij}^{int}k_{g,w}^{\tau 1}}{\mu_g}\left(\frac{\partial p_g^{\tau 1}}{\partial x_j^{\tau 1}}+\rho_g^{\tau 1}g_j\right)-\rho_v^{\tau 1}\frac{dk_{ij}^{int}k_{r,g}^{\tau 1}}{\mu_g}\left(\frac{\partial p_g^{\tau 1}}{\partial x_j^{\tau 1}}+\rho_g^{\tau 1}g_j\right)\\
&\quad-\rho_v^{\tau 1}\frac{k_{ij}^{int}dk_{r,g}^{\tau 1}}{\mu_g}\left(\frac{\partial p_g^{\tau 1}}{\partial x_j^{\tau 1}}+\rho_g^{\tau 1}g_j\right)-\rho_v^{\tau 1}\frac{k_{ij}^{int}k_{r,g}^{\tau 1}}{\mu_g}\left(d\left(\frac{\partial p_g^{\tau 1}}{\partial x_j^{\tau 1}}\right)+\rho_g^{\tau 1}g_j\right)\\
&\quad-d\phi^{\tau 1}S_r^{g,\tau 1}\bar{\tau}D_{v-g}\rho_g^{\tau 1}\frac{\partial}{\partial x_i^{\tau 1}}\left(\frac{\rho_v^{\tau 1}}{\rho_g^{\tau 1}}\right)-\phi^{\tau 1}dS_r^{g,\tau 1}\bar{\tau}D_{v-g}\rho_g^{\tau 1}\frac{\partial}{\partial x_i^{\tau 1}}\left(\frac{\rho_v^{\tau 1}}{\rho_g^{\tau 1}}\right)\\
&\quad\underbrace{-\phi^{\tau 1}S_r^{g,\tau 1}\bar{\tau}D_{v-g}d\rho_g^{\tau 1}\frac{\partial}{\partial x_i^{\tau 1}}\left(\frac{\rho_v^{\tau 1}}{\rho_g^{\tau 1}}\right)-\phi^{\tau 1}S_r^{g,\tau 1}\bar{\tau}D_{v-g}\rho_g^{\tau 1}d\left(\frac{\partial}{\partial x_i^{\tau 1}}\left(\frac{\rho_v^{\tau 1}}{\rho_g^{\tau 1}}\right)\right)}_{(2)}\\
&\quad\underbrace{-f_{w,i}^{\tau 1}\frac{\partial du_l^{\tau 1}}{\partial x_i^{\tau 1}}}_{(3)}+\underbrace{f_{w,l}^{\tau 1}\frac{\partial du_m^{\tau 1}}{\partial x_m^{\tau 1}}}_{(4)}-\underbrace{f_{v,i}^{\tau 1}\frac{\partial du_l^{\tau 1}}{\partial x_i^{\tau 1}}}_{(5)}+\underbrace{f_{v,l}^{\tau 1}\frac{\partial du_m^{\tau 1}}{\partial x_m^{\tau 1}}}_{(6)}
\end{aligned}
\tag{D–47}
$$

Where dk_{ij}^{int}, $dk_{r,w}^{\tau 1}$ and $dk_{r,g}^{\tau 1}$ depend on the chosen intrinsic permeability variation and water and gas permeability curve. However, it is noteworthy to mention the following developments which include the limit:

$$\begin{aligned} d\left(\frac{\partial p_w^{\tau 1}}{\partial x_j^{\tau 1}}\right) &= \frac{\partial p_w^{\tau 2}}{\partial x_j^{\tau 2}} - \frac{\partial p_w^{\tau 1}}{\partial x_j^{\tau 1}} = \frac{\partial p_w^{\tau 2}}{\partial x_i^{\tau 1}}\frac{\partial x_i^{\tau 1}}{\partial x_j^{\tau 2}} - \frac{\partial p_w^{\tau 1}}{\partial x_j^{\tau 1}} = \frac{\partial p_w^{\tau 2}}{\partial x_i^{\tau 1}}\left(\delta_{ij} - \frac{\partial du_i^{\tau 1}}{\partial x_j^{\tau 2}}\right) - \frac{\partial p_w^{\tau 1}}{\partial x_j^{\tau 1}} \\ &= \frac{\partial p_w^{\tau 2}}{\partial x_j^{\tau 1}} - \frac{\partial p_w^{\tau 2}}{\partial x_i^{\tau 1}}\frac{\partial du_i^{\tau 1}}{\partial x_j^{\tau 2}} - \frac{\partial p_w^{\tau 1}}{\partial x_j^{\tau 1}} = \frac{\partial dp_w^{\tau 1}}{\partial x_j^{\tau 1}} - \frac{\partial p_w^{\tau 1}}{\partial x_i^{\tau 1}}\frac{\partial du_i^{\tau 1}}{\partial x_j^{\tau 1}} \end{aligned} \tag{D–48}$$

$$\begin{aligned} d\left(\frac{\partial p_g^{\tau 1}}{\partial x_j^{\tau 1}}\right) &= \frac{\partial p_g^{\tau 2}}{\partial x_j^{\tau 2}} - \frac{\partial p_g^{\tau 1}}{\partial x_j^{\tau 1}} = \frac{\partial p_g^{\tau 2}}{\partial x_i^{\tau 1}}\frac{\partial x_i^{\tau 1}}{\partial x_j^{\tau 2}} - \frac{\partial p_g^{\tau 1}}{\partial x_j^{\tau 1}} = \frac{\partial p_g^{\tau 2}}{\partial x_i^{\tau 1}}\left(\delta_{ij} - \frac{\partial du_i^{\tau 1}}{\partial x_j^{\tau 2}}\right) - \frac{\partial p_g^{\tau 1}}{\partial x_j^{\tau 1}} \\ &= \frac{\partial p_g^{\tau 2}}{\partial x_j^{\tau 1}} - \frac{\partial p_g^{\tau 2}}{\partial x_i^{\tau 1}}\frac{\partial du_i^{\tau 1}}{\partial x_j^{\tau 2}} - \frac{\partial p_g^{\tau 1}}{\partial x_j^{\tau 1}} = \frac{\partial dp_g^{\tau 1}}{\partial x_j^{\tau 1}} - \frac{\partial p_g^{\tau 1}}{\partial x_i^{\tau 1}}\frac{\partial du_i^{\tau 1}}{\partial x_j^{\tau 1}} \end{aligned} \tag{D–49}$$

$$\begin{aligned} d\left(\frac{\partial}{\partial x_i^{\tau 1}}\left(\frac{\rho_v^{\tau 1}}{\rho_g^{\tau 1}}\right)\right) &= \frac{\partial \frac{\rho_v^{\tau 2}}{\rho_g^{\tau 2}}}{\partial x_j^{\tau 2}} - \frac{\partial \frac{\rho_v^{\tau 1}}{\rho_g^{\tau 1}}}{\partial x_j^{\tau 1}} = \frac{\partial \frac{\rho_v^{\tau 2}}{\rho_g^{\tau 2}}}{\partial x_i^{\tau 1}}\frac{\partial x_i^{\tau 1}}{\partial x_j^{\tau 2}} - \frac{\partial \frac{\rho_v^{\tau 1}}{\rho_g^{\tau 1}}}{\partial x_j^{\tau 1}} = \frac{\partial \frac{\rho_v^{\tau 2}}{\rho_g^{\tau 2}}}{\partial x_i^{\tau 1}}\left(\delta_{ij} - \frac{\partial du_i^{\tau 1}}{\partial x_j^{\tau 2}}\right) - \frac{\partial \frac{\rho_v^{\tau 1}}{\rho_g^{\tau 1}}}{\partial x_j^{\tau 1}} \\ &= \frac{\partial \frac{\rho_v^{\tau 2}}{\rho_g^{\tau 2}}}{\partial x_j^{\tau 1}} - \frac{\partial \frac{\rho_v^{\tau 2}}{\rho_g^{\tau 2}}}{\partial x_i^{\tau 1}}\frac{\partial du_i^{\tau 1}}{\partial x_j^{\tau 2}} - \frac{\partial \frac{\rho_v^{\tau 1}}{\rho_g^{\tau 1}}}{\partial x_j^{\tau 1}} = \frac{\partial d\left(\frac{\rho_v^{\tau 1}}{\rho_g^{\tau 1}}\right)}{\partial x_j^{\tau 1}} - \frac{\partial \frac{\rho_v^{\tau 1}}{\rho_g^{\tau 1}}}{\partial x_i^{\tau 1}}\frac{\partial du_i^{\tau 1}}{\partial x_j^{\tau 1}} \end{aligned} \tag{D–50}$$

After including all the different variations, the second term (D–46) of the water mass balance equation can finally be expressed as:

$$\begin{aligned} & f_{w,i}^{\tau 2}\frac{\partial x_k^{\tau 1}}{\partial x_j^{\tau 2}}det(F) + f_{v,i}^{\tau 2}\frac{\partial x_k^{\tau 1}}{\partial x_j^{\tau 2}}det(F) - f_{w,k}^{\tau 1} - f_{v,k}^{\tau 1} \\ &= -\rho_w^{\tau 1}\frac{p_w^{\tau 1}}{\chi_w}\frac{k_{ij}^{int}k_{r,w}^{\tau 1}}{\mu_w}\left(\frac{\partial p_w^{\tau 1}}{\partial x_j^{\tau 1}} + \rho_w^{\tau 1}g_j\right) - \rho_w^{\tau 1}\frac{dk_{ij}^{int}k_{r,w}^{\tau 1}}{\mu_w}\left(\frac{\partial p_w^{\tau 1}}{\partial x_j^{\tau 1}} + \rho_w^{\tau 1}g_j\right) - \rho_w^{\tau 1}\frac{k_{ij}^{int}dk_{r,w}^{\tau 1}}{\mu_w}\left(\frac{\partial p_w^{\tau 1}}{\partial x_j^{\tau 1}} + \rho_w^{\tau 1}g_j\right) \\ &\quad - \rho_w^{\tau 1}\frac{k_{ij}^{int}k_{r,w}^{\tau 1}}{\mu_w}\left(\frac{\partial dp_w^{\tau 1}}{\partial x_j^{\tau 1}} + d\rho_w^{\tau 1}g_j\right) + \rho_w^{\tau 1}\frac{k_{ij}^{int}k_{r,w}^{\tau 1}}{\mu_w}\left(\frac{\partial p_w^{\tau 1}}{\partial x_k^{\tau 1}}\frac{\partial du_k^{\tau 1}}{\partial x_j^{\tau 1}}\right) - \frac{m_v}{RT}dp_v^{\tau 1}\frac{k_{ij}^{int}k_{g,w}^{\tau 1}}{\mu_g}\left(\frac{\partial p_g^{\tau 1}}{\partial x_j^{\tau 1}} + \rho_g^{\tau 1}g_j\right) \\ &\quad - \rho_v^{\tau 1}\frac{dk_{ij}^{int}k_{r,g}^{\tau 1}}{\mu_g}\left(\frac{\partial p_g^{\tau 1}}{\partial x_j^{\tau 1}} + \rho_g^{\tau 1}g_j\right) - \rho_v^{\tau 1}\frac{k_{ij}^{int}dk_{r,g}^{\tau 1}}{\mu_g}\left(\frac{\partial p_g^{\tau 1}}{\partial x_j^{\tau 1}} + \rho_g^{\tau 1}g_j\right) - \rho_v^{\tau 1}\frac{k_{ij}^{int}k_{r,g}^{\tau 1}}{\mu_g}\left(\frac{\partial dp_g^{\tau 1}}{\partial x_j^{\tau 1}} + \rho_g^{\tau 1}g_j\right) \\ &\quad + \rho_v^{\tau 1}\frac{k_{ij}^{int}k_{r,g}^{\tau 1}}{\mu_g}\left(\frac{\partial p_g^{\tau 1}}{\partial x_k^{\tau 1}}\frac{\partial du_k^{\tau 1}}{\partial x_j^{\tau 1}}\right) - (1-\phi^{\tau 1})\left(\frac{(b-\phi^{\tau 1})(S_{r_w}^{\tau 1}dp_w^{\tau 1} + S_{r_g}^{\tau 1}dp_g) - d\sigma'^{\tau 1}}{(1-\phi^{\tau 1})K_s} + \frac{\partial du_m^{\tau 1}}{\partial x_m^{\tau 1}}\right)S_{r_g}^{\tau 1}\bar{\tau}D_{v-g}\rho_g^{\tau 1}\frac{\partial}{\partial x_i^{\tau 1}}\left(\frac{\rho_v^{\tau 1}}{\rho_g^{\tau 1}}\right) \\ &\quad - \phi^{\tau 1}dS_{r_g}^{\tau 1}\bar{\tau}D_{v-g}\rho_g^{\tau 1}\frac{\partial}{\partial x_i^{\tau 1}}\left(\frac{\rho_v^{\tau 1}}{\rho_g^{\tau 1}}\right) - \phi^{\tau 1}S_{r_g}^{\tau 1}\bar{\tau}D_{v-g}d\rho_g^{\tau 1}\frac{\partial}{\partial x_i^{\tau 1}}\left(\frac{\rho_v^{\tau 1}}{\rho_g^{\tau 1}}\right) \\ &\quad - \phi^{\tau 1}S_{r_g}^{\tau 1}\bar{\tau}D_{v-g}\rho_g^{\tau 1}\frac{\partial d\frac{\rho_v^{\tau 1}}{\rho_g^{\tau 1}}}{\partial x_j^{\tau 1}} + \phi^{\tau 1}S_{r_g}^{\tau 1}\bar{\tau}D_{v-g}\rho_g^{\tau 1}\frac{\partial \frac{\rho_v^{\tau 1}}{\rho_g^{\tau 1}}}{\partial x_i^{\tau 1}}\frac{\partial du_i^{\tau 1}}{\partial x_j^{\tau 1}} \\ &\quad - f_{w,i}^{\tau 1}\frac{\partial du_l^{\tau 1}}{\partial x_i^{\tau 1}} + f_{w,l}^{\tau 1}\frac{\partial du_m^{\tau 1}}{\partial x_m^{\tau 1}} - f_{v,i}^{\tau 1}\frac{\partial du_l^{\tau 1}}{\partial x_i^{\tau 1}} + f_{v,l}^{\tau 1}\frac{\partial du_m^{\tau 1}}{\partial x_m^{\tau 1}} \end{aligned} \tag{D–51}$$

By regrouping the two terms (D–45) and (D–51), the water mass balance equation becomes:

$$
\begin{aligned}
\int_{\Omega^{\tau 1}} p_w^{\star}\Bigg\{ & \rho_w^{\tau 1}\frac{dp_w^{\tau 1}}{\chi_w}\frac{\dot{p}_w^{\tau 1}}{\chi_w}\phi^{\tau 1}S_{r_w}^{\tau 1} + \rho_{w^{\tau 1}}\frac{dp_w^{\tau 1}}{\Delta t\chi_w}\phi^{\tau 1}S_{r_w}^{\tau 1} \\
& + \rho_w^{\tau 1}\frac{\dot{p}_w^{\tau 1}}{\chi_w}(1-\phi^{\tau 1})\left(\frac{(b-\phi^{\tau 1})(S_{r_w}^{\tau 1}dp_w^{\tau 1}+S_{r_g}^{\tau 1}dp_g)-d\sigma'^{\tau 1}}{(1-\phi^{\tau 1})K_s}+\frac{\partial du_m^{\tau 1}}{\partial x_m^{\tau 1}}\right)S_{r_w}^{\tau 1} \\
& + \rho_w^{\tau 1}\frac{\dot{p}_w^{\tau 1}}{\chi_w}\phi^{\tau 1}dS_{r_w}^{\tau 1} + \rho_w^{\tau 1}\frac{dp_w^{\tau 1}}{\chi_w}\frac{(b-\phi^{\tau 1})(S_{r_w}^{\tau 1}\dot{p}_w^{\tau 1}+S_{r_g}^{\tau 1}\dot{p}_g^{\tau 1})}{K_s}S_{r_w}^{\tau 1} \\
& - \rho_w^{\tau 1}\frac{(S_{r_w}^{\tau 1}\dot{p}_w^{\tau 1}+S_{r_g}^{\tau 1}\dot{p}_g^{\tau 1})}{K_s}S_{r_w}^{\tau 1}(1-\phi^{\tau 1})\left(\frac{(b-\phi^{\tau 1})(S_{r_w}^{\tau 1}dp_w^{\tau 1}+S_{r_g}^{\tau 1}dp_g)-d\sigma'^{\tau 1}}{(1-\phi^{\tau 1})K_s}+\frac{\partial du_m^{\tau 1}}{\partial x_m^{\tau 1}}\right) \\
& + \rho_w^{\tau 1}\frac{(b-\phi^{\tau 1})(2S_{r_w}^{\tau 1}dS_{r_w}^{\tau 1}\dot{p}_w^{\tau 1}+dS_{r_w}^{\tau 1}S_{r_g}^{\tau 1}\dot{p}_g^{\tau 1})}{K_s} + \rho_w^{\tau 1}\frac{(b-\phi^{\tau 1})(S_{r_w}^{\tau 1}dp_w^{\tau 1}+S_{r_g}^{\tau 1}dp_g^{\tau 1})}{K_s\Delta t}S_{r_w}^{\tau 1} \\
& + \rho_w^{\tau 1}\frac{(b-\phi^{\tau 1})(dS_{r_g}^{\tau 1}\dot{p}_g^{\tau 1})}{K_s}S_{r_w}^{\tau 1} + \rho_w^{\tau 1}\frac{dp_w^{\tau 1}}{\chi_w}\left((1-\phi^{\tau 1})\dot{\varepsilon}_v^{\tau 1}-\frac{\dot{\sigma}'^{\tau 1}}{K_s}\right)S_{r_w}^{\tau 1} \\
& + \rho_w^{\tau 1}\left((1-\phi^{\tau 1})\frac{\partial du_m^{\tau 1}}{\partial x_m^{\tau 1}}\left(\frac{1}{\Delta t}-\dot{\varepsilon}_v^{\tau 1}\right)-\frac{d\sigma'^{\tau 1}}{K_s\Delta t}\right)S_{r_w}^{\tau 1} + \rho_w^{\tau 1}\left((1-\phi^{\tau 1})\dot{\varepsilon}_v^{\tau 1}-\frac{\dot{\sigma}'^{\tau 1}}{K_s}\right)dS_{r_w}^{\tau 1} \\
& + \rho_w^{\tau 1}\frac{dp_w^{\tau 1}}{\chi_w}\phi^{\tau 1}\dot{S}_r^{w,\tau 1} + \rho_w^{\tau 1}(1-\phi^{\tau 1})\left(\frac{(b-\phi^{\tau 1})(S_{r_w}^{\tau 1}dp_w^{\tau 1}+S_{r_g}^{\tau 1}dp_g)-d\sigma'^{\tau 1}}{(1-\phi^{\tau 1})K_s}+\frac{\partial du_m^{\tau 1}}{\partial x_m^{\tau 1}}\right)\dot{S}_r^{w,\tau 1} \\
& + \rho_w^{\tau 1}\phi^{\tau 1}\frac{dS_{r_w}^{\tau 1}}{\Delta t} + \frac{m_v}{RT}\frac{dp_v^{\tau 1}}{\Delta t}\phi^{\tau 1}S_{r_g}^{\tau 1} \\
& + \frac{m_v}{RT}\dot{p}_v^{\tau 1}(1-\phi^{\tau 1})\left(\frac{(b-\phi^{\tau 1})(S_{r_w}^{\tau 1}dp_w^{\tau 1}+S_{r_g}^{\tau 1}dp_g)-d\sigma'^{\tau 1}}{(1-\phi^{\tau 1})K_s}+\frac{\partial du_m^{\tau 1}}{\partial x_m^{\tau 1}}\right)S_{r_g}^{\tau 1} \\
& + \frac{m_v}{RT}\dot{p}_v^{\tau 1}\phi^{\tau 1}dS_{r_g}^{\tau 1} + \frac{m_v}{RT}dp_v^{\tau 1}\frac{(b-\phi^{\tau 1})(S_{r_w}^{\tau 1}\dot{p}_w^{\tau 1}+S_{r_g}^{\tau 1}\dot{p}_g^{\tau 1})}{K_s}S_{r_g}^{\tau 1} \\
& - \rho_v^{\tau 1}\frac{(S_{r_w}^{\tau 1}\dot{p}_w^{\tau 1}+S_{r_g}^{\tau 1}\dot{p}_g^{\tau 1})}{K_s}S_g^{w,\tau 1}(1-\phi^{\tau 1})\left(\frac{(b-\phi^{\tau 1})(S_{r_w}^{\tau 1}dp_w^{\tau 1}+S_{r_g}^{\tau 1}dp_g)-d\sigma'^{\tau 1}}{(1-\phi^{\tau 1})K_s}+\frac{\partial du_m^{\tau 1}}{\partial x_m^{\tau 1}}\right) \\
& + \rho_v^{\tau 1}\frac{(b-\phi^{\tau 1})(dS_{r_w}^{\tau 1}\dot{p}_w^{\tau 1})}{K_s}S_g^{w,\tau 1} + \rho_v^{\tau 1}\frac{(b-\phi^{\tau 1})(S_{r_w}^{\tau 1}dp_w^{\tau 1}+S_{r_g}^{\tau 1}dp_g^{\tau 1})}{K_s\Delta t}S_{r_g}^{\tau 1} \\
& + \rho_v^{\tau 1}\frac{(b-\phi^{\tau 1})(S_{r_w}^{\tau 1}dS_{r_g}^{\tau 1}\dot{p}_w^{\tau 1}+2S_{r_g}^{\tau 1}dS_{r_g}^{\tau 1}\dot{p}_g^{\tau 1})}{K_s} + \frac{m_v}{RT}dp_v^{\tau 1}\left((1-\phi^{\tau 1})\dot{\varepsilon}_v^{\tau 1}-\frac{\dot{\sigma}'^{\tau 1}}{K_s}\right)S_{r_g}^{\tau 1} \\
& + \rho_v^{\tau 1}\left((1-\phi^{\tau 1})\frac{\partial du_m^{\tau 1}}{\partial x_m^{\tau 1}}\left(\frac{1}{\Delta t}-\dot{\varepsilon}_v^{\tau 1}\right)-\frac{d\sigma'^{\tau 1}}{K_s\Delta t}\right)S_{r_g}^{\tau 1} + \rho_v^{\tau 1}\left((1-\phi^{\tau 1})\dot{\varepsilon}_v^{\tau 1}-\frac{\dot{\sigma}'^{\tau 1}}{K_s}\right)dS_{r_g}^{\tau 1} \\
& + \frac{m_v}{RT}dp_v^{\tau 1}\phi^{\tau 1}\dot{S}_r^{g,\tau 1} + \rho_v^{\tau 1}(1-\phi^{\tau 1})\left(\frac{(b-\phi^{\tau 1})(S_{r_w}^{\tau 1}dp_w^{\tau 1}+S_{r_g}^{\tau 1}dp_g)-d\sigma'^{\tau 1}}{(1-\phi^{\tau 1})K_s}+\frac{\partial du_m^{\tau 1}}{\partial x_m^{\tau 1}}\right)\dot{S}_r^{g,\tau 1} \\
& + \rho_v^{\tau 1}\phi^{\tau 1}\frac{dS_{r_g}^{\tau 1}}{\Delta t} + \dot{M}_w^{\tau 1}\frac{\partial du_m^{\tau 1}}{\partial x_m^{\tau 1}} + \dot{M}_v^{\tau 1}\frac{\partial du_m^{\tau 1}}{\partial x_m^{\tau 1}}\Bigg\}d\Omega^{\tau 1}
\end{aligned}
$$

(continued on next page)

$$
\begin{aligned}
-\int_{\Omega^{\tau 1}} \frac{\partial p_w^{\star}}{\partial x_k^{\tau 1}} \Bigg\{ & -\rho_w^{\tau 1} \frac{p_w^{\tau 1}}{\chi_w} \frac{k_{ij}^{int} k_{r,w}^{\tau 1}}{\mu_w} \left(\frac{\partial p_w^{\tau 1}}{\partial x_j^{\tau 1}} + \rho_w^{\tau 1} g_j \right) d\Omega^{\tau 1} - \rho_w^{\tau 1} \frac{dk_{ij}^{int} k_{r,w}^{\tau 1}}{\mu_w} \left(\frac{\partial p_w^{\tau 1}}{\partial x_j^{\tau 1}} + \rho_w^{\tau 1} g_j \right) \\
& - \rho_w^{\tau 1} \frac{k_{ij}^{int} dk_{r,w}^{\tau 1}}{\mu_w} \left(\frac{\partial p_w^{\tau 1}}{\partial x_j^{\tau 1}} + \rho_w^{\tau 1} g_j \right) - \rho_w^{\tau 1} \frac{k_{ij}^{int} k_{r,w}^{\tau 1}}{\mu_w} \left(\frac{\partial dp_w^{\tau 1}}{\partial x_j^{\tau 1}} + d\rho_w^{\tau 1} g_j \right) + \rho_w^{\tau 1} \frac{k_{ij}^{int} k_{r,w}^{\tau 1}}{\mu_w} \left(\frac{\partial p_w^{\tau 1}}{\partial x_k^{\tau 1}} \frac{\partial du_k^{\tau 1}}{\partial x_j^{\tau 1}} \right) \\
& - \frac{m_v}{RT} dp_v^{\tau 1} \frac{k_{ij}^{int} k_{g,w}^{\tau 1}}{\mu_g} \left(\frac{\partial p_g^{\tau 1}}{\partial x_j^{\tau 1}} + \rho_g^{\tau 1} g_j \right) - \rho_v^{\tau 1} \frac{dk_{ij}^{int} k_{r,g}^{\tau 1}}{\mu_g} \left(\frac{\partial p_g^{\tau 1}}{\partial x_j^{\tau 1}} + \rho_g^{\tau 1} g_j \right) \\
& - \rho_v^{\tau 1} \frac{k_{ij}^{int} dk_{r,g}^{\tau 1}}{\mu_g} \left(\frac{\partial p_g^{\tau 1}}{\partial x_j^{\tau 1}} + \rho_g^{\tau 1} g_j \right) - \rho_v^{\tau 1} \frac{k_{ij}^{int} k_{r,g}^{\tau 1}}{\mu_g} \left(\frac{\partial dp_g^{\tau 1}}{\partial x_j^{\tau 1}} + \rho_g^{\tau 1} g_j \right) + \rho_v^{\tau 1} \frac{k_{ij}^{int} k_{r,g}^{\tau 1}}{\mu_g} \left(\frac{\partial p_g^{\tau 1}}{\partial x_k^{\tau 1}} \frac{\partial du_k^{\tau 1}}{\partial x_j^{\tau 1}} \right) \\
& - (1-\phi^{\tau 1}) \left(\frac{(b-\phi^{\tau 1})(S_{r_w}^{\tau 1} dp_w^{\tau 1} + S_{r_g}^{\tau 1} dp_g) - d\sigma'^{\tau 1}}{(1-\phi^{\tau 1}) K_s} + \frac{\partial du_m^{\tau 1}}{\partial x_m^{\tau 1}} \right) S_{r_g}^{\tau 1} \bar{\tau} D_{v-g} \rho_g^{\tau 1} \frac{\partial}{\partial x_i^{\tau 1}} \left(\frac{\rho_v^{\tau 1}}{\rho_g^{\tau 1}} \right) \\
& - \phi^{\tau 1} dS_{r_g}^{\tau 1} \bar{\tau} D_{v-g} \rho_g^{\tau 1} \frac{\partial}{\partial x_i^{\tau 1}} \left(\frac{\rho_v^{\tau 1}}{\rho_g^{\tau 1}} \right) - \phi^{\tau 1} S_{r_g}^{\tau 1} \bar{\tau} D_{v-g} d\rho_g^{\tau 1} \frac{\partial}{\partial x_i^{\tau 1}} \left(\frac{\rho_v^{\tau 1}}{\rho_g^{\tau 1}} \right) \\
& - \phi^{\tau 1} S_{r_g}^{\tau 1} \bar{\tau} D_{v-g} \rho_g^{\tau 1} \frac{\partial d \frac{\rho_v^{\tau 1}}{\rho_g^{\tau 1}}}{\partial x_j^{\tau 1}} + \phi^{\tau 1} S_{r_g}^{\tau 1} \bar{\tau} D_{v-g} \rho_g^{\tau 1} \frac{\partial \frac{\rho_v^{\tau 1}}{\rho_g^{\tau 1}}}{\partial x_i^{\tau 1}} \frac{\partial du_i^{\tau 1}}{\partial x_j^{\tau 1}} \\
& - f_{w,i}^{\tau 1} \frac{\partial du_l^{\tau 1}}{\partial x_i^{\tau 1}} + f_{w,l}^{\tau 1} \frac{\partial du_m^{\tau 1}}{\partial x_m^{\tau 1}} - f_{v,i}^{\tau 1} \frac{\partial du_l^{\tau 1}}{\partial x_i^{\tau 1}} + f_{v,l}^{\tau 1} \frac{\partial du_m^{\tau 1}}{\partial x_m^{\tau 1}} \Bigg\} d\Omega^{\tau 1} \\
= & -\Delta_3^{\tau 1}
\end{aligned}
\tag{D–52}
$$

D.3.4 Gas mass balance equation

The developments relative to the mass balance Equation (D–15) are treated, similarly to the water mass balance equation.

The first term can be expressed as a function of the different terms (1), (2), (3) and (4) as:

$$
\begin{aligned}
&\dot{M}_a^{\tau 2} det(F) + \dot{M}_{da}^{\tau 2} det(F) - \dot{M}_a^{\tau 1} - \dot{M}_{da}^{\tau 1} = \underbrace{d\dot{M}_a^{\tau 1}}_{(1)} + \underbrace{\dot{M}_a^{\tau 1}\frac{\partial du_m^{\tau 1}}{\partial x_m^{\tau 1}}}_{(3)} + \underbrace{d\dot{M}_{da}^{\tau 1}}_{(2)} + \underbrace{\dot{M}_{da}^{\tau 1}\frac{\partial du_m^{\tau 1}}{\partial x_m^{\tau 1}}}_{(4)} \\
&= \underbrace{\underbrace{\dot{\rho}_a^{\tau 1}\phi^{\tau 1}S_{r_g}^{\tau 1}}_{(1.1)} + \underbrace{\rho_a^{\tau 1}\dot{\phi^{\tau 1}}S_{r_g}^{\tau 1}}_{(1.2)} + \underbrace{\rho_a^{\tau 1}\phi^{\tau 1}\dot{S}_r^{g,\tau 1}}_{(1.3)}}_{(1)} + \underbrace{\underbrace{\dot{\rho}_{da}^{\tau 1}\phi^{\tau 1}S_{r_w}^{\tau 1}}_{(2.1)} + \underbrace{\rho_{da}^{\tau 1}\dot{\phi}^{\tau 1}S_{r_w}^{\tau 1}}_{(2.2)} + \rho_{da}^{\tau 1}\phi^{\tau 1}\dot{S}_{r_w}^{\tau 1}}_{(2)} + \underbrace{\dot{M}_a^{\tau 1}\frac{\partial du_m^{\tau 1}}{\partial x_m^{\tau 1}}}_{(3)} + \underbrace{\dot{M}_{da}^{\tau 1}\frac{\partial du_m^{\tau 1}}{\partial x_m^{\tau 1}}}_{(4)} \\
&= \underbrace{\frac{m_a}{RT}d\dot{p}_a^{\tau 1}\phi^{\tau 1}S_{r_g}^{\tau 1} + \frac{m_a}{RT}\dot{p}_a^{\tau 1}d\phi^{\tau 1}S_{r_g}^{\tau 1} + \frac{m_a}{RT}\dot{p}_a^{\tau 1}\phi^{\tau 1}dS_{r_g}^{\tau 1}}_{(1.1)} \\
&\quad + d\rho_a^{\tau 1}\cancel{(1-\phi^{\tau 1})}\frac{(b-\phi^{\tau 1})(S_{r_w}^{\tau 1}\dot{p}_w^{\tau 1} + S_{r_g}^{\tau 1}\dot{p}_g^{\tau 1})}{\cancel{(1-\phi^{\tau 1})}K_s}S_{r_g}^{\tau 1} - \rho_a^{\tau 1}\cancel{(1-\phi^{\tau 1})}\frac{d\phi^{\tau 1}(S_{r_w}^{\tau 1}\dot{p}_w^{\tau 1} + S_{r_g}^{\tau 1}\dot{p}_g^{\tau 1})}{\cancel{(1-\phi^{\tau 1})}K_s}S_{r_g}^{\tau 1} \\
&\quad + \rho_a^{\tau 1}\cancel{(1-\phi^{\tau 1})}\frac{(b-\phi^{\tau 1})(dS_{r_w}^{\tau 1}\dot{p}_w^{\tau 1})}{\cancel{(1-\phi^{\tau 1})}K_s}S_{r_g}^{\tau 1} + \rho_a^{\tau 1}\cancel{(1-\phi^{\tau 1})}\frac{(b-\phi^{\tau 1})(S_{r_w}^{\tau 1}d\dot{p}_w^{\tau 1} + S_{r_g}^{\tau 1}d\dot{p}_g^{\tau 1})}{\cancel{(1-\phi^{\tau 1})}K_s}S_{r_g}^{\tau 1} \\
&\quad + \rho_a^{\tau 1}\cancel{(1-\phi^{\tau 1})}\frac{(b-\phi^{\tau 1})(S_{r_w}^{\tau 1}dS_{r_g}^{\tau 1}\dot{p}_w^{\tau 1} + 2S_{r_g}^{\tau 1}dS_{r_g}^{\tau 1}\dot{p}_g^{\tau 1})}{\cancel{(1-\phi^{\tau 1})}K_s} \\
&\quad + \underbrace{d\rho_a^{\tau 1}\left((1-\phi^{\tau 1})\dot{\varepsilon}_v^{\tau 1} - \frac{\dot{\sigma}'^{\tau 1}}{K_s}\right)S_{r_g}^{\tau 1} + \rho_a^{\tau 1}\left((1-\phi^{\tau 1})d\dot{\varepsilon}_v^{\tau 1} - \frac{d\dot{\sigma}'^{\tau 1}}{K_s}\right)S_{r_g}^{\tau 1} + \rho_a^{\tau 1}\left((1-\phi^{\tau 1})\dot{\varepsilon}_v^{\tau 1} - \frac{\dot{\sigma}'^{\tau 1}}{K_s}\right)dS_{r_g}^{\tau 1}}_{(1.2)} \\
&\quad + \underbrace{d\rho_a^{\tau 1}\phi^{\tau 1}\dot{S}_r^{g,\tau 1} + \rho_a^{\tau 1}d\phi^{\tau 1}\dot{S}_r^{g,\tau 1} + \rho_a^{\tau 1}\phi^{\tau 1}d\dot{S}_r^{g,\tau 1}}_{(1.3)} + \underbrace{\frac{m_{da}}{RT}d\dot{p}_{da}^{\tau 1}\phi^{\tau 1}S_{r_w}^{\tau 1} + \frac{m_{da}}{RT}\dot{p}_{da}^{\tau 1}d\phi^{\tau 1}S_{r_w}^{\tau 1} + \frac{m_{da}}{RT}\dot{p}_{da}^{\tau 1}\phi^{\tau 1}dS_{r_w}^{\tau 1}}_{(2.1)} \\
&\quad + d\rho_{da}^{\tau 1}\cancel{(1-\phi^{\tau 1})}\frac{(b-\phi^{\tau 1})(S_{r_w}^{\tau 1}\dot{p}_w^{\tau 1} + S_{r_g}^{\tau 1}\dot{p}_g^{\tau 1})}{\cancel{(1-\phi^{\tau 1})}K_s}S_{r_w}^{\tau 1} - \rho_{da}^{\tau 1}\cancel{(1-\phi^{\tau 1})}\frac{d\phi^{\tau 1}(S_{r_w}^{\tau 1}\dot{p}_w^{\tau 1} + S_{r_g}^{\tau 1}\dot{p}_g^{\tau 1})}{\cancel{(1-\phi^{\tau 1})}K_s}S_{r_g}^{\tau 1} \\
&\quad + \rho_{da}^{\tau 1}\cancel{(1-\phi^{\tau 1})}\frac{(b-\phi^{\tau 1})(2S_{r_w}^{\tau 1}dS_{r_w}^{\tau 1}\dot{p}_w^{\tau 1} + S_{r_g}^{\tau 1}\dot{p}_g^{\tau 1})}{\cancel{(1-\phi^{\tau 1})}K_s} + \rho_{da}^{\tau 1}\cancel{(1-\phi^{\tau 1})}\frac{(b-\phi^{\tau 1})(S_{r_w}^{\tau 1}d\dot{p}_w^{\tau 1} + S_{r_g}^{\tau 1}d\dot{p}_g^{\tau 1})}{\cancel{(1-\phi^{\tau 1})}K_s}S_{r_w}^{\tau 1} \\
&\quad + \rho_{da}^{\tau 1}\cancel{(1-\phi^{\tau 1})}\frac{(b-\phi^{\tau 1})(dS_{r_g}^{\tau 1}\dot{p}_g^{\tau 1})}{\cancel{(1-\phi^{\tau 1})}K_s}S_{r_w}^{\tau 1} \\
&\quad + \underbrace{d\rho_{da}^{\tau 1}\left((1-\phi^{\tau 1})\dot{\varepsilon}_v^{\tau 1} - \frac{\dot{\sigma}'^{\tau 1}}{K_s}\right)S_{r_w}^{\tau 1} + \rho_{da}^{\tau 1}\left((1-\phi^{\tau 1})d\dot{\varepsilon}_v^{\tau 1} - \frac{d\dot{\sigma}'^{\tau 1}}{K_s}\right)S_{r_w}^{\tau 1} + \rho_{da}^{\tau 1}\left((1-\phi^{\tau 1})\dot{\varepsilon}_v^{\tau 1} - \frac{\dot{\sigma}'^{\tau 1}}{K_s}\right)dS_{r_w}^{\tau 1}}_{(2.2)} \\
&\quad + \underbrace{d\rho_{da}^{\tau 1}\phi^{\tau 1}\dot{S}_r^{w,\tau 1} + \rho_{da}^{\tau 1}d\phi^{\tau 1}\dot{S}_r^{w,\tau 1} + \rho_{da}^{\tau 1}\phi^{\tau 1}d\dot{S}_r^{w,\tau 1}}_{(2.3)} + \underbrace{\dot{M}_a^{\tau 1}\frac{\partial du_m^{\tau 1}}{\partial x_m^{\tau 1}}}_{(3)} + \underbrace{\dot{M}_{da}^{\tau 1}\frac{\partial du_m^{\tau 1}}{\partial x_m^{\tau 1}}}_{(4)}
\end{aligned}
\tag{D–53}
$$

Where:

$$d\dot{p}_g^{\tau 1} = \frac{dp_g^{\tau 1}}{\Delta t} \qquad \text{(D–54)} \qquad\qquad d\dot{p}_{dH_2}^{\tau 1} = \frac{dp_{dH_2}^{\tau 1}}{\Delta t}, \qquad \text{(D–55)}$$

After including all the variations including those introduced in Equations (D–43) and (D–44), the first term (D–53) of the air mass balance equation can be expressed as:

$$
\begin{aligned}
&\dot{M}_a^{\tau 2} det(F) + \dot{M}_{da}^{\tau 2} det(F) - \dot{M}_a^{\tau 1} - \dot{M}_{da}^{\tau 1} \\
&= \frac{m_a}{RT}\frac{dp_a^{\tau 1}}{\Delta t}\phi^{\tau 1} S_{r_g}^{\tau 1} + \frac{m_a}{RT}\dot{p}_a^{\tau 1}(1-\phi^{\tau 1})\left(\frac{(b-\phi^{\tau 1})(S_{r_w}^{\tau 1} dp_w^{\tau 1} + S_{r_g}^{\tau 1} dp_g) - d\sigma'^{\tau 1}}{(1-\phi^{\tau 1})K_s} + \frac{\partial du_m^{\tau 1}}{\partial x_m^{\tau 1}}\right) S_{r_g}^{\tau 1} \\
&\quad + \frac{m_a}{RT}\dot{p}_a^{\tau 1}\phi^{\tau 1} dS_{r_g}^{\tau 1} + \frac{m_a}{RT} dp_a^{\tau 1}\frac{(b-\phi^{\tau 1})(S_{r_w}^{\tau 1}\dot{p}_w^{\tau 1} + S_{r_g}^{\tau 1}\dot{p}_g^{\tau 1})}{K_s} S_{r_g}^{\tau 1} \\
&\quad - \rho_a^{\tau 1}\frac{(S_{r_w}^{\tau 1}\dot{p}_w^{\tau 1} + S_{r_g}^{\tau 1}\dot{p}_g^{\tau 1})}{K_s} S_{r_g}^{\tau 1}(1-\phi^{\tau 1})\left(\frac{(b-\phi^{\tau 1})(S_{r_w}^{\tau 1} dp_w^{\tau 1} + S_{r_g}^{\tau 1} dp_g) - d\sigma'^{\tau 1}}{(1-\phi^{\tau 1})K_s} + \frac{\partial du_m^{\tau 1}}{\partial x_m^{\tau 1}}\right) \\
&\quad + \rho_a^{\tau 1}\frac{(b-\phi^{\tau 1})(dS_{r_w}^{\tau 1}\dot{p}_w^{\tau 1})}{K_s} S_{r_g}^{\tau 1} + \rho_a^{\tau 1}\frac{(b-\phi^{\tau 1})(S_{r_w}^{\tau 1} dp_w^{\tau 1} + S_{r_g}^{\tau 1} dp_g^{\tau 1})}{K_s \Delta t} S_{r_g}^{\tau 1} \\
&\quad + \rho_a^{\tau 1}\frac{(b-\phi^{\tau 1})(S_{r_w}^{\tau 1} dS_{r_g}^{\tau 1}\dot{p}_w^{\tau 1} + 2S_{r_g}^{\tau 1} dS_{r_g}^{\tau 1}\dot{p}_g^{\tau 1})}{K_s} + \frac{m_a}{RT} dp_a^{\tau 1}\left((1-\phi^{\tau 1})\dot{\varepsilon}_v^{\tau 1} - \frac{\dot{\sigma}'^{\tau 1}}{K_s}\right) S_{r_g}^{\tau 1} \\
&\quad + \rho_a^{\tau 1}\left((1-\phi^{\tau 1})\frac{\partial du_m^{\tau 1}}{\partial x_m^{\tau 1}}\left(\frac{1}{\Delta t} - \dot{\varepsilon}_v^{\tau 1}\right) - \frac{d\sigma'^{\tau 1}}{K_s \Delta t}\right) S_{r_g}^{\tau 1} + \rho_a^{\tau 1}\left((1-\phi^{\tau 1})\dot{\varepsilon}_v^{\tau 1} - \frac{\dot{\sigma}'^{\tau 1}}{K_s}\right) dS_{r_g}^{\tau 1} + \frac{m_a}{RT} dp_a^{\tau 1}\phi^{\tau 1}\dot{S}_r^{g,\tau 1} \\
&\quad + \rho_a^{\tau 1}(1-\phi^{\tau 1})\left(\frac{(b-\phi^{\tau 1})(S_{r_w}^{\tau 1} dp_w^{\tau 1} + S_{r_g}^{\tau 1} dp_g) - d\sigma'^{\tau 1}}{(1-\phi^{\tau 1})K_s} + \frac{\partial du_m^{\tau 1}}{\partial x_m^{\tau 1}}\right)\dot{S}_r^{g,\tau 1} + \rho_a^{\tau 1}\phi^{\tau 1}\frac{dS_{r_g}^{\tau 1}}{\Delta t} \\
&\quad + \frac{m_{da}}{RT}\frac{dp_{da}^{\tau 1}}{\Delta t}\phi^{\tau 1} S_{r_w}^{\tau 1} + \frac{m_{da}}{RT}\dot{p}_{da}^{\tau 1}(1-\phi^{\tau 1})\left(\frac{(b-\phi^{\tau 1})(S_{r_w}^{\tau 1} dp_w^{\tau 1} + S_{r_g}^{\tau 1} dp_g) - d\sigma'^{\tau 1}}{(1-\phi^{\tau 1})K_s} + \frac{\partial du_m^{\tau 1}}{\partial x_m^{\tau 1}}\right) S_{r_w}^{\tau 1} \\
&\quad + \frac{m_{da}}{RT}\dot{p}_{da}^{\tau 1}\phi^{\tau 1} dS_{r_w}^{\tau 1} + \frac{m_{da}}{RT} dp_{da}^{\tau 1}\frac{(b-\phi^{\tau 1})(S_{r_w}^{\tau 1}\dot{p}_w^{\tau 1} + S_{r_g}^{\tau 1}\dot{p}_g^{\tau 1})}{K_s} S_{r_w}^{\tau 1} \\
&\quad - \rho_{da}^{\tau 1}\frac{(S_{r_w}^{\tau 1}\dot{p}_w^{\tau 1} + S_{r_g}^{\tau 1}\dot{p}_g^{\tau 1})}{K_s} S_{r_w}^{\tau 1}(1-\phi^{\tau 1})\left(\frac{(b-\phi^{\tau 1})(S_{r_w}^{\tau 1} dp_w^{\tau 1} + S_{r_g}^{\tau 1} dp_g) - d\sigma'^{\tau 1}}{(1-\phi^{\tau 1})K_s} + \frac{\partial du_m^{\tau 1}}{\partial x_m^{\tau 1}}\right) \\
&\quad + \rho_{da}^{\tau 1}\frac{(b-\phi^{\tau 1})(dS_{r_w}^{\tau 1}\dot{p}_w^{\tau 1})}{K_s} S_{r_w}^{\tau 1} + \rho_{da}^{\tau 1}\frac{(b-\phi^{\tau 1})(S_{r_w}^{\tau 1} dp_w^{\tau 1} + S_{r_g}^{\tau 1} dp_g^{\tau 1})}{K_s \Delta t} S_{r_w}^{\tau 1} \\
&\quad + \rho_{da}^{\tau 1}\frac{(b-\phi^{\tau 1})(S_{r_w}^{\tau 1} dS_{r_g}^{\tau 1}\dot{p}_w^{\tau 1} + 2S_{r_g}^{\tau 1} dS_{r_g}^{\tau 1}\dot{p}_g^{\tau 1})}{K_s} + \frac{m_{da}}{RT} dp_{da}^{\tau 1}\left((1-\phi^{\tau 1})\dot{\varepsilon}_v^{\tau 1} - \frac{\dot{\sigma}'^{\tau 1}}{K_s}\right) S_{r_w}^{\tau 1} \\
&\quad + \rho_{da}^{\tau 1}\left((1-\phi^{\tau 1})\frac{\partial du_m^{\tau 1}}{\partial x_m^{\tau 1}}\left(\frac{1}{\Delta t} - \dot{\varepsilon}_v^{\tau 1}\right) - \frac{d\sigma'^{\tau 1}}{K_s \Delta t}\right) S_{r_w}^{\tau 1} + \rho_{da}^{\tau 1}\left((1-\phi^{\tau 1})\dot{\varepsilon}_v^{\tau 1} - \frac{\dot{\sigma}'^{\tau 1}}{K_s}\right) dS_{r_w}^{\tau 1} + \frac{m_{da}}{RT} dp_a^{\tau 1}\phi^{\tau 1}\dot{S}_r^{w,\tau 1} \\
&\quad + \rho_{da}^{\tau 1}(1-\phi^{\tau 1})\left(\frac{(b-\phi^{\tau 1})(S_{r_w}^{\tau 1} dp_w^{\tau 1} + S_{r_g}^{\tau 1} dp_g) - d\sigma'^{\tau 1}}{(1-\phi^{\tau 1})K_s} + \frac{\partial du_m^{\tau 1}}{\partial x_m^{\tau 1}}\right)\dot{S}_r^{w,\tau 1} + \rho_{da}^{\tau 1}\phi^{\tau 1}\frac{dS_{r_w}^{\tau 1}}{\Delta t} \\
&\quad + \dot{M}_a^{\tau 1}\frac{\partial du_m^{\tau 1}}{\partial x_m^{\tau 1}} + \dot{M}_{da}^{\tau 1}\frac{\partial du_m^{\tau 1}}{\partial x_m^{\tau 1}}
\end{aligned}
\tag{D–56}
$$

The second term of the gas mass balance equation can be re-expressed by developing the different terms (1) to (6) as:

$$
\begin{aligned}
& f_{a,i}^{\tau 2}\frac{\partial x_k^{\tau 1}}{\partial x_j^{\tau 2}}det(F)+f_{da,i}^{\tau 2}\frac{\partial x_k^{\tau 1}}{\partial x_j^{\tau 2}}det(F)-f_{a,k}^{\tau 1}-f_{da,k}^{\tau 1}=f_{a,i}^{\tau 2}\frac{\partial x_k^{\tau 1}}{\partial x_j^{\tau 2}}\left(1+\frac{\partial du_i^{\tau 1}}{\partial x_j^{\tau 1}}\right)+f_{da,i}^{\tau 2}\frac{\partial x_k^{\tau 1}}{\partial x_j^{\tau 2}}\left(1+\frac{\partial du_i^{\tau 1}}{\partial x_j^{\tau 1}}\right)-f_{a,k}^{\tau 1}-f_{da,k}^{\tau 1} \\
&= \underbrace{df_{a,l}^{\tau 1}}_{(1)}-\underbrace{f_{a,i}^{\tau 1}\frac{\partial du_l^{\tau 1}}{\partial x_i^{\tau 1}}}_{(3)}+\underbrace{f_{a,l}^{\tau 1}\frac{\partial du_m^{\tau 1}}{\partial x_m^{\tau 1}}}_{(4)}+\underbrace{df_{da,l}^{\tau 1}}_{(2)}-\underbrace{f_{da,i}^{\tau 1}\frac{\partial du_l^{\tau 1}}{\partial x_i^{\tau 1}}}_{(5)}+\underbrace{f_{da,l}^{\tau 1}\frac{\partial du_m^{\tau 1}}{\partial x_m^{\tau 1}}}_{(6)} \\
&= -d\rho_a^{\tau 1}\frac{k_{ij}^{int}k_{r,g}^{\tau 1}}{\mu_g}\left(\frac{\partial p_g^{\tau 1}}{\partial x_j^{\tau 1}}+\rho_g^{\tau 1}g_j\right)-\rho_a^{\tau 1}\frac{dk_{ij}^{int}k_{r,g}^{\tau 1}}{\mu_g}\left(\frac{\partial p_g^{\tau 1}}{\partial x_j^{\tau 1}}+\rho_g^{\tau 1}g_j\right) \\
&\quad -\rho_a^{\tau 1}\frac{k_{ij}^{int}dk_{r,g}^{\tau 1}}{\mu_g}\left(\frac{\partial p_g^{\tau 1}}{\partial x_j^{\tau 1}}+\rho_g^{\tau 1}g_j\right)-\rho_a^{\tau 1}\frac{k_{ij}^{int}k_{r,g}^{\tau 1}}{\mu_g}\left(d\left(\frac{\partial p_g^{\tau 1}}{\partial x_j^{\tau 1}}\right)+\rho_g^{\tau 1}g_j\right) \\
&\quad -d\phi^{\tau 1}S_r^{g,\tau 1}\bar{\tau}D_{a-g}\rho_g^{\tau 1}\frac{\partial}{\partial x_i^{\tau 1}}\left(\frac{\rho_a^{\tau 1}}{\rho_g^{\tau 1}}\right)-\phi^{\tau 1}dS_{r_g}^{\tau 1}\bar{\tau}D_{a-g}\rho_g^{\tau 1}\frac{\partial}{\partial x_i^{\tau 1}}\left(\frac{\rho_a^{\tau 1}}{\rho_g^{\tau 1}}\right) \\
&\quad \underbrace{-\phi^{\tau 1}S_{r_g}^{\tau 1}\bar{\tau}D_{a-g}d\rho_g^{\tau 1}\frac{\partial}{\partial x_i^{\tau 1}}\left(\frac{\rho_a^{\tau 1}}{\rho_g^{\tau 1}}\right)-\phi^{\tau 1}S_{r_g}^{\tau 1}\bar{\tau}D_{a-g}\rho_g^{\tau 1}d\left(\frac{\partial}{\partial x_i^{\tau 1}}\left(\frac{\rho_a^{\tau 1}}{\rho_g^{\tau 1}}\right)\right)}_{(1)} \\
&\quad -d\rho_{da}^{\tau 1}\frac{k_{ij}^{int}k_{r,w}^{\tau 1}}{\mu_w}\left(\frac{\partial p_w^{\tau 1}}{\partial x_j^{\tau 1}}+\rho_w^{\tau 1}g_j\right)-\rho_{da}^{\tau 1}\frac{dk_{ij}^{int}k_{r,w}^{\tau 1}}{\mu_g}\left(\frac{\partial p_w^{\tau 1}}{\partial x_j^{\tau 1}}+\rho_w^{\tau 1}g_j\right) \\
&\quad -\rho_{da}^{\tau 1}\frac{k_{ij}^{int}dk_{r,w}^{\tau 1}}{\mu_w}\left(\frac{\partial p_w^{\tau 1}}{\partial x_j^{\tau 1}}+\rho_w^{\tau 1}g_j\right)-\rho_{da}^{\tau 1}\frac{k_{ij}^{int}k_{r,w}^{\tau 1}}{\mu_w}\left(d\left(\frac{\partial p_w^{\tau 1}}{\partial x_j^{\tau 1}}\right)+\rho_w^{\tau 1}g_j\right) \\
&\quad -d\phi^{\tau 1}S_{r_w}^{\tau 1}\bar{\tau}D_{da-w}\rho_w^{\tau 1}\frac{\partial}{\partial x_i^{\tau 1}}\left(\frac{\rho_{da}^{\tau 1}}{\rho_w^{\tau 1}}\right)-\phi^{\tau 1}dS_{r_w}^{\tau 1}\bar{\tau}D_{da-w}\rho_w^{\tau 1}\frac{\partial}{\partial x_i^{\tau 1}}\left(\frac{\rho_{da}^{\tau 1}}{\rho_w^{\tau 1}}\right) \\
&\quad \underbrace{-\phi^{\tau 1}S_{r_w}^{\tau 1}\bar{\tau}D_{da-w}d\rho_w^{\tau 1}\frac{\partial}{\partial x_i^{\tau 1}}\left(\frac{\rho_{da}^{\tau 1}}{\rho_w^{\tau 1}}\right)-\phi^{\tau 1}S_{r_w}^{\tau 1}\bar{\tau}D_{da-w}\rho_w^{\tau 1}d\left(\frac{\partial}{\partial x_i^{\tau 1}}\left(\frac{\rho_{da}^{\tau 1}}{\rho_w^{\tau 1}}\right)\right)}_{(2)} \\
&\quad -\underbrace{f_{a,i}^{\tau 1}\frac{\partial du_l^{\tau 1}}{\partial x_i^{\tau 1}}}_{(3)}+\underbrace{f_{a,l}^{\tau 1}\frac{\partial du_m^{\tau 1}}{\partial x_m^{\tau 1}}}_{(4)}-\underbrace{f_{da,i}^{\tau 1}\frac{\partial du_l^{\tau 1}}{\partial x_i^{\tau 1}}}_{(5)}+\underbrace{f_{da,l}^{\tau 1}\frac{\partial du_m^{\tau 1}}{\partial x_m^{\tau 1}}}_{(6)}
\end{aligned}
\tag{D–57}
$$

Where dk_{ij}^{int}, $dk_{r,w}^{\tau 1}$ and $dk_{r,g}^{\tau 1}$ depend on the chosen intrinsic permeability variation and water and gas permeability curve.

After including all the different variations, the second term (D–57) of the gas mass balance equation can finally be expressed as:

$$
\begin{aligned}
& f_{a,i}^{\tau 2}\frac{\partial x_k^{\tau 1}}{\partial x_j^{\tau 2}}det(F)+f_{da,i}^{\tau 2}\frac{\partial x_k^{\tau 1}}{\partial x_j^{\tau 2}}det(F)-f_{a,k}^{\tau 1}-f_{da,k}^{\tau 1} \\
&= -\frac{m_a}{RT}dp_a^{\tau 1}\frac{k_{ij}^{int}k_{g,w}^{\tau 1}}{\mu_g}\left(\frac{\partial p_g^{\tau 1}}{\partial x_j^{\tau 1}}+\rho_g^{\tau 1}g_j\right)-\rho_a^{\tau 1}\frac{dk_{ij}^{int}k_{r,g}^{\tau 1}}{\mu_g}\left(\frac{\partial p_g^{\tau 1}}{\partial x_j^{\tau 1}}+\rho_g^{\tau 1}g_j\right)-\rho_a^{\tau 1}\frac{k_{ij}^{int}dk_{r,g}^{\tau 1}}{\mu_g}\left(\frac{\partial p_g^{\tau 1}}{\partial x_j^{\tau 1}}+\rho_g^{\tau 1}g_j\right) \\
&\quad -\rho_a^{\tau 1}\frac{k_{ij}^{int}k_{r,g}^{\tau 1}}{\mu_g}\left(\frac{\partial dp_g^{\tau 1}}{\partial x_j^{\tau 1}}+\rho_g^{\tau 1}g_j\right)+\rho_a^{\tau 1}\frac{k_{ij}^{int}k_{r,g}^{\tau 1}}{\mu_g}\left(\frac{\partial p_g^{\tau 1}}{\partial x_k^{\tau 1}}\frac{\partial du_k^{\tau 1}}{\partial x_j^{\tau 1}}\right) \\
&\quad -(1-\phi^{\tau 1})\left(\frac{(b-\phi^{\tau 1})(S_{r_w}^{\tau 1}dp_w^{\tau 1}+S_{r_g}^{\tau 1}dp_g)-d\sigma'^{\tau 1}}{(1-\phi^{\tau 1})K_s}+\frac{\partial du_m^{\tau 1}}{\partial x_m^{\tau 1}}\right)S_{r_g}^{\tau 1}\bar{\tau}D_{a-g}\rho_g^{\tau 1}\frac{\partial}{\partial x_i^{\tau 1}}\left(\frac{\rho_a^{\tau 1}}{\rho_g^{\tau 1}}\right) \\
&\quad -\phi^{\tau 1}dS_{r_g}^{\tau 1}\bar{\tau}D_{a-g}\rho_g^{\tau 1}\frac{\partial}{\partial x_i^{\tau 1}}\left(\frac{\rho_a^{\tau 1}}{\rho_g^{\tau 1}}\right)-\phi^{\tau 1}S_{r_g}^{\tau 1}\bar{\tau}D_{a-g}d\rho_g^{\tau 1}\frac{\partial}{\partial x_i^{\tau 1}}\left(\frac{\rho_a^{\tau 1}}{\rho_g^{\tau 1}}\right) \\
&\quad -\phi^{\tau 1}S_{r_g}^{\tau 1}\bar{\tau}D_{a-g}\rho_g^{\tau 1}\frac{\partial d\frac{\rho_v^{\tau 1}}{\rho_g^{\tau 1}}}{\partial x_j^{\tau 1}}+\phi^{\tau 1}S_{r_g}^{\tau 1}\bar{\tau}D_{v-a}\rho_g^{\tau 1}\frac{\partial\frac{\rho_v^{\tau 1}}{\rho_g^{\tau 1}}}{\partial x_i^{\tau 1}}\frac{\partial du_i^{\tau 1}}{\partial x_j^{\tau 1}}-\frac{m_{da}}{RT}dp_{da}^{\tau 1}\frac{k_{ij}^{int}k_{r,w}^{\tau 1}}{\mu_w}\left(\frac{\partial p_w^{\tau 1}}{\partial x_j^{\tau 1}}+\rho_w^{\tau 1}g_j\right) \\
&\quad -\rho_{da}^{\tau 1}\frac{dk_{ij}^{int}k_{r,w}^{\tau 1}}{\mu_w}\left(\frac{\partial p_w^{\tau 1}}{\partial x_j^{\tau 1}}+\rho_w^{\tau 1}g_j\right)-\rho_{da}^{\tau 1}\frac{k_{ij}^{int}dk_{r,w}^{\tau 1}}{\mu_w}\left(\frac{\partial p_w^{\tau 1}}{\partial x_j^{\tau 1}}+\rho_w^{\tau 1}g_j\right) \\
&\quad -\rho_{da}^{\tau 1}\frac{k_{ij}^{int}k_{r,w}^{\tau 1}}{\mu_w}\left(\frac{\partial dp_w^{\tau 1}}{\partial x_j^{\tau 1}}+\rho_w^{\tau 1}g_j\right)+\rho_{da}^{\tau 1}\frac{k_{ij}^{int}k_{r,w}^{\tau 1}}{\mu_w}\left(\frac{\partial p_w^{\tau 1}}{\partial x_k^{\tau 1}}\frac{\partial du_k^{\tau 1}}{\partial x_j^{\tau 1}}\right) \\
&\quad -(1-\phi^{\tau 1})\left(\frac{(b-\phi^{\tau 1})(S_{r_w}^{\tau 1}dp_w^{\tau 1}+S_{r_w}^{\tau 1}dp_g)-d\sigma'^{\tau 1}}{(1-\phi^{\tau 1})K_s}+\frac{\partial du_m^{\tau 1}}{\partial x_m^{\tau 1}}\right)S_{r_w}^{\tau 1}\bar{\tau}D_{da-w}\rho_w^{\tau 1}\frac{\partial}{\partial x_i^{\tau 1}}\left(\frac{\rho_{da}^{\tau 1}}{\rho_w^{\tau 1}}\right) \\
&\quad -\phi^{\tau 1}dS_{r_w}^{\tau 1}\bar{\tau}D_{da-w}\rho_w^{\tau 1}\frac{\partial}{\partial x_i^{\tau 1}}\left(\frac{\rho_{da}^{\tau 1}}{\rho_w^{\tau 1}}\right)-\phi^{\tau 1}S_{r_w}^{\tau 1}\bar{\tau}D_{da-w}d\rho_w^{\tau 1}\frac{\partial}{\partial x_i^{\tau 1}}\left(\frac{\rho_{da}^{\tau 1}}{\rho_w^{\tau 1}}\right) \\
&\quad -\phi^{\tau 1}S_{r_w}^{\tau 1}\bar{\tau}D_{da-w}\rho_w^{\tau 1}\frac{\partial d\frac{\rho_{da}^{\tau 1}}{\rho_w^{\tau 1}}}{\partial x_j^{\tau 1}}+\phi^{\tau 1}S_{r_w}^{\tau 1}\bar{\tau}D_{da-w}\rho_w^{\tau 1}\frac{\partial\frac{\rho_{da}^{\tau 1}}{\rho_w^{\tau 1}}}{\partial x_i^{\tau 1}}\frac{\partial du_i^{\tau 1}}{\partial x_j^{\tau 1}} \\
&\quad -f_{a,i}^{\tau 1}\frac{\partial du_l^{\tau 1}}{\partial x_i^{\tau 1}}+f_{a,l}^{\tau 1}\frac{\partial du_m^{\tau 1}}{\partial x_m^{\tau 1}}-f_{da,i}^{\tau 1}\frac{\partial du_l^{\tau 1}}{\partial x_i^{\tau 1}}+f_{da,l}^{\tau 1}\frac{\partial du_m^{\tau 1}}{\partial x_m^{\tau 1}}
\end{aligned}
\tag{D–58}
$$

By regrouping the two terms (D–56) and (D–58), the gas mass balance equation becomes:

$$
\begin{aligned}
\int_{\Omega^{\tau 1}} p_g^{\star} \Bigg\{ & \frac{m_a}{RT}\frac{dp_a^{\tau 1}}{\Delta t}\phi^{\tau 1}S_{r_g}^{\tau 1} + \frac{m_a}{RT}\dot{p}_a^{\tau 1}\phi^{\tau 1}dS_{r_g}^{\tau 1} + \frac{m_a}{RT}dp_a^{\tau 1}\frac{(b-\phi^{\tau 1})(S_{r_w}^{\tau 1}\dot{p}_w^{\tau 1}+S_{r_g}^{\tau 1}\dot{p}_g^{\tau 1})}{K_s}S_{r_g}^{\tau 1} \\
& + \frac{m_a}{RT}\dot{p}_a^{\tau 1}(1-\phi^{\tau 1})\left(\frac{(b-\phi^{\tau 1})(S_{r_w}^{\tau 1}dp_w^{\tau 1}+S_{r_g}^{\tau 1}dp_g)-d\sigma'^{\tau 1}}{(1-\phi^{\tau 1})K_s}+\frac{\partial du_m^{\tau 1}}{\partial x_m^{\tau 1}}\right)S_{r_g}^{\tau 1} \\
& - \rho_a^{\tau 1}\frac{(S_{r_w}^{\tau 1}\dot{p}_w^{\tau 1}+S_{r_g}^{\tau 1}\dot{p}_g^{\tau 1})}{K_s}S_{g_w}^{\tau 1}(1-\phi^{\tau 1})\left(\frac{(b-\phi^{\tau 1})(S_r^{w,\tau 1}dp_w^{\tau 1}+S_{r_g}^{\tau 1}dp_g)-d\sigma'^{\tau 1}}{(1-\phi^{\tau 1})K_s}+\frac{\partial du_m^{\tau 1}}{\partial x_m^{\tau 1}}\right) \\
& + \rho_a^{\tau 1}\frac{(b-\phi^{\tau 1})(dS_{r_w}^{\tau 1}\dot{p}_w^{\tau 1})}{K_s}S_{r_g}^{\tau 1} + \rho_a^{\tau 1}\frac{(b-\phi^{\tau 1})(S_{r_w}^{\tau 1}dp_w^{\tau 1}+S_{r_g}^{\tau 1}dp_g^{\tau 1})}{K_s\Delta t}S_{r_g}^{\tau 1} \\
& + \rho_a^{\tau 1}\frac{(b-\phi^{\tau 1})(S_{r_w}^{\tau 1}dS_{r_g}^{\tau 1}\dot{p}_w^{\tau 1}+2S_{r_g}^{\tau 1}dS_{r_g}^{\tau 1}\dot{p}_g^{\tau 1})}{K_s} + \frac{m_a}{RT}dp_a^{\tau 1}\left((1-\phi^{\tau 1})\dot{\varepsilon}_v^{\tau 1}-\frac{\dot{\sigma}'^{\tau 1}}{K_s}\right)S_{r_g}^{\tau 1} \\
& + \rho_a^{\tau 1}\left((1-\phi^{\tau 1})\frac{\partial du_m^{\tau 1}}{\partial x_m^{\tau 1}}\left(\frac{1}{\Delta t}-\dot{\varepsilon}_v^{\tau 1}\right)-\frac{d\sigma'^{\tau 1}}{K_s\Delta t}\right)S_{r_g}^{\tau 1} + \rho_a^{\tau 1}\left((1-\phi^{\tau 1})\dot{\varepsilon}_v^{\tau 1}-\frac{\dot{\sigma}'^{\tau 1}}{K_s}\right)dS_{r_g}^{\tau 1} \\
& + \frac{m_a}{RT}dp_a^{\tau 1}\phi^{\tau 1}\dot{S}_{r_g}^{\tau 1} + \rho_a^{\tau 1}(1-\phi^{\tau 1})\left(\frac{(b-\phi^{\tau 1})(S_{r_w}^{\tau 1}dp_w^{\tau 1}+S_{r_g}^{\tau 1}dp_g)-d\sigma'^{\tau 1}}{(1-\phi^{\tau 1})K_s}+\frac{\partial du_m^{\tau 1}}{\partial x_m^{\tau 1}}\right)\dot{S}_{r_g}^{\tau 1} \\
& + \rho_a^{\tau 1}\phi^{\tau 1}\frac{dS_{r_g}^{\tau 1}}{\Delta t} \\
& + \frac{m_{da}}{RT}\frac{dp_{da}^{\tau 1}}{\Delta t}\phi^{\tau 1}S_{r_w}^{\tau 1} + \frac{m_{da}}{RT}\dot{p}_{da}^{\tau 1}(1-\phi^{\tau 1})\left(\frac{(b-\phi^{\tau 1})(S_{r_w}^{\tau 1}dp_w^{\tau 1}+S_{r_g}^{\tau 1}dp_g)-d\sigma'^{\tau 1}}{(1-\phi^{\tau 1})K_s}+\frac{\partial du_m^{\tau 1}}{\partial x_m^{\tau 1}}\right)S_{r_w}^{\tau 1} \\
& + \frac{m_{da}}{RT}\dot{p}_{da}^{\tau 1}\phi^{\tau 1}dS_{r_w}^{\tau 1} + \frac{m_{da}}{RT}dp_{da}^{\tau 1}\frac{(b-\phi^{\tau 1})(S_{r_w}^{\tau 1}\dot{p}_w^{\tau 1}+S_{r_g}^{\tau 1}\dot{p}_g^{\tau 1})}{K_s}S_{r_w}^{\tau 1} \\
& - \rho_{da}^{\tau 1}\frac{(S_{r_w}^{\tau 1}\dot{p}_w^{\tau 1}+S_{r_g}^{\tau 1}\dot{p}_g^{\tau 1})}{K_s}S_{r_w}^{\tau 1}(1-\phi^{\tau 1})\left(\frac{(b-\phi^{\tau 1})(S_{r_w}^{\tau 1}dp_w^{\tau 1}+S_{r_g}^{\tau 1}dp_g)-d\sigma'^{\tau 1}}{(1-\phi^{\tau 1})K_s}+\frac{\partial du_m^{\tau 1}}{\partial x_m^{\tau 1}}\right) \\
& + \rho_{da}^{\tau 1}\frac{(b-\phi^{\tau 1})(dS_{r_w}^{\tau 1}\dot{p}_w^{\tau 1})}{K_s}S_{r_w}^{\tau 1} + \rho_{da}^{\tau 1}\frac{(b-\phi^{\tau 1})(S_{r_w}^{\tau 1}dp_w^{\tau 1}+S_{r_g}^{\tau 1}dp_g^{\tau 1})}{K_s\Delta t}S_{r_w}^{\tau 1} \\
& + \rho_{da}^{\tau 1}\frac{(b-\phi^{\tau 1})(S_{r_w}^{\tau 1}dS_{r_g}^{\tau 1}\dot{p}_w^{\tau 1}+2S_r^{g,\tau 1}dS_{r_g}^{\tau 1}\dot{p}_g^{\tau 1})}{K_s} + \frac{m_{da}}{RT}dp_{da}^{\tau 1}\left((1-\phi^{\tau 1})\dot{\varepsilon}_v^{\tau 1}-\frac{\dot{\sigma}'^{\tau 1}}{K_s}\right)S_{r_w}^{\tau 1} \\
& + \rho_{da}^{\tau 1}\left((1-\phi^{\tau 1})\frac{\partial du_m^{\tau 1}}{\partial x_m^{\tau 1}}\left(\frac{1}{\Delta t}-\dot{\varepsilon}_v^{\tau 1}\right)-\frac{d\sigma'^{\tau 1}}{K_s\Delta t}\right)S_{r_w}^{\tau 1} + \rho_{da}^{\tau 1}\left((1-\phi^{\tau 1})\dot{\varepsilon}_v^{\tau 1}-\frac{\dot{\sigma}'^{\tau 1}}{K_s}\right)dS_{r_w}^{\tau 1} \\
& + \frac{m_{da}}{RT}dp_a^{\tau 1}\phi^{\tau 1}\dot{S}_{r_w}^{\tau 1} + \rho_{da}^{\tau 1}(1-\phi^{\tau 1})\left(\frac{(b-\phi^{\tau 1})(S_{r_w}^{\tau 1}dp_w^{\tau 1}+S_{r_g}^{\tau 1}dp_g)-d\sigma'^{\tau 1}}{(1-\phi^{\tau 1})K_s}+\frac{\partial du_m^{\tau 1}}{\partial x_m^{\tau 1}}\right)\dot{S}_{r_w}^{\tau 1} \\
& + \rho_{da}^{\tau 1}\phi^{\tau 1}\frac{dS_{r_w}^{\tau 1}}{\Delta t} + \dot{M}_a^{\tau 1}\frac{\partial du_m^{\tau 1}}{\partial x_m^{\tau 1}} + \dot{M}_{da}^{\tau 1}\frac{\partial du_m^{\tau 1}}{\partial x_m^{\tau 1}}\Bigg\}d\Omega^{\tau 1}
\end{aligned}
$$

(continued on next page)

$$
\begin{aligned}
-\int_{\Omega^{\tau 1}} \frac{\partial p_g^{\star}}{\partial x_k^{\tau 1}} \Bigg\{ & -\frac{m_a}{RT} d p_a^{\tau 1} \frac{k_{ij}^{int} k_{g,w}^{\tau 1}}{\mu_g} \left(\frac{\partial p_g^{\tau 1}}{\partial x_j^{\tau 1}} + \rho_g^{\tau 1} g_j \right) - \rho_a^{\tau 1} \frac{d k_{ij}^{int} k_{r,g}^{\tau 1}}{\mu_g} \left(\frac{\partial p_g^{\tau 1}}{\partial x_j^{\tau 1}} + \rho_g^{\tau 1} g_j \right) \\
& - \rho_a^{\tau 1} \frac{k_{ij}^{int} d k_{r,g}^{\tau 1}}{\mu_g} \left(\frac{\partial p_g^{\tau 1}}{\partial x_j^{\tau 1}} + \rho_g^{\tau 1} g_j \right) - \rho_a^{\tau 1} \frac{k_{ij}^{int} k_{r,g}^{\tau 1}}{\mu_g} \left(\frac{\partial d p_g^{\tau 1}}{\partial x_j^{\tau 1}} + \rho_g^{\tau 1} g_j \right) + \rho_a^{\tau 1} \frac{k_{ij}^{int} k_{r,g}^{\tau 1}}{\mu_g} \left(\frac{\partial p_g^{\tau 1}}{\partial x_k^{\tau 1}} \frac{\partial u_k^{\tau 1}}{\partial x_j^{\tau 1}} \right) \\
& - (1-\phi^{\tau 1}) \left(\frac{(b-\phi^{\tau 1})(S_{r_w}^{\tau 1} d p_w^{\tau 1} + S_{r_g}^{\tau 1} d p_g) - d\sigma'^{\tau 1}}{(1-\phi^{\tau 1}) K_s} + \frac{\partial d u_m^{\tau 1}}{\partial x_m^{\tau 1}} \right) S_{r_g}^{\tau 1} \bar{\tau} D_{a-g} \rho_g^{\tau 1} \frac{\partial}{\partial x_i^{\tau 1}} \left(\frac{\rho_a^{\tau 1}}{\rho_g^{\tau 1}} \right) \\
& - \phi^{\tau 1} d S_{r_g}^{\tau 1} \bar{\tau} D_{a-g} \rho_g^{\tau 1} \frac{\partial}{\partial x_i^{\tau 1}} \left(\frac{\rho_a^{\tau 1}}{\rho_g^{\tau 1}} \right) - \phi^{\tau 1} S_{r_g}^{\tau 1} \bar{\tau} D_{a-g} d \rho_g^{\tau 1} \frac{\partial}{\partial x_i^{\tau 1}} \left(\frac{\rho_a^{\tau 1}}{\rho_g^{\tau 1}} \right) \\
& - \phi^{\tau 1} S_{r_g}^{\tau 1} \bar{\tau} D_{a-g} \rho_g^{\tau 1} \frac{\partial d \frac{\rho_v^{\tau 1}}{\rho_g^{\tau 1}}}{\partial x_j^{\tau 1}} + \phi^{\tau 1} S_{r_g}^{\tau 1} \bar{\tau} D_{v-a} \rho_g^{\tau 1} \frac{\partial \frac{\rho_v^{\tau 1}}{\rho_g^{\tau 1}}}{\partial x_i^{\tau 1}} \frac{\partial d u_i^{\tau 1}}{\partial x_j^{\tau 1}} \\
& - \frac{m_{da}}{RT} d p_{da}^{\tau 1} \frac{k_{ij}^{int} k_{r,w}^{\tau 1}}{\mu_w} \left(\frac{\partial p_w^{\tau 1}}{\partial x_j^{\tau 1}} + \rho_w^{\tau 1} g_j \right) - \rho_{da}^{\tau 1} \frac{d k_{ij}^{int} k_{r,w}^{\tau 1}}{\mu_w} \left(\frac{\partial p_w^{\tau 1}}{\partial x_j^{\tau 1}} + \rho_w^{\tau 1} g_j \right) \\
& - \rho_{da}^{\tau 1} \frac{k_{ij}^{int} d k_{r,w}^{\tau 1}}{\mu_w} \left(\frac{\partial p_w^{\tau 1}}{\partial x_j^{\tau 1}} + \rho_w^{\tau 1} g_j \right) - \rho_{da}^{\tau 1} \frac{k_{ij}^{int} k_{r,w}^{\tau 1}}{\mu_w} \left(\frac{\partial d p_w^{\tau 1}}{\partial x_j^{\tau 1}} + \rho_w^{\tau 1} g_j \right) + \rho_{da}^{\tau 1} \frac{k_{ij}^{int} k_{r,w}^{\tau 1}}{\mu_w} \left(\frac{\partial p_w^{\tau 1}}{\partial x_k^{\tau 1}} \frac{\partial u_k^{\tau 1}}{\partial x_j^{\tau 1}} \right) \\
& - (1-\phi^{\tau 1}) \left(\frac{(b-\phi^{\tau 1})(S_{r_w}^{\tau 1} d p_w^{\tau 1} + S_{r_w}^{\tau 1} d p_g) - d\sigma'^{\tau 1}}{(1-\phi^{\tau 1}) K_s} + \frac{\partial d u_m^{\tau 1}}{\partial x_m^{\tau 1}} \right) S_{r_w}^{\tau 1} \bar{\tau} D_{da-w} \rho_w^{\tau 1} \frac{\partial}{\partial x_i^{\tau 1}} \left(\frac{\rho_{da}^{\tau 1}}{\rho_w^{\tau 1}} \right) \\
& - \phi^{\tau 1} d S_{r_w}^{\tau 1} \bar{\tau} D_{da-w} \rho_w^{\tau 1} \frac{\partial}{\partial x_i^{\tau 1}} \left(\frac{\rho_{da}^{\tau 1}}{\rho_w^{\tau 1}} \right) - \phi^{\tau 1} S_{r_w}^{\tau 1} \bar{\tau} D_{da-w} d \rho_w^{\tau 1} \frac{\partial}{\partial x_i^{\tau 1}} \left(\frac{\rho_{da}^{\tau 1}}{\rho_w^{\tau 1}} \right) \\
& - \phi^{\tau 1} S_{r_w}^{\tau 1} \bar{\tau} D_{da-w} \rho_w^{\tau 1} \frac{\partial d \frac{\rho_{da}^{\tau 1}}{\rho_w^{\tau 1}}}{\partial x_j^{\tau 1}} + \phi^{\tau 1} S_{r_w}^{\tau 1} \bar{\tau} D_{da-w} \rho_w^{\tau 1} \frac{\partial \frac{\rho_{da}^{\tau 1}}{\rho_w^{\tau 1}}}{\partial x_i^{\tau 1}} \frac{\partial d u_i^{\tau 1}}{\partial x_j^{\tau 1}} \\
& - f_{a,i}^{\tau 1} \frac{\partial d u_l^{\tau 1}}{\partial x_i^{\tau 1}} + f_{a,l}^{\tau 1} \frac{\partial d u_m^{\tau 1}}{\partial x_m^{\tau 1}} - f_{da,i}^{\tau 1} \frac{\partial d u_l^{\tau 1}}{\partial x_i^{\tau 1}} + f_{da,l}^{\tau 1} \frac{\partial d u_m^{\tau 1}}{\partial x_m^{\tau 1}} \Bigg\} d\Omega^{\tau 1} \\
= & -\Delta_4^{\tau 1}
\end{aligned}
\tag{D–59}
$$

D.4 Element stiffness matrix

The linearisation of the field equations leads to a linear auxiliary problem that can be expressed in matrix form as:

$$\int_{\Omega^{\tau 1}} \left[U^{\star,\tau 1}_{(x_1,x_2)}\right]^T \left[E^{\tau 1}\right] \left[dU^{\tau 1}_{(x_1,x_2)}\right] d\Omega^{\tau 1} = -\Delta_1^{\tau 1} - \Delta_2^{\tau 1} - \Delta_3^{\tau 1} - \Delta_4^{\tau 1} - \Delta_5^{\tau 1} \tag{D–60}$$

Where $\left[E^{\tau 1}\right]$ is the current element stiffness (tangent) matrix which contains all the terms of the linearised balance equations, and may be expressed in the following form:

$$\left[E^{\tau 1}\right] = \begin{bmatrix} E^{\tau 1}_{MM} & E^{\tau 1}_{WM} & E^{\tau 1}_{GM} & E^{\tau 1}_{TM} & E^{\tau 1}_{\nu M} & E^{\tau 1}_{\lambda M} \\ \mathbf{E^{\tau 1}_{MW}} & E^{\tau 1}_{WW} & E^{\tau 1}_{GW} & E^{\tau 1}_{TW} & E^{\tau 1}_{\nu W} & E^{\tau 1}_{\lambda W} \\ \mathbf{E^{\tau 1}_{MG}} & E^{\tau 1}_{WG} & E^{\tau 1}_{GG} & E^{\tau 1}_{TG} & E^{\tau 1}_{\nu G} & E^{\tau 1}_{\lambda G} \\ E^{\tau 1}_{MT} & E^{\tau 1}_{WT} & E^{\tau 1}_{GT} & E^{\tau 1}_{TT} & E^{\tau 1}_{\nu T} & E^{\tau 1}_{\lambda T} \\ E^{\tau 1}_{M\nu} & E^{\tau 1}_{W\nu} & E^{\tau 1}_{G\nu} & E^{\tau 1}_{T\nu} & E^{\tau 1}_{\nu\nu} & E^{\tau 1}_{\lambda\nu} \\ E^{\tau 1}_{M\lambda} & E^{\tau 1}_{W\lambda} & E^{\tau 1}_{G\lambda} & E^{\tau 1}_{T\lambda} & E^{\tau 1}_{\nu\lambda} & E^{\tau 1}_{\lambda\lambda} \end{bmatrix} \tag{D–61}$$

To compute the current element stiffness matrix, it is easier to separate the different parts of the coupled problem. The stiffness matrices of the coupling between the flow and the mechanical problems $\left[E^{\tau 1}_{MW}\right]$ and $\left[E^{\tau 1}_{MG}\right]$ are of interest in the present work, which attempts to determine the influence of the mechanics on the fluids.

D.4.1 Influence of the mechanics on water (E_{MW})

To determine the influence of the mechanics on the water, a different geometry for the configurations $\Omega^{\tau 1}$ and $\Omega^{\tau 2}$ as well as an identical pore water pressure can be assumed, so that the Equation (D–15) can be written as:

$$\begin{aligned}\int_{\Omega^{\tau 1}} \Bigg[& p_w^\star \left(d\dot{M}_w + d\dot{M}_v + \dot{M}_w \frac{\partial du_m^{\tau 1}}{\partial x_m^{\tau 1}} + \dot{M}_v \frac{\partial du_m^{\tau 1}}{\partial x_m^{\tau 1}} \right) \\ & - \frac{\partial p_w^\star}{\partial x_l^{\tau 1}} \left(df_{w,l}^{\tau 1} - f_{w,i}^{\tau 1} \frac{\partial du_l^{\tau 1}}{\partial x_i^{\tau 1}} + f_{w,l}^{\tau 1} \frac{\partial du_m^{\tau 1}}{\partial x_m^{\tau 1}} + df_{v,l}^{\tau 1} - f_{v,i}^{\tau 1} \frac{\partial du_l^{\tau 1}}{\partial x_i^{\tau 1}} + f_{v,l}^{\tau 1} \frac{\partial du_m^{\tau 1}}{\partial x_m^{\tau 1}} \right) \Bigg] d\Omega^{\tau 1} = -\Delta_3^{\tau 1}\end{aligned} \tag{D–62}$$

To further develop this previous equation, it is splitted in different parts by taking into account the expressions and derivatives of the masses of liquid water M_w and of water vapour M_v, and the mass flows of liquid water f_{w_i} and of water vapour f_{v_i}, so that:

$$\begin{aligned}& \int_{\Omega^{\tau 1}} p_w^\star \Bigg(\underbrace{\frac{\rho_w^B S_{r_w}^B}{\Delta t} \left(\phi^B \frac{\partial du_m}{\partial x_m} + (b-\phi^A) \frac{V^B}{V^A} \frac{\partial du_m}{\partial x_m} \right)}_{d\dot{M}_w} + \underbrace{\frac{\rho_v^B S_{r_g}^B}{\Delta t} \left(\phi^B \frac{\partial du_m}{\partial x_m} + (b-\phi^A) \frac{V^B}{V^A} \frac{\partial du_m}{\partial x_m} \right)}_{d\dot{M}_v} \Bigg) d\Omega^{\tau 1} \\ & + \int_{\Omega^{\tau 1}} p_w^\star \left(\dot{M}_w \frac{\partial du_m^{\tau 1}}{\partial x_m^{\tau 1}} + \dot{M}_v \frac{\partial du_m^{\tau 1}}{\partial x_m^{\tau 1}} \right) d\Omega^{\tau 1} \\ & - \int_{\Omega^{\tau 1}} \frac{\partial p_w^\star}{\partial x_l^{\tau 1}} \left(-f_{w,i}^{\tau 1} \frac{\partial du_l^{\tau 1}}{\partial x_i^{\tau 1}} + f_{w,l}^{\tau 1} \frac{\partial du_m^{\tau 1}}{\partial x_m^{\tau 1}} \right) d\Omega^{\tau 1} - \int_{\Omega^{\tau 1}} \frac{\partial p_w^\star}{\partial x_l^{\tau 1}} \left(-f_{v,i}^{\tau 1} \frac{\partial du_l^{\tau 1}}{\partial x_i^{\tau 1}} + f_{v,l}^{\tau 1} \frac{\partial du_m^{\tau 1}}{\partial x_m^{\tau 1}} \right) d\Omega^{\tau 1} \\ & - \int_{\Omega^{\tau 1}} \frac{\partial p_w^\star}{\partial x_l^{\tau 1}} \underbrace{\left(-\rho_w \frac{k_{r,w}}{\mu_w} \frac{\partial k_{lj}^{int}}{\partial \varepsilon_{ki}} \frac{\partial du_k}{\partial x_i} \left(\frac{\partial p_w}{\partial x_j} + \rho_w g_j \right) + \rho_w \frac{k_{lj}^{int} k_{r,w}}{\mu_w} \frac{\partial p_w}{\partial x_k} \frac{\partial du_k}{\partial x_j} \right)}_{df_{w,l}^{\tau 1}} d\Omega^{\tau 1} \\ & - \int_{\Omega^{\tau 1}} \frac{\partial p_w^\star}{\partial x_l^{\tau 1}} \Bigg(-\rho_v \frac{k_{r,g}}{\mu_g} \frac{\partial k_{lj}^{int}}{\partial \varepsilon_{ki}} \frac{\partial du_k}{\partial x_i} \left(\frac{\partial p_g}{\partial x_j} + \rho_g g_j \right) + \rho_v \frac{k_{lj}^{int} k_{r,g}}{\mu_g} \frac{\partial p_g}{\partial x_k} \frac{\partial du_k}{\partial x_j} \\ & \qquad \underbrace{-(b-\phi^A) \frac{\partial du_m}{\partial x_m} S_{r_g} \bar{\tau} D_{v-a} \rho_g \frac{\partial}{\partial x_j} \left(\frac{\rho_v}{\rho_g} \right) + \phi S_{r_g} \bar{\tau} D_{v-a} \rho_g \frac{\partial}{\partial x_k} \left(\frac{\rho_v}{\rho_g} \right) \frac{\partial du_k}{\partial x_j}}_{df_{v,l}^{\tau 1}} \Bigg) d\Omega^{\tau 1} \\ & = -\Delta_3^{\tau 1}\end{aligned} \tag{D–63}$$

To obtain the term of the stiffness matrix dealing with the coupling between the water flow and the mechanical problem, i.e. $\left[E_{MW}^{\tau 1}\right]$, each contribution coming from the water mass balance equation is computed individually:

Contribution from $d\dot{M}_w$

$$\begin{Bmatrix} dp_w^\star dx_1 \\ dp_w^\star dx_2 \\ FI \end{Bmatrix} = \frac{\rho_w^B S_{r_w}^B}{\Delta t} \begin{bmatrix} 0 & 0 & 0 & 0 \\ 0 & 0 & 0 & 0 \\ \phi^B + (b-\phi^A)\frac{V^B}{V^A} & 0 & 0 & \phi^B + (b-\phi^A)\frac{V^B}{V^A} \end{bmatrix} \begin{Bmatrix} \frac{\partial u_1}{\partial x_1} \\ \frac{\partial u_1}{\partial x_2} \\ \frac{\partial u_2}{\partial x_1} \\ \frac{\partial u_2}{\partial x_2} \end{Bmatrix} \tag{D–64}$$

Contribution from $d\dot{M}_v$

$$\begin{Bmatrix} dp_w^\star dx_1 \\ dp_w^\star dx_2 \\ FI \end{Bmatrix} = \frac{\rho_v^B S_{r_g}^B}{\Delta t} \begin{bmatrix} 0 & 0 & 0 & 0 \\ 0 & 0 & 0 & 0 \\ \phi^B + (b-\phi^A)\frac{V^B}{V^A} & 0 & 0 & \phi^B + (b-\phi^A)\frac{V^B}{V^A} \end{bmatrix} \begin{Bmatrix} \frac{\partial u_1}{\partial x_1} \\ \frac{\partial u_1}{\partial x_2} \\ \frac{\partial u_2}{\partial x_1} \\ \frac{\partial u_2}{\partial x_2} \end{Bmatrix} \tag{D–65}$$

Contributions from $\dot{M}_w$ and $\dot{M}_v$

$$\begin{Bmatrix} dp_w^\star dx_1 \\ dp_w^\star dx_2 \\ FI \end{Bmatrix} = \begin{bmatrix} 0 & 0 & 0 & 0 \\ 0 & 0 & 0 & 0 \\ \dot{M}_w + \dot{M}_v & 0 & 0 & \dot{M}_w + \dot{M}_v \end{bmatrix} \begin{Bmatrix} \frac{\partial u_1}{\partial x_1} \\ \frac{\partial u_1}{\partial x_2} \\ \frac{\partial u_2}{\partial x_1} \\ \frac{\partial u_2}{\partial x_2} \end{Bmatrix} \tag{D–66}$$

Contributions from f_w

$$\begin{Bmatrix} dp_w^\star dx_1 \\ dp_w^\star dx_2 \\ FI \end{Bmatrix} = \begin{bmatrix} -f_{w,1}^{\tau 1} + f_{w,1}^{\tau 1} & -f_{w,2}^{\tau 1} & 0 & f_{w,1}^{\tau 1} \\ f_{w,2}^{\tau 1} & 0 & -f_{w,1}^{\tau 1} & -f_{w,2}^{\tau 1} + f_{w,2}^{\tau 1} \\ 0 & 0 & 0 & 0 \end{bmatrix} \begin{Bmatrix} \frac{\partial u_1}{\partial x_1} \\ \frac{\partial u_1}{\partial x_2} \\ \frac{\partial u_2}{\partial x_1} \\ \frac{\partial u_2}{\partial x_2} \end{Bmatrix} \tag{D–67}$$

Contributions from f_v

$$\begin{Bmatrix} dp_w^\star dx_1 \\ dp_w^\star dx_2 \\ FI \end{Bmatrix} = \begin{bmatrix} -f_{v,1}^{\tau 1} + f_{v,1}^{\tau 1} & -f_{v,2}^{\tau 1} & 0 & f_{v,1}^{\tau 1} \\ f_{v,2}^{\tau 1} & 0 & -f_{v,1}^{\tau 1} & -f_{v,2}^{\tau 1} + f_{v,2}^{\tau 1} \\ 0 & 0 & 0 & 0 \end{bmatrix} \begin{Bmatrix} \frac{\partial u_1}{\partial x_1} \\ \frac{\partial u_1}{\partial x_2} \\ \frac{\partial u_2}{\partial x_1} \\ \frac{\partial u_2}{\partial x_2} \end{Bmatrix} \tag{D–68}$$

Contributions from $df_{w,l}^{\tau 1}$

$$\begin{Bmatrix} dp_w^\star dx_1 \\ dp_w^\star dx_2 \\ FI \end{Bmatrix} = -\rho_w \frac{k_{r,w}}{\mu_w} \left(\frac{\partial p_w}{\partial x_j} + \rho_w g_j \right) \begin{bmatrix} \frac{\partial k_{1j}^{int}}{\partial \varepsilon_{11}} & \frac{\partial k_{1j}^{int}}{\partial \varepsilon_{12}} & \frac{\partial k_{1j}^{int}}{\partial \varepsilon_{21}} & \frac{\partial k_{1j}^{int}}{\partial \varepsilon_{22}} \\ \frac{\partial k_{2j}^{int}}{\partial \varepsilon_{11}} & \frac{\partial k_{2j}^{int}}{\partial \varepsilon_{12}} & \frac{\partial k_{2j}^{int}}{\partial \varepsilon_{21}} & \frac{\partial k_{2j}^{int}}{\partial \varepsilon_{22}} \\ 0 & 0 & 0 & 0 \end{bmatrix} \begin{Bmatrix} \frac{\partial u_1}{\partial x_1} \\ \frac{\partial u_1}{\partial x_2} \\ \frac{\partial u_2}{\partial x_1} \\ \frac{\partial u_2}{\partial x_2} \end{Bmatrix} \tag{D–69}$$

$$\begin{Bmatrix} dp_w^\star dx_1 \\ dp_w^\star dx_2 \\ FI \end{Bmatrix} = \rho_w \frac{k_{r,w}}{\mu_w} \begin{bmatrix} k_{11}^{int} \frac{\partial p_w}{\partial x_1} & k_{12}^{int} \frac{\partial p_w}{\partial x_1} & k_{11}^{int} \frac{\partial p_w}{\partial x_2} & k_{12}^{int} \frac{\partial p_w}{\partial x_2} \\ k_{21}^{int} \frac{\partial p_w}{\partial x_1} & k_{22}^{int} \frac{\partial p_w}{\partial x_1} & k_{21}^{int} \frac{\partial p_w}{\partial x_2} & k_{22}^{int} \frac{\partial p_w}{\partial x_2} \\ 0 & 0 & 0 & 0 \end{bmatrix} \begin{Bmatrix} \frac{\partial u_1}{\partial x_1} \\ \frac{\partial u_1}{\partial x_2} \\ \frac{\partial u_2}{\partial x_1} \\ \frac{\partial u_2}{\partial x_2} \end{Bmatrix} \tag{D–70}$$

Contributions from $df_{v,l}^{\tau 1}$

$$\begin{Bmatrix} dp_w^\star dx_1 \\ dp_w^\star dx_2 \\ FI \end{Bmatrix} = -\rho_v \frac{k_{r,g}}{\mu_g} \left(\frac{\partial p_g}{\partial x_j} + \rho_g g_j \right) \begin{bmatrix} \frac{\partial k_{1j}^{int}}{\partial \varepsilon_{11}} & \frac{\partial k_{1j}^{int}}{\partial \varepsilon_{12}} & \frac{\partial k_{1j}^{int}}{\partial \varepsilon_{21}} & \frac{\partial k_{1j}^{int}}{\partial \varepsilon_{22}} \\ \frac{\partial k_{2j}^{int}}{\partial \varepsilon_{11}} & \frac{\partial k_{2j}^{int}}{\partial \varepsilon_{12}} & \frac{\partial k_{2j}^{int}}{\partial \varepsilon_{21}} & \frac{\partial k_{2j}^{int}}{\partial \varepsilon_{22}} \\ 0 & 0 & 0 & 0 \end{bmatrix} \begin{Bmatrix} \frac{\partial u_1}{\partial x_1} \\ \frac{\partial u_1}{\partial x_2} \\ \frac{\partial u_2}{\partial x_1} \\ \frac{\partial u_2}{\partial x_2} \end{Bmatrix} \tag{D–71}$$

$$\begin{Bmatrix} dp_w^{\star}dx_1 \\ dp_w^{\star}dx_2 \\ FI \end{Bmatrix} = \rho_v \frac{k_{r,g}}{\mu_g} \begin{bmatrix} k_{11}^{int}\frac{\partial p_g}{\partial x_1} & k_{12}^{int}\frac{\partial p_g}{\partial x_1} & k_{11}^{int}\frac{\partial p_g}{\partial x_2} & k_{12}^{int}\frac{\partial p_g}{\partial x_2} \\ k_{21}^{int}\frac{\partial p_g}{\partial x_1} & k_{22}^{int}\frac{\partial p_g}{\partial x_1} & k_{21}^{int}\frac{\partial p_g}{\partial x_2} & k_{22}^{int}\frac{\partial p_g}{\partial x_2} \\ 0 & 0 & 0 & 0 \end{bmatrix} \begin{Bmatrix} \frac{\partial u_1}{\partial x_1} \\ \frac{\partial u_1}{\partial x_2} \\ \frac{\partial u_2}{\partial x_1} \\ \frac{\partial u_2}{\partial x_2} \end{Bmatrix} \tag{D–72}$$

$$\begin{Bmatrix} dp_w^{\star}dx_1 \\ dp_w^{\star}dx_2 \\ FI \end{Bmatrix} = -(b-\phi^A) S_{r_g} \bar{\tau} D_{v-a} \rho_g \begin{bmatrix} \frac{\partial\left(\frac{\rho_v}{\rho_g}\right)}{\partial x_j} & 0 & 0 & \frac{\partial\left(\frac{\rho_v}{\rho_g}\right)}{\partial x_j} \\ \frac{\partial\left(\frac{\rho_v}{\rho_g}\right)}{\partial x_j} & 0 & 0 & \frac{\partial\left(\frac{\rho_v}{\rho_g}\right)}{\partial x_j} \\ 0 & 0 & 0 & 0 \end{bmatrix} \begin{Bmatrix} \frac{\partial u_1}{\partial x_1} \\ \frac{\partial u_1}{\partial x_2} \\ \frac{\partial u_2}{\partial x_1} \\ \frac{\partial u_2}{\partial x_2} \end{Bmatrix} \tag{D–73}$$

$$\begin{Bmatrix} dp_w^{\star}dx_1 \\ dp_w^{\star}dx_2 \\ FI \end{Bmatrix} = \phi S_{r_g} \bar{\tau} D_{v-a} \rho_g \begin{bmatrix} \frac{\partial\left(\frac{\rho_v}{\rho_g}\right)}{\partial x_1} & \frac{\partial\left(\frac{\rho_v}{\rho_g}\right)}{\partial x_1} & \frac{\partial\left(\frac{\rho_v}{\rho_g}\right)}{\partial x_2} & \frac{\partial\left(\frac{\rho_v}{\rho_g}\right)}{\partial x_2} \\ \frac{\partial\left(\frac{\rho_v}{\rho_g}\right)}{\partial x_1} & \frac{\partial\left(\frac{\rho_v}{\rho_g}\right)}{\partial x_1} & \frac{\partial\left(\frac{\rho_v}{\rho_g}\right)}{\partial x_2} & \frac{\partial\left(\frac{\rho_v}{\rho_g}\right)}{\partial x_2} \\ 0 & 0 & 0 & 0 \end{bmatrix} \begin{Bmatrix} \frac{\partial u_1}{\partial x_1} \\ \frac{\partial u_1}{\partial x_2} \\ \frac{\partial u_2}{\partial x_1} \\ \frac{\partial u_2}{\partial x_2} \end{Bmatrix} \tag{D–74}$$

$$
\begin{Bmatrix}
\frac{\partial f_{w,x}}{\partial u_i} \\
\frac{\partial f_{w,y}}{\partial u_i} \\
\frac{\partial S_{r_w}}{\partial u_i}
\end{Bmatrix} =
\begin{bmatrix}
\begin{array}{l}
\rho_w \frac{k_{r,w}}{\mu_w} \frac{\partial k_{1j}^{int}}{\partial \varepsilon_{11}} \left(\frac{\partial p_w}{\partial x_j} + \rho_w g_j \right) \\
-\rho_w \frac{k_{r,w}}{\mu_w} k_{11}^{int} \frac{\partial p_w}{\partial x_1} \\
+\rho_v \frac{k_{r,g}}{\mu_g} \frac{\partial k_{1j}^{int}}{\partial \varepsilon_{11}} \left(\frac{\partial p_g}{\partial x_j} + \rho_g g_j \right) \\
-\rho_v \frac{k_{r,g}}{\mu_g} k_{11}^{int} \frac{\partial p_g}{\partial x_1} \\
+(b-\phi^A) S_{r_g} \bar{\tau} D_{v-a} \rho_g \frac{\partial \left(\frac{\rho_v}{\rho_g} \right)}{\partial x_j} \\
-\phi S_{r_g} \bar{\tau} D_{v-a} \rho_g \frac{\partial \left(\frac{\rho_v}{\rho_g} \right)}{\partial x_1}
\end{array} &
\begin{array}{l}
\rho_w \frac{k_{r,w}}{\mu_w} \frac{\partial k_{1j}^{int}}{\partial \varepsilon_{12}} \left(\frac{\partial p_w}{\partial x_j} + \rho_w g_j \right) \\
-\rho_w \frac{k_{r,w}}{\mu_w} k_{12}^{int} \frac{\partial p_w}{\partial x_1} \\
+\rho_v \frac{k_{r,g}}{\mu_g} \frac{\partial k_{1j}^{int}}{\partial \varepsilon_{12}} \left(\frac{\partial p_g}{\partial x_j} + \rho_g g_j \right) \\
-\rho_v \frac{k_{r,g}}{\mu_g} k_{12}^{int} \frac{\partial p_g}{\partial x_1} \\
-\phi S_{r_g} \bar{\tau} D_{v-a} \rho_g \frac{\partial \left(\frac{\rho_v}{\rho_g} \right)}{\partial x_1} \\
+f_{w,2}^{\tau 1} + f_{v,2}^{\tau 1}
\end{array} &
\begin{array}{l}
\rho_w \frac{k_{r,w}}{\mu_w} \frac{\partial k_{1j}^{int}}{\partial \varepsilon_{21}} \left(\frac{\partial p_w}{\partial x_j} + \rho_w g_j \right) \\
-\rho_w \frac{k_{r,w}}{\mu_w} k_{11}^{int} \frac{\partial p_w}{\partial x_2} \\
+\rho_v \frac{k_{r,g}}{\mu_g} \frac{\partial k_{1j}^{int}}{\partial \varepsilon_{21}} \left(\frac{\partial p_g}{\partial x_j} + \rho_g g_j \right) \\
-\rho_v \frac{k_{r,g}}{\mu_g} k_{11}^{int} \frac{\partial p_g}{\partial x_2} \\
-\phi S_{r_g} \bar{\tau} D_{v-a} \rho_g \frac{\partial \left(\frac{\rho_v}{\rho_g} \right)}{\partial x_2}
\end{array} &
\begin{array}{l}
\rho_w \frac{k_{r,w}}{\mu_w} \frac{\partial k_{1j}^{int}}{\partial \varepsilon_{22}} \left(\frac{\partial p_w}{\partial x_j} + \rho_w g_j \right) \\
-\rho_w \frac{k_{r,w}}{\mu_w} k_{12}^{int} \frac{\partial p_w}{\partial x_2} \\
+\rho_v \frac{k_{r,g}}{\mu_g} \frac{\partial k_{1j}^{int}}{\partial \varepsilon_{22}} \left(\frac{\partial p_g}{\partial x_j} + \rho_g g_j \right) \\
-\rho_v \frac{k_{r,g}}{\mu_g} k_{12}^{int} \frac{\partial p_g}{\partial x_2} \\
+(b-\phi^A) S_{r_g} \bar{\tau} D_{v-a} \rho_g \frac{\partial \left(\frac{\rho_v}{\rho_g} \right)}{\partial x_j} \\
-\phi S_{r_g} \bar{\tau} D_{v-a} \rho_g \frac{\partial \left(\frac{\rho_v}{\rho_g} \right)}{\partial x_2} \\
-f_{w,1}^{\tau 1} - f_{v,1}^{\tau 1}
\end{array} \\
\hline
\begin{array}{l}
-\rho_w \frac{k_{r,w}}{\mu_w} \frac{\partial k_{2j}^{int}}{\partial \varepsilon_{11}} \left(\frac{\partial p_w}{\partial x_j} + \rho_w g_j \right) \\
-\rho_w \frac{k_{r,w}}{\mu_w} k_{21}^{int} \frac{\partial p_w}{\partial x_1} \\
+\rho_v \frac{k_{r,g}}{\mu_g} \frac{\partial k_{2j}^{int}}{\partial \varepsilon_{11}} \left(\frac{\partial p_g}{\partial x_j} + \rho_g g_j \right) \\
-\rho_v \frac{k_{r,g}}{\mu_g} k_{21}^{int} \frac{\partial p_g}{\partial x_1} \\
+(b-\phi^A) S_{r_g} \bar{\tau} D_{v-a} \rho_g \frac{\partial \left(\frac{\rho_v}{\rho_g} \right)}{\partial x_j} \\
-\phi S_{r_g} \bar{\tau} D_{v-a} \rho_g \frac{\partial \left(\frac{\rho_v}{\rho_g} \right)}{\partial x_1} \\
-f_{w,2}^{\tau 1} - f_{v,2}^{\tau 1}
\end{array} &
\begin{array}{l}
\rho_w \frac{k_{r,w}}{\mu_w} \frac{\partial k_{2j}^{int}}{\partial \varepsilon_{12}} \left(\frac{\partial p_w}{\partial x_j} + \rho_w g_j \right) \\
-\rho_w \frac{k_{r,w}}{\mu_w} k_{22}^{int} \frac{\partial p_w}{\partial x_1} \\
+\rho_v \frac{k_{r,g}}{\mu_g} \frac{\partial k_{2j}^{int}}{\partial \varepsilon_{12}} \left(\frac{\partial p_g}{\partial x_j} + \rho_g g_j \right) \\
-\rho_v \frac{k_{r,g}}{\mu_g} k_{22}^{int} \frac{\partial p_g}{\partial x_1} \\
-\phi S_{r_g} \bar{\tau} D_{v-a} \rho_g \frac{\partial \left(\frac{\rho_v}{\rho_g} \right)}{\partial x_1}
\end{array} &
\begin{array}{l}
\rho_w \frac{k_{r,w}}{\mu_w} \frac{\partial k_{2j}^{int}}{\partial \varepsilon_{21}} \left(\frac{\partial p_w}{\partial x_j} + \rho_w g_j \right) \\
-\rho_w \frac{k_{r,w}}{\mu_w} k_{21}^{int} \frac{\partial p_w}{\partial x_2} \\
+\rho_v \frac{k_{r,g}}{\mu_g} \frac{\partial k_{2j}^{int}}{\partial \varepsilon_{21}} \left(\frac{\partial p_g}{\partial x_j} + \rho_g g_j \right) \\
-\rho_v \frac{k_{r,g}}{\mu_g} k_{21}^{int} \frac{\partial p_g}{\partial x_2} \\
-\phi S_{r_g} \bar{\tau} D_{v-a} \rho_g \frac{\partial \left(\frac{\rho_v}{\rho_g} \right)}{\partial x_2} \\
+f_{w,1}^{\tau 1} + f_{v,1}^{\tau 1}
\end{array} &
\begin{array}{l}
\rho_w \frac{k_{r,w}}{\mu_w} \frac{\partial k_{2j}^{int}}{\partial \varepsilon_{22}} \left(\frac{\partial p_w}{\partial x_j} + \rho_w g_j \right) \\
-\rho_w \frac{k_{r,w}}{\mu_w} k_{22}^{int} \frac{\partial p_w}{\partial x_2} \\
+\rho_v \frac{k_{r,g}}{\mu_g} \frac{\partial k_{2j}^{int}}{\partial \varepsilon_{22}} \left(\frac{\partial p_g}{\partial x_j} + \rho_g g_j \right) \\
-\rho_v \frac{k_{r,g}}{\mu_g} k_{22}^{int} \frac{\partial p_g}{\partial x_2} \\
+(b-\phi^A) S_{r_g} \bar{\tau} D_{v-a} \rho_g \frac{\partial \left(\frac{\rho_v}{\rho_g} \right)}{\partial x_j} \\
-\phi S_{r_g} \bar{\tau} D_{v-a} \rho_g \frac{\partial \left(\frac{\rho_v}{\rho_g} \right)}{\partial x_2}
\end{array} \\
\hline
\begin{array}{l}
\frac{\rho_w^B S_{r_w}^B}{\Delta t} \left(\phi^B + (b-\phi^A) \frac{V^B}{V^A} \right) \\
+\frac{\rho_v^B S_{r_g}^B}{\Delta t} \left(\phi^B + (b-\phi^A) \frac{V^B}{V^A} \right) \\
+\dot{M}_w + \dot{M}_v
\end{array} &
0 &
0 &
\begin{array}{l}
\frac{\rho_w^B S_{r_w}^B}{\Delta t} \left(\phi^B + (b-\phi^A) \frac{V^B}{V^A} \right) \\
+\frac{\rho_v^B S_{r_g}^B}{\Delta t} \left(\phi^B + (b-\phi^A) \frac{V^B}{V^A} \right) \\
+\dot{M}_w + \dot{M}_v
\end{array}
\end{bmatrix}
\begin{Bmatrix}
\frac{\partial u_1}{\partial x_1} \\
\frac{\partial u_1}{\partial x_2} \\
\frac{\partial u_2}{\partial x_1} \\
\frac{\partial u_2}{\partial x_2}
\end{Bmatrix}
$$

D.4.2 Influence of the mechanics on air (E_{MA})

To determine the influence of the mechanics on the air, a different geometry for the configurations $\Omega^{\tau 1}$ and $\Omega^{\tau 2}$ as well as an identical gas pressure can be assumed, so that the Equation (D–16) can be written as:

$$\begin{aligned}
&\int_{\Omega^{\tau 1}} \left[p_g^\star \left(d\dot{M}_a + d\dot{M}_{da} + \dot{M}_a \frac{\partial du_m^{\tau 1}}{\partial x_m^{\tau 1}} + \dot{M}_{da} \frac{\partial du_m^{\tau 1}}{\partial x_m^{\tau 1}} \right) \right. \\
&\left. - \frac{\partial p_g^\star}{\partial x_l^{\tau 1}} \left(df_{a,l}^{\tau 1} - f_{a,i}^{\tau 1} \frac{\partial du_l^{\tau 1}}{\partial x_i^{\tau 1}} + f_{a,l}^{\tau 1} \frac{\partial du_m^{\tau 1}}{\partial x_m^{\tau 1}} + df_{da,l}^{\tau 1} - f_{da,i}^{\tau 1} \frac{\partial du_l^{\tau 1}}{\partial x_i^{\tau 1}} + f_{da,l}^{\tau 1} \frac{\partial du_m^{\tau 1}}{\partial x_m^{\tau 1}} \right) \right] d\Omega^{\tau 1} = -\Delta_4^{\tau 1}
\end{aligned} \tag{D–75}$$

To further develop the previous equation, it is splitted in different parts by taking into account the expressions and derivatives of the masses of dry air M_a and of dissolved air M_{da}, and the mass flows of dry air f_{a_i} and of dissolved air f_{da_i}, so that:

$$\begin{aligned}
&\int_{\Omega^{\tau 1}} p_g^\star \left(\underbrace{\frac{\rho_a^B S_{r_g}^B}{\Delta t} \left(\phi^B \frac{\partial du_m}{\partial x_m} + (b-\phi^A) \frac{V^B}{V^A} \frac{\partial du_m}{\partial x_m} \right)}_{d\dot{M}_a} + \underbrace{\frac{\rho_{da}^B S_{r_w}^B}{\Delta t} \left(\phi^B \frac{\partial du_m}{\partial x_m} + (b-\phi^A) \frac{V^B}{V^A} \frac{\partial du_m}{\partial x_m} \right)}_{d\dot{M}_{da}} \right) d\Omega^{\tau 1} \\
&+ \int_{\Omega^{\tau 1}} p_g^\star \left(\dot{M}_a \frac{\partial du_m^{\tau 1}}{\partial x_m^{\tau 1}} + \dot{M}_{da} \frac{\partial du_m^{\tau 1}}{\partial x_m^{\tau 1}} \right) d\Omega^{\tau 1} \\
&- \int_{\Omega^{\tau 1}} \frac{\partial p_g^\star}{\partial x_l^{\tau 1}} \left(-f_{a,i}^{\tau 1} \frac{\partial du_l^{\tau 1}}{\partial x_i^{\tau 1}} + f_{a,l}^{\tau 1} \frac{\partial du_m^{\tau 1}}{\partial x_m^{\tau 1}} \right) d\Omega^{\tau 1} - \int_{\Omega^{\tau 1}} \frac{\partial p_g^\star}{\partial x_l^{\tau 1}} \left(-f_{da,i}^{\tau 1} \frac{\partial du_l^{\tau 1}}{\partial x_i^{\tau 1}} + f_{da,l}^{\tau 1} \frac{\partial du_m^{\tau 1}}{\partial x_m^{\tau 1}} \right) d\Omega^{\tau 1} \\
&- \int_{\Omega^{\tau 1}} \frac{\partial p_a^\star}{\partial x_l^{\tau 1}} \left(-\rho_a \frac{k_{r,g}}{\mu_g} \frac{\partial k_{lj}^{int}}{\partial \varepsilon_{ki}} \frac{\partial du_k}{\partial x_i} \left(\frac{\partial p_g}{\partial x_j} + \rho_g g_j \right) + \rho_a \frac{k_{lj}^{int} k_{r,g}}{\mu_g} \frac{\partial p_g}{\partial x_k} \frac{\partial du_k}{\partial x_j} \right. \\
&\left. \underbrace{+(b-\phi^A) \frac{\partial du_m}{\partial x_m} S_{r_g} \bar{\tau} D_{v-a} \rho_g \frac{\partial}{\partial x_j} \left(\frac{\rho_v}{\rho_g} \right) - \phi S_{r_g} \bar{\tau} D_{v-a} \rho_g \frac{\partial}{\partial x_k} \left(\frac{\rho_v}{\rho_g} \right) \frac{\partial du_k}{\partial x_j}}_{df_{a,l}^{\tau 1}} \right) d\Omega^{\tau 1} \\
&- \int_{\Omega^{\tau 1}} \frac{\partial p_g^\star}{\partial x_l^{\tau 1}} \left(-\rho_{da} \frac{k_{r,w}}{\mu_w} \frac{\partial k_{lj}^{int}}{\partial \varepsilon_{ki}} \frac{\partial du_k}{\partial x_i} \left(\frac{\partial p_w}{\partial x_j} + \rho_w g_j \right) + \rho_{da} \frac{k_{lj}^{int} k_{r,w}}{\mu_w} \frac{\partial p_w}{\partial x_k} \frac{\partial du_k}{\partial x_j} \right. \\
&\left. \underbrace{-(b-\phi^A) \frac{\partial du_m}{\partial x_m} S_{r_w} \bar{\tau} D_{da-w} \rho_w \frac{\partial}{\partial x_j} \left(\frac{\rho_{da}}{\rho_w} \right) + \phi S_{r_w} \bar{\tau} D_{da-w} \rho_w \frac{\partial}{\partial x_k} \left(\frac{\rho_{da}}{\rho_w} \right) \frac{\partial du_k}{\partial x_j}}_{df_{da,l}^{\tau 1}} \right) d\Omega^{\tau 1} \\
&= -\Delta_4^{\tau 1}
\end{aligned} \tag{D–76}$$

To obtain the term of the stiffness matrix dealing with the coupling between the air flow and the mechanical problem, i.e. $\left[E_{MA}^{\tau 1}\right]$, each contribution coming from the air mass balance equation is computed individually:

Contribution from $d\dot{M}_a$

$$\begin{Bmatrix} dp_g^\star dx_1 \\ dp_g^\star dx_2 \\ FI \end{Bmatrix} = \frac{\rho_a^B S_{r_g}^B}{\Delta t} \begin{bmatrix} 0 & 0 & 0 & 0 \\ 0 & 0 & 0 & 0 \\ \phi^B + (b-\phi^A)\frac{V^B}{V^A} & 0 & 0 & \phi^B + (b-\phi^A)\frac{V^B}{V^A} \end{bmatrix} \begin{Bmatrix} \frac{\partial u_1}{\partial x_1} \\ \frac{\partial u_1}{\partial x_2} \\ \frac{\partial u_2}{\partial x_1} \\ \frac{\partial u_2}{\partial x_2} \end{Bmatrix} \tag{D–77}$$

Contribution from $d\dot{M}_{da}$

$$\begin{Bmatrix} dp_g^\star dx_1 \\ dp_g^\star dx_2 \\ FI \end{Bmatrix} = \frac{\rho_{da}^B S_{r_w}^B}{\Delta t} \begin{bmatrix} 0 & 0 & 0 & 0 \\ 0 & 0 & 0 & 0 \\ \phi^B + (b-\phi^A)\frac{V^B}{V^A} & 0 & 0 & \phi^B + (b-\phi^A)\frac{V^B}{V^A} \end{bmatrix} \begin{Bmatrix} \frac{\partial u_1}{\partial x_1} \\ \frac{\partial u_1}{\partial x_2} \\ \frac{\partial u_2}{\partial x_1} \\ \frac{\partial u_2}{\partial x_2} \end{Bmatrix} \tag{D–78}$$

Contributions from $\dot{M}_a$ and $\dot{M}_{da}$

$$\begin{Bmatrix} dp_g^\star dx_1 \\ dp_g^\star dx_2 \\ FI \end{Bmatrix} = \begin{bmatrix} 0 & 0 & 0 & 0 \\ 0 & 0 & 0 & 0 \\ \dot{M}_a + \dot{M}_{da} & 0 & 0 & \dot{M}_a + \dot{M}_{da} \end{bmatrix} \begin{Bmatrix} \frac{\partial u_1}{\partial x_1} \\ \frac{\partial u_1}{\partial x_2} \\ \frac{\partial u_2}{\partial x_1} \\ \frac{\partial u_2}{\partial x_2} \end{Bmatrix} \tag{D–79}$$

Contributions from f_a

$$\begin{Bmatrix} dp_g^\star dx_1 \\ dp_g^\star dx_2 \\ FI \end{Bmatrix} = \begin{bmatrix} -f_{a,1}^{\tau 1} + f_{a,1}^{\tau 1} & -f_{a,2}^{\tau 1} & 0 & f_{a,1}^{\tau 1} \\ f_{a,2}^{\tau 1} & 0 & -f_{a,1}^{\tau 1} & -f_{a,2}^{\tau 1} + f_{a,2}^{\tau 1} \\ 0 & 0 & 0 & 0 \end{bmatrix} \begin{Bmatrix} \frac{\partial u_1}{\partial x_1} \\ \frac{\partial u_1}{\partial x_2} \\ \frac{\partial u_2}{\partial x_1} \\ \frac{\partial u_2}{\partial x_2} \end{Bmatrix} \tag{D–80}$$

Contributions from f_{da}

$$\begin{Bmatrix} dp_g^\star dx_1 \\ dp_g^\star dx_2 \\ FI \end{Bmatrix} = \begin{bmatrix} -f_{da,1}^{\tau 1} + f_{da,1}^{\tau 1} & -f_{da,2}^{\tau 1} & 0 & f_{da,1}^{\tau 1} \\ f_{da,2}^{\tau 1} & 0 & -f_{da,1}^{\tau 1} & -f_{da,2}^{\tau 1} + f_{da,2}^{\tau 1} \\ 0 & 0 & 0 & 0 \end{bmatrix} \begin{Bmatrix} \frac{\partial u_1}{\partial x_1} \\ \frac{\partial u_1}{\partial x_2} \\ \frac{\partial u_2}{\partial x_1} \\ \frac{\partial u_2}{\partial x_2} \end{Bmatrix} \tag{D–81}$$

Contributions from $df_{a,l}^{\tau 1}$

$$\begin{Bmatrix} dp_g^\star dx_1 \\ dp_g^\star dx_2 \\ FI \end{Bmatrix} = -\rho_a \frac{k_{r,g}}{\mu_g} \left(\frac{\partial p_g}{\partial x_j} + \rho_g g_j \right) \begin{bmatrix} \frac{\partial k_{1j}^{int}}{\partial \varepsilon_{11}} & \frac{\partial k_{1j}^{int}}{\partial \varepsilon_{12}} & \frac{\partial k_{1j}^{int}}{\partial \varepsilon_{21}} & \frac{\partial k_{1j}^{int}}{\partial \varepsilon_{22}} \\ \frac{\partial k_{2j}^{int}}{\partial \varepsilon_{11}} & \frac{\partial k_{2j}^{int}}{\partial \varepsilon_{12}} & \frac{\partial k_{2j}^{int}}{\partial \varepsilon_{21}} & \frac{\partial k_{2j}^{int}}{\partial \varepsilon_{22}} \\ 0 & 0 & 0 & 0 \end{bmatrix} \begin{Bmatrix} \frac{\partial u_1}{\partial x_1} \\ \frac{\partial u_1}{\partial x_2} \\ \frac{\partial u_2}{\partial x_1} \\ \frac{\partial u_2}{\partial x_2} \end{Bmatrix} \tag{D–82}$$

$$\begin{Bmatrix} dp_g^\star dx_1 \\ dp_g^\star dx_2 \\ FI \end{Bmatrix} = \rho_a \frac{k_{r,g}}{\mu_g} \begin{bmatrix} k_{11}^{int} \frac{\partial p_g}{\partial x_1} & k_{12}^{int} \frac{\partial p_g}{\partial x_1} & k_{11}^{int} \frac{\partial p_g}{\partial x_2} & k_{12}^{int} \frac{\partial p_g}{\partial x_2} \\ k_{21}^{int} \frac{\partial p_g}{\partial x_1} & k_{22}^{int} \frac{\partial p_g}{\partial x_1} & k_{21}^{int} \frac{\partial p_g}{\partial x_2} & k_{22}^{int} \frac{\partial p_g}{\partial x_2} \\ 0 & 0 & 0 & 0 \end{bmatrix} \begin{Bmatrix} \frac{\partial u_1}{\partial x_1} \\ \frac{\partial u_1}{\partial x_2} \\ \frac{\partial u_2}{\partial x_1} \\ \frac{\partial u_2}{\partial x_2} \end{Bmatrix} \tag{D–83}$$

$$\begin{Bmatrix} dp_g^\star dx_1 \\ dp_g^\star dx_2 \\ FI \end{Bmatrix} = (b-\phi^A) S_{r_g} \bar{\tau} D_{v-a} \rho_g \begin{bmatrix} \frac{\partial \left(\frac{\rho_v}{\rho_g}\right)}{\partial x_j} & 0 & 0 & \frac{\partial \left(\frac{\rho_v}{\rho_g}\right)}{\partial x_j} \\ \frac{\partial \left(\frac{\rho_v}{\rho_g}\right)}{\partial x_j} & 0 & 0 & \frac{\partial \left(\frac{\rho_v}{\rho_g}\right)}{\partial x_j} \\ 0 & 0 & 0 & 0 \end{bmatrix} \begin{Bmatrix} \frac{\partial u_1}{\partial x_1} \\ \frac{\partial u_1}{\partial x_2} \\ \frac{\partial u_2}{\partial x_1} \\ \frac{\partial u_2}{\partial x_2} \end{Bmatrix} \tag{D–84}$$

$$\begin{Bmatrix} dp_g^\star dx_1 \\ dp_g^\star dx_2 \\ FI \end{Bmatrix} = -\phi S_{r_g} \bar{\tau} D_{v-a} \rho_g \begin{bmatrix} \frac{\partial\left(\frac{\rho_v}{\rho_g}\right)}{\partial x_1} & \frac{\partial\left(\frac{\rho_v}{\rho_g}\right)}{\partial x_1} & \frac{\partial\left(\frac{\rho_v}{\rho_g}\right)}{\partial x_2} & \frac{\partial\left(\frac{\rho_v}{\rho_g}\right)}{\partial x_2} \\ \frac{\partial\left(\frac{\rho_v}{\rho_g}\right)}{\partial x_1} & \frac{\partial\left(\frac{\rho_v}{\rho_g}\right)}{\partial x_1} & \frac{\partial\left(\frac{\rho_v}{\rho_g}\right)}{\partial x_2} & \frac{\partial\left(\frac{\rho_v}{\rho_g}\right)}{\partial x_2} \\ 0 & 0 & 0 & 0 \end{bmatrix} \begin{Bmatrix} \frac{\partial u_1}{\partial x_1} \\ \frac{\partial u_1}{\partial x_2} \\ \frac{\partial u_2}{\partial x_1} \\ \frac{\partial u_2}{\partial x_2} \end{Bmatrix} \tag{D–85}$$

Contributions from $df_{da,l}^{\tau 1}$

$$\begin{Bmatrix} dp_g^\star dx_1 \\ dp_g^\star dx_2 \\ FI \end{Bmatrix} = -\rho_{da} \frac{k_{r,w}}{\mu_w} \left(\frac{\partial p_w}{\partial x_j} + \rho_w g_j \right) \begin{bmatrix} \frac{\partial k_{1j}^{int}}{\partial \varepsilon_{11}} & \frac{\partial k_{1j}^{int}}{\partial \varepsilon_{12}} & \frac{\partial k_{1j}^{int}}{\partial \varepsilon_{21}} & \frac{\partial k_{1j}^{int}}{\partial \varepsilon_{22}} \\ \frac{\partial k_{2j}^{int}}{\partial \varepsilon_{11}} & \frac{\partial k_{2j}^{int}}{\partial \varepsilon_{12}} & \frac{\partial k_{2j}^{int}}{\partial \varepsilon_{21}} & \frac{\partial k_{2j}^{int}}{\partial \varepsilon_{22}} \\ 0 & 0 & 0 & 0 \end{bmatrix} \begin{Bmatrix} \frac{\partial u_1}{\partial x_1} \\ \frac{\partial u_1}{\partial x_2} \\ \frac{\partial u_2}{\partial x_1} \\ \frac{\partial u_2}{\partial x_2} \end{Bmatrix} \tag{D–86}$$

$$\begin{Bmatrix} dp_g^\star dx_1 \\ dp_g^\star dx_2 \\ FI \end{Bmatrix} = \rho_{da} \frac{k_{r,w}}{\mu_w} \begin{bmatrix} k_{11}^{int} \frac{\partial p_w}{\partial x_1} & k_{12}^{int} \frac{\partial p_w}{\partial x_1} & k_{11}^{int} \frac{\partial p_w}{\partial x_2} & k_{12}^{int} \frac{\partial p_w}{\partial x_2} \\ k_{21}^{int} \frac{\partial p_w}{\partial x_1} & k_{22}^{int} \frac{\partial p_w}{\partial x_1} & k_{21}^{int} \frac{\partial p_w}{\partial x_2} & k_{22}^{int} \frac{\partial p_w}{\partial x_2} \\ 0 & 0 & 0 & 0 \end{bmatrix} \begin{Bmatrix} \frac{\partial u_1}{\partial x_1} \\ \frac{\partial u_1}{\partial x_2} \\ \frac{\partial u_2}{\partial x_1} \\ \frac{\partial u_2}{\partial x_2} \end{Bmatrix} \tag{D–87}$$

$$\begin{Bmatrix} dp_g^\star dx_1 \\ dp_g^\star dx_2 \\ FI \end{Bmatrix} = -(b-\phi^A) S_{r_w} \bar{\tau} D_{da-w} \rho_w \begin{bmatrix} \frac{\partial\left(\frac{\rho_{da}}{\rho_w}\right)}{\partial x_j} & 0 & 0 & \frac{\partial\left(\frac{\rho_{da}}{\rho_w}\right)}{\partial x_j} \\ \frac{\partial\left(\frac{\rho_{da}}{\rho_w}\right)}{\partial x_j} & 0 & 0 & \frac{\partial\left(\frac{\rho_{da}}{\rho_w}\right)}{\partial x_j} \\ 0 & 0 & 0 & 0 \end{bmatrix} \begin{Bmatrix} \frac{\partial u_1}{\partial x_1} \\ \frac{\partial u_1}{\partial x_2} \\ \frac{\partial u_2}{\partial x_1} \\ \frac{\partial u_2}{\partial x_2} \end{Bmatrix} \tag{D–88}$$

$$\begin{Bmatrix} dp_g^\star dx_1 \\ dp_g^\star dx_2 \\ FI \end{Bmatrix} = \phi S_{r_w} \bar{\tau} D_{da-w} \rho_w \begin{bmatrix} \frac{\partial\left(\frac{\rho_{da}}{\rho_w}\right)}{\partial x_1} & \frac{\partial\left(\frac{\rho_{da}}{\rho_w}\right)}{\partial x_1} & \frac{\partial\left(\frac{\rho_{da}}{\rho_w}\right)}{\partial x_2} & \frac{\partial\left(\frac{\rho_{da}}{\rho_w}\right)}{\partial x_2} \\ \frac{\partial\left(\frac{\rho_{da}}{\rho_w}\right)}{\partial x_1} & \frac{\partial\left(\frac{\rho_{da}}{\rho_w}\right)}{\partial x_1} & \frac{\partial\left(\frac{\rho_{da}}{\rho_w}\right)}{\partial x_2} & \frac{\partial\left(\frac{\rho_{da}}{\rho_w}\right)}{\partial x_2} \\ 0 & 0 & 0 & 0 \end{bmatrix} \begin{Bmatrix} \frac{\partial u_1}{\partial x_1} \\ \frac{\partial u_1}{\partial x_2} \\ \frac{\partial u_2}{\partial x_1} \\ \frac{\partial u_2}{\partial x_2} \end{Bmatrix} \tag{D–89}$$

$$
\begin{Bmatrix}
\frac{\partial f_{a,x}}{\partial u_i} \\
\frac{\partial f_{a,y}}{\partial u_i} \\
\frac{\partial \dot{S}_a}{\partial u_i}
\end{Bmatrix} =
\begin{bmatrix}
\begin{array}{c}
\rho_a \frac{k_{r,g}}{\mu_g} \frac{\partial k_{1j}^{int}}{\partial \varepsilon_{11}} \left(\frac{\partial p_g}{\partial x_j} + \rho_g g_j \right) \\
-\rho_a \frac{k_{r,g}}{\mu_w} k_{11}^{int} \frac{\partial p_g}{\partial x_1} \\
+\rho_{da} \frac{k_{r,w}}{\mu_w} \frac{\partial k_{1j}^{int}}{\partial \varepsilon_{11}} \left(\frac{\partial p_w}{\partial x_j} + \rho_w g_j \right) \\
-\rho_{da} \frac{k_{r,w}}{\mu_w} k_{11}^{int} \frac{\partial p_w}{\partial x_1} \\
+(b-\phi^A) S_{r_w} \bar{\tau} D_{da-w} \rho_w \frac{\partial \left(\frac{\rho_{da}}{\rho_w} \right)}{\partial x_j} \\
-\phi S_{r_w} \bar{\tau} D_{da-w} \rho_w \frac{\partial \left(\frac{\rho_{da}}{\rho_w} \right)}{\partial x_1}
\end{array} &
\begin{array}{c}
\rho_a \frac{k_{r,g}}{\mu_g} \frac{\partial k_{1j}^{int}}{\partial \varepsilon_{12}} \left(\frac{\partial p_g}{\partial x_j} + \rho_g g_j \right) \\
-\rho_a \frac{k_{r,g}}{\mu_g} k_{12}^{int} \frac{\partial p_g}{\partial x_1} \\
+\rho_{da} \frac{k_{r,w}}{\mu_w} \frac{\partial k_{1j}^{int}}{\partial \varepsilon_{12}} \left(\frac{\partial p_w}{\partial x_j} + \rho_w g_j \right) \\
-\rho_{da} \frac{k_{r,w}}{\mu_w} k_{12}^{int} \frac{\partial p_w}{\partial x_1} \\
-\phi S_{r_w} \bar{\tau} D_{da-w} \rho_w \frac{\partial \left(\frac{\rho_{da}}{\rho_w} \right)}{\partial x_1} \\
+f_{a,2}^{\tau 1} + f_{da,2}^{\tau 1}
\end{array} &
\begin{array}{c}
\rho_a \frac{k_{r,g}}{\mu_g} \frac{\partial k_{1j}^{int}}{\partial \varepsilon_{21}} \left(\frac{\partial p_g}{\partial x_j} + \rho_g g_j \right) \\
-\rho_a \frac{k_{r,g}}{\mu_g} k_{11}^{int} \frac{\partial p_g}{\partial x_2} \\
+\rho_{da} \frac{k_{r,w}}{\mu_w} \frac{\partial k_{1j}^{int}}{\partial \varepsilon_{21}} \left(\frac{\partial p_w}{\partial x_j} + \rho_w g_j \right) \\
-\rho_{da} \frac{k_{r,w}}{\mu_w} k_{11}^{int} \frac{\partial p_w}{\partial x_2} \\
-\phi S_{r_g} \bar{\tau} D_{v-a} \rho_g \frac{\partial \left(\frac{\rho_v}{\rho_g} \right)}{\partial x_2} \\
-\phi S_{r_w} \bar{\tau} D_{da-w} \rho_w \frac{\partial \left(\frac{\rho_{da}}{\rho_w} \right)}{\partial x_2}
\end{array} &
\begin{array}{c}
\rho_a \frac{k_{r,g}}{\mu_g} \frac{\partial k_{1j}^{int}}{\partial \varepsilon_{22}} \left(\frac{\partial p_g}{\partial x_j} + \rho_g g_j \right) \\
-\rho_a \frac{k_{r,g}}{\mu_g} k_{12}^{int} \frac{\partial p_g}{\partial x_2} \\
+\rho_{da} \frac{k_{r,w}}{\mu_w} \frac{\partial k_{1j}^{int}}{\partial \varepsilon_{22}} \left(\frac{\partial p_w}{\partial x_j} + \rho_w g_j \right) \\
-\rho_{da} \frac{k_{r,w}}{\mu_w} k_{12}^{int} \frac{\partial p_w}{\partial x_2} \\
-(b-\phi^A) S_{r,g} \bar{\tau} D_{v-a} \rho_g \frac{\partial \left(\frac{\rho_v}{\rho_g} \right)}{\partial x_j} \\
+\phi S_{r,g} \bar{\tau} D_{v-a} \rho_g \frac{\partial \left(\frac{\rho_v}{\rho_g} \right)}{\partial x_2} \\
+(b-\phi^A) S_{r_w} \bar{\tau} D_{da-w} \rho_w \frac{\partial \left(\frac{\rho_{da}}{\rho_w} \right)}{\partial x_j} \\
-\phi S_{r_w} \bar{\tau} D_{da-w} \rho_w \frac{\partial \left(\frac{\rho_{da}}{\rho_w} \right)}{\partial x_2} \\
-f_{a,1}^{\tau 1} - f_{da,1}^{\tau 1}
\end{array} \\
\hline
\begin{array}{c}
\rho_a \frac{k_{r,g}}{\mu_g} \frac{\partial k_{2j}^{int}}{\partial \varepsilon_{11}} \left(\frac{\partial p_g}{\partial x_j} + \rho_g g_j \right) \\
-\rho_a \frac{k_{r,g}}{\mu_g} k_{21}^{int} \frac{\partial p_g}{\partial x_1} \\
+\rho_{da} \frac{k_{r,w}}{\mu_w} \frac{\partial k_{2j}^{int}}{\partial \varepsilon_{11}} \left(\frac{\partial p_w}{\partial x_j} + \rho_w g_j \right) \\
-\rho_{da} \frac{k_{r,w}}{\mu_w} k_{21}^{int} \frac{\partial p_w}{\partial x_1} \\
-(b-\phi^A) S_{r,g} \bar{\tau} D_{v-a} \rho_g \frac{\partial \left(\frac{\rho_v}{\rho_g} \right)}{\partial x_j} \\
+\phi S_{r_g} \bar{\tau} D_{v-a} \rho_g \frac{\partial \left(\frac{\rho_v}{\rho_g} \right)}{\partial x_1} \\
+(b-\phi^A) S_{r_w} \bar{\tau} D_{da-w} \rho_w \frac{\partial \left(\frac{\rho_{da}}{\rho_w} \right)}{\partial x_j} \\
+\phi S_{r_w} \bar{\tau} D_{da-w} \rho_w \frac{\partial \left(\frac{\rho_{da}}{\rho_w} \right)}{\partial x_1} \\
-f_{a,2}^{\tau 1} - f_{da,2}^{\tau 1}
\end{array} &
\begin{array}{c}
\rho_a \frac{k_{r,g}}{\mu_g} \frac{\partial k_{2j}^{int}}{\partial \varepsilon_{12}} \left(\frac{\partial p_g}{\partial x_j} + \rho_g g_j \right) \\
-\rho_a \frac{k_{r,g}}{\mu_w} k_{22}^{int} \frac{\partial p_g}{\partial x_1} \\
+\rho_{da} \frac{k_{r,w}}{\mu_w} \frac{\partial k_{2j}^{int}}{\partial \varepsilon_{12}} \left(\frac{\partial p_w}{\partial x_j} + \rho_w g_j \right) \\
-\rho_{da} \frac{k_{r,w}}{\mu_w} k_{22}^{int} \frac{\partial p_w}{\partial x_1} \\
+\phi S_{r_g} \bar{\tau} D_{v-a} \rho_g \frac{\partial \left(\frac{\rho_v}{\rho_g} \right)}{\partial x_1} \\
-\phi S_{r_w} \bar{\tau} D_{da-w} \rho_w \frac{\partial \left(\frac{\rho_{da}}{\rho_w} \right)}{\partial x_1}
\end{array} &
\begin{array}{c}
\rho_a \frac{k_{r,g}}{\mu_g} \frac{\partial k_{2j}^{int}}{\partial \varepsilon_{21}} \left(\frac{\partial p_g}{\partial x_j} + \rho_g g_j \right) \\
-\rho_g \frac{k_{r,g}}{\mu_g} k_{21}^{int} \frac{\partial p_g}{\partial x_2} \\
+\rho_{da} \frac{k_{r,w}}{\mu_w} \frac{\partial k_{2j}^{int}}{\partial \varepsilon_{21}} \left(\frac{\partial p_w}{\partial x_j} + \rho_w g_j \right) \\
-\rho_{da} \frac{k_{r,w}}{\mu_w} k_{21}^{int} \frac{\partial p_w}{\partial x_2} \\
+\phi S_{r_g} \bar{\tau} D_{v-a} \rho_g \frac{\partial \left(\frac{\rho_v}{\rho_g} \right)}{\partial x_2} \\
-\phi S_{r_w} \bar{\tau} D_{da-w} \rho_w \frac{\partial \left(\frac{\rho_{da}}{\rho_w} \right)}{\partial x_2} \\
+f_{a,1}^{\tau 1} + f_{da,1}^{\tau 1}
\end{array} &
\begin{array}{c}
\rho_a \frac{k_{r,g}}{\mu_g} \frac{\partial k_{2j}^{int}}{\partial \varepsilon_{22}} \left(\frac{\partial p_g}{\partial x_j} + \rho_g g_j \right) \\
-\rho_a \frac{k_{r,g}}{\mu_g} k_{22}^{int} \frac{\partial p_g}{\partial x_2} \\
+\rho_{da} \frac{k_{r,w}}{\mu_w} \frac{\partial k_{2j}^{int}}{\partial \varepsilon_{22}} \left(\frac{\partial p_w}{\partial x_j} + \rho_w g_j \right) \\
-\rho_{da} \frac{k_{r,w}}{\mu_w} k_{22}^{int} \frac{\partial p_w}{\partial x_2} \\
-(b-\phi^A) S_{r_g} \bar{\tau} D_{v-a} \rho_g \frac{\partial \left(\frac{\rho_v}{\rho_g} \right)}{\partial x_j} \\
+\phi S_{r_g} \bar{\tau} D_{v-a} \rho_g \frac{\partial \left(\frac{\rho_v}{\rho_g} \right)}{\partial x_2} \\
+(b-\phi^A) S_{r_w} \bar{\tau} D_{da-w} \rho_w \frac{\partial \left(\frac{\rho_{da}}{\rho_w} \right)}{\partial x_j} \\
-\phi S_{r_w} \bar{\tau} D_{da-w} \rho_w \frac{\partial \left(\frac{\rho_{da}}{\rho_w} \right)}{\partial x_2}
\end{array} \\
\hline
\begin{array}{c}
\frac{\rho_a^B (1-S_{r_w}^B)}{\Delta t} \left(\phi^B + (b-\phi^A) \frac{V^B}{V^A} \right) \\
+\frac{\rho_{da}^B S_{r_w}^B}{\Delta t} \left(\phi^B + (b-\phi^A) \frac{V^B}{V^A} \right) \\
+\dot{M}_a + \dot{M}_{da}
\end{array} &
0 &
0 &
\begin{array}{c}
\frac{\rho_a^B (1-S_{r_w}^B)}{\Delta t} \left(\phi^B + (b-\phi^A) \frac{V^B}{V^A} \right) \\
+\frac{\rho_{da}^B S_{r_w}^B}{\Delta t} \left(\phi^B + (b-\phi^A) \frac{V^B}{V^A} \right) \\
+\dot{M}_a + \dot{M}_{da}
\end{array}
\end{bmatrix}
\begin{Bmatrix}
\frac{\partial u_1}{\partial x_1} \\
\frac{\partial u_1}{\partial x_2} \\
\frac{\partial u_2}{\partial x_1} \\
\frac{\partial u_2}{\partial x_2}
\end{Bmatrix}
$$

D.5 Finite element formulation

Solving the numerical non-linear problem consists to obtain the equality between the global vector of internal nodal forces F_{I,m_n} and the global vector of external nodal forces F_{E,m_n}. The out of balance forces vector is computed as:

$$\begin{aligned} F_{OB,m_n} &= F_{E,m_n} - F_{I,m_n} \\ &= \sum_{IP} \left[\left(\dot{M}_a \mathcal{N}^{(n)} - f_{a,x} \frac{\partial \mathcal{N}^{(n)}}{\partial x_1} - f_{a,y} \frac{\partial \mathcal{N}^{(n)}}{\partial x_2} \right) det\left(J_{ij}\right) W_G \right] \end{aligned} \tag{D–90}$$

Where the generalised coordinates u_{m_n} are continuously interpolated over the element with classical linear interpolation functions $\mathcal{N}^{(n)}$.

In order to obtain $F_{OB,m_n} = 0$, generalised coordinates Δu_{m_n} are iteratively corrected by:

$$\Delta u_{m_n} = - \left[\frac{\partial F^t_{OB,l_k}}{\partial u_{m_n}} \right]^{-1} F^t_{OB,l_k} = - \left[K_{l_k m_n} \right]^{-1} F^t_{OB,l_k} \tag{D–91}$$

Where u_{m_n} is the vector of generalised coordinates gathering the mechanical and hydraulic degrees of freedom, with m the number of degrees of freedom of the node n, and $K_{l_k m_n}$ is the stiffness matrix at time step t.

The stiffness matrix $K_{l_k m_n}$ is computed analytically at each iteration by derivation of out of balance forces:

$$K_{l_k m_n} = \frac{\partial F_{OB,l_k}}{\partial u_{m_n}} \tag{D–92}$$

In the coupled finite element SGRT, each node is assigned thirteen degrees of freedom, namely one for the $x-$coordinate, one for the $y-$coordinate, one for the water pressure p_w, one for the air pressure p_g, one for the temperature T, four for the microdisplacement field ν_{ij}, and four for the Lagrange multiplier field λ_{ij}. The stiffness matrix is expressed in the following form:

$$\left[K\right] = \begin{bmatrix} E_{MM} & E_{WM} & E_{GM} & E_{TM} & E_{\nu M} & E_{\lambda M} \\ E_{MW} & E_{WW} & E_{GW} & E_{TW} & E_{\nu W} & E_{\lambda W} \\ \mathbf{E_{MG}} & E_{WG} & E_{GG} & E_{TG} & E_{\nu G} & E_{\lambda G} \\ E_{MT} & E_{WT} & E_{GT} & E_{TT} & E_{\nu T} & E_{\lambda T} \\ E_{M\nu} & E_{W\nu} & E_{G\nu} & E_{T\nu} & E_{\nu\nu} & E_{\lambda\nu} \\ E_{M\lambda} & E_{W\lambda} & E_{G\lambda} & E_{T\lambda} & E_{\nu\lambda} & E_{\lambda\lambda} \end{bmatrix} = \begin{bmatrix} \frac{\partial F_M}{\partial x_M} & \frac{\partial F_M}{\partial p_w} & \frac{\partial F_M}{\partial p_g} & \frac{\partial F_M}{\partial T} & \frac{\partial F_M}{\partial \nu} & \frac{\partial F_M}{\partial \lambda} \\ \frac{\partial F_W}{\partial x_M} & \frac{\partial F_W}{\partial p_w} & \frac{\partial F_W}{\partial p_g} & \frac{\partial F_W}{\partial T} & \frac{\partial F_W}{\partial \nu} & \frac{\partial F_W}{\partial \lambda} \\ \frac{\partial F_G}{\partial x_M} & \frac{\partial F_G}{\partial p_w} & \frac{\partial F_G}{\partial p_g} & \frac{\partial F_G}{\partial T} & \frac{\partial F_G}{\partial \nu} & \frac{\partial F_G}{\partial \lambda} \\ \frac{\partial F_T}{\partial x_M} & \frac{\partial F_T}{\partial p_w} & \frac{\partial F_T}{\partial p_g} & \frac{\partial F_T}{\partial T} & \frac{\partial F_T}{\partial \nu} & \frac{\partial F_T}{\partial \lambda} \\ \frac{\partial F_\nu}{\partial x_M} & \frac{\partial F_\nu}{\partial p_w} & \frac{\partial F_\nu}{\partial p_g} & \frac{\partial F_\nu}{\partial T} & \frac{\partial F_\nu}{\partial \nu} & \frac{\partial F_\nu}{\partial \lambda} \\ \frac{\partial F_\lambda}{\partial x_M} & \frac{\partial F_\lambda}{\partial p_w} & \frac{\partial F_\lambda}{\partial p_g} & \frac{\partial F_\lambda}{\partial T} & \frac{\partial F_\lambda}{\partial \nu} & \frac{\partial F_\lambda}{\partial \lambda} \end{bmatrix} \tag{D–93}$$

In this matrix, the non-diagonal components are related to the couplings between the degrees of freedom. The sub-matrices K_{MW} and K_{MG}, which integrate the influence of the mechanics on water and air can be analytically defined.

For K_{MW} it reads:

$$
\begin{aligned}
K_{MW} = \sum_{IP} \Bigg[& \left(\mathcal{N}^{(n)} d\dot{M}_w \frac{\partial \mathcal{N}^{(k)}}{\partial x_1} u_1 - \left(\frac{\partial \mathcal{N}^{(n)}}{\partial x_1} df_{w,x} + \frac{\partial \mathcal{N}^{(n)}}{\partial x_2} df_{w,y} \right) \frac{\partial \mathcal{N}^{(k)}}{\partial x_1} u_1 \right. \\
& \left. - \left(\frac{\partial \mathcal{N}^{(n)}}{\partial x_1} df_{w,x} + \frac{\partial \mathcal{N}^{(n)}}{\partial x_2} df_{w,y} \right) \frac{\partial \mathcal{N}^{(k)}}{\partial x_2} u_1 \right) det\,(J_{ij})\, W_G \Bigg] \\
+ \sum_{IP} \Bigg[& \left(\mathcal{N}^{(n)} d\dot{M}_w \frac{\partial \mathcal{N}^{(k)}}{\partial x_2} u_2 - \left(\frac{\partial \mathcal{N}^{(n)}}{\partial x_1} df_{w,x} + \frac{\partial \mathcal{N}^{(n)}}{\partial x_2} df_{w,y} \right) \frac{\partial \mathcal{N}^{(k)}}{\partial x_1} u_2 \right. \\
& \left. - \left(\frac{\partial \mathcal{N}^{(n)}}{\partial x_1} df_{w,x} + \frac{\partial \mathcal{N}^{(n)}}{\partial x_2} df_{w,y} \right) \frac{\partial \mathcal{N}^{(k)}}{\partial x_2} u_2 \right) det\,(J_{ij})\, W_G \Bigg] \\
= \sum_{IP} \Bigg[& \left(\mathtt{CMW1}\, \mathcal{N}^{(n)} \frac{\partial \mathcal{N}^{(k)}}{\partial x_1} u_1 \right. \\
& - \left(\mathtt{CMW2} \frac{\partial \mathcal{N}^{(n)}}{\partial x_1} + \mathtt{CMW6} \frac{\partial \mathcal{N}^{(n)}}{\partial x_2} \right) \frac{\partial \mathcal{N}^{(k)}}{\partial x_1} u_1 \\
& \left. - \left(\mathtt{CMW4} \frac{\partial \mathcal{N}^{(n)}}{\partial x_1} + \mathtt{CMW7} \frac{\partial \mathcal{N}^{(n)}}{\partial x_2} \right) \frac{\partial \mathcal{N}^{(k)}}{\partial x_2} u_1 \right) det\,(J_{ij})\, W_G \Bigg] \\
+ \sum_{IP} \Bigg[& \left(\mathtt{CMW1}\, \mathcal{N}^{(n)} \frac{\partial \mathcal{N}^{(k)}}{\partial x_2} u_2 \right. \\
& - \left(\mathtt{CMW8} \frac{\partial \mathcal{N}^{(n)}}{\partial x_1} + \mathtt{CMW9} \frac{\partial \mathcal{N}^{(n)}}{\partial x_2} \right) \frac{\partial \mathcal{N}^{(k)}}{\partial x_1} u_2 \\
& \left. - \left(\mathtt{CMW5} \frac{\partial \mathcal{N}^{(n)}}{\partial x_1} + \mathtt{CMW3} \frac{\partial \mathcal{N}^{(n)}}{\partial x_2} \right) \frac{\partial \mathcal{N}^{(k)}}{\partial x_2} u_2 \right) det\,(J_{ij})\, W_G \Bigg]
\end{aligned}
\tag{D–94}
$$

where the notation of each component of the sub-matrix K_{MW} is referenced as follows:

$$
\begin{Bmatrix} \frac{\partial f_{w,x}}{\partial u_i} \\ \frac{\partial f_{w,y}}{\partial u_i} \\ \frac{\partial \dot{S}_w}{\partial u_i} \end{Bmatrix} = \left[\begin{array}{c|c|c|c} \mathtt{CMW2} & \mathtt{CMW4} & \mathtt{CMW8} & \mathtt{CMW5} \\ \hline \mathtt{CMW6} & \mathtt{CMW7} & \mathtt{CMW9} & \mathtt{CMW3} \\ \hline \mathtt{CMW1} & 0 & 0 & \mathtt{CMW1} \end{array} \right] \begin{Bmatrix} \frac{\partial u_1}{\partial x_1} \\ \frac{\partial u_1}{\partial x_2} \\ \frac{\partial u_2}{\partial x_1} \\ \frac{\partial u_2}{\partial x_2} \end{Bmatrix} \tag{D–95}
$$

For K_{MG}, it gives:

$$
\begin{aligned}
K_{MG} = \sum_{IP} \Bigg[& \left(\mathcal{N}^{(n)} d\dot{M}_a \frac{\partial \mathcal{N}^{(k)}}{\partial x_1} u_1 - \left(\frac{\partial \mathcal{N}^{(n)}}{\partial x_1} df_{a,x} + \frac{\partial \mathcal{N}^{(n)}}{\partial x_2} df_{a,y} \right) \frac{\partial \mathcal{N}^{(k)}}{\partial x_1} u_1 \right. \\
& \left. - \left(\frac{\partial \mathcal{N}^{(n)}}{\partial x_1} df_{a,x} + \frac{\partial \mathcal{N}^{(n)}}{\partial x_2} df_{a,y} \right) \frac{\partial \mathcal{N}^{(k)}}{\partial x_2} u_1 \right) det\left(J_{ij}\right) W_G \Bigg] \\
+ \sum_{IP} \Bigg[& \left(\mathcal{N}^{(n)} d\dot{M}_a \frac{\partial \mathcal{N}^{(k)}}{\partial x_2} u_2 - \left(\frac{\partial \mathcal{N}^{(n)}}{\partial x_1} df_{a,x} + \frac{\partial \mathcal{N}^{(n)}}{\partial x_2} df_{a,y} \right) \frac{\partial \mathcal{N}^{(k)}}{\partial x_1} u_2 \right. \\
& \left. - \left(\frac{\partial \mathcal{N}^{(n)}}{\partial x_1} df_{a,x} + \frac{\partial \mathcal{N}^{(n)}}{\partial x_2} df_{a,y} \right) \frac{\partial \mathcal{N}^{(k)}}{\partial x_2} u_2 \right) det\left(J_{ij}\right) W_G \Bigg] \\
= \sum_{IP} \Bigg[& \left(\mathtt{CMA1} \mathcal{N}^{(n)} \frac{\partial \mathcal{N}^{(k)}}{\partial x_1} u_1 \right. \\
& - \left(\mathtt{CMA2} \frac{\partial \mathcal{N}^{(n)}}{\partial x_1} + \mathtt{CMA6} \frac{\partial \mathcal{N}^{(n)}}{\partial x_2} \right) \frac{\partial \mathcal{N}^{(k)}}{\partial x_1} u_1 \\
& \left. - \left(\mathtt{CMA3} \frac{\partial \mathcal{N}^{(n)}}{\partial x_1} + \mathtt{CMA5} \frac{\partial \mathcal{N}^{(n)}}{\partial x_2} \right) \frac{\partial \mathcal{N}^{(k)}}{\partial x_2} u_1 \right) det\left(J_{ij}\right) W_G \Bigg] \\
+ \sum_{IP} \Bigg[& \left(\mathtt{CMA1} \mathcal{N}^{(n)} \frac{\partial \mathcal{N}^{(k)}}{\partial x_2} u_2 \right. \\
& - \left(\mathtt{CMA8} \frac{\partial \mathcal{N}^{(n)}}{\partial x_1} + \mathtt{CMA9} \frac{\partial \mathcal{N}^{(n)}}{\partial x_2} \right) \frac{\partial \mathcal{N}^{(k)}}{\partial x_1} u_2 \\
& \left. - \left(\mathtt{CMA4} \frac{\partial \mathcal{N}^{(n)}}{\partial x_1} + \mathtt{CMA7} \frac{\partial \mathcal{N}^{(n)}}{\partial x_2} \right) \frac{\partial \mathcal{N}^{(k)}}{\partial x_2} u_2 \right) det\left(J_{ij}\right) W_G \Bigg]
\end{aligned}
\tag{D–96}
$$

where the notation of each component of the submatrix K_{MG} is referenced as follows:

$$
\begin{Bmatrix} \frac{\partial f_{a,x}}{\partial u_i} \\ \frac{\partial f_{a,y}}{\partial u_i} \\ \frac{\partial \dot{s}_a}{\partial u_i} \end{Bmatrix} = \left[\begin{array}{c|c|c|c} \mathtt{CMA2} & \mathtt{CMA3} & \mathtt{CMA8} & \mathtt{CMA4} \\ \hline \mathtt{CMA5} & \mathtt{CMA6} & \mathtt{CMA9} & \mathtt{CMA7} \\ \hline \mathtt{CMA1} & 0 & 0 & \mathtt{CMA1} \end{array} \right] \begin{Bmatrix} \frac{\partial u_1}{\partial x_1} \\ \frac{\partial u_1}{\partial x_2} \\ \frac{\partial u_2}{\partial x_1} \\ \frac{\partial u_2}{\partial x_2} \end{Bmatrix}
\tag{D–97}
$$

E Micro-scale hydraulic model

E.1 Hydraulic transmissivity functions

The constitutive Equations (IV–52)-(IV–55) used to describe the advective component of the multi-phase flow along a fracture and a tube embedded in the REV are respectively expressed as:

$$q_{\alpha_i} = -\frac{k_{r_\alpha}}{\mu_\alpha}\frac{1}{A}\kappa_{frac}\frac{\partial p_\alpha}{\partial x_i} = -\frac{k_{r_\alpha}}{\mu_\alpha}\frac{h_b^3}{12w}\frac{\partial p_\alpha}{\partial x_i} \tag{E–98}$$

$$q_{\alpha_i} = -\frac{k_{r_\alpha}}{\mu_\alpha}\frac{1}{A}\kappa_{tube}\frac{\partial p}{\partial x_i} = -\frac{k_{r_\alpha}}{\mu_\alpha}\pi\frac{D^4}{128w^2}\frac{\partial p}{\partial x_i} \tag{E–99}$$

where the parameters κ_{frac} and κ_{tube} represent the hydraulic conductivities of a fracture and a tube respectively. In order to obtain an analytical expression for this κ parameter, it is necessary to consider two specific channel flow models:

- **Fracture**: two closely-space parallel plates separated by an aperture h_b.
- **Tube**: A cylinder of diameter D_b.

The motion of compressible Newtonian fluids is described by the Navier-Stokes equations, which result from the application of the Reynolds transport theorem to the fluid density ρ and the momentum ρv_i. For the two defined geometries, the constitutive flow laws can be derived directly from Navier-Stokes equations, which allows to directly link the fluid velocity with the opening of the microscale constituent.

On the one hand, the conservation of mass reduces to conservation of volume if a constant density is considered and if there is no source or sink of mass:

$$\frac{\partial v_i}{\partial x_i} \tag{E–100}$$

On the other hand, the balance of the momentum integrates a source term that can be decomposed into the surface forces (normal and shear stresses) and the body forces, such as gravity. Considering Equation (E–100), the conservation of momentum gives the following formulation of the Navier-Stokes equations:

$$\rho\left(\frac{\partial v_i}{\partial t} + v_j\frac{\partial v_i}{\partial v_j}\right) = -\frac{\partial p}{\partial x_i} + \mu\frac{\partial^2 v_i}{\partial x_j^2} + f_i \tag{E–101}$$

where ρ is the fluid density, v_i are the components of the fluid velocity, t is the time, p is the pressure, μ is the dynamic viscosity and f_i is an external body force.

Fracture

Assuming that the flow between two parallel plates is a laminar flow $\left(v_j\frac{\partial v_i}{\partial x_j} = 0\right)$ under steady state conditions $\left(\frac{\partial v_i}{\partial t} = 0\right)$ as illustrated in Figure E–2a, the momentum Equation (E–101) reduces to Equation (E–102) when no body force is considered:

$$\frac{\partial^2 v_i}{\partial x_j^2} = \frac{1}{\mu}\frac{\partial p}{\partial x_i} \tag{E–102}$$

The following non-slip boundary conditions are considered at the walls:

$$v\left(x_2 = \pm\frac{h}{2}\right) = 0 \tag{E–103}$$

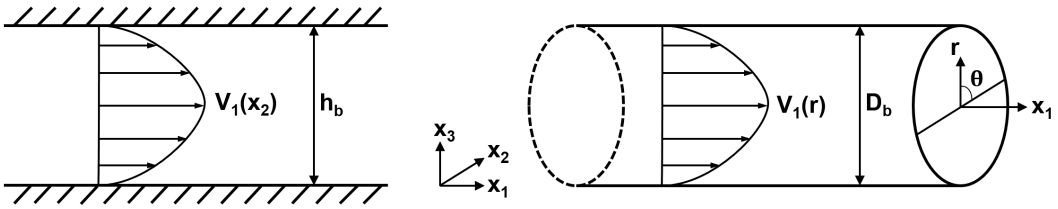

(a) (b)

Figure E–2 – Laminar fluid flow profiles (a) between two parallel plates and (b) in a circular pipe.

Moreover, the flow is only carried by the x_1 component $\left(\frac{\partial p}{\partial x_2} = 0\right)$, which leads to the following parabolic profile where the maximum velocity is reached in the middle of the channel:

$$v_1(x_2) = \frac{1}{2\mu}\left(\left(\frac{h_b}{2}\right)^2 - x_2^2\right)\frac{\mathrm{d}p}{\mathrm{d}x_1} \tag{E–104}$$

Then, averaging the velocity over the thickness h of the channel leads to:

$$\begin{aligned} q = \langle v_1 \rangle &= -\frac{1}{h_b}\int_{-\frac{h_b}{2}}^{\frac{h_b}{2}} v_1(x_2)dx_2 \\ &= -\frac{1}{h_b}\int_{-\frac{h_b}{2}}^{\frac{h_b}{2}} \frac{1}{2\mu}\left(\left(\frac{h_b}{2}\right)^2 - x_2^2\right)\frac{\mathrm{d}p}{\mathrm{d}x_1} \\ &= -\frac{h_b^2}{12}\cdot\frac{1}{\mu}\frac{\mathrm{d}p}{\mathrm{d}x_1} \end{aligned} \tag{E–105}$$

Using the distance s along the channel to generalize the example, this channel flow Equation (E–105) can be written:

$$q = -\frac{h_b^2}{12}\cdot\frac{1}{\mu}\frac{\mathrm{d}p}{\mathrm{d}s} \tag{E–106}$$

which is function of the fracture aperture h_b, and is equivalent to the Darcy's equation with a permeability equal to $k = \frac{h_b^2}{12}$ [Darcy, 1856].

Finally, projecting the flow obtained in Equation (E–105) over the REV of section $A = (w + h_b)^2 \simeq w^2$ assuming $w \gg h_b$, and considering a section of the fracture $A_{frac} = w \cdot h_b$, the following expression is obtained:

$$\begin{aligned} q &= -\frac{A_{frac}}{A}\frac{h_b^2}{12}\cdot\frac{1}{\mu}\frac{\mathrm{d}p}{\mathrm{d}x_1} \\ &= -\frac{1}{\mu}\frac{h_b^3}{12w}\frac{\partial p}{\partial x_i} \end{aligned} \tag{E–107}$$

which is similar to Equation (E–98) in saturated conditions, and allows to validate the parameter κ_{frac} by identification.

Tube

For case of flow in a circular pipe of radius r, the geometry is characterised by an axial symmetry as illustrated in Figure E–2b, which gives the following Navier-Stokes equations assuming a laminar flow under steady state conditions:

$$\begin{cases} -\frac{\partial p}{\partial x_1} + \mu\left[\frac{1}{r}\frac{\partial}{\partial r}\left(r\frac{\partial v_1}{\partial r}\right)\right] = 0 \\ -\frac{1}{r}\frac{\partial p}{\partial \theta} = 0 \\ -\frac{\partial p}{\partial r} = 0 \end{cases} \tag{E–108}$$

The following non-slip boundary conditions are considered at the walls:

$$v_1(r=0) \neq \infty \qquad \text{(E–109)} \qquad\qquad v_1(r=R) = 0 \qquad \text{(E–110)}$$

Moreover, for a flow carried by the x_1 component, the following parabolic profile is obtained where the maximum velocity is reached in the middle of the channel:

$$v_1(r) = \frac{1}{4\mu}\frac{\mathrm{d}p}{\mathrm{d}x_1}\left(r^2 - R^2\right) \tag{E–111}$$

Then, averaging the velocity over the section A_{tube} of the pipe related to the section of the REV A leads to:

$$\begin{aligned} q = \langle v_1 \rangle &= -\frac{1}{A}\int_0^R 2\pi r\, v_1(r)\, dr \\ &= -\frac{1}{A}\int_0^R \frac{1}{4\mu}\frac{\mathrm{d}p}{\mathrm{d}x_1}\left(r^2 - R^2\right) 2\pi r\, dr \\ &= -\frac{1}{A}\frac{\pi}{8\mu}\frac{\partial p}{\partial x_1}R^4 \end{aligned} \tag{E–112}$$

Finally, considering a REV of section $A = (w + h_b)^2 \simeq w^2$ and assuming that $R = D/2$, the following expression is obtained:

$$q = -\frac{\pi}{\mu}\frac{D^4}{128w^2}\frac{\partial p}{\partial x_1} \tag{E–113}$$

which is similar to Equation (E–99) in saturated conditions, and allows to validate the parameter κ_{tube} by identification.

E.2 Relative permeability functions

Supposing that a wetting phase (water) and a non-wetting phase (gas), are simultaneously flowing in the microstructure, the space occupied by one phase is logically not available for the flow of the other phase. As a consequence, the relative permeability is introduced in Equations (IV–52)-(IV–55) as a measure of the reduction in permeability of a given phase that occurs between partially and fully saturated conditions.

Assuming simple flow structures such as a planar interface for the fractures (Figure E–3a, [Fourar and Lenormand, 1998]) and a single circular cylinder for the tubes of the pore space (Figure E–3b, [Yuster, 1951]), it is possible to derive a model which takes into account the interference between the two phases through viscous considerations. In this co-axial two-phase flow, water is the wetting fluid in contact with the walls and the gas is the non-wetting fluid that flows in between.

Fracture

From the definition of the problem in Figure E–3a, it can be stated that the shear force on the two phases is similar at the interface given that the velocity of each phase is the same at the interface:

$$L \cdot w \cdot \mu_w \left(\frac{\mathrm{d}v_1}{\mathrm{d}x_2}\right)_w = L \cdot w \cdot \mu_g \left(\frac{\mathrm{d}v_1}{\mathrm{d}x_2}\right)_g \Longrightarrow \mu_w \left(\frac{\mathrm{d}v_1}{\mathrm{d}x_2}\right)_w = \mu_g \left(\frac{\mathrm{d}v_1}{\mathrm{d}x_2}\right)_g \tag{E–114}$$

where the area $L \cdot w$ vanishes out.

Then, deriving Navier-Stokes' Equation at the interface $\left(x_2 = \frac{h_g}{2}\right)$ in each stratum, from the form given in Equation (E–102), leads to:

$$\left(\frac{\mathrm{d}v_1}{\mathrm{d}x_2}\right)_w = \frac{h_g}{2\mu_w}\frac{\mathrm{d}p}{\mathrm{d}x_1} + C_w \qquad \text{(E–115)}$$

$$\left(\frac{\mathrm{d}v_1}{\mathrm{d}x_2}\right)_g = \frac{h_g}{2\mu_g}\frac{\mathrm{d}p}{\mathrm{d}x_1} + C_g \qquad \text{(E–116)}$$

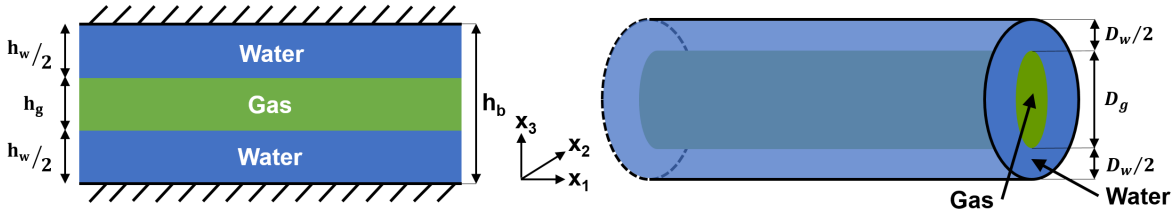

(a) (b)

Figure E–3 – Gas flow in between of water flows (a) in a fracture space and (b) in a circular pipe.

Due to the symmetry, the derivative of the velocity equals zero in the centre of the fracture $(x_2 = 0)$, which means that $C_g = 0$. Moreover, to satisfy Equation (E–114), it follows that:

$$\mu_w \cdot C_w = \mu_g \cdot C_g \qquad \text{(E–117)}$$

And it follows that $C_w = 0$.

Therefore, the generalise expression for the velocity gradient perpendicular to the direction of flow in a fracture reads:

$$\frac{\mathrm{d}v_1}{\mathrm{d}x_2} = \frac{x_2}{\mu}\frac{\mathrm{d}p}{\mathrm{d}x_1} \qquad \text{(E–118)}$$

Integrating this previous expression to give the velocity distribution perpendicular to the direction of flow leads to:

$$v_1 = \frac{x_2^2}{2\mu}\frac{\mathrm{d}p}{\mathrm{d}x_1} + \mathcal{Z} \qquad \text{(E–119)}$$

Applying this to the water phase, when $x_2 = \frac{h_b}{2}$, then $v_1 = 0$, and Equation (E–104) is obtained:

$$v_{1w} = \frac{1}{2\mu_w}\left(\left(\frac{h_b}{2}\right)^2 - x_2^2\right)\frac{\mathrm{d}p_w}{\mathrm{d}x_1} \qquad \text{(E–120)}$$

Thence, the velocity at the interface is:

$$v_{1i} = \frac{1}{2\mu_w}\left(\left(\frac{h_b}{2}\right)^2 - \left(\frac{h_g}{2}\right)^2\right)\frac{\mathrm{d}p}{\mathrm{d}x_1} \qquad \text{(E–121)}$$

The expression for the velocity distribution in the gas phase is:

$$v_{1g} = \frac{x_2^2}{2\mu_g}\frac{\mathrm{d}p_g}{\mathrm{d}x_1} + \mathcal{Z}_g \qquad \text{(E–122)}$$

And at the interface:

$$v_{1i} = \frac{1}{2\mu_g}\left(\frac{h_g}{2}\right)^2\frac{\mathrm{d}p}{\mathrm{d}x_1} + \mathcal{Z}_g \qquad \text{(E–123)}$$

Since the velocity of the two phases at the interface has been assumed to be the same, the Equations (E–121)-(E–123) may be equated and solved to find $\mathcal{Z}_g$. This expression for $\mathcal{Z}_g$ can be substituted in Equation (E–122) to obtain the velocity profile in the gas phase:

$$v_{1g} = \frac{-1}{2}\left[\frac{1}{\mu_w}\left(\left(\frac{h_b}{2}\right)^2 - \left(\frac{h_g}{2}\right)^2\right) + \frac{1}{\mu_g}\left(\left(\frac{h_g}{2}\right)^2 - x_2^2\right)\right]\frac{\mathrm{d}p_g}{\mathrm{d}x_1} \qquad \text{(E–124)}$$

Equations (E–120) and (E–124) give the velocity profile in the water and gas phases respectively. In order to derive the relative permeabilities, it is necessary to calculate the average velocity of each phase over the aperture.

For the liquid phase, it reads:

$$\begin{aligned} q_{1L} &= \frac{2}{h_b}\int_{\frac{h_b}{2}}^{\frac{h_b}{2}} \nu_{1w} \mathrm{d}x_2 \\ &= -\frac{h_b^2}{12}\left(1-\frac{3}{2}\frac{h_g}{h_b}+\frac{1}{3}\left(\frac{h_g}{h_b}\right)^3\right)\frac{1}{\mu_w}\frac{\mathrm{d}p_w}{\mathrm{d}x_1} \end{aligned} \tag{E–125}$$

Knowing that $\frac{h_g}{h_b} = \frac{h_b - h_w}{h_b} = 1 - S_r$, it follows that:

$$q_{lL} = -\frac{h_b^2}{12}\left(\frac{S_r^2}{2}(3-S_r)\right)\frac{1}{\mu_w}\frac{\mathrm{d}p_w}{\mathrm{d}x_1} \tag{E–126}$$

And for the gas phase, it reads:

$$\begin{aligned} q_{gL} &= \frac{2}{h_b}\int_{0}^{\frac{h_b}{2}} \nu_{1g} \mathrm{d}x_2 \\ &= -\frac{h_b^2}{12}\left(\frac{\mu_g}{\mu_w}\frac{3}{2}\left(\frac{h_g}{h_b}\right)\left(1-\frac{h_g}{h_b}\right)^2+\left(\frac{h_g}{h_b}\right)^3\right)\frac{1}{\mu_g}\frac{\mathrm{d}p_g}{\mathrm{d}x_1} \\ &= -\frac{h_b^2}{12}\left(\frac{3}{2}\mu_r S_r(1-S_r)(2-S_r)^2+(1-S_r)^3\right)\frac{1}{\mu_g}\frac{\mathrm{d}p_g}{\mathrm{d}x_1} \end{aligned} \tag{E–127}$$

where $\mu_r = \frac{\mu_g}{\mu_w}$ is the viscosity ratio.

And so, the following longitudinal flows are obtained for both phases respectively:

$$q_{lL} = -k_{r_w}\frac{h_b^2}{12}\frac{1}{\mu_w}\frac{\partial p_w}{\partial x_1} \tag{E–128}$$

$$q_{gL} = -k_{r_g}\frac{h_b^2}{12}\frac{1}{\mu_g}\frac{\partial p_g}{\partial x_1} \tag{E–129}$$

which gives the following relative permeabilities by identification:

$$k_{r_w} = \frac{S_r^2}{2}(3-S_r) \tag{E–130}$$

$$k_{r_g} = (1-S_r)^3 + \frac{3}{2}\mu_r S_r(1-S_r)(2-S_r) \tag{E–131}$$

Tube

From the definition of the problem in Figure E–3b, it can be stated that the shear force on the two phases is similar at the interface given that the velocity of each phase is the same at the interface:

$$2\pi r L\cdot\mu_w\left(\frac{\mathrm{d}\nu_1}{\mathrm{d}r}\right)_w = 2\pi r L\cdot\mu_g\left(\frac{\mathrm{d}\nu_1}{\mathrm{d}r}\right)_g \Longrightarrow \mu_w\left(\frac{\mathrm{d}\nu_1}{\mathrm{d}r}\right)_w = \mu_g\left(\frac{\mathrm{d}\nu_1}{\mathrm{d}r}\right)_g \tag{E–132}$$

where r is the radius of a cylindrical lamina, ν_1 is its linear velocity, μ_α is the viscosity of the fluid α the area $2\pi rL$ vanishes out.

Then, deriving Navier-Stokes' Equation at the interface $(r = 0)$ in each stratum, from the form given in Equation (E–111), leads to:

$$r\left(\frac{\mathrm{d}\nu_1}{\mathrm{d}r}\right)_w = \frac{1}{\mu_w}\frac{\mathrm{d}p}{\mathrm{d}x_1}\frac{r^2}{2} + C_w \qquad \text{(E–133)} \qquad\qquad r\left(\frac{\mathrm{d}\nu_1}{\mathrm{d}r}\right)_g = \frac{1}{\mu_g}\frac{\mathrm{d}p}{\mathrm{d}x_1}\frac{r^2}{2} + C_g \qquad \text{(E–134)}$$

Due to the symmetry, the derivative of the velocity equals zero in the centre of the fracture $(r = 0)$, which means that $C_g = 0$. Moreover, to satisfy Equation (E–132), it follows that:

$$\mu_w \cdot C_w = \mu_g \cdot C_g \qquad \text{(E–135)}$$

And it follows that $C_w = 0$.

Therefore, the generalise expression for the velocity gradient perpendicular to the direction of flow in a circular capillary reads:

$$\frac{\mathrm{d}\nu_1}{\mathrm{d}r} = \frac{1}{2\mu}\frac{\mathrm{d}p}{\mathrm{d}x_1}r \qquad \text{(E–136)}$$

Integrating this previous expression to give the velocity distribution perpendicular to the direction of flow leads to:

$$\nu_1 = \frac{1}{4\mu}\frac{\mathrm{d}p}{\mathrm{d}x_1}r^2 + \mathcal{Z} \qquad \text{(E–137)}$$

Applying this to the water phase, when $r = R$, then $\nu_1 = 0$, and Equation (E–111) is obtained:

$$v_{1w} = \frac{1}{4\mu_w}\frac{\mathrm{d}p_w}{\mathrm{d}x_1}\left(R^2 - r^2\right) \qquad \text{(E–138)}$$

Thence, the velocity at the interface where $r = r_i$ is:

$$v_{1i} = \frac{1}{4\mu_w}\frac{\mathrm{d}p}{\mathrm{d}x_1}\left(R^2 - r_i^2\right) \qquad \text{(E–139)}$$

The expression for the velocity distribution in the gas phase is:

$$v_{1g} = \frac{r^2}{4\mu_g}\frac{\mathrm{d}p_g}{\mathrm{d}x_1} + \mathcal{Z}_g \qquad \text{(E–140)}$$

And at the interface $r = r_i$:

$$v_{1i} = \frac{r_i^2}{4\mu_g}\frac{\mathrm{d}p}{\mathrm{d}x_1} + \mathcal{Z}_g \qquad \text{(E–141)}$$

Since the velocity of the two phases at the interface has been assumed to be the same, the Equations (E–139)-(E–141) may be equated and solved to find $\mathcal{Z}_g$. This expression for $\mathcal{Z}_g$ can be substituted in Equation (E–140) to obtain the velocity profile in the gas phase:

$$v_{1g} = \frac{1}{4}\left[\frac{R^2 - r_i^2}{\mu_w} + \frac{r_i^2 - r^2}{\mu_g}\right]\frac{\mathrm{d}p_g}{\mathrm{d}x_1} \qquad \text{(E–142)}$$

Equations (E–138) and (E–142) give the velocity profile in the water and gas phases respectively. In order to obtain the volume rate of the two phase, it is necessary to integrate the velocities over the proper range of radii.

The generalised equation is:

$$q = \int_{r_1}^{r_2} 2\pi r \nu_1 dr \qquad \text{(E–143)}$$

For the water phase, it reads:

$$\begin{aligned} q_{1L} &= \int_{r_1}^{R} \frac{2\pi r}{4\mu_w}\left(R^2 - r^2\right)\frac{\mathrm{d}p_g}{\mathrm{d}x_1}\mathrm{d}r \\ &= \frac{\pi}{8\mu_w}\left(R^4 - 2R^2 r_i^2 - r_i^4\right)\frac{\mathrm{d}p_w}{\mathrm{d}x_1} \\ &= \frac{\pi}{8\mu_w}\left(R^2 - r_i^2\right)^2\frac{\mathrm{d}p_w}{\mathrm{d}x_1} \end{aligned} \qquad \text{(E–144)}$$

Knowing that $\pi R^2 - \pi r_i^2$ is the area of the capillary through which water is flowing, then the water saturation in the system being considered would be:

$$S_w = \frac{\pi\left(R^2 - r_i^2\right)L}{\pi R^2 L} = \frac{R^2 - r_i^2}{R^2} \tag{E–145}$$

The relative permeability of a porous medium to a given phase is equal to the ratio of the flow rate of that phase in multiphase flow to the flow rate when it is the only phase present with the pressure gradient the same in both cases. On this basis, it is possible to calculate the relative permeability to the water phase as follows:

$$k_{r_w} = \frac{q_{lL}}{q} = \frac{\frac{\pi}{8\mu_w}\left(R^2 - r_i^2\right)^2 \frac{\mathrm{d}p_w}{\mathrm{d}x_1}}{\frac{\pi}{8\mu_w} R^4 \frac{\mathrm{d}p_w}{\mathrm{d}x_1}} = \left(\frac{R^2 - r_i^2}{R^2}\right)^2 \tag{E–146}$$

Substituting Equation (E–145) in this latter expression finally gives:

$$k_{r_w} = S_r^2 \tag{E–147}$$

which states that the relative permeability to water (the wetting phase) is dependent upon saturation only.

Making a proper substitution for the velocity of a lamina in the gas phase into Equation (E–143) and integrating between the proper limits should give the rate of gas flow:

$$\begin{aligned} q_{gL} &= \int_0^{r_i} \frac{2\pi r}{4}\left[\frac{\left(R^2 - r_i^2\right)}{\mu_w} + \frac{\left(r_i^2 - r^2\right)}{\mu_g}\right]\frac{\mathrm{d}p_g}{\mathrm{d}x_1}\mathrm{d}r \\ &= \frac{\pi}{8\mu_g L}\left[2(R^2 r_i^2 - r_i^4)\frac{\mu_g}{\mu_w} + r_i^4\right] \end{aligned} \tag{E–148}$$

Dividing this equation through by the equation for single phase flow of gas as was done in the case of water in order to obtain the relative permeability gives:

$$k_{r_g} = 2\left(\frac{r_i^2}{R^2} - \frac{r_i^4}{R^4}\right)\frac{\mu_g}{\mu_w} + \frac{r_i^4}{R^4} \tag{E–149}$$

The gas saturation in the capillary is thus expressed as:

$$S_{r_g} = \frac{\pi}{\pi}\frac{r_i^2}{R^2}\frac{L}{L} = \frac{r_i^2}{R^2} \tag{E–150}$$

Substituting this expression in Equation (E–149) finally gives:

$$\begin{aligned} k_{r_g} &= 2S_{r_g}(1 - S_{r_g})\frac{\mu_g}{\mu_w} + S_{r_g}^2 \\ &= 2\left(1 - S_{r_w}\right)S_{r_w}\frac{\mu_g}{\mu_w} + \left(1 - S_{r_w}\right)^2 \end{aligned} \tag{E–151}$$

It is worth noted that for gas and water two-phase flows, the terms encompassing the viscosity ratio $\mu_r = \frac{\mu_g}{\mu_w}$ are largely lower than the others and can be neglected.

F Geometric description of the MEGAS E5 injection piezometer

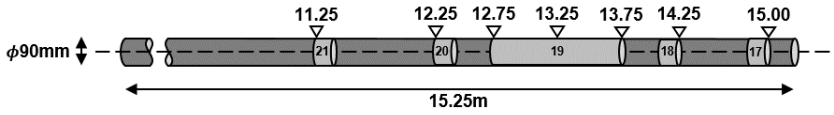

Figure F.4 – Design of the piezometer A.

Table F.1 – Parameters of the piezometer A, *after* [Volckaert et al., 1995].

Filter No.		A-17	A-18	A-19	A-20	A-21
Filter length	[cm]	9	9	100	9	9
Filter external diameter	[cm]	8.9	8.9	8.9	8.9	8.9
Filter internal diameter	[cm]	7.9	7.9	7.9	7.9	7.9
Filter porosity	[-]	0.3	0.3	0.3	0.3	0.3
Chamber internal diameter	[cm]	7.7	7.7	7.7	7.7	7.7
Micro-tube internal diameter	[cm]	0.2	0.2	0.2	0.2	0.2
Micro-tube length inside casing	[m]	15.7	14.95	13.95	12.95	11.95
Micro-tube in the gallery	[m]	1.35	1.35	1.35	1.35	1.35
Filter volume	[ml]	35.63	35.63	395.84	35.63	35.63
Chamber volume	[ml]	22.05	22.05	245.04	22.05	22.05
Micro-tube volume	[ml]	53.56	51.21	48.07	44.92	41.78
Total dead volume	[ml]	164.81	160.10	737.02	147.53	141.25